AIX-MARSEILLE UNIVERSITÉ

Faculté des Sciences

ECOLE DOCTORALE PHYSIQUE ET SCIENCES DE LA MATIERE ED352

LABORATOIRE D'ASTROPHYSIQUE DE MARSEILLE (LAM)

Thèse présentée pour obtenir le grade universitaire de docteur

Discipline: Sciences de l'Univers

Spécialité: Astrophysique et Cosmologie

Darko Donevski

Titre de la thèse: Identification et modelisation des galaxies distantes dans les relevés cosmologiques du satellite Herschel

Soutenue le 21/09/2018 devant le jury composé de:

Simona Mei	Université Paris-Diderot VII	Rapporteure
Stephen Serjeant	The Open University, UK	Rapporteur
Veronique Buat	LAM, Aix-Marseille Université	Directrice de thèse
Frederic Boone	IRAP, Toulouse	Codirecteur de thèse
Guilaine Lagache	LAM, Aix-Marseille Université	Examinateur
David Elbaz	CEA Paris-Saclay	Examinateur
Matthieu Bethermin	LAM, Aix-Marseille Université	Invité

Numéro national de thèse/suffixe local: 2017AIXM0001/001ED62

Résumé

Le but général de cette thèse est d'identifier et de caractériser des galaxies lointaines riches en poussières. Les travaux de ma thèse reposent essentiellement sur les données acquises par le satellite *Herschel* de l'Agence Spatiale Européenne, qui a pour la première fois détecté l'émission infrarouge de ce type de galaxies à de grandes distances correspondant à des décalages spectraux égaux ou supérieurs à 4.

La population de galaxies poussiéreuses ayant un fort taux de formation stellaire (Dusty Star Forming Galaxies, DSFGs) joue un rôle très important dans l'histoire de l'univers, avec des taux de formation d'étoiles allant de quelques centaines à quelques milliers de masses solaires par an. Les sondages infrarouges, comme ceux entrepris à l'aide du satellite Herschel, nous offrent l'opportunité de recenser de manière approfondie ces DSFGs jusqu'à de grands décalages spectraux.

Cependant, jusqu'à présent seul un petit nombre de DSFG détecté par Herschel ont été confirmés pour être à des décalages spectraux supérieurs à 4. Les modèles de formation et d'évolution des galaxies stipulent généralement que la population de DSFG à $z > 4$ sont les progéniteurs des galaxies elliptiques, observées dans les amas les plus massifs de l'univers local. L'abondance des DSFGs à $z > 4$ se révèle donc être décisive pour contraindre ces modèles ainsi que pour vérifier notre compréhension globale de l'univers lointain.

Le premier objectif de mon travail de recherche est d'identifier les candidates galaxies à $z > 4$ détectées sur des champs les plus larges possibles observés par Herschel et l'instrument SPIRE et d'examiner les propriétés statistiques de celles-ci. A cette fin, j'ai créé un nouvel algorithme de sélection dans le but d'augmenter substantiellement le nombre de candidates et de comprendre leur nature. Afin de surmonter le problème bien connu de confusion dû à la faible résolution spatiale des relevés IR et submillimétriques, j'ai introduit une méthode d'extraction de sources basée sur des connaissances à priori liée à la modélisation de distributions spectrales. J'ai appliqué cette

méthode aux champs du relevé à HeViCS (Herschel Virgo Cluster Survey), ce champ étant privilégié car il allie une grande surface et une bonne profondeur. J'ai défini des critères basés sur le modèle du corps noir, afin d'établir un recensement des DSFG possédant des couleurs dites rouges dans les bandes de l'instrument SPIRE, ces objets sont connus sous le nom de "500μm-risers". J'ai ainsi sélectionné 133 "500μm-risers au dessus du flux limite $S_{250} = 13$ mJy, ce qui constitue l'échantillon de DSFG rouges le plus profond jamais construit. Cet échantillon devrait permettre de dévoiler les progéniteurs des galaxies massives passives à $z \sim 2 - 3$.

Afin d'interpréter les statistiques de mes candidats 500μm-risers avec des modèles, j'ai étudié les différents biais influençant leur sélection. A cette fon, j'ai utilisé des simulations les plus récentes basées sur différents modèles phénoménologiques de galaxies. Le regroupement physique des galaxies est pris en compte dans ces simulations par une technique d'appariement d'abondance pour peupler les halos de matière noire d'un cône de lumière. J'ai démontré qu'une combinaison complexe du bruit, du regroupement de galaxies et de l'effet de lentille gravitaionnelle forte avait un très fort impact sur le nombre d'objets identifiés et sur la distribution en décalage spectral des 500μm-risers. Mes résultats montrent que la tension existante entre les modèles et les observations peut être au moins partiellement résolue par la prise en compte de ces biais.

A partir de la population des 500μm-risers j'ai estimé le flux SPIRE et la densité du taux de formation d'étoiles corrigée par l'effet de lentille gravitationnelle forte à des décalages spectraux z compris entre 4 et 5 et j'ai trouvé une valeur proche de la valeur totale précédemment mesurée en infrarouge. Cela indique que la sélection en couleur ne représente pas un effet limitatif à la recherche des galaxies poussiéreuses les plus massives à très grandes distances.

Etant donné que les DSFGs semblent évoluer dans les halos les plus massifs, leurs associations pourraient servir de balises pour des proto-amas en formation, comme celà a été démontré par une combinaison de données des satellites Planck et Herschel. La dernière partie de mon travail a visé à comprendre dans quelle mesure notre identification des DSFGs tracent les surdensités des façon efficace. Pour répondre à cette question, j'ai proposé une nouvelle méthode permettant de caractériser les propriétés physiques des DSFGs dans des candidats proto-amas préalablement sélectionnés par *Planck*. J'ai effectué une étude d'un cas identifié dans un de nos champs HeViCS. Je me suis appuyé sur des images profondes provenant du relevé NGVS au télescope Canada-France-Hawaii (Next generation Virgo Survey), combinées à des données infrarouges.

J'ai également utilisé le code d'ajustement spectral CIGALE pour déterminer les propriétés de ces galaxies et prédire l'émission de leurs poussières. J'ai ensuite réalisé des simulations basées sur des modèles panchromatiques de galaxies afin de comprendre au mieux les résultats des ajustements spectraux.

Abstract

The main goal of this Thesis is to detect and characterise very distant, dusty star-forming galaxies (DSFGs). The work presented in this Thesis is mainly based on data acquired by the European Space Agency's $Herschel$ Space Observatory, which for the first time imaged the infrared emission of this type of galaxy at great distances corresponding to redshifts $z \geq 4$.

Over the last few decades, great progress has been made in our understanding of the star formation history of the Universe. It has become apparent that observing at rest-frame UV and optical wavelengths is insufficient as a large fraction of the star formation is dust obscured. The $Herschel$ SPIRE photometer was often used to directly map large areas at wavelengths of 250 μm, 350 μm and 500 μm, covering in total more than 1000 square degrees. Thanks to the extensive observational studies carried out during the last two decades, we learn that DSFGs have a redshift peak at $z \sim 2$, matching the cosmic time where galaxies have formed most of their young, massive stars. However, it remains extremely challenging to use *Herschel* for identifying a tail extending towards much higher redshifts ($z > 4$). As a result, until recently only a small number of $Herschel$-selected DSFGs at $z > 4$ were known, most of them strongly gravitationally lensed.

The known population of massive DSFGs at $z > 4$ are amongst the most prodigious sources across the history of the Universe, with high star formation rates between a hundred to few thousands solar masses per year. The existing models of galaxy formation and evolution generally state that DSFGs at $z > 4$ are the progenitors of elliptical galaxies observed in the most massive clusters of the local Universe. Therefore, the abundance of DSFGs at $z > 4$ proves to be crucial to constrain these models as well as to check our general understanding of the star formation in distant Universe.

One of the main goals of this Thesis is to assemble candidate $z > 4$ galaxies detected in

a large area survey observed by *Herschel*-SPIRE and to examine the statistical properties and environments of these systems.

The key difficulty with observations at FIR wavelengths is the limited sensitivity and coarse angular resolution of *Herschel*. It has been known that blending of sources in FIR observations has a noticeable effect on the number counts derived from such observations. In order to partially overcome this problem, I introduce prior-based source extraction linked with the SED modelling. I applied this novel approach to the *Herschel* Virgo Cluster Survey field (HeViCS), the deepest contiguous 55 deg^2 field observed by *Herschel*. I define model-based selection function to make a census of DSFGs with fluxes rising from 250 μm to 500 μm, so-called "500 μm-risers" (Donevski, Buat, et al. 2018, $\mathrm{A\&A}, 614\mathrm{A}, 33\mathrm{D}$). I select 133 500 μm-risers down to $S_{250} = 13.2$ mJy, which is the faintest sample of $500\,\mu$m-risers selected to date (Chapter 2). The sample contains some of the most luminous DSFGs at $z > 4$, and it is expected to unveil progenitors of massive quiescent galaxies observed at $z \sim 2 - 3$.

I use different SED templates to test the systematics and accuracy of estimated infrared luminosities and redshifts. (Chapter 3). In this Thesis I provide a comprehensive analysis of biases that affect the selection of 500 μm-risers (Chapter 4). I put the observed statistics in the context of galaxy evolution using different phenomenological models. I construct mock catalogues based on these models and evaluate the number density of our 500 μm-risers. I also create end-to-end simulations based on adopted models. The physical clustering is included by using a sub-halo abundance matching technique to populate the dark-matter halos of a light cone with modelled galaxies. The analysis based on simulations show that complex combinations of noise, source clustering and galaxy-galaxy lensing have crucial impact on measured counts and redshift distribution of 500 μm-risers. Correcting for all these observational biases, I estimate star-formation rate density at $4 < z < 5$ with the 500 μm-risers and found it to be close to the total value measured in infrared. (Chapter 5).

Since high-z DSFGs appear to grow in the most massive dark matter halos, it has been recently pointed out that their associations (i.e. multiple dusty sources at the same redshift located within a small area on the sky) can serve as beacons of galaxy protoclusters in formation. An important question related to protoclusters is addressed in the last part of this Thesis: how can we characterise environments of high-redshift DSFGs ? (Chapter 6)

To answer on this question, I firstly investigate can 500 μm-risers be used as signposts

of overdensities at $z > 4$. I then focus my work on development of a new method which is intended to help the understanding of the dust emission and physical properties of galaxies in a high-z protocluster candidate PHZ282 initially identified by *Planck*. To resolve the cold peak observed with *Planck*, I aim to model infrared luminosities of optically detected sources from Next Generation Virgo Cluster Survey (NGVS). I combine SED fitting with dust SED modelling, and predict the infrared luminosities for more than a thousand of galaxies that comprise one *Planck* detection. I show that there exist potentially significant concentrations of physically associated DSFGs at $z > 2$ below the SPIRE detection limit.

The Thesis opens a number of interesting roads for further research, which are thoroughly discussed in Chapter 7.

Contents

List of Figures

List of Tables

Prologue

> I imagine that the two cities,
> especially when they're reduced for
> practical purposes to two points on a
> map, can represent the two objects,
> and the trajectory between them
> represents the emptiness between
> them. For a week and a half now,
> Paris and Marseille, without needing
> to look for more or less important
> circles on the route map, are only
> two abstract poles that allow us to
> describe the space between them,
> and perceive within it...
>
> Julio Cortazar and Carol Dunlop,
> *Autonauts of the Cosmoroute*

It has recently been discovered that long before Salvador Dali or Pablo Piccaso, in some of the oldest Spanish caves, the very first (but unknown) artists had decorated the cave's walls by making geometrical lines and patterns. The artists had made such an art by applying a red paint on the walls, moulding that paint around their hands, and making the long-lasting echoes of an ancient storytelling full of lines which, I presume, reflected a metamorphosis of their everyday's lives and dreams. The full identity of these ancient painters remained unknown and archaeologists have long assumed that a cave art was a process typical only for *Homo sapiens*. The other group of humans with large-brains, the *Neandertals* (Homo neanderthalensis.), had also lived in the time which is now associated to the dawn of a European cave art, but it has been thought that

only *Homo sapiens* reached the cognitive level sufficiently high for creating the pieces of a symbolic and abstract art[a].

In the time of writing this thesis, I have read an issue of *Scientific American*, and an article written by K. Wong, staying fascinated by the evidences that change our understanding of the history of humanity. Archaeologists reported that some of those images found in several Spanish caves (e.g. Cueva de los Aviones) are actually far older than the earliest known fossils of Homo sapiens in Europe, implying that they must have instead been created by Neandertals. The human-made ornaments are found to be at least 65 thousands of years old, much older than previously known early artistic designs discovered in Africa. The findings opened a new window into our understanding of Neandertals. The findings also raise some of key questions about the origin of storytelling and the use of symbolic art and mural-making, the categories that were always assumed "straightforwardly" for distinguishing the Homo sapiens and other humans. The storytelling as a combination of abstract descriptions, realisations of human dreams, complex interactions, painted figures, colours, interplays between the shadow and light, cave's warmth and coolness, in other word luminosities... It seems that archaeology and extragalactic astronomy have a plenty of similarities, and they both are trying to deal with the process known as "evolution".

The evolution is classically defined as *change in the heritable characteristics of biological populations over successive generations* and from this it is not difficult to understand that everything about nature is about evolution. So the Universe itself and all building elements contained in it. If we just replace the word "biological" with the word "galactic" in aforementioned definition of evolution, we will get the most general information about the topic contained in this thesis - how galaxies evolve over cosmic time. There is, however, a huge difference between investigating evolution of galaxies and evolution of humanity. What makes the difference is what we defined as the *problem of scales*.

In general, galaxy formation and evolution consist of two widely complex aspects : (i) physics and (ii) initial (+ boundary) cosmological conditions. Their combination is known to be the leading factor in shaping the evolution of galaxies. However, as in many other branches of science, we today witness the remarkable diversity that encompasses the formation and evolution of objects in space. The physical processes deeply involved in galaxy formation are known to cover more than 20 orders of magnitude in physical

[a]based on K.Wong, Scientific American, 23/02/2018, Ancient Cave Paintings Clinch the Case for Neandertal Symbolism. https://www.scientificamerican.com/article/ancient-cave-paintings-clinch-the-case-for-neandertal-symbolism1/

size, from the scale of the Universe itself down to the smaller scales typical of individual stars. Interestingly, galaxies do not have a clearly defined "life cycle" like stars do have. Spatial scales are just the tip of the iceberg - the much prominent difficulty comes with time scales. To illustrate how young is our investigation of those questions, let us go back to 1929, the year when Edwin Hubble created the first galaxy classification scheme known as the Hubble tuning-fork diagram. Hubble partitioned galaxies into different morphological types as ellipticals, normal or barred spirals (such as our own Milky Way), and irregulars. Nevertheless, the tuning fork diagram shows an evolution from simple to complex with no temporal associations intended. Galaxies evolve on very long time scales, typically more than hundreds of millions of years. This number significantly exceeds the typical lifetime of a human, which is still less than 100 years. Even the estimated total age of humanity (which is usually assumed to be $\sim$280 000 years) is way shorter than the evolutionary scale from the galaxy point of view, which can be confirmed by extensively re-observing the patch of the sky with different astronomical instruments in longer time intervals, e.g. of more than several decades. After some time, we will still consider that we are observing the same system, and although we could do nothing related to that fact, we can apply some of the most natural things related to the human imagination - a prediction.

Astronomers today agree that galaxies evolve. One such evolutionary picture is related to massive local elliptical galaxies, and it is believed that they are formed from disk galaxies, followed by spectacular intergalactic collisions know as galaxy mergers. However, we need the multiple lines of converging evidences to confirm some of those evolutionary pictures. The problem that "time-scale" set on our ability to explore the changes of galaxies through various cosmic epochs, implies that the only possible way we can constrain the evolution of galactic sources is by analysing whole populations of objects. Doing that, we cannot just feel a pleasure being spectators, but we can also take an advantage drawing the (evolutionary) links between these galaxies. In other words - creating our own storytelling. With the new generation of observing instruments, we can ,assign the $statistical$ approaches, observing the cosmos at various epochs and linking the galaxy populations of different ages.

Fifty three years ago, a group of Caltech physicists led by Gerry Neugebauer and Tom Soifer brought to the forefront of extragalactic science the infrared astronomy, the part of the electromagnetic spectrum that has been underexploited at that time. Despite the fact that William Herschel discovered thermal infrared radiation back in 1800, a

very little progress has been made in the field of infrared astronomy until Neugebauer and Soifer. They discovered ten objects that were only thermally visible, and just four years later, the list of these infrared objects had grown to thousands. Poetically saying, with the time we learnt the infrared astronomy holds the "seven keys" to our cosmic origins, revealing how planets, stars, cosmic elements, and even the earliest galaxies and subsequent clusters and small scale cluster progenitors had formed. That means, with the development of modern infrared space instrumentation, we can now reach and connect not just earliest objects seen in optical, but also the most distant places which beauty is hidden by dust - *the inner spots of space imagination*.

One of the greatest South American writers of all time, Julio Cortazar, once wrote that the best scientific explorations are those which "discover dusty, parallel highways, that perhaps only exist in the imagination of those who dream of it." It is then necessary - *first scientific calculations* - to make such exploration in small stages, because "if dusty, parallel highways exist, they do not just involve a different physical space, but also another time. We are then just intergalactic travellers that observe from afar the rapid ageing of those who remain subject to the laws we know... we take the path that leads through a little wood, fool of other travellers, confusion and collisions..."

In this Thesis I adopt most of these wise advices of Julio Cortazar. In fact, the Thesis is an effort of shedding new light on the evolution of "hidden dusty highways", a.k.a dusty galaxies in the Universe. Modern space-based infrared observatories showed that only a billion years after the Big Bang there were dusty galaxies that have frenetic star-forming activities barely seen by largest optical telescopes. These activity is just the enthusiastic response of the distant phenomenon, yet fully unexplored. The main goal of my "adventure" is to show how can we exploit large infrared extragalactic surveys in order to understand the statistical view of evolution of these remarkably distant and dusty objects.

Marseille, July 2018

CHAPTER 1

High-redshift dusty, star-forming galaxies: the context of galaxy evolution

One of the main goals of modern astronomy is to understand how the structure of the Universe evolved, that means how were the primordial density fluctuations converted into the structures (e.g. galaxies and galaxy clusters) we see in the present time. In other words, we question how the heterogeneous structures we see at the present, have been formed from the (not-fully) homogeneous beginning. The stars are the known building blocks of these structures, made of luminous groups of particles called baryons. On one hand, baryons as visible constituents of these structures represent only insignificant fraction of the total mass of the Universe (it accounts for the less than 1% of the total budget of the Universe). On the other hand, it is widely accepted that baryons trace the underlying dark matter distribution, and thus it is vital to develop the methods to reconstruct the process of the stellar mass build-up in galaxies and thus study the structure formations within the Universe. In this Chapter I give a brief overview

of the basic theoretical framework within which our current understanding of galaxy formation and evolution has been developed. I particularly emphasize the importance of studying dusty, star-forming galaxies.

1.1. Emergence of ΛCDM framework for galaxy evolution

The leading protagonists of this Thesis are galaxies far from our own Milky Way. Back in 1913, Vesto Slipher was the first who measured the redshift of extragalactic objects (Slipher 1913). Slipher noted that the (spectroscopic) faintness of extragalactic objects were the main reason for the lack of redshift measurements by that time. The object he targeted was the M31 or "Andromeda nebula" (today known as "Andromeda galaxy"). A decade after this pioneering work of Slipher, in 1925, Edwin Hubble used distances estimated from Cepheid variables to demonstrate that some sources are really extragalactic, individual galaxies, comparable with the size, shape and luminosity to our Milky Way (Hubble, E 1926). Despite the early work of Slipher, it is still widely (but wrongly) accepted that Hubble's discovery actually marked the beginning of extragalactic astronomy. Since then, a great progress has been made in observing distant, extragalactic sources. In fact, only four years after the discovery that galaxies are truly extragalactic objects, Hubble made his subsequent breakthrough achievement: he showed that the recession velocities of galaxies are falling in linear relation to their distances (Hubble 1929), allowing for the first time the observational evidence for expanding Universe. Hubble's discovery was obtained with use of 24 nearby galaxies for which both measured velocities and distances were available. Interestingly, most of the obtained velocities were from the pioneering spectroscopic observations by Slipher, although no reference is given in Hubble's paper.[a]. Hubble measured the galaxy distances with greater accuracy than what was achieved before him. He measured apparent brightnesses of the stars, but also did analysis for some more distant galaxies in the sample, where all four galaxies are located in the Virgo cluster (source: http://www.pnas.org/content/112/11/3173).

Because the all galaxies we know are now observed over cosmological lengths and different time scales, the description of their formation and evolution must involve cosmological context. The cosmology is needed for studying the properties of space-time

[a]It is thus important, from my point of view, that astronomical community recognise and reward with appropriate citations the pioneers who push the field forward.

on large scales, as stated in seminal works of Einstein, de-Sitter and Lemaitre (Lemaitre 1931, Einstein et al. 1932). Today we understand that the Universe consists not only of visible matter, but also of components of invisible matter and even invisible energy. (Spergel 2015, Ostriker et al. 1973). Current cosmological observations of the Universe support the Λ-cold dark matter model (ΛCDM, e.g. P. J. Peebles et al. 2003). The ΛCDM is the model of the Universe which is widely accepted as the standard paradigm since the beginning of the 1980s. The letter Λ represents the cosmological constant, which is associated to a dark energy component that is used to explain the contemporary detection of accelerating expansion of space which works against the attractive gravity force. The cold dark matter is postulated such that it accounts for these gravitational effects observed in very large-scales. The cold dark matter is not baryonic, which means that it does not contain protons, electrons and/or neutrons. From the latest cosmological measurements the main parameters of the model are found to be (Planck Collaboration, 2016): $\Omega_M = 0.307$, $\Omega_\Lambda = 0.693$, and $H_0 = 67.8$ km/s/Mpc for the Hubble constant. It means that baryonic matter, dark matter and dark energy contribute to the total mass-energy of the Universe this at 5 $\%$, 26$\%$ and 69$\%$, respectively. Also, according to the same measurements, the best estimate of the age of the Universe is 13.79 ± 0.38 billion years.

Structure formations

The main assumption of our current view of galaxy formation and evolution is that galaxies form within the dark matter (DM) halos. The DM halos are specifically defined as the regions of invisible (and thus "dark") matter whose average density is usually assumed to be around 200 times the critical density of the Universe (H. Mo et al. 2010). The dark matter is known to only interacts gravitationally and it is thus assumed to be "collisionless", even if it is not fully precise statement. Even the first evidences of the existence of dark matter date back to 1930's (Zwicky 1933), only recently the astronomical community started to understand the complex role of DM in galaxy evolution.[b] From the theoretical viewpoint, the structure formation is still surrounded by a lot of uncertain details. It is widely assumed that In the "cosmic dark ages" that appeared in the cosmic era following the Universe's recombination time (∼378 000 years after the

[b]For example, one of these evidences were inferred from the analysis of low amplitudes of cosmic microwave background (CMB) anisotropies. The low amplitude of the CMB anisotropies implies that the inhomogeneities must have been very small at the epoch of recombination.

Big Bang), the small initial fluctuations of the scalar field started to grow, giving the rise to the process of structure formation. Immediately after their formation, structures had started their evolution caused by the gravitational instabilities. Today's galaxy formation theory usually separates the structure formation into two different regimes: the linear growth governed by small fluctuations, and the non-linear regime with larger perturbations, leading to the emergence of non-linear objects (H. Mo et al. 2010, Spergel 2015). As a result, the fluctuations had created enormous areas controlled by gravitation. It is thus thought that the primordial baryon-photon fluid should trace the DM distribution. Following such an interplay, the gas fell into the gravitational potential wells of DM halos, leading to the increase of density which became massive enough to overcome the internal gas pressure. The whole system then collapsed, inducing the process known as nuclear fusion, which, after some time, released the energy as an output of the nuclear process, supporting the birth to the first stars in the Universe (Barkana et al. 2001). Today we know that the stars are just a very small part of large structures contained in visible Universe. The condensed matter is embedded in large web-like filaments and galaxy haloes, which are responsible for the formation of structures even larger than galaxies: galaxy groups, cluster progenitors, galaxy clusters and galaxy superclusters.The most accepted theory which describes the evolution of galaxies from the appearance of first baryons in the Universe to these largest structures is the *hierarchical structure-formation* model (Press et al. 1974). The hierarchical theory considers a so-called "bottom-up" formation scenario where the DM halos agglomerated together causing their clustering; the cosmic baryons then resulted from the cooling and gas-condensation within the potential wells provided by these DM halos, and whose merging history later affect the galaxy population contained. The full interpretation of DM-baryon relation is currently only partially understood, and the main part of our understanding is reached from observations which shown that fluctuations of the galaxy number density in the local Universe are directly proportional to the DM density (e.g. Schneider 2015).

At present, the physical nature of dark matter and dark energy are unknown, even after several observational breakthroughs of detecting their imprints (see e.g. Schneider 2015 for a detailed historical overview). At very early cosmic times the perturbations were still in linear regime, and the size of an overdense regions were increasing along with the expansion of the Universe, until they reached the critical density after which they started to collapse. Since it is not possible to systematically study such an early

cosmic epoch from the observational point of view, in order to better understand the processes and issues related to structure formation and evolution, astronomers built cosmological simulations. I will later describe in detail different recipes used for their build-up as well as their main aspects. Here is just important to note that classical N-body simulations include only dark matter that interacts gravitationally. Even simplistic, when performed with large dynamic range (that means with large numbers of particles per virialized structure), the N-body simulations can successfully trace the formation of DM halos (e.g. Prada et al. 2012, V. Springel 2005). They show that DM halos are even more complex substructures than what was initially thought, which is particularly reflected on our understanding of satellite galaxies (Somerville and R. Davé 2015). Ideally, to have a clearer view on evolutionary timeline, we should follow the evolution of each satellite halo and the host (central) DM halo from their birth until they merging or splitting (e.g. Fakhouri et al. 2008, P. J. E. Peebles 1982). The other important result from simulations is environmental dependence of halo formation, meaning that there exist a correlation between the time of forming the galaxy-sized DM halos and the density of their environment (Sheth et al. 2004). However, even the most refined cosmological simulations constructed to date have limitations. These limitations will be later discussed in details and here I note that the most prominent issue is their unability to precisely predict the distribution of galaxies made up of baryonic matter (see Somerville and R. Davé 2015 for a review).

1.2. Star formation in galaxies

As already stated, beside the dark energy and collisionless dark matter, the Universe is filled with baryonic particles. It is widely thought that the primordial baryon-photon fluid closely follow the distribution of DM halos, which seems as a natural consequence of their joint grow into the observed structures. Within the framework of the ΛCDM paradigm, the baryons does not collapse uniformly onto a DM halo (e.g. Davé et al. 2010, Somerville and R. Davé 2015, H. Mo et al. 2010). In fact, differently to DM halos, the baryon matter collapses with undergoing collisions. The primordial gas becomes compressed, producing accretion shocks that firstly heat the gas, which later starts to cool, collapsing into a disc and making the conditions for star formation. One of structures that had grown and formed across all scales within the DM halo (occupying tens of parsecs) are giant molecular clouds (GMCs) (H. Mo et al. 2010). The GMCs

represent very dense areas, having molecular hydrogen densities $n_{H2} \approx 100cm^3$, which is orders of magnitude above the density of ionised hydrogen in other regions of the interstellar medium (ISM). There are several theories that explain processes which trigger and suppress (quench) star formation activity in galaxies. They all generally agree that star formation in galaxies proceeds through the conversion of cold molecular gas (e.g. H_2) to the stars, which is in line with observations of locally star-forming galaxies (see McKee et al. 2007). Nevertheless, while the idea of an energy input from star formation was proposed long time ago (McKee et al. 2007), we still do not understand fully what is the exact process which allow individual stars to form.This led to the long standing problem, addressed by many observational and theoretical studies - the problem related to one of the main questions of modern astronomy: *how do galaxies actually use their molecular gas to form stars?* In the Universe, there are two usual channels for stellar mass production: slow (continuous) way, and short (usually very intense, bursting) way (see e.g. Tacconi et al. 2008, Davé et al. 2010, Mancuso et al. 2016, Ellison, Sánchez, et al. 2018).

On one hand, the star formation process can be maintained very long at a steady level, led by the process known as "cold gas accretion" from the intergalactic medium (IGM). On the other hand, the stellar build-up is often connected to galaxy-galaxy mergers, since it has been known that star formation can be catalysed via interaction of gas-rich dwarf galaxies (see e.g. Dekel et al. 2009, Sánchez Almeida et al. 2014, Ellison, Patton, et al. 2010). The diffuse gas replenishes the interstellar medium (ISM) of interacting galaxies, giving the fuel to the star formation (see e.g. Dekel et al. 2009). On top of it, the collisions of more massive galaxies known as major mergers of gas-rich systems are known to be important players in stellar production (Abruzzo et al. 2018 Lee et al. 2017, Tacconi et al. 2008). They can trigger intense and short-lived bursts of star formation. These prodigious, so-called starburst galaxies (SBs) can build hundreds or even thousands stars per year, much faster than "normal" star-forming galaxies.

Within the framework of the hierarchical model of galaxy formation and evolution, the violent events such as formation of SB galaxies, have decisive role in increasing their sizes and stellar masses over cosmic time. The extensive hydrodynamical parsec-scale simulations (e.g. Di Matteo et al. 2008, Renaud et al. 2014) have confirmed that, along with the global enhancement of the gas surface density caused by inflows induced in interactions, SB activity of galaxy mergers can be controlled by changes in the inner structure of the ISM. For example, galaxy interactions could increase the ISM turbu-

lence and help to compress the diffuse gas reservoirs (Renaud et al. 2014). Tidal shocks that accompany these interactions are also known to leave the significant observational imprints (e.g. Donevski and Prodanović 2015, Stroe et al. 2014). Recently, various lines of investigations presented rapidly increasing evidences that early galaxies contain more cold gas compared to their local analogues. Such a difference indicates that they could form more stars even without being very efficient (e.g. Geach, Smail, et al. 2011, Magdis, Rigopoulou, E. Daddi, et al. 2017). While both channels of star-formation are known, it still remains unclear which of them dominates the star formation histories of galaxies (see McKee et al. 2007 for the review). Another, still unanswered but vital question is why turbulence triggered by mergers lead to SB activity, rather than strengthening the pressure of molecular gas against the gravitational collapse.

To measure what is the rate in which galaxies convert their molecular gas reservoirs to the stars, we often aim to estimate star formation efficiency of galaxies ($\mathrm{SFE} \equiv \mathrm{SFR}/M_{gas}$). This simplified formula clearly illustrates that galaxies with high star formation efficiency must have correspondingly very low gas depletion timescales ($\tau_{depl} \equiv M_{gas}/\mathrm{SFR}$). Likewise, they are only able to maintain their present SFR for a short time related to burst. As shown in numerous studies, these galaxies will deplete their gas reservoirs on time-scales between 10 and 150 Myr (e.g. Tacconi et al. 2008, Lee et al. 2017), which makes their gas-star conversion much faster (an order of magnitude) than in isolated discs Renaud et al. 2014).

Now, to answer the important question *which mechanism dominates star formation history of galaxies in our Universe*, observational astronomers decided to build statistically large samples of objects seen at various distances, with the main goal to determine their SFRs and stellar masses. Observations that are performed so far shield a picture where most of galaxies have SFRs that are almost linearly related to their present stellar mass, in other words - proportional to the number of stars they have already produced. Such a tight relation is found in star-forming galaxies over different cosmic epochs and stellar masses and is called the "*main sequence*" of star-forming galaxies (Brinchmann and Ellis 2000). The galaxy main sequence (MS) is usually defined in the literature as an observed strong empirical relationship between the galaxy mass and the SFR and it was first analysed in large data samples in Brinchmann and Ellis 2000, and after revisited by Noeske et al. 2007. Very soon after these influential works, rapidly increasing number of studies analysed different population of galaxies in the context of their main sequence (Schreiber, Pannella, Elbaz, et al. 2015, Whitaker et al. 2015, Leja et al. 2015,

Elbaz, Dickinson, et al. 2011, Rodighiero, Daddi, et al. 2011 Daddi, Dickinson, et al. 2007, Noeske et al. 2007, Speagle et al. 2014, Brinchmann, Charlot, et al. 2004). As presented at Fig.1.1, there are also populations of galaxies that show offset from the sequence: they are so-called "red and dead" (usually used to describe passive galaxies in the very local Universe) and/or "quiescent" galaxies (QGs), which is the term used for passive galaxies at higher-z. Both of these populations are no longer forming newly born stars. However, it is very important to say that some galaxies that look "read and dead" in reach clusters at $z > 0.5 - 1.2$ can also be found with still active areas of star formation, as shown in recent study of Bonaventura et al. 2017. Even not so common, such findings posses a challenge to the accepted picture of galaxy evolution (Ragone-Figueroa et al. 2018). On the other hand, SB galaxies are forming stars at much higher rates compared to MS, expressing a clear bimodality in respect to the MS. Starbursts are commonly defined as galaxies that have systematic offset to the MS by factor of 3 and above (Rodighiero, Daddi, et al. 2011). However, it is Important to be highlighted here - the line which separates MS and SB galaxies is not well-defined and it is a matter of constant investigation and debate (see e.g Elbaz, Dickinson, et al. 2011, Daddi, Elbaz, et al. 2010, Caputi et al. 2017).

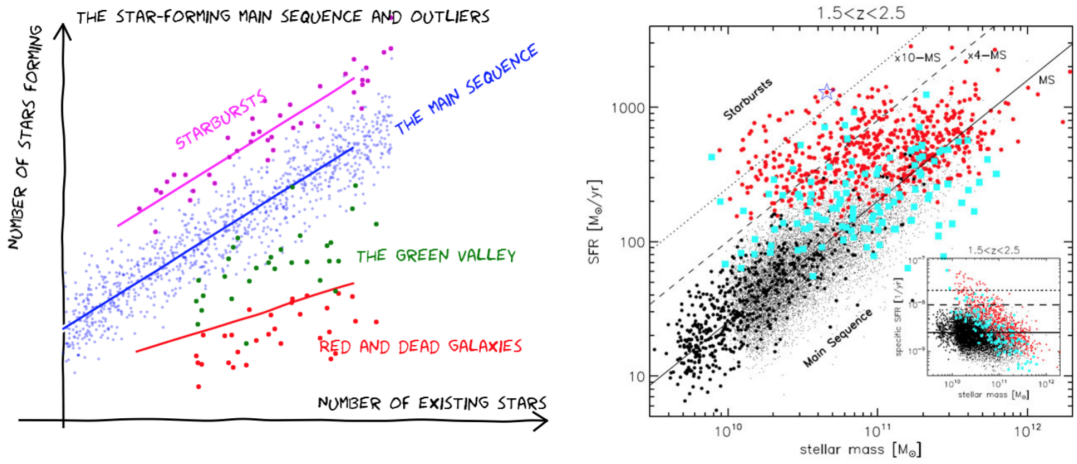

Figure 1.1.: Left: The cartoon form of a galaxy main sequence (credit: CANDELS collaboration); Right: The star formation rate as a function of stellar mass for wide range of galaxies analysed in Rodighiero, Daddi, et al. 2011, while galaxies from different selections and different fields are marked with various symbols. The solid black line indicates the MS, while the dotted lines represent the SBs.

The cartoon representation of main sequence seen in Fig.1.1 looks quite simple and

illustrates how the galaxies are linked relative to their MS positions (S. Eales et al. 2018, Magnelli, Lutz, et al. 2014, Elbaz, Hwang, et al. 2010). The prevailing theoretical picture states that star-forming galaxies gradually move along the MS, enlarging their masses, then simultaneously increasing the level of star formation until being terminated ("quenched", e.g. Conselice 2014, Gabor et al. 2010). In such, the galaxy is falling off the MS, reaching the region between the two extremes (so called "green valley") and then moves towards the passive end of the MS space. From an observational point of view, such a theoretical picture is very elegant and intuitively easy to understand, showing that the narrowness of the SFR–$M_\star$ relation implies that SFR in galaxies must be steady over very long time scales (Mancuso et al. 2016). However, this claim is somewhat controversial - the physical meaning of the galaxy main sequence is a debatable topic, and what particularly puzzles the scientists is how important are mergers in triggering SB activity. The rate of major mergers is theoretically predicted to steadily increase with redshift, which implies that we could expect more starbursting events in the past (see e.g. Elbaz, Leiton, et al. 2017, Kartaltepe et al. 2010, P. F. Hopkins et al. 2010). While the existence of a tight connection between SFR and $M_\star$ is anticipated, the fact that more than 75$\%$ of all star-forming galaxies have SFRs within a scatter of only 0.3 dex per given mass remains as a big challenge for theoretical models (e.g. Jorryt Matthee et al. 2018, Schreiber, Elbaz, Pannella, Ciesla, T. Wang, Koekemoer, et al. 2016). However, Kelson 2014 find that stochastic star formation would also create a MS correlation, and that the existence of the MS does not put any stronger constraints on the uniformity of star formation efficiencies. From this point, it is crucial to understand the time variability of star formation histories in galaxies, which remains crucial to interpret the observed MS of galaxies (e.g. L. Ciesla, D. Elbaz, et al. 2017).

As mentioned above, one of key unresolved issues is role of galaxy mergers in driving the stellar mass growth over different cosmic epochs. Recent numerical simulations found that mergers are efficient in triggering additional instability of the gas through compressive tidal forces, effectively allowing a substantial fraction of this gas to collapse and form new stars within short timescales (Renaud et al. 2014, Fig.1.2). Contrary to that, some observational works suggest the different possibility which would make overall contribution of "major" mergers to cosmic stellar mass growth much smaller than expected. The reason for such a claim is coming from results of handful of available observational statistical studies (e.g. Schreiber, Pannella, Elbaz, et al. 2015, Mantha et al. 2017). Those studies found disagreement between empirically measured merger

Rates and model predictions. Along with this, they also found that mergers negligibly enhance SFRs at higher redshifts ($z > 2$), when bulk of present stellar mass was already assembled. Relatively small size of current statistical datasets, coupled with the difficulty in observationally identifying genuine merger pairs, makes it challenging to properly answer on aforementioned question and quantify the true contribution of minor and major mergers to stellar mass growth at different epochs (e.g. Martin et al. 2017).

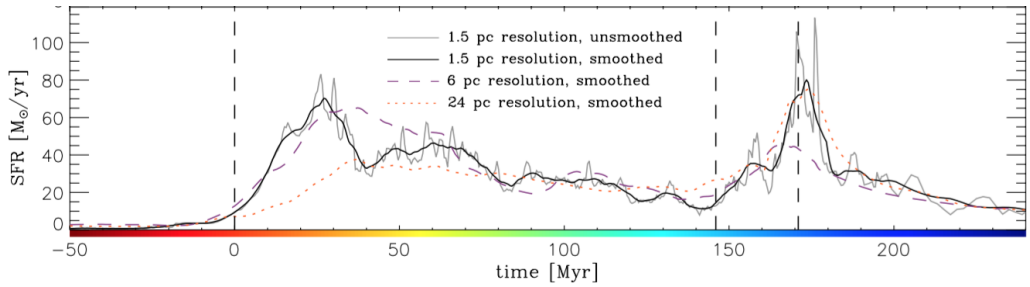

Figure 1.2.: Star formation history of low-redshift galaxy merger seen in hydrodinamical, parsec-resolution simulation. The gas excess caused by compressive turbulence translates into an enhanced star formation activity and drives the merger to the starburst regime. Solid, dashed and dotted lines represent the data from different resolution-runs for which convergence is reached. (credit: F.Renaud)

1.2.1. Dust in galaxies

While the dominant component of the ISM is molecular/atomic gas, there are important contributions to the energy related to star formation which comes from the dust particles. Dust plays important role in determining the formation of galaxies and their stars. Together with their role in inducing the inducing the formation of molecular clouds in galaxies, dust grains absorb UV light and re-process it into infrared bands, dramatically affecting the observed galaxy spectra. The dust consists of sub-micron sized grains that are typically made of graphites (C) and silicates Si. Our knowledge of their emission is accompanied with several fundamental problems, and the most important one is that microscopic structure of the dusty interstellar grains and their size distribution are still poorly known (see e.g. Galliano et al. 2011).

The overall nature of dust emission is thermal (Blain, Barnard, et al. 2003, Juvela et al. 2013). The vast majority of the dust in galaxies is located within the diffuse ISM, being heated by interstellar radiation field (ISRF). The smaller part of dust is enclosed

within the photo-dissociation region (PDR). The earlier models of dust formation in galaxies (e.g. Dwek et al. 1992, Dale and Helou 2002, see also Magdis, Daddi, et al. 2012) assumed that ISRF is constant, but it has been recently found (Béthermin, Daddi, Magdis, Lagos, et al. 2015, Schreiber, Pannella, Elbaz, et al. 2015) that the interstellar radiation strength is redshift dependent. The range of temperatures under which dusty grains are exposed are usually found to be between 20 K and 180 K, depending on intensity of the ISRF, the grain sizes and their optical properties (Dwek et al. 1992,Blain, Barnard, et al. 2003. Draine 2006, Dale, G. Helou, et al. 2014, Draine, Aniano, et al. 2014). If these grains reside closer to a powerful source of interstellar radiation, higher dust temperatures can be produced, sometimes even above 2000 K. The dust heating is also present in very high-z galaxies since the influence of CMB radiation on dust temperature starts to be non-negligible. The basic parameters necessary for describing the emission from dust grains are a dust temperature ($T_{\rm d}$) and the dust emissivity (ϵ_ν). Here I note that $T_{\rm d}$, represents the cold-dust temperature in the ISM. The distribution of a $T_{\rm d}$ in galaxy describes the nature and environment of each silicate or carbon grain. The dust radiative transfer models and observations of locally bright dusty galaxies support the picture where continuum emission from dusty grains in most of these systems can be successfully described with the optically thin modified blackbody (MBB) radiation (see the discussion in Blain, Barnard, et al. 2003, Casey, Berta, et al. 2012 and Casey, Narayanan, et al. 2014). The MBB model together with some other, more refined and complex models, will be discussed in detail in Chapter 2. Here I just describe the principle basic form of the dust emission that is relevant to observations of DSFGs presented in this Thesis.

Modelling the dust emission of galaxies is essential to understand the physics of dust obscured galaxies. It requires deep understanding on the galaxy Spectral Energy Distribution (SED) which is described by stellar, dust and gas content of galaxies, together with their physical properties. As SFR is closely related to galaxy dust properties, it is thus important to have the data which cover the total IR wavelength range, that means both the "Wien" and "Rayleigh-Jeans" side of the thermal SED. In general, the thermal part of the SED is usually expressed as (Blain, Barnard, et al. 2003):

$$S_\nu \propto \nu^\beta B_\nu(T_{\rm d}) \tag{1.1}$$

Here S_ν is the flux density at a given wavelength (frequency), B_ν is the Planck function

$((2hc^2)/\lambda^5/(e^{hc/\lambda\kappa T}-1)$, or in Reyleigh-Jeans regime $2\kappa T_{\rm d}\nu^2/c^2$), whilst it is common to plot these flux density values as a function of wavelength as $S_\nu(\lambda)$, where $\lambda = c/\nu$.

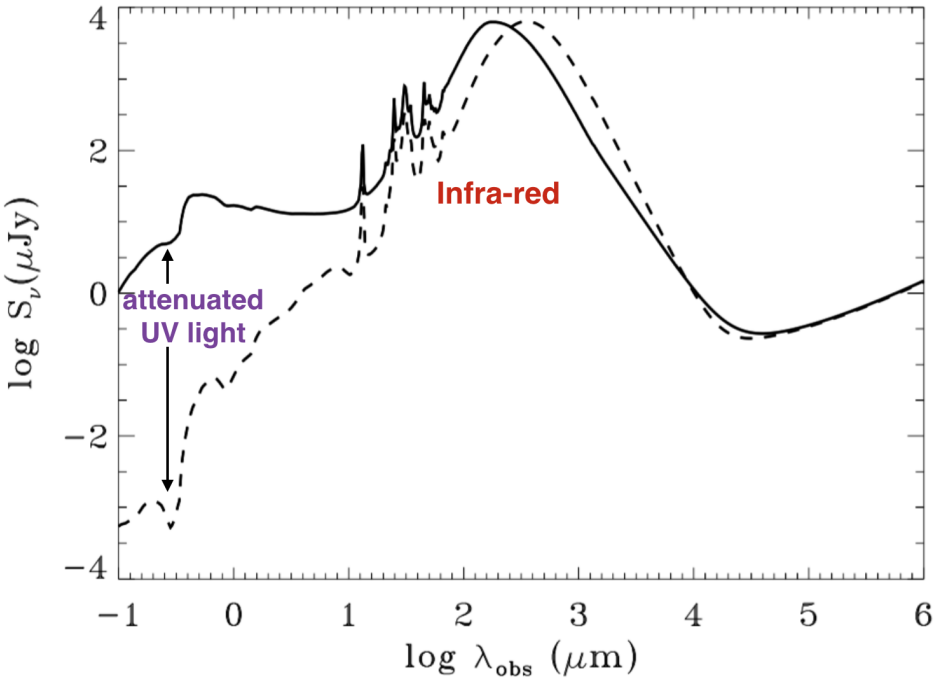

Figure 1.3.: Simulated SED of strongly obscured and less obscured galaxies. The figure shows an SED of a galaxy in two different stages of evolution. The solid line represents the galaxy at the beginning of its life, when only a mild dust attenuation is present, while the dashed line shows the galaxy in a more evolved (and dusty) stage, when most of the UV light has been absorbed and re-emitted at higher wavelengths by the dust (image credit: adopted and modified based on Fig.1, C. Mancuso, PhD Thesis).

Galaxy SED analysis based on single-temperature MBB models[c] thus are important not only in estimating $T_{\rm d}$ and β of DSFGs, but also in comparing dust masses inferred by MBB models and more refined template-based methods (e.g. Draine and A. Li 2007, Dale, G. Helou, et al. 2014).The dusty part of electromagnetic spectrum is made up of different components that are heated at non-uniform temperatures, which makes the dusty emission fairly complex for studying (e.g. Dale, G. Helou, et al. 2014, Galliano et al. 2011, Dwek et al. 1992). The MIR continuum side ($\lambda < 30\mu$m), mainly arises by

[c]More recently, there are other approaches which modelled the thermal SED as a combination of two modified blackbodies of different temperatures. The cold component dominates the long-wavelength side, and a warmer component dominating at mid-infrared wavelengths (Loretta Dunne et al. 2001, Galametz et al. 2012).

the emission from polycyclic aromatic hydrocarbons (PAHs) and absorption bands from silicate and amorphous carbon grains. On top of that, the MIR wavelengths can be under strong active galactic nuclei (AGN) contamination. The dust heated in galaxies may have two different features in FIR part of SED: the diffuse dust (cirrus) being heated by old stars, and the dust in molecular clouds heated by younger stars, which is a more direct tracer of the star formation processes occurring inside the HII regions (Rowlands et al. 2014). Dusty particles are important to understand the physical nature of obscured processes of star formation, since they scatter and absorb the optical and ultraviolet (UV) light emitted by young stars. Thus the measured intensity of the radiation is heavily reduced, and in Fig.1.3 I present the SED of a galaxy illustrating different levels of dust obscuration.

We need to rely on FIR SED fitting if we want to extract basic physical properties of galaxy dust emission: its IR luminosity which is in direct relation to obscured SFR, the dust temperature and the dust mass. Having in hand the redshift of a dusty source, we can make an estimate of its bolometric IR luminosity by integrating the observed SED over the total IR wavelength range. This range is usually assumed to be 8-1000 μm.

$$L_{\rm IR} = \int_{8\mu{\rm m}}^{1000\mu{\rm m}} 4\pi D_L(z)^2 S_\nu(\lambda) d\lambda, \tag{1.2}$$

Here $D_L(z)^2$ is luminosity distance, whilst $S_\nu(\lambda)$ is a flux density of a source at given wavelength.

For standard spiral galaxies with relatively low FIR luminosities (e.g. several $10^{10} L_\star$) the dust emission is found to be essentially extended, reaching the same scale as the stellar disk with the size of ~ 10 kpc. Such emission is mostly correlated with molecular gas rich regions of star-formation that are distributed within the galaxy (Casasola et al. 2017). In these regions the dust is heated by the hot, young OB stars, more massive than $8{\rm M}_\odot$ whose lifetime is $\lesssim 10$ Myr. From the resolved structure of extensively studied lower-z IR luminous galaxies such as IC1614, we now know that the great majority of the IR emission arises in a much smaller, (sub-kpc) regions within a merger (e.g. Murphy et al. 2013). It is plausible to expect that a significant fraction of the energy produced in IR could be a consequence of an AGN surrounded by a dense gas and dust. This material imposes significant extinction on the AGN emission in the optical and UV wavebands (Fritz et al. 2006). Alternatively, another powerful source for dust emission is an ongoing centrally fragmented burst which is mainly fuelled by gas coming from the interacting pair of galaxies. In the case of AGN heating, the SED would be is expected

to peak at shorter wavelengths (in the MIR part) and the MIR SED would be flatter in comparison to a more extended star-formation source (Symeonidis, Vaccari, et al. 2013).

1.2.2. Dust as a star-formation rate tracer

The most subtle care to be considered when trying to infer the SFR from UV emission is that, especially in star forming galaxies, the star-forming processes occur in dust enshrouded environments. It causes that UV emission is suppressed in favour of the IR reprocessed light. Therefore, the IR emission of star-forming galaxies can give information on the level of obscured star formation in these structures. However, it is also known that especially for those galaxies that are forming stars at lower rates, not all the UV light is reprocessed by the dust (J. Matthee et al. 2017, Schreiber, Pannella, Elbaz, et al. 2015). Since the amount of dust is expected to be strictly connected to the formation of stars, it implies that if the star formation process is slow (so the production of dust), the result will be a not fully dust obscured galaxy. In such a case, the solely IR emission can underestimate the true (intrinsic) SFR, since we know that UV light can actively trace it. The one way to estimate SFR in galaxies by combining such tracers is through a following relation :

$$\mathrm{SFR}_{\mathrm{tot}} = K_{\mathrm{UV}} \times L_{\nu}(\mathrm{UV}) + K_{\mathrm{IR}} \times L_{\nu}(\mathrm{IR}) \tag{1.3}$$

The $L_{\nu}(\mathrm{UV})$ does not take into account the dust extinction, and the conversion factors can be estimated based on modelled relations (Kennicutt and Evans 2012).

However, for most of the distant galaxies that are heavily obscured and undetected even in large optical surveys, it means that their stellar light is fully reprocessed by dust. Assuming this fact, we can infer the star formation rate from L_{IR} only. In this example, the Eq.1.3 is reduced to:

$$\mathrm{SFR}_{\mathrm{tot}} = K_{IR} \times L_{\nu}(\mathrm{IR}) \tag{1.4}$$

Although the IR luminosity only traces star formation obscured by dust, observations show that in most of the massive star-forming galaxies the obscured star formation activity dominates (e.g. J. A. Zavala, I. Aretxaga, et al. 2018, Faisst et al. 2017, Mancuso et al. 2016, Buat, Giovannoli, et al. 2010). These dust-obscured galaxies are the main population of interest in my Thesis. Here I refer to dusty star-forming galaxies (DSFGs

hereafter) for all star-forming galaxies that are selected from IR and/or submm data. This definition can encompasses a great diversity of objects (e.g. Casey, Narayanan, et al. 2014). In literature, high-z dusty sources typically selected at wavelengths 850μm or longer are often called "Submillimeter galaxies (SMGs)", while equivalent distant sources selected from FIR are defined as dusty star forming galaxies. In this Thesis, I did not want to make distinction between the two. Instead, I assume that DSFG is much more appropriate definition which in general better describes the nature of sources I aim to investigate.

1.2.3. Sources of contamination

The way of using the dust emission as a star formation indicator simply relies on the total IR budget estimated for a given source. Regardless on that fact, the detailed shape of the SED is important, since it encodes the physical conditions in the ISM in which the emitting small, dusty grains reside. Theoretical works (Dwek et al. 1992, Blain, Barnard, et al. 2003) agreed that dusty grains will equilibrate to a temperature that increases with the intensity of the local radiation field. The grain re-emission scales with $\propto T^{4+\beta}$ whilst the dust emissivity index is typically β=1.5–2.3 (Blain, Barnard, et al. 2003, Casey, Narayanan, et al. 2014).

It has been shown that in the local Universe more than a half of the IR luminosity in QGs originates in the ISM thermal emission, which is not always related to star formation. The dust is instead heated from older, dying stars, oppositely to SBs and SF galaxies which are heated by younger stars (e.g. Lonsdale, Persson, et al. 1984; Sodroski et al. 1997; L. Dunne et al. 2011). This trend has also been observed out to higher redshifts ($z \sim 3$, Glazebrook et al. 2017, Salim et al. 2015, Toft et al. 2014). When the star formation increases, however, the fraction of emitted dust coming from older stars (e.g. the fractal galactic structure known as cirrus) decreases consequently (Bianchi et al. 2017, Buat, Heinis, et al. 2014). This implies that for strongly star-forming galaxies which are of main interest in this Thesis, it accounts only for a small percentage of the total IR emission (Rowlands et al. 2014). Along with the interstellar radiation field (ISF) connected to young stars, the dust can also be heated by active galactic nuclei (AGN) within galaxies. It is assumed that in high redshift galaxies which contain moderately luminous AGNs, stellar-heated emission dominates over AGN-heated emission in the FIR part of the spectra (Urry et al. 1995, Hatziminaoglou et al. 2008, Eilat Glikman

et al. 2006, Sajina et al. 2006, Symeonidis, Vaccari, et al. 2013. One way to disentangle between star-forming and AGN components is via equivalent width of PAHs, since it is known that sources hosting AGN typically have very small PAH equivalent widths in IR bright local galaxies (Murphy et al. 2013, Armus et al. 2007). Generally saying, a careful SED fitting to the AGN portion of the spectra can account for the fraction of IR luminosity produced by AGN activity. This is proven to be not an easy task, but it is a way to prevent overestimation of the calculated star formation rate (e.g. L. Ciesla, Charmandaris, et al. 2015, Calistro Rivera, Lusso, et al. 2016, Małek et al. 2017). Most of studies which aimed to disentange the IR emission from AGNs and star formation have analysed mid-IR continuum data sets (e.g. Eilat Glikman et al. 2006, Sajina et al. 2006, Symeonidis, Vaccari, et al. 2013, Satyapal et al. 2017) or a combination of the mid-IR continuum and spectral lines (Magdis, Rigopoulou, Hopwood, et al. 2014). Very recent theoretical results shade a new light on star-forming-AGN connection, stating that the true number density of AGNs may be underestimated due to poor template-fitting choices (see Roebuck et al. 2016).

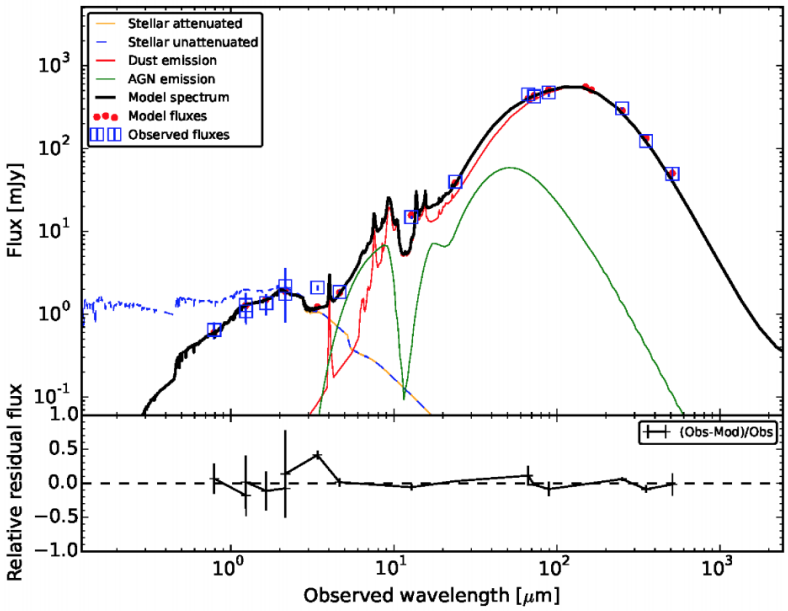

Figure 1.4.: Example of the best SED fit model made with SED fitting code `CIGALE` (Noll et al. 2009), for a dusty galaxy at $z = 0.2$. Observed fluxes are plotted with open blue squares while filled red circles correspond to the model fluxes. The final best model is plotted as a solid black line. The blue, yellow, green and red lines represents the different contributions to the galaxy SED, and their meaning is noted in legend. We see that, in this example, total dust emission (red line) experiences significant contribution from AGN component (green line). The relative residual fluxes are plotted at the bottom (credit: Małek et al. 2017).

.

1.3. The advent of infrared astronomy

The largest part of the IR light emitted by galaxies is absorbed by water vapour and carbon dioxide (CO_2) in the Earth's atmosphere. The IR light can pass (at least partially) through the atmospheric window only in few narrow wavelength regions and reach the ground-based IR/submm telescopes. In addition, the Earth's atmosphere causes another but significant issue: the atmosphere itself radiates in the IR bands, creating additional thermal component to the one expected from space objects. From the Figure 1.5 we can see that our atmospheric layer is opaque over most of the FIR wavelengths, which implies that ground-based facilities are substantially limited to submm/mm wavelengths by using only high-altitude telescopes such as the James Clerk Maxwell Telescope (JCMT) mounted at Hawaiian Mauna Kea or LABOCA instrument

mounted in APEX in Chile. Most FIR observations have thus to be conducted from space. It is only during the last decades that IR space-launched satellites such are Herschel and Spitzer, or their predecessors, e.g. *IRAS* allowed to detect and study DSFGs and thus complement ground based submm single dish observations. A critical limitation related to the selection of distant DSFGs, is telescope's instrumentation, particularly the one applied for large extragalactic surveys. I will later discuss the impact of these limitations on selection effects, critical when hunting distant galaxies and characterising their nature. At this stage it is important to say that throughout the last decade the FIR SED coverage has been significantly expanded to other wavelengths due to instrumental improvements. In the following I briefly highlight the history of IR facilities used for discovery of DSFGs (Tables 1.1 and 1.2).

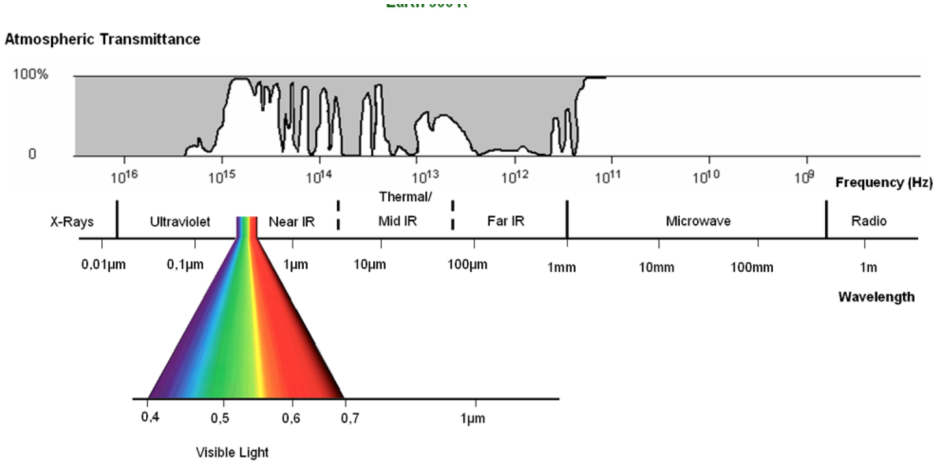

Figure 1.5.: Atmospheric transmission window, which shows the level at which an emitting photon is absorbed as a function of its wavelength. It can be seen that only longer radio waves, optical light, the hardest gamma-rays, and FIR radiation in a few windows can pierce the Earth's atmosphere and reach the sea level. Observations at all other wavebands including most of FIR (e.g. between 70 μm to 500 μm) should be carried out above the atmosphere. Credit: http://coolcosmos.ipac.caltech.edu/infrared_universe

1.3.1. An overview of infrared telescopes

The extragalactic IR astronomy is in a time of great progress. Expecting the launch of the James Webb Space Telescope (JWST; space-based near and mid-IR telescope), we are extensively analysing data sets from ground-based FIR and submm/mm interferometers and single-dish observatories such are the Atacama Large Millimeter Array (ALMA), Northern Extended Millimeter Array (NOEMA), Submillimeter Array (SMA),

Table 1.1.: List of the most important space-based and balloon facilities used for detection of dusty galaxies

Telescope	Launch	Instrument	Wavebands	Beamsize	Reference
Herschel	2009	PACS	100 μm 160 μm	8″ 13″	Poglitsch et al. 2010
		SPIRE	250 μm 350 μm 500 μm	18″ 25″ 36″	Pilbratt et al. 2010
IRAS	1983	IRAS	12-60 μm	0.5′-2′	Neugebauer et al. 1984
ISO	1995	ISOPHOT	15-180 μm	7″-80″	Lemke et al. 1996
CSO	2002	Sharc-II	350 μm	9″	C. D. Dowell et al. 2003
Spitzer	2003	MIPS	24-160 μm	6″-38″	Rieke et al. 2004
AKARI	2006	FIS	65-160 μm	26″-64″	Murakami et al. 2007
BLAST	2008	BLAST	250-500 μm	33″-66″	Devlin et al. 2009
WISE	2009	WISE	12-22 μm	6.5″-12″	Wright et al. 2010
Planck	2009	HFI	345 μm-3 mm	5′-10′	Tauber et al. 2010

SCUBA-2 and SPT, enable the detection and physical characterization of DSFGs out to the Universe's earliest epochs.

For the DSFGs at high-redshifts ($z \geq 4$), aimed to be explored in this Thesis, both space-based MIR and ground-based submm/mm surveys miss the position of the rest-frame FIR peak that is known to shapes the dusty SEDs of DSFGs. To partially suppress the problem, most of studies enforce the extrapolation through averaged template SEDs,which is compulsory in order to characterise the energy budget of near-IR selected samples.

Table 1.2.: List of the current ground-based telescopes used for detection of dusty galaxies

Telescope	Year	Instrument	Wavebands	Beamsize	Reference
			Single-dish telescopes		
JCMT	1998	SCUBA-2 [a]	450 μm, 850 μm	7″, 14″	Holland et al. 2013
LMT	2005	AzTEC	1.1 mm	6″	G. W. Wilson et al. 2008
APEX	2006	LABOCA	870 μm	19″	Siringo et al. 2009
SPT	2008	SPT	1.4 mm, 2.0 mm	63″, 69″	Siringo et al. 2009
IRAM 30m	2015	NIKA-2	1.5 mm, 2.6 mm	11″, 17″	Calvo et al. 2016
			Interferometers		
NOEMA[b]	1992	NOEMA	1.3 - 3mm	0.4″ – 3.7″	Guilloteau et al. 1992
SMA	2004	SMA	350 μm-1.3 mm	0.25″, 5.″	Ho et al. 2004
ATCA	2008	SPT	1.4 mm, 2.0 mm	63″, 69″	W. E. Wilson et al. 2011
ALMA	2013	ALMA	650 μm-3 mm	0.1″, 4.5″	Wootten et al. 2009

Notes: (a) Initial SCUBA telescope has been operating from 1997-2005 in same wavebands. The SCUBA-2 is operating from 2011; (b) PdBI became NOEMA after several upgrades at 2016. Today array consists of eight 15m telescopes.

1.3.2. *Herschel* space observatory

Most of the work in this Thesis is based on data collected by *Hercshel* Space Observatory. The *Hercshel* Space Observatory (Pilbratt et al. 2010) is the fourth cornerstone mission in European Space Agency (ESA) science programme. *Hercshel* was successfully launched on 14th May 2009. from French Guiana (http://sci.esa.int/herschel/). With its cooled 3.5 m (in diameter) primary mirror, *Hercshel* is still the largest observatory that has been ever sent to explore the Universe. *Hercshel* was actively operating between 2009 and 2013, and it is the first space observatory which combined the sensitivity and large aperture over the longer wavelength FIR ranges (from 100 μm to 500μm)[d]. *Hercshel* has three on-board instruments: the Heterodyne Instrument for FIR (HIFI, de Graauw et al. 2010), the Photodetector Array Camera and Spectrometer (PACS, Poglitsch et al. 2010) and the Spectral and Photometric Imaging Receiver (SPIRE, Griffin et al. 2010) had their first light soon after. The spectral window observed with *Hercshel* covers the cold and the dusty universe: from dust-enshrouded sources at great distances, down to small scales of stellar formation and planetary bodies. A high-level description of the *Hercshel* Space Observatory is given in Pilbratt et al. 2010, while more details are given in the *Hercshel* Observers' Manual.

As can be seen from Table 1.1, pre-*Herschel* space telescopes explored dusty Universe in wavebands below 250 μm. Due to the Doppler shift of their thermal SED, most of the potentially high-z DSFGs are expected to have their peak at longer wavelengths. Thus, the launch of the *Herschel* Space Observatory improved the situation and offered to the astronomical community unprecedented size and depth for studying the DSFGs. For example, the *Herschel* covered large areas on the sky (as now, more than 1000 square degrees of the sky has been explored) providing statistically significant data sets of DSFGs which serve for a wide range of science goals (see e.g. S. J. Oliver, L. Wang, et al. 2010, Lutz 2014). The large part of the total *Herschel's* observing time was devoted to big galaxy surveys (Lutz 2014). In particular, *Herschel* provided important advantages for the study of galaxy evolution as compared to *Planck* telescope and its ancestors. The first is possibility to directly measure the level of the dust re-emission in galaxies, even above the peak of star-formation in the Universe, distances that were mainly unexplored by optical telescopes. Secondly, thanks to *Herschel* FIR imaging and photometry, which is now finalised for more than a million of galaxies, and covers approximately 1300 deg^2

[d] In the present thesis I refer to this range as the "FIR", leaving the "submm" terminology to ground-based surveys typically performed at 850 μm and longer millimetre wavelengths.

on the sky, it is possible to reach the better understanding of the physical conditions of the ISM in DSFGs, e.g. by measuring their dust masses (S. Eales et al. 2018, Groves et al. 2015). The full comparison of instrumental sensitivities and abilities to observe larger area on the sky is illustrated on Fig. 1.7, which is a schematic comparison discussed in Casey, Narayanan, et al. 2014.

1.4. The road to distant DSFGs

It has been theoretically predicted that the extragalactic background light, which represents the integrated radiation connected to various sources at all redshifts in the Universe, should also contains a contribution from the dust emission of galactic objects (Partridge et al. 1967). The first confirmation for such a claim appeared In the early 1990s - the FIR Absolute Spectrophotometer (FIRAS) aboard the space-based *Cosmic Background Explorer* (COBE) estimated the total SED of the Universe at FIR and submm wavelengths above 150 μm. Along with initial observations of nearby galaxies made with IRAS, it has been proved that significant portion of that extragalactic light ($\sim 50\%$), so-called the Cosmic Infrared Background (CIB), is actually IR-emitted. (Puget et al. 1996, Lagache, Abergel, et al. 1999, Hauser et al. 2001, Magnelli, Lutz, et al. 2014, M. Béthermin, Dole, Lagache, et al. 2011). Since it was speculated that CIB is almost essentially connected to the process of star-formation (with a much smaller contribution coming from AGNs), it becomes clear that the main implication of this discovery is that optical observations alone eventually missing an important piece of the dusty star-formation in the Universe. The early COBE measurements along with galaxy surveys performed at optical wavelengths, showed the existence of a population of galaxies that are enshrouded in dust and/or numerous dusty areas within optically-detected sources. Since most of the systems were discovered in our local, extragalactic surroundings, it implied a crucial question related to the topic discussing the dusty Universe - *What is the contribution of higher-z DSFGs to the CIB?*

1.4.1. Resolving the cosmic infrared background

The flux distribution of DSFGs responsible for CIB is one of critical statistical parameters related to our understanding of the evolution of baryon matter in the Universe, and it can be considered as a gateway to our knowledge of early galaxy formation and

evolution (e.g. Béthermin, Daddi, Magdis, Sargent, et al. 2012, Franceschini et al. 2010, Lagache, J.-L. Puget, et al. 2005).

The very first attempts of mapping the FIR emission over large areas date-back to the pioneering Infrared Astronomical Satellite (IRAS) (Neugebauer et al. 1984). The IRAS was launched in 1983, being equipped with detectors that cover wavelengths 12-100 μm. IRAS was the first space-based observatory which completed a full-sky survey at IR wavelengths. Some of the remarkable science results that came-out from the IRAS are observation of some of the IR-brightest local galaxies, together with two extremely bright high-redhsift systems at $z > 2$ whose flux is found to be significantly boosted by the effect of gravitational lensing (Houck et al. 1984, Broadhurst et al. 1995). The brightest local galaxies discovered with IRAS are now known as (U)LIRGs which stands for (Ultra-)luminous Infrared Bright Galaxies. LIRGs and ULIRGs are traditionally defined as galaxies with luminosities $L_{IR} > 10^{11} L_{\odot}$ and $L_{IR} \geq 10^{12} L_{\odot}$ respectively (D. B. Sanders et al. 1988, see also Lonsdale, Farrah, et al. 2006).

With the launch of Infrared Space Observatory (Lemke et al. 1996) back in 1995, astronomers received a much deeper view of dusty galaxies at both mid-IR and FIR wavelengths. As compared to IRAS, ISO improved the detector technology, being able to probe wavelengths from 2.5 μm to 240 μm with better resolution. However, ISO was not designed for performing an all-sky survey. Instead of it, ISO selected almost 32 000 sources with the goal to provide the deeper images than IRAS (with almost 1000 times better detection sensitivity). The largest open time survey that was conducted with ISO was ELAIS, (European Large Area ISO Survey, Seb Oliver et al. 2000), which undertake the imaging over 20 deg^2 and probing intermediate redshift of objects at $z \sim 1$ (Serjeant, Carramiñana, et al. 2004). Although the discovery of local LIRGs and ULIRGs showed that optical surveys potentially miss the most of heavily dust-obscured SF and SB systems, such extremely dusty galaxies turned out to be rare compared to "normal" galaxies (e.g. UV bright, blue spirals) seen in the local Universe. Therefore, these sources alone could not explain the CIB.

The astronomical IR community carefully prepared the way to overcome the drawbacks seen in pioneering IR missions. These efforts resulted with another progress happened in 1997, when the 850 μm deep blank field observations with the Submillimeter Common-User Bolometer Array (SCUBA) on the James Clerk Maxwell Telescope (JCMT) directly spotted population of high-z DSFGs that are extremely bright at FIR/submm wavelengths and barely visible (or even invisible) in the optical (Barger

et al. 1998, David H. Hughes et al. 1998, see Blain, Smail, et al. 2002 for the review). Such ground-breaking results revolutionised the field of galaxy dusty formation and evolution, gathering the study of high-z DSFGs into one of the growing branches of a modern observational cosmology. At the beginning of this century, the *Spitzer* Space Telescope opened still unused windows for MIR surveys as well as the direct MIR spectroscopy of faint high-z dusty galaxies (see the review by Soifer et al. 2008). At the same time, the *AKARI* mission (Murakami et al. 2007) made detailed MIR photometric coverage with slightly lower sensitivity (see Figure 1.5 for comparison). As a result of these two space-based MIR projects, galaxies with a wide range of inferred SFRs, stellar masses, and AGN luminosities extended their IR properties, providing a way to look at their energetics. Later support from balloon and ground-based submm/mm single dish facilities, improved our understanding of galaxies initially selected with *Spitzer* or *AKARI*.

Unfortunately, it appeared very clear that one of the striking limitations of FIR/submm missions, that makes it difficult to resolve the faint sources contributing to the CIB, is *confusion noise* (Condon 1974 Dole, Lagache, et al. 2006). The confusion noise consists as a superposition of signals from fainter galaxies fluctuating in the cosmic background, and arises as a result of the limited resolution of telescopes operating in IR, and the steep source counts of the galaxy populations selected at these wavelengths. The limited angular resolution states that IR-selected sources cannot be distinguished from each other easily, and the total sum of their IR fluxes creates an significant uncertainty in the maps.

Although sources with IR fluxes below the confusion limit cannot be fully spotted and resolved, there exist a large collection of statistical methods that are utilized in order to partially investigate the statistics (e.g. the number counts) of these fainter objects. One of the commonly used methods is called "probability of deflection analysis" or $P(D)$, and aims to recover the pixel intensity histograms in FIR maps (Patanchon et al. 2009). As a complement to the $P(D)$ technique, another popular recipe is based on weighting the covariance between the confusion-limited FIR maps and source positions obtained from *Spitzer*-MIPS 24 μm detections. The method is dubbed "source stacking" (e.g. Marsden et al. 2009, Serjeant, Dye, et al. 2008). These two methods, however, can also be biased by the contamination of the measured flux by fainter clustered sources, which is an important issue that will be discussed throughout the Thesis. At this point, it is worth to note that clustering is specifically important at higher distances ($z > 2$), where

the small-scale grouping of distant sources is usually found more stronger as compared to those signal measured at intermediate redshifts (e.g. Wilkinson et al. 2017).

As a relic of galaxy formation and evolution emitted at IR wavelengths, the CIB opened a new era of our understanding of dusty Universe and increased the number of stadies which aimed to characterise the statistical behaviour of galaxies responsible for CIB. Elbaz, Cesarsky, Fadda, et al. 1999 succeed in resolving the CIB with ISOCAM instrument, observing the Lockman hole and Marano field. They found that more than a half of the CIB can be resolved into point sources observed in MIR at 15 μm. At larger wavelengths, initial COBE and ISO missions failed to resolve the CIB at sufficient level (Dole, Gispert, et al. 2001) due to the instrumental sensitivity and angular resolution. By using SED models to extend the estimates above the wavelengths covered with ISOCAM, Elbaz, Cesarsky, Chanial, et al. 2002 derived that around 65% of the background peaking at 140 μm is due to point sources with median $z \sim 0.8$, detected with ISOCAM. The situation in this field has been constantly improving with the newer generation of telescopes, such are *Spitzer* (e.g. Dole, Lagache, et al. 2006) and *Herschel* (e.g. Magnelli, Popesso, et al. 2013, M. Béthermin, Dole, Lagache, et al. 2011). For example, Dole, Lagache, et al. 2006 found that *Spitzer* detected sources contribute 79% at 24 μm and 69% at 160 μm, finding that total CIB emission peaks close to 150 μm. As anticipated, with the advent of *Herschel*, today is known that the average redshift of dusty sources which contribute to the CIB increases with the wavelength - approximately 75% of CIB is accounted by individually resolved galaxies. For SPIRE wavelengths 250-500 μm, about half of the CIB is emitted by sources at z =1.04, 1.20, and 1.25 respectively (Béthermin, Le Floc'h, et al. 2012, Magnelli, Popesso, et al. 2013). Despite the increasing median redshift of the resolved sources,the increasing confusion noise makes that the partitioned fraction is lower at SPIRE wavelenghts (250–500 μm), making 15–16$\%$ of the CIB resolved (M. Béthermin, Dole, Lagache, et al. 2011).

1.4.2. Detectability of high-redshift DSFGs

To understand the star-formation in early cosmic times, the distant, dusty galaxies are of particular interest. Once we achieve a good understanding of distant star formation, we will be close in picking the essential piece of the jigsaw puzzle called dusty galaxy formation and evolution. With more statistical properties in hand (e.g. redshift distribution, SEDs, luminosity functions, clustering properties), we can estimate the SFR of distant

DSFGs more accurately and characterise their environments and physical nature. We can further investigate the overlap/difference in the properties of the objects selected with different methods. The fastest and more direct way of selecting the DSFGs in wide sky areas is via FIR-selection (*Herschel*) or submm selection (SPT, SCUBA-2). We thus need to apply the source detection methods and selection techniques suitable for building statistically rich data samples of the high-z DSFGs. This process is not trivial, due to instrumental limitation of *Herschel* (e.g. its sensitivity and resolution). Additionally, it is expected that their detectability varies with source's dust temperature and intrinsic SED shape (see e.g. Fig.7 from Casey, Narayanan, et al. 2014). On top of that, it is pointed out (Béthermin, De Breuck, et al. 2015) that depth of surveys and wavelength which we use to select the population of interest, lead to the sources with different redshift distribution. However, the situation is quite complex and a compromise must be reached between the longer wavelength selection and the surveying efficiency (defined as the number of extracted sources per an observing hour). Also, at longer wavelengths the proper source identification is problematic due to the larger beam sizes (for SPIRE and SPT, a beam size is drastically increasing with wavelengths, from 250 μm to 1.4mm, see Table 1). All these aspects are very important to consider, since the nature of the galaxies that are found in larger surveys is very broad and source's luminosities varying much more compared to those found in smaller surveys. In the following I describe what we can learn about populations of dusty galaxies from large dedicated surveys. Firstly, I briefly introduce two important tools that allow us to detect the high-z DSFGs.

(a) Negative K-correction

The selection of high-redshift DSFGs benefit from the effect known as "negative K-correction" (see Blain, Barnard, et al. 2003). The K-correction enables us to convert the magnitude (or flux) observed for a source at redshift z to a rest-frame magnitude, while taking into account the shape of its redshifted SED. It is defined as the K(z) term in the following equation (Hogg 1999):

$$\mathrm{m} = \mathrm{M} + 5(\log \mathrm{D_L} - 1) + \mathrm{K(z)} \tag{1.5}$$

The K-correction depends only on the inferred shape of the galaxy's SED, and it is independent of the correction between apparent to absolute magnitudes. In the case of FIR and submm observations, the detectable flux density at an observed frequency ν from a galaxy with bolometric luminosity L at redshift z can be approximated as (Casey,

Narayanan, et al. 2014):

$$S_\nu \propto \frac{\upsilon^{\beta+2}}{4\pi D_L^2} \propto \begin{cases} (1+z)^{\beta-2}, & \text{for } 0 < z \leq 3 \\ (1+z)^{\beta-1.5}, & \text{for } z > 3 \end{cases} \tag{1.6}$$

The copious number of observations confirmed that emission slope in high-redshift DSFGs is in the range found to be $1.5 < \beta < 2.2$. It implies that thermal flux density of DSFGs remains nearly constant as their redshift increases. This is the one of key features that allow detections of distant DSFGs for a range of wavelengths between 250 μm and up to several millimetres.

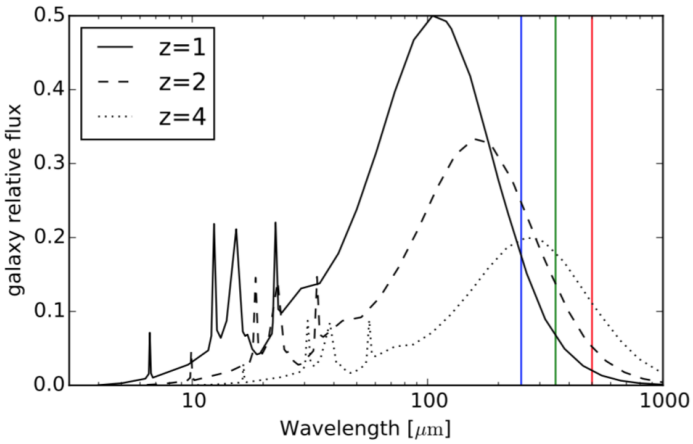

Figure 1.6.: Demonstration of negative K-correction across the SPIRE bands using the M82 SED. The observed flux remains relatively constant across the SPIRE bands, while for shorter wavebands fluxes drastically decrease with increasing redshifts. For mm bands, K-correction works even better than in SPIRE bands, causing nearly unchanged fluxes of DSFGs across a wide range of cosmic epochs ($1 < z < 10$, see Fig.3 in Casey, Narayanan, et al. 2014). Image courtesy: C.Clark.

(b) Strong lensing

By studying the large samples of galaxies, astronomers spotted that very massive objects in the Universe are sometimes found to reside between a distant source and the observer - in other words, they can act as "lenses" and bend the light which travels from the background source. Such effect is called gravitational lensing, and it can magnify and distort the image of the distant object (Kneib et al. 2011, Abdelsalam et al. 1998, Blandford et al. 1986). The gravitational magnification of fainter sources by foreground galaxies (and galaxy clusters) has been widely used and tested in FIR/submm astron-

omy, since it allows the unprecedented investigation of objects that would be otherwise undetected in most of surveys. Strongly lensed DSFGs are important for several reasons: (i) due to the luminosity boosting and increase of their detected angular size, the distant dusty galaxies can be studied down to sub-kpc scales (Enia et al. 2018). This precision is achieved in the last decade for sub-mm/mm selected sources across the peak of the cosmic star formation history (e.g. Negrello et al. 2017, Wardlow, Malhotra, et al. 2014, Swinbank, I. Smail, et al. 2010); (ii) the observed, lensed morphology is determined by the content and spatial distribution of the total (baryonic+dark) matter of the foreground galaxy; therefore, thanks to the unprecedented imaging possibilities at mm wavelengths, now provided by ALMA/NOEMA/SMA, gravitational lensing allows the detection of lower-mass sub-structures, and their abundance can be used to test the prediction of galaxy formation models (Kneib et al. 2011). As I will show later, the gravitational lensing has very important role in the discoveries of some of the most distant DSFGs (Strandet, Weiss, Vieira, et al. 2016).

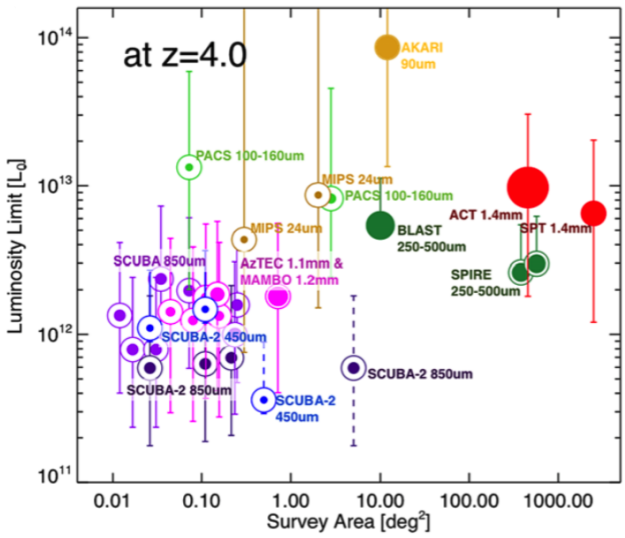

Figure 1.7.: Schematic representation of different FIR telescopes along with the *Herschel* space observatory. Plotted is area against sensitivity, in solar luminosities. Survey depth in solar luminosities is determined from the range of plausible SEDs while size of the circle represents beamsize (Casey, Narayanan, et al. 2014).

1.4.3. Number counts

One of most important goals when studying the galaxies is to unveil their physical nature. Since the DSFGs are very distant and often without clear counterparts at shorter wavelengths, studying their statistics gives us a valuable information about their evolution. Measurements of the number density of DSFGs detected in a cosmological survey per unit area, placed in different flux density bins can provide an insight into the evolution of the selected population of sources. Number counts are usually expressed in a differential form as dN/dS, describing the number of objects falling into a chosen flux bin, or in an integral form, $N(>S)$, corresponding to the total number of objects with flux densities above S. The observed differential counts are usually best fitted by either a Schechter-type function (i.e. Peng et al. 2010):

$$\frac{dN}{dS} = (\frac{N_0}{S_0})^{-\alpha} \exp(-\frac{S}{S_0}), \tag{1.7}$$

or a double power-law (i.e. M. Pannella et al. 2015):

$$\frac{dN}{dS} = (\frac{N_0}{S_0})^{-\alpha} \exp(-\frac{S}{S_0}); \;\; S \leq S_0, \tag{1.8}$$

$$\frac{dN}{dS} = (\frac{N_0}{S_0})^{-\beta} \exp(-\frac{S}{S_0}); \;\; S \geq S_0, \tag{1.9}$$

where N_0, S_0 and β are parameters of the fit.

In a flat Euclidean universe, which contains uniformly distributed sources, the number counts are expected to vary as $(\frac{dN}{dS}) \propto S^{-\frac{5}{2}}$. If the population of sources is evolving (e.g. their luminosity or number density changes with redshift), then the slope of the observed counts will deviate from the Euclidean value. Steep number counts can suggest that the number of luminous sources decreases over time. Recent observations indeed suggest very steep count slope for dusty DSFGs at high-redshifts (Koprowski et al. 2017, Asboth et al. 2016). Although the number counts from large IR surveys might seem easy to measure, it is actually very challenging considering the complexity of biases that affect their measurements (their analysis is in the heart of this Thesis, but see also the recent discussion in Bethermin et al. 2017 and Asboth et al. 2016). Shortly, the fluxes of selected sources should be de-boosted and the whole extracted sample has to be corrected for multiplicity and incompleteness (see the Monte Carlo procedure explained in Casey, Narayanan, et al. 2014).

Then, if we know the redshift distribution of selected sources, we can further convert

our measured number counts into a function $\Phi(L)$ describing the number of galaxies per unit luminosity and unit volume (Press et al. 1974). To investigate eventual evolution in an observed population, the luminosity function is usually determined separately in several different redshift bins, and their characteristic values are obtained from LF fitting in the chosen redshift range. Studies of the FIR luminosity function all show strong evolution of these parameters, which implies that the contribution of dusty galaxies to the total luminosity density increases towards higher redshift (Bethermin et al. 2017, Koprowski et al. 2017, Gruppioni et al. 2013, Magnelli, Lutz, et al. 2014).

1.4.4. Cosmic star formation history

The stars that are formed within galaxies do not have a constant rate of their production over cosmic time. The simplest example of such a claim is our own Milky Way. Today we know that the stars in our Galaxy have very different ages, with the oldest stars ageing around 12 billion years, and the youngest ones are being presently born (e.g. the fampus stellar nursery known as Orion nebula, with the estimated age of around 3 millions of years). We can directly observe this evolution chasing the objects at high redshift, with very high SFRs. The difference of their colours compared to those galaxies observed locally is a result of star-formation processes and an ageing of the stellar population. An efficient way to address some essential questions in galaxy formation and evolution related to stellar content is via panchromatic modelling (from UV to IR and radio wavelengths) of the stellar emission history in the Universe. Some of these questions are: What is the fraction of the luminous baryons observed today that were placed in galaxies at early times?; What is the physical role of dust in following the star formation events in the distant Universe? (see P. Madau et al. 2014). The better quantify the evolutionary changes of the stellar build-up over cosmic time, astronomers are now able to estimate so-called "star formation rate density" (SFRD), defined as the total star formation occurring per unit time and volume at a given epoch (P. Madau et al. 2014, Speagle et al. 2014, Lutz 2014).

The standard way in determining the SFRD of galaxies is by considering the rest-frame UV selected galaxy samples (see e.g. Bouwens et al. 2007, Piero Madau et al. 1996). This is because the galaxy emission in the UV is dominated by young, short-lived, very massive stars, thus assumed to be a great SFR calibrator (Kennicutt 1998, Buat, Giovannoli, et al. 2010). There are numerous data sets that can be combined in order to

study a large number of UV-selected objects over most of the galaxy evolutionary time, from $z = 0$ to $z = 11.1$ (the later is the redshift where the most distant known source has been detected (Oesch et al. 2016). However, as it has been already noted, the UV light is heavily absorbed in the most massive galaxies that contain a substantial amount of dust (e.g. Fujimoto, M. Ouchi, T. Shibuya, et al. 2017, Faisst et al. 2017, Buat, Noll, et al. 2012). The main line in overcoming this problem is to directly detect the dust re-processed UV radiation. The bottle between UV- and IR-tracers was following the first estimates of SFRD, back in 1996: S. J. Lilly et al. 1996 and Piero Madau et al. 1996 calculated the SFRD based on UV-data available at that time, applying very simplistic correction for the contribution of dust. Their results were soon after found to suffer from significant underestimation, mostly due to the missing contribution of dusty galaxies (Rowan-Robinson, Mann, et al. 1997). This debatable start of SFRD estimates clearly illustrated how important are IR surveys, and in the last decade a large number of them focused on determining the contribution of DSFGs to the cosmic SFRD. The later studies bring the more accurate estimates and the good overall agreement between the UV- and IR-derived SFRDs, particularly for $z \sim 2 - 3$, but there is still no consensus about their ratios at largest distances, since the most of the data are still available through the UV, but not at FIR wavelengths (e.g. Lutz 2014, Rowan-Robinson, S. Oliver, et al. 2016).

With the launch of cutting-edge space mission such as *Herschel*, a new scientific possibilities are enabled. Since the *Herschel* selection offers a possibility to build flux-limited samples, galaxies with higher FIR luminosities can be detected to greater distances than fainter sources. However, the expected contribution of fainter galaxies is significant, so the derived SFRD critically depends on how deep and how far the IR luminosity function (LF) can be explored. This is vital, since the redshift evolution of LFs should be properly constructed prior to determining the SFRD. The IR luminosity function is usually computed by the $1/V_{\rm max}$ method (Schmidt 1968, Gruppioni et al. 2013). This $1/V_{\rm max}$ method is non-parametric and does not require any assumptions on the shape of LF, but derives the LF directly from the available data. In this method the maximum redshift is the one at which a source with luminosity L_{IR} would still be detectable based on the flux limits of the given observational survey (see e.g. Schmidt 1968, Koprowski et al. 2017). Since $1/V_{\rm max}$ method does not provide any functional shape on LF, to describe the continuous form of LF the astronomers often fit the data with Schechter function which is given in the form: $\Phi_{sc}(L, z) = \Phi_\star (L/L_\star)^\alpha \exp(-L/L_\star)$. Here $\Phi_\star$ is the normalisation parameter, α is the faint-end slope, while $L_\star$ is the luminosity that

disentangle between the power-law and the exponential fit. The luminosity functions can be further used to calculate the evolution of the dust-obscured SFRD (see Kennicutt and Evans 2012 and Kennicutt 1998):

$$\mathrm{SFR_{IR}}(z) = K_{\mathrm{IR}} \times L_{\nu}(z)_{\mathrm{IR}} \tag{1.10}$$

Here , $L_{\nu}(z)_{IR}$ is defined as the IR co-moving luminosity:

$$L_{\nu}(z)_{IR} = \int_{L_{\mathrm{lim}}}^{\infty} L\phi(L,z)\mathrm{d}L, \tag{1.11}$$

where L_{lim} is the limiting luminosity of the survey at the given redshift. The commonly used conversion factor is given as (Kennicutt and Evans 2012): $\mathrm{SFR_{IR}}(M_{\odot}\, yr^{-1}) = 1.71 \times 10^{-10}\, L_{IR}\, (L_{\odot})$. As I will explain later in the text, the shape of the IR luminosity function is poorly constrained if compared to the rest-frame UV luminosity function of galaxies (see Koprowski et al. 2017, Casey, Zavala, et al. 2018). To fully investigate is LF of a certain population evolves with redshift, galaxies should be placed in different redshift bins. The IR luminosity functions estimated for galaxies at high redshift differ at both the faint and bright end, and such difference depends on the data and selection functions that are used to probe the given population. At the fainter end, the available data are frequently incomplete, and thus rarely constrain the slope of the LF. This is a prominent issue when investigating the evolution of population of dusty galaxies at high-z. Because of this, it is common to perform extrapolation of a faint-end slope based on measurements at lower redshifts. However, such extrapolations are subject of large and uncertain estimations of total IR luminosity densities (Grazian et al. 2015, Asboth et al. 2016). Due to incomplete constraints on the shape of IR LF, more recent studies adopt a continuous double power law and a broken double power law fit to data, with slopes that show some redshift dependence (Casey, Zavala, et al. 2018).

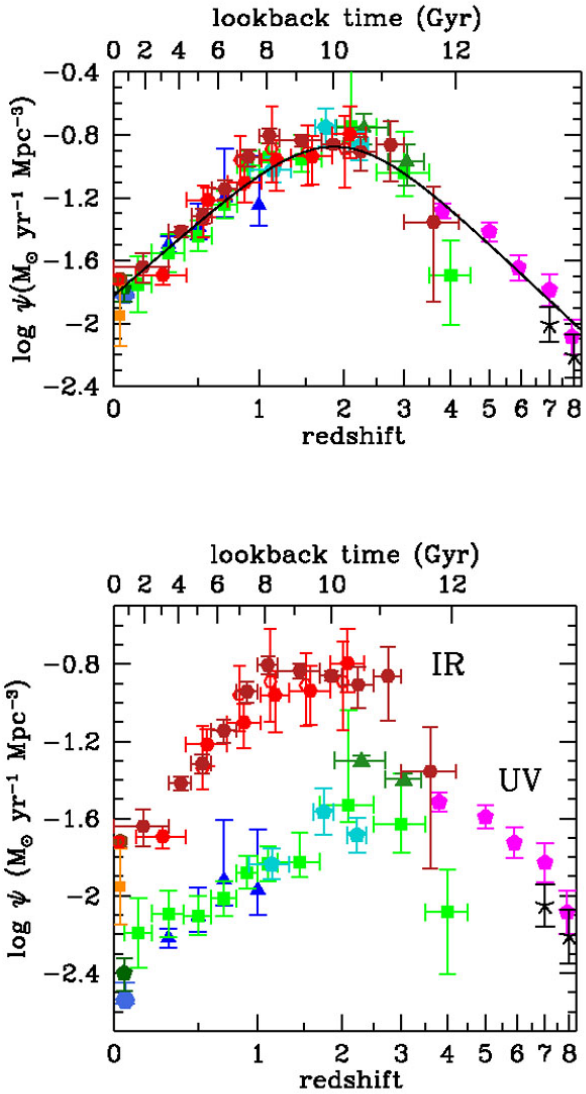

Figure 1.8.: Star formation rate density of the Universe at different redshifts - the data compiled until 2014 (P. Madau et al. 2014). The top figure shows the best fit to a range of datasets in the infrared, as well as UV data corrected for dust attenuation, while the lower figure shows the IR and the dust-uncorrected UV estimates.

Conducting the comprehensive analysis of a largest sample of available multiwavelength datasets (from UV to IR and submm), P. Madau et al. 2014 showed that there is a general consensus in placing the peak of star formation activity in the Universe around $z \sim 2$. The studies also agree there is a declining trend towards higher redshifts. They, however, do not agree about the level of this decline. While some studies predict sharp decrease of nuclear star-formation activity above $z > 4$ (e.g. Koprowski

et al. 2017), stating the UV-estimates are others are much more optimistic and claim that level of dust-obscured star-formation at $z > 4$ is only mildly below the global peak (Rowan-Robinson, S. Oliver, et al. 2016). Additionally, it is also stated that the majority of star-formation activity happens in galaxies that reside in the main sequence of star-forming galaxies (e.g., Schreiber, Pannella, R. Leiton, et al. 2017, Elbaz, Leiton, et al. 2017, M. Pannella et al. 2015). At a given stellar mass, the typical SFR of galaxies belonging to MS dramatically evolved through the cosmic time, continuously going to the lower area of the MS plane. Such a "downhill" of star-forming activity makes that formerly starbursting galaxies reach the values which are order of magnitude below relative to their positions at $z = 2$ (Schreiber, Elbaz, Pannella, Ciesla, T. Wang, Koekemoer, et al. 2016, Grazian et al. 2015). This transition can be explained either by a progressive depletion of molecular gas reservoirs (e.g., Lee et al. 2017, Tacconi et al. 2008) together with an additional decline of the star-formation efficiency over the same period of time (e.g. Schreiber, Pannella, Elbaz, et al. 2015, Murphy et al. 2013).

The situation at high-redshifts, especially at $z \geq 4$ is still much less clear. This is mostly due to limited data samples which is the consequence of instrumental limitations and lack of well-defined selection techniques for producing the suitable data samples. Over the past decade, most of our knowledge of the early Universe has been based on the analyses of stellar activity observed in the rest-frame UV-to-optical. The HST selected sources allow extragalactic astronomers to detect galaxies even into the re-ionization period (e.g. Hoag et al. 2018, Inoue et al. 2016, Oesch et al. 2016). Nevertheless, as noted above, in the absence of direct mid-IR or FIR measurements, accurately correcting for interstellar dust absorption remains a long-standing matter of contention.[e]

Until recently, very small number of $z > 4$ DSFGs were known (e.g. P. Cox et al. 2011, Weiß, C. De Breuck, et al. 2013), and due to the lack of statistically significant data sets, the accurate estimates of the luminosity function at $z > 4$ were not possible. To overcome the problem of noise related to high source density, stacking methods are commonly applied in order to derive the average SFR and molecular gas mass from existing data sets (e.g., Schreiber, Pannella, Elbaz, et al. 2015, Béthermin, Daddi, Magdis,

[e]Because the dust grains efficiently absorb optical/UV stellar light, it is therefore natural to expect a tight relation between the UV and the IR produced by this interplay. Such correlation is called the IRX-β relation (e.g. Meurer et al. 1999, Álvarez-Márquez et al. 2016, Calzetti et al. 2000, D. Narayanan et al. 2018). However, it is highly uncertain at high redshifts (D. Narayanan et al. 2018, Ferrara et al. 2017) and for galaxies at $z > 4$ cannot be reliable way of estimating their young stellar content (Spitler et al. 2014).

Lagos, et al. 2015, Magdis, Daddi, et al. 2012). The main problem with stacking technique lies in the fact that it needs to be carefully corrected for the effect of source blending and clustering, which is not a trivial task (e.g. Béthermin, Daddi, Magdis, Lagos, et al. 2015). The situation has been changing in the last two years. *Herschel* cosmological surveys in combination with SCUBA-2 follow ups reviewed the estimations of a SFRD for large data sets of DSFGs selected to be at $z \geq 3-5$ (Bourne, L. Dunne, et al. 2016). However, if we want to select candidate galaxies that are even more distant, we can quickly start to suffer from intricate biases which can affect estimated intrinsic SFRs of distant DSFGs. The careful treatment of systematic biases is thus very important while making big datasets with candidate high-z DSFGs (Bethermin et al. 2017, Mancuso et al. 2016). I will introduce the wide range of observational effects in the next Chapter, and investigate them in detail within the Thesis.

1.5. Population of high-z DSFGs: overview and challenges

What do we learn from existing studies of DSFGs?

The observed population of massive, dusty high-z galaxies are some of the most powerful star-forming sources across the cosmic history, having prodigious SFRs between a few hundred to even thousands solar masses per year (Fudamoto et al. 2017, Narayanan et al. 2015, Michałowski, C. C. Hayward, et al. 2014, Riechers, Bradford, et al. 2013). Thanks to the fact that numerous and detailed follow-ups were carried out during the last two decades, we learn that DSFGs are typically high-redshift galaxies, with their redshift peaking at $z \sim 2.2$ (Miettinen et al. 2015, Swinbank, J. M. Simpson, et al. 2014, Pearson, Eales, et al. 2013, Michałowski, J. S. Dunlop, et al. 2012). They have large IR luminosities ($> 10^{12} L_{\odot}$), and large gas reservoirs ($> 10^{10} M_{\odot}$, e.g. J. A. Zavala, I. Aretxaga, et al. 2018, Bothwell, Ian Smail, et al. 2013, Swinbank, Ian Smail, et al. 2012). It is also generally accepted that the ISM of DSFGs is mainly turbulent which might reflect the complexity connected to the number of physical processes related to galaxy assembly and the associated gas heating (e.g. galaxy merging, gas accretion, disk fragmentation, AGN/SF feedback). It is also widely thought that such immense activity only last through restricted time period, until the available gas reservoirs become fully depleted (Calistro Rivera, Hodge, et al. 2018, Magdis, Rigopoulou, E. Daddi, et al. 2017). For this reason, the monstrous IR emission seen in DSFG is thought to be rather short with typical time scales of ~ 100 Myr, making this galaxy population rare

in the local universe. This is reflected through its number density - the intrinsic volume of the DSFG population increases by 3 orders of magnitude from $z = 0$ to $z = 2.5 for f$ (Béthermin, Daddi, Magdis, Lagos, et al. 2015).

To address the nature of the large dust-obscured star formation seen in distant DSFGs, and consequently probe the formation and evolution of the most massive galaxies, recent studies use advent of ground based interferometric facilities i.e. ALMA, NOEMA and SMA. These are offering astronomers to map high-z DSFGs with angular resolutions of $< 0.3''$. As a consequence, some ALMA studies have reported effective radii $R_e \sim 0.3 - 3$ kpc (Oteo, Ivison, Negrello, et al. 2017, Ikarashi, Ivison, Caputi, I. Aretxaga, et al. 2015, Hodge, Carilli, et al. 2013). The radii of DSFGs observed with ALMA are small compared to expectations from studies which are based on radio continuum and/or molecular (mostly CO) emission (e.g. Calistro Rivera, Hodge, et al. 2018, Sharda et al. 2018, Karim et al. 2013). The compact submm sizes of DSFGs, including recent reports of the existence of sub-kpc scale starburst cores (Ikarashi, Ivison, Caputi, Nakanishi, et al. 2017), also suggests that the intense star-formation activity might be quenched by AGN, as observed in some luminous quasars (QSOs) (Maiolino et al. 2012). These morphology analyses should be taken with caution, since it has been found that dusty continuum sizes in DSFGs are very dependent on the data analysis and weighting schemes applied in order to create the interferometric maps (Hodge, Swinbank, et al. 2016). In addition, the most distant systems ($z > 4$) detected with *Herschel* are found to share variety of dust continuum morphologies, resembling from mostly smooth disks with extended star formation to more compact sources, isolated and interacting (Riechers, Leung, et al. 2017). All these findings state that care must be exercised when extrapolating morphological properties of dust continuum observations to conclusions about the molecular gas phase of the ISM. This is somewhat in contradiction to the recent findings from state-of-the art zoom-in simulations (Liang et al. 2018). They suggest that single-band FIR/submm techniques can reliably constrain the molecular ISM masses of both main-sequence (MS) and starburst (SB) galaxies.

1.5.1. Hunting the large number of DSFGs at $z > 4$

Methods

Optical/near-IR selection techniques commonly employed to isolate distant DSFGs in large quantities have revealed some individual examples of massive starbursts out to

$z = 5.3$ (Capak et al. 2011). Nonetheless, as mentioned earlier the dust extinction leads to an effective bias against systematic selection of the most massive, dusty galaxies at those wavelengths. At the same time, deep blank-field ALMA campaigns (which were not based on colour pre-selection, e.g. J. S. Dunlop et al. 2017, Walter et al. 2016), have failed to yield a population of $z > 4$ dusty sources.

The selection of $z > 4$ DSFGs is now routinised with use of deep large-area surveys (e.g. for areas larger than 10 deg^2) at FIR and submm wavelengths with the South Pole Telescope (SPT, Vieira et al. 2013, Strandet, Weiss, Vieira, et al. 2016) and *Herschel*. The major trade-off following these selections is that selection based on bright millimetre flux shows a very broad redshift distribution ($1.1 < z < 6.9$, Weiß, C. De Breuck, et al. 2013, Strandet, Weiss, C. De Breuck, et al. 2017). Additionally, SPT observations are taken at just one wavelength and may be unrepresentative for the whole dusty population of the most massive galaxies in the early Universe. The prime advantage of hunting $z > 4$ galaxies with *Herschel* is that large surveys can probe the peak of the dust-emission SED in high-redshift galaxies, making it suitable for colour-based selection. Considering this, one of the most popular methods that has been applied last years, is based on drafting the *Herschel* sources with extremely red SPIRE colours, thus potentially very high-z candidates (Riechers, Bradford, et al. 2013, Strandet, Weiss, C. De Breuck, et al. 2017). However, even some exciting discoveries have been reported in the last decade (e.g. Miller, Chapman, et al. 2018, Oteo, Ivison, L. Dunne, et al. 2017, Riechers, Bradford, et al. 2013, Combes et al. 2012, P. Cox et al. 2011), the nature of source selection and follow-up make it difficult to draw any information on underlying population statistics. This highlights the importance of using very large *Herschel* surveys to find and systematically study these distant objects, both from observational and modelling sides.

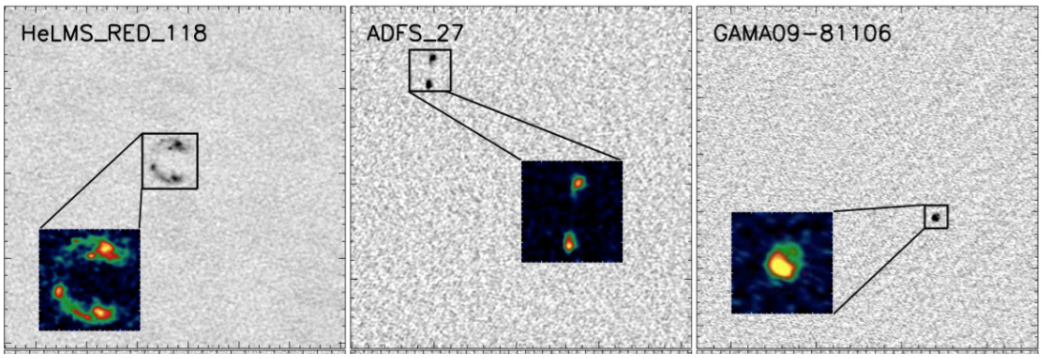

Figure 1.9.: Example of ALMA observations of some $z > 4$ candidates from the H-ATLAS survey. This example reveals variety of morphologies seen in systematically selected ultrared, SPIRE sources - lensing galaxy, possible interacting pair and isolated case. Image credit: Oteo, Ivison, Negrello, et al. 2017.

Confusion problem

A challenge in studying the properties of high-z *Herschel* DSFGs is the coarse angular resolution, especially related to the SPIRE passbands. The existing list of techniques which aim to de-blend the *Herschel* sources is extensive. The known de-blending methods make frequent use of different positional priors as input information (e.g. Elbaz, Hwang, et al. 2010, Swinbank, J. M. Simpson, et al. 2014, M. Béthermin, Dole, Cousin, et al. 2010, Roseboom, S. J. Oliver, et al. 2010). The most common positional information used for SPIRE source extraction and photometry is position of objects detected with *Spitzer*. For example, to compute SPIRE fluxes a new generation de-blending tool called XID+ (Hurley et al. 2017) employs Bayesian inference methods in combination with positional priors from resolved observations at 3.6μm and/or 24μm. As compared to maximum likelihood methods, this approach has an advantage by giving access to the full posterior probability (PDF) of the flux distribution. However it might still have some limitations, and certainly the most important one is inability to find the genuine high-z sources in situation where not all the priors are included in the initial list. Such a de-blending approach assumes that all *Herschel* sources are detectable in the deep 3.6μm and 24 μm images, and thus introduces a bias against fainter galaxies which fall below the detection limit (see Magdis, D. Elbaz, et al. 2011 for discussion). Additionally, there are several techniques that combine both positional and SED information (Pearson, Wang, Hurley, et al. 2018, T. P. MacKenzie et al. 2014, Liu et al. 2017). In this Thesis, I will present a new tool which combines positional prior information along with modelled SEDs in order to better constrain the SPIRE fluxes.

Investigating the source confusion in SPIRE images is important for answering on question: *What is the physical nature of source blending?* Cowley, Lacey, Carlton M. Baugh, et al. 2016 and Hayward 2013 examine the effect of the coarse angular resolution of the single-dish telescope beam (that means, the one used to produce FIR surveys) on the observed galaxy number counts. They make the prediction that a significant fraction ($\sim 45-50\%$) of the bright single-dish detected DSFGs are multiple sources blended into one source. The physical nature of this multiplicity, that means whether the galaxies are physically associated or only chance projections, has not been revealed yet and it is a matter of current debate in modern extragalactic IR astronomy.

1.5.2. Estimating the redshifts of DSFGs at $z > 4$

To study the nature and distribution of distant DSFGs we need to obtain their redshifts. The redshift acquisition of DSFGs is a difficult task due to significant extinction in the rest-frame UV and optical, where are most of the emission-line redshift indicators typically applied in the literature. In general, high-redshift DSFGs may be studied in detail with either photometric or spectroscopic redshift identifications. Photometric redshift estimation is observationally cheaper compared to spectroscopy, but less reliable. The constant increase of available multiwavelength data in deep extragalactic fields significantly improved this situation (e.g. Ilbert et al. 2009). Considering the IR wavelengths mainly inspected in this Thesis, an alternate form of photometric redshift determination is by using the shape (colour) of the FIR/submm SEDs (e.g. Aretxaga, Hughes, et al. 2007, Yuan et al. 2015). This is mostly applied in large statistical samples selected with SPIRE or SPT, for which optical-NIR counterparts are not available.

Another way to derive redshifts of DSFGs is via observations of atomic/molecular emission lines at submm/mm wavelengths which can be related unambiguously to the dusty continuum source (see Carilli et al. 2013 and Solomon et al. 2005 for comprehensive reviews). This method has only become competitive recently with the increased bandwidth of facilities such as IRAM 30m, ALMA, NOEMA and NIKA2 (see e.g. Weiß, Ivison, et al. 2009, T. Y. Li et al. 2016, Dessauges-Zavadsky et al. 2015). Most of observations of DSFGs at $z > 4$ are unresolved, and studies of the global molecular gas excitation play an important role in constraining their distances and average molecular-gas properties. Molecular gas is often inferred from the luminosity in ISM cooling lines (e.g. carbon-monoxide, CO). Targeting the molecular CO at high-z in the most luminous and

extreme starburst systems with interferometric observations, around 40 DSFGs at $z > 4$ have been already confirmed (e.g. Strandet, Weiss, C. De Breuck, et al. 2017, Fudamoto et al. 2017, Riechers, Leung, et al. 2017, Weiß, C. De Breuck, et al. 2013). In addition to ^{12}CO, there is also advantage of eventually detected O[III] line (Inoue et al. 2016) and carbon emission line. With the advent of ALMA, the O[III] line detected in infrared at 55 μm and 88 μm is frequently used as a redshift estimator. It originates from HII regions, and it is also valuable alternative way for studying gas-phase metallicities. The O[III] line is less affected by extinction compared to optical spectral lines, and in combination with some other fine structure transition lines such as N[II] it can be applied as diagnostical tool for very high-z galaxy metallicity (J. L. Wardlow et al. 2017, Rigopoulou et al. 2018, Hashimoto et al. 2018). The [CII] fine structure transition at 158 μm is the dominant cooling line of cool interstellar gas, and it is known as the brightest of all emission lines from DSFGs at high-z. It has been found that the line is barely affected by dust attenuation (Bothwell, Maiolino, et al. 2016, Papadopoulos et al. 2004, Lagache, Cousin, et al. 2018). There is a clear advantage of tracing the C[II], because at $z > 4$ the [CII] line is redshifted to the submm/mm wavelengths and becomes observable using ground based facilities such as ALMA. Apart from redshift confirmation, many useful physical parameters can be derived from this line, and there is a growing interest in using the [CII] as a probe of the physical conditions of the gas in galaxies, and as a SFR indicator (see Lagache, Cousin, et al. 2018).

1.5.3. The nature and evolution of high-z DSFGs

The space density of massive galaxies at high redshift is an important constraint on cosmological models as DM halos are growing rapidly and have to be massive and abundant enough to host them. Knowing the prevalence of dust-obscured star-formation is essential at $z > 4$, when the cosmic time becomes a compelling constraint on the physical processes involved in producing cosmic dust, metals and stars seen in galaxies.[f]

Dusty star forming galaxies at high-redshifts thus provide a unique inventory for investigating different ranges of topics. In the following I will highlight some of the most prominent of them.

[f] It has been confirmed observationally that the role of DSFGs within the overall galaxy population becomes more important with increasing stellar mass, and grows rapidly with increasing redshift (Martis et al. 2016).

(a) Evolutionary sequence of galaxies

Galaxy clusters with cores that are rich with early-type galaxies (ETGs, e.g. relatively passive ellipticals and lenticulars) are beacons for the densest regions in the DM distribution. In the local Universe, these galaxy clusters host the majority of ETGs, which harbour more than a half of the present-day stellar mass. Thus studying their cosmic evolution we can place invaluable constraints on models of galaxy formation (e.g. V. Springel 2005, Lacey et al. 2016, Narayanan et al. 2015). ETGs obey a tight colour-magnitude scaling relation, where magnitude equates roughly to $M_{\star}$. This is known as the "red sequence", in which more massive galaxies are usually redder having older stellar populations and less ongoing star formation (e.g. Bower et al. 1998, Baldry et al. 2004). The nature of that colour transformation, from blue, active star-forming systems, to red and passive structures is poorly understood as well as mechanisms which lead to star-formation shut-off, or quenching (see Conselice 2014 for a review). Furthermore, ETGs in local galaxy clusters appear redder (and thus more massive, since they follow the scaling relation) as their distance to the centre of the cluster decreases (Bernardi et al. 2006), the fact which is later used for the concept of "cosmic downsizing" (Chiang, Overzier, K. Gebhardt, et al. 2017, Cowie, Songaila, et al. 1996).

In local massive galaxy clusters the quenching effect can be brought either via process known as "ram pressure stripping" (e.g. Gunn et al. 1972) or by process called "starvation" (Larson et al. 1980, Elbaz, Daddi, et al. 2007, Gabor et al. 2010). By following the evolutionary picture which place massive structures in connection to more distant interacting systems (e.g. Philip F. Hopkins, Hernquist, et al. 2008), a simple question remains: *Are the most-massive ETGs which reside in the centres of galaxy clusters, actually remnants of high-z mergers ?* The large number of distant QGs have been recently observed at $z \sim 2-3$ (see e.g. Glazebrook et al. 2017, Gobat et al. 2012, Kriek et al. 2008). Because the stellar populations observed in the bulge of these QGs at $z \sim 2-3$ seem to have formed in a rapid way and at early cosmic times, their existence strongly suggests that intense star-formation events are not rare even in the early Universe. This evolutionary path points to DSFGs as the progenitors of compact QGs galaxies and large local ellipticals (e.g. Toft et al. 2014, Ivison, Lewis, et al. 2016). It additionally implies that massive DSFGs are common at $z \geq 4$ (e.g. Oteo, Ivison, Negrello, et al. 2017, Miettinen et al. 2015). It is worth to note here that the significant number of very high-redshift QGs posses a serious challenge to galaxy formation models. It requires a very bursty and efficient conversion of baryons from the hosting DM halos to stellar masses

at $4 < z < 7$. Simple scheme which describes the formation of elliptical galaxies from distant DSFGs is presented at Fig.1.10.

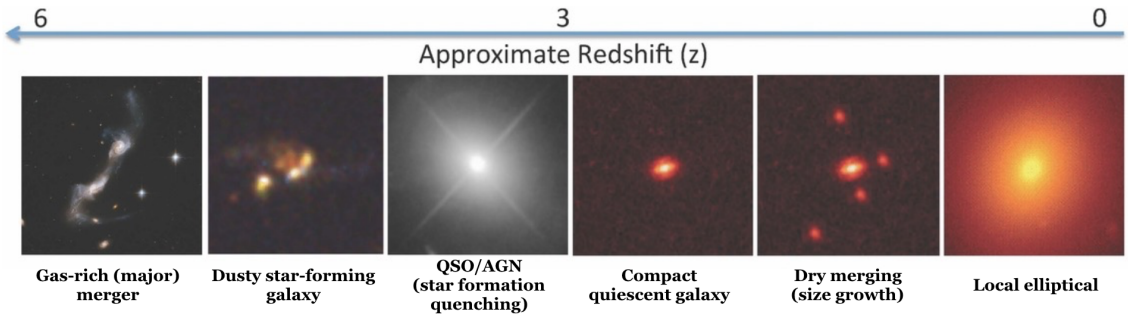

Figure 1.10.: Schematic representation of the development of elliptical galaxies (Toft et al. 2014).This graphic shows the evolutionary sequence in the growth of massive elliptical galaxies over 13 billion years, as gleaned from space-based and ground-based telescopic observations. The growth of this class of galaxies is quickly driven by rapid star formation and mergers with other galaxies; Image credit: NASA, ESA, S. Toft (Niels Bohr Institute), and A. Feild (STScI)

(b) Studying the environments of DSFGs

The DM halos with wide range of masses and redshifts exhibit different clustering strengths (Jing et al. 2007, Tinker et al. 2008). Because of this, by measuring the clustering signal of DSFGs we can obtain the information related to masses of the DM halos that DSFGs inhabit. This information is one of crucial constraints for evolutionary path of DSFGs, and it describes how their host-DM halos evolve with time. Therefore, observations of the early evolution of large scale structure are gateways for testing galaxy formation theories. Numerous observational efforts have been probed in order to identify distant cluster progenitors ("protoclusters"), usually defined as diffuse collection of haloes ("overdensities"). These halos are assumed to merge at some time of their evolution, and make the final large DM halo at very local redshifts.[g] The problem is that, as we approach the earlier cosmic times, the galaxies that are in protoclusters become difficult to distinguish from field galaxies due to the absence of a well-placed red sequence or a hot intracluster medium (Overzier 2016). Thus, the apparent sign for the presence of a distant protocluster is the relatively large abundance of galaxies and associated diffuse gas flocked in angular/redshift space. To find such a distant structures, the main

[g]This definition is widely used, but too simplistic, and in Chapter 6 I discuss the problem of clustering scales related to protocluster search. I refer to Muldrew et al. 2015 for a very nice discussion about how we define a term protocluster.

techniques applied in observations are based on this observational trademarks (Miley et al. 2008, Steidel et al. 1998). Since it is found that extreme population of bright DSFGs appear to grow in the most massive DM halos, it has been recently pointed out that large collections of DSFGs can be probed as beacons of galaxy protoclusters (Chiang, Overzier, K. Gebhardt, et al. 2017, Overzier 2016, Hayward 2013). The coherent picture which connects brightest DSFGs and their DM halos is only partially supported by the most recent observations: the Universe's largest galaxy clusters likely built the most of their massive ($M > 10^{11} M_{\odot}$) objects in simultaneous, short-lived bursts, before being virialized structure. Such a conclusion emerges from copious datasets on $z > 2$ protoclusters and the characteristics of their members, star-forming systems and AGNs (Casey 2016). From the observational point of view, catching these structures during the peak time of their growth and stellar mass assembly is extremely challenging. It requires observational campaigns that are capable to unveil the massive and bright DSFGs, signposts of protoclusters, but also it requires wide enough surveys in order to capture the rarest objects. At present, very small number of such systems at $z > 4$ have been confirmed so far (Marrone et al. 2018, Pavesi et al. 2018, Oteo, Ivison, Negrello, et al. 2017, Hayward, Chapman, et al. 2018, H. Dannerbauer, Lehnert, Emonts, et al. 2017, Smolčić et al. 2017, Casey 2016,Combes et al. 2012, Daddi, Dannerbauer, et al. 2009). The large field and all sky surveys such as the *Planck* or *Herschel* are thus suitable for selection of distant clusters made by overdense DSFGs.

A sample of 2154 high-z candidate structures has been found using *Planck's* all-sky maps (Planck Collaboration, Ade, Aghanim, Arnaud, Aumont, Baccigalupi, Banday, Barreiro, Bartolo, Battaner, Benabed, Benoit-Lévy, et al. 2016). The full nature of these systems and their member galaxies is not fully confirmed, since more than 200 of them were reported overdense in DSFGs, but only two are spectroscopically confirmed to date. Negrello et al. 2017 studied the number counts of extragalactic sources expected from low angular resolution surveys such as *Planck*. They concluded that several luminous IR/sub-mm sources clustered on the scale of the instrument beam may actually be unresolved (or marginally resolved) dusty source. Their individual components could be either chance projections along the line of sight, or physically associated structure. Greenslade et al. 2018 and Clements, Braglia, Hyde, et al. 2014 have further demonstrated that some *Planck* sources indeed trace overdensities of DSFGs. Therefore the bulk of *Planck* compact and cold high-z candidates might resolve into high-z clusters or even protoclusters of DSFGs when they are examined with a higher resolution instru-

ment such as SPIRE. However, there is an open important question: how complete are tracers of DSFGs at all distances ? A seminal work related to this problem was done by Miller, Hayward, et al. 2015 who exploited a set of hybrid simulations investigating how DSFGs trace protoclusters. Because of their rarity, Poissonian noise causes significant scatter in the DSFGs overdensity at fixed DM clustering, and it is more prominent at lower redshifts ($z < 2.5$). This results suggest caution if we simply interpret that large-scale structures at high-z can be traced by any bright DSFG associations.

(c) Investigating the co-evolution between starbursts and supermassive black holes (SMBH)

As everything in the Universe, the co-evolution between stars and supermassive black holes (SMBHs) in galaxies is also shaped by complexity of different physical processes (gravitational effects, gas heating/cooling, SMBH fueling, AGN and stellar feedback). All these effects ranges within the scales from several parsecs to several tens of megaparsecs (Satyapal et al. 2017, Kocevski et al. 2015). The existing studies now agree that for MS galaxies star formation and SMBH accretion are intrinsically linked (e.g. Philip F. Hopkins, T. J. Cox, et al. 2008). A sub-sample of bright DSFGs are also known to harbour monstrous SMBHs that are heavily dust-enshrouded (e.g. Trakhtenbrot et al. 2018). It is widely assumed that SMBHs are preferentially triggered as AGNs during later stages of galaxy mergers (see Fig.1 in Philip F. Hopkins, Hernquist, et al. 2008, Donley et al. 2018). A significant fraction of the IR luminosity of these galaxies can actually be driven by heating physical mechanisms, placed and raised in AGN, rather than being star formation dominated (see e.g. Decarli et al. 2017, L. Ciesla, Charmandaris, et al. 2015, Alonso-Herrero et al. 2013, Blain, Assef, et al. 2013, Casey, Berta, et al. 2012). In fact, there are variety of evidences which suggest that these galaxy may serve as precursors to luminous quasars (QSOs), and assist in finding the site of a rapid growth of central BHs. Thus, probing the AGN content of DSFGs provides essential limits on their evolutionary history. Recent investigations of star-formation-to-SMBHs relation, exploited uniqueness of combining ALMA and deep radio (VLA) data to study "in-situ" co-evolution at the peak epoch of galaxy assembly (Rujopakarn et al. 2018, Trakhtenbrot et al. 2018). In their study, Rujopakarn et al. 2018 have localised the sub-kpc sites of SMBH growth in distant ($z > 3$) galaxies, finding evidences for spatial connection with regions of intense, obscured star formation. In addition to this study, Rodighiero, Brusa, et al. 2015 investigated the connection between the star-formation

and SMBHs using large data sets of COSMOS galaxies at $1.5 < z < 2.5$, finding the great diversity of their star-forming properties and showing that the ratio between BH accretion rate and SFR of MS galaxies is mass dependent, contrary to some earlier works.

1.5.4. Are local (U)LIRGs and high-redshift DSFGs same?

Despite being representative population for the study of dusty galaxy formation and evolution, the detailed nature for a large number of DSFGs at $z > 4$ is severally limited by a combination of reasons: first, they are at high redshift and thus have small apparent sizes which requires follow-up with high spatial resolution Fujimoto, M. Ouchi, Y. Ono, et al. 2016, Oteo, Smail, et al. 2017, J. M. Simpson et al. 2014, Hodge, Carilli, et al. 2013); secondly, they are highly dust-obscured, meaning that they are extremely faint at rest-frame UV/optical wavelengths. Because of these reasons, in literature there exist copious number of examples which take advantage of analysing low redshift analogues of more distant DSFGs, in order to achieve the more detailed view of their physics (e.g. Oteo, Smail, et al. 2017, D. Sanders et al. 2004). With *Herschel* we got an unprecedented view of dusty properties of local IR-bright sources, complementing the detailed, multiwavelength view of individual, local dusty galaxies, which cannot be easily probed at largest distances even with the most powerful submm telescopes available. However, the question whether or not local ULIRGs are true analogues of more distant DSFGs is still under the extensive debate (see Casey, Narayanan, et al. 2014 for the review). Both the recent observations (Magnelli, Lutz, et al. 2014) and simulations (Somerville and R. Davé 2015, Davé et al. 2010) have suggested that the DSFGs are mix of SBs and massive star-forming galaxies, where the most luminous DSFGs are usually associated to major merger events, while fainter of them are being associated with turbulent, star-forming discs. There are still considerable uncertainties in the derived physical properties of DSFGs (e.g. Michałowski, J. S. Dunlop, et al. 2012, Schreiber, Elbaz, Pannella, Ciesla, T. Wang, Koekemoer, et al. 2016), which affects our perspective related to question how DSFGs are linked to the general picture of dusty galaxy evolution.

(U)LIRGs are extreme local sources, but generally found to be a very rare population in the local Universe, having a space density of several orders of magnitude lower compared to normal star-forming galaxies (D. Sanders et al. 2004). Follow-up observations (e.g. Lotz et al. 2011, Alonso-Herrero et al. 2013) show that vast majority of (U)LIRGs

are found in major disk mergers, and that the central few hundred parsecs (pc) of their nuclear regions harbour very large masses of gas and dust (Elbaz, Hwang, et al. 2010, Lotz et al. 2011, P. F. Hopkins et al. 2010, Casey, Narayanan, et al. 2014). Thus a natural question appears: if high-z DSFGs are far more common than local (U)LIRGs, does this imply that interactions and major mergers dominate the SFRD at early cosmic times? The general expectation is that galaxy mergers were much more frequent in the past, because the Universe was overall more homogeneous: today, most of the structures that could merge have already did it. For example, Philip F. Hopkins, D. Croton, et al. 2010 predicts that major mergers (with a mass ratio of at least 1/3) occurred every 40 Gyr per a galaxy seen today, while this number falls down to every 4 Gyr if we consider the early Universe, at the time it was 10 Gyr ago - that means ten times more frequently. Similar trends were found in observations: Delahaye et al. 2017 reported that the fraction of bright galaxies in pairs is only 0.8% today, but was closer to 8% about 10 Gyr ago; a similar factor of ten difference. However, linking observed pair fractions with actual merger rates is difficult. While these numbers are corrected for chance galaxy projections, without having precise velocity measurements in hand, it is unknown what fraction of tidally interacting pairs will actually end-up in mergers.

Moreover, there are some recent evidences that complicates this discussion: by using 20 low–z DSFG analogs selected with criteria that their total IR luminosities and dust temperature match to those of the high-redshift DSFGs, Oteo, Smail, et al. 2017 found evidence that low–z DSFGs also are very diverse population. They have morphologies ranging from isolated sources resembling star-forming disks to systems in interaction or group of galaxies.

Considering the physical parameters that shape the SEDs of DSFGs, It is now widely accepted that there exist a redshift evolution of T_d of DSFGs. Magdis, Daddi, et al. 2012 were the first who proposed that the T_d of MS galaxies increases with the distance in the Universe, explaining the rising trend with correlation to the redshift evolution of the mean intensity of the radiation field which heats the dust. In similar manner, Béthermin, Daddi, Magdis, Lagos, et al. 2015 found an increase of T_d, extending this analysis to $z \sim 3.5$ by stacking on a stellar mass-selected sample ($M_\star > 2.1\times10^{10}h^{-1}M_\odot$) of galaxies derived from `ultraVista` data (O. Ilbert, McCracken, et al. 2013) in the COSMOS field. These findings suggest a break to the fundamental gas-metallicity relation (Mannucci et al. 2010), which connects gas metallicity to SFR and stellar/dust mass, found to be redshift independent for $z \leq 2$. As a consequence, such break has the effect of

reducing the gas metallicity (and the dust mass too) at a given stellar mass for $z \geq 2$. All this results in hotter dust temperatures, compared to what would be implied by simply extrapolating the gas-metallicity relation from lower redshifts (e.g Cowley, M. Béthermin, et al. 2017).

1.6. Can the observed number of high-z DSFGs be explained with physical models ?

Throughout the last decade, an extensive attention has been given to the studies of the formation of DSFGs and their DM halos by applying different classes of computing simulations. In general, the modelling of observed number of DSFGs related to density of DM halos depends upon three different parameters: (1) The fraction of DM halos containing a galaxy (or halo occupation rate), which is measured to be $\sim 40\%$ at $z \sim 5$; (2) The fraction of baryonic particles converted into stars (Hayward 2013; and (3) The amount of cosmic time that is required for the formation of stars after virialisation. The difference in both scale and leading physical processes between aforementioned hierarchical halo merging and star formation means that simulations cannot investigate both processes directly. Based on how they model the IR/submm emission, we can broadly split models in four groups : Semi-Analytical Models (SAMs), Cosmological simulations known as Smoothed-particle Hydrodynamics (SPHs) , Idealised/Hybrid Simulations and Phenomenological Models.

SAMs use analytical prescriptions for connecting the evolution of the molecular gas partitioned by the occupied DM halo. The baryons are discretely divided into several components such are gas halo, gas disc, stellar bulge etc, where each of these component has idealised spatial, thermal and velocity profile (Schaye et al. 2015, Vogelsberger et al. 2014). Some of the most known SAMs which are used to test the formation and evolution of DSFGs are: `GALFORM` (Lacey et al. 2016, C. M. Baugh et al. 2005), `Santa Cruz SAM` (Somerville, Gilmore, et al. 2012), `L-GALAXIES` (Henriques et al. 2015, V. Springel 2005, D. J. Croton, Volker Springel, et al. 2006), SAGE (D. J. Croton, Stevens, et al. 2016) and GAS (Cousin et al. 2016). SAMs generally treat many physical processes like star formation, stellar feedback or galaxy merging, using assumptions that differ considerably amongst SAMs, even though all these models are fine-tuned to match key observational parameters.

SPHs (e.g. Narayanan et al. 2015, Schaye et al. 2015, Volker Springel et al. 2018, Vogelsberger et al. 2014, Davé et al. 2010, V. Springel 2005) simultaneously solve the equations of gravity and hydrodynamics for DM, gas and stars. SPHs can calculate the anisotropic distribution and gas flows in unprecedented details and with fewer list of applied approximations than SAMs, and thus provide detailed predictions for the internal structure of DM halos and galaxies, rather than just their global properties.

As a complementary method to SPHs, a number of studies have also explored the formation of DSFGs via idealised/hybrid simulations (Hayward, Desika Narayanan, et al. 2013). The name of this group of models reflects the fact that galaxy baryons have been initialised with idealised conditions. These are generally disk galaxies, or mergers between two disks. The advantage of idealised/hybrid simulations over SAMs and SPHs is their relatively high resolution (a few-100pc). In order to infer cosmological statistics from idealised/hybrid simulations, Hayward, Desika Narayanan, et al. 2013 combined the submm duty cycles as a function of galaxy mass and merger ratio. They did not model the DSFG population in an "ab initio" way, but make the physical properties to be consistent with observations. To model the dusty SED of DSFGs, they apply Monte Carlo radiative transfer method, and reached the good agreement with the observed redshift distribution of distant DSFGs. However, the model failed to explain the observed number of most massive DSFGs at $z > 4$ (Hayward, Desika Narayanan, et al. 2013).

The models listed above are complementary, and have their own benefits and drawbacks. SAMs and idealised/hybrid simulations are quite flexible, requiring a relatively modest computational time in comparison to SPHs which are much more time-consuming. The SPHs may catch the full complexity of gas-stellar dynamics in a way that SAMs cannot, which is serviceable when studying, for example, the smaller details of gas accretion onto massive galaxies. They ar still very limited by the high computational cost which is mandatory if one wants to resolve very small scales over larger cosmological volumes.[h] Concerning idealised/hybrid models, they are unlike SPHs or SAMs in that they cannot be evolved forward to infer the properties of the descendants of high-z DSFGs. All in all, the models are found to have some remarkable agreements between the statistical properties of model DSFGs (e.g. they are able to form galaxies with specified luminosities, and match their number density), but are otherwise unable to simultaneously match

[h] It has been pointed out only recently that SPHs have reached sufficient volume to make precision predictions for clustering on cosmologically relevant scales and to reproduce some of the fundamental observations of the local galaxy population (Schaye et al. 2015, Volker Springel et al. 2018).

some physical properties such are SFRs, gas fractions and environments (Narayanan et al. 2015). More specifically, most of simulations cannot reproduce the observed number of most massive DSFGs at $z > 4$ with the use of known physics. As an example, Popping et al. 2017 recently probed new recipes in SAMs in order to track-down the dust content of galaxies from $z = 0$ to $z = 9$. They find that most of SAMs can successfully explain the trends between stellar- and dust mass in the local Universe, but in the same time fail to reproduce high dust mass as found in galaxies at $z \sim 5 - 6$. Some studies refer this to eventual "impossible early galaxy problem" (see e.g. Steinhardt et al. 2016). There are several lines of investigations proposed to overcome this issue (Safarzadeh, Lu, et al. 2017, Mancuso et al. 2016, Narayanan et al. 2015 and Lacey et al. 2016). Nonetheless, there is a sharp disagreement between proposed solutions, reflected mostly on number of major mergers and use of initial stellar mass functions. As an illustration, Hayward, Desika Narayanan, et al. 2013 concluded that oppositely to the conventional claims, brightest DSFGs are not merger-dominated starbursts. The same authors found that the observed number counts are affected by observational (multiplicity) effects, and do not support models which blindly use top-heavy IMF to describe existence of distant DSFGs. Since results of the simulations strongly depend on the wide range of initial conditions, more observational constraints from star formation activity at different epochs are needed to fine-tune these models and to properly determine the initial conditions.

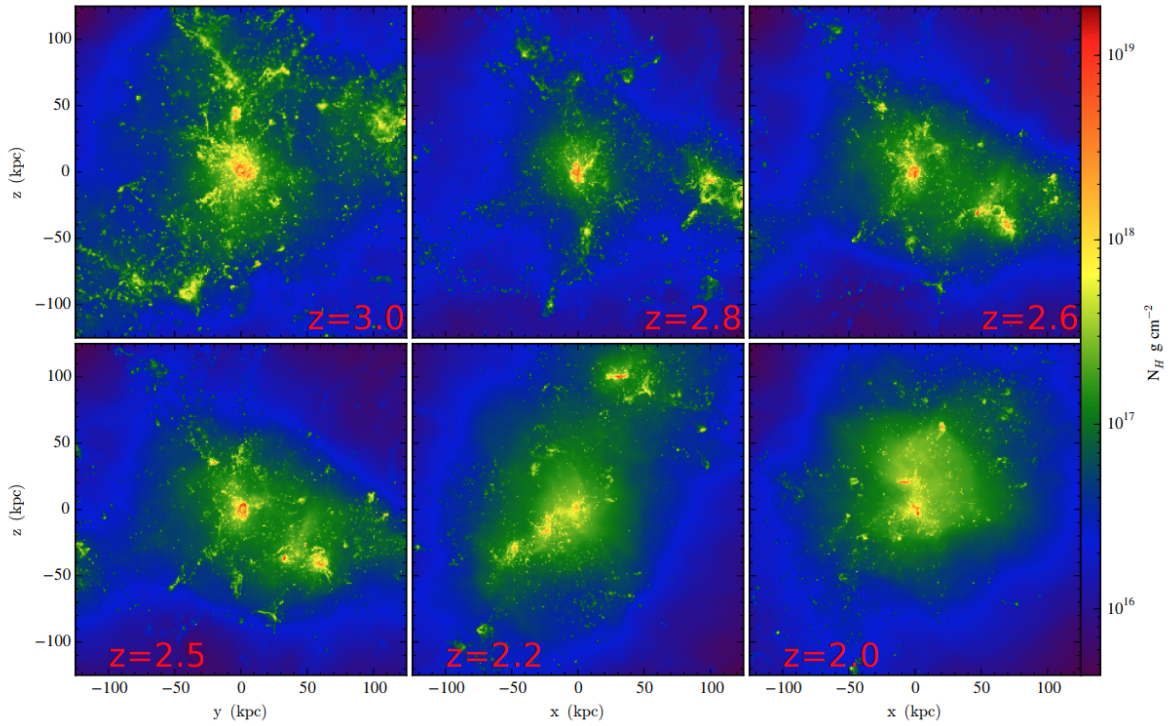

Figure 1.11.: DSFGs seen in hydrodynamical zoom galaxy simulations utilising the new code GIZMO (Narayanan et al. 2015). Surface density projection maps of 250 kpc region around central dusty, star-forming galaxy between redshifts $z \approx 2-3$. The dust emission region probed in surveys typically encompasses a central galaxy in a massive halo that is undergoing a protracted bombardment phase by numerous dark matter sub-halos. Some of brightest DSFGs arise from numerous galaxies within the beam in a rich environment (bottom right panel). Image credit: Narayanan et al. 2015

As an alternative to aforementioned three groups of models, there are also phenomenological (that means, not being *ab initio*) models of galaxy formation and evolution (Franceschini et al. 2010, Béthermin, Daddi, Magdis, Sargent, et al. 2012, Cai et al. 2013).These models (commonly refer in literature as "*backward evolution models*") are designed to infer constraints on the prevalence and characteristics of the DSFG population at $z > 4$ using bulk statistical measurements. They are built directly from assumptions of the IR galaxy luminosity function and from known characteristics of averaged SEDs. The new generation of these models fairly well interpret the multiband IR/submm number counts, but due to different modelling prescriptions there are significant differences according to the predicted redshift distribution of DSFGs and their flux correlations in the IR/mm bands (Cai et al. 2013, Schreiber, Elbaz, Pannella, Ciesla,

T. Wang, Koekemoer, et al. 2016, Bethermin et al. 2017, Mancuso et al. 2016, Casey, Zavala, et al. 2018). Additionally, it has been found that galaxy clustering has very important impact on the observed statistics of DSFGs at high-z ($z > 3 - 4$). Namely, Cowley, Lacey, Carlton M. Baugh, et al. 2016 and M. Béthermin, Kilbinger, et al. 2014 show that the impact of clustering on the extraction of sources from confusion-limited *Herschel* surveys might be actually stronger than initially thought. Following these findings, some models aimed to incorporate physical clustering (e.g. Bethermin et al. 2017, Hayward, Desika Narayanan, et al. 2013). To do so, they apply so-called sub-halo abundance matching technique (Conroy et al. 2006, Simha et al. 2012)[i] to populate the DM halos of a light cone which is constructed from the large volume cosmological simulations such as `Bolshoi-Planck` (Rodríguez-Puebla et al. 2016) or `Multidark` (Prada et al. 2012). The main strength of those phenomenological models is that they are suitable to easily generate mock catalogues of galaxies over larger volumes, which on the one hand can be compared to observational data to test the model assumptions and constrain the model parameters, and on the other hand, can be used to interpret statistics from large cosmological surveys. This method is advantageous over other similar methods since it is initiated in observational data, but the main uncertainty is whether locally-calibrated "averaged" SED templates can be applicable to variety of galaxies at the same luminosity at high-z (see the discussion in Cowley, M. Béthermin, et al. 2017).

1.7. Thesis outline and big questions

One of the main goals of this Thesis is to assemble candidate $z > 4$ galaxies detected in a large area survey observed by *Herschel*-SPIRE and to examine the statistics and nature of these sources. Another important goal of my work is shedding a new light on investigation of environments of high-z DSFGs. In the Thesis I attempt to address and answer on variety of specific questions. These questions are in the limelight of following chapters:

- **How to take advantage of large Herschel surveys, and use them to systematically select the most massive galaxies at very high redshifts ($z \geq 4$)? (Chapter**

[i](Subhalo abundance matching assumes that one (sub)halo property, such as peak circular velocity, determines properties of the galaxy hosted in each (sub)halo such as its luminosity or stellar mass. This assumption implies that the dependence of galaxy luminosity functions and the galaxy stellar mass function on environmental density is determined by the corresponding halo density dependence.

2) I create a novel selection algorithm in order to substantially increase the number of candidate DSFGs at $z \geqslant 4$ and explain their statistics (Donevski et al. 2018, A&A, 614, A33). To overcome the source confusion problem, I introduced prior-based source extraction linked with the SED modelling. The code (`MBB-fitter`) that I extensively tested for this purpose is developed by Frederic Boone and HLS team. I use the code for the source photometry. I further defined model-based selection function to make a census of DSFGs with red SPIRE colours, so-called "$500\,\mu$m-risers".I applied this novel selection approach to the *Herschel* Virgo Cluster Survey field (HeViCS, Davies, Baes, et al. 2010), the deepest contiguous 55 deg^2 field observed by *Herschel*.

- **How to accurately infer the statistical properties of "$500\,\mu$m-risers"? (Chapter 3)** The novel selection algorithm I implemented in HeViCS led to the selection of some of the most luminous DSFGs expected to lie at very high-redshifts ($z > 4$). I present different methods in order to estimate distribution of photometric redshifts of 500μm-risers along with their total IR luminosities and colour-flux distribution. By comparing our findings to other similar studies, I highlight the importance of carefully de-blending SPIRE-selected high-z candidates. To make statistical constraints of selected high-z candidates in the context of galaxy evolution, I calculate differential number counts of 500 μm-risers. Throughout this Chapter I extensively discuss how our selection relates to methods implemented in other studies and how and why they differ. I analyse which category of sources might potentially be missed when applying different techniques to find 500 μm-risers in wide extragalactic *Herschel* fields.

- **What challenges the use of red Herschel sources to constrain models ? (Chapter 4)** To put our method in the proper context of galaxy evolution and to fully understand the tension between observations and models introduced in previous Section, it is thus vital to investigate the variety of observational biases. Accurately correcting the selected number density of 500 μm-risers for all the observational effects has been found to be an intricate task (e.g. Cowley, Lacey, Baugh, and S. Cole 2015, Bethermin et al. 2017). Hence I decide to produce an extensive analysis dedicated to this issue. I combine different phenomenological models of galaxy evolution and study how the selection biases shape the overall statistics and nature of 500 μm-risers. To understand the role of resolution effects and physical

clustering, I primarily used and tested the latest simulation made by M.Bethermin, which includes physical clustering, modelled by assigning abundance matching technique to populate the DM halos of a light cone with mock galaxies (SIDES simulation, Bethermin et al. 2017). To simulate the whole selection procedure of 500 μm-risers, I built mock SPIRE maps and filled them with sources that are sampled from different models. One important conclusion from this Chapter is that complex combination of noise, source clustering and strong lensing may have crucial impact on measured density and redshift distribution of "500 μm-risers". Such a quantified observational biases show that existing tension between models and observations can be at least partially solved, but small discrepancy is still present for unlensed DSFGs.

- **What is the nature of DSFGs selected with our technique?(Chapter 5)**

  With remarkably high median $L_{\rm IR}$ and $\rm SFR$, 500 μm-risers appear as one of the most extreme and rarest DSFGs at $z > 4$. In order to develop a better understanding of the population of 500 μm-risers, I aim to inspect the exact nature of these seemingly extreme systems. In particular, I use a model based approach, and analyse how the strong lensing, source multiplicity and small scale clustering shape observed properties of 500 μm-risers? To reach this goal, I again (as in Chapter 4) apply model-based approach. The work I have done in this Chapter was to employ realistic end-to-end simulations in order to explore all diverse effects that could impact estimated statistical properties (e.g $L_{\rm IR}$ and SFR) of individual objects.Analyses performed in this Chapter revealed that selection of 500 μm risers leads to the population of high-z sources: individual, likely isolated, unlensed starbursts, but also strongly lensed galaxies and physically connected pairs and groups of high-z DSFGs. I also use simulation made by M. Bethermin and quantify the effect of small scale clustering based on SPIRE colours. I further estimated the flux and lensing-corrected star formation rate density at $4 < z < 5$ with the "500 μm-risers".

- **How dense are the environments of 500 μm-risers? How can we resolve and characterise recently discovered candidate high-z overdensities selected with *Planck*? (Chapter 6)**

  Since high-z DSFGs appear to grow in the most massive DM halos, it has been recently claimed that associations of distant DSFGs can act as beacons of distant

galaxy protoclusters. In the first part of Chapter 6, I analyse environments of very high-redshift ($z > 4 - 6$) candidate DSFGs. I employ both simulations and observations to evaluate the density of regions centred around 500 μm-risers selected with our technique. As an addition to this, in `Appendix B` I present my external collaborative work in Subaru Hyper Supreme Camera (HSC)-Protocluster Survey Project (PI: Y. Matsuda). The project aims to understand the nature of DSFGs in some of the most distant protoclusters confirmed so far ($z > 5.5$), initially selected as strong overdensities of Lyman-α emitters (LAEs) (Tamura et al. 2009, Masami Ouchi et al. 2005). Results of my analysis are incorporated in one submitted proposal as co-I (PI: Fujimoto) and two scientific papers that I co-authored: Harikane et al. (submitted to ApJ) and Fujimoto et al. (to be submitted).

In the second part of Chapter 6 I focus my work on a new idea and tool which intends to characterise physical properties of galaxies in high-z protocluster candidate PHZ282, initially identified by *Planck*. I use a state-of-the art SED fitting and modelling code CIGALE, developed at LAM, and explore a wide range of galaxies detected in optical (NGVS, Ferrarese et al. 2012). Combining SED fitting and SED modelling methodologies, I estimate $L_{\rm IR}$ and star-forming properties for more than a thousand of galaxies that comprise one *Planck* detection. I show that there exist potentially significant concentration of physically associated DSFGs at $z > 2$ that are slightly below the SPIRE detection limit.

The results presented in this Chapter are used for my first-authored paper in preparation that I will circulate and submit this fall. I hope that with this new idea, we open a creative playground for better characterisation of candidate large scale structures selected from wide-field and all-sky surveys. This approach would particularly be useful in the era of big surveys expected in the nearest future (e.g. *Euclid*, SKA).

CHAPTER 2

Selection of 500 μm-risers in the *HeViCS* field

Table of contents:

2.1. Introduction

Large FIR surveys, such as those conducted with the *Herschel* Space Observatory, provide a unique opportunity to build a thorough census of DSFGs over cosmic time using a wide and blind search concept. The *Herschel* SPIRE photometer (Griffin et al. 2010) was often used for mapping large areas at wavelengths of 250 μm, 350 μm and 500 μm. *Herschel* surveys cover in total a huge area of more than 1000 square degrees. The redshift peak of most *Herschel*-detected sources matches with the time where galaxies have formed most of their stars ($z \sim 2$, Casey, Narayanan, et al. 2014, Pearson, Eales, et al. 2013, Lapi et al. 2011, Amblard et al. 2010).

However, until recently, only a small number of SPIRE selected DSFGs at $z > 4$ were known. Considering that the rest-frame dust SED of a galaxy typically peaks between 70 and 100 μm, the FIR colours of sources in *Herschel* SPIRE bands can be used to select candidate high-redshift dusty objects. To search for $z \gtrsim 4$ candidates, there is a growing interest to exploit the objects with red SPIRE colours[a], with rising flux densities from 250 to 500 microns (so-called "500 μm-risers"). Such galaxies should lie at $z \gtrsim 4$ unless they have dust temperatures that are notably lower than is seen in local FIR-bright analogues (Asboth et al. 2016, Yuan et al. 2015, Dowell et al. 2014, Roseboom, Ivison, et al. 2012).

If the selection of 500 μm-risers is free of contaminants such are blended systems and powerful non-thermal sources (e.g. QSOs), it is expected to provide us insight into extreme forms of obscured star formation at high-z. Recently, literature on dusty high-z galaxies has rapidly flourished, including a handful of serendipitously discovered 500 μm-risers (e.g. Daddi, Dannerbauer, et al. 2009, P. Cox et al. 2011, Capak et al. 2011, Combes et al. 2012, Vieira et al. 2013, Miettinen et al. 2015, Negrello et al. 2017). Since significant fraction of these sources were spectroscopically confirmed to lie at $z > 4$, it demonstrates that selecting those with red SPIRE colours is efficient way for identifying a tail extending towards higher redshifts ($z > 4$).

However, most of initial findings had serious shortcomings - being primarily focused on individual (usually strongly lensed) candidates, their overall statistics was limited to few objects with red SPIRE colours.

Even if *Herschel* offers a direct insight into the IR emission of objects at $z > 4$, there

[a] Throughout this thesis I adopt the following terminology regarding colours of IR-detected sources: red colours and red sources refer to 500 μm-risers, while "350 μm peakers" refer to galaxies having SED peak at 350 μm.

are critical limitations, such as sensitivity of detectors and low spatial resolution. These are responsible for biases such as source confusion. The sensitivity of SPIRE allows for the direct detection of only the brightest and thus rarest objects at the tip of the luminosity function (e.g. $L_{\rm IR} > 7 \times 10^{12} L_{\odot}$; Fudamoto et al. 2017, Casey, Narayanan, et al. 2014, Karim et al. 2013). The challenge now is using wide *Herschel* surveys to find and systematically study, large, homogeneous samples of rare, extremely luminous DSFGs.

To probe the larger number of 500 μm-risers, several recent works used map-search technique (Asboth et al. 2016, Dowell et al. 2014, Ivison, Lewis, et al. 2016). The study of Dowell et al. 2014 analysed maps of three different extragalactic fields observed as part of the HerMES (*Herschel* Multi-tiered Extragalactic Survey, S. J. Oliver, L. Wang, et al. 2010) program, while Ivison, Lewis, et al. 2016 and Asboth et al. 2016 probed much wider but shallower areas of the H-ATLAS (Herschel Astrophysical Terahertz Large Area Survey, Eales, Dunne, et al. 2010) and HeLMS (HerMES Large Mode Survey) fields, respectively (see Section 2.1 for details about field properties). These led to the discovery of the most distant DSFGs known to date: SPIRE selected HFLS3 at $z = 6.34$ (Riechers, Bradford, et al. 2013) and G09-83808 at $z = 6.02$ (J. A. Zavala, Montaña, et al. 2017, Fudamoto et al. 2017). The most distant 500 μm-riser is SPT0311-58 at $z = 6.902$ (Strandet, Weiss, C. De Breuck, et al. 2017), initially discovered with SPT. Furthermore, selecting the 500 μm-risers from lowest-resolution *Herschel* SPIRE-maps, Dowell et al. 2014 and Asboth et al. 2016) claimed significant underprediction of observed number of 500 μm-risers, finding one order of magnitude higher number density than predicted by the existing models (e.g. Hayward 2013, Béthermin, Daddi, Magdis, Sargent, et al. 2012).

In this Section I aim to introduce a slightly different approach to build a statistically significant sample of red, potentially $z > 4$ sources and estimate their observed statistical properties. The new selection scheme I propose is motivated by the size and the depth of the field I chose to investigate. *Herschel* Virgo Cluster Survey (HeViCS, Davies, Baes, et al. 2010) is deeper than the one used in the analysis of Asboth et al. 2016 and Ivison, Lewis, et al. 2016, and larger than the area analysed by Dowell et al. 2014. The novelty here is that our source selection method combines both positional and SED information to estimate source photometry. Due to the lack of higher-resolution *Spitzer* data that can be used as priors for source extraction, I decide to create selection function for candidate DSFGs at $z > 4$ relaying on SPIRE data only. To verify the method, I

extensively tested our approach with simulations.

2.2. Herschel Virgo Cluster Field

HeViCS is a fully sampled survey that covers a region centered at the Virgo cluster (Davies, Baes, et al. 2010, Davies, Bianchi, et al. 2012)[b]. It is one of the largest uniform Herschel surveys, and its main advantage is its sensitivity and uniformity of data. In this survey, $Herschel$ observed four overlapping fields (labelled as V1-V4) in fast parallel-mode. The total entire survey region is 84 square degrees, where 55 square degrees are observed at unvarying depth with eight orthogonal cross scans (see Auld et al. 2013 and Pappalardo, Bendo, et al. 2015 for more details). It is also worth to note that an innovative map-making process has been developed in order to remove all instrumental artefacts such as glitches, finite bolometer time response, electronic filtering and thermal drift (see Auld et al. 2013).

[b] http://www.hevics.org/

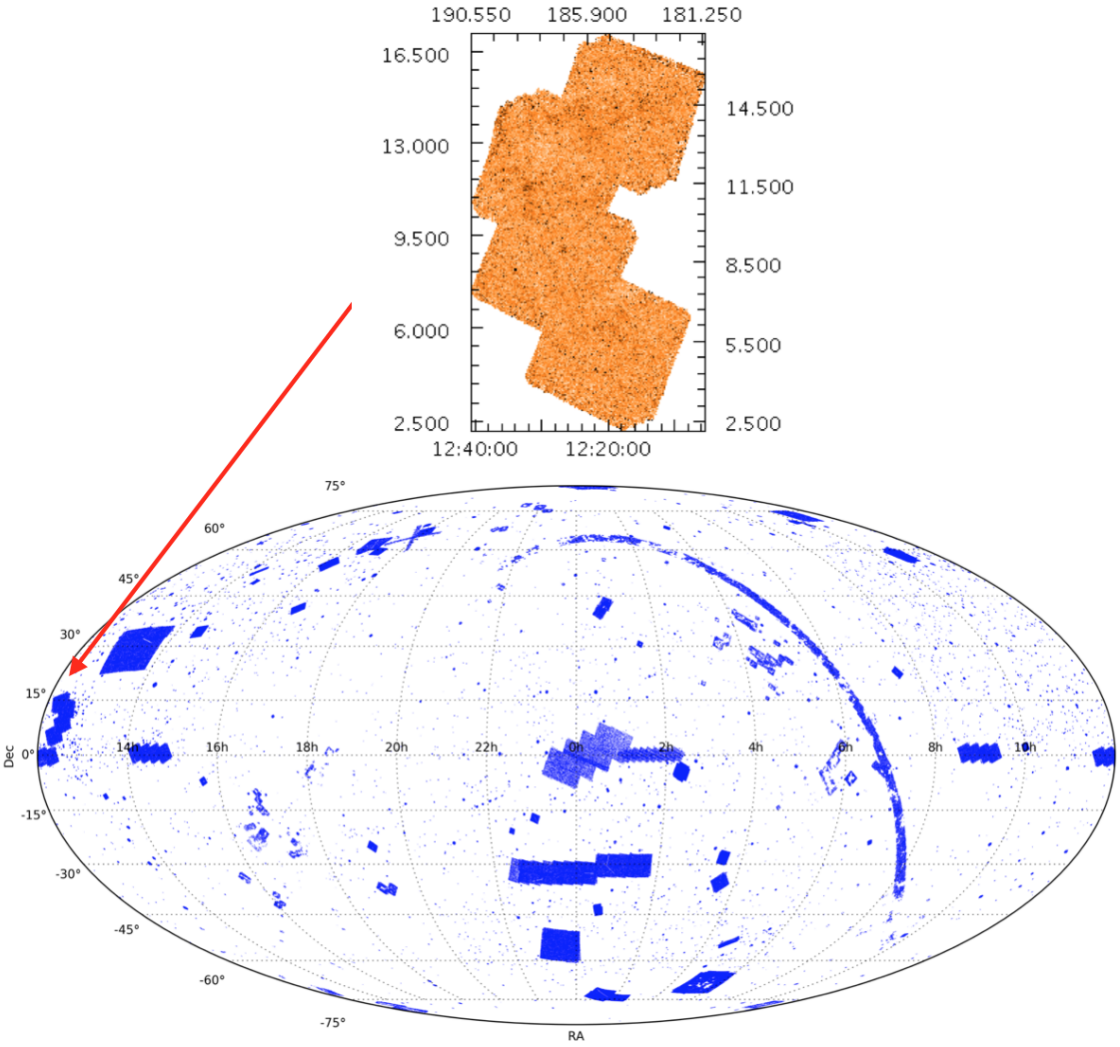

Figure 2.1.: All-sky Aitoff projection of the sky areas observed with *Herschel*. The map shows observations performed over *Herschel* extragalactic fields, as well as numerous individual targets. HeViCS field is denoted with the red arrow. Upper panel of this figure shows the four overlapping areas in the HeViCS field observed with the SPIRE instrument.

HeViCS observations reached a depth close to the confusion limit at the shortest SPIRE wavelength (250 μm). Because of the number of repeated scans, instrumental noise is significantly reduced in HeViCS maps, giving the 1σ levels of 4.9, 4.9, and 5.5 mJy at 250 μm, 350 μm, and 500 μm, respectively (Auld et al. 2013). In the overlapped, deeper regions recorded by 16 scans, these values are even smaller, namely 3.5, 3.3, and 4.0 mJy. Due to the presence of bright sources, global noise estimation is not a straightforward task. I excluded bright sources from the map by masking them, and after their removal the global noise was derived from the variance of the map. It reaches

the 1σ values of 6.58, 7.07, and 7.68 mJy (250 μm, 350 μm, and 500 μm, respectively) for a major area covered by eight cross-scans. The extensive contributor to the overall noise measured in HeViCS maps is confusion noise, usually defined as the the variance in the sky map due to the fluctuations of unresolved sources inside the SPIRE beam. The confusion is calculated using the relation $\sigma_{\rm conf} = \sqrt{\sigma^2_{\rm tot} - \sigma^2_{\rm inst}}$, where $\sigma_{\rm tot}$ is the total noise measured in the map, and $\sigma_{\rm inst}$ is the instrumental noise. Values determined for the confusion noise are 4.4, 5.2, and 5.5 mJy at the 250 μm, 350 μm, and 500 μm bands, respectively, and are almost identical to the ones presented in Auld et al. 2013. These values are also close to the confusion noise measured in HerMES maps, within twice the uncertainty of 3σ-clipping estimates from Nguyen et al. 2010 (3.8 mJy, 4.7 mJy, and 5.2 mJy at the 250 μm, 350 μm, and 500 μm bands, respectively).[c]

Although the primary goal of HeViCS was to study the galaxies within the Virgo Cluster itself, the described characteristics of the survey offer a great laboratory to study the statistics of background dusty sources - this thesis is the first work which performed systematic analysis and selection of such data. In this thesis I use only SPIRE data. In parallel, each HeViCS tile has been observed by the *Herschel* PACS instrument, but the depth of PACS data ($5\sigma_{tot}$ =70 mJy at $100\,\mu$m, Pappalardo, Bizzocchi, et al. 2016) is not sufficient to directly detect our FIR-rising sources. PACS data at 100 μm and 160 μm are added together to optical-NIR maps from the Next Generation Virgo Cluster Survey (NGVS, Ferrarese et al. 2012) in Chapter 6 analysing ancillary data.

2.2.1. An overview of other *Herschel* fields

There are several large *Herschel* fields (e.g. with an observed area $\theta > 10$ deg^2) used for detection of 500 μm-risers[d]. A summary of their properties is shown in Table. All the values are taken from the literature (S. J. Oliver, Bock, et al. 2012, Wang et al. 2014). The *H*-ATLAS survey (Eales, Smith, et al. 2010) is used to select red candidates by Ivison, Lewis, et al. 2016. *H*-ATLAS is designed to uniformly cover 600 deg^2 of sky, but with its two scans, the survey did not reach the level of confusion noise at 250 μm. Studies by Asboth et al. 2016 and Dowell et al. 2014 acquired data from different fields which are part of the HerMES survey (S. J. Oliver, Bock, et al. 2012). The HerMES survey observed 380deg^2 of the sky. The survey has a hierarchical structure

[c] This estimates makes the HeViCS field the deepest local cluster field ever observed with *Herschel*.
[d] Apart from the fields presented in the Table 2.1, there is also the *Herschel* Lensing Survey (HLS), a large dedicated survey of 40 X-luminous local clusters (PI:Egami)

Table 2.1.: Properties of different large fields mapped by *Herschel*

Field	Mode	N(rep)	Time [hr]	Area [deg^2]	Noise level in mJy 5σ at 250 μm
(1)	(2)	(3)	(4)	(5)	(6)
HeViCS	Parallel	8	286	55	30.5
H-ATLAS	Parallel	2	600	550	56.0
HerMES					
FLS	Parallel	2	17.1	6.7	25.8
Bootes NDWFS	Parallel	2	28	10.5	25.8
ELAIS-N2	Parallel	2	28	12.28	25.8
Lockman-Swire	Parallel	4	71.2	16	13.6
XMM-LSS SWIRE	Parallel	4	71.2	18.87	25.8
HeLMS	Sp.Fast	2	103.4	274	64.0

Notes: Columns (1) Name of the field observed by *Herschel*; (2) *Herschel* observing mode ; (3) The total number of repeats of the observing mode in the set; (4) Total time of observations; (5) Field area of good pixels; (6) Total noise from the literature. Noise is calculated using the relation $\sigma_{\rm tot} = \sqrt{\sigma^2_{\rm conf} + \sigma^2_{\rm inst}}$; The bottom six fields are areas with different design levels nested as a part of HerMES: Total area covered in HerMES is 380 deg^2. Shallow HeLMS field covers the area of 274 deg^2, and deeper Level 1 - Level 6 fields cover the total area of about 80 deg^2. FLS and Lockman-SWIRE have been used to probe 500 μm-risers selection by Dowell et al. 2014, while Asboth et al. 2016 applied the same selection method in the HeLMS field.

containing seven levels, ranging from very deep observations of clusters to wider fields with varying size and depth. The largest (and the shallowest) observed area is HeLMS, with its 274deg^2. HeViCS maps consist of two or four times more scans compared to other fields listed in Table. This leads to a reduction of instrumental noise by a factor of $\sqrt{2}$. The global 250 μm noise in HeViCS is smaller than in H-ATLAS and HeLMS. However, it is still higher than in other HerMES fields, showing that confusion is a very compelling supplier to the noise budget for point sources in the HeViCS field. I clarified that statement by repeating our analysis of regions overlapped between the tiles, which have greater coverage. No significant noise reduction has been found, implying that the

maps are dominated by confusion noise.

2.2.2. Map filtering

Prior to performing source extraction on SPIRE maps, I reduce the background contamination. It has been found that 250 μm map of V2 field in HeViCS is particularly strongly affected by galactic cirrus emission. This contamination peaks at around 150 μm (Bracco et al. 2011), implying that it could be prominent just in the shortest SPIRE band. The main effect of cirrus emission is to increase the confusion in the maps, but the small-scale structure within it can also lead to spurious detections in the catalogues.

To overcome the cirrus contamination problem, I follow the method applied by Pappalardo, Bendo, et al. 2015 (see also Valiante et al. 2016). Using the `SExtractor` (Bertin et al. 1996) I re-grid the nominal 250 μm map into meshes larger than the pixel size. The `SExtractor` makes an initial pass through the pixel data, and computes an estimator for the local background in each mesh of a grid that covers the whole adopted frame. Following the suggestion given by Bradley et al. 2017, the value of the background in each mesh is then estimated by using $2.5 \times \mathrm{M_{med}} - 1.5 \times \mathrm{M_{avg}}$, where $\mathrm{M_{med}}$ and $\mathrm{M_{avg}}$ are the median and the mean inside each mesh. If $\mathrm{M_{avg}} - \mathrm{M_{med}}/\mathrm{st.dev} > 0.3$ then the median is used instead.

Finally, the background map is obtained by linearly interpolating between the cells. I apply repetitive iterations in order to precisely estimate the mean and standard deviation of the pixel value distribution in boxes. I remove outlying pixels at each iteration for that purpose. An important step in the procedure I used is the choice of the box size, since it is vital to suppress the background estimation being affected by the presence of bright objects and fluctuated noise. The adopted box size should generally be larger than the typical size of sources in SPIRE image, but small enough to encapsulate any fluctuation of the background. I therefore fix the mesh size to 8 image pixels, adopting the same parameters from Pappalardo, Bendo, et al. 2015. The local background is clipped iteratively to reach $\pm 3\sigma$ convergence around its median.

To test the reliability of the background estimation, I used boxes with the size of 0.5×0.5 deg^2 covering different regions with strong and weak cirrus emission in the V2 field (right panel of Fig. 2.2). If the background subtraction works properly, we should measure relatively small variations in the total number of sources detected in each box. After the background subtraction, the number of sources appears uniform for

regions with different cirrus emission which is illustrated in Figure 2.4. I thus use the background subtracted map as an input for the source-extraction process described in the following section.

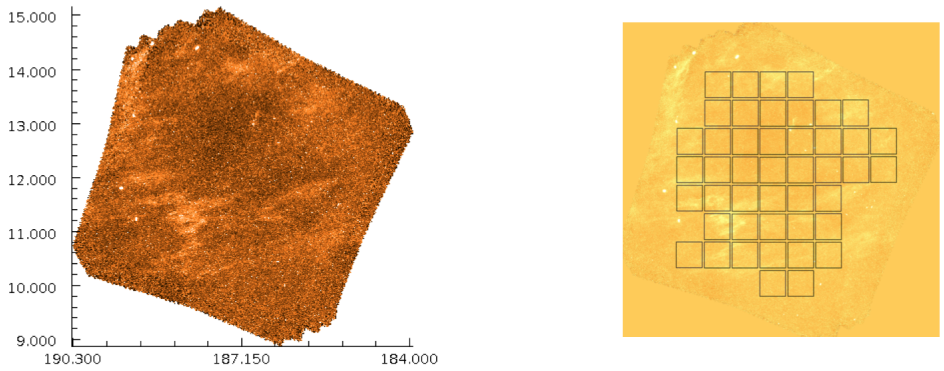

Figure 2.2.: Left panel presents the initial 250μm map of the V2 field which is significantly affected by cirrus emission. Right panel shows the boxes (0.5×0.5 deg^2) used to test the reliability of the cirrus subtraction.

2.3. Extraction of sources

Blind SPIRE source catalogues have been produced for HeViCS (Pappalardo, Bendo, et al. 2015) and they are included in the latest release of a large *Herschel*-SPIRE Point Source Catalogue (HSPSC). [e] Nonetheless, when the density of sources is very high, which is the case in the highly crowded HeViCS field, blind source extraction cannot separate blended point sources in an efficient way. Additionally, it remains difficult to properly cross-match sources at different wavelengths, since central positions from blind catalogues are not well constrained. To deal with source multiplicity I chose to perform extraction of 350 μm and 500 μm fluxes at the exact a priori position of 250 μm band detections, allowing much more precise identification. The potential limitation of such a method is that we might be eventually miss some 500μm-risers that are not included in the prior list after the first iteration of source extraction. It is clear that careful creation of a prior list is of high importance, and I thus run the method iteratively adding new sources that may appear in the residuals at each iteration. In the following, I provided details about the source extraction, source de-blending and final source selection.

[e] https://www.cosmos.esa.int/web/herschel/spire-point-source-catalogue

2.3.1. Bayesian point source detection

The choice of source extraction method is a very important initial step in order to obtain the reliably deep catalogue of 250 μm prior sources. Some of the recent studies (e.g C. Pearson et al. 2014, Wang et al. 2014) compared different widely used codes appropriate for point source extraction and agreed that at the faintest levels of large 250 μm maps, the `SUSSEXtractor` (Savage et al. 2007), a source-finding algorithm optimised for *Herschel* detected point-sources, works slightly better than other algorithms in terms of source detection and estimation of their signal-to-noise ratios. Therefore, I use `SUSSEXtractor` to create the catalogue of galaxies detected in the 250 μm map as a prior to extract the flux densities at longer wavelengths. To perform the de-blended SPIRE photometry, I implement the novel technique where source de-blending and modified blackbody (MBB) fitting are combined in the same procedure (Section 2.4). As an additional check, in `Appendix` I present my results of an extensive comparison of performances of different codes with the aim to compute the completeness of 250 μm catalogues down to $3\sigma_{\rm conf}$.

`SUSSEXtractor` (Savage et al. 2007) is a Bayesian peak-finding algorithm which treats each potential source location (for example, the centre of image pixel) individually, and considers two possible models at each location: it uses an empty-sky model and a source model. For the given models, parameters and likelihoods are estimated, and then the models are compared in order to determine whether a source is present at certain location. The fully Bayesian approach assumes a prior knowledge about point-spread function (PSF), P_i, which is centred on the potential source location, and which is dimensionless (normalised such that its integral is unity).

The source model is given in the form:

$$m_i = FP_i + B_{\rm source}\,, \tag{2.1}$$

where m_i is the intensity of the sky at location i, F is the flux density of the source, P_i is value at location i of the point-spread function (centred at the source position), and B is the (uniform) background intensity under the source.

`SUSSEXtractor` task is implemented in the newest release of HIPE data processing system (`http://herschel.esac.esa.int/hipe/`) and it requires an image, noise map and error map as input, along with parameters for the Full Width Half Maximum (FWHM) and detection threshold. It further implements aforementioned Bayesian for-

malism such that analytically calculates the likelihood assuming a prior model (described with Eq.2.1.) for the source model. It is important to note that only those sources above some specified detection threshold can be considered as reliable detections (http://herschel.esac.esa.int/Docs/SPIRE/html/spire_om.html).

The likelihood is defined as the probability of the data given the model and a set of parameters, and here it is in the form of normal distribution:

$$\mathcal{L} \equiv P(D|\theta, H) = A \exp\left(-\chi^2/2\right) \tag{2.2}$$

where P is the probability, D is the data, H is the hypothesis (model) assumed, A is a constant (such that the probability when integrated over all possible values of the data will sum to unity). Furthermore,

$$\chi^2 = \sum_{i=1}^{N_{\rm data}} \left[\frac{d_i - m_i(\theta)}{\sigma_i}\right]^2 , \tag{2.3}$$

where the summation is over a local region around the source position being considered, d_i is the intensity of the sky at location i, and σ_i is the Gaussian instrumental noise associated to the certain pixel. The value which is given under the summation sign is a noise-weighted residual. In principle, lower the noise means higher the weight. The model works under assumption of a flat-prior, meaning that it is equal across all parametric space and it is essentially an "uninformative" prior. Therefore no assumptions are made about the source's parameters (i.e. no initial guesses are made about the real (physical) fluxes) (Savage et al. 2007).

2.3.2. Source extraction algorithm

In the following I explain the source-extraction pipeline that I create in order to detect and select candidate high-z DSFGs in the HeViCS field (see Fig.2.8 for a graphical description):

1. I run `SUSSEXtractor` using a fully overlapping HeViCS 250 μm map. The code works on the point source calibrated Level 2 *Herschel* SPIRE maps. The code creates a point response function (PRF)-filtered image, smoothed with the PRF. In `SUSSEXtractor`, the PRF is assumed to be Gaussian by default, with the full-width-at-half-maximum (FWHM) provided by the FWHM parameter. I apply values of

17.6", 23.9", and 35.2" at 250, 350, and 500 μm, respectively. Subsequently, pixel sizes at these bands are 6", 10", and 14". The algorithm searches for a local maximum which is the highest pixel value within a distance defined by pixel region. The position assigned to the possible source is then refined by fitting a quadratic function to certain pixels in the PRF-filtered image.

To search for even fainter sources that are closer to the confusion limit and usually masked/hidden in highly confused fields like HeViCS, I perform an additional step looking for detections in residual maps. Applying such an additional step increases the total number of sources by around 4%. Errors in the position estimated to be a source are determined as 0.6 times the ratio of the FWHM to the signal-to-noise ratio (S/N), up to a maximum of 1.0 pixel, as suggested in the literature (Ivison, Greve, et al. 2007, Wang et al. 2014).

2. I build an initial list of 250 μm sources selecting all point sources above the threshold=3 (Bayesian criteria in `SUSSEXtractor`). It corresponds to $S_{250} \gtrsim 3\sigma_{\rm conf}$. As a result of the source extraction pipeline at 250-micron maps, I listed 94309 sources, similarly distributed among the four (V1-V4) fields.

3. For efficient de-blending, I applied grouping algorithm which is used to separate sources into optimum groups (Density Based Scan, DBScan) provided within machine learning package `scikit-learn` [f]. The algorithm searches for sources whose PSF profiles overlap, i.e. it decides whether or not the profile of a given galaxy extends into the fitting region of any other source. Applying the DBScan algorithm I found 12135 grouped sources.

   Final list of 250 μm detections is divided into a "no-neighbour" list of sources (250 μm sources without another detection inside the 500 μm beam, 82174 sources in total) and a "group" list with all sources that have overlapped PSF profiles (12135 sources in total). The final catalogue contains column that represent the group ID number assigned to each source. Prior to assigning the initial 250 μm list as an input to our MBB fitting procedure, I remove potentially extended sources from the prior 250 μm catalogue.

[f] http://scikit-learn.org/stable/modules/clustering.html

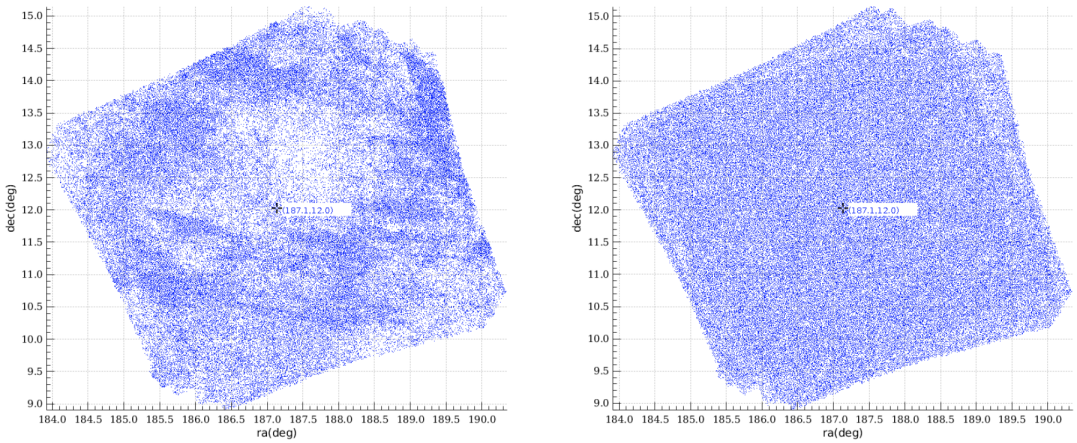

Figure 2.3.: Difference between point source detections from unfiltered (left) and filtered V2 map (right). The centre of V2 field labelled with black cross is very close to the peak of the X-ray emission associated to the dominant local cluster galaxies. Non-uniform density seen at the left panel appears strongly correlated with the intensity of galactic cirrus. This effect is removed after the background subtraction, as can be seen on the right panel.

2.3.3. Extended sources

The Virgo cluster is one of the richest local clusters and we may expect to have a significant number of extended sources. Objects that are extended on the SPIRE beam scale (see Wang et al. 2014 or Rigby, Maddox, et al. 2011) are not expected to be accurately identified with point-source extracting algorithms, and large galaxies may be misidentified as multiple point sources. To solve this problem, I implement the method used in Pappalardo, Bendo, et al. 2015 and Wang et al. 2014. They define a mask using the recipe of `SExtractor`, which detects a source when a fixed number of contiguous pixels is above a σ-threshold estimated from the background map. I keep the same value tested in Pappalardo, Bendo, et al. 2015: 70 contiguous pixels above $1.2\,\sigma$.

In this case, most of the sources larger than 0.7 arcmin^2 at 250μm are rejected from the sample. Additionally, I cross-match all remaining HeViCS 250 μm detections with their nearest (within 36") counterpart in the *2MASS* Extended Source Catalog (Jarrett et al. 2000). I remove any detection supposed to be a counterpart with a Kron elliptical aperture semi-major larger than 9". In total I suppressed 812 sources from the analysis, thus decreasing the number of 250 μm detections in the parent list from 94309 to 93497.

The list of sources detected at 250 μm down to 13.2 mJy, cleaned from galactic cirrus

contaminants and extended sources, is further used as an a priori list for our simultaneous modified blackbody fitting.

2.4. Source photometry: `Modified blackbody fitter`

As described in *Section* 2.1, our maps are limited by confusion noise caused by the high density of sources relative to the resolution of the *Herschel* instrument. In cases where SPIRE images have multiple sources per beam, measured fluxes might be biased if we treat several blended sources as one. Several different approaches for source "de-blending" exist in the literature. We can broadly separate these algorithms into three groups: firstly, there are de-blending methods that use only positional priors as input information (e.g. Elbaz, Hwang, et al. 2010, Swinbank, J. M. Simpson, et al. 2014, M. Béthermin, Dole, Cousin, et al. 2010, Roseboom, S. J. Oliver, et al. 2010). The second group of de-blenders consists of methods which combine positional information with statistical techniques (Hurley et al. 2017, Safarzadeh, Ferguson, et al. 2015); for example, Safarzadeh, Ferguson, et al. 2015 and Hurley et al. 2017 developed the codes based on the Monte Carlo Markov Chain (MCMC) sampling for prior source detections, and while Safarzadeh, Ferguson, et al. 2015 used Hubble Space Telescope (HST) H-band sources as a positional argument, Hurley et al. 2017 developed a similar MCMC-based prior-extraction (XID+) for *Spitzer* 24 μm or IRAC (e.g. 3.6 μm) detections. The XID+ [g] offers a full posterior probability of galaxy photometry and it is successfully used for fields such as COSMOS, for which the deep, shorter wavelength data are well provided. While aforementioned algorithms seem to be efficient in obtaining Bayesian PDFs for all imposed priors, they might still have limiting cases, the most important ones are the low efficiency to recognise the true high-z obscured source in situations where the DSFGs of interests are not included in the initial list. Finally, a third group of de-blenders apply SED modelling techniques as an addition to positional arguments (T. P. MacKenzie et al. 2014, Shu et al. 2016, Merlin et al. 2016, Liu et al. 2017). For example, Liu et al. 2017 progressively de-confuse FIR maps starting from sources initially found in *Spitzer*24 μm and VLA 1.4 GHz data. Shu et al. 2016 perform slightly different approach to select $z > 2$ candidates in GOODS-N field. They constructed a so-called "500 μm/24 μm ratio map" by dividing the nominal 500 μm image with the smoothed 24 μm map. In this way, the contamination of lower-z sources is expected to be significantly reduced

[g] http://herschel.sussex.ac.uk/XID_plus/build/html/index.html

since they have much lower 500 μm/24 μm ratios compared to high-z counterparts. On top of that, XID+ has been recently tested with the combination of SED priors, by SED fitting ancillary optical and near-IR data to obtain flux priors (see Pearson, Wang, van der Tak, et al. 2017). All these methods have their advantages and obstacles, and the most important is their dependence on shorter-wavelength priors, and limited ability to recognize the true position of a source which remains absent in ancillary datasets.

Due to the lack of *Spitzer* data for the HeViCS field, we have no opportunity to use positional priors from shorter-wavelength surveys, and I based the analysis on SPIRE data instead. I use the most recent models to test the whole procedure of selecting 500 μm-risers in Section 4.1.

`MBB-fitter` is a code developed by Frederic Boone and collaborators from HLS team, with the main goal to extract sources from multiwavelength bolometric observations (Boone et al, in prep.). It is used in Boone et al. 2013 to identify a *Herschel* SPIRE μm dropout source, one of the first moderately FIR luminous candidates at $z > 4$. The `MBB-fitter` combines positional priors and spectral information of sources such that SEDs of fitted galaxies follow the modified blackbody shape given the model defined by Blain, Barnard, et al. 2003. The MBB de-blending approach presented in this Thesis is thus very similar to the photometric method applied by T. P. MacKenzie et al. 2014, with the difference that later uses slightly different initial MBB model and MCMC algorithm with Gibbs sampling to determine the uncertainties of model parameters. The MBB fit to (F)IR data is the most simplistic SED fit. Although such a model cannot encapsulate a global complexity of astrophysical processes in a galaxy, it is very useful for statistically significant samples, since it can account for a wide variety of DSFG SEDs.

Formalism

The formalism described below is taken from Boone et al. in prep. who described the technical aspects of the code and its initial test are in much more details. Shortly, in `MBB-fitter`, the map (M) of a sky region is described as a (regular) grid corresponding to the sky flux density distribution convolved by the point spread function (PSF) of an instrument and sampled in pixels. In this case, $M_i = M(\alpha_i, \delta_i)$ refers to the value of the map at the i^{th} pixel with coordinates α_i, δ_i. Following this, it can be assumed that the sources have a frequency-independent morphology. The flux density distributions in the three-dimensional (3D) space $s_k(\alpha, \delta, \nu)$, where ν is frequency, can thus be decomposed

into a spatially distributed term and an SED term:

$$M_{ij} = M(\alpha_i, \delta_i, \nu_j) = [\sum_{k=1}^{N_{sources}} f_k(\nu_j)\tilde{s}_k(\alpha - \alpha_k, \delta - \delta_k) \otimes PSF_j]_i, \tag{2.4}$$

where PSF_j is the PSF of the map at a given frequency (ν_j), and $N_{sources}$ is the number of sources considered for the fitting, with its reference coordinates $(\alpha_\kappa, \delta_\kappa)$. It is assumed that the thermal continuum SED of galaxies in the FIR domain can be modelled as a MBB of the form (Blain, Barnard, et al. 2003)

$$f(\nu, T_\mathrm{d}, \beta, \gamma) \propto \begin{cases} \nu^{3+\beta}/[exp(h\nu/kT_\mathrm{d}) - 1], \ if\ \nu < \nu_\mathrm{w} \\ \nu^{-\gamma}, \ if\ \nu \geq \nu_\mathrm{w} \end{cases}, \tag{2.5}$$

where ν_w is the lower boundary of Wien's regime, h is the Planck constant, and k is the Stefan-Boltzmann constant. Thus, Eq.2.5 describes a general model for a set of maps at different wavelengths.

The normalised SED is defined with:

$$\bar{f}(\nu, T_\mathrm{d}, \beta, \gamma) \propto \frac{f(\nu, T_\mathrm{d}, \beta)}{\int_{\nu_\mathrm{min}}^{\nu_\mathrm{max}} f(\nu, T_\mathrm{d}, \beta, \gamma) d\nu} \tag{2.6}$$

Applying previous equation, one can define the flux of a source at redshift z observed at the frequency ν_obs. It is given by:

$$f(\nu, T_\mathrm{d}, \beta, \gamma, z) = \frac{(1+z) L_\mathrm{IR} \bar{f}((1+z)\nu_\mathrm{obs}, T_\mathrm{d}, \beta, \gamma)}{4\pi D_\mathrm{L}^2}, \tag{2.7}$$

where D_L^2 is a luminosity distance which is a function of a redshift.

There are also possibility that at redshifts higher than $z > 6$ the heating of dust by the cosmic microwave background (CMB) may becomes significant. It then needs to be taken into account in the model for the observed SED. The `MBB-Fitter` quantifies the effect of the CMB on the SED shape following da Cunha et al. 2013 and applying the correction factor to the SED:

$$C_\mathrm{CMB}(\nu_{obs}, T_d, \beta) = \frac{B_\nu[T_d(z)] - B_\nu[T_{CMB}(z)]}{B_\nu[T_d(z)]}, \tag{2.8}$$

where B_ν is the Planck function, $T_\mathrm{CMB} = 2.73$ K, $T_\mathrm{CMB}(z) = (1+z)T_\mathrm{CMB}$ and $T_d(z)$=$(T_\mathrm{d}^{4+\beta} + T_\mathrm{CMB}^{4+\beta}[(1+z)^{4+\beta}] - 1)^{\frac{1}{4+\beta}}$. Each source SED is defined by a set of parameters arranged

into a vector of the form $P_\kappa = [L_{\mathrm{IR}_\kappa}, T_{\mathrm{d}_\kappa}, z_\kappa, \beta_\kappa, \gamma_\kappa]$, where z_κ is the redshift of a given source, β_κ is its emissivity index, γ_κ is the index of the power law to substitute the Wien's regime, and L_{IR} is the IR luminosity as defined in Eq.1.2. This model is parametrised by the source SED parameters, P_κ, and coordinates $\alpha_\kappa, \delta_\kappa$. The total number of parameters is therefore N_{par}=$N_\mathrm{s} \times (N_{SED_{\mathrm{par}}} + 2)$, where $N_{SED_{\mathrm{par}}}$ is the number of SED parameters and N_s is the number of sources.

The set of parameters given in equations introduced above reflects the global properties of the source. There are important degeneracies to be considered, that means different values of parameters which may give undistinguishable SEDs. This is one of the main challenges when using the FIR peak as a redshift indicator; dust temperature and the redshift are completely degenerate (see e.g. Pope and Chary 2010).

Model fitting

A model defined by equations 2.5, 2.6, 2.8, and 2.9, can be compared to a set of observed maps and its fidelity can be assessed with a figure of merit such as the chi-square, defined as the sum of the pixel deviations:

$$\chi(P)^2 = \sum_i^{N_{\mathrm{pix}}} \sum_j^{N_{\mathrm{freq}}} \frac{(M_{ij}(P) - \tilde{M}_{ij})^2}{\sigma_{ij}^2}, \tag{2.9}$$

where $\tilde{M}_{ij}$ is the multiwavelength set of maps, σ_{ij} is the Gaussian noise level of the i-th pixel of the map at the j-th frequency, N_{pix} is the number of accounted pixels, while N_{freq} represents the number of maps, which is equal to the number of different frequencies used.

The parameter P is the global parameter vector and its components are the N_{par} parameters:

$$P = \{P_1, \alpha_1, \delta_1, P_2, \alpha_2, \delta_2, ...P_{N_{sources}}, \alpha_{N_{sources}}, \delta_{N_{sources}}\} \tag{2.10}$$

Extracting the sources from the multiwavelength set of maps is then equivalent to finding the values of the parameters P that minimize $\chi^2(P)$. The code has implemented the method described above with the IDL progamming language. In the current version of `MBB-fitter` the source positions are always fixed, i.e. the coordinates are assumed to be known and a prior catalogue needs to be provided at input. Despite this limitation it is still possible to use this implementation to extract unknown sources from the maps. This can be done by running iteratively the method and add new sources that may

appear in the residuals following each iteration.

To find the minimum of the χ^2 function in the space of parameters, the code uses the Levenberg-Marquardt algorithm which is a standard technique for solving non-linear least squares problems by iteratively searching for the best fit. This particular implementation is drawn from a robust routine called MINPACK while the latest version of `MPFit` package (Markwardt 2009) returns an estimation of the errors on the parameters based on the covariance matrix. The uncertainties on the flux values can then be obtained by varying the best fit L_{IR} with $\pm\sigma$.

The `MBB-fitter` also introduces the simple way to protect from different features that could bias the fit. It is not necessary to include all the pixels of maps in the χ^2 computation, and it can be restricted to a subset of pixels (contiguous or not). In this way we mask out parts of an image and sky regions without prior sources can be excluded from the fitting-procedure (such an example is illustrated at Fig.2.4). An example of colour-redshift diagram of modelled sources (assumed to be blackbodies) is presented in Fig.2.6. In Fig.2.5 I presented an example of a simulated de-blending between the two sources, along with the best-fit models and residuals. In this example the two sources at different redshifts are blended together (the one at $z = 1.3$ with $L_{\rm IR} = 11.9 L_{\odot}$ and another one at $z = 3.0$ with $L_{\rm IR} = 12.5 L_{\odot}$).

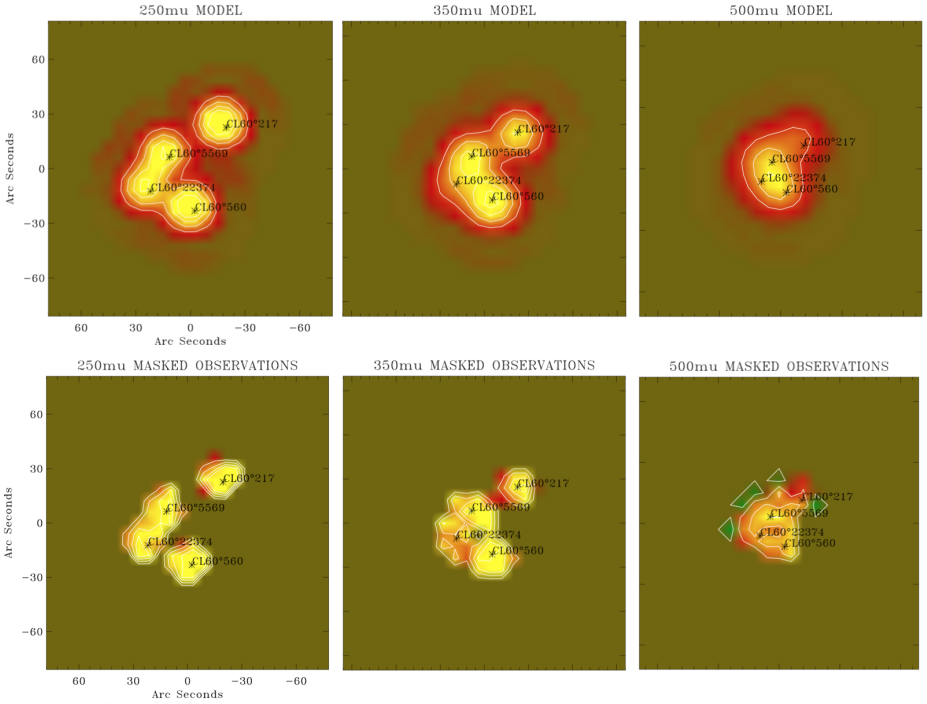

Figure 2.4.: Example of grouped sources and their subtracted MBB models (upper panel) along with masked regions considered for the fit (lower panel).

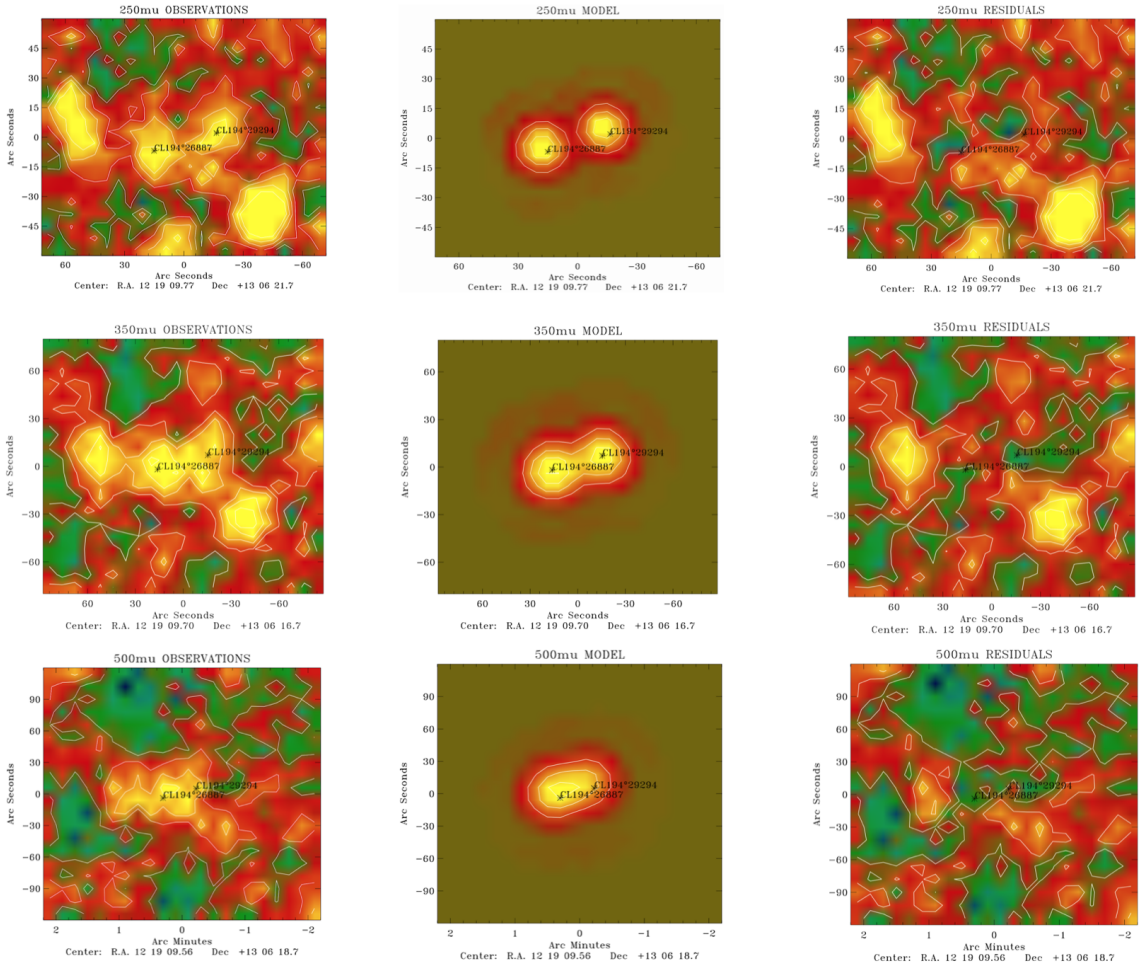

Figure 2.5.: Example of simultaneous prior-source de-blending with `MBB-fitter`. Simulated example shows clustered 250 μm detections. Columns from left to right: 250 μm, 350 μm, and 500 μm maps of sources (first column), subtracted models (second column) and residuals (third column). For simplicity, n this example two central sources are considered for the fitting.

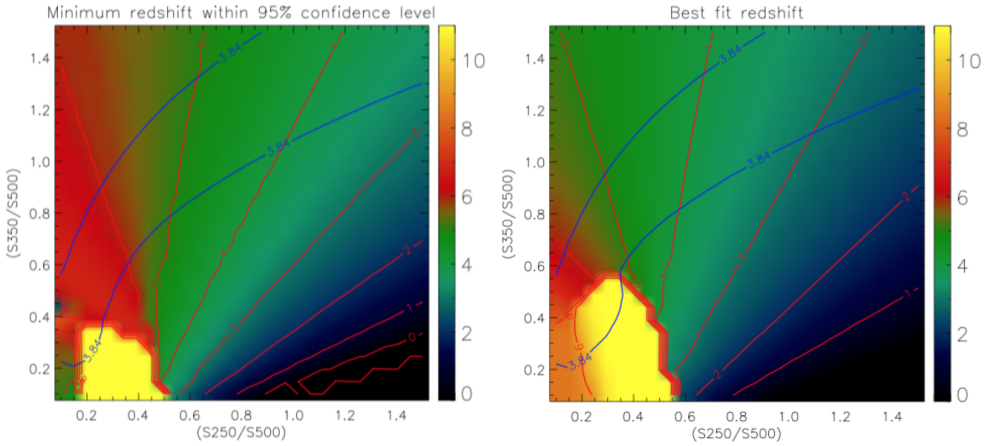

Figure 2.6.: SPIRE colour-redshift diagram related to the chosen MBB model. The figure illustrates connection between observed colours and expected redshifts of sources modelled with MBBs, depending on a chosen β and $T_{\rm d}$. Plotted against all possible SPIRE colours are simulated sources with $T_{\rm d}$=45 K and $\beta = 1.8$ (left) and $T_{\rm d}$=35 K and $\beta = 1.8$ (right). The red lines represent the redshift tracks, whose values rise from right to left. The coloured background indicates the average redshift in the colour-colour space. The blue lines define the 95% confidence limit region. For our final 500 μm-risers selection I kept only those de-blended sources whose χ^2 fitting values resides inside the 95% confidence area ($\chi^2 < 3.84$).

2.4.1. Photometry procedure

I impose the list of 250 μm detected sources as a prior list, and use `MBB-fitter` to perform two-step photometry process: (1) simultaneously fitting the sources affected by surrounding source-blend (12135 sources in total), and (2) performing the photometry of sources that are more isolated without a surrounding companion inside the beam (81362 sources in total). I set emission spectral slope and dust temperature to be fixed at $\beta = 1.8$ and $T_{\rm d} = 38 \pm 9$ K respectively. These values are chosen to provide a very good description of the data and they are based on our current knowledge of dust temperatures in SPIRE-detected sources (e.g. Riechers, Leung, et al. 2017, Schreiber, Pannella, R. Leiton, et al. 2017, Dowell et al. 2014, Swinbank, J. M. Simpson, et al. 2014, Symeonidis, Vaccari, et al. 2013, Lapi et al. 2011).

2.4.2. Final data sample of 500 μm-risers

I select the final list of 133 500 μm-risers over the area of 55 deg^2. Selected sources fulfil criteria accepted for the final cut: $S_{500} > S_{350} > S_{250}$, $S_{250} > 13.2$ mJy and $S_{500} > 30$ mJy. The full selection algorithm is illustrated in the left side of Fig. 2.7, while the catalogue is presented in `Appendix A`.

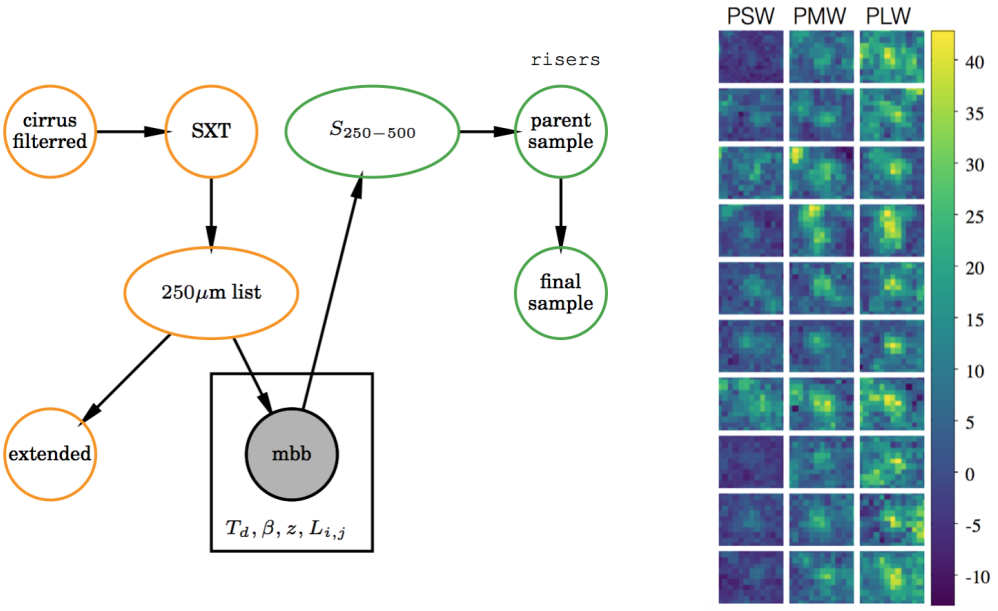

Figure 2.7.: `Left:` Schematic representation of our selection of 500 μm-risers. Coloured in orange are segments of source extraction prior to using `MBB-fitter`; these are (from upper left, following the arrows) cirrus filtering; `SUSSEXtractor` list of initial (threshold=3) 250 μm detections; and final "prior" list cleaned from extended sources. Enveloped by black square are parameters considered for the fitting procedure with `MBB-fitter`. Coloured in green are selection steps: (i) MBB photometry ($S_{250-500}$) at SPIRE wavelengths using 250 μm priors; (ii) parent list of 500 μm-risers (140 sources in total), not cleaned from strong synchrotron contaminants; and (iii) final list of 500 μm-risers (133 in total) after excluding QSOs. Applied selection criteria are: $S_{500} > S_{350} > S_{250}$, $S_{250} > 13.2$ mJy, and $S_{500} > 30$ mJy; `Right:` 2D image cutouts of 500 μm-risers that fulfil our final selection criteria. Colourbar shows fluxes measured in mJy.

I perform several tests and chose to set the flux density cut in the 500 μm band at $S_{500} \simeq 30$ mJy, which is related to 4σ above total noise measured in HeViCS maps. Using this value, we reach a completeness level of $\sim 80\%$ at 500 μm for the whole

HeViCS catalogue (see Fig.2.9) avoiding larger uncertainties in colours due to lower S/Ns (see also Chapter 4.2). A 250 μm flux cut ($S_{250} > 13.2$ mJy) corresponds to $S_{250} > 3\sigma_{conf}$ after applying an iterative 3σ clipping to remove bright sources (Section 2.1). The statistics of our selection, including correction for different biases and influence of contaminants, is analysed in Section 4.2 and Section 4.3.

Amongst the final 500 μm-risers (133 in total), 21 reside in groups, having in average 1.3 ± 0.2 additional 250 μm detections inside the 500 μm beam. Example two-dimensional (2D) cutouts of several 500μm-risers from our final sample are presented in the right panel of Fig.2.7. Strong radio sources that have flat spectra and very prominent FIR emission (7 objects in total) have been removed from our final list of 500μm-risers in the HeViCS field; these objects may have colours similar to those of dusty, star-forming systems that we are interested in selecting. Contamination due to radio-bright galaxies is eliminated by cross-matching existing radio catalogues: HMQ (Flesch 2015), NVSS (Condon et al. 1998), FIRST (Helfand et al. 2015) and ALFA ALFA (Giovanelli et al. 2007). All identified radio-bright sources are classified as QSOs, and I analyse them in more details in Section 3.6.

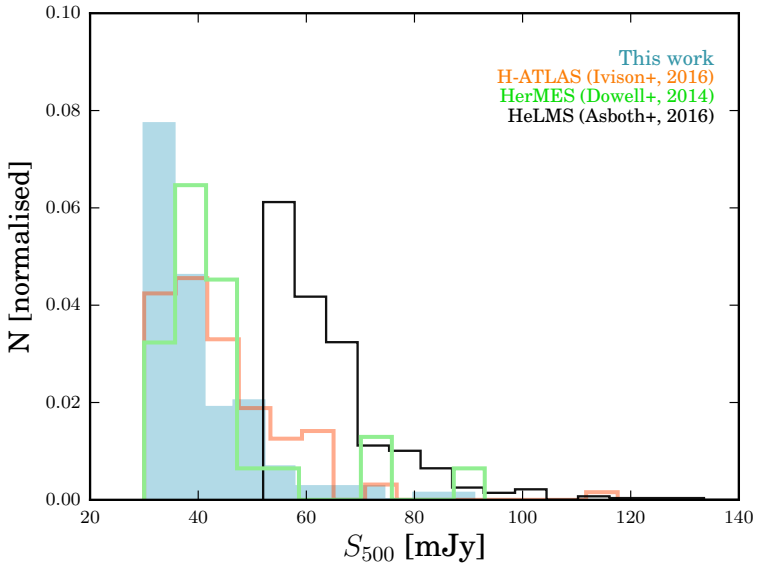

Figure 2.8.: Normalised distribution of 500 μm fluxes of 500 μm-risers. The filled blue area indicates our sample, while samples of Ivison, Lewis, et al. 2016, Dowell et al. 2014 and Asboth et al. 2016 are represented by orange, green and black lines, respectively.

In Fig.2.8 I show actual flux distribution of 500 μm-risers selected in this work, along

with red sources from other studies. We see that our catalogue contains, on average, more fainter objects than other existing samples. The median 500 μm flux of a sample presented in this work is 38 ± 4 mJy, while median fluxes found in Dowell et al. 2014, Asboth et al. 2016, and Ivison, Lewis, et al. 2016 are 45 mJy, 65 mJy, and 47 mJy, respectively. Therefore, our selection is arguably the faintest sample of 500 μm-risers available.[h] The underlying flux distribution of selected galaxies might still be affected by strong gravitational lensing, which I discuss in detail in Section 5.2. Along with galaxy-galaxy lensing, cluster-lens amplification might affect measured fluxes. The effect is the strongest when the deflector is located half-way between the observer and the lensed object (e.g. Kneib et al. 2011). Strong lensing events are thus more numerous for clusters at $0.1 < z < 0.5$ (Johnson et al. 2014). The Virgo cluster is very close along the line of sight ($z = 0.003$) and for this reason we expect negligible impact on SPIRE fluxes of 500 μm-risers. Colours of sources selected in this work, together with colours of 500 μm-risers with spectroscopic redshifts from other studies, are plotted in Fig.3.7 in the next Chapter, when luminosity-redshfit range of selected sources is discussed. The median observed colour of this sample is $S_{500}/S_{350} = 1.11 \pm 0.10$, whereas median colours from Dowell et al. 2014, Asboth et al. 2016, and Ivison, Lewis, et al. 2016 are $S_{500}/S_{350} = 1.08$, $S_{500}/S_{350} = 1.20$, and $S_{500}/S_{350} = 1.23$, respectively. In Section 4.1.5 and Section 4.2 I quantify and discuss the impact of the noise on observed colours.

2.5. Data quality assessment and conventional completeness

In this section, I determine the reliability and the conventional completeness of our catalogue using priors at 250 μm. I also verify the flux accuracy in the `MBB-fitter`, and the precision in the determination of the source position in `SUSSEXtractor`.

2.5.1. Reliability of prior 250 μm catalogue

A spurious detection may happen as a result of noise in the map pixels (due to a small number of bolometer samples, each with a significant uncertainty), or as a result of other factors contributing to the detector signal, such as cosmic ray glitches that are

[h] Based on our current knowledge of 500 μm-risers known in literature, we expect their average dust temperature is slightly higher than in DSFGs at $z < 4$. I thus probe our fitting procedure over selected 133 sources once again, but now applying wider priors $T_{\rm d} = [38, 52]$ K. I find much poorer result of the fit, with wider χ^2 distribution. I thus kept our initial fitting results for the further analysis.

eventually unremoved by the pipeline.

The reliability of 250 μm prior list is an important value for measuring the total number counts rather than for selection of 500μm-risers, since we expect that eventually spurious sources would be present in one waveband but not in all three SPIRE bands. However, since our prior list is based on faint 250 μm detections close to the confusion limit, I perform an analysis of possible false detections by injecting fake sources into noise maps. I use a permutation method similar to that applied by Auld et al. 2013. When the noise in the data is due entirely to instrumental effects, the probability that a detection is genuine (or spurious) can be estimated from the S/N ratio of the source. However, in these *Herschel*-SPIRE data, the dominant source of noise is confusion, that is, the measurement of the flux density of any particular source being contaminated by the flux density of neighbouring sources. This means that the S/N ratio of a detection cannot be used in any straightforward way to give the probability that it is spurious.

The number of such spurious detections that would arise from instrumental noise may be estimated using the so-called "jacknife" method. The method takes maps and catalogues generated from the two halves of the data for each HeViCS field. Since real sources should appear in each half of the data, they should not be present in the jackknife map, even at substantially low signal-to-noise. In that sense, the jackknife map represents pure noise. I built maps using the two halves of the eight HeViCS-scans and calculate two difference maps:

$$\mathrm{M_{diff}} = \pm\frac{\mathrm{M_1} - \mathrm{M_2}}{2}, \tag{2.11}$$

where M1 and M2 are the maps built with the first and the last four scans. This procedure removes the confusion noise, considering only the uncertainties due to the instrument. The subtraction is done in two different permutations because a cosmic ray can give a positive or negative spike depending on the map considered. I search for spurious sources using (`SUSSEXtractor` and found 65 fake detections over the whole HeViCS field. However the position of the most of false sources are confined to the external regions of the map, where the number of bolometer samplings is low. In the final catalogue, I considered only regions of the field with a sampling redundancy ≥ 35, therefore ignoring all the sources on the map borders. This implies that we can reasonably assume that there are no false detections due to glitches or different noise properties in different scans in the regions considered for the source extraction.

2.5.2. Completeness and flux accuracy

To check the quality of data analysis, I perform tests of conventional completeness and flux accuracy. Since our catalogue is based on a priori 250-μm positions, in this subsection I focused my analysis to inspect that band, following the same approach from Wang et al. 2014. Calculating the completeness in a catalogue of sources selected at a single wavelength is straightforward, since the detection efficiency only depends on the signal-to-noise ratio of these sources. Here, I present completeness only for our prior-based SPIRE catalogue, without testing the novel selection function introduced in previous section. However, for the final sample of 500 μm risers, which has a complex selection function, correction factors will also depend on the colours of our sources, so evaluation of our selection and its corrections require careful and refined analysis based on predictions from different models, which must include treatment of lensing and clustering. These simulations and corresponding analysis will be presented in details in Chapter 4.

To make the quality assessment of our HeViCS catalogue, here I use Monte Carlo method, which is widely employed technique in the literature for characterising the efficiency of different source extraction algorithms. It was first outlined by Eales, Lilly, et al. 2000, and it has been updated for point source identification in *Herschel* extragalactic surveys such as HerMES and *H*-ATLAS (Rigby, Maddox, et al. 2011, M. W. L. Smith et al. 2012, Wang et al. 2014), Valiante et al. 2016).

I artificially add 1000 Gaussian sources projecting them at randomised positions to the real 250 μm data, before convolving with the beam. Since our photometry is based on prior list, simulated sources have the same assigned coordinates over all three SPIRE maps. The FWHM values that I used to convolve are 17.6", 23.9", and 35.2", that is, values I consider for `SUSSEXtractor` detections. In each HeViCS field I add sources spanning the wide range of flux densities separated in different flux bins (first bin starts from 1-5 mJy, then 5-10 mJy, 10-20 mJy, 20-30 mJy and so on, up to 90-100 mJy). I perform the source extraction pipeline extracting the list of recovered point sources using `SUSSEXtractor` and searching for matched detections.

The HeViCS field is significantly crowded and we can perform missmatch with an unrelated source close to the input (x, y) coordinate. I match the input to output catalogue considering source distances smaller than half of the 250 μm beam size (9"), measured from the centre of the 250 μm detection. Quality assessment results are summarised in Table 2.2 and Fig.2.9. I calculate completeness by considering the number of injected sources with certain flux density S that are recovered in the simulated maps as

Table 2.2.: The completeness fraction at SPIRE wavebands measured by injecting artificial sources into real SPIRE maps. Input fluxes are given in the first column, while percentages of detected sources (average values per bin) are given in the subsequent columns.

Flux [mJy]	V1 [250 μm]	V2 [250 μm]	V3 [250 μm]	V4 [250 μm]
5	0.18	0.14	0.17	0.19
10	0.37	0.40	0.39	0.38
15	0.59	0.64	0.63	0.61
25	0.84	0.91	0.93	0.93
35	0.94	0.97	0.96	0.97
45	0.97	0.98	0.98	0.98
55	0.98	0.99	0.99	0.99
65	0.98	1.0	1.0	0.99
75	0.99	1.0	1.0	1.0
85	1.0	1.0	1.0	1.0
95	1.0	1.0	1.0	1.0
	[350 μm]	[350 μm]	[350 μm]	[350 μm]
5	0.14	0.19	0.12	0.11
10	0.30	0.43	0.29	0.28
15	0.57	0.64	0.53	0.55
25	0.79	0.83	0.78	0.76
35	0.92	0.94	0.93	0.93
45	0.97	0.98	0.98	0.97
55	0.98	0.99	0.99	0.98
65	0.99	1.0	0.99	0.99
75	0.99	1.0	1.0	1.0
85	1.0	1.0	1.0	1.0
95	1.0	1.0	1.0	1.0
	[500 μm]	[500 μm]	[500 μm]	[500 μm]
5	0.10	0.09	0.11	0.11
10	0.21	0.20	0.18	0.18
15	0.39	0.44	0.43	0.42
25	0.69	0.68	0.68	0.73
35	0.91	0.88	0.89	0.94
45	0.98	0.99	0.98	0.99
55	0.99	0.99	0.99	0.99
65	0.99	1.0	1.0	0.99
75	0.99	1.0	1.0	1.0
85	1.0	1.0	1.0	1.0
95	1.0	1.0	1.0	1.0

real detections. The plotted completeness curves are the best-fitting logistic functions, describing the completeness as a function of input flux. We can see that positions of recovered sources do not show any significant offset to assigned inputs. More than 70 % of sources with $S_{250} > 13.2$ mJy have an offset lower than 6", which is smaller than a

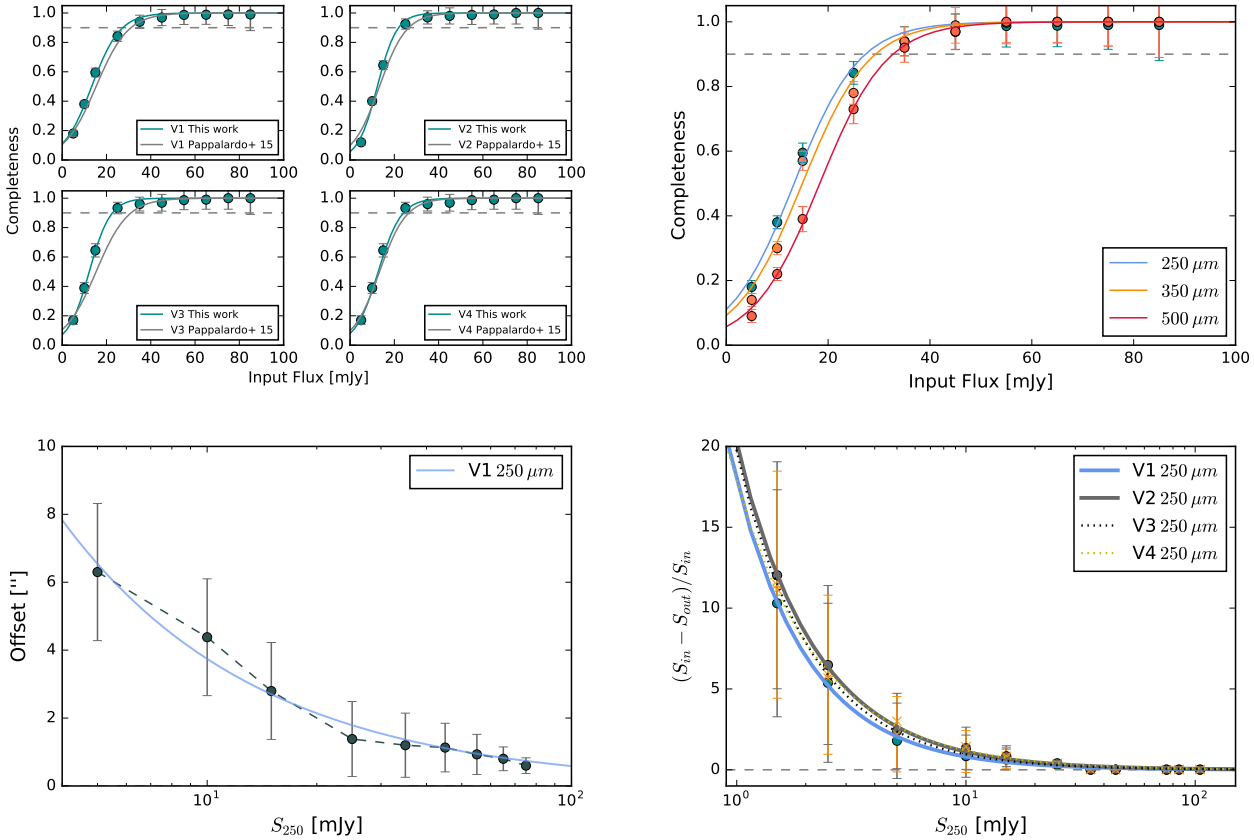

Figure 2.9.: For the HeViCS fields: Completeness at 250 μm band compared to Pappalardo, Bendo, et al. 2015 (upper left), SPIRE completeness for the V1 field (upper right), positional accuracy (average radial offset; lower left), and flux boosting, that is the flux difference as a function of input flux (lower right). Simulated (input) flux S_{in} is plotted on the x-axis for all subplots, while S_{out} refers to observed flux.

250 μm pixel size. I find that completeness and flux accuracy are consistent over all four HeViCS fields. The top left panel in Fig.2.9 shows our completeness result compared to one obtained by Pappalardo, Bendo, et al. 2015, confirming that with our `MBB-fitter` we can reach lower flux levels with fairly small flux biases, as can be seen from the bottom-right panel of Fig.2.9.

With the measured numbers in hand, we can adjust the detection cut to see variations in completeness, which are connected to the function of input flux density. The completeness of our 250 μm maps shows a trend of fast decrease below $\sim$ 25 mJy, and reaches $\sim$ 50% at $\sim$ 13.2 mJy, the value I choose as the lowest cut for our prior S_{250} list. To fit the completeness fraction as a function of input flux I use the generalised logistic function (Eq.9 from Wang et al. 2014). The fitted logistic curve reaches 90%

completeness at $S_{250} = 22$ mJy, being saturated at the level of 250 μm fluxes larger than 40 mJy. Very similar result is obtained for 350 μm. For the 500 μm band, the completeness is above 90% at $S_{500} > 35$ mJy, and above 80% at $S_{500} > 30$ mJy. I apply the latter 500 μm flux as the threshold for our final selection of 500 μm-risers. The bottom right panel in Fig.2.9 shows that fluxes of sources below $S_{250} = 7 - 10$ mJy are systematically overestimated due to "flux-boosting".

I also quantify the range of statistical outliers present in our measurements. Outlier contamination is measured as a function of output flux density. Sources are considered as contaminants if their output fluxes are more than 3σ above the value inferred for injected sources. Considering the lowest detection threshold in the 250 μm band (13.2 mJy) we found a low sample contamination of 2.7%.

2.6. Appendix: Comparison of 250 μm catalogues that are built by various extraction methods

Along with selection algorithm presented in previous sections, I additionally tested several other ways of producing prior catalogues that can be used to effectively de-blend photometry at longer wavelengths. I compare two other extraction codes and tested their performance in real and simulated maps. StarFinder (Diolaiti et al. 2000) is IDL source finding algorithm designed for stellar fields. It models the data as the summation of beam-smoothed point sources and iteratively detects, fits, and removes sources with decreasing fluxes. Sources do not have to be isolated to be found by StarFinder, but instead the algorithm attempts to untangle flux from neighbouring sources so flux is not double counted. The algorithm is iterative, finding sources at lower and lower signal-to-noise. StarFinder is developed to deblend sources but the ideal image to deblend would be crowded stellar field like a globular cluster or open star cluster.

Table 2.3.: Number of detected sources above the given detection threshold (quality flag>3 which corresponds to $3\sigma_{\rm conf}$).

250μm catalogue	number of sources at 250 μm	source density [per sq.deg]
HeViCS (SUSSEXtractor)	94309	1714
HeViCS (DAOphot)	80101	1456
HeViCS (StarFinder)	90265	1640
ELAIS-N2	21483	1760

The HIPE implementation of DAOphot incorporates the classic DAOPHOT algorithm (Stetson 1987), using the FIND and APER procedures in the IDL. The image is smoothed with the DAOPHOT convolution kernel, derived from the point response function, and the resulting smoothed image is searched for peaks, which are taken to be the positions of the point sources. Then the source flux densities are estimated using aperture photometry. The HIPE DAOphot algorithm also calculates an aperture correction automatically and returns a list of sources found in the input image along with their photometry.

The result of source extraction on 250μm maps is summarized in Table 2.3, while the result of completeness is illustrated in Fig.2.10. In the Table 2.3 we can see the number of 250 μm detections above the chosen flux cut. The three source extraction algorithms are tested, while I also show the result from the public catalogue of ELAIS-N2 as a control sample to compare with this work. The ELAIS-N2 is assumed to be a good proxy for anticipated source density since it is a large field with the depth at 250 μm similar as HeViCS. This case study confirmed that at flux levels at $S_{250} \gtrsim 35-40$ mJy all methods perform fairly well, while the combination of using `SUSSEXtractor` priors and **MBB-fitter** photometry returns the best result at faintest flux levels and reach the higher completeness at 250 μm (Fig.2.10).

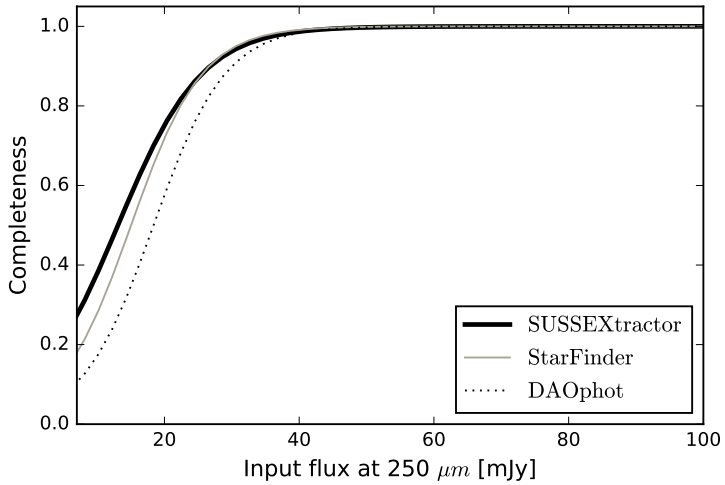

Figure 2.10.: Detection performance of the three algorithms used for this test case. The test is performed on simulated maps (see Section 2.5). For flux levels larger than 40 mJy all of them perform fairly well. At the faint end of the curve, the method which combines `SUSSEXtractor` priors and `MBB-fitter` photometry gives the best result.

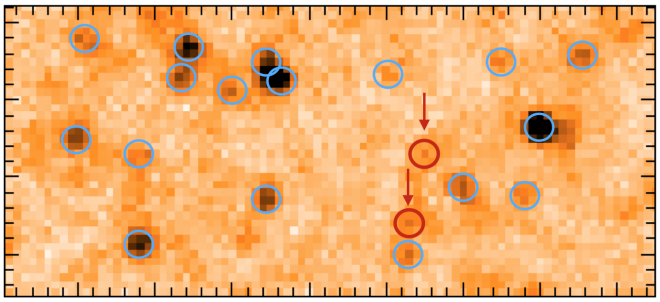

Figure 2.11.: Zoomed segment of the 250 μm map, showing the sources that are missed with StarFinder and DAOphot (red arrows), but detected with our extraction procedure.

CHAPTER 3

Statistical properties of SPIRE selected 500 μm-risers

Table of contents:

Introduction

Without confirmed spectroscopic redshifts of our sources, we are limited to the FIR properties of SPIRE-selected 500 μm-risers. Nevertheless, our data may be very useful in providing approximate redshift/luminosity distributions of statistical samples and candidates for follow-ups. In this Section I aim to accomplish this goal by performing several tests. In principle, having used priors on $T_{\rm d}$, we can obtain redshifts from the best-fit MBB SED and then compute the $L_{\rm IR}$. Since degeneracies between model parameters limit the information that can be derived from a MBB SED, here I decide to additionally probe a wider range of SED templates to test their consistency with the dust temperature I adopt. This is important for our estimation of IR luminosity of selected 500 μm-risers, since our MBB model has too simplistic description of the mid-IR part of the SED.

The photometric redshifts of 500μm-risers estimated with MBB model are compared to those from other templates in Section 3.1. The estimated total IR luminosities are presented in Section 3.2. I further make a direct comparison between the colours of our 500 μm-risers to those with known redshifts collected from the literature (Section 3.3).To put the statistics of selected high-z candidates in the context of galaxy evolution, in Section 3.4 I calculated differential number counts of 500 μm-risers. In Section 3.5 I discuss how does our selection relate to methods implemented in other studies. I further analyse which category of sources might potentially be missed when applying different techniques to find 500 μm-risers in wide extragalactic *Herschel* fields.

3.1. Expected redshift distribution of 500 μm-risers

Traditionally, two complementary approaches have been used in the literature to measure the photometric redshifts (z_{phot}) of galaxies via the shape of their FIR SEDs. One method uses a library of template SEDs (e.g. Aretxaga, D. H. Hughes, et al. 2003), while the other uses a small set of template SEDs, assumed to be representative (e.g Kirkpatrick et al. 2017, Lapi et al. 2011).

The approach based on different template SEDs has already been applied in studies of candidate high-z DSFGs (Dowell et al. 2014, Ivison, Lewis, et al. 2016, Duivenvoorden et al. 2018). For example, Ivison, Lewis, et al. 2016 take different well-sampled SED templates assumed to be representative, to calculate the z_{phot} and $L_{\rm IR}$ of SPIRE selected

sources. Because blindly employing these templates does not offer a full understanding of the potential systematics and uncertainties, Ivison, Lewis, et al. 2016 tested the reliability of template SEDs on the brightest sample of H-ATLAS DSFGs ($2 < z < 6$, $S_{500} > 50$ mJy). They quantified offset between estimated photometric redshifts and the known spectroscopic redshifts as $\mu = \Delta z/(1 + z_{spec})$, where $\Delta z = z_{phot} - z_{spec}$.

To compare the z_{phot} distribution of 500 μm-risers selected with our MBB approach, I decide to follow the same approach of Ivison, Lewis, et al. 2016 and to test how accurate the chosen SED templates are for our data. The first step in such testing is to build of a control data set. Since the reliability of a template is highly sensitive on the control data set, the best way to confront z_{phot} and z_{spec} is to probe 500 μm-risers selected in exactly the same manner as I did in the HeViCS field. Though no such data are currently available in HeViCS, I compile 30 known 500 μm-risers found in different extragalactic fields for which redshifts are available (J. A. Zavala, I. Aretxaga, et al. 2018, Riechers, Leung, et al. 2017, Fudamoto et al. 2017, Strandet, Weiss, Vieira, et al. 2016, Dowell et al. 2014). The majority of these sources (65%) are selected from SPIRE data, while the rest are strongly lensed 500 μm-risers initially selected from SPT. Hence I employ this "training" data set to analyse the efficiency of different SEDs in reproducing known redshifts.

3.1.1. The choice of SED templates

Along with the MBB model presented in Chapter 2, I adopt well-sampled SEDs of various DSFGs to estimate the redshifts of our 500 μm-risers. I make a careful choice of templates, aiming to overcome potential differences between local and high-redshift DSFGs (e.g. Symeonidis, Vaccari, et al. 2013, Magdis, Daddi, et al. 2012). All the SEDs presented here are also used in work of Ivison, Lewis, et al. 2016 and Duivenvoorden et al. 2018, and comparison of redshift distributions amongst different selection can be easily performed. The chosen templates are listed in Fig.3.1. They are: M82 (compact local starburst, Polletta et al. 2007); Arp220 (an interacting local ULIRG Rangwala et al. 2011); HFLS3 (SPIRE selected 500 μm-riser at $z = 6.34$; Riechers, Bradford, et al. 2013); "Cosmic Eyelash" (strongly lensed DSFG at $z = 2.3$; Swinbank, I. Smail, et al. 2010); G15.141 (strongly lensed DSFG at $z = 4.2$; Lapi et al. 2011). Finally, I also include templates synthesised for a wide range of DSFGs discovered in various surveys: GOODS-N (Pope, Chary, et al. 2008, hereafter Pope08), H-ATLAS (Pearson, Eales, et

al. 2013, hereafter P13) and ECDF-S (Swinbank, J. M. Simpson, et al. 2014, hereafter ALESS).

The Pope08 template is made of 13 DSFGs selected from *Spitzer* 24 μm data, covering the redshift range $2 < z < 2.5$. It covers the mid-IR to radio wavelength range. The P13 template is built from a subset of 40 H-ATLAS survey sources with accurately measured redshifts in the range from 0.5 to 4.5, and including the 500 μm-riser at $z = 4.4$ discovered by P. Cox et al. 2011. The template adopts two dust components with different temperatures. Here I use the same best-fit values as found in Pearson, Eales, et al. 2013: $T_{\rm cold} = 23.9$ K, $T_{\rm hot} = 46.9$ K, and the ratio between the masses of cold and warm dust of 30.1. ALESS template describes 52 ALMA observed sources that are selected at 870 μm in the Extended Chandra Deep Field South. The ALESS sources have mean redshift at 2.4 ± 0.2, with the redshift distribution featuring a high-z tail, having 20% of the DSFGs at $z > 3$.

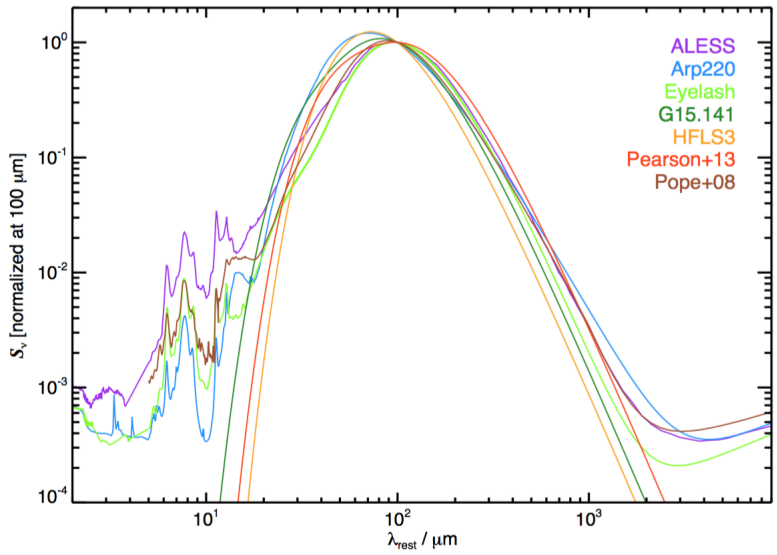

Figure 3.1.: Rest frame SED templates probed in this work normalized in flux at 100 μm. The choice of templates is the same as in Ivison, Lewis, et al. 2016 and Duivenvoorden et al. 2018. (Image credit: Ivison, Lewis, et al. 2016).

3.1.2. The validation of chosen SED templates

I further test adopted SED templates against the control data set of high-z DSFGs. For a given template I quantify its offset ($\mu = \Delta z/(1 + z_{spec})$) and root-mean-square scatter ($\sigma_{\rm RMS}$). I find that the HFLS3, M82 and G15.141 are less accurate fitting choices due to their large offset ($\langle\mu\rangle > 0.25$) and large scatter ($\sigma_{\rm RMS} > 0.3$). I thus left them unused for

the final z_{phot} and $L_{\rm IR}$ computation. Amongst other SEDs that worked fairly well, the synthesized template P13 shows the best performance. This is mainly expected given the fact that P13 has already been confirmed in the literature as a good framework for calculating z_{phot} of SPIRE sources (Oteo, Ivison, Negrello, et al. 2017, Rawle et al. 2016, Ivison, Lewis, et al. 2016). More recently, Bakx et al. 2018 found that P13 template is also accurate for strongly lensed SPIRE galaxies at $z > 3$.

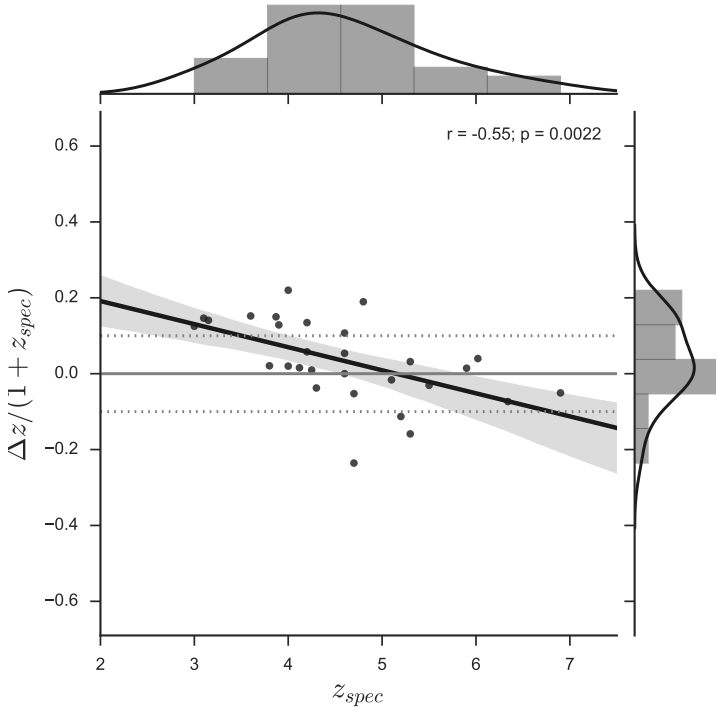

Figure 3.2.: For the P13 template: offset between estimated and true redshift quantified as $\mu = \Delta z/(1+z_{spec})$ as a function of z_{spec}. The black line with the corresponding shaded region represents linear fit of the form: $\Delta z/(1+z_{spec}) = -0.062 \times z_{spec}$. The similar slope of a linear fit is present if we apply ALESS or Pope08 SED.

In Fig.3.2 I illustrate how the z_{phot} estimated with the P13 template compare to z_{spec} of 500 μm risers from the control data set. The linear fit in the same figure indicates a slight decreasing trend for $\Delta z/(1 + z_{spec})$ with redshift. Such a behaviour suggests that we may underestimate the z_{phot} of some of the galaxies due to a rising $T_{\rm d}$ of the spectroscopic sample towards higher redshifts (e.g. Hayward, Jonsson, et al. 2012, Kirkpatrick et al. 2017, Ivison, Lewis, et al. 2016).[a]

[a]Duivenvoorden et al. 2018 found the similar linearly decreasing trend in their SED template analysis. They applied photometric code `EAZY` with a range of galaxy templates to determine the full redshift PDF of 500 μm-risers selected in Asboth et al. 2016.

Table 3.1.: Photometric redshift accuracy related to SED templates.

	MBB*	P13	ALESS	Pope08	Arp220	Eyelash	G15	M82	HFLS3
$\langle\mu\rangle$	0.12	-0.09	-0.12	0.09	-0.2	0.15	0.24	-0.26	0.29
$\langle\sigma_{\rm RMS}\rangle$	0.18	0.20	0.23	0.21	0.24	0.2	0.31	0.35	0.33

Here $\langle\mu\rangle$ and $\langle\sigma_{\rm RMS}\rangle$ are median offset and scatter between z_{phot} estimated with listed SED templates and spectroscopic redshifts of the control data set. I test the performance of MBB model fixing the emission slope $\beta = 1.8$ and using a prior in the dust temparature ($T_{\rm d} = 40 \pm 10$K). By applying several tests I found that use of a wide unfiorm prior ($20 < T_{\rm d} < 60$K) lead to much larger χ^2.

3.1.3. Summary of photometric redshift estimates

To estimate the z_{phot} of our 500 μm-risers, along with MBB I use SED templates found to be reliable within the adopted temperature range (Section 3.1.2), and fit them to our FIR fluxes.

For the MBB model introduced in Section 2.4, the FIR peak depends linearly on both the z and the inverse of the $T_{\rm d}$, causing the $T_{\rm d} - z$ degeneracy (Blain, Barnard, et al. 2003, Pope and Chary 2010). Because of the degeneracy, one cannot obtain constraints on most individual parameters of the MBB model using only SED data: a prior information is needed. To make a reasonable choice of priors on β and $T_{\rm d}$, I investigate the described test sample of 30 known 500 μm-risers. The median $T_{\rm d}$ for such a sample is $T_{\rm d} = 38 \pm 9$ K (Strandet, Weiss, Vieira, et al. 2016, Riechers, Bradford, et al. 2013, Dowell et al. 2014). Therefore I use this information and set Gaussian prior at $T_{\rm d} = 38 \pm 9$ K. The choice of β is arbitrary, likely $1.5 < \beta < 2.1$ (Casey, Narayanan, et al. 2014, T. P. MacKenzie et al. 2014, Roseboom, Ivison, et al. 2012). For sake of simplicity I keep power-law slope fixed at $\beta = 1.8$, which is the value in the middle of that range. For chosen $T_{\rm d}$ and β, I determine a median redshift of 4.2 ± 0.55. Due to the aforementioned degeneracy in $(1+z)/T_{\rm d}$ space, decreasing the peak of the $T_{\rm d}$ distribution, i.e. from 38 K to 33 K for the fixed β, the measured redshift peak decreases to $\hat{z} = 3.69$ (with 33% of sources at $z > 4$).

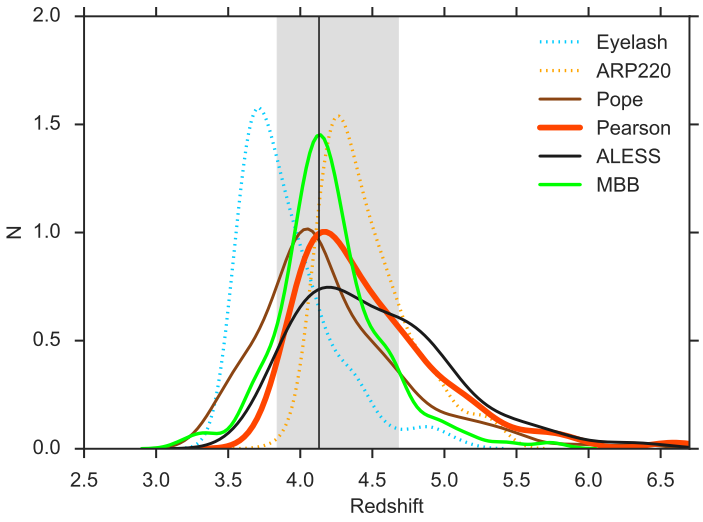

Figure 3.3.: Redshift distribution estimated with our MBB method, related to distributions obtained from different templates employed in this analysis. The vertical line and grey shaded region illustrate the median and corresponding interquartile range when we linearly combine results from all templates.

Table 3.2.: Median photometric redshifts of our 500 μm-risers and attributed errors.

	MBB $T_{\rm d} = 38 \pm 9$K	P13	ALESS	Pope	Arp220	Eyelash
$\langle z_{phot} \rangle$	$4.2^{+0.55}_{-0.55}$	$4.27^{+0.52}_{-0.37}$	$4.3^{+0.71}_{-0.53}$	$4.04^{+0.62}_{-0.46}$	$4.35^{+0.45}_{-0.33}$	$3.73^{+0.5}_{-0.4}$
$\langle \chi^2 \rangle$	0.87	0.83	0.95	1.1	1.34	1.18

We can now check how the results would change when applying different choice of templates. For single galaxy templates the redshifts are 3.73 and 4.3 for "Cosmic Eyelash" and Arp220 respectively. On the another hand, all synthesized templates show a very good consistency having the median redshift in the range $4.1 < z_{phot} < 4.35$. The errors on the median were determined using a bootstrap method, where I randomly sampled 133 sources from the redshift distribution 1000 times. The kernel density estimation (KDE) of photometric redshifts is plotted in Fig.3.3, while the median z_{phot} and $\langle \chi^2 \rangle$ related to each SED are listed in Table.3.2. The vertical line and shaded region of the plot depicts the total median redshift and corresponding interquartile range:

$4.19^{+0.5}_{-0.33}$.

3.1.4. Comparing the estimated z_{phot} distribution to other studies

In the following I compare our z_{phot} distribution to those estimated in other studies. As an example here, I adopt the z_{phot} distribution from P13 template to be representative ($z_{phot} = 4.27^{+0.52}_{-0.37}$).

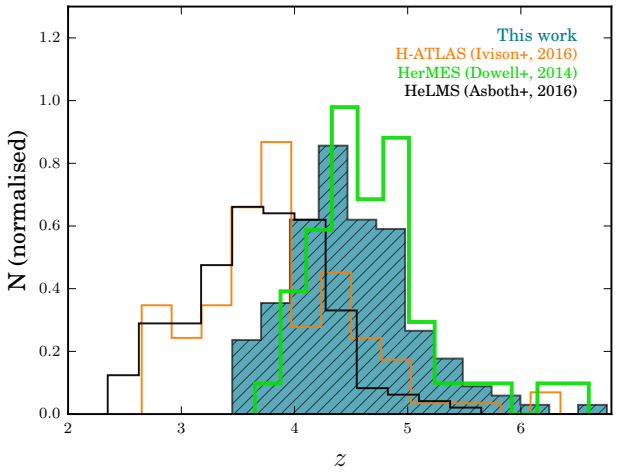

Figure 3.4.: Normalised distribution of estimated photometric redshifts of red DSFGs in different studies. Note that z_{phot} in studies of Ivison, Lewis, et al. 2016 and Duivenvoorden et al. 2018 are determined with SPIRE and SCUBA-2 data, whilst for this work and Dowell et al. 2014 only SPIRE photometry were available for z_{phot} computation.

To determine an average z_{phot} for 500 μm-risers selected in HerMES fields, Dowell et al. 2014 used an MCMC method to fit the optically thick MBB model with fixed dust emissivity and rest-frame wavelength peak for each source. They found $\langle z \rangle = 4.7 \pm 0.9$. For DSFGs selected in *H*-ATLAS Ivison, Lewis, et al. 2016 found $\hat{z} = 3.7 \pm 0.7$, while for those selected in the HeLMS field Duivenvoorden et al. 2018 estimated $\hat{z} = 3.6 \pm 0.9$. The median value of our sample matches the 1σ uncertainty range of photometric redshifts reported in other studies. The redshift distribution of all known studies of 500μm-risers is presented in Fig.3.4.

Although our estimates of z_{phot} are consistent to those found in other works, it is clear from Fig.3.4 that the peaks of the redshift distribution of galaxies from this work and those fromDowell et al. 2014 are higher than in the other two studies. There are two

main reasons for such difference. Firstly, for HeLMS and *H*-ATLAS, z_{phot} are computed with use of SPIRE and 850 μm SCUBA-2 data, whilst for this work and Dowell et al. 2014 only SPIRE were available. Working with SPIRE/SCUBA-2 data, Cowie, Barger, et al. 2017, Duivenvoorden et al. 2018 and Roseboom, Ivison, et al. 2012 found that SPIRE photometry alone overestimate the z_{phot} by factor of $\Delta z \approx 0.3$ due to the lack of constraints on the peak of the FIR emission. On the other hand, the catalogues of Ivison, Lewis, et al. 2016 and Asboth et al. 2016 may be contaminated by a non-negligible fraction of $z < 4$ galaxies due to relaxed colour criteria ($S_{500}/S_{350} > 0.85$) used in Ivison, Lewis, et al. 2016 [b], and very high confusion noise measured in HeLMS (Asboth et al. 2016). The later causes the selection threshold being much brighter than in our work, potentially introducing selection biases such as strong lensing (e.g.Negrello et al. 2017) and source blending (e.g. Bethermin et al. 2017). In Section 4.2 and 4.3 I use different models to extensively analyse how the noise, strong lensing and resolution effects impact the observed colours and redshift distribution of $500\,\mu$m-risers. The influence of selection wavelengths and various colour-cuts on expected z_{phot} is discussed in Section 4.4.

3.2. Estimating the IR luminosity

To compute the total IR luminosity I again test the MBB SED along with more complex SEDs introduced in previous section. The estimated median $L_{\rm IR}$ for each corresponding template is presented in Table.3.3. The obtained values favour the presence of very luminous IR systems regardless of the chosen template - in 90% of cases selected $500\,\mu$m-risers have $L_{IR} \geq 10^{13} L_{\odot}$, with minimum and maximum values of $L_{IR} = 8.1 \times 10^{12} L_{\odot}$ and $L_{IR} = 5.1 \times 10^{13} L_{\odot}$, respectively. For example, assuming again P13 to be representative for the whole population of selected 500 μm-risers, I obtain median IR luminosity $\hat{L_{IR}} = 1.94 \times 10^{13} L_{\odot}$. The result is again in consistency with Dowell et al. 2014 and Ivison, Lewis, et al. 2016. Ivison, Lewis, et al. 2016 report the median value $L_{IR} = 1.3^{+0.7}_{-0.5} \times 10^{13} L_{\odot}$, while Dowell et al. 2014 find $L_{IR} = 2.1 \times 10^{13} L_{\odot}$.

[b] In the catalogue of Ivison, Lewis, et al. 2016, $\sim 15\%$ of sources are selected with different colour criteria than ours, and are not $500\,\mu$m-risers.

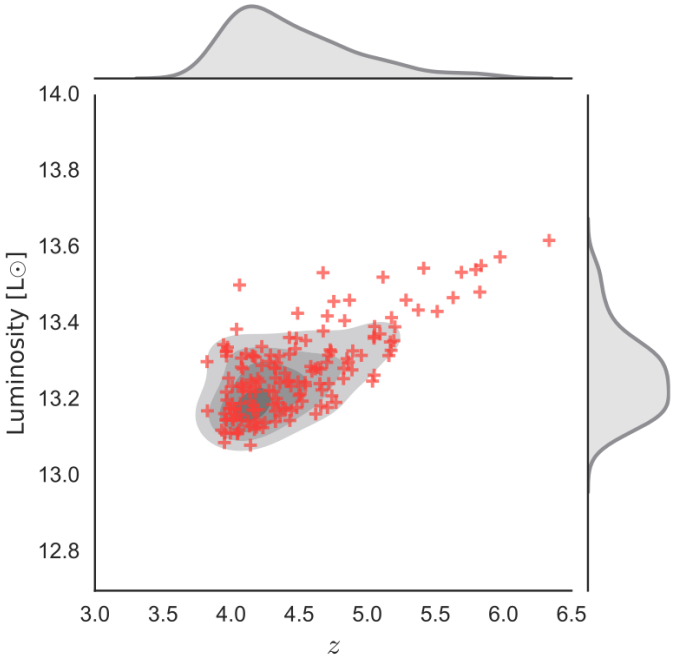

Figure 3.5.: Infrared luminosity of our 500μm-risers (y-axis) as a function of redshift. Red crosses represent values estimated with the P13 template. For the fitting I imposed the same best parameters as in Pearson, Eales, et al. 2013: T_{cold} = 23.9 K, T_{hot} = 46.9 K, and a cold-to-hot dust mass ratio equal to 30.1.

Table 3.3.: Median IR luminosities of our 500 μm-risers.

	MBB	P13	ALESS	Pope	Arp220	Eyelash
$\hat{L_{IR}}$	$1.15 \times 10^{13} L_\odot$	$1.94 \times 10^{13} L_\odot$	$1.65 \times 10^{13} L_\odot$	$1.36 \times 10^{13} L_\odot$	$1.09 \times 10^{13} L_\odot$	$1.19 \times 10^{13} L_\odot$

Comparing estimated $L_{\rm IR}$ among templates, we can see from Table.3.3 that synthesised templates (P13, ALESS and Pope08) reveal larger apparent luminosities than single galaxy templates. It leads to the conclusion that the average 500 μm-riser is more luminous than a typical ULIRG (e.g. Arp220), located at a same redshift. The $L_{\rm IR}$ estimate from MBB is also slightly lower then those measured with P13 - the difference arises from the fact that single-temperature MBB model cannot fully catch the mid-IR excess of the SED at the Wien side. In Fig.3.5 I illustrate the L_{IR}-redshift trend of our 500 μm-risers. It can be seen that the expected luminosity distribution is heavy-tailed towards the higher redshifts. This indicates that extreme DSFGs are present at redshfits above the interquartile range, but could also indicate strong gravitational lensing

or unresolved blending. It is notable that the vast majority of the brightest red DSFGs selected by *Herschel* have been revealed as either lensed galaxies, groups/clusters of starburst galaxies (Oteo, Ivison, L. Dunne, et al. 2017), starbursts with buried AGN (Strandet, Weiss, C. De Breuck, et al. 2017), or some combination of the three (e.g. Riechers, Leung, et al. 2017). It would strongly suggests a limit to the IR luminosity of individual DSFGs (Fudamoto et al. 2017). Our selection function results with the faintest known catalogue of 500 μm-risers (see Fig.2.11), and we expect that fraction of strongly lensed sources would be smaller than in other existing selections. In Section 5.2 I introduce the method of using models to correct for the effect of multiplicity and lensing on derived $L_{\rm IR}$.

3.3. Colour-redshift comparison to red DSFGs from the literature

In this section I investigate if the colours of our sources are consistent with high-z observations. The observed colour-colour diagram related to the MBB model used in this work is presented in Fig.3.6, and it illustrates the aforementioned temperature-redshift degeneracy. The shape of our colours is model dependent, since we forced photometric points to follow modelled MBB SED track presented in Section 2.4. To better understand how these colours relate to those found in other studies of 500 μm-risers, I introduce 12 of the 500 μm-risers for which spectroscopic redshifts are known to be at $z > 4$. [c]

The unlensed 500 μm-risers at $z > 4$ are available from H-ATLAS (marked with red diamonds in Fig.3.7). Their redshifts are confirmed via systematic ALMA/NOEMA 3 mm scan, which was the first spectral scan of a larger number of SPIRE selected red DSFGs (J. A. Zavala, I. Aretxaga, et al. 2018, Fudamoto et al. 2017, Oteo, Ivison, Negrello, et al. 2017). Other known 500 μm-risers at $z > 4$ are brighter, strongly lensed sources (50$<S_{500} <$ 100 mJy). They are detected in HeLMS and HerMES fields (marked with red stars in Fig.3.7): HFLS3, Riechers, Bradford, et al. 2013; FLS1, Dowell et al. 2014, HELMS-RED4, Asboth et al. 2016), while the rest are initially found with SPT at 1.4 mm, but SPIRE observations later reveal that they are also 500μm-risers. Example of

[c] There also exist 18 sources that have known redshifts $3 < z < 4$. Here, for the sake of simplicity, I plotted just those that are at $z > 4$ and have 500 μm fluxes within the same range as our observations (30 mJy$< S_{500} <$ 100 mJy).

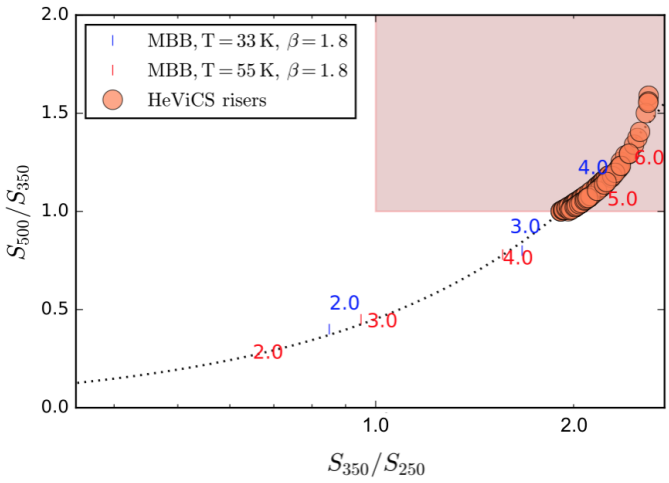

Figure 3.6.: SPIRE colour-colour diagram of 500μm-risers related to our MBB model. The blue and red labels show different modelled redshifts associated to chosen $T_{\rm d}$.

such objects are SPT0113-46 at $z = 4.2$ (Weiß, C. De Breuck, et al. 2013) and the most distant known dusty starburst SPT0311-58 at $z = 6.9$ (Strandet, Weiss, C. De Breuck, et al. 2017).

In Fig.3.7 I present colours of our 500 μm-risers along with those introduced above. Redshift tracks of typical starbursts Arp 220 and Cosmic Eyelash are added for comparison. From the Fig.3.7 we see that the colours of our sources agree rather well with a large number of red DSFGs at $z > 4$ found in different studies. There are some exceptions, one of them being the most distant 500 μm-riser, SPT0311-58 at $z = 6.9$. The possible reason for this might be the contribution from AGN, since it has been shown that SPT0311-58 likely experiences additional mechanical energy input via AGN-driven outflows(Strandet, Weiss, C. De Breuck, et al. 2017). There are also examples of sources with redshifts somewhat lower than what would be expected from their very red colours. Such an example is the 500 μm-riser at $z = 4.2$ (Weiß, C. De Breuck, et al. 2013), a strongly lensed red source with colours very similar to those of known 500 μm-risers at $z > 6$. However this source has an estimated $T_{\rm d}$ of 30 K, which is much lower compared to the median dust temperature of 500 μm-risers with similar colours ($z \sim 6$, $T_{\rm d} = 52$K, J. A. Zavala, Montaña, et al. 2017, Riechers, Bradford, et al. 2013).

Finally, I draw attention to some interesting 500 μm-risers selected in this work. According to our template-based z_{phot} distribution, the "reddest" sources from our data ($S_{500}/S_{350} > 1.3$) have estimated photometric redshifts in the range $5.7 < z_{phot} < 6.7$. In the literature all known 500 μm-risers at $z > 6$ fulfil these so-called "ultra-red" require-

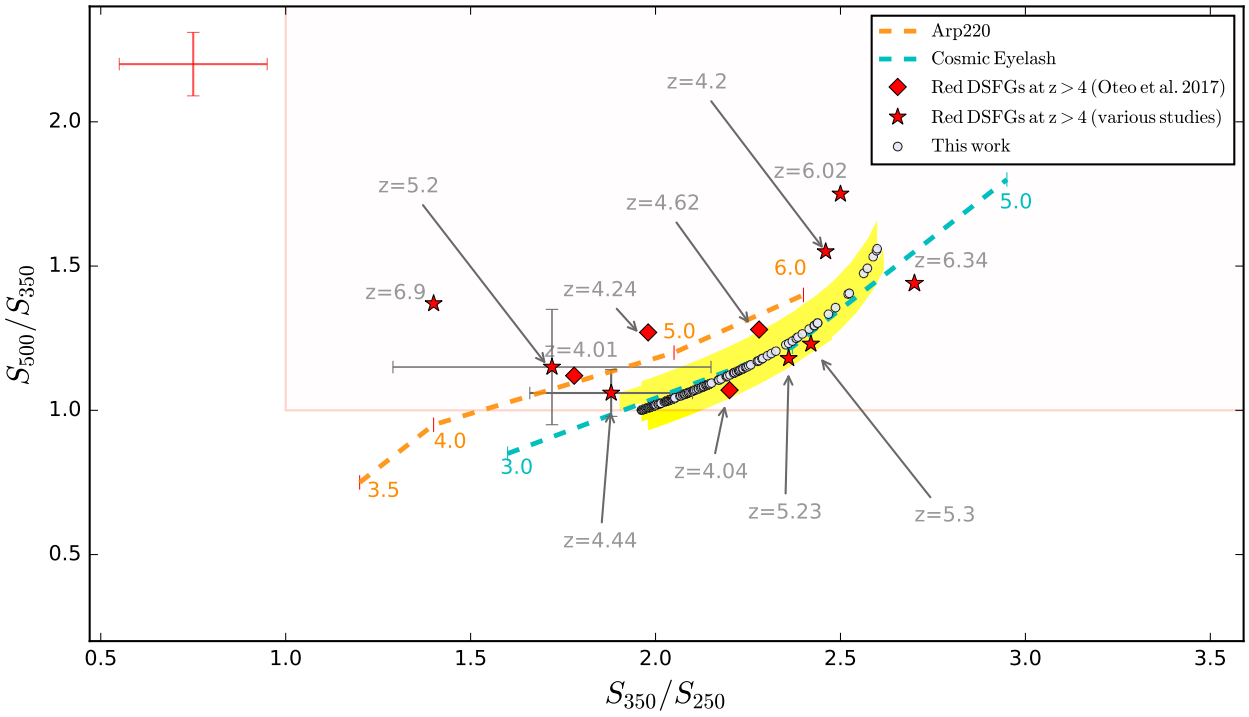

Figure 3.7.: SPIRE colour-colour diagram of 500 μm-risers, overlaid with redshift tracks of Arp 220 (Rangwala et al. 2011) and Cosmic Eyelash (Swinbank, I. Smail, et al. 2010). Galaxies selected in this work are represented with circles, while yellow shaded regions describe uncertainties related to the chosen emissivity ($1.5 < \beta < 2.1$). For comparison we show 500 μm-risers selected in different studies and with known spectroscopic redshifts. Sources marked with red stars are: $z = 6.34$ (HFLS3 , Riechers, Bradford, et al. 2013), $z = 6.02$ (G09-8988, J. A. Zavala, Montaña, et al. 2017), $z = 4.44$ (FLS 5, Dowell et al. 2014), $z = 5.3$ (FLS 1, Dowell et al. 2014), $z = 5.2$ (HELMS-RED4, Asboth et al. 2016), $z = 4.04$ (GN20, Daddi, Dannerbauer, et al. 2009), $z = 6.9$ (SPT0311-58 Strandet, Weiss, C. De Breuck, et al. 2017) and $z = 4.2$ (SPT0113-46, Weiß, C. De Breuck, et al. 2013). Sources marked with red diamonds are unlensed DSFGs from Oteo, Ivison, Negrello, et al. 2017. For some of known sources we plot their colour uncertainties. Representative colour uncertainty (1σ) for our sample is plotted in the upper-left corner.

ments (J. A. Zavala, Montaña, et al. 2017, Strandet, Weiss, C. De Breuck, et al. 2017, Riechers, Bradford, et al. 2013). I selected seven such sources in the present sample, and I highlight them as potentially $z > 6$ candidates. They are catalogued as HVS 5, HVS 6, HVS 21, HVS 35, HVS 47, HVS 75, HVS 85 and HVS 94. I also stress that five of our 500 μm-risers (HVS27, HVS60, HVS 64, HVS115 and HVS 130) reside in potential

overdense regions unveiled by *Planck* (Planck Collaboration, Ade, Aghanim, Arnaud, Aumont, Baccigalupi, Banday, Barreiro, Bartolo, Battaner, Benabed, A. Benoit-Lévy, et al. 2016). If these overdensities are not just part of random fluctuations in the galaxy number density within the *Planck* beam, this makes them candidate protoclusters of high-z DSFGs (Greenslade et al. 2018, Smolčić et al. 2017, Oteo, Ivison, L. Dunne, et al. 2017, Clements, Braglia, Petitpas, et al. 2016). I extensively discussed this possibility in the Chapter 6 of this Thesis.

3.4. Differential number counts

Measurements of the number density of galaxies detected in a cosmological survey, and their distribution in different flux bins can provide an insight into the evolution of the selected population of sources and put strong constrains on the galaxy formation theory (see e.g. Hayward 2013 or Casey, Narayanan, et al. 2014). The advantage of using number counts to retrieve the information about selected population is that no redshift information is needed, and it can be easily compared amongst different samples. The number of sources is often given either in a raw (uncorrected) form, or in a flux deboosted form, usually represented with power-law fits (see Clauset et al. 2007 for a review). In this section I measure the raw 500 μm differential number counts along with their integral values, and test our selection in respect to previous studies.

I determine our counts placing 133 $500\,\mu$m-risers in seven logarithmic flux bins between 30 mJy and 100 mJy. The total raw number density of $500\,\mu$m-risers in 55 deg^2 of HeViCS is $N = 2.41$ sources per deg^2, with the corresponding 1σ uncertainty of 0.34. Along with differential counts, I also compute integral number counts, which are simply obtained by counting all $500\,\mu$m-risers in a given sky area above the 500 μm flux.The differential and integral number counts are presented in Table 3.4. From the Fig.3.8 we can see that the slope of our differential counts is very steep between 30 mJy and 55 mJy, suggesting a strong decline in the number of brighter 500 μm-risers. Since it is known that bright-end of FIR/submm number counts is dominated by brightest local spirals, powerful AGNs and strongly-lensed FIR-luminous galaxies (see Negrello et al. 2017, Wardlow, Malhotra, et al. 2014), the relatively small number density of brighter 500 μm-risers indicates that our selection is not mainly affected by these contaminants. The counts presented here are uncorrected for non-red interlopers, galaxy clustering and incompleteness, and they are thus a biased estimator of the intrinsic distribution of

selected DSFGs. In Section 4.1 I introduce the model-based method that fully inspects and quantifies biases which govern the shape of observed distribution. On top of that, the slight departure from the steep power-law shape towards the brighter fluxes is usually explained with the effect of strong lensing (e.g. Negrello et al. 2017). In Section 5.2 I again use a model-based approach to determine the number counts of strongly-lensed DSFGs in our catalogue.

Table 3.4.: Differential and integral number counts.

Flux (500 μm)		Diff. counts	Int.counts [(1)]
S_{min}	S_{max}	dN/dS	$N(> S_{min})$
[mJy]	[mJy]	[$\times 10^{-4}$mJy^{-1}deg^{-2}]	[deg^{-2}]
30	40	1527± 164	2.41± 0.22
40	50	581± 90	0.91±0.14
50	60	145±51	0.29±0.09
60	70	72±36	0.14±0.05
70	90	27±15	0.07±0.03
90	110	9±5	0.02±0.01

(1) In order to calculate the cumulative (integral) number counts I have summed over all the 500 μm-risers above the specified flux density (S_{min}). Here I present raw differential and integrated number counts.

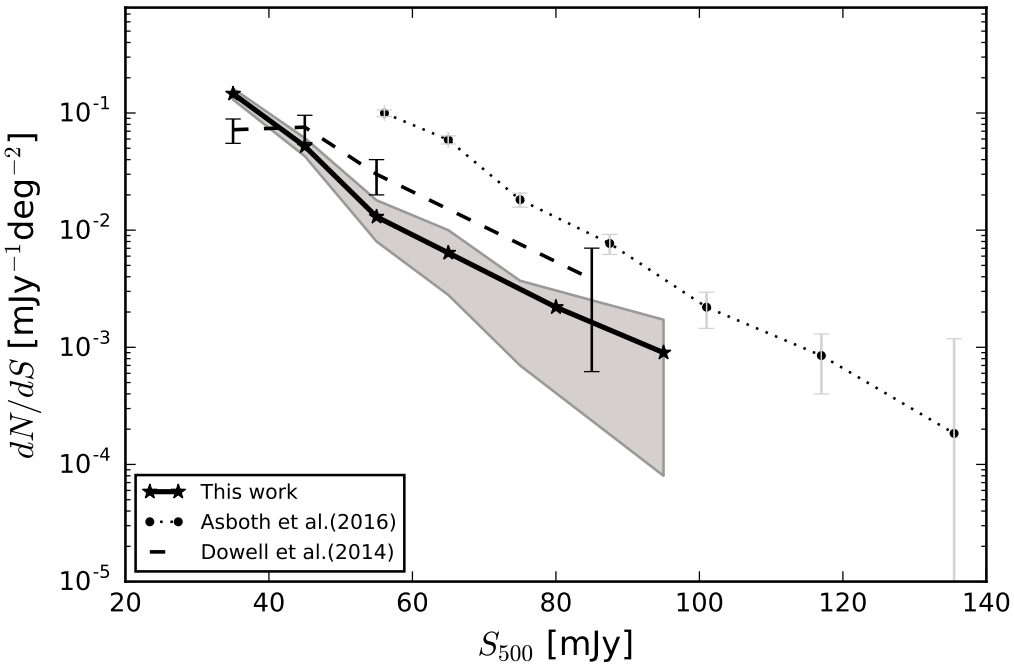

Figure 3.8.: Raw differential number counts of 500 μm-risers from several studies. HeViCS number counts are presented with black stars, connected with a full, black line. Counts from Asboth et al. 2016 are indicated with black circles and connected with dotted lines, whilst observational findings of Dowell et al. 2014 are presented with dashed black lines. Shaded area is associated to 1σ Poisson error-bars, while for the brightest flux bin with low statistics of sources, I assume the upper 95% confidence level.

To compare the number of selected 500 μm-risers to other existing selections, in Fig.3.8 I show raw differential number measured by Asboth et al. 2016 and Dowell et al. 2014. These studies applied the so-called "difference map" method (DMAP) to select red DSFGs. The method homogenizes beams to the size of 500 μm, and creates the DMAP where SPIRE images are all smoothed to an identical angular resolution. Prior to source identification, a carefully weighted combination of the three SPIRE maps is formed such that I applied the relation from Dowell et al. 2014: $D = 0.920 \times M_{500} - 0.392 \times M_{250}$, where M_{500} and M_{250} are the smoothing values after matching SPIRE maps to the 500 μm resolution. To select 500 μm-risers, they then performed a red colour map-based search, starting from the lowest-resolution 500 μm maps.

While our measurements show fairly good agreement with number counts reported by Dowell et al. 2014 especially in lower flux bins, they are well below the values measured by Asboth et al. 2016. Depending on the chosen flux bin, the discrepancy factor

ranges from 3 to 10. The significant offset between our measurements and those from Asboth et al. 2016 might be due to several effects. Firstly, Asboth et al. 2016 included possible blends in their final catalogue under the assumption that at least one component of a blend is a red DSFG. This introduces a non-negligible number of contaminants, which is the effect I analyse in Section 4.2. Secondly, Bethermin et al. 2017 simulated the DMAP selection in their mock catalogues and found the number of observed $500\ \mu$m-risers to be higher by a factor of 5 compared to genuine (modelled) sources. They concluded that a combination of noise, resolution effects, and the steepness of flux density distributions produces numerous red artefacts that match $500\ \mu$m-risers criteria in DMAP. In Section 4.2.1 I present a detailed analysis of the effect of noise on our selection.

3.5. Comparing our selection to DMAP: an observational view

In order to better understand the differences between selections, in this Section I aim to make a HeViCS catalogue of $500\ \mu$m-risers using the exact DMAP method described in Asboth et al. 2016 and Dowell et al. 2014. The main goal of this exercise is to compare the numbers and colours of such selected sample to our de-blended catalogue of 133 $500\ \mu$m-risers.

I start my analysis by creating three smoothed maps at SPIRE bands following the recipe of Dowell et al. 2014. They implemented the optimal matched filter for the 500 μm map, and construct the smoothing kernels that produce the same effective source shape at other SPIRE wavelengths. The purpose of such a filtered map (DMAP) is to have a substantially reduced confusion limit while sources represented with red SPIRE colours remain brighter as compare to nominal SPIRE maps. Dowell et al. 2014 experimented with various linear combinations using all three maps, but surprisingly, they have found that including a 350 μm term does not improve the efficiency of the source selection. To make the DMAP from nominal HeViCS images, I thus accept the same best coefficients found in their work: $\mathrm{D} = 0.920 \times M_{500} - 0.392 \times M_{250}$.

Moreover, for the sake of consistency, I extract the sources and compute their fluxes with StarFinder, which is the code used both in Asboth et al. 2016 and Dowell et al. 2014.[d] I measure the SPIRE photometry at 500 μm positions, listing all the sources with

[d]Some recent studies (e.g. Wang et al. 2014) showed that although StarFinder is very efficient source extraction algorithm, it is not fully suitable for the photometry at fainter SPIRE flux levels ($S_{500} < 30 - 40$ mJy). Investigating the blind catalogues in HerMES fields, Wang et al. 2014 found that StarFinder detects fewer sources than SUSSEXtractor at $S_{250} < 4\sigma$, at the same time suffering from

D-value above 4σ (1652 sources in total). To select 500μm-risers I impose DMAP selection criteria: the first selected group of sources fulfil the requirements of Dowell et al. 2014 ($S_{500} > S_{350} > S_{250}$, $D > 27$ mJy and S_{500} >30mJy), and contains 148 sources in total. Subsequently, I found 87 sources while following the criteria proposed by Asboth et al. 2016: $S_{500} > S_{350} > S_{250}$, $D > 31$ mJy and S_{500} >52mJy.

The total density of sources that are selected according to criteria of Dowell et al. 2014 are mildly above our estimates (148 vs.133 sources, for the total observed area of 55deg^2). Oppositely, the number of 500 μm-risers from the selection of Asboth et al. 2016 is factor of 5 above our estimates when we consider the same flux range ($S_{500} > 52$ mJy, 87 vs. 17 sources).

The another way to check eventual difference between selections is via observed SPIRE colours. In Fig.3.9 I plot S_{500}/S_{350} vs. 500 μm flux for 500 μm-risers selected in the HeViCS field. The black circles represent the sources that fulfil our criteria, whilst the blue stars are sources selected from DMAP and follow the criteria of Asboth et al. 2016. We see that significant number of galaxies from DMAP sample have systematically higher S_{500}/S_{350} compare to DSFGs selected with our de-blending algorithm. If we consider the same flux range and compare measured colours, we find that median value of our selection ($S_{500}/S_{350} = 1.11$) agrees with Dowell et al. 2014 ($S_{500}/S_{350} = 1.08$), but not with selection of Asboth et al. 2016 ($S_{500}/S_{350} = 1.20$). As we suspect before, the impact of noise seems to be a prominent factor for colour selection, and I analyse it with simulations presented in Section 4.2.1.

How to explain the difference between observed number counts?

The DMAP selection of 500 μm-risers only requires that objects have red SPIRE colour and are detected in 500 μm maps. This method, however, does not require a clear detection at 250 μm and 350 μm, because that could bias against the reddest objects. While this assumption is reasonable if we do not want to miss those candidates with very faint 250 μm fluxes (e.g. "250 μm dropouts"), it severally affects the overall statistics because it could pollute the final catalogue with the large number of observed red artefacts (see the discussion from Bethermin et al. 2017 and Duivenvoorden et al. 2018).

As a first check to see how dense are regions that host sources from the DMAP sample, I probe apertures of 40", 50" and 60" and measure the cumulative 500 μm flux around

significant flux boosting at blindly detected 500 μm sources.

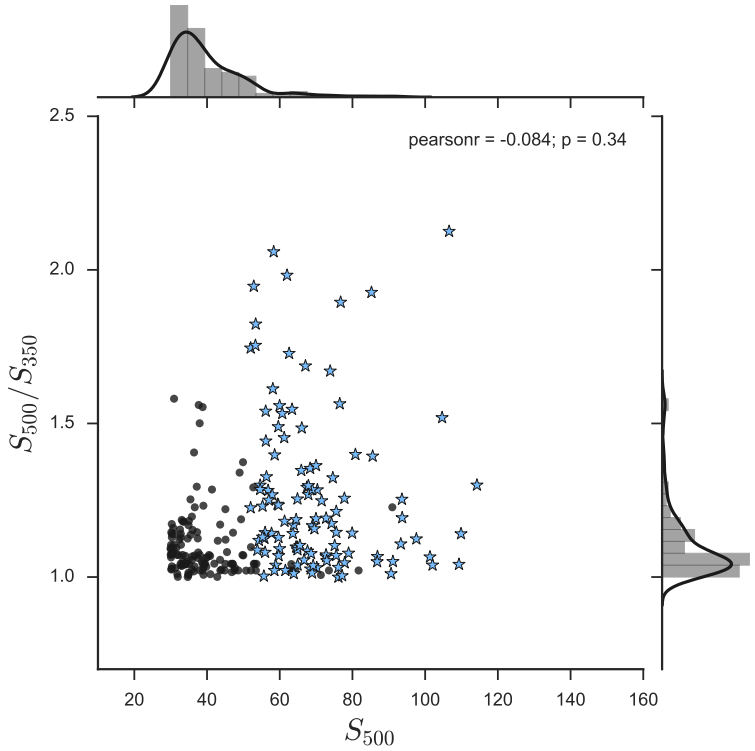

Figure 3.9.: Comparison of observed colours of 500 μm-risers detected in the HeViCS field with our method (black circles) and DMAP (Asboth et al. 2016, blue stars).

the DMAP selected risers and 500 μm-risers selected with our method. For the same "on-sky" area, the DMAP objects reveal much steeper (factor of 1.3) rise of cumulative flux than 500 μm-risers selected with our technique. It strongly suggests that DMAP galaxies systematically reside in denser regions compare to those from this work.

For 500 μm-risers selected in HeViCS with the DMAP method, I analyse colours estimated with our simultaneous de-blending method. Applying this, the number of 500 μm-risers selected with Asboth et al. 2016 criteria dropped significantly - from 87 to 43. I find that 80% of DMAP sources with anomalously red colours ($S_{500}/S_{350} > 1.5$) are actually blended with one or two 250 μm companions inside the 500 μm beam. Since $> 50\%$ of selected 500 μm-risers are rejected with our de-blended method, it strongly indicates that blending of sources in a combination with some additional factor (e.g. physical clustering or lensing) may be responsible in producing observed (artificial) red colours in SPIRE maps. Recently, Duivenvoorden et al. 2018 analysed the original sample of Asboth et al. 2016 and refined the colours of SPIRE selected sources with SCUBA-2 observations. They report a similar fraction ($\sim 60\%$) of observed contaminants. In Sec-

tion 4.1.5 I use simulated maps and accomplish the analysis of noise effects and sources clustering on the observed red colours in different selections. [e]

(a) Which category of sources does the `MBB-fitter` miss?

The potential limitation of our de-blending method is that `MBB-fitter` uses theoretical *Herschel* PSF and than masks the slightly extended objects, thus producing accurate fit to point-like objects. In that way we could miss some fraction of the flux. If semi-extended source is a genuine 500 μm-riser, its intrinsic colour is much redder than what is measured with the `MBB-fitter` due to the missed flux. However, these objects are very rare, and one such semi-extended 500 μm-riser is known from the literature - it is recently confirmed to be a core of a large protocluster of galaxies at $z = 4.002$ (Oteo, Ivison, L. Dunne, et al. 2017). The other eventual weakness is that `MBB-fitter` retrieves a bad χ^2 for a source having flatter SPIRE SED (e.g $S_{350} \sim S_{250}$) or SEDs that are more complex than single-temperature MBBs. In literature the vast majority of these flat, dusty sources are found to be AGN-dominated (see the next subsection) but we cannot not rule-out the possibility that some distant sources may be missed due to relatively simplistic SED model used as a prior for our selection. In Section 4, I thus perform extensive analysis over galaxies modelled with more refined SEDs, in order to test the completeness of our selection method.

(b) Which sources DMAP misses ?

The selection method presented in this Thesis targets the vastly point-like 500 μm-risers and from Fig.2.11 we see that they are in average fainter than DSFGs selected with the `DMAP`. Hence I inspect what fraction of our 133 500 μm-risers is potentially missing if we follow `DMAP` criteria. In Fig.3.10 I plot 500 μm fluxes of our galaxies, against the different `D`-value cuts applied in Dowell et al. 2014 and Asboth et al. 2016.

I find 29 sources that are below the D-value threshold used in Dowell et al. 2014). These objects are covered with a red square in Fig.3.10. The number of missed sources is even larger if we apply the selection cut from Asboth et al. 2016 (58 missed sources in total). In Fig.3.10 I illustrate some examples where our and `DMAP` selections disagree: (1) In the upper panel, the SPIRE emission is found to be flat, causing the `MBB-fitter` to return very bad fit ($\chi^2 > 3.84$). Later inspection confirmed that the source is WISE-

[e] Duivenvoorden et al. 2018 also try statistical technique aiming to find explanation for the high SFRs in the sample of Asboth et al. 2016. They look at the density of WISE-1 and SDSS sources inside the 36" beam. By comparing to the expected (field) value, they found significant, factor of 3 increase of WISE-1 and SDSS sources close to the centre of extracted 500 μm-risers. They concluded that such a trend is likely implying high fraction of strongly lensed galaxies within their data.

detected quasar at $z = 2.3$; (2) The mid panel shows the two faint 250 μm blends. They together produce observed red colour in the DMAP, but after applying our de-blending technique the source is characterised as a combination of two 350 μm-peakers; (3) The bottom panel shows the case where the source is selected as a 500 μm-riser with the method of Dowell et al. 2014. However, the flux measured with MBB-fitter is not sufficiently high to be selected in the final catalogue ($S_{500} < 30$ mJy).

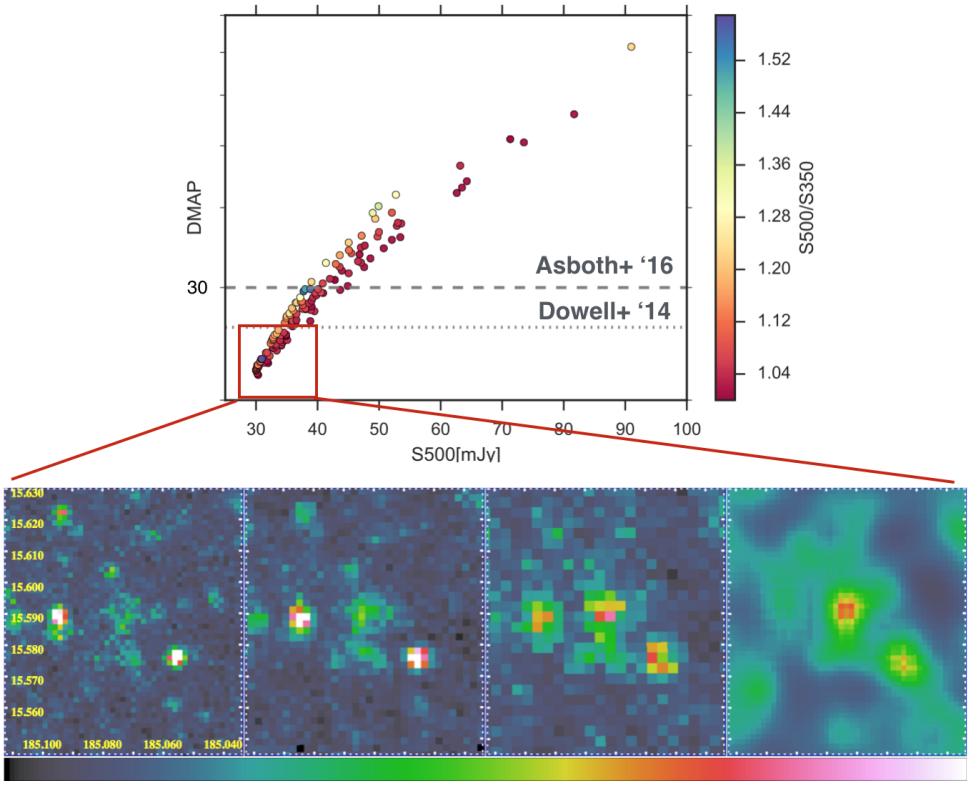

Figure 3.10.: The 500 μm flux of galaxies selected in this work (133 in total) against their D-values calculated following the equation from Asboth et al. 2016 and Dowell et al. 2014: $D = 0.920 \times M_{500} - 0.392 \times M_{250}$. Horizontal lines are attributed to different cuts used in Asboth et al. 2016 and Dowell et al. 2014. Below is an example of a source that is missed with the DMAP method due to its unsufficiently high S/N ratio in DMAP (S/N<4).

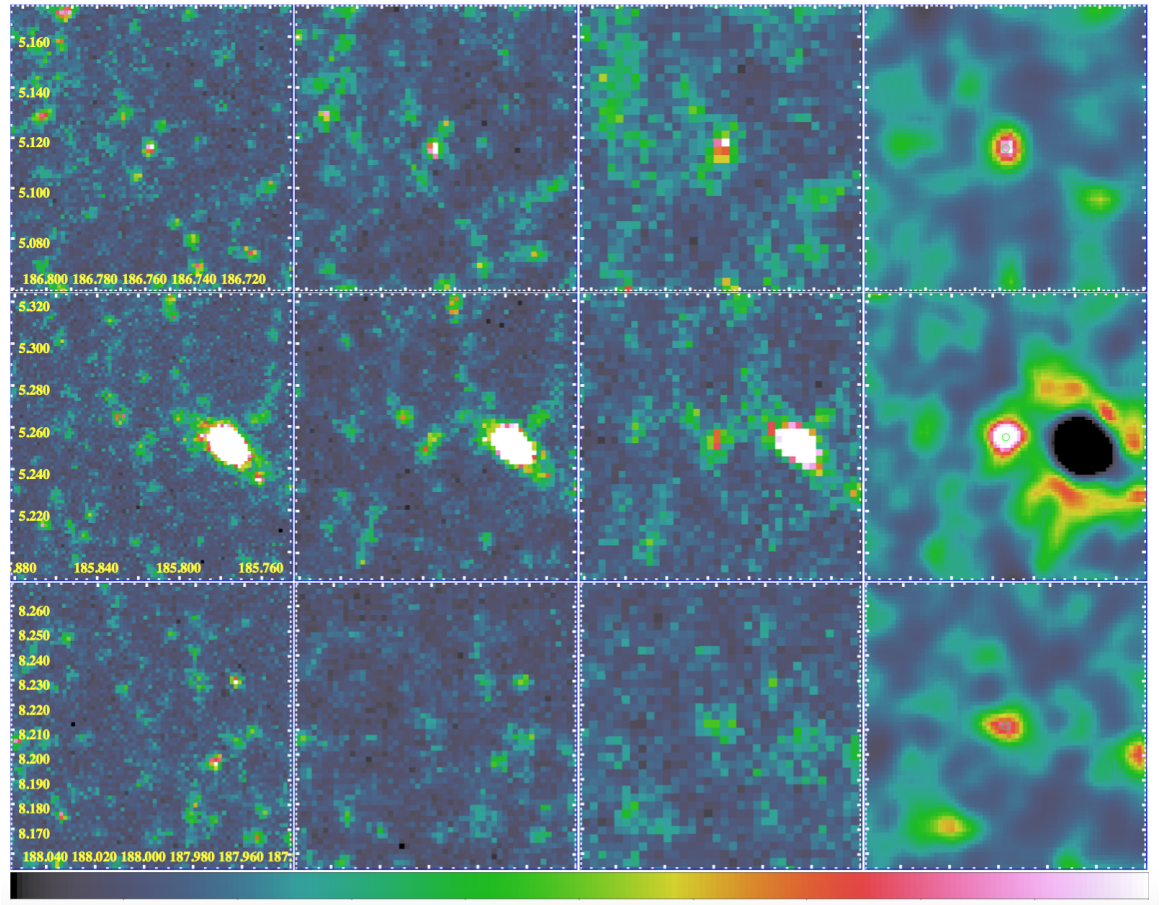

Figure 3.11.: Examples of DMAP-selected 500 μm-risers that are differently characterised with our selection method. Maps at 250 μm, 350 μm, 500 μm and DMAP are showed from left to right respectively. The top panel shows the sources that is observed as 500 μm-riser with DMAP. However, it has a flat SPIRE SED, and it is later confirmed to be a QSO at $z = 2.3$. The mid panel shows the example of two faint blends which produce 500 μm-riser on DMAP. Our method characterise the detection as a combination of 350 μm-peakers. The bottom panel illustrates the case where the source satisfies the 500 μm-riser criteria from Dowell et al. 2014, but is missed with our technique, due to unsufficiently high 500 μm flux measured with MBB-fitter ($S_{500} < 30$ mJy).

3.6. Appendix: Dusty quasars

It has been already shown that radio bright AGNs (QSOs, blazars) may have SPIRE colours similar to those of high-z DSFGs (Wardlow, Malhotra, et al. 2014). The radio emission from AGN-like objects may be either due to star formation in the QSO-host galaxy, to a strong radio-jet expelled by the SMBH, or to relativistic, radio electrons

accelerated in a wide, radiative outflow (Symeonidis, Giblin, et al. 2016). Hence 500μm-riser selection may be drastically polluted by synchrotron-dominated sources whose FIR emission is not entirely SF related (see e.g E. Glikman et al. 2018, for the recent discovery of very red, dusty QSO at $z > 2$). As mentioned in Section 2.5, I clean our final list of 500 μm-risers against these sources (7 objects in total). Since I measure significant FIR emission close to their position, it is interesting to briefly investigate its nature.

Between the 7 objects removed from the final list, 3 of them are known radio-loud QSOs/blazars, with catalogued L-band 1.4 GHz radio emission larger than 1 mJy (5.04 mJy, 799.97 mJy and 6.2 mJy respectively). They have redshifts well below $z \sim 4$ ($0.6 < z < 1.0$). The brightest radio source amongst them is catalogued as J122222.5+041316 in the FIRST radio database (Helfand et al. 2015). The source has $z_{spec} = 0.964$ and according to the classical PSF-fitting photometry performed with `SUSSEXtractor` or `StarFinder` it could pass our red colour criteria, but it cannot be fitted accurately with the `MBB-fitter` and the resulted χ^2 is very high ($\chi^2 > 10$).

Apart from the three known QSOs detected as very bright radio objects, the other four QSOs are found in the Half Million Quasar catalogue (HMQ, Flesch 2015). They are optically bright galaxies, all very close to the position of our SPIRE detection (r<5"). Their spectroscopic redshifts are very high, ranging from $3.1 < z < 4.5$. None of these four QSOs are present in existing all sky radio catalogues. Nevertheless, it does not necessarily mean that their contribution to the total $L_{\rm IR}$ is negligible. Here I present a brief analysis in order to understand their connection to the measured SPIRE emission. I first determine the expected radio emission limit of our final group of 133 $500\,\mu$m-risers through FIR-radio correlation (e.g Yun et al. 2001), under assumption that all selected sources are indeed star-forming galaxies with redshifts determined in Section 3.1:

$$q_{IR} = \log\left(\frac{F_{\rm FIR}}{3.75 \times 10^{12}{\rm W}m^{-2}}\right) - \log\left(\frac{S_{1.4}}{{\rm W}m^{-2}Hz^{-1}}\right), \tag{3.1}$$

where $S_{1.4}$ is the continuum radio emission flux at 1.4 GHz per frequency such that $S_{1.4} \propto \nu^{-\alpha}$ and α is the radio spectral index, positive in the vast majority of sources. $F_{\rm FIR}$ is the rest-frame FIR dust emission flux. From this I find that for our $z \sim 4$ candidates 1.4 GHz fluxes are ranging between 25 μJy and 105 μJy. Assuming the faintest level of existing radio surveys covering the Virgo Cluster (∼0.75-1 mJy at 1.4 GHz, Helfand et al. 2015), we can reveal just local cluster members and radio bright

quasars, but not high-z DSFGs. At present, all known radio bright QSO objects in Virgo are at $z < 3$. [f]

The range of determined 1.4 GHz fluxes is consistent with the fact that these sources are undetected in a shallow all sky surveys. However, FIR-radio correlation cannot be accurate if one estimating a radio flux of QSOs from their SPIRE emission only. In other words, if we impose additional synchrotron contribution to both radio and IR, the correlation may break.

To prevail the problem, I use the QSO SED from Polletta et al. 2007, add the WISE fluxes and calculate the AGN contribution to the total L_{IR}. The WISE colours of these objects are consistent with those of QSOs usually found in the literature (W1-W2>0.8, Ma et al. 2015). Fitting the optical to mid-IR photometry I find dust luminosities to be in the range of $8 \times 10^{12}\ L_{\odot} < L_{IR} < 1.5 \times 10^{13}\ L_{\odot}$. This range is within 1σ agreement with the determined $L_{\rm IR}$ of 500 μm-risers, presented in Section 3.2. From this I conclude that high-z QSOs produce significant contribution to the measured SPIRE flux and I keep them removed from our final sample.

Some recent studies have enlarged the sample of *Herschel* - detected optically selected QSOs (e.g. Ma et al. 2015). They, however, claim a statistically large group of objects for which SEDs are mostly due to the cold-dust components within the host galaxies. This is consistent for sources being heated by active star formation. However, lacking the L_{IR} correlation with the M_{BH} or the L_X of QSOs, this could also support a likely scenario where their thermal SED is not AGN-driven. Thus, our subsample of QSO-like objects could be a very interesting case study for probing the connection between AGN activity and host galaxy star-formation.

[f] Existing large sky radio catalogues are not deep enough to distinguish between very dusty radio-dominated galaxies at $z > 2$ and star-forming systems. This will be addressed with the Evolutionary Map of the Universe (EMU survey, Norris et al. 2011) which will soon make a deep (10", rms=10 μJy/beam) continuum maps covering Virgo.

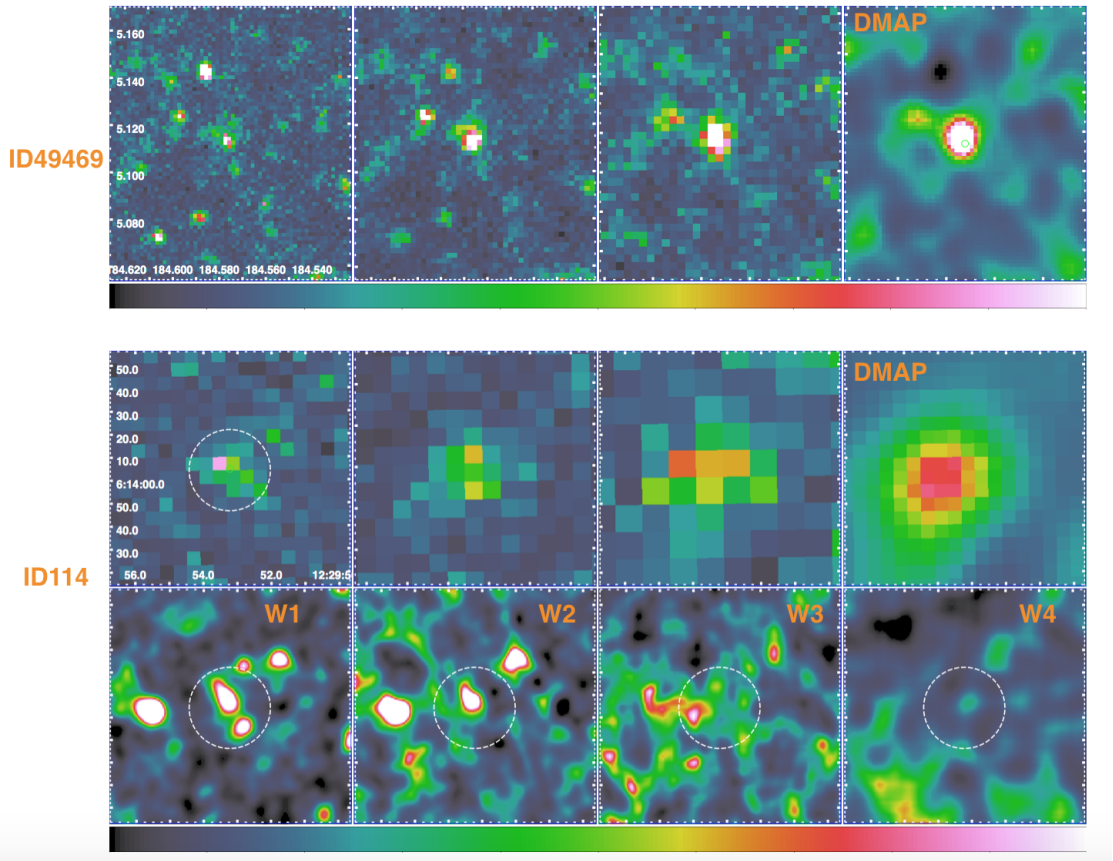

Figure 3.12.: Example of sources that are rejected from our final catalogue due to their flat SPIRE spectra (upper panel), and high dust luminosity associated to high-z QSO ($z = 4$, lower panel). SPIRE maps (250 μm, 350 μm and 500 μm) and DMAP are showed from left to right respectively. The W1, W2, W3 and W4 are WISE maps at 3.4 μm, 4.8 μm, 12 μm and 22 μm respectively. The yellow circle shows the size of 500 μm beam.

CHAPTER 4

Comparison to galaxy evolution models

Table of contents:

Introduction

The estimated distribution of redshifts and IR luminosities presented in the previous Chapter implies that our selection of 500 μm-risers might be a powerful tool in building large samples of candidate high-z DSFGs. However, while our estimates of L_{IR} and z agree fairly well to other studies, we see that different selections might lead to very diverse results in terms of observed colours and number densities of selected 500 μm-risers. To put our method in the proper context of galaxy evolution and to fully understand the eventual tension between observations and models, it is thus crucial to investigate a complexity of observational biases. Since the FIR surveys are affected by large beam-sizes of present instruments and increasing numbers of fainter sources close to the confusion limit, accurately correcting the selection of 500 μm-risers for all the observational effects has been found as an highly intricate task (e.g. Cowley, Lacey, Baugh, and S. Cole 2015, Bethermin et al. 2017). The best possible way to achieve this goal is to rely on an intrinsic shape of counts of 500 μm-risers. Such corrections should assume an underlying galaxy model which successfully reproduces the observed statistics of DSFGs.

In the Section 4.1 I introduce the newest phenomenological models of galaxy evolution, while in Section 4.2 I employ mock catalogues and compare our results with expectations from the models. To properly model our selection I introduce a novel way to simulate the effects of both instrumental and confusion noise on predicted number counts and redshifts of 500 μm-risers. The full understanding of tensions between observations and models remains challenging, and it requires using exactly the same algorithm on simulated maps with the true noise properties and physically motivated clustering over large area. Therefore, to better evaluate our selection procedure, in Section 4.3 I present the use of realistic "end-to-end" simulations. These simulations are employed to generate SPIRE maps from the mock catalogues and include the galaxy clustering.

4.1. Models

In the literature there are a number of methods aiming to predict the evolution of number counts at different IR/submm wavelengths. To model our observation process, in

this work I consider galaxy evolution models based on multiband surveys.[a] Globally, such models rely on the combination of observed SED templates of galaxies and luminosity functions. Additionally, we expect that sources having a peak in their FIR SEDs at wavelengths between 350 and 500 μm contaminate the sample of "500 μm-risers". These objects can make observational artefacts (e.g. fake red colours on the maps) caused by the positive noise fluctuations. It is then very important to have models that predict proper number of such contaminants, which is crucial for checking the systematics in the detection rate of 500 μm-risers. I adopt galaxy models of Béthermin, Daddi, Magdis, Sargent, et al. 2012, Schreiber, Elbaz, Pannella, Ciesla, T. Wang, Koekemoer, et al. 2016 and Bethermin et al. 2017, hereafter denoted as B12, S16 and B17 respectively. These models were built on *Herschel* data and found to accurately match the total IR number counts.[b] In the following I will firstly explain basic formalisms under which the models were built. After that, I will outline the basic differences between the models. A summary of the models and their main ingredients is given in Table 4.1.

Common to all models adopted in this work is their usage of the stellar mass function (SMF) as a starting point from which properties of galaxies are generated. The stellar mass function (SMF) is described by a double Schechter function:

$$\phi(\mathrm{M}_*)d(\mathrm{M}_*) = \exp(-\frac{\mathrm{M}_*}{M^*})[\Phi_1^*(\frac{\mathrm{M}_*}{M^*})^{\alpha_1} + \Phi_2^*(\frac{\mathrm{M}_*}{M^*})^{\alpha_2}]\frac{d(\mathrm{M}_*)}{\mathrm{M}^*}, \tag{4.1}$$

where M^* is the characteristic mass of the Schechter break, Φ_1^* and Φ_2^* are normalisations, and α_1 and α_2 are the power-law slopes at low mass.

All the models assume that only galaxies classified as star-forming have FIR outputs. In passive galaxies, some residual emission of cirrus heated by the old stellar populations has been observed (e.g. Glazebrook et al. 2017). However, at a given stellar mass, these galaxies usually have dust luminosities lower by at least one order of magnitude than galaxies on the main sequence (e.g. Viero et al. 2014).

For a given redshift and stellar mass, the models share the same general description of star-forming galaxies, with SFR assigned based on the dichotomy model of M. T. Sargent et al. 2012. It decomposes the bolometric FIR-luminosity function into main sequence (MS) and starburst (SB) galaxies. The MS galaxies are described as secularly evolving galaxies with a tight correlation between stellar mass and SFR, while SB galax-

[a] An additional reason for choosing the phenomenological models comes from the fact that at present none of the physically-motivated semi-analytical models have been fine-tuned to properly describe at the same time the observed SPIRE counts and the redshift distribution of observed DSFGs.

[b] B17 is additionally "trained" to match the most recent ALMA counts at 870 μm.

Table 4.1.: Comparison of models used in our analysis.

	Models		
	B12 Bethermin+, '12	B17 Bethermin+ '17	S16 Schreiber+, '15
Formalism(1)	2SFM	2SFM	2SFM
sSFR(2)	evolves up to $z = 2.5$	evolves up to $z = 4$	evolves continuously
Dispersion ($\sigma_{\rm MS}$)(3)	0.15 dex	0.3 dex	0.3 dex
Strong lensing	Yes	Yes	No
Passive galaxies	Yes	Yes	Yes
Evolution of $T_{\rm d}$	up to $z = 2$	up to $z = 4$	continuous
AGN contribution	Yes	Yes	No

(1) Two SF mode formalism. Stellar mass function (SMF) is described by a double Schechter function: $\phi(\mathrm{M}_*)d(\mathrm{M}_*) = exp(-\frac{\mathrm{M}_*}{M^*})[\Phi_1^*(\frac{\mathrm{M}_*}{M^*}) + \Phi_2^*(\frac{\mathrm{M}_*}{M^*})]$, where M^* is the characteristic mass of the Schechter break. The M^* is the redshift invariant in the B12, and evolves with redshift in the other two presented models. For redshifts $z > 4$, B17 assumes a single Schechter function fixing Φ_1^* at zero, while S16 adopts double Schechter fitting to results of Grazian et al. 2015 for $4.5 < z < 7$. (2) The specific star-formation rate, defined as sSFR=SFR/M_*. In B12 the sSFR increases with redshift up to $z = 2.5$ and than flattens. This trend is independent of the chosen range of stellar masses. In S16 and B17 the evolution is different, see Eq. 6 in Bethermin et al. 2017; (3) Modelled width of the main sequence (as log-normal scatter).

ies show an positive offset from the MS (usually assumed to be $4 \times \mathrm{MS}$), thus expressing high specific SFRs (sSFR = SFR/$\mathrm{M}_\star$). Such an approach has been shown to successfully reproduce the observed flux and redshift distributions from the MIR-to-FIR regime (Elbaz, Leiton, et al. 2017, M. Pannella et al. 2015, Béthermin, Daddi, Magdis, Lagos, et al. 2015). The decomposition on MS and SB galaxies is double log-normal, with the form:

$$\begin{aligned} \log_{10}\left(\frac{SFR_{MS}}{M_\odot yr^{-1}}\right) = \log_{10}\left(\frac{M_\star}{10^9 M_\odot}\right) - m_0 + a_0 \log_{10}(1+z) \\ -a_1\left[\max\left(0, \log_{10}\left(\frac{M_\star}{10^9 M_\odot} - m_1 + a_1 \log_{10}(1+z)\right)\right)\right]^2 \end{aligned} \tag{4.2}$$

The precise functional form is arbitrary, but the parametrisation choice is physically motivated and aims to explicitly describe the two regimes observed in Schreiber, Pannella, Elbaz, et al. 2015, namely a sequence of slope unity whose normalization increases with redshift (first and second term in Eq.4.2, and a "bending" that vanishes both at low masses and high redshifts (last term in Eq.4.2). The best-fit parameters are found to be: $m_0 = 0.5$, $\alpha_0 = 1.3$, $m_0 = 0.36$, $\alpha_0 = 2.5$.

The SEDs are assigned to each of modelled galaxies in order to derive their SPIRE fluxes from their total IR luminosities. The models use dust emission libraries (Draine and A. Li 2007) which describe the interstellar dust as a mixture of carbonaceous and amorphous silicate grains, and also take into account that their size distributions are chosen to realistically "mimic" the observed extinction in the Milky Way (MW), the Large Magellanic Cloud (LMC),and the Small Magellanic Cloud (SMC). The properties of these grains are parametrised by the so-called PAH index (q_{PAH}), and it is defined as the fraction of the dust mass in the form of PAH grains. In SEDs, the majority of the dust is heated by a radiation field, so the SED shape is mainly controlled by the galaxy type (MS or SB) and the mean intensity of the radiation field $\langle U \rangle$. The later parameter controls the energy of the radiation field to which each grain is exposed. For example, for grains that are sufficiently big to be thermalised, an energy increase is coupled with the enhanced dust temperature and vice versa (Dale and Helou 2002). All models presented here consider evolution of $\langle U \rangle$ with redshift, which is observed for main sequence galaxies (Magdis, Daddi, et al. 2012, Béthermin, Daddi, Magdis, Lagos, et al. 2015, Schreiber, Elbaz, Pannella, Ciesla, T. Wang, and Franco 2018). We will see later that the models use slightly different relations to describe observed trends.

The modelled galaxies are distributed around the main sequence by randomly draw-

ing the SFR of each source using a log-normal distribution. The scatter around the main sequence is non-negligible and it is accounted in these models.

To reproduce IR number counts, the models link SFR and $L_{\rm IR}$. The latter is directly derived from the estimation of SFR using the Kennicutt 1998 conversion factor ($K = 1.71 \times 10^{-10}\, M_{\odot}\, yr^{-1}$) after converting to Chabrier IMF. As explained in Chapter 1 of this Thesis, in dust-obscured star-forming galaxies the bulk of the UV emitted light is absorbed by dust and re-emitted in the IR. Less massive galaxies have smaller dust attenuation and a significant part of the star-formation can be detected in UV. The models split the total SFR into UV and IR component ($\mathrm{SFR} = \mathrm{SFR_{UV}} + \mathrm{SFR_{IR}}$) assuming the best fit relation between $M_{\star}$ and dust obscuration found in Heinis et al. 2014. Such a decomposed IR luminosity is then determined as:

$$\mathrm{L_{IR}}\ (L_{\odot}) = \frac{\mathrm{SFR_{IR}}}{K} = \frac{\mathrm{SFR}}{K} \times f_{\rm IR}^{\rm SF}(M_{\star}), \tag{4.3}$$

where $f_{\rm IR}^{\rm SF}(M_{\star})$ describes how the mean ratio between $\mathrm{SFR_{UV}}$ and $\mathrm{SFR_{IR}}$ varies with $M_{\star}$.

Differences between the models are described briefly in the following paragraphs - the most important are scatter from the MS, parameters chosen to fit stellar masses, redshift evolution of a dust temperature and treatment of galaxy-galaxy lensing.

B12 (Béthermin, Daddi, Magdis, Sargent, et al. 2012)

The B12 model describes the SMF as a Schechter function with a redshift invariant characteristic mass parameter (see Eq. 4 in Béthermin, Daddi, Magdis, Sargent, et al. 2012, and Peng et al. 2010 for more details). The IR SED template is based on Draine and A. Li 2007 models, while the mean radiation field $\langle U \rangle$ is described with the following form:

$$\langle U \rangle = \langle U \rangle_0 \times (1 + \min(z, z_{\langle U \rangle}))^{\gamma_U}, \tag{4.4}$$

where $\langle U \rangle_0$ is the mean radiation field in local MS galaxies, γ_U is the parameter which describes evolution of the radiation field with redshift and $z_{\langle U \rangle}$ is the redsfhit where $\langle U \rangle$ flattens. In B12 $\langle U \rangle$ evolves with redshift up to $z = 2.0$ and then flattens. The dispersion of the MS log-normal distribution is σ_{MS}=0.15 dex, following M. T. Sargent et al. 2012 and Salmi et al. 2012. B12 includes the effect of strong lensing reckoning

the magnification rate PDF from the model of Hezaveh et al. 2011:

$$\frac{d^2N}{d\log L_{\rm IR} dV}|_{\rm lensed} = \int_{\mu>2}^{\infty} \frac{dP(\mu,z)}{d\log\mu} \frac{d^2N}{d\log L_{\rm IR}} dV|_{\rm initial}\, d\log\mu. \tag{4.5}$$

Here $dP(\mu,z)/d\log\mu$ is a lensing magnification PDF, while $d^2N/d\log L_{\rm IR}dV$ is the luminosity function. The strongly lensed sources contribute $\sim 20\%$ to the brightest-end IR counts (PLW $\gtrsim 100$ mJy). The AGN contribution is statistically associated based on results from Aird et al. 2012 and Mullaney et al. 2011. At SPIRE wavelengths, AGN's have negligible contribution (3% at $z > 2$).

B17 (Bethermin et al. 2017)

The B17 model is a significantly upgraded version of the B12 model. In B17, the MS scatter is updated ($\sigma_{\rm MS}$=0.3 dex) in order to match the SMFs observed in O. Ilbert, Arnouts, E. Le Floc'h, et al. 2015 and Schreiber, Pannella, Elbaz, et al. 2015. The model uses a new parametric form to fit the redshift evolution of the radiation field $\langle U\rangle$:

$$\log_{10}\left[\langle U\rangle_{MS}\right] = \log_{10}\left[\langle U\rangle_{MS}(z=0)\right] + 0.25\times z. \tag{4.6}$$

The T_d evolution in MS star-forming galaxies stops at $z = 4$ (instead at $z = 2.0$ as in B12) and remains constant at higher values. Contribution of AGNs and strong lensing effects are modelled as in B12. The weak lensing is additionally modelled with magnifications that are randomly drawn from a Gaussian distribution, while their width and mean values are derived based on a cosmological simulation of Hilbert et al. 2007. The B17 model (as well as S16) accounts for the relative excess of the modelled SPIRE fluxes caused by source clustering. The excess is estimated by comparing the stacked fluxes measured in the simulated maps with modelled fluxes. The 2 sq.deg. catalogue based on this model is publicly available (Simulated Infrared Dusty Extragalactic Sky, SIDES, Bethermin et al. 2017).

S16 (Schreiber, Elbaz, Pannella, Ciesla, T. Wang, Koekemoer, et al. 2016)

In S16, MS galaxies are modelled based on a stellar mass and redshift from Schreiber, Pannella, Elbaz, et al. 2015 and M. Pannella et al. 2015. The scatter of the main sequence is $\sigma_{\rm MS}$=0.3 dex. Randomly-selected galaxies (5%) are placed in the SB mode

by enhancing their SFR by a factor of approximately five. The distribution of stellar masses is described by a double power-law Schechter fit, with parameters evolving with redshift. These parameters are chosen according to observational data from Schreiber, Pannella, Elbaz, et al. 2015 (see also Grazian et al. 2015). A new set of template SEDs is used to model the dust emission of star-forming galaxies. These SEDs are based on the physically motivated dust model of Galliano et al. 2011. The model uses following empirical relation to link together T_d and the radiation field intensity:

$$\frac{\langle U \rangle}{U_\odot} = \left(\frac{T_d}{18.2}\right)^{5.57}. \tag{4.7}$$

The library describes T_d ranging from 15 to 100 K, and its redshift evolution is modelled as:

$$T_{\rm d}[{\rm K}] = \begin{cases} 4.65 \times (z-2) + 31, & \text{for MS} \\ T_{\rm d}^{\rm MS} + 6.6 \times \log_{10}({\rm R_{SB}}), & \text{for SB} \end{cases} \tag{4.8}$$

The "starburstiness" term R_{SB} is used to quantify the SFR offset between MS and SB galaxies ($\mathrm{R_{SB}} = \mathrm{SFR/SFR_{MS}}$). Dependence of sSFR on the stellar mass shows that sSFR is constant at lower masses, and drops at the highest masses, $M > 10^{10.5} M_*$ (e.g. Schreiber, Pannella, Elbaz, et al. 2015, Whitaker et al. 2015, Magnelli, Lutz, et al. 2014). This trend is similar to the one used in B17, but different from the fit used in B12. To summarise, in S16 both sSFR and $T_{\rm d}$ evolve continuously with redshift, which is not the case for the other two models (see 3). Effects of strong lensing and AGNs are not included in the model.

Main limitations of presented models

Despite their simplicity, the phenomenological models presented here above provide some of the best fits achieved to the IR/submm number counts, including source counts per redshift slice in the SPIRE bands, which were poorly reproduced by semi-analytical models and the pre-*Herschel* generation of phenomenological models (see Casey, Zavala, et al. 2018, Cowley, M. Béthermin, et al. 2017, Dowell et al. 2014 and Casey, Narayanan, et al. 2014 for comprehensive discussions). However, the models adopted in this work have some limitations that are worth mentioning here.

- The lack of data points on the Rayleigh-Jeans tail of the SED at $z > 4$ require that T_d is fixed to the extrapolated value from lower redshifts. At $3 < z < 4$,

B17 assumes the same evolution for MS and SB galaxies ($\langle U \rangle_{MS} = \langle U \rangle_{SB}$). At $z > 4$, the model assumes a plateau, since a simple extrapolation could lead to unphysically-high dust temperatures.

- B17 implements a sharp SFR limit at $1000\ M_{\odot}\mathrm{yr}^{-1}$, and the SFR of each modelled galaxy is re-drawn under the condition to be lower than this limit. This sharp limit is applied in order to properly match the observed 870 μm number counts of SPIRE selected galaxies. Karim et al. 2013, Hodge, Carilli, et al. 2013, Simpson et al. 2015 investigated ALMA data of ALESS galaxies and showed that the bright end of the number counts at 870 μm is significantly overestimated and that none of the single, bright components they analysed have a SFR significantly above $1000\ M_{\odot}\mathrm{yr}^{-1}$. However, systematic, wide-survey selections of candidate DSFGs at $z > 4$ unveiled some objects with estimated $SFR > 1000 - 1500\ M_{\odot}\mathrm{yr}^{-1}$, implying that SFR limit is probably not so sharp (Oteo, Ivison, Negrello, et al. 2017, Riechers, Bradford, et al. 2013). Bethermin et al. 2017 decide to keep the SFR limit for the present version of B17 model, but as stated in their work, the full physical origin of this SFR cut is not completely clear.

- Weak lensing in B17 is modelled as a simplified Gaussian distribution. The number of sources with a magnification between 1.5 and 2 might be slightly underestimated compared to recent numerical simulations (e.g.Takahashi et al. 2017, Hilbert et al. 2007).

- The scatter on the main sequence is assumed to be constant both with mass and redshift. This is mainly due to difficulties to measure the dispersion (Buat, Heinis, et al. 2014, Jorryt Matthee et al. 2018).[c]

4.2. Mock catalogues

In order to simulate our selection criteria I set mock catalogues based on models described in the previous section. Such approach will allow comparison of number counts

[c]Some crucial information may be encoded in the scatter of MS, and its dependence on stellar mass and cosmic time. For example, it can be investigated what makes the difference between growing rates of galaxies, or what are the important evolutionary time-scales?; how important is the influence of the environment inside the halo (e.g. density of satellite galaxies).

of "observed" 500 μm-risers to the ones predicted by different models.[d]

Namely, for the B12 model I retrieve the SPIRE catalogue which is a result of 500 deg^2 simulations (Béthermin, Daddi, Magdis, Sargent, et al. 2012). I also retrieve the catalogue created by the B17 model covering the area of 274 deg^2. The size of the simulated area is equal to the size of the HeLMS field, thus perfectly suited for a comparison of our selection technique to the one used by Asboth et al. 2016. With the S16 model, I generated a mock catalogue myself using the C++ routine (`gencat`) written as a suite of Empirical Galaxy Generator Code (`EGG`, C. Schreiber et al. 2017). The `gencat` routine uses the prescriptions from S16 and generates the fluxes of each galaxy in an arbitrary number of bands simultaneously. I thus produce the mock SPIRE catalogue covering the size of the HeViCS field (55 deg^2). The mock catalogue consists of 5.7 millions of galaxies covering the redshift range $0 < z < 8$.

The catalogues based on B12, B17, and S16 cover sufficiently large areas to offer accurate inspection of our selection method. I further apply our 500 μm-risers selection criteria ($S_{500} > S_{350} > S_{250}$, $S_{250} > 13.2$ mJy and S_{500} >30 mJy) to modelled sources. When implemented on mock catalogues, our selection results in a differential distribution presented on the left panel of Fig.4.1. We see that observed counts are in a good agreement with B12, but slightly above other two models. The observed counts are somewhat steeper at the fainter end and flatter at the brighter end ($S_{500} > 80 - 90$ mJy) which is due to flux magnification by gravitational lensing (Negrello et al. 2017). The influence of lensing is clearly reflected in the counts modelled with the S16. The model does not take into account strong lensing and counts steeply decline above 60 mJy. Our differential number counts show the best agreement with B12, but I note that recent interferometric observations of DSFGs in the COSMOS field (see Bethermin et al. 2017 for more details) suggest that the B12 model likely overpredicts the number counts at 500 μm fluxes below 50 mJy by a factor of two to three. The main reason for such an overprediction is that the measurements upon which the B12 model was initially built favoured a scenario with no evolution of $\langle U \rangle$ at $z > 2$. The model thus produces colder SEDs and consequently higher FIR/submm counts. At the time of working on this analysis, we learned it is no longer favoured. The new number counts are observed to be lower (e.g. Brisbin et al. 2017, Rawle et al. 2016). I thus mainly focus my further analysis on B17 and S16. The number density of 500 μm-risers which satisfy our

[d] In the following, I make the distinction between intrinsic and observed quantities. The former ones are the true, modelled properties of galaxies, free of measurement errors and systematics. The latter are measured values, affected by biases.

selection in B17 and S16 is 0.45 deg^{-2} and 0.40 deg^{-2}, respectively. Predictions of B17 are consistent with the 1σ error bars of observed counts in the higher flux bins (60 mJy$< S_{500} <$ 100 mJy). In lower flux bins (30 mJy$< S_{500} <$ 60 mJy) observed source density show a factor of 1 to 6 discrepancy with B17 and S16 depending on the chosen bin. However, it is clear that we have a much better agreement with galaxy models than previous studies (Asboth et al. 2016) who claim observational discrepancy of an order of magnitude. Hence it is crucial to understand the relation between predictions and observations if we model observational effects. Accordingly, in Section 4.1.3 I discuss in detail the effects of simulated noise on measured counts.

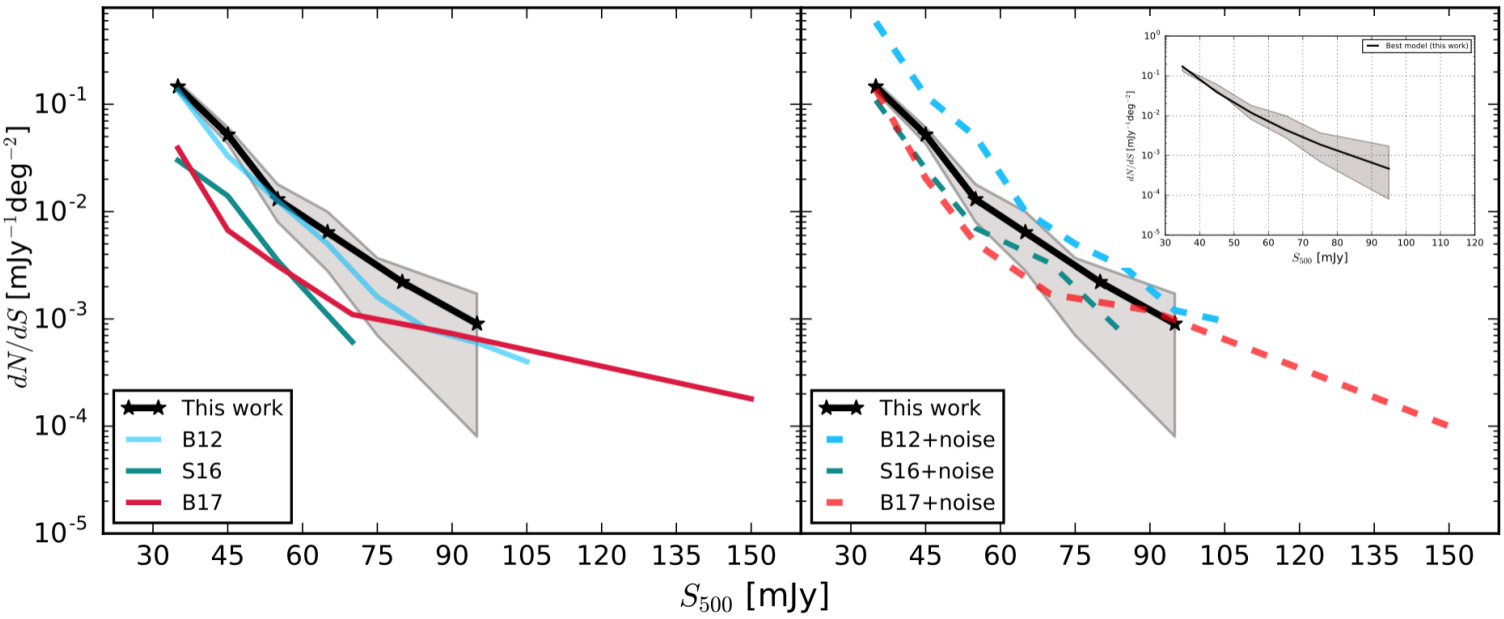

Figure 4.1.: Observed differential number counts of 500 μm-risers in the HeViCS field (black line) compared to models. Expected values from models are over-plotted as coloured lines. Grey, shaded area has the same meaning as in Fig.3.8.*Left*: Comparison of observed and modelled counts. Models are represented by full, coloured lines: cyan for B12 (Béthermin, Daddi, Magdis, Sargent, et al. 2012), red for B17 (Bethermin et al. 2017), and green for S16 (Schreiber, Elbaz, Pannella, Ciesla, T. Wang, Koekemoer, et al. 2016). The effect of simulated noise is ignored. *Right*: Comparison between observed and modelled counts if the effect of noise is simulated. The effect of confusion and instrumental noise is simulated by adding a random Gaussian noise to the modelled fluxes. Differential counts are then represented by dashed, coloured lines. The best-fit power law on observed data is presented in the inner subplot.

4.2.1. Effects of noise on measured counts

The results described in previous Section neglect the effect of noise on the modelled number counts of 500 μm-risers. However, it has been recently shown (Duivenvoorden et al. 2018, Cowley, Lacey, Baugh, and S. Cole 2015, Bethermin et al. 2017) that careful treatment of observational effects should be performed when comparing counts with models. Therefore, I simulate the effect of both confusion and instrumental noise by adding a random Gaussian noise drawn from the values measured in the HeViCS field (Section 2.1).

Considering the addition of noise, the number of simulated sources that are observed as 500 μm-risers in B17 jumps to 473, resulting in an increase of number counts from 0.45 per deg^2 to 1.73 per deg^2. We obtain a very similar result with S16 - a number density increases from 0.4 per deg^2 to 1.54 per deg^2. As a consequence, observed values match predictions from B17 and S16 in the faintest 500 μm flux regime, and have very small offset in the next two flux bins. The agreement is reached again for fluxes above 60 mJy. The comparison between observations and models with simulated Gaussian noise is illustrated in the right panel of Fig.4.1. The significant increase of counts in the lowest two flux bins is clearly seen, while the line slopes do not express significant change compared to intrinsic ones (left panel in Fig.4.1).

In order to compare our results with the models in a more quantitative way, I fit a power law to our differential counts. The best model is of the form

$$\frac{dN}{dS} = N_0 S^{-\gamma}, \tag{4.9}$$

where $\gamma = 5.93$, and $\log N_0 = 8.37$. The best fit is presented as an right-panel inner plot in Fig.4.1. I further compute the χ^2 between our best-fit model and counts predicted by B17 and S16 in corresponding flux bins. I find the *p*-values of 0.7 and 0.47 for S16 and B17 models respectively. Since these *p*-values are greater than commonly accepted thresholds of 0.05[e], they do not suggest that the modelled differential counts from B17 and S16 differ significantly from our model within the same flux range. Even though this simple calculation shows that observed and modelled differential counts are largely consistent if we account for the effect of noise, any differences in the number counts, even if they are within the 1σ Poisson error bars, still carry importance. In the next Section I conduct end-to-end simulations to inspect what is the fraction of

[e]In statistics, the *p*-value smaller than 0.05 indicates strong evidence against the null hypothesis.

Table 4.2.: Comparison of modelled number counts before and after adding the Gaussian noise. Counts are calculated by imposing our criteria to select 500 μm-risers.

	Predicted density of 500 μm-risers [(1)]	Faint 500 μm-risers [(2)] ($S_{500} < 30$ mJy)
B17	0.45 deg^{-2} (51% lensed)	-
B17 + noise	1.73 deg^{-2} (24% lensed)	52 %
S16	0.4 deg^{-2}	-
S16 +noise	1.54 deg^{-2}	67 %

(1) Modelled density of 500 μm-risers before and after the addition of random Gaussian noise. Criteria used to select 500 μm-risers are: $S_{500} > S_{350} > S_{250}$, $S_{250} > 13.2$ mJy and $S_{500} > 30$ mJy. Numbers reported in brackets refer to the percentage of strongly lensed galaxies; (2) Contribution of contaminants that are intrinsically red sources, but with intrinsic fluxes below our flux limit ($S_{500} < 30$mJy).

potentially missing and contaminant sources, while in the Chapter 5 I discuss the effects of multiplicity, strong lensing and clustering in greater details.

I find that noise often tends to increase the number of 500 μm-risers that have intrinsic 500 μm fluxes slightly below 30 mJy, but they pass our flux criterion after the addition of noise. As shown in Table 4.2, contribution of these sources to observed 500 μm-risers varies between 52 and 67%.

The noise also has the effect in changing the relative contribution of modelled lensed and unlensed 500 μm-risers. The percentage of weakly lensed and non-lensed 500 μm-risers in B17 increases from 49% (intrinsic fluxes) to 76% (intrinsic fluxes+Gaussian noise). I did a closer inspection to this and found that noise modelled group reveals that weak lensing ($1 < \mu < 2$) is an important player to the modelled flux for the significant number of sources (166 out of 473, or 35%). Fainter, weakly lensed DSFGs selected with our method can fulfil our final 500 μm-risers criteria more often, because they are on a positive fluctuation side of the lensing magnification. In principle, it means that this combination has an non-negligible role in producing observed 500 μm-risers

even without the strongly lensing.

Systematic studies of 500 μm-risers known from the literature show different results as respect to models. For the wide and shallow HeLMS field, Asboth et al. 2016 observed an order of magnitude discrepancy. Because the distribution of number counts measured in Asboth et al. 2016 is much steeper than in our work, the noise increases the number of observed 500 μm-risers drastically. Bethermin et al. 2017 simulate the selection procedure of Asboth et al. 2016 on their mock catalogues, and concluded that such a strong increase of measured counts is due to combination of noise and clustering. They measure a boosting of observed number counts by factor of nine due to noise, which is three times higher than the modelled increase of observed 500 μm-risers in our field (first raw in Table 4.2). This leads to the conclusion that the effect of noise is more prominent for shallower fields, while for deeper fields (e.g. HeViCS and deep HerMES fields analysed in Dowell et al. 2014) it has just a mild impact on measured number counts.

4.2.2. Effect of noise on the redshift distribution

In the following I investigate how the noise influences redshift distribution of 500 μm-risers. To achieve this goal I compare the redshift distribution of 500μm-risers that pass our selection criteria before and after adding the noise.

I illustrate my findings in Fig.4.2, where I plot the redshift distribution of modelled sources concerning B17. The galaxies that fulfil our selection criteria are plotted in the upper panel. They do not show large differences in the peak of their redshift distribution when we add noise. More precisely, for B17 and S16 the intrinsic median redshifts are $\langle z \rangle = 3.91 \pm 0.6$ and $\langle z \rangle = 4.49 \pm 0.55$ respectively. With the addition of noise, corresponding medians drop to $\langle z \rangle = 3.61 \pm 0.52$ and $\langle z \rangle = 3.97 \pm 0.55$. It is worth to note that S16 does not require any limit on maximum SFR and does not include lensing, so modelled 500 μm-risers are assumed to have high intrinsic SFRs ($\mathrm{SFR} > 1000\ M_{\odot} yr^{-1}$). As I explain in Section 4.1, this is not the case with B17, which attaches higher lensing magnifications to the highest-redshift 500 μm-risers, in order to scale SFRs to a maximum limit of 1000 $M_{\star} yr^{-1}$. Having combined with the fact that SEDs in S16 are slightly warmer than in B17, it mainly explains why intrinsic 500 μm-risers in S16 are at average higher redshifts than those from B17. Beside that, we see that even the number of contaminants increases, observed high-z tail is also expanding due to the

noise. I find three sources at $6.2 < z < 7.2$ that additionally pass our final selection due to positive noise fluctuations. Their colours are intrinsically red and adding the noise does not make them more "redder", but instead boosting their observed S_{500} fluxes above our selection limit.

To check how the noise shapes the redshift distribution of sources from other selections, I simulate exact DMAP criteria from Asboth et al. 2016 and Dowell et al. 2014 on our mock catalogues. To simulate the effect of noise for these two selections, I use the noise values for HeLMS and HerMES, as provided in Asboth et al. 2016 and Dowell et al. 2014. In Fig.4.2 I plot the distributions associated to these two selections. The median redshifts before and after modelling the noise, are annotated with dashed red and black lines accordingly.

The overall redshift distribution of sources selected with the method of Dowell et al. 2014 shows fairly good agreement with our sample. Intrinsic 500 μm-risers have median $\langle z \rangle = 4.23 \pm 0.56$ in B17, and $z = 4.83 \pm 0.42$ in S16. The corresponding medians became lower with the influence of noise: $\langle z \rangle = 3.53 \pm 0.5$ and $\langle z \rangle = 3.93 \pm 0.45$. However, when we model the selection of Asboth et al. 2016, median redshifts before and after adding the noise decrease from $\langle z \rangle = 4.18 \pm 0.62$ to $z = 3.02 \pm 0.45$ for B17, and from $\langle z \rangle = 4.4 \pm 0.55$ to $z = 3.28 \pm 0.42$ for S16. The reason for such a big change is that relative contribution of DSFGs at $z < 4$ increases dramatically: from 20% to 88% in B17, and from 15% to 72% in S16. On top of that, the number of 500 μm-risers at $z > 4$ remains almost constant, causing the highest redshift tail stay unextended, oppositely to the trend we observe following our method. Presented facts lead to the conclusion that noise in wide and shallower fields such as HeLMS, strongly influences not just differential number counts, but also the redshift distribution of selected 500 μm-risers.

It is beneficial here to understand which populaton of sources are expected to act as "observed" 500 μm-risers, and whether DSFGs can commonly pass our selection criteria with the additional support of Gaussian noise. To do so, in Fig.4.3 I plot the change of intrinsic colours and redshifts due to the noise, as respect to the strength of the mean radiation field. Observed galaxies can be broadly split in two groups: the first are those 500 μm-risers whose intrinsic colour (S_{500}/S_{350}) does not significantly change with the noise. In this case, noise acts just as an additional flux contributor. The vast majority of such galaxies are $z > 5$ DSFGs with warmer SEDs ($\langle U \rangle > 50 U_{\odot}$). The second group of sources are weakly lensed, colder DSFGs ($\langle U \rangle < 35\, U_{\odot}$). The noise changes

their intrinsic colours and fluxes more intensely since they are both very close to our selection limit.

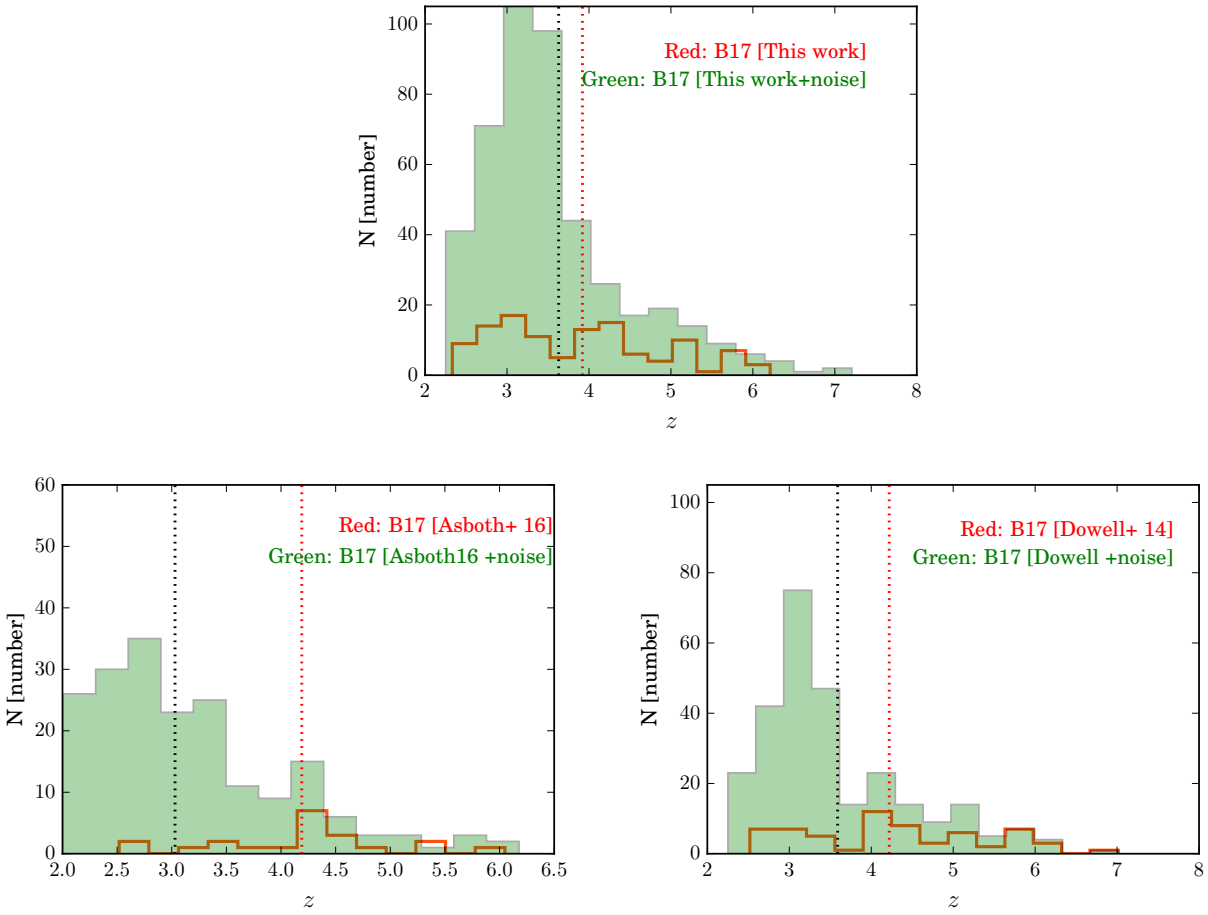

Figure 4.2.: Redshift distribution of 500μm-risers in B17 related to our selection (upper panel) and the DMAP selection (lower pannel) from Asboth et al. 2016 (left) and Dowell et al. 2014 (rigth). Red and green colours are modelled redshifts of intrinsic and observed 500 μm-risers, respectively. Here I refer to observed 500 μm-risers those sources which fulfil selection criteria after we add simulated noise. Red and black dotted lines illustrate the difference between modelled medians before and after adding the noise, respectively.

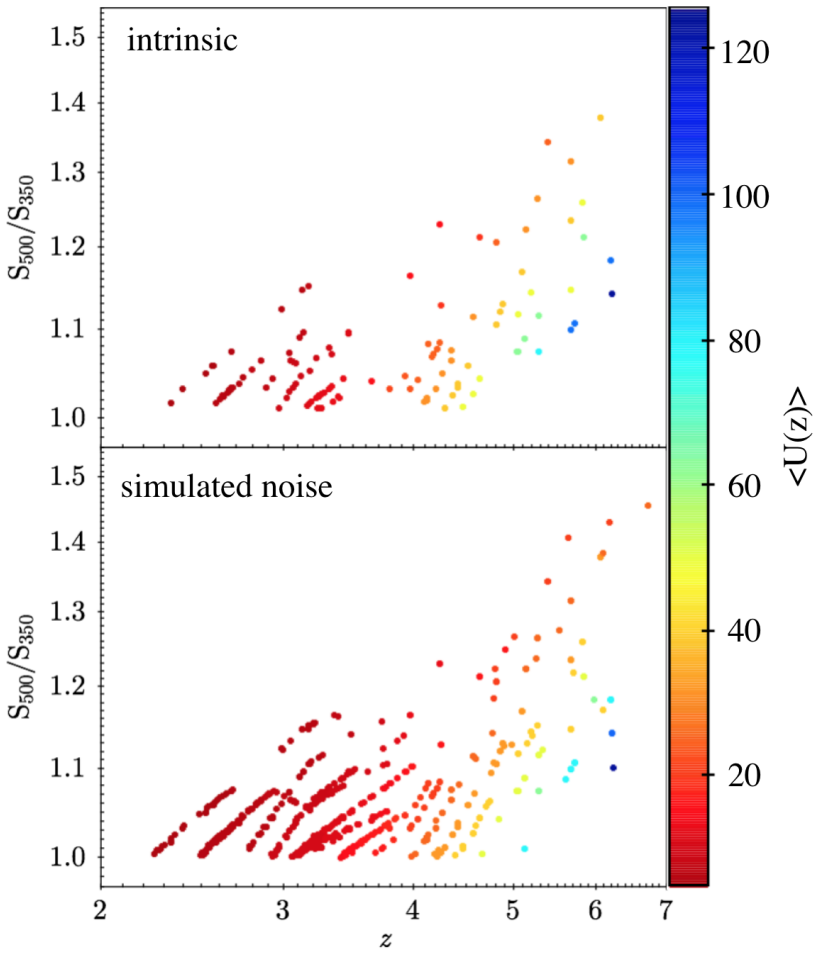

Figure 4.3.: Modelled 500 μm-risers which fulfil our selection criteria in B17 before and after adding the noise. Intrinsic and observed colours are presented in the upper and lower panel respectively, and plotted as a function of redshift, coloured with the intensity of a mean radiation field ($\langle U(z) \rangle$). According to Eq.4.7 which links together T_d and the radiation field intensity, i.e. $\langle U \rangle = 50\, U_{\odot}$ corresponds to $T_d = 37$K.

4.3. Simulated maps

Simulated realistic maps are needed to explore the exact nature of selected sources and the full complexity of biases that shape *Herschel* SPIRE selection of 500 μm-risers. These systematic effects are mostly induced by the limited angular resolution combined with the noise and lensing effects, and also due to method we chose to extract sources and compute photometry (fluxes and corresponding uncertainties). Having used two different models, B17 and S16, I aim to uncover systematic uncertainty of the detection

rate of 500 μm-risers. This is a crucial step if we want to test and understand our selection algorithm - it is necessary to count the galaxies we potentially miss and to determine fraction of contaminants.

The simplest way to generate the position of each galaxy is to draw their positions uniformly on the sky sphere, within the sky region that is covered by the simulated survey. The stellar mass functions used in B17 and S16 ensure that we will get a correct sky density of objects over the whole simulated area. However, as I note in the Section 1, within the ΛCDM-cosmology, galaxies are forming large-scale structures by following the history of merging of their DM-halos, that means they have tendency to be "clustered" in the sky. Hence, it is highly important to simulate clustering in order to generate realistic connections between sources and their positions in mock maps .

Sky positions of galaxies in S16 are clustered based on deep observations in GOODS-N field. Schreiber, Pannella, Elbaz, et al. 2015 found that observed clustering signal between $1''$ and $5'$ is well described with the single power law. To further produce mock sky positions that resemble these observations, S16 uses Soneira et al. 1978 algorithm, which produces a two-point correlation function with a power-law shape. In S16 it is of the form $\omega(\theta) \sim \theta^{-\gamma}$, where θ is an angular distance between two objects, and $\gamma = -0.9$.

Concerning B17, I decide to use the simulation with physically clustered sources (SIDES, Bethermin et al. 2017) as the starting point. The full procedure of making the simulation is described in Bethermin et al. 2017 and here I outline the most important steps. To provide the information about the large-scale clustering of dark matter haloes, Bethermin et al. 2017 make mock light cones derived from a publicly available cosmological Bolshoi-Planck simulation (Rodríguez-Puebla et al. 2016). Halos are identified by the phase-space `RockStar` halo finder (Behroozi et al. 2013). To link stellar mass to DM halos and subhalos, B17 uses abundance matching formalism between the halo catalogues and the modelled stellar mass functions (Behroozi et al. 2013, Hayward 2013). The size of initial simulation presented in Bethermin et al. 2017 is 2 deg^2, and in order to increase the statistics I make eight realisations, drawing the galaxies from the larger, 274 deg^2 catalogue following the same luminosity distribution.[f] The galaxies are thus placed on the sky at coordinates with a fixed angular correlation, to preserve their positions from cosmological simulation. The galaxies in our mock maps cover the wide range of stellar masses, from 10^8 $M_\odot$ to 10^{12} $M_\odot$, which ensures that simulated maps

[f]The catalogue contains sources modelled to be at $z > 2$, generated using the prescriptions of the 2SFM formalism described above.

contain a realistic confusion.

I generate a set of mock SPIRE maps with the use of Empirical Galaxy Generator Code (EGG, C. Schreiber et al. 2017). The clustered catalogues described above are converted into simulated images assigning theoretical *Herschel*-SPIRE PSFs to sources and using the same noise properties as measured in our real HeViCS images. The mock maps related to B17 and S16 cover the same area, 16 deg^2 each, which is equal to one of the four HeViCS fields. As shown in Section 2.4, our source extraction lead to a homogeneous distribution of sources over all HeViCS fields, so we can easily extrapolate our results for the total observed area of 55 deg^2. I show an example of simulated SPIRE images (source and noise) in Fig.4.4.

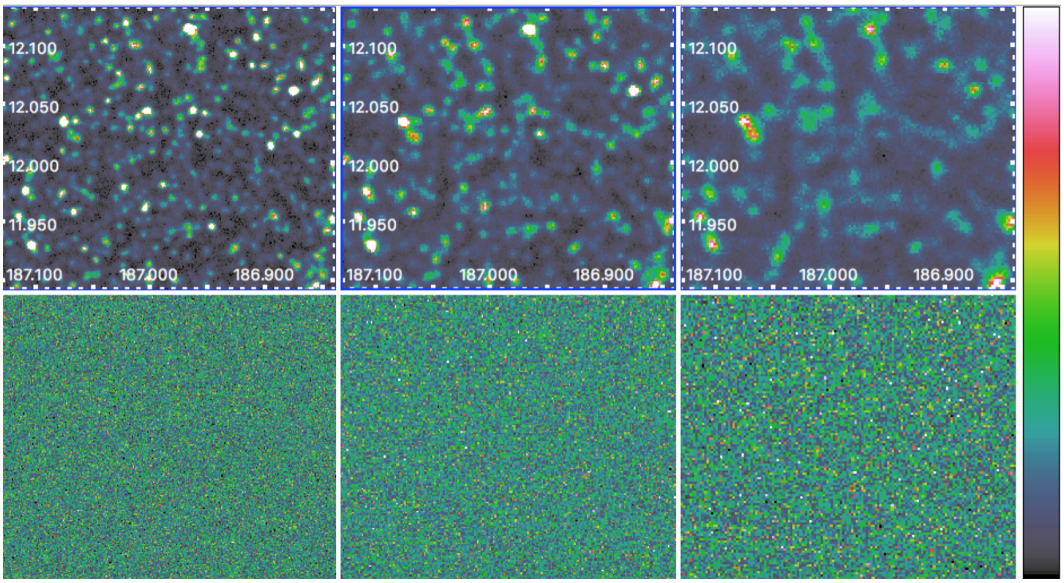

Figure 4.4.: Simulated SPIRE maps (upper panel), and corresponding noise maps (bottom panel). From left to right the maps are at 250 μm, 350 μm and 500 μm respectively.

I apply the same source-detection pipeline as I do in our raw HeViCS maps. As expected from the analysis performed with mock catalogues in Section 4.2, I disclose three groups of sources:

- Intrinsic 500 μm-risers
- Contaminants (both red and non-red)
- Missed 500 μm-risers

Below I describe each category of objects in more details. Results from the simulations are summarised in Fig.4.5, while in Fig.4.6 I plot an example 2D-cutout images of detected and missed sources.

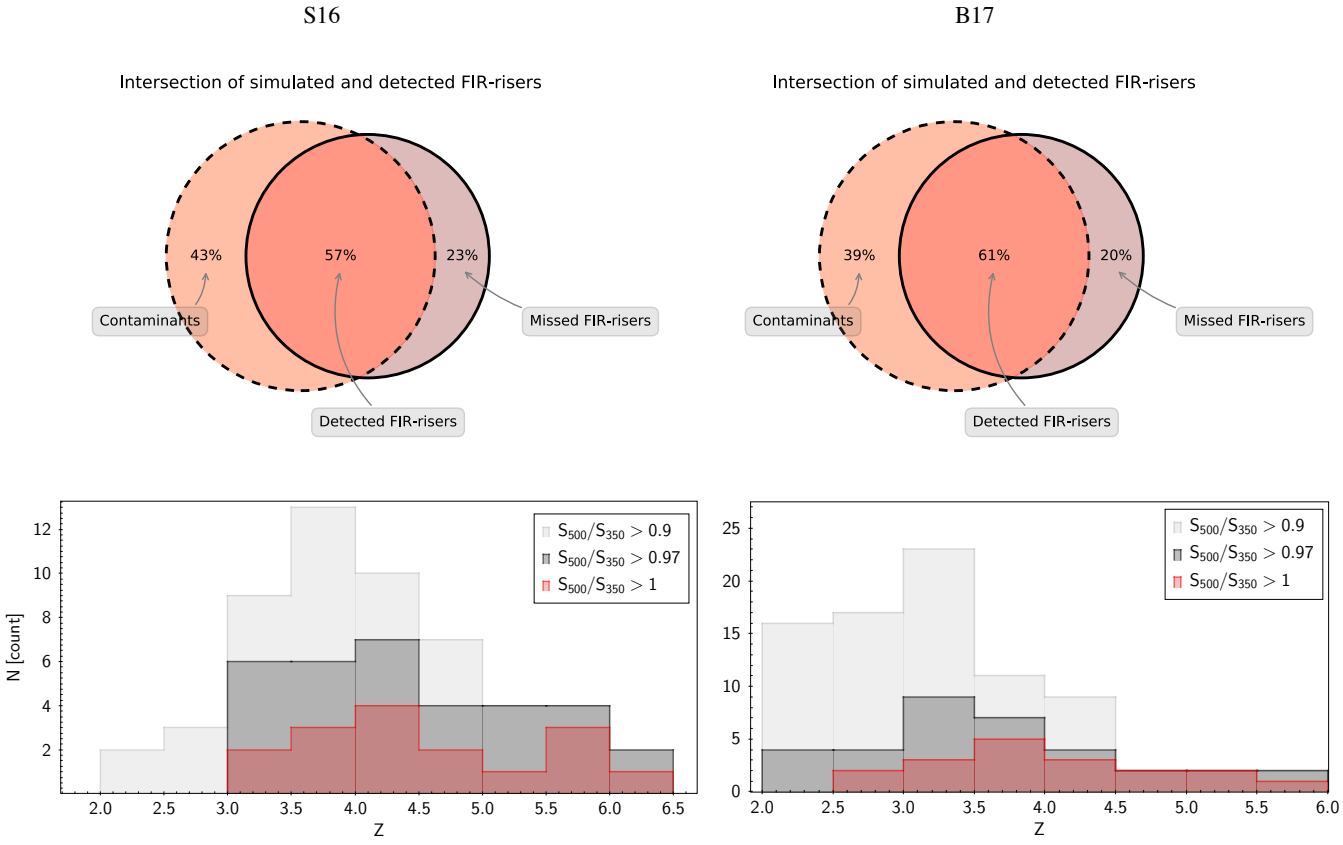

Figure 4.5.: *Upper panels*: Galaxies detected in mock maps. "FIR-riser" criteria are imposed as for real HeViCS maps ($S_{500} > S_{350} > S_{250}$, $S_{250} > 13.2$ mJy, $S_{500} > 30$ mJy). Intersected area coloured in dark orange depicts recovered 500 μm-risers. Light orange area represents detected contaminants. Violet area represents missed sources. Those are genuinely 500 μm-risers, but they are not present in our final catalogue, since we observed their fluxes or colours slightly below the limit of selected 500 μm-risers. *Lower panels*: Redshift distribution of galaxies observed in mock maps. Different S_{500}/S_{350} colour cuts are imposed. These cuts are related to statistical properties of the confusion noise, which is the greatest contributor to colour uncertainties. (see also Table 6). Left and right panels refer to S16 and B17, respectively.

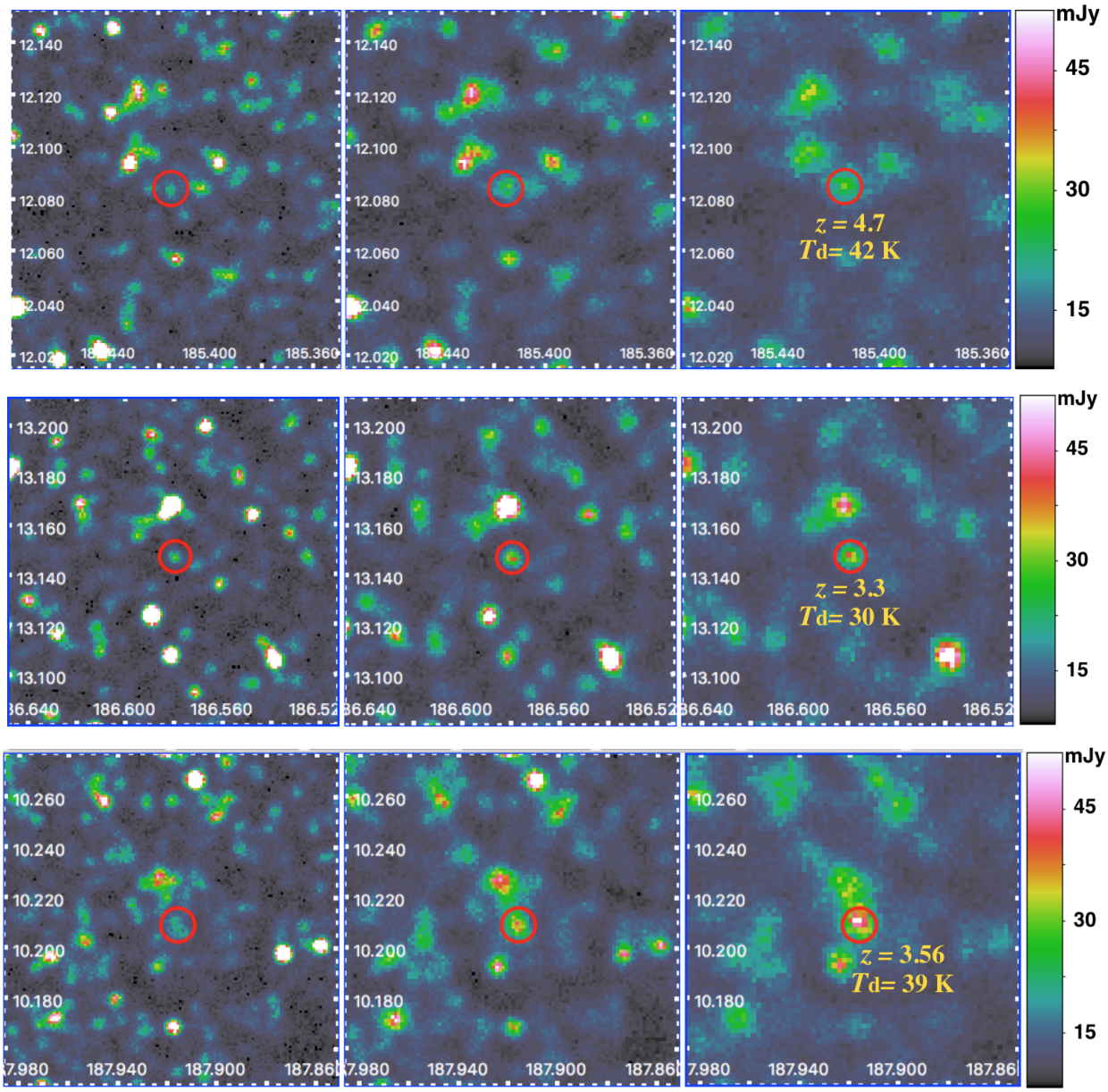

Figure 4.6.: Example 2D-cutouts of high-z DSFG from our simulations. The red circle has diameter of 36", which is a beam size at 500 μm. The upper panel presents the simulated 500 μm-riser at $z = 4.7$ which we successfully recover. The source's 500 μm flux is at the edge of our detection threshold ($S_{500} = 30.7$mJy). It is a weakly lensed DSFG with the warmer SED ($T_d = 42$K), Middle panel depicts the intrinsic 500 μm-riser that we did not select. The missed source is at $z = 3.3$ and we observe it as a 350μm peaker. It is intrinsically strongly lensed ($\mu = 2.7$), colder DSFG ($T_d = 30$K). The lower panel illustrates an example of a contaminant DSFG. It is not entirely "spurious" source, since its redshift is $z = 3.56$. Nevertheless, the source is observed as 500 μm-riser, but intrinsically it is a 350 μm-peaker blended with another 350 μm-peaker at $z = 3.25$.

1. *Recovered 500 μm-risers*

   The dark orange region in Fig.4.5 indicates the fraction of recovered sources. These are objects with both intrinsic and observed properties matching our selection criteria ($S_{500} > S_{350} > S_{250}$, $S_{250} > 13.2$ mJy and S_{500} >30 mJy). The relative contribution of recovered 500 μm-risers is 57% for S16 and 61% for B17. The redshift distribution of recovered 500 μm-risers is plotted in the lower panel of Fig.4.5. Following S16, all recovered galaxies are at $z > 3$, with the median redshift $\langle z \rangle = 4.56 \pm 0.54$. The B17 model has a comparable high redshift tail, but this model peaks at lower redshift, causing the median value ($\langle z \rangle = 3.91 \pm 0.62$) to be lower than in S16. Galaxies that we recover have $L_{\rm IR} > 1.5 \times 10^{12} L_{\odot}$ and very wide range of dust temperatures, from 28 K to 54 K, which is wider than in known observational studies (see Section 3.1). However, the selection is slightly biased towards warmer sources, since median $T_{\rm d}$ is found to be 41 K.

2. *Contaminants*

   The light-orange region in Fig.4.5 indicates a fraction of contaminants (39% for B17 and 43% for S16). These are observed as 500 μm-risers, but their intrinsic colours and/or fluxes are not matching our selection criteria. The contaminants consist of two different populations of sources: The first ones are faint 500 μm-risers, with modelled 500 μm fluxes not bright enough for the final inclusion in catalogue of 500 μm-risers selected with our criteria ($S_{500} < 30$ mJy). They are dominating this group of objects, since their relative contribution is found to be 60% for B17 and 72% for S16. The second population of contaminants are intrinsically 350 μm-peakers with narrowly ranged colours (0.9<S_{500}/S_{350}<1.0). The normalised redshift distribution of these sources is shown in Fig.4.7. The most of contaminants at $2 < z < 4$ are either weakly lensed sources, or colder galaxies blended with another high-z source. As shown in Bethermin et al. 2017, the weakly-lensed 500 μm-risers are on average 6% more magnified than the average magnification at $2 < z < 4$. Weak lensing can be then considered as an additional noise on the flux. That means, the sources that fall on a positive fluctuation of the galaxy magnification can easily fulfil the flux criterion, thus being observed as 500 μm-risers. For contaminants at $z > 4$, I find that there are more complex combination of effects which cause their observed fluxes/colours. I indicate them with arrows and annotate the different reasons As I will discuss in more details in

Section 5.3, 350 μm-peakers at $3 < z < 4.5$ are much strongly clustered than those at lower redshits. They thus produce non-negligible 500 μm flux excess.

All detected contaminants are high-z DSFGs, with 85% of sources found to be at $z > 3$. Their redshift distribution peaks at 3.48 for B17 ($z_{min} = 2.12$ and $z_{max} = 7.01$), and 4.17 for S16 ($z_{min} = 3.08$ and $z_{max} = 7.56$). I thus conclude that contaminants are not purely spurious objects. They are DSFGs with $L_{IR} > 3 \times 10^{12}\, L_{\odot}$ and $M_{*} > 10^{10.5} M_{\odot}$. Interestingly, as we predicted in previous Section, complex combination of effects (clustering, lensing, noise, SED type) supports the selection of some very high-z ($z > 6$) sources that are intrinsically below our selection limit. The most distant ones have warmer SEDs ($T_{\rm d} > 45$ K), with the difference that in S16 they are all isolated SB galaxies, while in B17 50% are SB galaxies, and the other half are more strongly magnified MS galaxies.

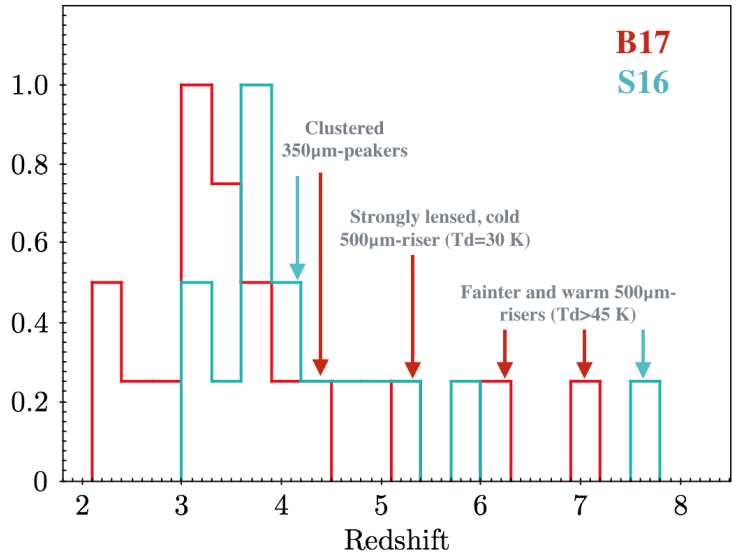

Figure 4.7.: Redshift distribution of contaminants observed in our simulations. The most distant contaminants observed at $z > 4$ are annotated with arrows (red for B17, cyan for S16). They illustrate how the complex combination of effects causes the detection of high-z contaminants that are below our selection limit. At redshifts $z > 3.5$, clustering plays important role, since it increases with redshift. For sources modelled in B17, strong lensing of some of very distant 350 μm-peakers also pushes their fluxes above the selection threshold. The most distant ones are warm starbursts.

3. *Missed 500 μm-risers*

With our extraction procedure I detect all modelled 500 μm-risers from simulated

maps. However there is a fraction of sources (20% and 23%, for B17 and S16 respectively) for which I failed to properly recover their fluxes and/or colours. These sources correspond to a violet region in Fig.4.5. $S_{500}/S_{350} < 1$ or $S_{500} < 30$ mJy. The redshifts of missed 500 μm-risers reveal that 30% of them are galaxies at $z > 4$ while the rest are strongly lensed, very cold sources at $z \sim 3$. In both models, the missed galaxies have much smaller median $L_{\rm IR}$ compare to recoverd ones. For example, for B17, it is $L_{\rm IR} = 2.1 \times 10^{12} L_{\odot}$, compared to $L_{\rm IR} = 7.9 \times 10^{12} L_{\odot}$. Missed 500 μm-risers have both colours and fluxes very close to the selection threshold. In our simulated maps, they often immerse in complex blends, having a brighter, blue source inside the 500μm beam. Therefore, some of our missed sources pass both 250 μm and 500 μm flux selection cuts, but their observed colours are non-red. Another reason why we are potentially missing some objects is because our simultaneous de-blending technique assumes that all sources have MBB SEDs. For those cases where 500 μm-risers are blended with the source whose SED cannot be described well with MBB, we can over- or undersubtract total flux, leaving some high-z candidates uncatalogued. One way to solve this issue is inclusion of more sophisticated SEDs in our code, which is not a trivial task since such a procedure requires additional multiwavelength information about blends (see e.g., Pearson, Wang, Hurley, et al. 2018, Safarzadeh, Ferguson, et al. 2015).

Colours of sources observed in simulated maps

To measure the variations of observed and modelled colours, I define two quantities. The first one measures a difference between catalogued intrinsic colours (without addition of noise) and catalogued modelled colours (with the addition of simulated noise). I dub this quantity the "modelled reddening", and define it as:

$$\Delta_{mod} = \left(\frac{S_{500} + \sigma_{500}}{S_{350} + \sigma_{350}}\right) - \left(\frac{S_{500}}{S_{350}}\right)_{\rm intrinsic}, \tag{4.10}$$

where σ_{500} and σ_{350} are 1σ total noise ratios measured at 500 μm and 350μm respectively (see Section 2.1). The second quantity is a difference between colours observed in our mock maps and intrinsic ones. This quantity is "observed reddening", given as:

$$\Delta_{obs} = \left(\frac{S_{500}}{S_{350}}\right)_{\rm map} - \left(\frac{S_{500}}{S_{350}}\right)_{\rm intrinsic}, \tag{4.11}$$

where $\left(\frac{S_{500}}{S_{350}}\right)_{\rm map}$ and $\left(\frac{S_{500}}{S_{350}}\right)_{\rm intrinsic}$ are observed and intrinsic colours respectively. Ideally Δ_{obs} should be zero, but in reality the noise fluctuations along with other effects cause observed value never be the same as the true one. I further compare Δ_{obs} and Δ_{mod}. The differences between intrinsic and observed colours of recovered 500 μm-risers are presented in Table 4.3. We see that the largest Δ_{obs} and Δ_{obs} are measured for the lowest flux bin, where we expect the largest flux uncertainties due to the lower S/N.

The colours of recovered sources are observed somewhat "redder" than original ones. Such a difference between intrinsic and observed colours is expected from our analysis in Section 4.2.1. For missed 500 μm-risers, I find negative median values for both Δ_{map} and Δ_{mod}. It means that noise tend to push the colours of these galaxies slightly blue-wards (see the Table 4.3 and Fig.4.8). As we can see, the change of colours is small, but for selection functions based on certain colour cuts, even such small differences are important. I consider these variations in the next Section, when I analyse the suitability of other colour criteria for selecting DSFGs at $z > 4$ (Section 4.4).

Table 4.3.: Intrinsic vs. observed colours of simulated 500 μm-risers. Catalogue and maps are based on B17.

Flux bin	$S_{500}/S_{350}^{(1)}$ [B17$_{cat}$]	$S_{500}/S_{350}^{(2)}$ [B17$_{map}$]	$\Delta^{(3)}$ (observed)	$\Delta^{(4)}$ (missed)
30-40 mJy	1.03± 0.09	1.07± 0.1	0.04 (0.012)	-0.03 (-0.004)
40-50 mJy	1.10± 0.05	1.12±0.06	0.02 (0.009)	-0.005 (0.002)
$>$ 50 mJy	1.15±0.11	1.16±0.18	0.01 (0.008)	

(Column 1) Catalogued intrinsic colours from B17. Noise is not simulated; (Column 2) Colours measured in simulated maps; (Column 3) Δ_{obs} (left raw) and Δ_{mod} (right, in brackets); (Column 4) The same as in Column 3, but for 500 μm-risers that are missing from our final selection.

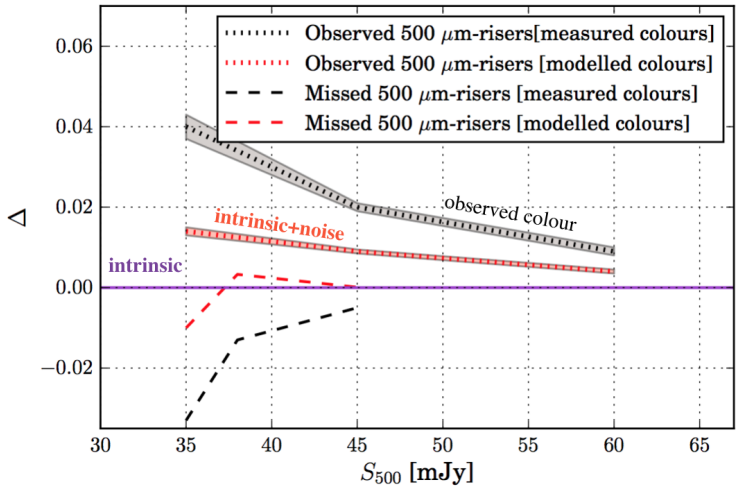

Figure 4.8.: Both observed and modelled reddening parameter (here for simplicity labelled Δ), plotted as a function of 500 μm-flux. Note that red colours on the plot correspond to Δ_{obs}, while black lines are related to Δ_{mod}. Observed and missed 500 μm-risers are plotted with dotted and dashed lines respectively. We see that for missing 500 μm-risers, both observed and modelled colours are poorly reddened by the noise, which is opposite trend compared to sources that are observed as 500 μm-risers.

On the detectability of intrinsic 500 μm-risers

The relative contribution of 500 μm-risers we recover with our method (61%) is not as high as the value claimed by Asboth et al. 2016. They perform end-to-end simulations to test their detection pipeline, and report no missing sources and the purity of almost 90%. It means that just 10% of all sources contained in their final catalogue are contaminants. However, I find significant differences between our simulations. While in this work I create simulated images adopting intrinsic colours of sources that have been drawn directly from the mock catalogues, Asboth et al. 2016 use B12 to create the maps, but omitting all modelled 500 μm-risers. They instead create noise maps and inject 500 μm-risers with the number density and SPIRE colours fixed to the median values measured in their raw maps. Such an approach may lead to serious biases, since the number of detected 500 μm-risers in HeLMS is order of magnitude higher as compared to the existing models. The relative contribution to the extracted number counts of intrinsically non-red sources, which matches the selection criteria because of the noise and resolution effects, might be then severely underestimated due to the very high number of injected 500 μm-risers in their simulation. On top of that, I simulate

clustering in our maps, which is not the case in the simulation of Asboth et al. 2016.

Considering the Δ_{obs} presented in Table 4.3 and Fig.4.7, it appears evident that distinguishing between the red and non-red DSFGs is very challenging, even for those extragalactic fields with significantly reduced instrumental noise. As expected, colour uncertainties are increasing towards the lower fluxes causing that we miss to select 20% of galaxies in the final 500 μm-riser catalogue. To search for missing "risers", I analyse the full catalogue of sources detected in mock maps, finding that with $S_{500}/S_{350} > 0.9$ the number of missed 500 μm-risers falls to zero independently of the chosen model. Nevertheless, blindly imposing this cut in order to catch all 500 μm-risers above $S_{500} = 30$ mJy does not come without the cost. The contribution of contaminants becomes very high, from 57% (S16) to 77% (B17). I thus conclude that some flexibility on a colour/flux threshold is needed to account for the effect of noise, lensing and clustering. Such flexibility is important not just to reduce the number of missed intrinsic 500 μm-risers, but also to unveil potentially non-red galaxies at $z > 4$. I examine this goal in the next Section.

4.4. Modifying the criteria: can we select a larger number of candidate DSFGs at $z > 4$?

The primary idea behind the 500 μm-riser method is in creating the well controlled function that systematically selects candidate $z > 4$ DSFGs with the lowest possible fraction of contaminants from lower redshifts. However, according to models used in this work, sources at $z > 4$ are not just 500 μm-risers. This prediction is also in line with observations, since there are examples of DSFGs at $z > 4$ that are 350 μm-peakers (e.g. Pope, Montaña, et al. 2017, Miettinen et al. 2015, Capak et al. 2011). It is thus important to investigate how can we relax the criteria in order to select even larger number of DSFGs at $z > 4$. To achieve this, here I use B17 and examine a grid of colour/flux cuts from SPIRE data. The goal of such a test is twofold: to find the colour/flux threshold that increases the number of modelled DSFGs at $z > 4$, and to invest the expected contribution of interlopers (sources at $z < 4$).

I decide to confront different flux cuts, based on the completeness values (from $50\% - 80\%$ in 10% step). The upper flux cut is then identical as in our original selection ($S_{250} > 13.2$mJy, $S_{500} \geq 30$mJy), while the lowest limit is $S_{500} \geq 18$mJy. I further

explore the grid of colours, starting from $S_{500}/S_{350} = 0.85$. The motivation to chose $S_{500}/S_{350} = 0.85$ as a starting point is based on model predictions: $S_{500}/S_{350} = 0.85$ is the lowest limit for which B17 predicts the 250 μm detected source at $z > 4$.

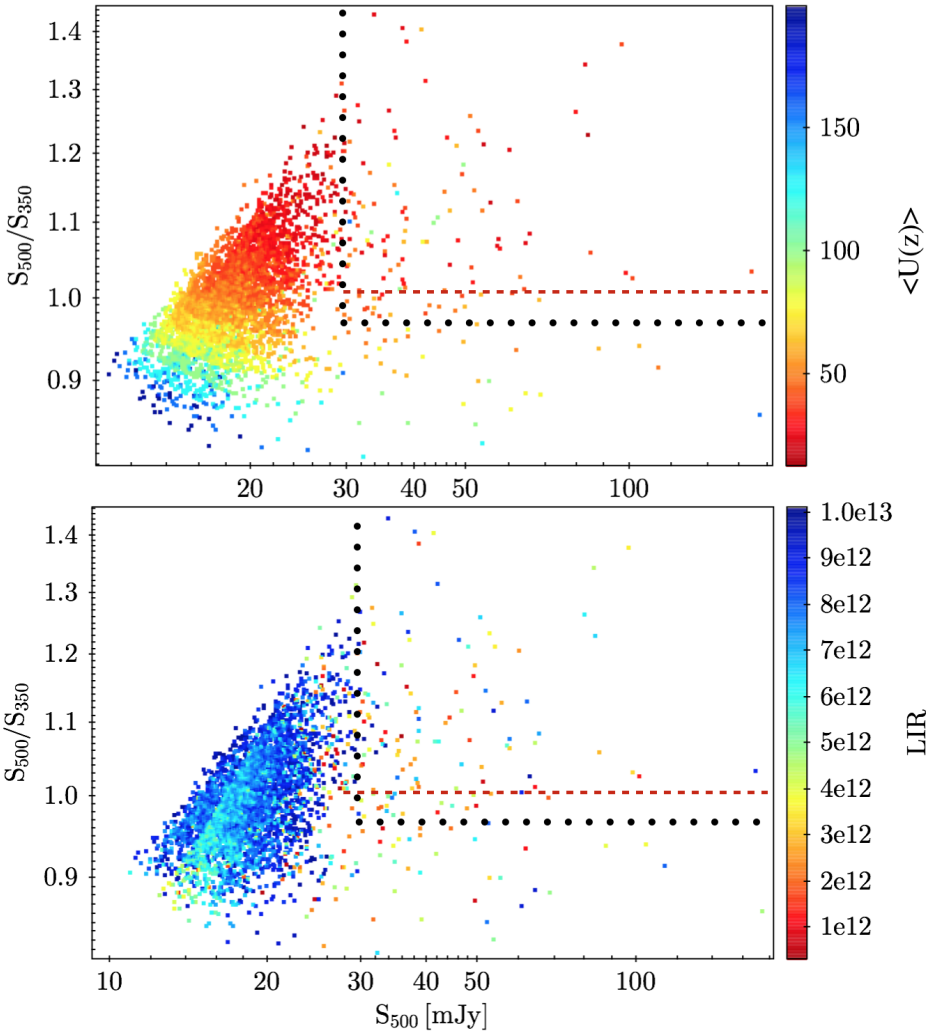

Figure 4.9.: Modelled colours and 500 μm fluxes for all sources being at $z > 4$ according to B17. Scattered points are coloured based on their modelled mean radiation field (upper panel), and modelled $L_{\rm iR}$ (lower panel). The red line depicts the selection of 500 μm-risers imposed in our work, whilst black, dotted lines cover the sources that fulfil the best alternative colour criteria: $S_{500}/S_{350} > 0.97$ and $S_{500} > 30$ mJy.

On Fig.4.9 I plot all sources modelled to be at $z > 4$ in B17, if we impose the same 250 μm detection limit as we did in our real maps ($S_{250} > 13.2$ mJy). Note that these sources account just for the 250 μm limit, but they do not impose any limitation on 500μm. The upper and lower panel illustrate the colours and fluxes of modelled sources, related to

their $\langle U \rangle$ and $L_{\rm IR}$ respectively. We see that B17 predicts that a large number of DSFGs at $z > 4$ should be contained in our prior 250 μm catalogue (950 sources over 55 deg^2). As we can see from the Fig.4.9, applying only 500 μm-riser criteria (the region enveloped with red line), we reach just the "leading edge" of the whole population of DSFGs at $z > 4$. The main difficulty in selecting the rest of distant sources are thus not coming from the colour criterion, but due to confusion which restricts secure detections at 350μm and 500 μm. The vast majority of galaxies we miss to select from SPIRE data are fainter DSFGs.[g]

In Fig.4.10 I present results of my analysis. I find that for $S_{500} = 30$ mJy, we can slightly downgrade the colour criteria to $S_{500}/S_{350} = 0.97$. In this case the redshift distribution is still more dominated by sources at $z > 4$, having median value $z = 3.69$. In other words, the proposed colour cut works well against the lower-z contaminants, limiting their contribution to a maximum of 18% at $2 < z < 3$. On the other hand, degrading the 500 μm flux leads to a significant increase of selected DSFGs at $z > 4$ by $\sim 10 - 12\%$. However, there is no flux/colour combination for which the median redshift stays above $z = 3.5$. In the lower panel of Fig.4.10 I show the best combination for which difference between the two "reddest" colours gives the small difference in redshifts, however both of them being at $z < 3.5$. Concerning this, the proposed selection function can be used as a baseline for uncovering more DSFGs at $z > 4$ from existing SPIRE catalogues. In the next Chapter of the Thesis, for the purpose of comparison to other existing selections, I keep investigating our initial 500μm-risers criteria.

From this analysis we see that even significantly relaxed selection functions does not have the power to detect most DSFGs at $z > 4$. Following this, it appears that one of the most important questions related to *Herschel* surveys remains unanswered: *How can we find the distant DSFGs beyond the confusion limit?* In Chapter 6 I present a new approach which aims to deal with this problem.

[g] In the Section 5.3 I also present measurements of their angular correlation function, showing they fainter 350 μm-peakers are much strongly clustered than other galaxies at $4 < z < 4.5$.

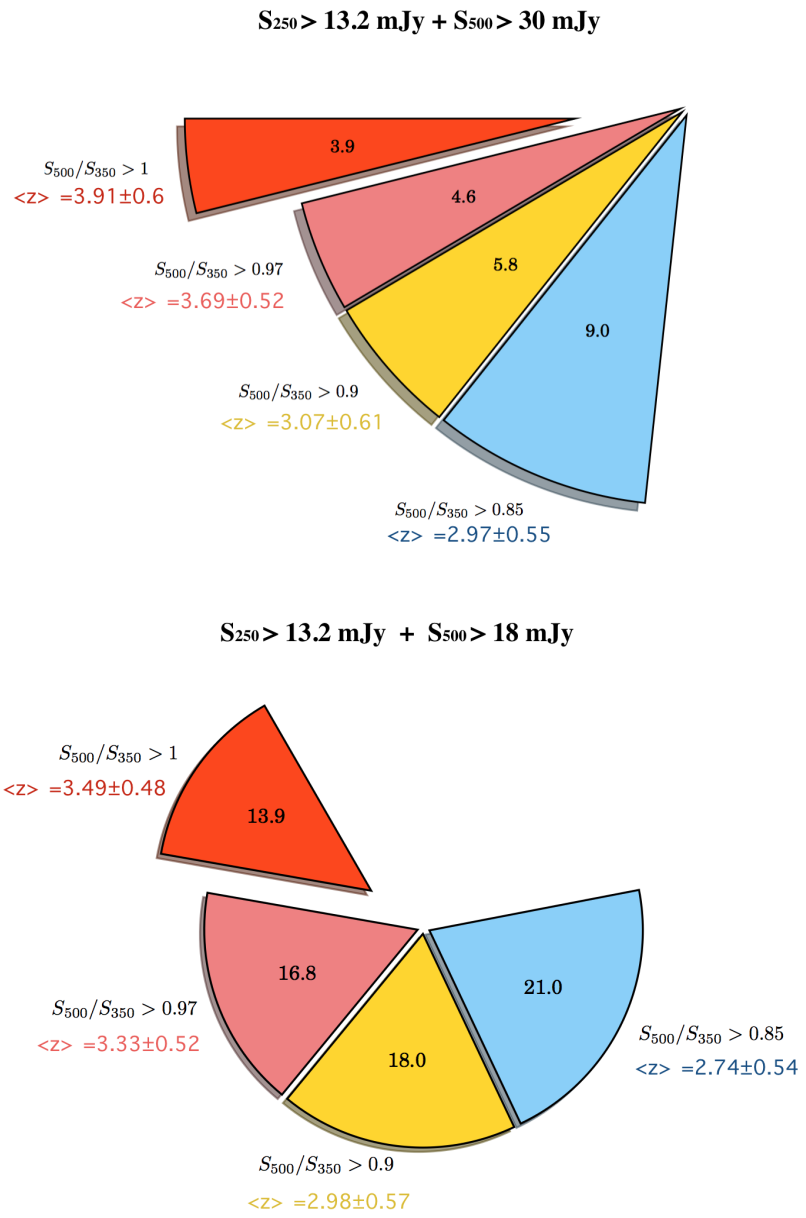

Figure 4.10.: Comparison of different selection criteria for candidate $z > 4$ DSFGs. Coloured pie-chart slices illustrate various cuts we test. Numbers inside each of coloured areas are relative contributions (in percentages) of DSFGs detected to be at $z > 4$ if we impose given 250 μm limit. The median redshifts are assigned to each combination, and reflect the contribution of low-z contaminants. The colour criteria presented in the upper panel are combined with the flux cut: $S_{250} > 13.2$ mJy and $S_{500} > 30$ mJy. Results related to relaxed detection flux cut ($S_{500} > 2.7\sigma \approx 18$mJy) are shown in the lower panel. From the lower panel we see that relaxing the 500 μm flux limit we can increase the relative contribution of DSFGs at $z > 4$ by more than 10%, but at the same we time pollute our sample with more than 50% of galaxies at $z < 4$.

CHAPTER 5

Characterising the 500 μm-risers

Table of contents:

Introduction

In the literature, the vast majority of known DSFGs at $z > 4$ selected by *Herschel* have been revealed as either strongly lensed galaxies, interacting groups/protoclusters of high-z objects, DSFGs with obscured AGN, or eventually the combination of these groups of sources (e.g. Miller, Chapman, et al. 2018, J. A. Zavala, Montaña, et al. 2017, Fudamoto et al. 2017, Riechers, Leung, et al. 2017, Oteo, Ivison, Negrello, et al. 2017, P. Cox et al. 2011). In order to develop a better understanding of the population of 500 μm-risers, we should determine the exact nature of these seemingly extreme systems by exploring all diverse effects that could impact estimated properties (e.g $L_{\rm IR}$) of individual objects. In this Chapter I use a model-based approach and undertake a comprehensive analysis of selected sources aiming to answer on question "*What are 500 μm-risers?*".

The SPIRE instrument has a large beam size, and ALMA follow-ups of brightest DSFGs have demonstrated that many of these sources are often resolved in multiple components. If contribution of multiple galaxies to the measured flux is non-negligible, 500 μm-risers will remain less extreme systems than previously thought, regardless of the question are contributed objects physically interacting with each other or not. The physical nature of source multiplicity and its impact on single-dish selections is widely considered as one of the "hot topics" of modern IR astronomy (Hayward, Chapman, et al. 2018, Bethermin et al. 2017, Narayanan et al. 2015). I analyse the effect of source multiplicity on observed SPIRE flux in Section 5.1. Even if one of main ideas behind the fainter (down to $S_{250} = 13.2$ mJy) selection of 500 μm-risers is to unveil existence of a significant population of unlensed DSFGs at $z > 4$, we should account for possibility that strong lensing magnify sources even at $S_{500} = 30$ mJy. In Section 5.2 I present the statistical method of modelling the strongly lensing fraction of 500 μm-risers selected with our technique. To further place 500 μm-risers within the broader context of galaxy formation and evolution, we need to evaluate their clustering properties, which are in correlation to masses of the host DM halos. It has been shown (Cowley, Lacey, Carlton M. Baugh, et al. 2016, Karim et al. 2013) that the blending of multiple galaxies into a single source enveloped by the telescope beam causes an artificial boost in the angular clustering signal compared to that of individual, "real" galaxies. Since the observed clustering of DSFGs is often used to infer the halo occupation number and typical masses of the DM halos containing these galaxies, the "blending bias" could lead in overesti-

mation of estimated halo masses (Cowley, M. Béthermin, et al. 2017). In Section 5.3 I apply angular cross-correlation analysis to study the clustering of simulated DSFGs at $2.5 < z < 4.5$, and to model its impact on the observed statistics of 500 μm-risers. The analysis presented here is the first of this kind which is based on modelled SPIRE colours of galaxies, and computes changes of their clustering signal with redshift. In Section 5.4 I estimate the lensing-corrected cosmic star formation rate density of 500 μm-risers at $4 < z < 5$.

5.1. Problem of multiplicity

One serious drawback for a proper characterisation of 500μm-risers is our limited knowledge of source multiplicity. Taking into account coarse angular resolution of SPIRE instrument, it is suitable to expect that the flux of single-dish sources would be emitted by several galaxies. The single source is thus very often comprised of blends that are either physically independent (chance projections) and/or associated (galaxy pairs).

The problem of multiplicity has long been recognised (e.g. Hayward 2013, Chapin et al. 2011, H. Dannerbauer, Lehnert, Lutz, et al. 2002), but constraining the prevalence and nature of blends appears very challenging. This is mostly due to the fact that vast majority of available higher-resolution instruments at other wavebands (e.g. MIR or radio) do not benefit from K-correction, and with the exception of ALMA, there are no higher-resolution instruments operating at the same wavelengths that are used for IR-selection of candidate distant DSFGs. There are different claims from studies found in the literature regarding the influence of multiplicity of DSFGs on single-dish surveys (Hayward, Chapman, et al. 2018, Hill et al. 2018, Wardlow, Simpson, et al. 2018, Bethermin et al. 2017, Geach, Dunlop, et al. 2017, Chen et al. 2016, Cowley, Lacey, Baugh, and S. Cole 2015, Simpson et al. 2015, Hodge, Carilli, et al. 2013). Their conclusions are tightly related to selection criteria and instruments used to measure the flux and different definitions of "multiplicity" adopted in these works. Traditionally, the multiplicity of DSFGs is defined as number of components that are resolved within a single dish detected DSFG and contribute to at least 10% of the single-dish flux at the given wavelength (e.g. Cowley, Lacey, Baugh, and S. Cole 2015). Some suggest that multiplicity fraction may be dependent on the observed FIR flux, where brighter DSFGs are more likely to have multiple components (Hodge, Carilli, et al. 2013, Karim et al. 2013, Bussmann et al. 2015, Simpson et al. 2015, Geach, Dunlop, et al. 2017). These

assumptions are based mostly on strongly lensed DSFGs, since these are known to be very bright in FIR bands.[a]

The multiplicity of DSFGs has been extensively studied at 850μm from both an observational and theoretical point of view (e.g. Hayward 2013, Cowley, Lacey, Baugh, and S. Cole 2015, Muñoz Arancibia et al. 2015, Simpson et al. 2015, Geach, Dunlop, et al. 2017, Hayward, Chapman, et al. 2018). Oppositely, the problem is much less explored for SPIRE sources (see Bethermin et al. 2017). A recent multiplicity study of SPIRE data was performed by Scudder et al. 2016. These authors analysed the fraction of galaxies contributing to fluxes at 250 μm for sources detected based on *Spitzer* priors in the COSMOS field. They conclude that a significant fraction of DSFGs are composed of multiple sources emitting at 250 μm, with the brightest component contributing $\sim 65\%$ at 30 mJy. The analysis of Scudder et al. 2016 considers galaxies with photometric redshifts up to $z = 3.5$ and $S_{250} > 30$ mJy. However, in the literature there is no systematic theoretical study of multiplicity based on colour-selected *Herschel* sources. On the observational side, multiplicities of 500 μm-risers are usually serendipitously observed (Marrone et al. 2018, Riechers, Leung, et al. 2017, Oteo, Ivison, Negrello, et al. 2017, Fudamoto et al. 2017), while the first systematic sub-mm survey of multiplicity of various red DSFGs is still ongoing (Greenslade et al, in prep.).

5.1.1. Impact of resolution effects on the flux of 500 μm-risers

Since we work with SPIRE data only, here I present multiplicity analysis based on simulations. I follow the same approach that has already been implemented for SPIRE and SCUBA-2 selected DSFG, in order to find the ratio between the brightest modelled source and the brightest observed source (Bethermin et al. 2017, Cowley, Lacey, Baugh, and S. Cole 2015). I use the catalogue of 500 μm-risers detected in our mock maps, and for each source I search for the catalogued, brightest counterpart in the radius no larger than half of the corresponding FWHM. I then measure the ratio between the modelled flux of this brightest galaxy from mock catalogues and the total single-dish flux observed in simulated maps. I place computed values in different flux bins. The comparison between the brightest galaxy flux to single-dish source flux is presented in Fig.5.1.

For 250 μm, 71 to 85$\%$ of observed flux is emitted by the brightest galaxy. For both

[a] As noted in Chapter 2, the vast majority of $z > 3-4$ DSFGs with $S_{500} > 100$ mJy, are biased towards stronger magnifications.

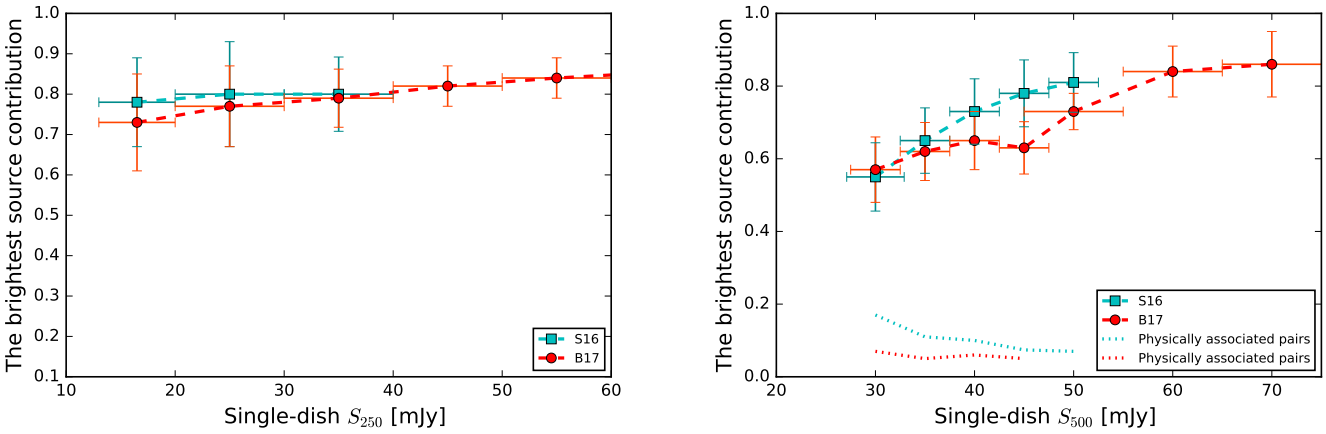

Figure 5.1.: Ratio of brightest galaxy component flux to single-dish source flux for 500 μm-risers detected in our mock maps. Results are plotted for 250 μm maps (left) and 500 μm maps (right). Horizontal error bars indicate the width of the chosen flux bin, while vertical error bars show the standard deviation of the distribution. Plotted with dashed red and cyan lines in the right panel is average contribution of physically associated pairs of galaxies in B17 and S16 respectively.

models we witness the same trend, with the slight increase towards higher 250 μm fluxes. The total 250 μm flux is largely affected by the presence of other source in the lowest flux bin. This expectation is in agreement with our colour analysis from previous Chapter, where we find the faintest detections also express the largest reddening. Repeating the same analysis for 500 μm map, I find the similarly rising trend, but with a lower average fraction due to much stronger resolution effects. In the lowest 500 μm flux bin, the contribution to the total flux from the brightest source drops to 55-57% for both models. In other flux bins the fractional contribution increases and reaches $\sim 80\%$ at $S_{500} > 50$ mJy. On the one hand, the faint-end of 500 μm-risers ($30 < S_{500} < 40$ mJy), experiences the large impact of multiples which comes from the fact that blends are in average high-z sources ($\langle z \rangle = 2.37 \pm 0.35$), intrinsically below our 250 μm detection cut, but with fluxes being larger at 350 μm and 500 μm, due to the shift of the peak of their SEDs. On the other hand, the brighter-end of 500 μm-risers ($S_{500} > 50$) appears mildly boosted by nearby sources. At these flux levels, the models predict that SPIRE sources are essentially either local SF galaxies, loud AGNs or strongly lensed DSFGs. Combined with the fact that clustering of nearby objects is significantly weaker than at higher redshift (e.g. Wilkinson et al. 2017), this may explain why the brighter 500 μm-risers have a smaller contamination to their total single-dish flux. However, this is

only true when careful de-blending based on 250 μm priors is performed.

Bethermin et al. 2017 used 2 deg^2 mock maps to probe the impact of multiple sources on all simulated SPIRE detections down to $S_{250} = 30$ mJy. They apply a slightly different source photometry technique based on positional priors, but the findings presented here are in very good agreement with their results, with marginally higher measured fraction at 500 μm, but still consistent within the uncertainty. Unfortunately, our results are very hard to compare to those from other observational studies. For example, Scudder et al. 2016 based their analysis exclusively on 250 μm fluxes, selecting just those sources for which they have both 3.6 μm and 24μm catalogued detections inside the given 500 μm beam. Sources that do not fulfil such criteria were immediately rejected. This highly biases the sample against the reddest DSFGs, since we expect most of 500 μm-risers being fainter than 5σ at 24μm (Dowell et al. 2014).

5.1.2. Multiplicity of single-dish sources: physically associated or not?

To roughly quantify the multiplicity rate of our single-dish measurements, I assume each SPIRE detection being multiple if it has another catalogued source within the beam, with the flux contributing 10% and more. Considering B17 (S16), such a defined multiplicity rate is $31^{+5}_{-7}\%$ ($34^{+4}_{-4}\%$), and $37^{+5}_{-7}\%$ ($44^{+6}_{-5}\%$) at 250 μm and 500 μm respectively. To better understand these galaxies, I aim to quantify the contribution of physically related and unrelated sources. I measure the fraction of the 500 μm flux emitted by galaxies residing at a similar redshift as the brightest catalogued one. I assume that galaxies are physical pairs if their redshift difference is $|\Delta z| < 0.01$ and their projected co-moving distance is no larger than 100 kpc (Hayward 2013, Fensch et al. 2017, Stach et al. 2018). For the sources detected at $z = 4$, such a limit corresponds to 14" in angular scale. I then search for all possible galaxy pairs in our mock catalogues. I find the ratio between randomly projected blends and physically related galaxies is 79% vs. 21%. Closer inspection of our galaxy pairs reveals that they are intrinsic 350 μm-peakers at $z > 3$. They have been found at distances 4" or closer to the central source. Since their 250 μm fluxes are below our detection threshold, they are missing from the prior catalogue, and hence cannot be used for the de-blending. For S16, their maximum contribution to the total flux is at 30 mJy (17%), while for B17 is even lower (8%), showing no significant changes with input fluxes. I measure that the majority of counterparts are physically unassociated, which is in line with the same conclusions

from Hayward, Chapman, et al. 2018, Wardlow, Simpson, et al. 2018, Cowley, Lacey, Baugh, and S. Cole 2015 and also with Hayward 2013,who perform a similar analysis with simulated submm-selected DSFGs.

Results from this analysis seem to be in a good agreement with recent interferometric observations of Greenslade et al. (to be submitted). They conduct a Submillimeter Array (SMA) follow up program for 36 500 μm-risers selected from various fields and report a multiplicity rate of 33%. They found the brightest component contributes in average $\sim$ 70% to the total flux measured with SMA. The analysis presented in this Section strengthen the importance of using interferometric observations of the dust continuum emission to directly test our predictions based on models.

5.2. Strong lensing

Considering the increase with redshift of the optical depth to lensing and the magnification bias, we should also account for the possibility that some number of our 500 μm-risers are strongly lensed (Bethermin et al. 2017, Negrello et al. 2017, Cai et al. 2013). Without interferometric data allowing us to identify the true lensing fraction of our 500 μm-risers, we cannot precisely correct for the lensed population in our final sample. I thus investigate their relative contribution by making the comparison with recent ALMA/NOEMA follow-up results of 500 μm-risers selected in other fields (H-ATLAS, HerMES and HeLMS, Oteo, Ivison, Negrello, et al. 2017, see also Fudamoto et al. 2017), and using predictions from B17. My findings are summarised in Fig.5.2 and Table 5.1.

The sample used for high-resolution ALMA follow-up in Oteo, Ivison, Negrello, et al. 2017 contains 44 red DSFGs. They were chosen from initial selection candidate $z > 4$ DSFGs presented in Ivison, Lewis, et al. 2016, Asboth et al. 2016, and Dowell et al. 2014. The sources span a wide range of 500 μm fluxes, from 30 mJy to 162 mJy. I note here that a sample is highly incomplete, accounting for only the reddest sources whose colours are consistent with high photometric redshifts, estimated to be $z_{phot} \sim 4 - 6$. Observed fraction of strongly lensed galaxies in Oteo, Ivison, Negrello, et al. 2017 is 40 $\%$ (18 out of 44). To make this heterogeneous sample suitable for comparison with our sources and therefore model predictions, I split it into three subsamples according to methods used for their selections, more precisely: 21 source from Ivison, Lewis, et al. 2016, 13 sources from Asboth et al. 2016, and 10 sources from Dowell et al. 2014. In

Fig.5.2 I present the 500 μm flux distribution of our sample alongside the sub-samples drawn from Oteo, Ivison, Negrello, et al. 2017. We see that 500 μm-risers selected in our work have average fluxes fainter than those from other three studies.The observed number of strongly lensed objects in H-ATLAS, HerMES, and HeLMS is presented in the second column of Table 5.1. As expected, due to its bright average 500 μm flux, the sub-sample of 500 μm-risers in HeLMS contains the largest fraction of lensed sources (75%), while the lowest observed fraction is for H-ATLAS (23%).

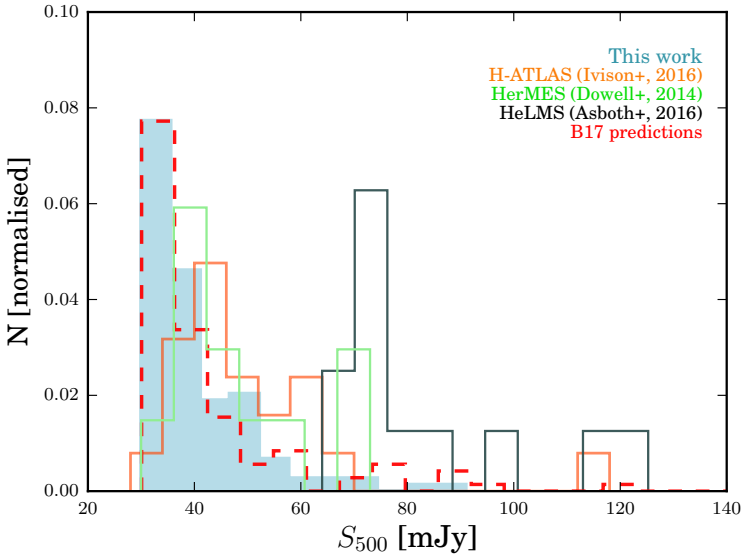

Figure 5.2.: Flux distribution of 500 μm-risers from this work (coloured blue area) compared to 500 μm-risers considered for a submillimetre interferometric follow-up in different studies. Orange, black, and green stepfilled lines represent sub-samples selected from Ivison, Lewis, et al. 2016, Asboth et al. 2016, and Dowell et al. 2014, respectively. Flux distribution of red sources from the B17 that are modelled applying the same selection criteria presented in this work is represented by the dashed red line.

I further use B17 and consider the same selection criteria as in corresponding studies (Ivison, Lewis, et al. 2016, Asboth et al. 2016, Dowell et al. 2014). For each sub-sample I examine the range of fluxes identical to what is presented in Oteo, Ivison, Negrello, et al. 2017 and simulate the effect of noise for each field separately (see Section 4.2.1). Our modelled lensing fractions are presented in the last column of Table 5.1. We see there exists a very good match between model predictions and observations, which gives confidence to our model-based approach. The predicted contribution of strongly lensed sources to our sample of 500 μm-risers is 24^{+6}_{-5}%. In Fig.5.3 I present observed differ-

Table 5.1.: A relative contribution of strongly lensed sources to 500 μm-risers selected in different studies (1):

	Median S_{500} [mJy]	Lensed [observed]	Lensed [modelled (B17)]
H-ATLAS	45 ± 14	23^{+13}_{-11} % (5/21)	28^{+8}_{-9} %
HeLMS	78 ± 19	69^{+21}_{-25} % (9/13)	75^{+10}_{-13} %
HerMES	47 ± 9	40^{+10}_{-8} % (4/10)	36^{+9}_{-7} %
This work	38 ± 4	-	24^{+6}_{-5}%

Notes: Flux distribution of 500 μm-risers from this work compared to 44 red DSFGs presented in Oteo, Ivison, Negrello, et al. 2017. These are H-ATLAS, HerMES, and HeLMS sub-samples observed with ALMA and NOEMA at 870 μm, 1 mm, and 3 mm (Oteo, Ivison, Negrello, et al. 2017, Fudamoto et al. 2017). The second column shows median 500 μm fluxes along with the median 500 μm flux from this work. The relative contribution of observed, strongly lensed sources in various selections is shown in the third column. The fourth column shows the relative contribution of modelled, strongly lensed sources from B17. A relative contribution of strongly lensed sources is modelled applying the same selection cuts of 500 μm-risers for tabulated extragalactic fields.

ential number counts along with predictions from B17, plotting separately modelled unlensed and lensed differential counts. Highly magnified 500 μm-risers start to contribute more than 50% to the observed population $S_{500} > 52$ mJy. I then use $S_{500} = 52$ mJy as a flux cut to separate between fainter (mainly unlensed) and brighter (mainly lensed) regime of 500 μm-risers. Considering the 500 μ fluxes of our 500 μm-risers, we find that most of our sources (119 out of 133, or 89%) reside in the mainly unlensed regime. Transferred to the model predictions, it means that only 17% of the modelled strongly magnified galaxies are expected to lie at a fainter flux regime ($S_{500} < 52$ mJy) where most of our sources reside.

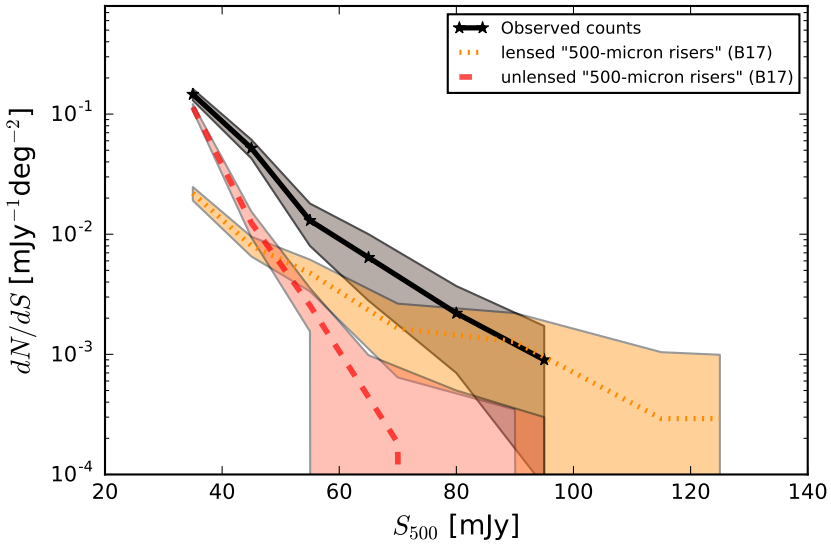

Figure 5.3.: Differential number counts modelled with B17, resolved on unlensed 500 μm-risers (red) and strongly lensed population 500 μm-risers (orange). Differential number density of 500 μm-risers observed in our field is presented with the black line. Shaded areas correspond to 1σ uncertainties in number counts.

The median redshift of modelled, strongly lensed sources is $\hat{z} = 4.2 \pm 0.4$, whilst median magnification differs by $\hat{\mu} = 4.1 \pm 1.1$ and $\hat{\mu} = 7.1 \pm 3.5$ for the fainter and brighter flux regime, respectively. This implies that strong lensing can affect the observed luminosity function of our 500 μm-risers and lowers the fraction of intrinsically bright sources. I thus apply aforementioned median magnifications to correct the observed fluxes IR luminosities estimated in Chapter 3. I thus randomly chose sources from our catalogue to correct for lensing, namely 17% of sources at $S_{500} < 52$ mJy, and 83% at $S_{500} > 52$ mJy. These percentages correspond to predictions from B17. I

then adopt aforementioned median magnification from B17 that corresponds to a chosen regime ($\mu = 4.2$ for unlensed, and $\mu = 7.1$ for lensed regime of "500 μm-risers"), and produce the observed, lensing-corrected luminosity distribution. After correcting for lensing, we expect to have 24% of galaxies with luminosities falling in the range $1.3 \times 10^{12} L_{\odot} < L_{\rm IR} < 10^{13} L_{\odot}$, and 76% of sources with $L_{\rm IR} > 10^{13} L_{\odot}$. These corrections are important and should be take into account when determining the contribution to the cosmic star formation rate density of red DSFGs (see Section 5.4).

5.3. Clustering of high-z DSFGs

To further characterise 500 μm-risers and place them in a wider context of galaxy formation and evolution, we should explore the tendency of galaxies to cluster by following the merging history of their DM halos which is a consequence developed from the initial conditions in the density field (see Chapter 1).

However, it has been shown in the literature that clustering measurement of DSFGs is a challenging task (e.g. Cowley, Lacey, Baugh, Cole, et al. 2017, Wilkinson et al. 2017, M. Béthermin, Kilbinger, et al. 2014, Xia et al. 2012, Cooray et al. 2010). For bright DSFGs usually selected in large *Herschel* surveys a significant difficulty is their sparse number density, such that wide surveys are required to yield sufficient galaxy pairs for the clustering measurements to be estimated robustly. Another issue is the lack of adequate spectroscopic redshifts for the larger samples obtained from wide surveys, so studies often make use of IR colours to generate a qualitative redshift distribution. Cowley, Lacey, Carlton M. Baugh, et al. 2016 were the first who make systematic study of clustering redshift evolution of DSFGs at $z > 2$. They analysed DSFGss modelled with the `GALFORM` semi-analytical galaxy formation model of Lacey et al. 2016 and show that confusion due to the single-dish beam could boost the observed clustering measurements by a factor of ~ 2 relative to the intrinsic values over all angular scales (the effect known as "blending bias").

In the literature, however, there are no existing clustering measurements of colour selected SPIRE sources at different redshifts. Such measurements are particularly important if we want to test evolutionary hints in source's clustering.

5.3.1. Angular clustering of high-z DSFGs

To analyse the clustering properties of colour-selected DSFGs I aim to evaluate their angular two-point correlation function (2pCF). The function, usually denoted with $\omega(\theta)$, represents a measure of the excess probability, compared with a random distribution, of finding a galaxy at an angular separation θ from another galaxy at the same redshift (P. J. E. Peebles 1982, H. J. Mo et al. 1992). The 2pCF provides a robust way of tracing the dependence of large-scale structure on galaxy properties and evolution through redshift.To evaluate this function, we need to know the underlying redshift distribution of the source samples. I decide to use B17 catalogue with physically clustered positions of galaxies (see Section 4.3). In B17 light cones are created from cosmological simulations, and the model is calibrated to match ALMA 870 μm counts successfully, which is important to partially suppress the blending issues mentioned in previous paragraph. For measuring the angular 2pCF I apply the Landy $\&$ Szalay (Landy et al. 1993) formalism, which is the widely used standard procedure described by:

$$\omega(\theta) = \frac{DD(\theta) - 2DR(\theta) + RR(\theta)}{RR(\theta)}, \tag{5.1}$$

where $DD(\theta), 2DR(\theta)$ and $RR(\theta)$ are the galaxy-galaxy, galaxy-random and random-random normalised pair counts with separations between $\theta \pm \theta/2$.

I calculate errors using the bootstrap method described in Leauthaud et al. 2011 and Norberg et al. 2008. I run 100 bootstrap realisations from which I calculate the 1σ variation for each bin.

In order to check applied methodology and clustering properties of DSFGs modelled with B17 model, I firstly measure the averaged 2pCF at $1 < z < 4$, for all galaxies that have observed (that means modelled+noise) 250 μm flux above the detection threshold we chose for our prior catalogue ($S_{250} = 13.2$ mJy). The broad redshift range of this clustering measurement is used to be the same as the one from Cowley, Lacey, Baugh, Cole, et al. 2017, which is the only known theoretical study of clustering evolution of high-z DSFGs. The later study is performed at different selection wavelength (850 μm),however even the two estimates cannot be fully compared, I plotted them together for the sake of clarity.

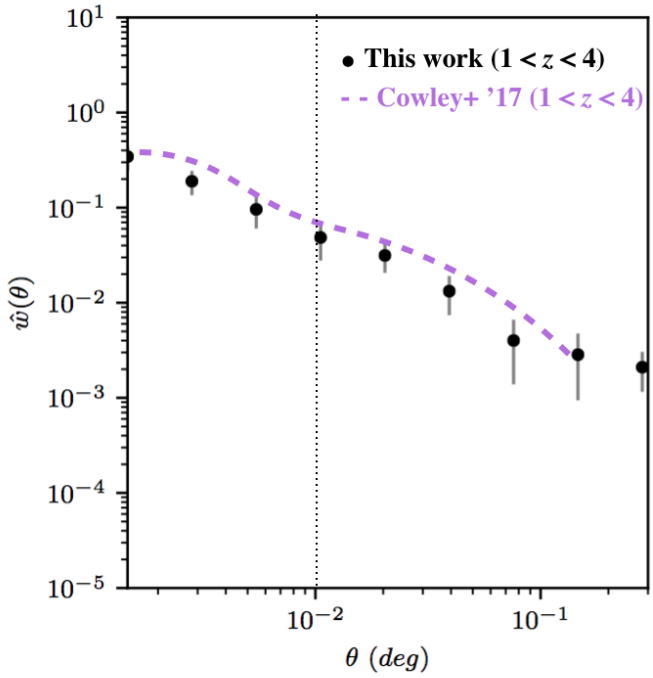

Figure 5.4.: Modelled angular two-point correlation function of DSFGs, modelled from B17 (black points). The clustering is averaged for the redshift range $1.0 < z < 4.0$. As an example, with dashed magenta I plot correlation function observed in simulated maps of modelled DSFGs selected from longer wavelengths (Cowley, Lacey, Baugh, Cole, et al. 2017). For the sake of argument, I restrict the redshift range of our sample to be the same as in Cowley, Lacey, Baugh, Cole, et al. 2017. The vertical dotted line marks the SPIRE 500 μm beam size (36").

From Fig.5.4, we see the evidence for non-linear clustering, as also stated in Cowley, Lacey, Baugh, Cole, et al. 2017. Also, if we consider uncertainty due to field-to-field variance which is find to be factor of $\sim 1.5 - 1.6$ in Cowley, Lacey, Carlton M. Baugh, et al. 2016, the agreement between the best fit from Cowley, Lacey, Baugh, Cole, et al. 2017 and our estimates is very good. This result allows us to rely on the same formalism to probe the 2pCF for modelled DSFGs, separated by their SPIRE colours. I measure the 2pCF at $2.5 < z < 4.5$ for three groups of DSFGs: all galaxies irrespective of colours, 500 μm-risers and 350 μm-peakers defined as same as in Section 4 ($0.8 < z < 1.0$)[b]. Observational SPIRE studies are limited for selecting the sources well above

[b]In this particular case, the more precise definition of this population of dusty galaxies might be "contaminant non-red sources". They are defined as $S_{350}/S_{250} > 1$ and $0.8 < S_{500}/S_{350} < 1$, and in Section 4.2 I show how they can be observed redwards due to different biases. It is thus important to inspect their clustering properties, to understand why they often pass our criteria of 500 μm-risers.

the confusion limit. The background is thus hard to estimate, and the completeness of such catalogue can vary depending on the local source density. Here we work with models, so we can significantly improve our statistics and reduce the error bars. I decide to probe all galaxies with $\mathrm{SFR} > 30 M_{\odot} yr^{-2}$, which roughly corresponds to 1mJy at 250 μm. Such a selection offers us to account for large number of sources that are potentially missed in prior catalogues. To further reduce the uncertainty of clustering measurements, I placed the colour-selected DSFGs in narrower redshift bins ($\Delta z = 1.0$). The result is presented in Fig.5.5. We can note that average 2pCF of DSFGs at both redshift ranges is stronger than average 2pCF measured for all galaxies at $1 < z < 4$. This indicates that clustering of DSFGs at $z < 2.5$ is much weaker than at $z > 2.5$, in line with findings from Wilkinson et al. 2017. They combined FIR/submm data together with deep K-band data from UKIDSS Ultra-deep survey, exploring the sources up to $z = 3.2$. They reach the same conclusion as we do, stating that low clustering amplitudes likely reflect the scenario in which lower-redshift DSFGs ($0 < z < 2$) live in low density environments. Clustering properties of modelled red and non-red DSFGs at $2.5 < z < 3.5$ do not show significant offset from the averaged population. However, moving to $3.5 < z < 4.5$ the measured offset is much larger. This is particularly evident for 350μm-peakers. Sources which have $S_{500}/S_{350} > 0.8$ show offset to the average population of DSFGs in all angular scales, which indicates that redder SPIRE galaxies may generally have more satellites (responsible for increase of smaller-scale clustering signal) and live in more overdense environments (which may explain increase of larger-scale clustering signal). Therefore, even the statistics of sources with brighter fluxes ($S_{500} > 30$ mJy) is not high in SIDES simulation, the results of our modelled 2pCF can have important consequences on selection methods of cluster progenitors at very high-z, which is the idea I discuss extensively in the Section5.5.

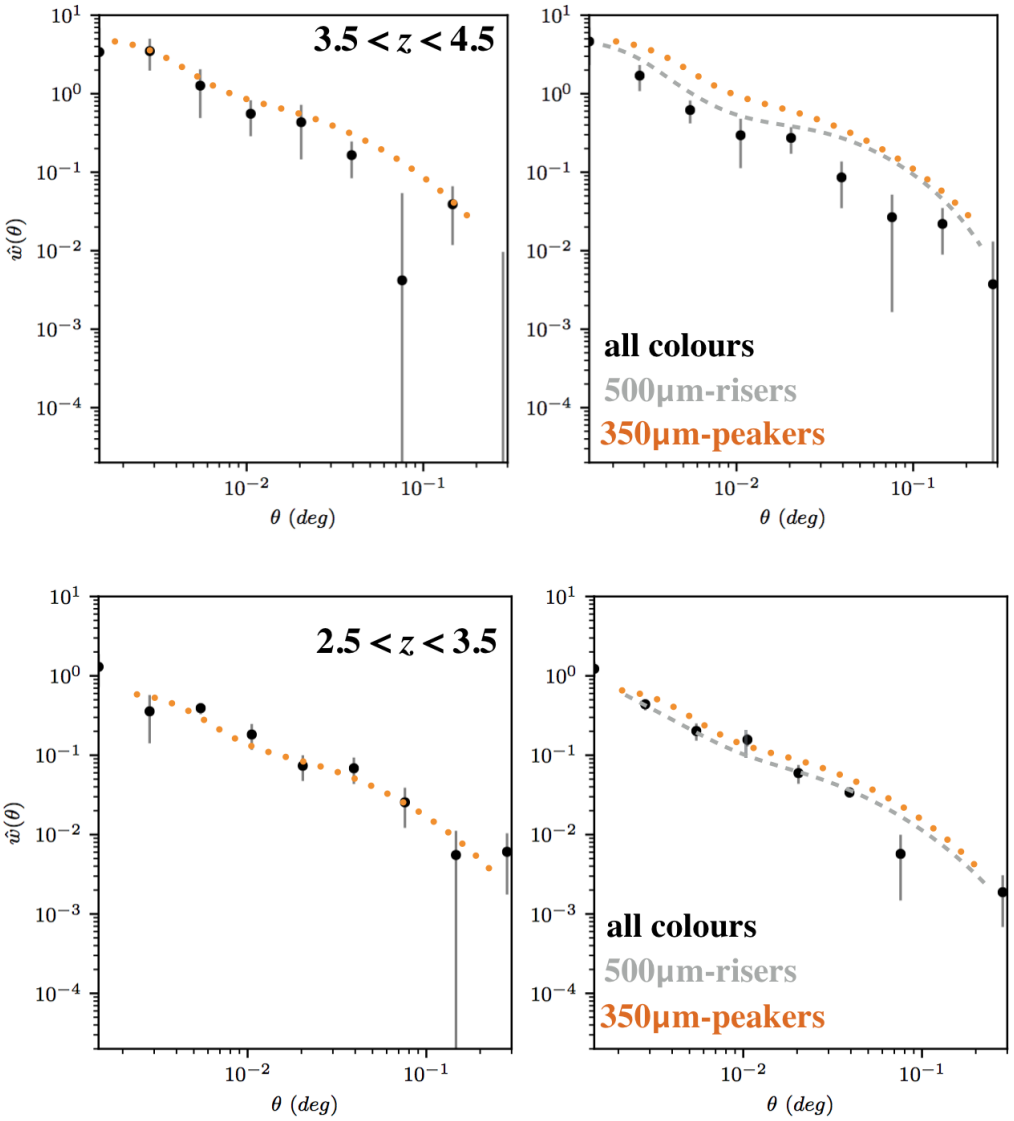

Figure 5.5.: The two-point correlation function of non-red DSFGs (350 μm-peakers, selected as galaxies having $0.8 < S_{500}/S_{350} < 1.0$ and averaged population at the same redshift (irrespective of colours). Clustering is measured for the two different redshift ranges. The best fit to the data is placed on the lower panels, and then plotted on the right panels for the sake of clarity.

5.3.2. Impact of clustering on the observed statistics of 500μm-risers

As an important potential outcome of our 2pCF analysis is that a stronger clustering of sources with certain colours can make observational imprint on the number of selected high-z galaxies ($z > 4$). This idea is already tested in Bethermin et al. 2017 for the case

of red source selection performed by Asboth et al. 2016.[c] Here I explore how the clustering of high-z DSFGs influences observed statistics of 500 μm-risers. To do so, I produce 16deg^2 map with galaxies modelled with B17 without performing any clustering treatment, that saying - cosmic variance is not taken into account and sources are randomly distributed on the sky. I perform the same selection procedure over these unclustered maps as I do in Section 4 for our clustered maps. Since we expect that the number of detections varies according to the realisation of the noise, I apply 100 realisations to estimate the median number of selected 500μm-risers. As a result, I find the total number of sources observed in unclustered maps ($1.25^{+0.9}_{-0.5}$ deg^{-2}) lower by factor of 1.4 as compared to number densities from clustered 16 deg^2 map. This boosting factor caused by clustering is somewhat lower but consistent with the one found by Bethermin et al. 2017 ($1.7^{+1.9}_{-0.7}$). However, both results seem to be in contradiction to conclusions from Dowell et al. 2014. They use the DMAP method, and measure the counts of 500 μm-risers on both simulated unclustered and clustered maps. They report that clustering does not have any measurable effect on their false detections. Nonetheless, their simulations is notably different than ours, since they consider purely clustering in the plane of the sky. When using more physically-based, clustering model, it can be shown that contaminant sources (i.e. 350 μm-peakers with colours close to our final colour-cut) are more strongly clustered than previously thought. The disagreement with Dowell et al. 2014 strongly indicates that the impact of clustering on the extraction of sources from confusion-limited surveys should be carefully considered. When using too simplified simulations, contribution of contaminants to the selection of 500μm-risers can be largely underestimated.

5.4. Star-formation rate density

Bright, individually detected 500 μm-risers are important for understanding the evolution of massive systems. Here I test if such a selection is suitable to measure the total SFR density (SFRD). To do so, I assume the statistical properties of selected 500 μm-risers and estimate SFRD at $4 < z < 5$ applying the equation (Vincoletto et al. 2012,

[c] For SPIRE data, it has already been shown that clustering has a non-negligible effect on the $P(D)$ analysis, particularly at 500 μm where blending bias increases measured fluxes up to 15% (M. Béthermin, Kilbinger, et al. 2014).

Hogg 1999):

$$\rho_*(z) = \frac{\sum SFR_{\rm IR}}{\frac{4\pi}{3}\int_{z=4}^{z=5} \frac{c/H_0}{\sqrt{\Omega_{\rm M}(1+z)^3+\Omega_\Lambda}} dz}, \tag{5.2}$$

where $\rho_*(z)$ is SFRD, defined as a total sum of SFRs per co-moving volume, while SFR_{IR} is determined from IR luminosity. The denominator in Eq.5.2 is the co-moving volume contained within $4 < z < 5$, and IR luminosity is converted to SFR applying the standard conversion formula from Kennicutt 1998:

$$\mathrm{SFR_{IR}}(M_\odot\ yr^{-1}) = 1.71 \times 10^{-10}\ L_{\rm IR}\ (L_\odot). \tag{5.3}$$

I apply our selection criteria to model (B17). Since B17 provides a magnification factor for each source, I further use the modelled, lensing-corrected luminosities and redshift distribution of $500\ \mu$m-risers. I also correct for the number of missed and contaminant sources applying the result from our simulations (Fig.4.5, Section 4.3). I place IR luminosities in a wide bin by the co-moving volume per deg^2. Scaling with the observed area and applying cosmological parameters $\Omega_{\rm M} = 0.307$, $\Omega_\Lambda = 0.693$, and $H_0 = 67.8$ km/s/Mpc (Planck Collaboration, Ade, Aghanim, Arnaud, Ashdown, et al. 2016), we find that $\mathrm{SFRD} = 1.99 \times 10^{-4}$ M$_\odot\ yr^{-1}$ Mpc^{-3} for $500\ \mu$m-risers at $4 < z < 5$. This result is shown with a filled red star in Fig.5.6. Uncertainties ($\pm 1.4 \times 10^{-4}$) are determined by Monte Carlo bootstrapping. I additionally cross-check this result by making the same estimation of SFRD but adopting IR luminosities estimated from template-based $L_{\rm IR} - z$ distribution (see Section 3.2). The IR luminosities are corrected for the effect of strong lensing as explained in Section 5.2. Applying this, I find $\mathrm{SFRD} = 2.87 \times 10^{-4}$ M$_\odot\ yr^{-1}$ Mpc^{-3}. I first compare our estimate to the one of Duivenvoorden et al. 2018. They measured the SFRD for 500μm-risers in HeLMS field, applying IR luminosities estimated from SPIRE and SCUBA-2 data. The model-based SFRD estimation presented here is consistent with Duivenvoorden et al. 2018. However, our observed SFRD is factor of two higher, but still within the 1σ uncertainty. The main cause of the difference is much larger fraction of contaminant galaxies at $z < 4$ they find in their initial selection, which results with lower density of sources estimated to be at $z > 4$ compared to our selection. Their estimate would be even lower if corrected for lensing. In contrary, there is an offset between the study of Dowell et al. 2014 and our own. Much larger SFRD found in their study may be explained by the fact that Dowell et al. 2014 predict substantially higher IR luminosities for their galaxies (median value is $3.5 \times 10^{13}\ L_\odot$, compared to

$1.9 \times 10^{13}\ L_{\odot}$, which is the median value find in this work). Additionally, Dowell et al. 2014 did not try to correct the IR luminosities for lensing magnifications.

Furthermore, we can use the shape of the luminosity function to correct for the fainter red sources. I extrapolate the contribution of 500μm-risers to SFRD - firstly by removing 500 μm flux limit (thus accounting for red sources fainter than $S_{500} < 30$ mJy), and then I remove the lower 250 μm flux cut, thus accounting for all 500 μm-risers below the *Herschel* sensitivity limit. Extrapolated contributions are depicted by empty red triangles in Fig.5.6. Here I assume the luminosity distribution from B17, but I should

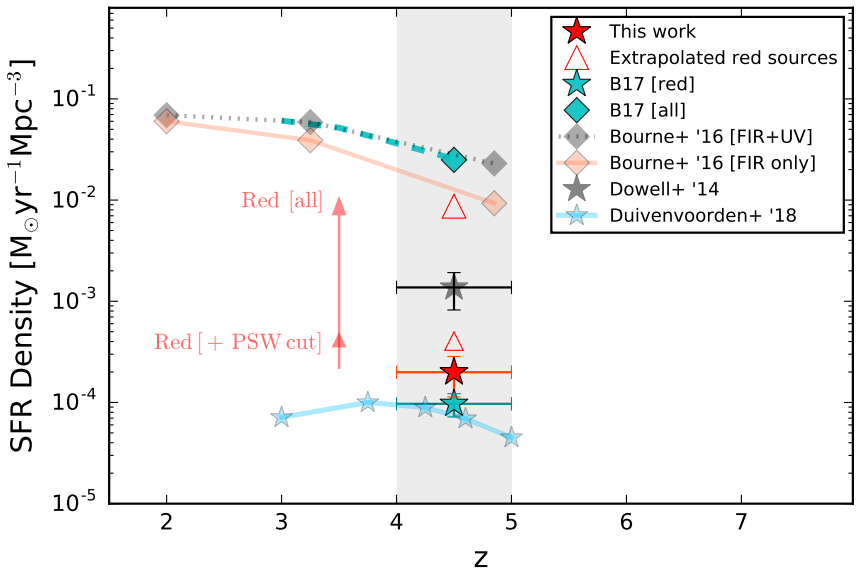

Figure 5.6.: SFRD as a function of redshift. The filled red star indicates our measurement. The estimated SFRDs of extrapolated 500 μm-risers are shown with empty red-edged triangles: smaller when 250 μm cut is imposed ($S_{250} > 13.2$ mJy), and larger if all flux cuts are removed. Flux corrections are annotated with arrows. We show for comparison results from other 500 μm-riser selections: B17 (cyan), Dowell et al. 2014 (black) and Duivenvoorden et al. 2018 (blue). Horizontal bars reflect the bin size. FIR and total FIR+UV observed SFRD (Bourne, J. S. Dunlop, et al. 2017), as well as total simulated SFRD (B17), are marked with diamonds.

mention that we obtain a very similar result (higher by a factor of 1.2) by applying the luminosity function from S16. As expected, the largest portion of sources responsible for a stellar budget at $z > 4$ is missed due to sensitivity limitations of *Herschel* instruments and not to colour selection.

The contribution of the emission of DSFGs to the total IR luminosity functions up to

$z = 5$ is partially investigated (e.g. Koprowski et al. 2017, Bourne, L. Dunne, et al. 2016, Rowan-Robinson, S. Oliver, et al. 2016, P. Madau et al. 2014, Gruppioni et al. 2013, Burgarella et al. 2013). Attempting to extend the cosmic SFRD up to $z = 6$, Rowan-Robinson, S. Oliver, et al. 2016 exploited existing 500 μm $Herschel$ selections of $500\,\mu$m-risers. They report no decline in dust-obscured SFRDs in the range $z = 3 - 6$, and very high SFRD values at $4 < z < 5$, an order of magnitude higher than our estimation. Given the severe over-prediction of the 850 μm number counts produced by the Herschel IR LFs (Bethermin et al. 2017), we may conclude that the high SFRD reported from Rowan-Robinson, S. Oliver, et al. 2016 probably reflects problems in proper $L_{IR} - z$ estimation, arising from the large-beam long-wavelength SPIRE data, as well as other biases described in this Chapter. Our result is in much better agreement with studies of Bourne, L. Dunne, et al. 2016 (marked with diamonds in Fig.5.6), who use deeper millimetre imaging to reduce the effects of confusion on cosmic SFRD measurements.

CHAPTER 6

Characterising the environments of dusty star-forming galaxies

Table of contents:

Introduction

Today we know that clusters of galaxies are largest virialised structures in an observable Universe, and assuming that most of them can be found locally, they are well explored systems. This is not the case with their more distant progenitors. The recent theoretical models suggests that protoclusters[a] may have dominated SFRD in the first two billion of years of cosmic time (Muldrew et al. 2015, Chiang, Overzier, K. Gebhardt, et al. 2017). This is due to the fact that the fraction of the cosmic volume filled by protoclusters increases by more than three orders of magnitude from $z = 0$ to $z = 7$ (Chiang, Overzier, K. Gebhardt, et al. 2017). Therefore, by quantifying the contribution to SFRD of different environments as a function of cosmic remains as the one of the most important tasks at the time of large, multiband surveys.

Motivated by these predictions, there are numerous observational efforts which aim to identify high-z (e.g. $z > 2$) protoclusters (see Overzier 2016 for a review). Despite the hundreds of candidates reported so far, just a small number of detections have been done in random fields. On one hand, the problem with detecting the protoclusters is that classical techniques used for cluster detection (e.g. via extended X-ray emission or via overabundance of optically red galaxies) do not work well at higher redshfits due to cosmological dimming. On the other hand, the majority of protocluster candidates are biased towards the mapped areas around those objects that are previously known as fairly good signposts of cluster progenitors; e.g. Lyman-α blobs (Tamura et al. 2009, Lemaux et al. 2017), high-z radio galaxies (Hatch et al. 2014, Miley et al. 2008), X-ray selected massive systems (Brodwin et al. 2015, Mei et al. 2015), or the most distant quasars (Stiavelli et al. 2005, Decarli et al. 2017). In the last decade, some environments are also find overabundant of bright DSFGs at $z \sim 2 - 3$ (e.g. Chiang, Overzier, and Karl Gebhardt 2013, Smolčić et al. 2017, Kato et al. 2016, Casey 2016, Rigby, Hatch, et al. 2014, Clements, Braglia, Hyde, et al. 2014, Valtchanov et al. 2013, Daddi, Dannerbauer, et al. 2009). Consequently, large field and all sky surveys such as *Herschel* and *Planck* are considered ideal for targeting the larger number of rare DSFGs, that will be further explored as potential protocluster members. The problem is here that majority of surveys aimed to study the clustering of DSFGs close to the peak of their

[a] As noted in the Chapter 1, the term "protocluster" is often used to describe the cluster progenitor at $z > 1.5$, commonly seen as diffuse collection of DM halos. However, while some define a protocluster as all the DM haloes at a given redshift progressing to merge and make the final cluster, others define the protocluster as the most massive progenitor DM halo, sometimes referred to as the main DM halo (e.g. Overzier 2016).

star-formation ($z \sim 2$), while selection and characterisation of dusty environments towards the higher redshift tail ($z > 4$) remains very challenging due to instrumental limitations, unknown properties of sources and lack of efficient selection techniques. As a result, only few protocluster candidates at $z > 4$ have been confirmed so far, all of them being serendipitous detections within the brightest DSFGs in small and deep fields such as COSMOS or UDS (Pavesi et al. 2018, H. Dannerbauer, Lehnert, Emonts, et al. 2017, Smolčić et al. 2017, Kato et al. 2016, Capak et al. 2011,Daddi, Dannerbauer, et al. 2009).

To select candidate overdensities at $z > 4$ in a more systematic manner, there is a growing interest of probing the surroundings of 500 μm-risers (Oteo, Ivison, L. Dunne, et al. 2017). This is due to assumption that such extreme events of obscured star-formation trace the most massive DM halos, and therefore large scale structures. Observational support to such idea recently came from Oteo, Ivison, L. Dunne, et al. 2017 and Miller, Chapman, et al. 2018 who reported two uttermost forms of high-z overdensities, SMM-J004224 and SPT2349-5 correspondingly. Both systems are 500 μm-risers, whereas their core regions (only 40" in size) reveal 10 and 14 DSFGs resolved with ALMA. With redshifts confirmed to be $z_{spec} = 4.002$ and $z_{spec} = 4.31$ respectively, the IR-derived SFR of these two protoclusters is $\sim 15000\ M_{\odot} yr^{-1}$.

Nevertheless, 500 μm-risers have very low number density ($< 2\text{deg}^2$, see Chapter 4), and to probe much larger space volume and thus increase the statistics of candidate overdensities, some studies take advantage of a blind search of luminous CIB peaks seen by *Planck* (e.g. Greenslade et al. 2018). The moderate $5'$ resolution of *Planck* has a clear benefit when we hunt the clustered structures in the early Universe: a beam size of $5'$ corresponds to a physical size of $\sim 2.5 - 2.6$ Mpc at $z \sim 2$, which matches the size of smaller scale clustering as seen in observations and simulations (Muldrew et al. 2015). To extend the search for such rare structures, the *Planck* team recently provide the list of 2151 high-z candidates based on the colour-selection method, likely at $1.5 < z < 2.5$ (PHZs, *Planck* collaboration XXIX, 2016[b], see also Planck Collaboration, Aghanim, Altieri, et al. 2015).

Nevertheless, because of the limited sensitivity and resolution of *Planck*, the nature of the PHZ sources is still uncertain and only two of them are spectroscopically confirmed to date (Kneissl et al. 2018, Flores-Cacho et al. 2016). This motivates some studies to

[b]Planck Collaboration, Ade, Aghanim, Arnaud, Aumont, Baccigalupi, Banday, Barreiro, Bartolo, Battaner, Benabed, Benoit-Lévy, et al. 2016

question are the large number of PHZ objects in fact statistical fluctuations of the CIB, rather than physically clustered sources (Negrello et al. 2017).

Aforementioned facts reflect differences between selection strategies and bring the two crucial questions that we should address at this stage. The first one is: *How does the efficiency of using DSFGs as protocluster tracers change with redshifts DSFGs?* Miller, Hayward, et al. 2015, did a "counts-in-cells" analysis in N-body simulation and found that associations of DSFGs at $z < 2.5$ are poor and noisy footmarks of the most massive DM halos. Since SPIRE overdensities within PHZ's peak at $z \approx 1.9 - 2$ (Kneissl et al. 2018, MacKenzie et al. 2017), lower than for protoclusters detected around 500 μm-risers ($\hat{z} = 3.2 \pm 0.2$, Lewis et al. 2017) it implies that these two different selections do not trace the most massive DM halos with same efficiency. This urges caution if we "*a-priori*" assume that any association of DSFGs signposts distant protoclusters.

The second important question is: *How can we resolve and characterise individual galaxies that give rise to the dust excess seen by Planck?* To date, 237 PHZ objects were analysed by inspecting SCUBA-2 and/or ALMA detections targeted around bright SPIRE sources associated to PHZ peaks (Kneissl et al. 2018, MacKenzie et al. 2017, Planck Collaboration, Aghanim, Altieri, et al. 2015, Planck Collaboration, Ade, Aghanim, Argüeso, Arnaud, Ashdown, Aumont, Baccigalupi, Banday, et al. 2016 Clements, Braglia, Hyde, et al. 2014). Such approach has been proven very efficient for confirming statistical overdensities of DSFGs that are significantly above the confusion level, but as stated by MacKenzie et al. 2017 almost $85 - 90\%$ of the total *Planck* emission remains unresolved. Here I aim to go beyond approaches previously known in literature, and test the novel idea: our goal is to use the SED fitting technique as the main tool to model the $L_{\rm IR}$ and other physical properties of all optical/NIR sources within the PHZ peak. With this new technique, we have no need in performing de-blending in the real SPIRE maps as usually seen in techniques used to break through the confusion limit (Pearson, Wang, van der Tak, et al. 2017, Liu et al. 2017). Instead, the fidelity of our analysis can be tested via sets of simulated SPIRE maps.

The Chapter is organised as follows: In Section 6.1 I present a comprehensive analysis of environments of very high-redshift ($z > 4 - 6$) candidate DSFGs. In the first part of this Section, I employ both simulations and observations in order to evaluate how dense are environments of 500 μm-risers selected with our technique. In Section 6.2 I present the data analysis and statistical properties of PHZ282 which is a *Planck* high-z candidate we use for our case study. Furthermore, in Section 6.3 I explain our novel idea based

on SED fitting and SED modelling, which aims to characterise the sources that give rise to dust emission excess observed in PHZ282(Planck Collaboration, Aghanim, Altieri, et al. 2015, Planck Collaboration, Ade, Aghanim, Arnaud, Aumont, Baccigalupi, Banday, Barreiro, Bartolo, Battaner, Benabed, Benoit-Lévy, et al. 2016). I conclude this Section with our results, and directions for the future work. Related to this topic, in Appendix B I describe my external collaborative work within HSC-Protocluster Search project, where I complemented my method of selecting 500 μm-risers with SCUBA-2 data in order to investigate the DSFGs in some of the most distant protoclusters confirmed so far ($z > 5.5$).

6.1. Probing the environment of 500 μm-risers

6.1.1. Insight from simulations

To better understand connection between 500 μm-risers selected in this work and their environments, I firstly perform a brief systematic analysis based on simulations. As shown in Section 5.3, modelled dusty galaxies exhibit a redshift-dependent clustering signal; as we advance to higher redshifts ($z > 3.5 - 4.5$), the clustering signal of DSFGs with redder SPIRE colours ($S_{500}/S_{350} > 0.8$) increases by factor of 4-5 than in average population of galaxies. To briefly check the DM halo masses of red DSFGs modelled in SIDES 2deg^2 simulation, I undertake the high-z ($2 < z < 7$) unlensed sources that have red colour and observed 250 μm fluxes above the threshold I impose for our prior catalogue. To build the larger statistics just for this purpose I did not impose any limit on their 500 μm flux. In Fig.6.1 I plot these sources, placed in $M_{halo} - \mathrm{SFR}$ plane, and colour coded for their stellar mass.

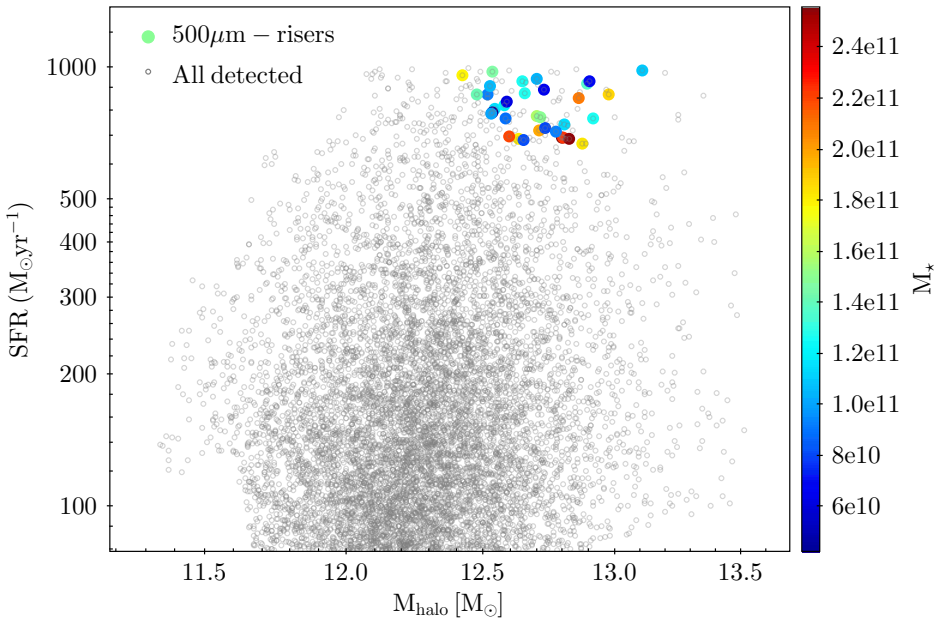

Figure 6.1.: Relation of SFR and DM halo mass for the unlensed SPIRE sources that are detectable at 250 μm in B17 model ($z > 2$, $\theta = 2\text{deg}^2$, the noise effect added) and have the "observed" red colour after the modelling of noise. The sources are colour coded for the stellar mass. A specific flux cut at 500 μm is not imposed for this case.

We see that selected, unlensed 500 μm-risers mostly reside in the high SFR-end for a given DM halo mass. This is in a good agreement with recent findings from "zoom-in" and idealised cosmological simulations (Miller, Chapman, et al. 2018, Narayanan et al. 2015). With mock maps I further check how dense are environments around our 500 μm-risers. The advantage of using simulations over analysing the real data is that all sources detected in our 250μm catalogue can be complemented with other modelled sources below the SPIRE confusion limit. In that case, we significantly reduce uncertainties of our overdensity estimations.

The question is now: *What is the best observing strategy for probing environments around 500 μm-risers ?* Concerning the larger scale environments, the theoretical studies of N-body simulations have been usually showing that the progenitors of $z = 0$ DM halos with masses $> 10^{15} M_\odot$ extend over length-scales of around 5-15 cMpc at $z > 4$, corresponding to an angular scale of larger than degree (Chiang, Overzier, K. Gebhardt, et al. 2017, Lovell et al. 2018, Chiang, Overzier, and Karl Gebhardt 2013). On the other hand, as a best way to probe the correspondingly bright protocluster core, the same theoretical models propose angular distances $< 1.5' - 2'$ from the signpost. For the sake of

easier comparison to known studies, here I consider the same scale ($2' \times 2'$) probed in Pavesi et al. 2018, Oteo, Ivison, L. Dunne, et al. 2017, Smolčić et al. 2017). Additionally, in `Appendix B` I present a data analysis related to larger scale ($6' \times 6'$) overdensities of DSFGs discovered in optically selected protoclusters from HSC-protocluster project (Toshikawa, Kashikawa, R. Overzier, et al. 2014, Harikane, Masami Ouchi, Yoshiaki Ono, et al. 2018).

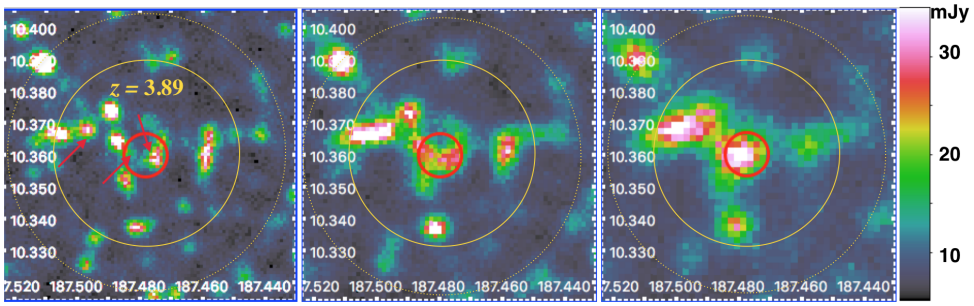

Figure 6.2.: Overdensity of sources at $z = 3.89 \pm 0.01$, centred around the 500 μm-riser observed in simulated map. Red arrows mark those physically associated members that are above our detection threshold at 250 μm. Full and dotted circle represent the 2' and 3' aperture respectively. Red circle illustrates the FWHM size at 500 μm (36").

I undertake the positions of 500 μm-risers detected from mock maps, and search for associations of galaxies in a chosen angular scale. I consider the sources as physical associations if their redshifts are within $\Delta z = 0.016$ in respect to the redshifts of their signposts (Smolčić et al. 2017). Applying such criteria, I find one overdensity totalling 12 DSFGs at $z = 3.89 \pm 0.015$. The three out of 12 DSFGs have 250 μm fluxes above the detection limit we impose for our prior catalogue while other sources are fainter, thus "hidden" in confusion (Fig.6.2). The total star-formation rate of clustered sources is modelled to be $\mathrm{SFR} = 2170 M_{\odot} yr^{-1}$. To compute the statistical significance of these associations I employ an "overdensity parameter" defined as (Morselli et al. 2014):

$$\delta(> S) = \frac{N(> S)}{N(> S)_{field}} - 1, \tag{6.1}$$

where $N(> S)$ is a measured number of physically associated DSFGs above the chosen detection threshold, and $N(> S)_{field}$ is the model-expected number of DSFGs in the same redshift within the given circular area. According to the above definition, the higher the value of $\delta(> S)$, the higher the probability that the identified dense environment is a genuine protocluster/galaxy group (Smolčić et al. 2017, Chiang, Overzier,

and Karl Gebhardt 2013).

To measure the significance of derived $\delta(>S)$, I randomly injected 1000 apertures in our mock map. I find the overdensity parameter $\delta(>S) = 5 \pm 0.3$. In other words, we are 99.99% confident that detected region is overdense by a factor of 5 compared to the field. The $\delta(>S)$ is radially dependent and shows decreasing trend when moving from $1'$ to $2'$.

The total SFR for this overdensity is smaller than the SFR estimated for SMM-J004224 and SPT2349-5. Their total SFRs are estimated to be larger than $6000\ M_{\odot} yr^{-1}$, with corresponding DM halo masses of $4 \times 10^{13}\ M_{\odot}$ and $1.7 \times 10^{13}\ M_{\odot}$ respectively. The result we reach from simulations can be only understood as a support to the idea that at least some number of 500 μm-risers reside in high-z overdensities (e.g. protoclusters). There is, however, a notable difference to the systems mentioned above: SMM-J004224 and SPT2349-5 have extremely large number of DSFGs concentrated in very small areas ($20" - 40"$), and it is difficult to asses their exact evolution or compare them easily to simulated structures. In fact, Miller, Chapman, et al. 2018 show that there is no existing simulation which can explain high "curve-of-growth" of the total flux of SPT2349-5 at such a small scale. Interestingly, both SMM-J004224 and SPT2349-5 have extended $500\ \mu$m emission in respect to the beam, with the emitted region extending up to $2'$. They are thus observed as anomalously large "red blob" compared to the most of known 500 μm-risers which appear more compact/point-like (see e.g. Ivison, Lewis, et al. 2016, Oteo, Ivison, Negrello, et al. 2017, Oteo, Ivison, L. Dunne, et al. 2017).

6.1.2. Insight from HeViCS SPIRE maps

I further check whether our catalogue of 133 500 μm-risers contains any source with comparably wide 500μm emission, accompanying a large number of 250 μm detections concentrated in a small area ($r < 2'$). I find two such cases, both of them having 500 μm-emission extending up to $1.7'$, which is very similar to what is observed in SMM-J004224 and SPT2349-5. I show these two systems in Fig.6.3. To probe their larger scale environment, I additionally search for all associated red DSFGs within the $6'$, lowering the 500 μm threshold to 3σ (22mJy), in order to increase the completeness. For both of our signposting 500 μm-risers, the two fainter red DSFGs has been found. I estimate their photometric redshifts as in Section 3.1, and find to be lower than the z_{phot} of their signposts. Determined z_{phot} of signpost are $z = 4.57 \pm 0.5$ and $z = 4.11 \pm 0.52$, and

for associated red sources $z = 3.65 \pm 0.61$ and $z = 3.18 \pm 0.59$ respectively. Nevertheless, a proper redshift comparison is not possible with SPIRE data only, while increase of colour uncertainties with decreasing 500 μm flux makes their z_{phot} estimation even more complicated (see Section 4.3). Unfortunately, HeViCS field is not deeply covered at submm/radio wavelengths, and the two listed sources also remain uncovered by optical-NIR NGVS data, due to slightly different survey design as compared to HeViCS (see Ferrarese et al. 2012). Hence, we cannot make any certain conclusion about their physical relation to our 500 μm-risers, except that the two targets are very promising candidates for future interferometric follow-ups. Last year, my colleague Steven Duivenvoorden (Univ. of Sussex, UK) and myself propose a deep SCUBA-2 observations including those two systems, but our proposal was not accepted.

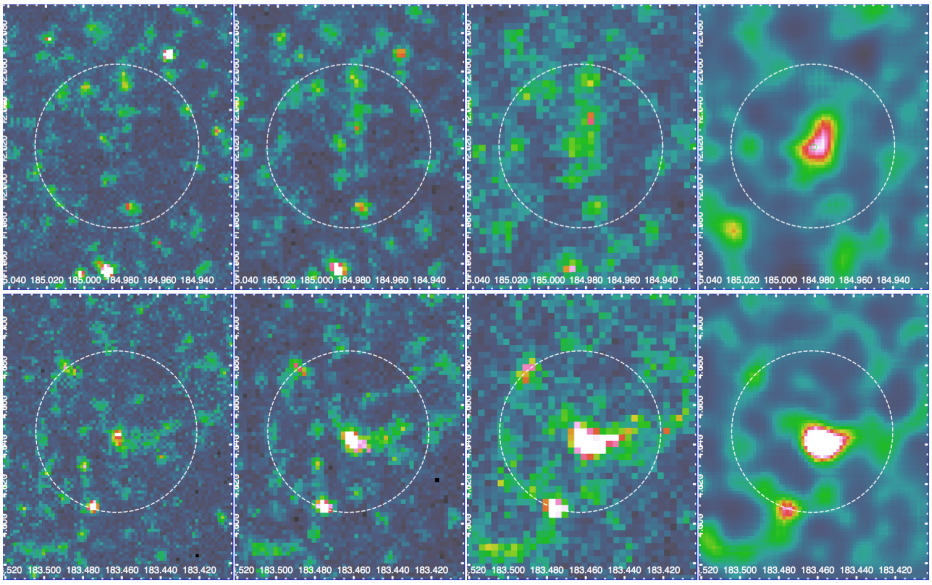

Figure 6.3.: Examples of two galaxies from our final sample of 500 μm-risers, whose 500 μm emission region is extending to ∼arcmin level. They are considered suitable to be probed as overdensity candidates. Presented maps are 250μm, 350μm, 500 μm and the DMAP, from left to right respectively. The DMAP is shown together with nominal SPIRE maps to better illustrate the extension of 500 μm emission above the confusion noise. The circle illustrate the 2' aperture within which we search for associated red sources.

Method of linking observed 500 μm-risers to distant overdensities is promising, but highly uncertain if we rely only on IR data. These are major caveats:

- The accuracy of $z - phot$ based on IR/submm data is lower at $z > 4$ compared to lower redshifts, as I already show in Chapter 3.

- When analysing number counts of candidate DSFG associations, and compare their density in respect to the field, the observational effects (noise, clustering) should be carefully simulated. Such a refined modelling would significantly reduce the measured overdensity and thus ruled-out non-negligible number of false overdensity candidates. Additionally, the intrinsic L_{IR} of associated DSFGs depend on the multiplicity and gravitational lensing, so corrections should be applied in order to get proper intrinsic values.

- The optical identifications are necessary if one want to accurately constrain the total stellar mass and the mass of DM halo. This is crucial for reconstructing the fate high-z protoclusters towards the present epoch.

Due to limitations described here above, it is important to perform higher-resolution observations of selected 500 μm-risers and their surroundings. On top of that, while in the previous section I analyse the environments centred around 500 μm-risers, it is important to investigate the general environment of distant DSFGs, both on smaller and larger scales, without requiring that 500 μm-risers necessarily reside in the centre of the overdensity. This spring I received a great opportunity to conduct such a test, since I have been invited to join Subaru Hyper Supreme Camera (HSC)-Protocluster Survey Project (PI: Y. Matsuda). The main aim of the project is to characterise dust properties of some of the most distant overdensities confirmed to date. In Appendix B I briefly describe the main lines of project along with my contribution. Results that are described in Appendix B will soon appear in two scientific papers: Harikane et al. (submitted to ApJ) and Fujimoto et al. (to be submitted to ApJ).

6.2. Planck's dusty source PHZ282

In this Section, I present my work related to new idea which aims to resolve the excess, submm peaks selected by *Planck* (PHZs, Planck Collaboration, Ade, Aghanim, Arnaud, Aumont, Baccigalupi, Banday, Barreiro, Bartolo, Battaner, Benabed, Benoit-Lévy, et al. 2016). I firstly describe the PHZ catalogue from which our source of interest is drawn, and then describe a new technique which we impose in order to derive physical properties of galaxies that are beyond the SPIRE confusion limit.

PHZ catalogue

The *Planck's* List of High-redshift Source Candidates (the "PHZ" catalogue hereafter) includes 2151 sources distributed over 26% of the sky, with photometric redshifts estimated to be $z \sim 2$. The list serves as complementary data set to the *Planck* Catalogue of Compact Sources (Planck Collaboration, Ade, Aghanim, Argüeso, Arnaud, Ashdown, Aumont, Baccigalupi, Banday, et al. 2016), which has been made in *Planck*-HFI and LFI bands. The PHZ list uses the advantage of the spectral coverage in higher-frequency bands, between 857 and 353 GHz. It is important to note at this stage that PHZ selected sources suppose to be different from those in Sunyaev-Zel'dovich Catalogue (PSZ2; Planck Collaboration, Aghanim, Arnaud, et al. 2016), since the former mainly use to track the dust emission from DSFGs, while the later mainly searches for a signature of the hot intracluster gas in potential clusters.

The PHZ catalogue is based on colour selection which requires detections at $> 4\sigma$ in HFI bands. The first criterion ($S_{545}/S_{857} > 0.5$) is used to avoid the cold galactic cirrus emission, while the second colour criterion ($S_{353}/S_{545} < 1$) is applied to avoid contamination from radio sources (Planck Collaboration, Ade, Aghanim, Argüeso, Arnaud, Ashdown, Aumont, Baccigalupi, Balbi, et al. 2011).

PHZ sources in the HeViCS field

The total area of HeViCS contain 11 PHZ sources. I refer their basic statistical properties in Table 6.1. I complement each of *Planck* detections with our SPIRE data, and estimate the overdensity parameter $\delta(> N)$ for their 250μm detections. I also check is there any extended ($\sim 1' - 1.5'$), red 500 μm emission, similar to what is find in Miller, Chapman, et al. 2018. The procedure I undertake to estimate $\delta(> N)$ is the same as I do for 500 μm risers in Section 6.1. I additionally search through existing all-sky radio catalogues described in Section 3.6 in order to probe eventual connection between PHZ peaks and bright radio sources.

For one source, PHZ1228, I find a strong evidence of being gravitationally lensed candidate, because its SPIRE emission is completely aligned (with positional offset of just 1") with the large, local elliptical galaxy at $z = 0.47$ seen in NGVS data.

Table 6.1.: Planck high-redshift candidates

	PHZ candidates					
	HeViCS detections	250μm overdensity	NGVS cover	$S_{1.4}$ >0.7 mJy	Cirrus	Ext 500μm
PHZ683	18	6.2σ	-	No	No	Yes
PHZ432	16	4.0σ	-	Yes	No	Yes
PHZ578	15	3.7σ	Yes	No	Yes	No
PHZ282	14	3.5σ	Yes	Yes	No	No
PHZ970	12	3.2σ	Yes	No	No	No
PHZ1718	11	2.8σ	Yes	No	No	Yes
PHZ1228(lens)	10	2.5σ	Yes	No	No	Yes
PHZ1246	9	2σ	Yes	No	No	Yes
PHZ1490	7	No	Yes	No	No	No
PHZ2065	6	No	-	Yes	No	No
PHZ2112	5	No	Yes	No	No	No

A study case: PHZ282

In order to resolve the total dust emission observed with *Planck* and to provide a novel way of understanding determine the nature of these red peaks in the CIB, we chose to make a study case on one of 11 PHZ sources within the HeViCS field: the source's ID is PHZ282, with position coordinates (R.A.,Dec)= (186.951; 10.239, in degrees). The PHZ282 resides in the V3 field of HeViCS which is unaffected by strong cirrus emission.The PHZ282 is one of the PHZ sources for which we find $> 3\sigma$ overdensity at 250 μm; it has 14 detections at 250μm inside the beam of *Planck*, out of which 6 sources are characterised as 350 μm-peakers in our HeViCS catalogue. Interestingly, there is only one 350 μm-peaker with emitting flux above 5σ ($S_{350} \approx 35$mJy). Likewise, PHZ282 appears less extreme compared to all known PHZ sources identified so far, which are find to have usually extremely bright/or lensed central SPIRE source (Cañameras et al.

2015, Flores-Cacho et al. 2016, MacKenzie et al. 2017, Kneissl et al. 2018). By fitting the single-temperature MBB to *Planck* data, the photometric redshift of PHZ282 estimated by the *Planck* team is in the range $1.93 < z < 2.9$ if T_d varies from 25 K to 35 K (Planck Collaboration, Ade, Aghanim, Argüeso, Arnaud, Ashdown, Aumont, Baccigalupi, Balbi, et al. 2011). The PHZ282 also benefits from deep optical/NIR data created for the study of Virgo cluster (Next Generation Virgo Cluster Survey, NGVS; Ferrarese et al. 2012). Because of this, we consider PHZ282 as a great test example for interpreting the nature of *Planck's* most luminous peaks, and to test our approach based on dust SED modelling.

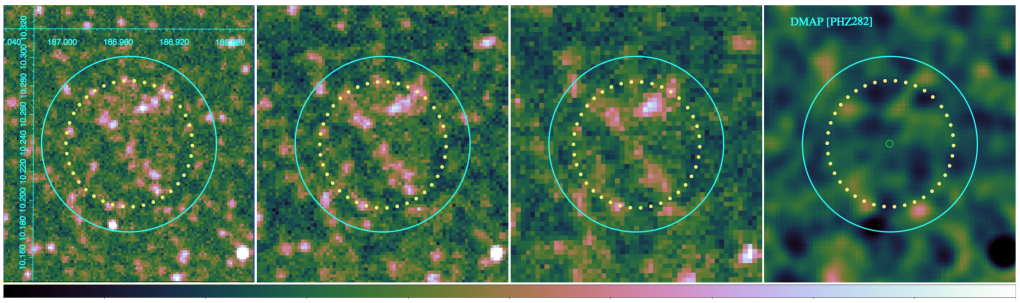

Figure 6.4.: PHZ282seen in SPIRE maps (250μm, 350 μm and 500 μm)and corresponding DMAP (from left to right respectively). The DMAP shows no significant contrast for the "red" emission, typical for sources expected to be at $z > 3-4$. The yellow circle illustrates the size of the Planck's beam, while for with the cyan line I mark the area with the corresponding 3' radius.

6.2.1. Data analysis

Planck vs. SPIRE emission in PHZ282

The *Planck* 857 GHz (300 μm) and 545 GHz (500μm) bandpasses are well matched with SPIRE 350 μm and 500 μm bands, so they are often used in order to check how different is the total flux observed by these two instruments (Greenslade et al. 2018). I use our catalogued SPIRE fluxes de-blended with `MBB-fitter` and perform two-step analysis on 350 μm and 500 μm maps. Firstly, I check whether summing the fluxes of all point sources detected with SPIRE can adequately match *Planck* flux. Secondly, I make photometry using an circular aperture with the same size as *Planck* beam (150" in radius). In both cases, I find that SPIRE emission at 350 μm and 500μm cannot explain the *Planck* flux. In Table 6.2 I present the relative contribution of point sources to the *Planck* flux at two different wavelengths. We see that almost half of the *Planck's* flux remains unknown if we consider only SPIRE detected point sources. We thus need to

Table 6.2.: A SPIRE view of 545 GHz and 857 GHz flux observed in PHZ282

N	$S_{350}^{Herschel}/S_{857}^{Planck}$	$S_{350}^{Herschel}/S_{857}^{Planck}$	$S_{500}^{Herschel}/S_{545}^{Planck}$	$S_{500}^{Herschel}/S_{545}^{Planck}$
(250 μm)	point sources	aperture	point sources	aperture
14	0.48	0.74	0.41	0.72

understand which sources below the confusion limit contribute to the rest of the *Planck's* flux. The observed differences of *Planck/Herschel* fluxes are listed in Table 6.2.

The result presented above is not surprising, and it is in line with findings from MacKenzie et al. 2017 and Planck Collaboration, Ade, Aghanim, Arnaud, Ashdown, et al. 2016. They show that accounting the SPIRE detections it appears that the *Planck* L_{IR} estimates are about 2 to 3 times larger than the integrated luminosities of the SPIRE detected galaxy members inside the PHZ sources. As pointed by the Planck Collaboration, Ade, Aghanim, Arnaud, Aumont, Baccigalupi, Banday, Barreiro, Bartolo, Battaner, Benabed, Benoit-Lévy, et al. 2016 despite the initial care to perform the careful selection by applying a flux threshold at 500mJy at 545GHz, the flux boosting can still reach 20% for fluxes around 0.5 Jy. This may explain a some part of the discrepancy we see between *Planck* and *Herschel*. However, even if we correct for flux boosting, there is a still remaining discrepancy which suggests that the *Planck* estimates integrated over a $5'$ beam include a component that is barely traced by SPIRE because of confusion. In the following part of this Section, I propose and discuss a novel method which aims to resolve the dust peak observed by *Planck* by combining SED fitting of optically detected sources and dust SED modelling based on energy-balance. To achieve this goal, I firstly complement our lower resolution FIR/submm data with higher resolution optical and mid-IR data.

NGVS data

The PHZ282 is covered at wavelengths from 0.365 μm to 1 μm with optical data from the Next Generation Virgo Cluster Survey (NGVS, Ferrarese et al. 2012). The NGVS is an optical imaging survey totalling 104 deg^2 centred on the Virgo cluster, and it overlaps 85% of the HeViCS field. Currently, the complete survey area has been observed with 0.6"-1" FWHM in the $u^{\star}giz$-bands and one third in the r-band. All the data are

obtained with the MegaCam instrument, mounted on the CFHT in Hawaii[c]. The NGVS team provide me with a catalogue and images covering the $4' \times 4'$ area targeting the PHZ282. The catalogue cut is made based on the deepest i-band, which has superb seeing distribution at $< 0".6$. The 5σ detection is achieved at 25.2 mag (Ferrarese et al. 2012), while here I decide to use slightly deeper magnitude cut at 26 AB mag in i-band which downgrades the S/N, but offers us to capture some fainter and potentially higher-z sources. In such I list 1360 NGVS sources inside the PHZ282 (and 3209 sources within a $4' \times 4'$ region surrounding *Planck's* peak).

WISE photometry

The Wide-field Infrared Survey Explorer (WISE, Wright et al. 2010) has mapped the entire sky with 5σ point source sensitivities better than 0.08, 0.11, 1 and 6 mJy in bands centred on wavelengths of 3.4 μm, 4.6μm, 12μm and 22 μm (W1-W4 bands respectively), which is much more sensitive than previous wide field surveys at the same frequencies. The latest AllWISE Release[d] includes a source catalogue of nearly 750 million sources, a database of photometry in the individual frames at each source position, and "Atlas Images" coadded matched-filtered images.

However, due to the coarse resolution of WISE compared to CFHT, simple source matching could result either in missed astrometry matches or incorrect colours. We thus decide to create de-blended catalogue for the purpose of our study, by using `Tractor` code (Lang et al. 2016) which has already been tested for de-blending MIR-images (e.g. Nyland et al. 2017). Shortly, the `Tractor` is a code for optimizing or sampling from models of astronomical objects. The approach is generative: given astronomical sources (in our case NGVS detections) and a model description of the image properties, the code itself produces pixel-space based estimates simulating what would be observed in the images. In other words, we can obtain magnitudes in lower resolution images starting from higher-resolution priors, by modelling the profiles of sources. To infer the properties of sources of interest we need to write a `Python` "driver" script manually, which read our data and immediately create objects describing our data. The first mandatory step in the source modelling procedure is thus to determine the fiducial survey pass band, and for this I chose the deepest i-band in NGVS. I adopt source profiles given by

[c] http://astrowww.phys.uvic.ca/~lff/NGVS/Home.html
[d] AllWISE Data Release Products, http://wise2.ipac.caltech.edu/docs/release/allwise/expsup/

the code: exponential and general-Sersic model. For the sake of consistency with original WISE data, I use ALLWISE PSF model to convolve with our models. As a result of our procedure we obtain secure photometry for 155 sources down to 0.035 mJy in W1 (17.8 mag [Vega]).[e] Additionally, by cross-matching with the latest Gaia Data Release 2 (Gaia DR2), I remove 42 stars from our final sample. The catalogue contains 155 WISE sources inside the PHZ282, which is 15% more than in original blind WISE catalogue covering the same area. The nominal and residual W1 maps are present in the upper panel of Fig. 6.5. As an addition, I apply criteria presented in Bilicki et al. 2016 to check the number of potentially strong radio sources, and find 9 QSO candidates in total. One of them is a known high-z QSO at $z = 3.165$ (Pâris et al. 2018). I do not remove these radio sources from our final inclusion, since some of them may contribute to the potential overdensity we want to investigate.

As a consistency check, I compare computed magnitudes for sources that are present in both (allWISE and Tractor) catalogues (mid-panel of Fig. 6.5). The very good match confirms reliability of our method. Corresponding $i_{\rm AB}$ magnitudes are shown in the lower panel of Fig. 6.5 along with the distribution of other NGVS detections inside the PHZ282. We see that WISE sources have in average brighter $i_{\rm AB}$ than other NGVS sources. This is in line with studies who conventionally place WISE sources at $0.5 < z < 1.0$ (e.g. Glowacki et al. 2017). The more detailed analysis on our WISE sources will be provided at the end of this Section.

[e] Although multi-band photometric catalogues offers important advantage over existing one, the accuracy of WISE photometry is less robust for NGVS sources that are not well-described by a given model. This is prominent for either fainter NGVS sources and/or more complex, semi-extended WISE regions.

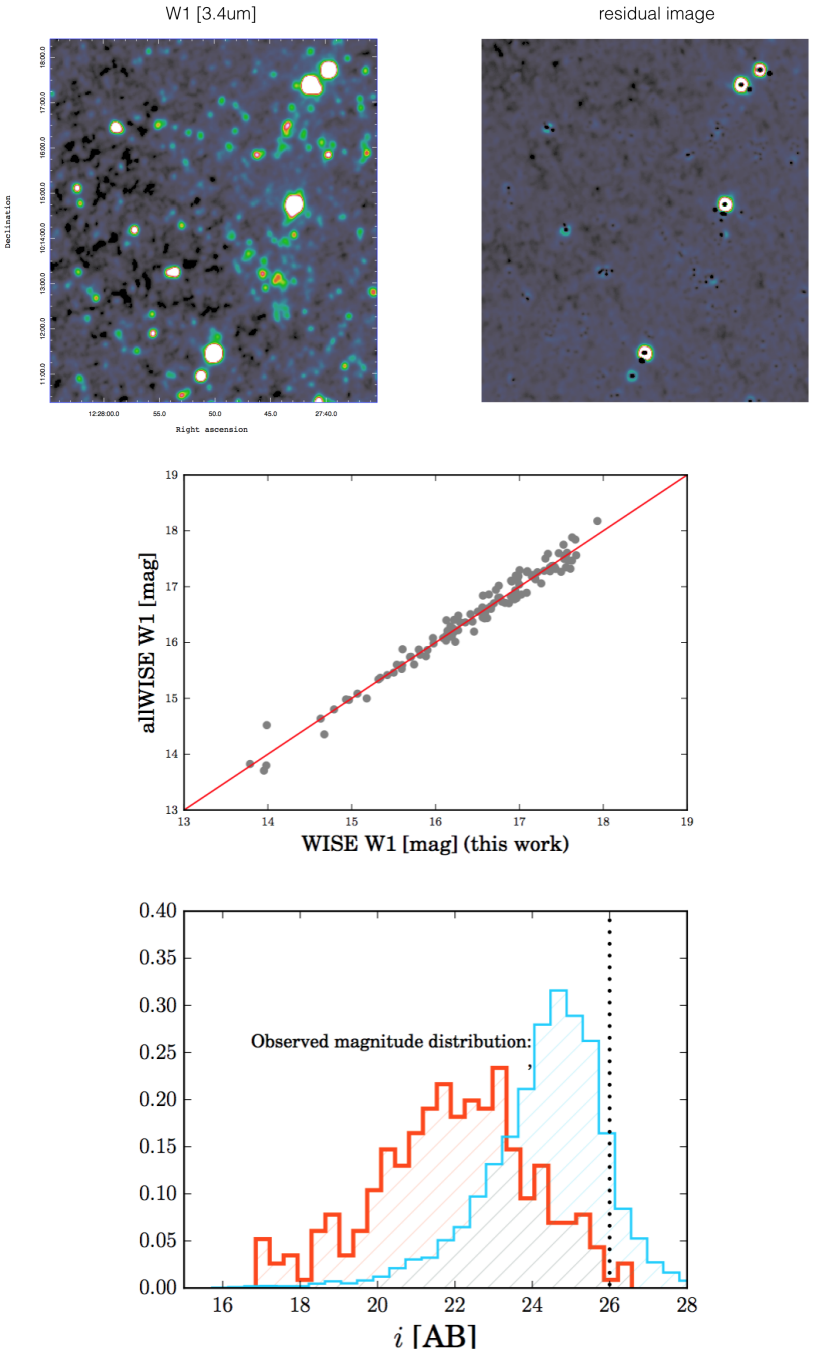

Figure 6.5.: Example of our forced photometry result for the W1 band. Upper panel: Nominal and residual image ($4' \times 4'$ in size) centred around the peak PHZ282 (left and right respectively). Mid-panel: Comparison between photometry results obtained with our method and those from allWISE release for the matched sources. Bottom panel: Magnutude distribution for all sources detected in NGVS (blue) and those with W1 (< 17.8 mag[Vega]). Dotted line shows our limiting magnitude in i-band.

6.2.2. Photometric redshifts and Gaussian kernel density estimates

We use the template-based code `Le Phare` (O. Ilbert, Arnouts, McCracken, et al. 2006) to estimate photometric redshifts. `Le Phare` is a code specifically designed for high-redshift studies and uses priors for $i > 20$ mag galaxies, built with observed data. The code has been already applied and tested for the purpose of estimating z_{phot} in CFHT data (Raichoor et al. 2014), which have shown that `Le Phare` provided very satisfactory results. Here we use a standard set of SED templates provided in Ilbert et al. 2009. `Le Phare` also uses distribution prior $N(z)$ as a function of the i-band magnitude to remove the risk of catastrophic failures between the Balmer and Lyman breaks (Ilbert, private communication). As suggested in Ilbert et al. 2009, such option is necessary when lacking NIR data. The accuracy of z_{phot} is estimated via comparison to z_{spec} from different fields. The uncertainty increases with redshift (Raichoor et al. 2014) and since our field lacks with r-band observations this affects the z_{phot} accuracy such that scatter increases as $\sigma \sim 0.04 \times (1 + z)$. We find reliable z_{phot} (within 99% confidence) for 1249 out of 1360 objects in total.

Along with z_{phot}, another useful statistical parameter that comes from our NGVS data is the source's density in respect to distribution of SPIRE-detected sources in PHZ282. At 250 μm and 350 μm the SPIRE overdensity stands out clearly with respect to the field in the map, while the same feature has a lower contrast at 500 μm. I apply an iterative Gaussian kernel density (KDE) estimate on our NGVS sources. I compute the optimal kernel width at any point within the map, based on the local density of detected sources. The reddest region in the KDE map in Fig.6.6 thus gives the highest overdensity of sources with 3σ significance. As we can see, the shape of NGVS overdensity closely follows brighter structure seen in SPIRE maps.

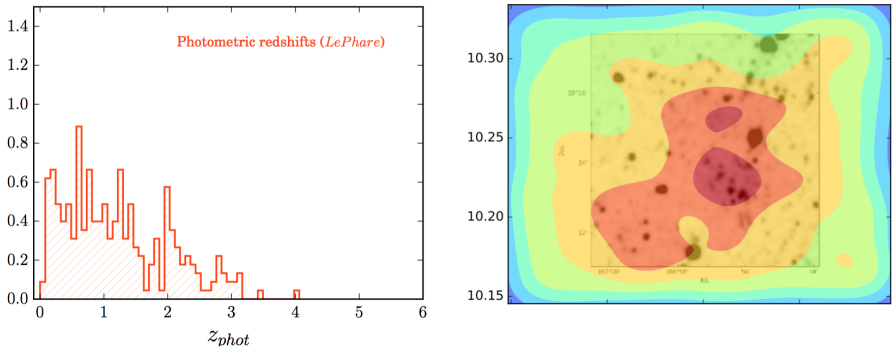

Figure 6.6.: Left panel: Template-based redshift estimates from `Le Phare`. The sources accepted for our final inclusion are those within 99% confidence (1249 in total). Right panel: KDE as an illustration of overabundance of optical detections in respect to the SPIRE and WISE map. The contour levels are from 1 to 5σ with respect to the background KDE rms noise. The light green colour delineates the region with relative coverage above 50%. The reddest area is the KDE region which reflects the largest overdensity (with 4σ) of NGVS sources. In the background we plot WISE W1 map which covers $4' \times 4'$ area centred in the PHZ282. We see that larger red region contains some very bright WISE sources, which is not the case in the smaller, northern red area.

6.3. Resolving the dust emission of PHZ282: A novel approach based on SED-fitting

After making the catalogue which contains NGVS and NGVS+WISE photometry with corresponding photometric redshifts, we are ready to proceed and test our novel approach. The method aims to resolve and characterise the excess dust emission seen by *Planck*. As stated above, I want to explore a wide range of galaxies applying SED-fitting methodology, making the predictions for their $L_{\rm IR}$ and star-forming properties. The method, if confirmed, would provide several advantages over existing techniques which deal with the confusion applying positional and/or SED priors as a step before the direct de-blending in the real SPIRE maps. Our technique is structured within several steps, described in following subsections. Firstly, I explain the use of a main tool applied for our SED fitting analysis. Secondly, I present the main results based on our SED fitting procedure, giving the particular attention on characterisation of sources which we classified as candidate DSFGs ($L_{IR} > 10^{11}\ L\odot$). Lastly, I present our ongoing work and

important directions for the future.

6.3.1. Tools: CIGALE

We use Code Investigating GALaxy Emission (CIGALE; Noll et al. 2009, Boquien et al. in prep.) as a tool for our SED fitting and modelling analysis. CIGALE is a state-of-the-art SED modelling and fitting code, which combines UV-optical stellar SED with a dust component emitting in the IR. The code fully preserves the energy balance between dust absorbed emission and light re-emitted in IR. For the purpose of our analysis, here I use CIGALE v0.11 (Boquien et al., in prep)[f]. I employ CIGALE for SED fitting and to calculate wide range of physical parameters for each NGVS source. The number of options provided by CIGALE is large but designed in a modular way that allows to manually select some of them.

CIGALE parameters

SED model components and parameters used in this analysis are presented in Table 6.2. The choices are based on some of the most recent prescriptions that are extensively tested on large multiband datasets, thus optimised for a wide range of galaxies (Malek et al. submitted to A&A; see also L. Ciesla, D. Elbaz, et al. 2017 and Pearson, Wang, Hurley, et al. 2018). In the following I briefly summarise the choice of parameters noted in Table 6.3.

I use a double exponentially decreasing star-formation history (SFH) for the old and young stellar populations. As explained in Buat, Heinis, et al. 2014, commonly used exponentially declining/ delayed SFH cannot produce a reliable fits to wide range of observed data. L. Ciesla, D. Elbaz, et al. 2017 also reach the similar conclusion employing simulations. The e-folding time of the two stellar populations (old and young) in the SFH was matched to that of Pearson, Wang, Hurley, et al. 2018. I use Bruzual & Charlot stellar population synthesis model (BC03, Bruzual et al. 2003) together with a Chabrier IMF (Chabrier 2003). I fix metallicity to the solar value. In order to model the effects of dust on the integrated spectral properties for the large variety of galaxies, I adopt a double power-law recipe for dust attenuation described in Lo Faro et al. 2017. It is based on prescriptions from the model of S. Charlot et al. 2000, with individual power laws for the birth clouds (BCs) and interstellar medium (ISM). This recipe is

[f] https://gitlab.lam.fr/cigale/cigale

Table 6.3.: Parameters used for modelling the SEDs with CIGALE. All ages/times are given in Gyr.

Parameter	Values	Description
	Star Formation History	
τ_{main}	1.0, 1.8, 3.0, 5.0, 7.0	e-folding time (main)
τ_{burst}	10.0	e-folding time (burst)
f_{burst}	0.001, 0.1, 0.20, 0.30	Mass fraction of the late burst
Age	0.5, 1.0, 2.0, 3.0, 4.5, 6.0, 7.5, 9.0, 10.0, 11.0, 12.0	Population age (main)
Burst age	0.001, 0.05, 0.08, 0.11, 0.3	Age of the late burst
	Stellar emission	
IMF	Chabrier 2003	Initial mass function
Z	0.02	Metallicity (0.02) in Solar
Separation age	0.01	Age difference between old and young population
	Dust attenuation	
A_v^{BC}	0.3, 0.8, 1.2, 3.3, 3.8	V-band attenuation
slope BC	-0.7	Power law slope of BC attenuation
BC to ISM factor	0.3, 0.5, 0.8, 1.0	Ratio of the BC-to-ISM attenuation
slope ISM	-0.7	ISM attenuation power law slope
	Dust emission	
q_{PAH}	0.47, 1.12, 3.9	Mass fraction of PAH
$U_{\min}$	0.1, 5.0, 25.0	Minimum radiation field
α	2.0	Dust emission power law slope
γ	0.02	Illuminated fraction
	AGN emission	
r_{ratio}	60.	Maximum to minimum radii of the dust torus
τ	1.0, 6.0	Optical depth at 9.7$\vert mu$m
β	-0.5	Coefficient for the gas density function of the torus
γ	0.0	γ coefficient for the gas density function of the torus
Opening angle	100°	γ Opening angle of the torus
ψ	0.001, 89.99	Angle between eq.axis and line of sight
$frac_{AGN}$	0.0, 0.1, 0.25, 0.8	AGN fraction

based on age-dependent attenuation (Lo Faro et al. 2017). Dust luminosity is predicted based on preserved energy balance, modelled with Draine, Aniano, et al. 2014, which is an update based upon Draine & Li (2007) IR emission model. For WISE sources I chose to quantify the contribution of AGNs to the total predicted L_{IR}. I assign AGN model by Fritz et al. 2006[g]. The parameters in the AGN model were matched to those from L. Ciesla, Charmandaris, et al. 2015. Due to computational reasons I somewhat reduced the number of guesses on *fracAGN* (we model four different values).

The compiled catalogue that we impose for SED fitting contains 1249 galaxies with reliable redshifts, out of which 155 galaxies have a full NGVS and WISE photometry. I chose to set upper limits on SPIRE fluxes to all catalogued sources. To do so, I firstly carefully define a masked region, 36" in a size around each of our 250 μm detections. For NGVS sources delineated by the masked region (425 in total), corresponding SPIRE flux is than set as an upper limit. Giving the large difference in optical/FIR instrument resolutions, this approach seems more precise than the one which simply matched closest priors, which can wrongly connect neighbouring pairs of points and produce unreliable estimates of their physical parameters. For the rest of NGVS sources (824 in total) that fall outside the masked region, limiting amplitudes in SPIRE are given by setting the maximum flux to be equal to $1\sigma_{conf}$ measured in HeViCS (see Section 2.1).[h] The same is then applied for sources without reliable WISE photometry, with the difference that I set limit only to W1 band ($1\sigma_{conf}^{\rm WISE} = 20{\rm mag}_{\rm Vega}$).

Taking into account panchromatic information from the SED, with CIGALE we can then derive the physical properties of galaxies such as $M_\star$, instantaneous SFRs, dust attenuation, $L_{\rm IR}$ and corresponding AGN contribution[i]. .

In the next section I present main findings of our analysis.

6.3.2. Results

Estimating $L_{\rm IR}$ of NGVS sources

One of main goals of our SED fitting analysis is to provide the estimate of $L_{\rm IR}$ for all galaxies that fall inside the area of PHZ282. In Fig.6.7 I plot their $L_{\rm IR}$ and $M_\star$ along with

[g]Fritz et al. 2006 models preserve the energy balance which matches the philosophy used by CIGALE

[h]This is important since we do not know FIR colours of sources that are below the SPIRE confusion limit.

[i]For each parameter, a probability distribution function (PDF) analysis is made. The output value is the likelihood-weighted mean value of the PDF and the error associated is the likelihood-weighted standard deviation

their $i_{\rm AB}$. We should take caution here since lack of stronger FIR constraints produces large uncertainties in our $l_{\rm IR}$ estimates, which are in average 45%. We also observe variations of $L_{\rm IR}$ with stellar mass, such that more massive galaxies in average tend to be more luminous. This is in line with predictions from recent studies (e.g. Williams et al. 2018, Schreiber, Elbaz, Pannella, Ciesla, T. Wang, Koekemoer, et al. 2016); these works suggest that, on one hand, most massive galaxies (e.g. $M_\star > 10^{11} M_\odot$) with low IR luminosity have correspondingly low dust temperatures ($T_d < 25$K) indicative of a reduced star formation efficiency. On the other hand, the same studies found that lower $L_{\rm IR}$ in low mass galaxies at higher redshifts ($z > 1$) is possibly linked to their lower metallicities ($L_{\rm IR}$).

The observed peak for WISE-detected sources in PHZ282 is at $i_{\rm AB} = 23.2 \pm 0.35\, mag$ which implies that more than a half of IR-bright galaxies with $L_{\rm IR} > 10^{11} L_\odot$ are detected only in NGVS, but not in WISE data.

Having estimated the census of $L_{\rm IR}$ inside the area observed by *Planck*, we can check whether the total contribution summed over all NGVS sources now explains L_{IR} and $\rm SFR$ measured by *Planck* team. Even uncorrected for completeness[j] and with large uncertainties for modelled $L_{\rm IR}$, our derived estimates show a good agreement with L_{IR} and $\rm SFR$ which are calculated fitting the MBB SED with $T_d = 35K$ to *Planck* data. Comparison of these two results is presented in Table 6.4.

For sources that are detected in WISE bands, with CIGALE I also measure the relative contribution of the dusty torus of the AGN to the total IR luminosity ("AGN fraction") . I find that average fraction $frac_{AGN} = 14 \pm 2\%$. Interestingly, the AGN fraction is found to be much larger in WISE detected galaxies which are IR-bright and have redder $g - z$ colours. I discuss the nature of these IR-luminous WISE galaxies later.

[j] I performed an initial completeness test based on panchromatic model of Schreiber, Elbaz, Pannella, Ciesla, T. Wang, Koekemoer, et al. 2016. We find that for galaxies with $M_\star > 10^{8.5} M_\odot$ we reach completeness of 79% corresponding to the magnitude cut we chose.

Table 6.4.: Total SFR and $L_{\rm IR}$ of PHZ282

PHZ282		
Method	$L_{\rm IR}$ $[L_\odot]$	SFR $[M_\odot yr^{-1}]$
Planck source (MBB fit)$_(T_d = 35K)$	1.16×10^{14}	28182
NGVS sources (CIGALE)	1.33×10^{14}	29113

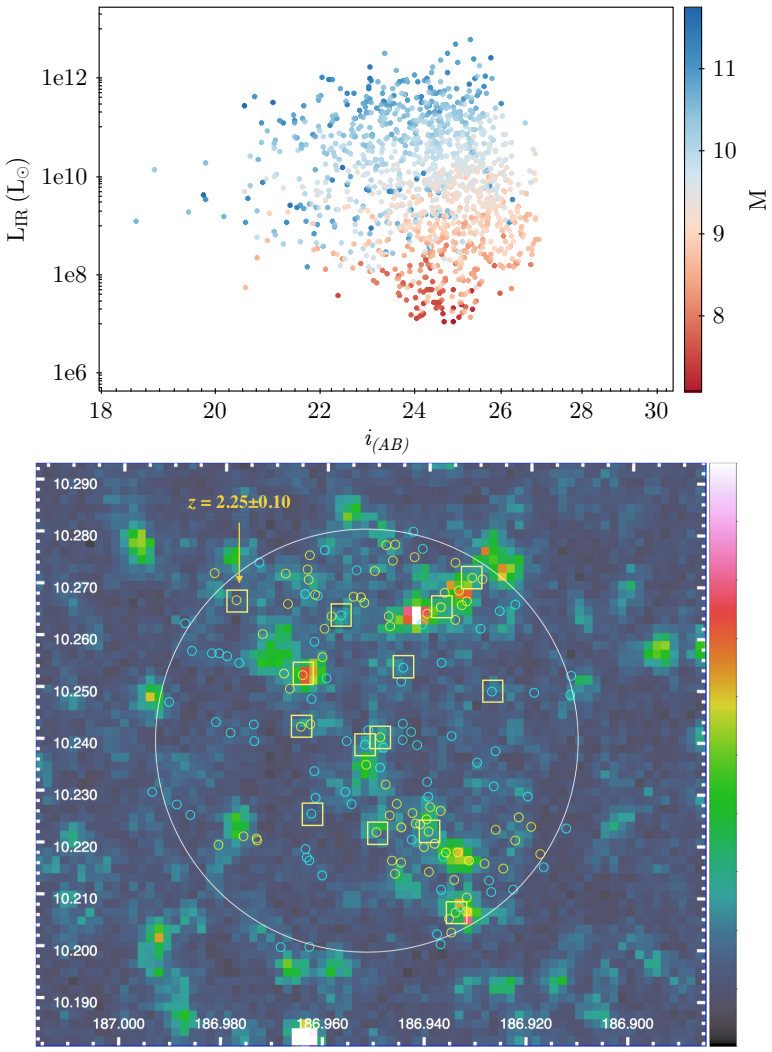

Figure 6.7.: Upper panel: $L_{\rm IR}$ and $M_\star$ estimated via SED fitting with CIGALE, as a function of observed i-band magnitudes. Bottom panel: SPIRE 250 μm map overplotted with galaxies having $L_{\rm IR} > 10^{11} L_\odot$, arbitrarily split in two groups: $L_{\rm IR} > 5 \times 10^{11} L_\odot$, which roughly corresponds to SFR $\geq 50 M_\odot yr^{-1}$ (yellow circles); and $10^{11} L_\odot < L_{\rm IR} < 5 \times 10^{11} L_\odot$ which corresponds to SFR $\leq 50 M_\odot yr^{-1}$ (blue circles). We mark with squares those sources that follows the observed peak of the redshift distribution for brighter DSFGs, find to be $z = 2.25 \pm 0.10$ (see the next subsection). The radius of white circle matches the beam size of Planck (5′).

Quantifying the relation of galaxies to the MS

To shed a light on the evolutionary picture of sources contained within PHZ282, it is important to characterise their star-forming properties, e.g their position in respect to main sequence. In Figure 6.8 I present SFR vs. $\mathrm{M}_{\star}$ for all galaxies related to PHZ282, colour-coded for their redhsifts. The Figure reveals a mixing of two likely distinct populations, SF galaxies and those with high masses in average and and very low SFRs (typical for quiescent (QSc) galaxies). I test the robustness of our findings by providing the best fit to our data and comparing to known studies (e.g. Schreiber, Pannella, Elbaz, et al. 2015, Pearson, Wang, Hurley, et al. 2018. To do so, I assume the simple power-law which is the simplest form found to reliably model the MS in a number of studies (Johnston et al. 2015). It is given by: $\log(\mathrm{SFR}) = \alpha \log(M_{\star}) + \beta$. I simply split the data into a series of redshift slices with 0.5 step, and use the single power law functional expression to estimate the fit within each bin. The best fits are shown as inner plot in Figure 6.8. With this I determine how the normalisation β and the slope α of the SF-MS evolve. Both α and β are find to steadily evolve with redshift, with the difference that α evolves slowly from 0.7 to 1.2, and normalisation slope β increases much strongly with redshift, from 0.95 to 1.94 at $0.5 < z < 3.5$. Both the evolution and observed range of values are in consistency with findings from Schreiber, Elbaz, Pannella, Ciesla, T. Wang, Koekemoer, et al. 2016, Pearson, Wang, van der Tak, et al. 2017, see also Jorryt Matthee et al. 2018. For example, Pearson, Wang, van der Tak, et al. 2017 use different methods based on MCMC to derive a scatter and evolution of β, which they found increasing from 0.92 to 1.77 at $0.5 < z < 3.5$. They suggest that increase of β with the redshift is likely a consequence of high-mass galaxies having enhanced star formation efficiency with respect to the low-mass galaxies.

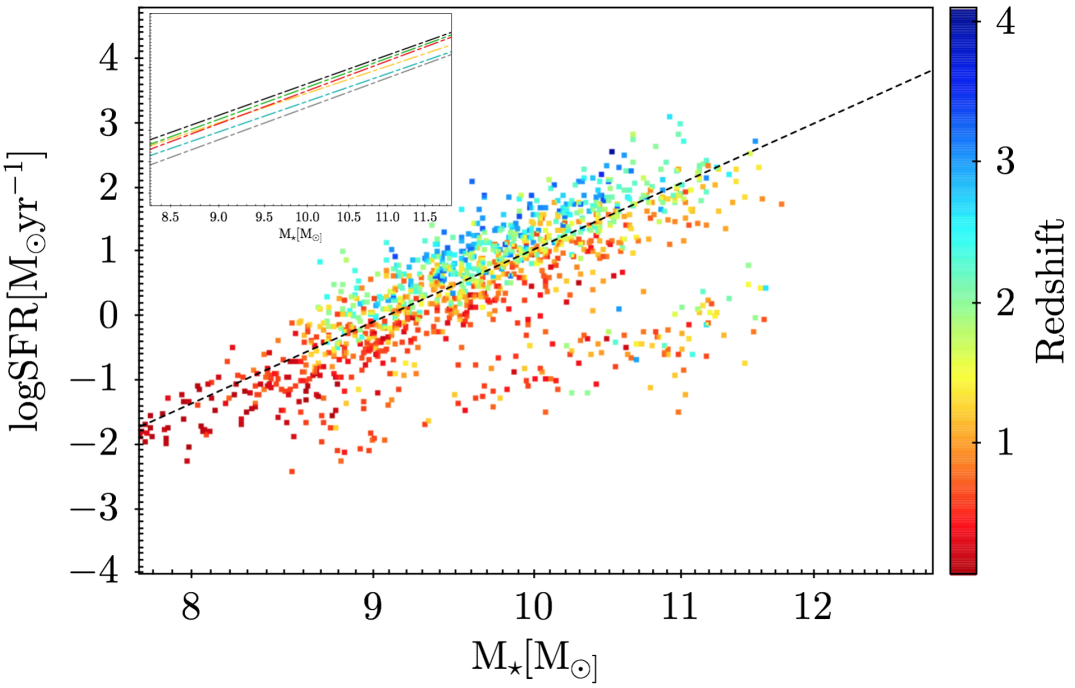

Figure 6.8.: The SFR vs. $M_\star$ of galaxies within PHZ282. Points are coloured for their photometric redshifts. The solid line is the best fit to the average sample, while the inner plot show the fitted MS trends splitted per redshift bins ($\Delta z = 0.5$). Hence a coloured dashed lines reflect the evolution of a normalisation factor β ($0 < z < 3.5$, from bottom to the top line).

As a result of our combined SED fitting and $L_{\rm IR}$ modelling procedure, we find 67 galaxies that have $L_{IR} > 5{\times}10^{11}(L_\odot)$ which roughly corresponds to $SFR > 50 M_\odot yr^{-1}$.[k] In the following I refer to them as "brighter DSFGs". The number of brighter DSFGs contribute 7% to the total number of NGVS sources inside the PHZ282. To deeply investigate their nature, it is crucial to estimate what is their position relative to the star-formation MS. To do so, I measure their "starburstiness" (RSB), which is defined as an offset of galaxy's SFR to the SFR expected for the MS (Elbaz, Dickinson, et al. 2011, Schreiber, Pannella, Elbaz, et al. 2015). Since I find a good match to a general fit of MS described in Pearson, Wang, Hurley, et al. 2018, I adopt their parametrisation (their Eq.9), and compute RSB for 67 brighter DSFGs in our sample.

I find that 13 out of 67 brighter DSFGs lie a factor of 3 above the MS (shown as a grey region in Fig.6.9), while 7 of them are modelled to be factor of 4 above the MS (which corresponds to RSB>0.6). They are thus experiencing an enhanced star-

[k] I should note here that the cut I chose for candidate DSFGs is completely arbitrary, and the main conclusion does not change if we assume slightly upper or lower L_{IR} cut.

forming activity consistent of being characterised as starbursts. I find that the redshift distribution of those 67 brighter DSFGs reaches a strong peak at $z = 2.25 \pm 0.1$, as illustrated in histograms in the lower panel of Fig.6.9. In the right panel of Fig.6.9 I show the redsfhit distribution of these sources disentangled on different stellar masses. We see that higher-redshift peak is dominated by galaxies having $\mathrm{M}_{\star} < 10^{11} M_{\odot}$. Even if accounting for large uncertainties of our estimates, it is very unlikely that such a large number of DSFGs at the similar redshift within the area of 2.5' is a result of random fluctuations. This argument for such conclusion is strengthen when we plot the position of these sources in respect to the 250 μm map, which unveils that majority of our DSFGs at $z \sim 2.25$ nicely follow the brighter SPIRE structure (Fig. 6.7).

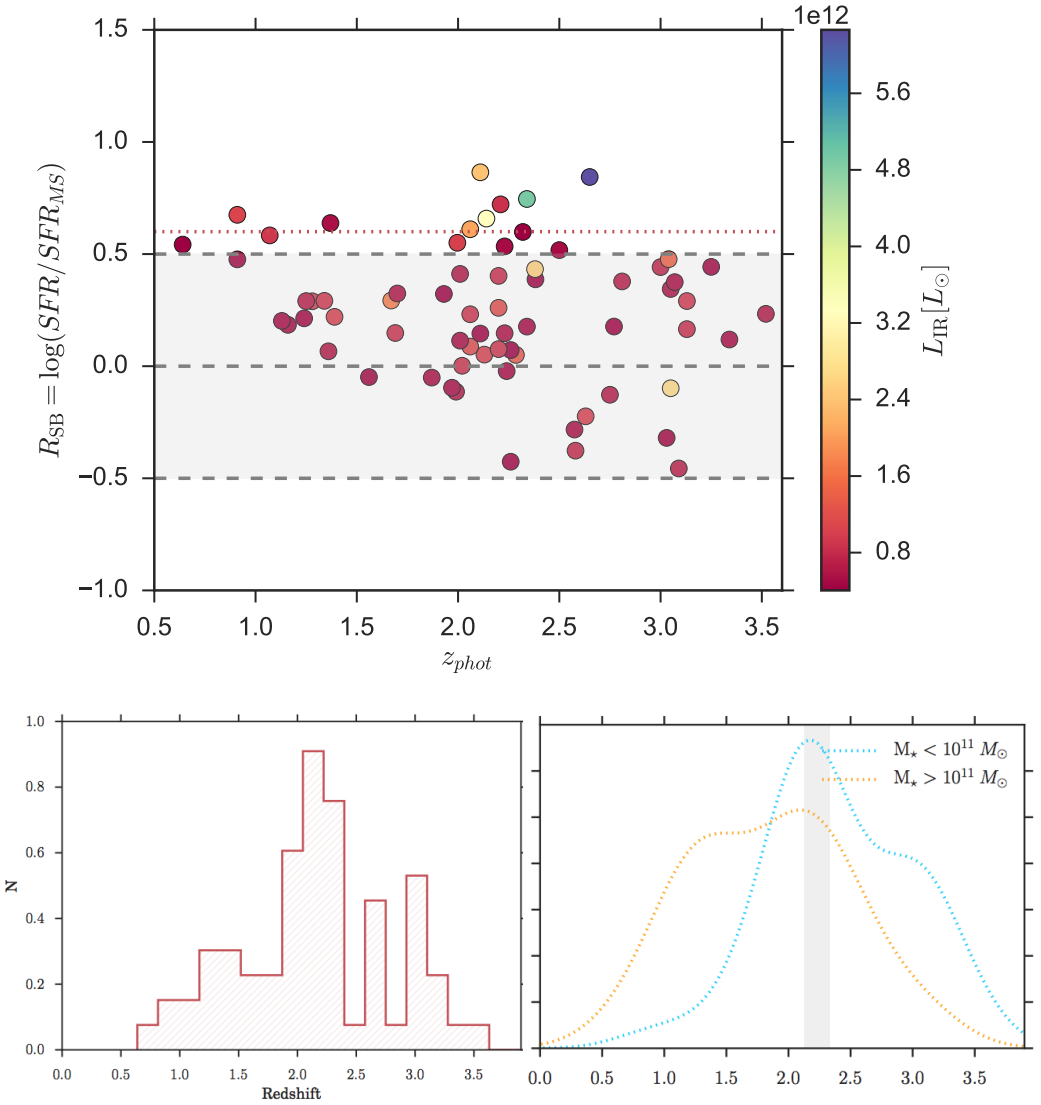

Figure 6.9.: The main finding of our analysis; `Upper panel:` Starburstiness (RSB) which is the ratio of the measured SFR to the SFR expected for the main sequence (using the relation at the respective redshift). To parametrise SFR at the MS I apply the form given by Schreiber, Elbaz, Pannella, Ciesla, T. Wang, Koekemoer, et al. 2016. Our RSB is plotted against redshift, and colour-coded for $L_{\rm IR}$. A factor of 3 offset around the MS is indicated by shaded grey region. The dotted red line represents the threshold which is commonly used to describe SB galaxies - 4×MS. `Lower panel:` Redshift distribution of our DSFGs (left), and the same distribution separated by their stellar masses (right). This shows that the most massive DSFGs dominate at redshifts below the median, as indicated with grey area ($z = 2.25 \pm 0.1$).

The nature of WISE detections in PHZ282

Amongst 67 brighter DSFGs presented in previous subsection, there are 29 WISE detected galaxies. I apply widely used colour criteria based on W1, W2 and i-band (e.g. Noboriguchi et al. 2018, Glowacki et al. 2017) to see how these sources would be classified. By applying the colour criterion W1-W2>0.8 (Glowacki et al. 2017), I find three candidate strong QSOs that are IR-bright, one of them being spectroscopically confirmed QSO at $z = 3.165$ (Pâris et al. 2018). It can also be found that 17 out of 29 WISE-detected, IR-bright sources fulfil the criteria: $i - W4_{\rm AB} > 7$ and W1-W2<0.8, consistent of being classified as Dust Obscured Galaxies (DOGs, Noboriguchi et al. 2018, Toba et al. 2018). In the literature, the DOGs are known as bright, 22μm-selected sources with strong obscuration at optical wavelengths.

We find that DOGs from our sample are massive galaxies ($M > 3 \times 10^{10}$), having the peak of their redshift distribution at $z = 1.2$ which is consistent with other studies of DOGs (e.g. Toba et al. 2018). We additionally check $(g - z)_{AB}$ colours of our DOGs, as suggested by Noboriguchi et al. 2018. The average and the standard deviation of $(g - z)_{AB}$ are found to be 2.19 ± 0.41, which is significantly redder than the average $(g - z)_{AB}$ colour for the rest of the NGVS sources (see right panel on Figure 6.12). Inspecting the other (non-DOG) WISE detected sources with very red $(g - z)_{AB}$ colours, we find a non-negligible number of galaxies (12 in total) with very low SFR (logSFR<-1), thus candidate QGs. Their $(g - z)_{AB}$ colour is very red, similarly to those of DOGs, therefore a caution should be taken when we pre-select QGs considering $g - z$ colours alone, as suggested by some studies (Bilicki et al. 2016).

Concerning DOGs, I also find a higher median AGN fraction (30%) than in the rest of our WISE sources (18%). It is thus likely that WISE selected DOGs are powered by AGN, which is a scenario that follow the formation of gas-rich mergers, as proposed by Noboriguchi et al. 2018. This is also in line with some other studies which reported that WISE-selected DOGs are widely distributed over SFR–$M_\star$ plane at $z \sim 1$ (Bilicki et al. 2016). Tsai et al. 2015 perform an extensive SED analysis on DOGs, and show that the most luminous are typically characterized by a rising power law continuum of hot dust in the near-IR indicating that their mid-IR luminosity is dominated by AGN. Due to their significant AGN and star forming activity, our subsample of WISE detected DOGs can provides us an important laboratory to probe the maximum phase of the co-evolution of galaxies and SMBHs.[1]

[1]Interestingly, one of the most IR-luminous galaxies reported in the literature is WISE selected DOG

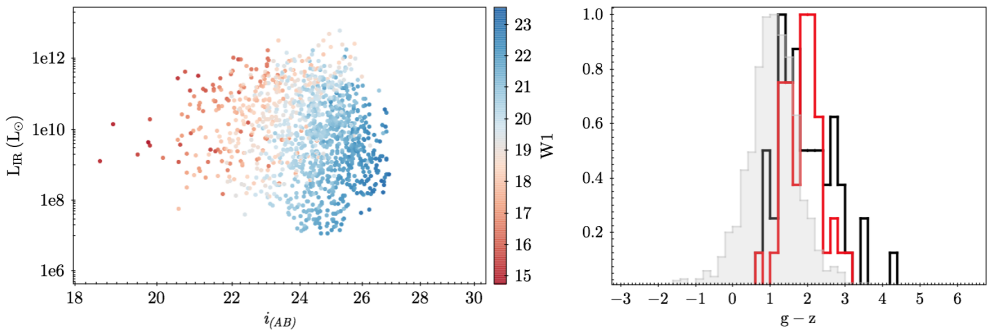

Figure 6.10.: Left: Dust luminosities estimated with CIGALE, plotted versus $i_{\rm AB}$ and colour coded for W1 magnitudes obtained with `Tractor`. Only those magnitudes below 17.8 mag for W1 are reliable, since for W1>17.8 mag we assign only upper limits based on `Tractor's` Bayesian output, which suffers from large uncertainties. Nonetheless, it can be seen that the vast majority of fainter i-band sources (e.g. $i_{\rm AB} > 24$ mag) are not sufficiently bright at 3.4 μm to be detected in WISE W1 map; Right: Observed $g-z$ colours for different galaxy subsamples: the grey stepfilled area shows the colour distribution of all NGVS detections, red line depicts the DOGs, while the black line illustrates unclassified WISE galaxies with very low SFR (logSFR<-1). Here we exclude QSO candidates from the plot. Their optical colours are much bluer ($g-z \sim 0.5$) compare to the rest of WISE selected sources.

6.3.3. A present and future work

Throughout Section 6.3 I present a methodology and early results to answer the question: *How can excess dust emission seen by Planck be resolved and characterised?* With the currently available data set presented in Section 6.3, these results are affected with high-uncertainties, especially related to derived stellar masses and predicted IR luminosities. However, we believed that the results create a promising ground for future investigation, and we are now in a stage of making more refined analysis. There are two main lines that we should use to reach our final goal:

- *Modelling side:* We employ newly updated dust SED libraries from Schreiber, Elbaz, Pannella, Ciesla, T. Wang, and Franco 2018 and Bethermin et al. 2017. The goal is to use our $L_{\rm IR}$ as an input, and compute monochromatic SPIRE fluxes based on adopted SEDs. In Fig.6.11 I illustrate an example of such an estimate performed with an updated dust SED library of Bethermin (M.Bethermin, private communi-

at $z = 2.25$ and it is stated that extreme IR luminosity ($L_{\rm IR} = 1.2 \times 10^{14}\, L\odot$ corresponds to the peak of AGN (Tsai et al. 2015)

cation) while currently I am also repeating the same analysis with use of updated library of Schreiber, Elbaz, Pannella, Ciesla, T. Wang, and Franco 2018. The SED library used in Bethermin et al. 2017 is based on Magdis, Daddi, et al. 2012 SED library (see the Section 4.1 for the more detailed explanation). The fine redshift grid is created by following the parametric evolution of the mean radiation field, while the monochromatic flux is then an array defined as a function of observed wavelength and redshift. The updated SED library presented in Schreiber, Elbaz, Pannella, Ciesla, T. Wang, and Franco 2018 has three degrees of freedom: the normalization (either $L_{\rm IR}$ or $M_{\rm dust}$), the dust temperature, and the IR8 (or $f_{\rm PAH}$). Since the peak of FIR emission is not constrained for our sources, the dust temperature must be fixed, while the value of $f_{\rm PAH}$ can be taken from Eq.16 of Schreiber, Elbaz, Pannella, Ciesla, T. Wang, and Franco 2018 and evaluated at the redshift of the galaxy. For each value of $T_{\rm d}$ allowed in the fit, the templates (provided in rest-frame quantities) are translated to the observer frame and integrated under the filter response curves of the available photometry. The number of sources that should be extracted in our real maps based on SPIRE fluxes obtained from SED library applied in B17 is slightly higher than the number of our real 250 μm detections (19 vs.14). To better understand and interpret the differences, I am currently finishing the writing of a tool that creates simulated maps based on estimated monochromatic SPIRE fluxes. The fidelity of results will be then assessed as a figure of merit by varying the different input parameters (e.g $T_{\rm d}$) and quantifying the differences between the fluxes measured in modelled and real maps.

- *Observing side:* As a supplement to the present study based on SED modelling, we also need high-resolution follow-ups (particularly in submm domain) to confirm that the candidate DSFGs are really physically associated. All of our 67 brighter DSFGs have stellar masses larger than $10^{10} M_{\odot}$, and to study high-z galaxies at lower masses we require instruments such as ALMA and JWST. As an illustration to this need, in Fig.6.12 I plot a very small area around the centre of PHZ282, where two starbursts are find in a close proximity (indicated with arrows), both of them undetected in u-band. Both sources have RSB>0.6, and their modelled 250 μm fluxes are close to the detection limit of SPIRE. We have one detection in our real maps which is 5" away from these sources. This highlights the importance of making follow-up observations with suitable submm instruments such as ALMA or NOEMA in order to unveil the interplay between environments and DSFGs that

may remain hidden in noise.

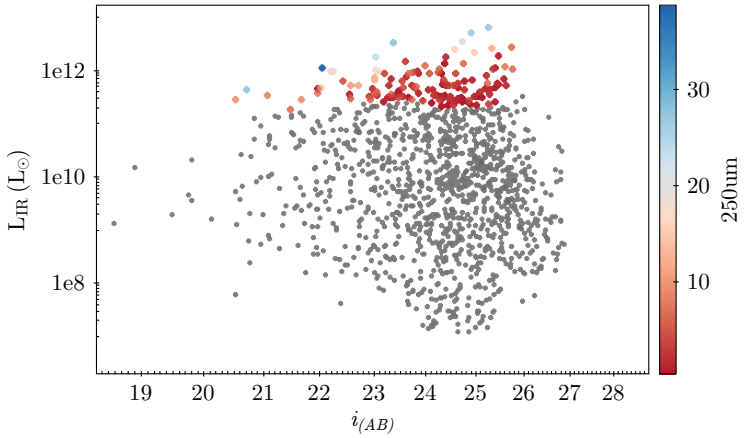

Figure 6.11.: Example of modelled monochromatic 250 μm fluxes. These fluxes are predicted with use of updated dust SED library applied in B17 model (M.Bethermin, private communication).

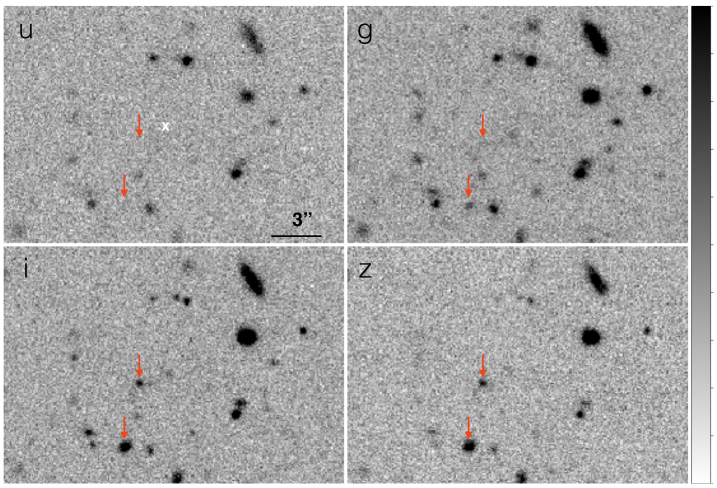

Figure 6.12.: Central region around the core of PHZ282. In a distance smaller than 5" from the centre of PHZ282, I mark two NGVS sources for which we find the star-formation excess by factor of 3-4. They are both undetected in u-band, and have modelled $L_{\rm IR} > 10^{11.8}\,L_\odot$ which correspond to $\sim$ 10 mJy at 250 μm. This flux is just slightly below the detection limit of our SPIRE maps. This example is used to highlights the necessity of performing interferometric follow-ups of such candidates, in order to unveil their redshifts and dusty nature, as well as influence of the environment on their estimated physical properties.

CHAPTER 7

Summary and future prospects

You will be required to do wrong no matter where you go. Everywhere in the Universe.

Philip K. Dick, *Do Androids Dream of Electric Sheep?*

Summary

In this Thesis, I present how the large extragalactic fields observed with *Herschel* can be used in order to understand the statistical properties, nature and environments of distant DSFGs. The largest part of my work is concerned with a comprehensive analysis of statistics and nature of 500 μm-risers, a candidate very distant ($z > 4$) population of sources, characterised with rising fluxes in SPIRE bands ($S_{500} > S_{350} > S_{250}$). To partially suppress a source confusion problem I apply a novel extraction and photometry method which combines positional and SED priors. I define a following selection function: $S_{500} > S_{350} > S_{250}$, $S_{250} > 13.2$ mJy and $S_{500} > 30$ mJy. I apply such a defined criteria on wide and deep HeViCS field, resulting in 133 500 μm-risers. This statistically significant sample substantially increases the number of known candidate DSFGs at $z > 4$ (Chapter 2). The estimated median IR luminosity ($\hat{L_{IR}} = 1.94 \times 10^{13} L_{\odot}$) of selected sources strengthen the expectations that the vast majority of our 500 μm-risers are linked to the prodigious star-formation events (Chapter 3).

To put the statistics of selected 500 μm-risers in cosmological framework, I use phenomenological models of galaxy evolution (Chapter 4) that are able to simultaneously reproduce the FIR and submm observations at various angular resolutions. I construct mock catalogues based on these models and study the statistics of our 500 μm-risers. I model the effect of instrumental and confusion noise on number counts and redshifts of 500 μm-risers. From this analysis I find that both the density of sources and their redshift distribution are very sensitive to the source extraction method and depth of the field we chose to investigate. I also find that contribution of strongly lensed galaxies predicted by models is not dominant (24%) if we perform selection based on simultaneous de-blending of sources down to 13.2 mJy at 250 μm.

It is known that the one of the key difficulties with observations at FIR wavelengths is the coarse angular resolution of *Herschel* which causes that superimposed signal of multiple galaxies known as blending has a noticeable effect on the derived number counts.

To fully investigate its impact on the selection of 500 μm-risers I generate SPIRE maps from different mock catalogues and incorporate physical clustering based on abundance matching recipe. This allows me to evaluate the impact of several observational biases on our selection. I find that our technique is able to recover $\sim 60\%$ of genuine 500 μm-risers. I measure the correlation function between modelled, colour-selected galaxies at different redshift bins, and find that correlation signal for 350 μm-peakers and 500 μm-risers is the strongest at $3.5 < z < 4.5$ (Section 5.3). It is responsible for a factor of 1.4 boost of number counts compared to underlying intrinsic value. An important consequence which comes from this result is that existing tension between observations and galaxy models can be partially solved if we carefully account for all observational effects such as noise, lensing (weak and strong) and the clustering of sources at high-z. However, even correcting for all selection biases, a small discrepancy (factor of 1.3 - 1.5) between observations and phenomenological models still remains if we consider only intrinsically bright, unlensed DSFGs at $z > 4$. Such an offset is significantly smaller than in previous studies who claim that models underpredict the number of 500 μm-risers by an order of magnitude. Despite this fairly good agreement, the results of my statistical analysis strongly indicate that we have yet to extract and understand all the information present in the data produced by *Herschel*.

An important part of this Thesis was focused on an investigation of environments of high-z DSFGs (Chapter 6). On the one hand, I show that a number of 500 μm-risers reside in overdense regions at $z > 3 - 4$, tracing the most massive DM halos. On the other hand, I present a method for resolving the dust emission in candidate distant sources ($z \sim 2$) selected by *Planck*. I study the PHZ282, which is one of sources that is fully covered with SPIRE data in the HeViCS field. I apply a methodology based on SED fitting and $L_{\rm IR}$ modelling, and conclude that there is a significant peak in the redshift distribution of DSFGs at $z = 2.25 \pm 0.1$ which give rise to the total flux observed with *Planck*.

Future prospects

The sample which contains systematically selected 500 μm-risers might become a benchmark for our understanding of how galaxies formed and evolved in the very distant Universe. However, although I significantly enlarge the known sample of candidate DSFGs at $z > 4$, it must be acknowledged that estimated photometric redshifts, as well

as the fraction of spurious sources are highly uncertain in the parent catalogue of 500 μm-risers. Since this, I highlight the necessity of additional observations and further refinement of selection technique presented in this Thesis.

From the ***observational point of view***, there is large progress to be made in providing the pieces necessary to reconstruct the nature of distant DSFGs throughout the whole electromagnetic spectra. A better understanding of lensing fraction and physical meaning of source multiplicity of 500 μm-risers will be achieved with NOEMA, ALMA and SMA. While ALMA, NOEMA and SMA can follow-up hundreds of high-z DSFGs, their small field of view and narrow bandwidth strongly limits the sensitivity and efficiency to conduct larger unbiased surveys. This can be currently performed at 1.1 mm and 2 mm with NIKA-2 camera ($\theta = 12$" and $\theta = 18$" respectively) mounted on IRAM 30m telescope, and with LMT telescope (1-3 mm) in Mexico. Spectroscopic millimetre observations will also significantly improve the estimated SFRs of 500 μm-risers by measuring their *gas content*, namely: ionised gas (using [NII] line at 205 μm), atomic gas (using [CII] at 158 μm) and molecular gas (using CO). Another valuable source of information about the small-scale environment of 500 μm-risers will be achieved by measuring the ratio between [NII] and [CII]. It determines whether or not a significant fraction of the [CII] emission comes from diffuse ionised gas, not directly associated with the dense star-forming gas. This will be particularly important to test our assumption that a non-negligible number of 500 μm-risers may reside in distant protoclusters.

Future *James Webb Space Telescope (JWST)* will provide a great synergy to ALMA. It will probe the wavelength range between 0.7 μm and 25.5 μm and revolutionise the near-IR view of 500 μm-risers. In particular, *JWST* will be able to derive accurate estimates of the AGN contribution to 500 μm-risers, and provide important constraints on the gas reservoirs of these sources from various near-IR and mid-IR lines, resulting from a PAH cooling process.

Combining high-resolution imaging of the stellar continuum (with *JWST*) and dust continuum (with ALMA and NOEMA) we can test our model-based estimates of relative contribution of *galaxy mergers* to selected 500 μm-risers. Additionally, the combination of mm and mid-IR observations will allow us to compare *galaxy morphologies and sizes* of 500 μm-risers. Having these information in hand, we can test the hypothesis that DSFGs at $z > 4$ are connected to the formation of the most massive galaxies, being triggered by major mergers, and then evolving into compact quiescent galaxies via quenching in a QSO phase.

Along with current and future instruments that are designed to cover IR and mm part of the spectra, forthcoming large area *radio interferometers* such as SKA (it will operate from 50 MHz to 14 GHz) and Next Generation VLA (ngVLA, 1 GHz to 116 GHz) will open a new discovery space for sources selected in this work. Their advantage is ability to probe higher rest-frame radio frequencies (> 10 GHz) with increasing redshift, where emission of galaxies becomes dominated by thermal (free-free) radiation, thus offering a robust, dust-unbiased measurement of SFRs of our 500 μm-risers.

An important complementary method that can be used to probe the nature of 500 μm-risers is *intensity mapping*. This method does not resolve individual galaxies but it has the advantage that it is sensitive to faint sources. Cross-correlation of multiple lines (e.g. [CII], [OI] and [NII]) will enable multiple probes of the different phases of the ISM, which is key to understanding the interplay between energetic sources, and the gas and dust at $z > 4$.

Concerning the protocluster candidates and *large-scale environment* of distant DSFGs selected in this Thesis, the particular interest will be in combining measurements from NIKA-2, along with future optical-NIR telescopes such are *Euclid* and LSST. All these instruments offer large instantaneous field of view: 6.5' for NIKA2; 0.5 deg^2 for *Euclid*, and 6.5 deg^2 for LSST. Having combined wide-field data of candidate protoclusters with mm-spectroscopy of their member galaxies, we can build a census of their stellar and star-forming properties, and test our method based on SED modelling. Such a detailed study is a way to determine the nature of bright, cold peaks in the CIB selected by *Planck*.

From the *theoretical point of view*, recent models suggest that early galaxy formation may be dominated by the central regions of the most massive *dusty overdensities*, and that star formation evolved inside-out to galaxies in underdense regions. The prediction that DSFGs are systematically reside in more massive halos in the early Universe may be one of crucial predictions of structure formation. Protoclusters thus remains as excellent cosmic laboratories for studying hierarchical galaxy growth. It is expected that such growth catalysed through mergers increases relative to star formation in comparison to the field. Since such a growth is catalysed through mergers that are more common in protoclusters relative to the field, it would results in a different evolution of the galaxy SMF for protocluster and field galaxies. This idea is pointed by several simulations based on SAMs (Muldrew et al. 2018). Quantification of the associated galaxies can be gained from mapping the evolution of the galaxy SMF in protoclusters and confronting

it with simulations. However, such evolution has not yet been measured, mostly due to relatively small sample sizes existing to date. The future large surveys, LSST and *Euclid*, will help in solving this issue by detecting a large number of new protoclusters (more than thousands), while in the same time the environmental dependence of the galaxy SMF will be obtained with *JWST*. This will be achieved even for masses below the $M \sim 10^9 M_{\odot}$. This clearly reflects how important is the synergy between the different (both present and future) astronomical instruments.

Last but not least, I highlight the importance of making more refined ***simulations*** of DSFGs in the future, since they are crucial to properly place detected sources in the context of galaxy formation and evolution. In this Thesis I show that interpretation of observed statistics with models remains as a very challenging task. The self-consistent simulations that include physical clustering based on sub-halo abundance matching technique are difficult to conduct on wide areas because they need both a large-volume DM simulation and a high-mass resolution to resolve the most of faint galaxies responsible for confusion. The refined simulations that will be conducted in the future must include physical effect of gravitational lensing (strong and weak) on mock images. It is possible to do so by assigning the mass distribution predicted by different cosmological simulations along the line of sight that is used to generate the mock images. It is also important to test other methods which connect modelled galaxies to DM halos, since it is still an open question does the galaxy-halo relation vary with environments. Lastly, the QSO-phase of galaxies and the growth of SMBHs is not specifically treated in existing simulations, and I point here the importance of them to be carefully modelled, particularly because the DSFG and QSO phases have been shown to be tightly connected.

Bibliography

[1] Hanadi M. Abdelsalam et al. “Non-parametric reconstruction of cluster mass distribution from strong lensing: modelling Abell 370.” In: 294 (Mar. 1998), pp. 734–746. DOI: 10.1046/j.1365-8711.1998.01356.x. arXiv: astro-ph/9707207.

[2] M. W. Abruzzo et al. “Identifying Mergers Using Quantitative Morphologies in Zoom Simulations of High-Redshift Galaxies”. In: ArXiv e-prints (Mar. 2018). arXiv: 1803.02374.

[3] J. Aird et al. “PRIMUS: The Dependence of AGN Accretion on Host Stellar Mass and Color”. In: 746, 90 (Feb. 2012), p. 90. DOI: 10.1088/0004-637X/746/1/90. arXiv: 1107.4368.

[4] Almudena Alonso-Herrero et al. “Local Luminous Infrared Galaxies. III. Co-evolution of Black Hole Growth and Star Formation Activity?” In: 765, 78 (Mar. 2013), p. 78. DOI: 10.1088/0004-637X/765/2/78. arXiv: 1301.4015.

[5] J. Álvarez-Márquez et al. “Dust properties of Lyman-break galaxies at z ˜ 3”. In: 587, A122 (Mar. 2016), A122. DOI: 10.1051/0004-6361/201527190. arXiv: 1512.04120.

[6] A. Amblard et al. “Herschel-ATLAS: Dust temperature and redshift distribution of SPIRE and PACS detected sources using submillimetre colours”. In: 518, L9 (July 2010), p. L9. DOI: 10.1051/0004-6361/201014586. arXiv: 1005.2412.

[7] Aretxaga, D. H. Hughes, et al. “Breaking the ‘redshift deadlock’- II. The redshift distribution for the submillimetre population of galaxies”. In: 342 (July 2003), pp. 759–801. DOI: 10.1046/j.1365-8711.2003.06560.x. eprint: astro-ph/0205313.

[8] Aretxaga, Hughes, et al. “The SCUBA Half Degree Extragalactic Survey - IV. Radio-mm-FIR photometric redshifts”. In: 379 (Aug. 2007), pp. 1571–1588. DOI: 10.1111/j.1365-2966.2007.12036.x. arXiv: astro-ph/0702503.

[9] L. Armus et al. “Observations of Ultraluminous Infrared Galaxies with the Infrared Spectrograph on the Spitzer Space Telescope. II. The IRAS Bright Galaxy Sample”. In: 656 (Feb. 2007), pp. 148–167. DOI: 10.1086/510107. arXiv: astro-ph/0610218 [astro-ph].

[10] V. Asboth et al. “HerMES: a search for high-redshift dusty galaxies in the HerMES Large Mode Survey – catalogue, number counts and early results”. In: Monthly Notices of the Royal Astronomical Society 462.2 (2016), p. 1989. DOI: 10.1093/mnras/stw1769. eprint: /oup/backfile/Content_public/Journal/mnras/462/2/10.1093_mnras_stw1769/2/stw1769.pdf. URL: +%20http://dx.doi.org/10.1093/mnras/stw1769.

[11] R. Auld et al. “The Herschel Virgo Cluster Survey - XII. FIR properties of optically selected Virgo cluster galaxies”. In: 428 (Jan. 2013), pp. 1880–1910. DOI: 10.1093/mnras/sts125. arXiv: 1209.4651.

[12] T. J. L. C. Bakx et al. “The Herschel Bright Sources (HerBS): sample definition and SCUBA-2 observations”. In: 473 (Jan. 2018), pp. 1751–1773. DOI: 10.1093/mnras/stx2267. arXiv: 1709.01514.

[13] Ivan K. Baldry et al. “Quantifying the Bimodal Color-Magnitude Distribution of Galaxies”. In: 600 (Jan. 2004), pp. 681–694. DOI: 10.1086/380092. arXiv: astro-ph/0309710.

[14] A. J. Barger et al. “Submillimetre-wavelength detection of dusty star-forming galaxies at high redshift”. In: 394 (July 1998), pp. 248–251. DOI: 10.1038/28338. arXiv: astro-ph/9806317 [astro-ph].

[15] R. Barkana et al. “In the beginning: the first sources of light and the reionization of the universe”. In: 349 (July 2001), pp. 125–238. DOI: 10.1016/S0370-1573(01)00019-9. eprint: astro-ph/0010468.

[16] C. M. Baugh et al. “Can the faint submillimetre galaxies be explained in the Λ cold dark matter model?” In: 356 (Jan. 2005), pp. 1191–1200. DOI: 10.1111/j.1365-2966.2004.08553.x.

[17] Peter S. Behroozi et al. "The ROCKSTAR Phase-space Temporal Halo Finder and the Velocity Offsets of Cluster Cores". In: 762, 109 (Jan. 2013), p. 109. DOI: 10.1088/0004-637X/762/2/109.

[18] M. Bernardi et al. "A Search for the Most Massive Galaxies: Double Trouble?" In: 131 (Apr. 2006), pp. 2018–2034. DOI: 10.1086/499770. arXiv: astro-ph/0510696.

[19] E. Bertin et al. "SExtractor: Software for source extraction." In: 117 (June 1996), pp. 393–404. DOI: 10.1051/aas:1996164.

[20] M. Béthermin, H. Dole, M. Cousin, et al. "Submillimeter number counts at 250 μm, 350 μm and 500 μm in BLAST data". In: 516, A43 (June 2010), A43. DOI: 10.1051/0004-6361/200913910. arXiv: 1003.0833 [astro-ph.CO].

[21] M. Béthermin, H. Dole, G. Lagache, et al. "Modeling the evolution of infrared galaxies: a parametric backward evolution model". In: 529, A4 (May 2011), A4. DOI: 10.1051/0004-6361/201015841. arXiv: 1010.1150.

[22] M. Béthermin, M. Kilbinger, et al. "Clustering, host halos, and environment of z ˜ 2 galaxies as a function of their physical properties". In: 567, A103 (July 2014), A103. DOI: 10.1051/0004-6361/201423451. arXiv: 1405.0492.

[23] Béthermin, Daddi, Magdis, Lagos, et al. "Evolution of the dust emission of massive galaxies up to z = 4 and constraints on their dominant mode of star formation". In: 573, A113 (Jan. 2015), A113. DOI: 10.1051/0004-6361/201425031. arXiv: 1409.5796.

[24] Béthermin, Daddi, Magdis, Sargent, et al. "A Unified Empirical Model for Infrared Galaxy Counts Based on the Observed Physical Evolution of Distant Galaxies". In: 757, L23 (Oct. 2012), p. L23. DOI: 10.1088/2041-8205/757/2/L23. arXiv: 1208.6512.

[25] Béthermin, De Breuck, et al. "The influence of wavelength, flux, and lensing selection effects on the redshift distribution of dusty, star-forming galaxies". In: 576, L9 (Apr. 2015), p. L9. DOI: 10.1051/0004-6361/201525718.

[26] Béthermin, Le Floc'h, et al. "HerMES: deep number counts at 250 μm, 350 μm and 500 μm in the COSMOS and GOODS-N fields and the build-up of the cosmic infrared background". In: 542, A58 (June 2012), A58. DOI: 10.1051/0004-6361/201118698. arXiv: 1203.1925 [astro-ph.CO].

[27] Bethermin et al. “The impact of clustering and angular resolution on far-infrared and millimeter continuum observations”. In: ArXiv e-prints, arXiv:1703.08795 (Mar. 2017). arXiv: 1703.08795v2.

[28] S. Bianchi et al. “The Herschel Virgo Cluster Survey. XX. Dust and gas in the foreground Galactic cirrus”. In: 597, A130 (Jan. 2017), A130. DOI: 10.1051/0004-6361/201629013. arXiv: 1609.05941.

[29] Maciej Bilicki et al. “WISE SuperCOSMOS Photometric Redshift Catalog: 20 Million Galaxies over 3/pi Steradians”. In: The Astrophysical Journal Supplement Series 225, 5 (July 2016), p. 5. DOI: 10.3847/0067-0049/225/1/5.

[30] Blain, Roberto Assef, et al. “WISE Detections of Known QSOs at Redshifts Greater than Six”. In: 778, 113 (Dec. 2013), p. 113. DOI: 10.1088/0004-637X/778/2/113. arXiv: 1310.2301.

[31] Blain, V. E. Barnard, et al. “Submillimetre and far-infrared spectral energy distributions of galaxies: the luminosity-temperature relation and consequences for photometric redshifts”. In: 338 (Jan. 2003), pp. 733–744. DOI: 10.1046/j.1365-8711.2003.06086.x. eprint: astro-ph/0209450.

[32] Blain, Smail, et al. “Submillimeter galaxies”. In: 369 (Oct. 2002), pp. 111–176. DOI: 10.1016/S0370-1573(02)00134-5. arXiv: astro-ph/0202228.

[33] Roger Blandford et al. “Fermat’s Principle, Caustics, and the Classification of Gravitational Lens Images”. In: 310 (Nov. 1986), p. 568. DOI: 10.1086/164709.

[34] N. R. Bonaventura et al. “Red but not dead: unveiling the star-forming far-infrared spectral energy distribution of SpARCS brightest cluster galaxies at 0 < z < 1.8”. In: 469 (Aug. 2017), pp. 1259–1281. DOI: 10.1093/mnras/stx722.

[35] F. Boone et al. “An extended Herschel drop-out source in the center of AS1063: a normal dusty galaxy at z = 6.1 or SZ substructures?” In: 559, L1 (Nov. 2013), p. L1. DOI: 10.1051/0004-6361/201322552. arXiv: 1308.6707 [astro-ph.CO].

[36] M. S. Bothwell, R. Maiolino, et al. “Galaxy metallicities depend primarily on stellar mass and molecular gas mass”. In: 595, A48 (Oct. 2016), A48. DOI: 10.1051/0004-6361/201527918.

[37] M. S. Bothwell, Ian Smail, et al. “A survey of molecular gas in luminous submillimetre galaxies”. In: 429 (Mar. 2013), pp. 3047–3067. DOI: 10.1093/mnras/sts562. arXiv: 1205.1511.

[38] N. Bourne, J. S. Dunlop, et al. “Evolution of cosmic star formation in the SCUBA-2 Cosmology Legacy Survey”. In: 467 (May 2017), pp. 1360–1385. DOI: 10.1093/mnras/stx031. arXiv: 1607.04283.

[39] N. Bourne, L. Dunne, et al. “The Herschel-ATLAS Data Release 1 - II. Multi-wavelength counterparts to submillimetre sources”. In: 462 (Oct. 2016), pp. 1714–1734. DOI: 10.1093/mnras/stw1654. arXiv: 1606.09254.

[40] R. J. Bouwens et al. “UV Luminosity Functions at z~4, 5, and 6 from the Hubble Ultra Deep Field and Other Deep Hubble Space Telescope ACS Fields: Evolution and Star Formation History”. In: 670 (Dec. 2007), pp. 928–958. DOI: 10.1086/521811. arXiv: 0707.2080 [astro-ph].

[41] Richard G. Bower et al. “The colour-magnitude relation as a constraint on the formation of rich cluster galaxies”. In: 299 (Oct. 1998), pp. 1193–1208. DOI: 10.1046/j.1365-8711.1998.01868.x. arXiv: 8711.1998.

[42] A. Bracco et al. “Herschel-ATLAS: statistical properties of Galactic cirrus in the GAMA-9 Hour Science Demonstration Phase Field”. In: 412 (Apr. 2011), pp. 1151–1161. DOI: 10.1111/j.1365-2966.2010.17971.x. arXiv: 1011.0725.

[43] Larry Bradley et al. astropy/photutils: v0.4. Oct. 2017. DOI: 10.5281/zenodo.1039309. URL: https://doi.org/10.5281/zenodo.1039309.

[44] Brinchmann, Charlot, et al. “The physical properties of star-forming galaxies in the low-redshift Universe”. In: 351 (July 2004), pp. 1151–1179. DOI: 10.1111/j.1365-2966.2004.07881.x. arXiv: astro-ph/0311060.

[45] Brinchmann and Ellis. “The Mass Assembly and Star Formation Characteristics of Field Galaxies of Known Morphology”. In: 536 (June 2000), pp. L77–L80. DOI: 10.1086/312738. arXiv: astro-ph/0005120.

[46] Drew Brisbin et al. “An ALMA survey of submillimeter galaxies in the COSMOS field: Multiwavelength counterparts and redshift distribution”. In: 608, A15 (Nov. 2017), A15. DOI: 10.1051/0004-6361/201730558.

[47] Tom Broadhurst et al. “A Gravitational Lens Solution for the IRAS Galaxy FSC 10214+4724”. In: 450 (Sept. 1995), p. L41. DOI: 10.1086/316774. arXiv: astro-ph/9505013.

[48] M. Brodwin et al. "The Massive and Distant Clusters of WISE Survey. III. Sunyaev-Zel'dovich Masses of Galaxy Clusters at z1". In: 806, 26 (June 2015), p. 26. DOI: 10.1088/0004-637X/806/1/26. arXiv: 1410.2355.

[49] G. Bruzual et al. "Stellar population synthesis at the resolution of 2003". In: 344 (Oct. 2003), pp. 1000–1028. DOI: 10.1046/j.1365-8711.2003.06897.x.

[50] V. Buat, E. Giovannoli, et al. "Measures of star formation rates from infrared (Herschel) and UV (GALEX) emissions of galaxies in the HerMES fields". In: 409 (Nov. 2010), pp. L1–L6. DOI: 10.1111/j.1745-3933.2010.00916.x. arXiv: 1007.1857.

[51] V. Buat, S. Heinis, et al. "Ultraviolet to infrared emission of z > 1 galaxies: Can we derive reliable star formation rates and stellar masses?" In: 561, A39 (Jan. 2014), A39. DOI: 10.1051/0004-6361/201322081. arXiv: 1310.7712.

[52] V. Buat, S. Noll, et al. "GOODS-Herschel: dust attenuation properties of UV selected high redshift galaxies". In: 545, A141 (Sept. 2012), A141. DOI: 10.1051/0004-6361/201219405.

[53] D. Burgarella et al. "Herschel PEP/HerMES: the redshift evolution $(0 \leq z \leq 4) of dustattenuationa$ $IR) starformationratedensity$". In: 554, A70 (June 2013), A70. DOI: 10.1051/0004-6361/201321651. arXiv: 1304.7000.

[54] R. S. Bussmann et al. "HerMES: ALMA Imaging of Herschel-selected Dusty Star-forming Galaxies". In: 812, 43 (Oct. 2015), p. 43. DOI: 10.1088/0004-637X/812/1/43. arXiv: 1504.05256.

[55] Z.-Y. Cai et al. "A Hybrid Model for the Evolution of Galaxies and Active Galactic Nuclei in the Infrared". In: 768, 21 (May 2013), p. 21. DOI: 10.1088/0004-637X/768/1/21. arXiv: 1303.2335 [astro-ph.CO].

[56] Gabriela Calistro Rivera, J. A. Hodge, et al. "Resolving the ISM at the peak of cosmic star formation with ALMA - The distribution of CO and dust continuum in z 2.5 sub-millimetre galaxies". In: ArXiv e-prints, arXiv:1804.06852 (Apr. 2018), arXiv:1804.06852. arXiv: 1804.06852.

[57] Gabriela Calistro Rivera, Elisabeta Lusso, et al. "AGNfitter: A Bayesian MCMC Approach to Fitting Spectral Energy Distributions of AGNs". In: 833, 98 (Dec. 2016), p. 98. DOI: 10.3847/1538-4357/833/1/98.

[58] M. Calvo et al. "The NIKA2 Instrument, A Dual-Band Kilopixel KID Array for Millimetric Astronomy". In: Journal of Low Temperature Physics 184 (Aug. 2016), pp. 816–823. DOI: 10.1007/s10909-016-1582-0. arXiv: 1601.02774 [astro-ph.IM].

[59] D. Calzetti et al. "The Dust Content and Opacity of Actively Star-forming Galaxies". In: 533 (Apr. 2000), pp. 682–695. DOI: 10.1086/308692. eprint: astro-ph/9911459.

[60] R. Cañameras et al. "Planck's dusty GEMS: The brightest gravitationally lensed galaxies discovered with the Planck all-sky survey". In: 581, A105 (Sept. 2015), A105. DOI: 10.1051/0004-6361/201425128. arXiv: 1506.01962.

[61] Capak et al. "A massive protocluster of galaxies at a redshift of z˜5.3". In: 470 (Feb. 2011), pp. 233–235. DOI: 10.1038/nature09681. arXiv: 1101.3586 [astro-ph.CO].

[62] K. I. Caputi et al. "Star Formation in Galaxies at z 4-5 from the SMUVS Survey: A Clear Starburst/Main-sequence Bimodality for Hα Emitters on the SFR-M* Plane". In: 849, 45 (Nov. 2017), p. 45. DOI: 10.3847/1538-4357/aa901e.

[63] C. L. Carilli et al. "Cool Gas in High-Redshift Galaxies". In: Annual Review of Astronomy and Astrophysics 51 (Aug. 2013), pp. 105–161. DOI: 10.1146/annurev-astro-082812-140953. arXiv: 1301.0371.

[64] V. Casasola et al. "Radial distribution of dust, stars, gas, and star-formation rate in DustPedia$\star/xreface - ongalaxies$". In: 605, A18 (Sept. 2017), A18. DOI: 10.1051/0004-6361/201731020. arXiv: 1706.05351.

[65] Casey. "The Ubiquity of Coeval Starbursts in Massive Galaxy Cluster Progenitors". In: 824, 36 (June 2016), p. 36. DOI: 10.3847/0004-637X/824/1/36.

[66] Casey, S. Berta, et al. "A Redshift Survey of Herschel Far-infrared Selected Starbursts and Implications for Obscured Star Formation". In: 761, 140 (Dec. 2012), p. 140. DOI: 10.1088/0004-637X/761/2/140. arXiv: 1210.4928.

[67] Casey, Narayanan, et al. "Dusty star-forming galaxies at high redshift". In: 541 (Aug. 2014), pp. 45–161. DOI: 10.1016/j.physrep.2014.02.009. arXiv: 1402.1456.

[68] Casey, Zavala, et al. "The Brightest Galaxies in the Dark Ages: Galaxies' Dust Continuum Emission During the Reionization Era". In: ArXiv e-prints, arXiv:1805.10301 (May 2018), arXiv:1805.10301. arXiv: 1805.10301.

[69] Gilles Chabrier. "Galactic Stellar and Substellar Initial Mass Function". In: Publications of the Astronomical Society of the Pacific 115 (July 2003), pp. 763–795. DOI: 10.1086/376392.

[70] Edward L. Chapin et al. "A joint analysis of BLAST 250-500 μm and LABOCA 870 μm observations in the Extended Chandra Deep Field-South". In: 411 (Feb. 2011), pp. 505–549. DOI: 10.1111/j.1365-2966.2010.17697.x. arXiv: 1003.2647 [astro-ph.CO].

[71] Stéphane Charlot et al. "A Simple Model for the Absorption of Starlight by Dust in Galaxies". In: 539 (Aug. 2000), pp. 718–731. DOI: 10.1086/309250.

[72] Chen et al. "The SCUBA-2 Cosmology Legacy Survey: Multiwavelength Counterparts to 10^3 Submillimeter Galaxies in the UKIDSS-UDS Field". In: 820, 82 (Apr. 2016), p. 82. DOI: 10.3847/0004-637X/820/2/82.

[73] Jacopo Chevallard et al. "Modelling and interpreting spectral energy distributions of galaxies with BEAGLE". In: 462 (Oct. 2016), pp. 1415–1443. DOI: 10.1093/mnras/stw1756.

[74] Chiang, Overzier, and Karl Gebhardt. "Ancient Light from Young Cosmic Cities: Physical and Observational Signatures of Galaxy Proto-clusters". In: 779, 127 (Dec. 2013), p. 127. DOI: 10.1088/0004-637X/779/2/127. arXiv: 1310.2938.

[75] Chiang, Overzier, K. Gebhardt, et al. "Galaxy Protoclusters as Drivers of Cosmic Star Formation History in the First 2 Gyr". In: 844, L23 (Aug. 2017), p. L23. DOI: 10.3847/2041-8213/aa7e7b. arXiv: 1705.01634.

[76] L. Ciesla, V. Charmandaris, et al. "Constraining the properties of AGN host galaxies with spectral energy distribution modelling". In: 576, A10 (Apr. 2015), A10. DOI: 10.1051/0004-6361/201425252.

[77] L. Ciesla, D. Elbaz, et al. "The SFR-M_* main sequence archetypal star- formation history and analytical models". In: 608, A41 (Dec. 2017), A41. DOI: 10.1051/0004-6361/201731036.

[78] Clauset et al. "Power-law distributions in empirical data". In: ArXiv e-prints, arXiv:0706.1062 (June 2007), arXiv:0706.1062. arXiv: 0706.1062 [physics.data-an].

[79] Clements, Braglia, A. K. Hyde, et al. "Herschel Multitiered Extragalactic Survey: clusters of dusty galaxies uncovered by Herschel and Planck". In: 439 (Apr. 2014), pp. 1193–1211. DOI: 10.1093/mnras/stt2253. arXiv: 1311.5758.

[80] Clements, Braglia, G. Petitpas, et al. “H-ATLAS: a candidate high redshift cluster/protocluster of star-forming galaxies”. In: 461 (Sept. 2016), pp. 1719–1733. DOI: 10.1093/mnras/stw1224. arXiv: 1605.06433.

[81] F. Combes et al. “A bright z = 5.2 lensed submillimeter galaxy in the field of Abell 773. HLSJ091828.6+514223”. In: 538, L4 (Feb. 2012), p. L4. DOI: 10.1051/0004-6361/201118750. arXiv: 1201.2908.

[82] J. J. Condon. “Confusion and Flux-Density Error Distributions”. In: 188 (Mar. 1974), pp. 279–286. DOI: 10.1086/152714.

[83] J. J. Condon et al. “The NRAO VLA Sky Survey”. In: 115 (May 1998), pp. 1693–1716. DOI: 10.1086/300337.

[84] Charlie Conroy et al. “Modeling Luminosity-dependent Galaxy Clustering through Cosmic Time”. In: 647 (Aug. 2006), pp. 201–214. DOI: 10.1086/503602. arXiv: astro-ph/0512234.

[85] Christopher J. Conselice. “The Evolution of Galaxy Structure Over Cosmic Time”. In: Annual Review of Astronomy and Astrophysics 52 (Aug. 2014), pp. 291–337. DOI: 10.1146/annurev-astro-081913-040037. arXiv: 1403.2783.

[86] A. Cooray et al. “HerMES: Halo occupation number and bias properties of dusty galaxies from angular clustering measurements”. In: 518, L22 (July 2010), p. L22. DOI: 10.1051/0004-6361/201014597.

[87] M. Cousin et al. “Metal enrichment in a semi-analytical model, fundamental scaling relations, and the case of Milky Way galaxies”. In: 589, A109 (May 2016), A109. DOI: 10.1051/0004-6361/201527734.

[88] Cowie, A. J. Barger, et al. “A Submillimeter Perspective on the GOODS Fields (SUPER GOODS). I. An Ultradeep SCUBA-2 Survey of the GOODS-N”. In: 837, 139 (Mar. 2017), p. 139. DOI: 10.3847/1538-4357/aa60bb. arXiv: 1702.03002.

[89] Cowie, Antoinette Songaila, et al. “New Insight on Galaxy Formation and Evolution From Keck Spectroscopy of the Hawaii Deep Fields”. In: 112 (Sept. 1996), p. 839. DOI: 10.1086/118058. arXiv: astro-ph/9606079.

[90] Cowley, M. Béthermin, et al. “The far infra-red SEDs of main sequence and starburst galaxies”. In: 467 (May 2017), pp. 1231–1248. DOI: 10.1093/mnras/stx165. arXiv: 1607.05717.

[91] Cowley, Lacey, Carlton M. Baugh, et al. "The clustering evolution of dusty star-forming galaxies". In: 461 (Sept. 2016), pp. 1621–1641. DOI: 10.1093/mnras/stw1069.

[92] Cowley, Lacey, Baugh, and S. Cole. "Simulated observations of sub-millimetre galaxies: the impact of single-dish resolution and field variance". In: 446 (Jan. 2015), pp. 1784–1798. DOI: 10.1093/mnras/stu2179. arXiv: 1406.0855.

[93] Cowley, Lacey, Baugh, Cole, et al. "Blending bias impacts the host halo masses derived from a cross- correlation analysis of bright submillimetre galaxies". In: 469 (Aug. 2017), pp. 3396–3404. DOI: 10.1093/mnras/stx928.

[94] P. Cox et al. "Gas and Dust in a Submillimeter Galaxy at z = 4.24 from the Herschel Atlas". In: 740, 63 (Oct. 2011), p. 63. DOI: 10.1088/0004-637X/740/2/63. arXiv: 1107.2924.

[95] Darren J. Croton, Volker Springel, et al. "The many lives of active galactic nuclei: cooling flows, black holes and the luminosities and colours of galaxies". In: 365 (Jan. 2006), pp. 11–28. DOI: 10.1111/j.1365-2966.2005.09675.x.

[96] Darren J. Croton, Adam R. H. Stevens, et al. "Semi-Analytic Galaxy Evolution (SAGE): Model Calibration and Basic Results". In: The Astrophysical Journal Supplement Series 222, 22 (Feb. 2016), p. 22. DOI: 10.3847/0067-0049/222/2/22.

[97] E. da Cunha et al. "On the Effect of the Cosmic Microwave Background in High-redshift (Sub-)millimeter Observations". In: 766, 13 (Mar. 2013), p. 13. DOI: 10.1088/0004-637X/766/1/13. arXiv: 1302.0844.

[98] Daddi, Dannerbauer, et al. "Two Bright Submillimeter Galaxies in a z = 4.05 Protocluster in Goods-North, and Accurate Radio-Infrared Photometric Redshifts". In: 694 (Apr. 2009), pp. 1517–1538. DOI: 10.1088/0004-637X/694/2/1517. arXiv: 0810.3108.

[99] Daddi, Dickinson, et al. "Multiwavelength Study of Massive Galaxies at z˜2. I. Star Formation and Galaxy Growth". In: 670 (Nov. 2007), pp. 156–172. DOI: 10.1086/521818. arXiv: 0705.2831.

[100] Daddi, Elbaz, et al. "Different Star Formation Laws for Disks Versus Starbursts at Low and High Redshifts". In: 714 (May 2010), pp. L118–L122. DOI: 10.1088/2041-8205/714/1/L118. arXiv: 1003.3889.

[101] Dale and Helou. "The Infrared Spectral Energy Distribution of Normal Star-forming Galaxies: Calibration at Far-Infrared and Submillimeter Wavelengths". In: 576 (Sept. 2002), pp. 159–168. DOI: 10.1086/341632.

[102] Dale, G. Helou, et al. "A Two-parameter Model for the Infrared/Submillimeter/Radio Spectral Energy Distributions of Galaxies and Active Galactic Nuclei". In: 784, 83 (Mar. 2014), p. 83. DOI: 10.1088/0004-637X/784/1/83. arXiv: 1402.1495.

[103] H. Dannerbauer, M. D. Lehnert, B. H. C. Emonts, et al. "The implications of the surprising existence of a large, massive CO disk in a distant protocluster". In: ArXiv e-prints (Jan. 2017). arXiv: 1701.05250.

[104] H. Dannerbauer, M. D. Lehnert, D. Lutz, et al. "Properties of Millimeter Galaxies: Constraints from K-Band Blank Fields". In: 573 (July 2002), pp. 473–484. DOI: 10.1086/340762.

[105] Davé et al. "The nature of submillimetre galaxies in cosmological hydrodynamic simulations". In: 404 (May 2010), pp. 1355–1368. DOI: 10.1111/j.1365-2966.2010.16395.x. arXiv: 0909.4078.

[106] J. I. Davies, M. Baes, et al. "The Herschel Virgo Cluster Survey. I. Luminosity function". In: 518, L48 (July 2010), p. L48. DOI: 10.1051/0004-6361/201014571. arXiv: 1005.3054.

[107] J. I. Davies, S. Bianchi, et al. "The Herschel Virgo Cluster Survey - VIII. The Bright Galaxy Sample". In: 419 (Feb. 2012), pp. 3505–3520. DOI: 10.1111/j.1365-2966.2011.19993.x. arXiv: 1110.2869.

[108] Th. de Graauw et al. "The Herschel-Heterodyne Instrument for the Far-Infrared (HIFI)". In: 518, L6 (July 2010), p. L6. DOI: 10.1051/0004-6361/201014698.

[109] R. Decarli et al. "Rapidly star-forming galaxies adjacent to quasars at redshifts exceeding 6". In: 545 (May 2017), pp. 457–461. DOI: 10.1038/nature22358.

[110] A. Dekel et al. "Formation of Massive Galaxies at High Redshift: Cold Streams, Clumpy Disks, and Compact Spheroids". In: 703 (Sept. 2009), pp. 785–801. DOI: 10.1088/0004-637X/703/1/785. arXiv: 0901.2458 [astro-ph.GA].

[111] A. G. Delahaye et al. "Galaxy Merger Candidates in High-redshift Cluster Environments". In: 843, 126 (July 2017), p. 126. DOI: 10.3847/1538-4357/aa756a.

[112] M. Dessauges-Zavadsky et al. “Molecular gas content in strongly lensed z 1.5-3 star-forming galaxies with low infrared luminosities”. In: 577, A50 (May 2015), A50. DOI: 10.1051/0004-6361/201424661. arXiv: 1408.0816.

[113] M. J. Devlin et al. “Over half of the far-infrared background light comes from galaxies at z=1.2”. In: 458 (Apr. 2009), pp. 737–739. DOI: 10.1038/nature07918. arXiv: 0904.1201 [astro-ph.CO].

[114] P. Di Matteo et al. “On the frequency, intensity, and duration of starburst episodes triggered by galaxy interactions and mergers”. In: 492 (Dec. 2008), pp. 31–49. DOI: 10.1051/0004-6361:200809480. arXiv: 0809.2592.

[115] E. Diolaiti et al. “StarFinder: an IDL GUI-based code to analyze crowded fields with isoplanatic correcting PSF fitting”. In: Adaptive Optical Systems Technology. Ed. by P. L. Wizinowich. Vol. 4007. July 2000, pp. 879–888. DOI: 10.1117/12.390377. eprint: astro-ph/0004101.

[116] H. Dole, R. Gispert, et al. “FIRBACK: III. Catalog, source counts, and cosmological implications of the 170 mu m ISO”. In: 372 (June 2001), pp. 364–376. DOI: 10.1051/0004-6361:20010449. arXiv: astro-ph/0103434.

[117] H. Dole, G. Lagache, et al. “The cosmic infrared background resolved by Spitzer. Contributions of mid-infrared galaxies to the far-infrared background”. In: 451 (May 2006), pp. 417–429. DOI: 10.1051/0004-6361:20054446. arXiv: astro-ph/0603208.

[118] D. Donevski, V. Buat, et al. “Towards a census of high-redshift dusty galaxies with Herschel. A selection of ”500 μm-risers””. In: 614, A33 (June 2018), A33. DOI: 10.1051/0004-6361/201731888.

[119] D. Donevski and T. Prodanović. “Possible breaking of the FIR-radio correlation in tidally interacting galaxies”. In: 453 (Oct. 2015), pp. 638–644. DOI: 10.1093/mnras/stv1653.

[120] J. L. Donley et al. “Evidence for Merger-driven Growth in Luminous, High-z, Obscured AGNs in the CANDELS/COSMOS Field”. In: 853, 63 (Jan. 2018), p. 63. DOI: 10.3847/1538-4357/aa9ffa.

[121] C. D. Dowell et al. “SHARC II: a Caltech submillimeter observatory facility camera with 384 pixels”. In: Millimeter and Submillimeter Detectors for Astronomy. Ed. by T. G. Phillips et al. Vol. 4855. Feb. 2003, pp. 73–87. DOI: 10.1117/12.459360.

[122] Dowell et al. “HerMES: Candidate High-redshift Galaxies Discovered with Herschel/SPIRE”. In: The Astrophysical Journal 780.1 (2014), p. 75. URL: http://stacks.iop.org/0004-637X/780/i=1/a=75.

[123] B. T. Draine. “On the Submillimeter Opacity of Protoplanetary Disks”. In: 636 (Jan. 2006), pp. 1114–1120. DOI: 10.1086/498130. eprint: astro-ph/0507292.

[124] B. T. Draine, G. Aniano, et al. “Andromeda’s Dust”. In: 780, 172 (Jan. 2014), p. 172. DOI: 10.1088/0004-637X/780/2/172. arXiv: 1306.2304.

[125] B. T. Draine and A. Li. “Infrared Emission from Interstellar Dust. IV. The Silicate-Graphite-PAH Model in the Post-Spitzer Era”. In: 657 (Mar. 2007), pp. 810–837. DOI: 10.1086/511055. eprint: astro-ph/0608003.

[126] S. Duivenvoorden et al. “Red, redder, reddest: SCUBA-2 imaging of colour-selected \textit{Herschel} sources”. In: ArXiv e-prints (Jan. 2018). arXiv: 1801.07266.

[127] J. S. Dunlop et al. “A deep ALMA image of the Hubble Ultra Deep Field”. In: 466 (Apr. 2017), pp. 861–883. DOI: 10.1093/mnras/stw3088. arXiv: 1606.00227.

[128] Loretta Dunne et al. “The SCUBA Local Universe Galaxy Survey - II. 450-μm data: evidence for cold dust in bright IRAS galaxies”. In: 327 (Nov. 2001), pp. 697–714. DOI: 10.1046/j.1365-8711.2001.04789.x. arXiv: astro-ph/0106362 [astro-ph].

[129] L. Dunne et al. “Herschel-ATLAS: rapid evolution of dust in galaxies over the last 5 billion years”. In: 417 (Oct. 2011), pp. 1510–1533. DOI: 10.1111/j.1365-2966.2011.19363.x. arXiv: 1012.5186.

[130] E. Dwek et al. “Dust-gas interactions and the infrared emission from hot astrophysical plasmas”. In: 30 (1992), pp. 11–50. DOI: 10.1146/annurev.aa.30.090192.000303.

[131] S. Eales et al. “The new galaxy evolution paradigm revealed by the Herschel surveys”. In: 473 (Jan. 2018), pp. 3507–3524. DOI: 10.1093/mnras/stx2548. arXiv: 1710.01314.

[132] Eales, Dunne, et al. “The Herschel ATLAS”. In: Publications of the Astronomical Society of the Pacific 122 (May 2010), p. 499. DOI: 10.1086/653086. arXiv: 0910.4279.

[133] Eales, Lilly, et al. “The Canada-UK Deep Submillimeter Survey. IV. The Survey of the 14 Hour Field”. In: 120 (Nov. 2000), pp. 2244–2268. DOI: 10.1086/316823. arXiv: astro-ph/0009154.

[134] Eales, Smith, et al. “Mapping the interstellar medium in galaxies with Herschel/SPIRE”. In: 518, L62 (July 2010), p. L62. DOI: 10.1051/0004-6361/201014536. arXiv: 1005.2113.

[135] A. Einstein et al. “On the Relation between the Expansion and the Mean Density of the Universe”. In: Proceedings of the National Academy of Science 18 (Mar. 1932), pp. 213–214. DOI: 10.1073/pnas.18.3.213.

[136] Elbaz, Cesarsky, P. Chanial, et al. “The bulk of the cosmic infrared background resolved by ISOCAM”. In: 384 (Mar. 2002), pp. 848–865. DOI: 10.1051/0004-6361:20020106. arXiv: astro-ph/0201328.

[137] Elbaz, Cesarsky, D. Fadda, et al. “Source counts from the 15 mu m ISOCAM Deep Surveys”. In: 351 (Nov. 1999), pp. L37–L40. arXiv: astro-ph/9910406 [astro-ph].

[138] Elbaz, Daddi, et al. “The reversal of the star formation-density relation in the distant universe”. In: 468 (June 2007), pp. 33–48. DOI: 10.1051/0004-6361:20077525. arXiv: astro-ph/0703653.

[139] Elbaz, Dickinson, et al. “GOODS-Herschel: an infrared main sequence for star-forming galaxies”. In: 533, A119 (Sept. 2011), A119. DOI: 10.1051/0004-6361/201117239. arXiv: 1105.2537.

[140] Elbaz, Hwang, et al. “Herschel unveils a puzzling uniformity of distant dusty galaxies”. In: 518, L29 (July 2010), p. L29. DOI: 10.1051/0004-6361/201014687. arXiv: 1005.2859.

[141] Elbaz, Leiton, et al. “Starbursts in and out of the star-formation main sequence”. In: ArXiv e-prints (Nov. 2017). arXiv: 1711.10047.

[142] Sara L. Ellison, David R. Patton, et al. “Galaxy pairs in the Sloan Digital Sky Survey - II. The effect of environment on interactions”. In: 407 (Sept. 2010), pp. 1514–1528. DOI: 10.1111/j.1365-2966.2010.17076.x. arXiv: 1002.4418.

[143] Sara L. Ellison, Sebastian F. Sánchez, et al. “Star formation is boosted (and quenched) from the inside-out: radial star formation profiles from MaNGA”. In: 474 (Feb. 2018), pp. 2039–2054. DOI: 10.1093/mnras/stx2882.

[144] A. Enia et al. "The Herschel-ATLAS: magnifications and physical sizes of 500-μm-selected strongly lensed galaxies". In: 475 (Apr. 2018), pp. 3467–3484. DOI: 10.1093/mnras/sty021.

[145] A. L. Faisst et al. "Are High-redshift Galaxies Hot? Temperature of z 5 Galaxies and Implications for Their Dust Properties". In: 847, 21 (Sept. 2017), p. 21. DOI: 10.3847/1538-4357/aa886c. arXiv: 1708.07842.

[146] Onsi Fakhouri et al. "The nearly universal merger rate of dark matter haloes in ΛCDM cosmology". In: 386 (May 2008), pp. 577–592. DOI: 10.1111/j.1365-2966.2008.13075.x. arXiv: 0710.4567 [astro-ph].

[147] J. Fensch et al. "High-redshift major mergers weakly enhance star formation". In: 465 (Feb. 2017), pp. 1934–1949. DOI: 10.1093/mnras/stw2920. arXiv: 1610.03877.

[148] A. Ferrara et al. "The infrared-dark dust content of high redshift galaxies". In: 471 (Nov. 2017), pp. 5018–5024. DOI: 10.1093/mnras/stx1898. arXiv: 1607.01824.

[149] L. Ferrarese et al. "The Next Generation Virgo Cluster Survey (NGVS). I. Introduction to the Survey". In: 200, 4 (May 2012), p. 4. DOI: 10.1088/0067-0049/200/1/4.

[150] E. W. Flesch. "The Half Million Quasars (HMQ) Catalogue". In: 32, e010 (Mar. 2015), e010. DOI: 10.1017/pasa.2015.10. arXiv: 1502.06303.

[151] I. Flores-Cacho et al. "Multi-wavelength characterisation of z ˜ 2 clustered, dusty star-forming galaxies discovered by Planck". In: 585, A54 (Jan. 2016), A54. DOI: 10.1051/0004-6361/201425226. arXiv: 1510.01585.

[152] A. Franceschini et al. "Galaxy evolution from deep multi-wavelength infrared surveys: a prelude to Herschel". In: 517, A74 (July 2010), A74. DOI: 10.1051/0004-6361/200912622. arXiv: 0906.4264.

[153] J. Fritz et al. "Revisiting the infrared spectra of active galactic nuclei with a new torus emission model". In: 366 (Mar. 2006), pp. 767–786. DOI: 10.1111/j.1365-2966.2006.09866.x. eprint: astro-ph/0511428.

[154] Y. Fudamoto et al. "The most distant, luminous, dusty star-forming galaxies: redshifts from NOEMA and ALMA spectral scans". In: 472 (Dec. 2017), pp. 2028–2041. DOI: 10.1093/mnras/stx1956. arXiv: 1707.08967.

[155] S. Fujimoto, M. Ouchi, Y. Ono, et al. "ALMA Census of Faint 1.2 mm Sources Down to ˜ 0.02 mJy: Extragalactic Background Light and Dust-poor, High-z Galaxies". In: 222, 1 (Jan. 2016), p. 1. DOI: 10.3847/0067-0049/222/1/1. arXiv: 1505.03523.

[156] S. Fujimoto, M. Ouchi, T. Shibuya, et al. "Demonstrating a New Census of Infrared Galaxies with ALMA (DANCING-ALMA). I. FIR Size and Luminosity Relation at z = 0-6 Revealed with 1034 ALMA Sources". In: 850, 83 (Nov. 2017), p. 83. DOI: 10.3847/1538-4357/aa93e6. arXiv: 1703.02138.

[157] J. M. Gabor et al. "How is star formation quenched in massive galaxies?" In: 407 (Sept. 2010), pp. 749–771. DOI: 10.1111/j.1365-2966.2010.16961.x. arXiv: 1001.1734.

[158] M. Galametz et al. "Mapping the cold dust temperatures and masses of nearby KINGFISH galaxies with Herschel". In: 425 (Sept. 2012), pp. 763–787. DOI: 10.1111/j.1365-2966.2012.21667.x. arXiv: 1207.1301 [astro-ph.CO].

[159] F. Galliano et al. "Non-standard grain properties, dark gas reservoir, and extended submillimeter excess, probed by Herschel in the Large Magellanic Cloud". In: 536, A88 (Dec. 2011), A88. DOI: 10.1051/0004-6361/201117952. arXiv: 1110.1260.

[160] Geach, Dunlop, et al. "The SCUBA-2 Cosmology Legacy Survey: 850 μm maps, catalogues and number counts". In: 465 (Feb. 2017), pp. 1789–1806. DOI: 10.1093/mnras/stw2721.

[161] Geach, Smail, et al. "On the Evolution of the Molecular Gas Fraction of Star-Forming Galaxies". In: 730, L19 (Apr. 2011), p. L19. DOI: 10.1088/2041-8205/730/2/L19. arXiv: 1102.3694.

[162] R. Giovanelli et al. "The Arecibo Legacy Fast ALFA Survey. III. H I Source Catalog of the Northern Virgo Cluster Region". In: 133 (June 2007), pp. 2569–2583. DOI: 10.1086/516635. eprint: astro-ph/0702316.

[163] K. Glazebrook et al. "A massive, quiescent galaxy at a redshift of 3.717". In: 544 (Apr. 2017), pp. 71–74. DOI: 10.1038/nature21680. arXiv: 1702.01751.

[164] Eilat Glikman et al. "A Near-Infrared Spectral Template for Quasars". In: 640 (Apr. 2006), pp. 579–591. DOI: 10.1086/500098. arXiv: astro-ph/0511640.

[165] E. Glikman et al. "A highly magnified gravitationally lensed red quasar at z = 2.5 with significant flux anomaly: Uncovering a missing population". In: ArXiv e-prints, arXiv:1807.05434 (July 2018), arXiv:1807.05434. arXiv: 1807.05434 [astro-ph.GA].

[166] M. Glowacki et al. "WISE data as a photometric redshift indicator for radio AGN". In: ArXiv e-prints, arXiv:1709.08634 (Sept. 2017), arXiv:1709.08634. arXiv: 1709.08634.

[167] R. Gobat et al. "The Early Early Type: Discovery of a Passive Galaxy at z _{spec} 3". In: 759, L44 (Nov. 2012), p. L44. DOI: 10.1088/2041-8205/759/2/L44. arXiv: 1210.4299.

[168] A. Grazian et al. "The galaxy stellar mass function at 3.5 $\leq z \leq$ 7.5 $in the CANDELS/UDS, GOOD South, and HUDF fields$". In: 575, A96 (Mar. 2015), A96. DOI: 10.1051/0004-6361/201424750. arXiv: 1412.0532.

[169] J. Greenslade et al. "Candidate high-z proto-clusters among the Planck compact sources, as revealed by Herschel-SPIRE". In: (Jan. 2018). DOI: 10.1093/mnras/sty023. arXiv: 1712.07141.

[170] M. J. Griffin et al. "The Herschel-SPIRE instrument and its in-flight performance". In: 518, L3 (July 2010), p. L3. DOI: 10.1051/0004-6361/201014519. arXiv: 1005.5123 [astro-ph.IM].

[171] B. A. Groves et al. "Dust Continuum Emission as a Tracer of Gas Mass in Galaxies". In: 799, 96 (Jan. 2015), p. 96. DOI: 10.1088/0004-637X/799/1/96. arXiv: 1411.2975.

[172] C. Gruppioni et al. "The Herschel PEP/HerMES luminosity function - I. Probing the evolution of PACS selected Galaxies to z 4". In: 432 (June 2013), pp. 23–52. DOI: 10.1093/mnras/stt308. arXiv: 1302.5209.

[173] S. Guilloteau et al. "The IRAM interferometer on Plateau de Bure". In: 262 (Sept. 1992), pp. 624–633.

[174] James E. Gunn et al. "On the Infall of Matter Into Clusters of Galaxies and Some Effects on Their Evolution". In: 176 (Aug. 1972), p. 1. DOI: 10.1086/151605.

[175] Yuichi Harikane, Masami Ouchi, Yoshiaki Ono, et al. “GOLDRUSH. II. Clustering of galaxies at z 4-6 revealed with the half- million dropouts over the 100 deg² area corresponding to 1 Gpc³”. In: Publications of the Astronomical Society of Japan 70, S11 (Jan. 2018), S11. DOI: 10.1093/pasj/psx097.

[176] Yuichi Harikane, Masami Ouchi, Takatoshi Shibuya, et al. “SILVERRUSH. V. Census of Lyα, [O III] λ5007, Hα, and [C II] 158 μm Line Emission with $\sim$1000 LAEs at z = 4.97.0 Revealed with Subaru/HSC”. In: 859, 84 (June 2018), p. 84. DOI: 10.3847/1538-4357/aabd80.

[177] Takuya Hashimoto et al. “The onset of star formation 250 million years after the Big Bang”. In: 557 (May 2018), pp. 392–395. DOI: 10.1038/s41586-018-0117-z.

[178] N. A. Hatch et al. “Why z > 1 radio-loud galaxies are commonly located in protoclusters”. In: 445 (Nov. 2014), pp. 280–289. DOI: 10.1093/mnras/stu1725. arXiv: 1409.1218.

[179] E. Hatziminaoglou et al. “Properties of dusty tori in active galactic nuclei - I. The case of SWIRE/SDSS quasars”. In: 386 (May 2008), pp. 1252–1264. DOI: 10.1111/j.1365-2966.2008.13119.x. arXiv: 0802.2458.

[180] Michael G. Hauser et al. “The Cosmic Infrared Background: Measurements and Implications”. In: Annual Review of Astronomy and Astrophysics 39 (Jan. 2001), pp. 249–307. DOI: 10.1146/annurev.astro.39.1.249. arXiv: astro-ph/0105539.

[181] Hayward. “The star formation rate and stellar mass limits for submillimetre galaxies implied by recent interferometric observations”. In: 432 (May 2013), pp. L85–L89. DOI: 10.1093/mnrasl/slt047. arXiv: 1304.1154.

[182] Hayward, S. C. Chapman, et al. “Observational constraints on the physical nature of submillimetre source multiplicity: chance projections are common”. In: (Feb. 2018). DOI: 10.1093/mnras/sty304. arXiv: 1802.00452.

[183] Hayward, Patrik Jonsson, et al. “How to distinguish starbursts and quiescently star-forming galaxies: the ’bimodal’ submillimetre galaxy population as a case study”. In: 424 (Aug. 2012), pp. 951–970. DOI: 10.1111/j.1365-2966.2012.21254.x.

[184] Hayward, Desika Narayanan, et al. “Submillimetre galaxies in a hierarchical universe: number counts, redshift distribution and implications for the IMF”. In: 428 (Jan. 2013), pp. 2529–2547. DOI: 10.1093/mnras/sts222. arXiv: 1209.2413.

[185] S. Heinis et al. “HerMES: dust attenuation and star formation activity in ultraviolet-selected samples from z 4 to 1.5”. In: 437 (Jan. 2014), pp. 1268–1283. DOI: 10.1093/mnras/stt1960.

[186] D. J. Helfand et al. “The Last of FIRST: The Final Catalog and Source Identifications”. In: 801, 26 (Mar. 2015), p. 26. DOI: 10.1088/0004-637X/801/1/26. arXiv: 1501.01555.

[187] Bruno M. B. Henriques et al. “Galaxy formation in the Planck cosmology - I. Matching the observed evolution of star formation rates, colours and stellar masses”. In: 451 (Aug. 2015), pp. 2663–2680. DOI: 10.1093/mnras/stv705. arXiv: 1410.0365.

[188] Y. D. Hezaveh et al. “Effects of Strong Gravitational Lensing on Millimeter-wave Galaxy Number Counts”. In: 734, 52 (June 2011), p. 52. DOI: 10.1088/0004-637X/734/1/52. arXiv: 1010.0998.

[189] S. Hilbert et al. “Strong lensing optical depths in a ΛCDM universe”. In: 382 (Nov. 2007), pp. 121–132. DOI: 10.1111/j.1365-2966.2007.12391.x. eprint: astro-ph/0703803.

[190] Ryley Hill et al. “High-resolution SMA imaging of bright submillimetre sources from the SCUBA-2 Cosmology Legacy Survey”. In: 477 (June 2018), pp. 2042–2067. DOI: 10.1093/mnras/sty746.

[191] P. T. P. Ho et al. “The Submillimeter Array”. In: 616 (Nov. 2004), pp. L1–L6. DOI: 10.1086/423245. eprint: astro-ph/0406352.

[192] A. Hoag et al. “HST Grism Observations of a Gravitationally Lensed Redshift 9.5 Galaxy”. In: 854, 39 (Feb. 2018), p. 39. DOI: 10.3847/1538-4357/aaa9c2. arXiv: 1709.03992.

[193] J. A. Hodge, C. L. Carilli, et al. “High-resolution Spectroscopic Imaging of CO in a z = 4.05 Proto-cluster”. In: 776, 22 (Oct. 2013), p. 22. DOI: 10.1088/0004-637X/776/1/22. arXiv: 1307.4763.

[194] J. A. Hodge, A. M. Swinbank, et al. “Kiloparsec-scale Dust Disks in High-redshift Luminous Submillimeter Galaxies”. In: 833, 103 (Dec. 2016), p. 103. DOI: 10.3847/1538-4357/833/1/103. arXiv: 1609.09649.

[195] D. W. Hogg. "Distance measures in cosmology". In: ArXiv Astrophysics e-prints, arXiv:astro-ph/9905116 (May 1999). eprint: astro-ph/9905116.

[196] W. S. Holland et al. "SCUBA-2: the 10 000 pixel bolometer camera on the James Clerk Maxwell Telescope". In: 430 (Apr. 2013), pp. 2513–2533. DOI: 10.1093/mnras/sts612. arXiv: 1301.3650 [astro-ph.IM].

[197] P. F. Hopkins et al. "Mergers, active galactic nuclei and 'normal' galaxies: contributions to the distribution of star formation rates and infrared luminosity functions". In: 402 (Mar. 2010), pp. 1693–1713. DOI: 10.1111/j.1365-2966.2009.15990.x. arXiv: 0911.1131 [astro-ph.CO].

[198] Philip F. Hopkins, Thomas J. Cox, et al. "A Cosmological Framework for the Co-Evolution of Quasars, Supermassive Black Holes, and Elliptical Galaxies. II. Formation of Red Ellipticals". In: The Astrophysical Journal Supplement Series 175 (Apr. 2008), pp. 390–422. DOI: 10.1086/524363. arXiv: 0706.1246 [astro-ph].

[199] Philip F. Hopkins, Darren Croton, et al. "Mergers in ΛCDM: Uncertainties in Theoretical Predictions and Interpretations of the Merger Rate". In: 724 (Dec. 2010), pp. 915–945. DOI: 10.1088/0004-637X/724/2/915. arXiv: 1004.2708.

[200] Philip F. Hopkins, Lars Hernquist, et al. "A Cosmological Framework for the Co-Evolution of Quasars, Supermassive Black Holes, and Elliptical Galaxies. I. Galaxy Mergers and Quasar Activity". In: The Astrophysical Journal Supplement Series 175 (Apr. 2008), pp. 356–389. DOI: 10.1086/524362. arXiv: 0706.1243 [astro-ph].

[201] J. R. Houck et al. "Unidentified point sources in the IRAS minisurvey." In: 278 (Mar. 1984), pp. L63–L66. DOI: 10.1086/184224.

[202] E.P. Hubble, E. "Extragalactic nebulae." In: 64 (Dec. 1926). DOI: 10.1086/143018.

[203] E. Hubble. A Relation between Distance and Radial Velocity among Extra-Galactic Nebulae. Mar. 1929. DOI: 10.1073/pnas.15.3.168.

[204] David H. Hughes et al. "High-redshift star formation in the Hubble Deep Field revealed by a submillimetre-wavelength survey". In: 394 (July 1998), pp. 241–247. DOI: 10.1038/28328. arXiv: astro-ph/9806297.

[205] P. D. Hurley et al. "HELP: XID+, the probabilistic de-blender for Herschel SPIRE maps". In: 464 (Jan. 2017), pp. 885–896. DOI: 10.1093/mnras/stw2375. arXiv: 1606.05770.

[206] S. Ikarashi, R. J. Ivison, K. I. Caputi, I. Aretxaga, et al. "Compact Starbursts in z 3-6 Submillimeter Galaxies Revealed by ALMA". In: 810, 133 (Sept. 2015), p. 133. DOI: 10.1088/0004-637X/810/2/133. arXiv: 1411.5038.

[207] S. Ikarashi, R. J. Ivison, K. I. Caputi, K. Nakanishi, et al. "Extremely Red Submillimeter Galaxies: New z 4-6 Candidates Discovered using ALMA and Jansky VLA". In: 835, 286 (Feb. 2017), p. 286. DOI: 10.3847/1538-4357/835/2/286. arXiv: 1701.01448.

[208] O. Ilbert, S. Arnouts, E. Le Floc'h, et al. "Evolution of the specific star formation rate function at z 1.4 Dissecting the mass-SFR plane in COSMOS and GOODS". In: 579, A2 (July 2015), A2. DOI: 10.1051/0004-6361/201425176. arXiv: 1410.4875.

[209] O. Ilbert, S. Arnouts, H. J. McCracken, et al. "Accurate photometric redshifts for the CFHT legacy survey calibrated using the VIMOS VLT deep survey". In: 457 (Oct. 2006), pp. 841–856. DOI: 10.1051/0004-6361:20065138.

[210] O. Ilbert, H. J. McCracken, et al. "Mass assembly in quiescent and star-forming galaxies since z 4 from UltraVISTA". In: 556, A55 (Aug. 2013), A55. DOI: 10.1051/0004-6361/201321100. arXiv: 1301.3157.

[211] Ilbert et al. "Cosmos Photometric Redshifts with 30-Bands for 2-deg²". In: 690 (Jan. 2009), pp. 1236–1249. DOI: 10.1088/0004-637X/690/2/1236. arXiv: 0809.2101.

[212] Akio K. Inoue et al. "Detection of an oxygen emission line from a high-redshift galaxy in the reionization epoch". In: Science 352 (June 2016), pp. 1559–1562. DOI: 10.1126/science.aaf0714.

[213] R. J. Ivison, T. R. Greve, et al. "The SCUBA HAlf Degree Extragalactic Survey - III. Identification of radio and mid-infrared counterparts to submillimetre galaxies". In: 380 (Sept. 2007), pp. 199–228. DOI: 10.1111/j.1365-2966.2007.12044.x. eprint: astro-ph/0702544.

[214] R. J. Ivison, A. J. R. Lewis, et al. "The Space Density of Luminous Dusty Star-forming Galaxies at z 4: SCUBA-2 and LABOCA Imaging of Ultrared Galaxies from Herschel-ATLAS". In: 832, 78 (Nov. 2016), p. 78. DOI: 10.3847/0004-637X/832/1/78. arXiv: 1611.00762.

[215] T.-H. Jarrett et al. "2MASS Extended Sources in the Zone of Avoidance". In: 120 (July 2000), pp. 298–313. DOI: 10.1086/301426. eprint: astro-ph/0005017.

[216] Jing et al. "The Dependence of Dark Halo Clustering on Formation Epoch and Concentration Parameter". In: 657 (Mar. 2007), pp. 664–668. DOI: 10.1086/511130. arXiv: astro-ph/0610099 [astro-ph].

[217] T. L. Johnson et al. "Lens Models and Magnification Maps of the Six Hubble Frontier Fields Clusters". In: 797, 48 (Dec. 2014), p. 48. DOI: 10.1088/0004-637X/797/1/48. arXiv: 1405.0222.

[218] Russell Johnston et al. "The evolving relation between star formation rate and stellar mass in the VIDEO survey since z = 3". In: 453 (Nov. 2015), pp. 2540–2557. DOI: 10.1093/mnras/stv1715.

[219] M. Juvela et al. "The degeneracy between dust colour temperature and spectral index. Comparison of methods for estimating the β(T) relation". In: 556, A63 (Aug. 2013), A63. DOI: 10.1051/0004-6361/201220910. arXiv: 1305.2130.

[220] A. Karim et al. "An ALMA survey of submillimetre galaxies in the Extended Chandra Deep Field South: high-resolution 870 μm source counts". In: 432 (June 2013), pp. 2–9. DOI: 10.1093/mnras/stt196. arXiv: 1210.0249 [astro-ph.CO].

[221] Jeyhan S. Kartaltepe et al. "A Multiwavelength Study of a Sample of 70 μm Selected Galaxies in the COSMOS Field. II. The Role of Mergers in Galaxy Evolution". In: 721 (Sept. 2010), pp. 98–123. DOI: 10.1088/0004-637X/721/1/98. arXiv: 1006.4956.

[222] Y. Kato et al. "Herschel protocluster survey: a search for dusty star-forming galaxies in protoclusters at z = 2-3". In: 460 (Aug. 2016), pp. 3861–3872. DOI: 10.1093/mnras/stw1237. arXiv: 1605.07370.

[223] D. D. Kelson. "Decoding the Star-Forming Main Sequence or: How I Learned to Stop Worrying and Love the Central Limit Theorem". In: ArXiv e-prints (June 2014). arXiv: 1406.5191.

[224] Kennicutt. "Star Formation in Galaxies Along the Hubble Sequence". In: 36 (1998), pp. 189–232. DOI: 10.1146/annurev.astro.36.1.189. eprint: astro-ph/9807187.

[225] Kennicutt and Evans. "Star Formation in the Milky Way and Nearby Galaxies". In: Annual Review of Astronomy and Astrophysics 50 (Sept. 2012), pp. 531–608. DOI: 10.1146/annurev-astro-081811-125610. arXiv: 1204.3552.

[226] A. Kirkpatrick et al. "A Controlled Study of Cold Dust Content in Galaxies from z = 0-2". In: 843, 71 (July 2017), p. 71. DOI: 10.3847/1538-4357/aa76dc. arXiv: 1705.10846.

[227] J.-P. Kneib et al. "Cluster lenses". In: 19, 47 (Nov. 2011), p. 47. DOI: 10.1007/s00159-011-0047-3. arXiv: 1202.0185 [astro-ph.CO].

[228] Rüdiger Kneissl et al. "Using ALMA to resolve the nature of the early star-forming large-scale structure PLCK G073.4-57.5". In: ArXiv e-prints, arXiv:1804.06581 (Apr. 2018), arXiv:1804.06581. arXiv: 1804.06581.

[229] Dale D. Kocevski et al. "Are Compton-thick AGNs the Missing Link between Mergers and Black Hole Growth?" In: 814, 104 (Dec. 2015), p. 104. DOI: 10.1088/0004-637X/814/2/104.

[230] M. P. Koprowski et al. "The evolving far-IR galaxy luminosity function and dust-obscured star formation rate density out to z5." In: 471 (Nov. 2017), pp. 4155–4169. DOI: 10.1093/mnras/stx1843. arXiv: 1706.00426.

[231] Mariska Kriek et al. "The Detection of a Red Sequence of Massive Field Galaxies at z 2.3 and Its Evolution to z 0". In: 682 (Aug. 2008), pp. 896–906. DOI: 10.1086/589677. arXiv: 0804.4175.

[232] Lacey et al. "A unified multiwavelength model of galaxy formation". In: 462 (Nov. 2016), pp. 3854–3911. DOI: 10.1093/mnras/stw1888. arXiv: 1509.08473.

[233] G. Lagache, A. Abergel, et al. "First detection of the warm ionised medium dust emission. Implication for the cosmic far-infrared background". In: 344 (Apr. 1999), pp. 322–332. arXiv: astro-ph/9901059.

[234] G. Lagache, M. Cousin, et al. "The [CII] 158 μm line emission in high-redshift galaxies". In: 609, A130 (Feb. 2018), A130. DOI: 10.1051/0004-6361/201732019.

[235] G. Lagache, J.-L. Puget, et al. "Dusty Infrared Galaxies: Sources of the Cosmic Infrared Background". In: 43 (Sept. 2005), pp. 727–768. DOI: 10.1146/annurev.astro.43.072103.150606. eprint: astro-ph/0507298.

[236] Stephen D. Landy et al. "Bias and Variance of Angular Correlation Functions". In: 412 (July 1993), p. 64. DOI: 10.1086/172900.

[237] Dustin Lang et al. The Tractor: Probabilistic astronomical source detection and measurement. Astrophysics Source Code Library. Apr. 2016. ascl: 1604.008.

[238] A. Lapi et al. “Herschel-ATLAS Galaxy Counts and High-redshift Luminosity Functions: The Formation of Massive Early-type Galaxies”. In: 742, 24 (Nov. 2011), p. 24. DOI: 10.1088/0004-637X/742/1/24. arXiv: 1108.3911.

[239] R. B. Larson et al. “The evolution of disk galaxies and the origin of S0 galaxies”. In: 237 (May 1980), pp. 692–707. DOI: 10.1086/157917.

[240] Alexie Leauthaud et al. “A Theoretical Framework for Combining Techniques that Probe the Link Between Galaxies and Dark Matter”. In: 738, 45 (Sept. 2011), p. 45. DOI: 10.1088/0004-637X/738/1/45.

[241] N. Lee et al. “The fine line between normal and starburst galaxies”. In: 471 (Oct. 2017), pp. 2124–2142. DOI: 10.1093/mnras/stx1753. arXiv: 1710.02757.

[242] J. Leja et al. “Reconciling the Observed Star-forming Sequence with the Observed Stellar Mass Function”. In: 798, 115 (Jan. 2015), p. 115. DOI: 10.1088/0004-637X/798/2/115. arXiv: 1407.1842.

[243] G. Lemaitre. “Expansion of the universe, A homogeneous universe of constant mass and increasing radius accounting for the radial velocity of extra- galactic nebulae”. In: 91 (Mar. 1931), pp. 483–490. DOI: 10.1093/mnras/91.5.483.

[244] B. C. Lemaux et al. “The VIMOS Ultra Deep Survey: Emerging from the Dark, a Massive Proto- Cluster at z 4.57”. In: ArXiv e-prints, arXiv:1703.10170 (Mar. 2017), arXiv:1703.10170. arXiv: 1703.10170.

[245] D. Lemke et al. “ISOPHOT - capabilities and performance.” In: 315 (Nov. 1996), pp. L64–L70.

[246] A. J. R. Lewis et al. “Ultra-Red Galaxies Signpost Candidate Proto-Clusters at High Redshift”. In: ArXiv e-prints, arXiv:1711.08803 (Nov. 2017), arXiv:1711.08803. arXiv: 1711.08803.

[247] Tony Y. Li et al. “Connecting CO Intensity Mapping to Molecular Gas and Star Formation in the Epoch of Galaxy Assembly”. In: 817, 169 (Feb. 2016), p. 169. DOI: 10.3847/0004-637X/817/2/169.

[248] Lichen Liang et al. “Submillimetre flux as a probe of molecular ISM mass in high-z galaxies”. In: 478 (July 2018), pp. L83–L88. DOI: 10.1093/mnrasl/sly071.

[249] S. J. Lilly et al. “The Canada-France Redshift Survey: The Luminosity Density and Star Formation History of the Universe to Z approximately 1”. In: 460 (Mar. 1996), p. L1. DOI: 10.1086/309975. arXiv: astro-ph/9601050 [astro-ph].

[250] D. Liu et al. ""Super-deblended" Dust EmissiPope et al. 2010on in Galaxies: I. the GOODS-North Catalog and the Cosmic Star Formation Rate Density out to Redshift 6". In: ArXiv e-prints, arXiv:1703.05281 (Mar. 2017). arXiv: 1703.05281.

[251] B. Lo Faro et al. "Characterizing the UV-to-NIR shape of the dust attenuation curve of IR luminous galaxies up to z
2". In: 472 (Dec. 2017), pp. 1372–1391. DOI: 10.1093/mnras/stx1901. arXiv: 1707.09805.

[252] C. J. Lonsdale, D. Farrah, et al. "Ultraluminous Infrared Galaxies". In: Astrophysics Update 2, Springer Praxis Books. ISBN 978-3-540-30312-1. Praxis Publishing Ltd, Chichester, UK, 2006, p. 285. 2006, p. 285. DOI: 10.1007/3-540-30313-8_9.

[253] C. J. Lonsdale, S. E. Persson, et al. "Infrared observations of interacting/merging galaxies." In: 287 (Dec. 1984), pp. 95–107. DOI: 10.1086/162666.

[254] J. M. Lotz et al. "The Major and Minor Galaxy Merger Rates at z 1.5". In: 742, 103 (Dec. 2011), p. 103. DOI: 10.1088/0004-637X/742/2/103. arXiv: 1108.2508.

[255] Christopher C. Lovell et al. "Characterising and identifying galaxy protoclusters". In: 474 (Mar. 2018), pp. 4612–4628. DOI: 10.1093/mnras/stx3090.

[256] D. Lutz. "Far-Infrared Surveys of Galaxy Evolution". In: 52 (Aug. 2014), pp. 373–414. DOI: 10.1146/annurev-astro-081913-035953. arXiv: 1403.3334.

[257] Z. Ma et al. "Co-evolution of Extreme Star Formation and Quasars: Hints from Herschel and the Sloan Digital Sky Survey". In: 811, 58 (Sept. 2015), p. 58. DOI: 10.1088/0004-637X/811/1/58. arXiv: 1501.01240.

[258] T. P. MacKenzie et al. "Disentangling a group of lensed submm galaxies at z
2.9". In: 445 (Nov. 2014), pp. 201–212. DOI: 10.1093/mnras/stu1623. arXiv: 1312.0950.

[259] MacKenzie et al. "SCUBA-2 follow-up of Herschel-SPIRE observed Planck over-densities". In: 468 (July 2017), pp. 4006–4017. DOI: 10.1093/mnras/stx512. arXiv: 1703.02074.

[260] Piero Madau et al. "High-redshift galaxies in the Hubble Deep Field: colour selection and star formation history to z~4". In: 283 (Dec. 1996), pp. 1388–1404. DOI: 10.1093/mnras/283.4.1388. arXiv: astro-ph/9607172 [astro-ph].

[261] P. Madau et al. "Cosmic Star-Formation History". In: 52 (Aug. 2014), pp. 415–486. DOI: 10.1146/annurev-astro-081811-125615. arXiv: 1403.0007.

[262] Magdis, Daddi, et al. “The Evolving Interstellar Medium of Star-forming Galaxies since z = 2 as Probed by Their Infrared Spectral Energy Distributions”. In: 760, 6 (Nov. 2012), p. 6. DOI: 10.1088/0004-637X/760/1/6. arXiv: 1210.1035.

[263] Magdis, D. Elbaz, et al. “GOODS-Herschel: a population of 24 μm dropout sources at z < 2”. In: 534, A15 (Oct. 2011), A15. DOI: 10.1051/0004-6361/201117649. arXiv: 1108.0838.

[264] Magdis, D. Rigopoulou, E. Daddi, et al. “Dust and gas in star-forming galaxies at z 3. Extending galaxy uniformity to 11.5 billion years”. In: 603, A93 (July 2017), A93. DOI: 10.1051/0004-6361/201731037. arXiv: 1705.06296.

[265] Magdis, D. Rigopoulou, R. Hopwood, et al. “A Far-infrared Spectroscopic Survey of Intermediate Redshift (Ultra) Luminous Infrared Galaxies”. In: 796, 63 (Nov. 2014), p. 63. DOI: 10.1088/0004-637X/796/1/63. arXiv: 1409.5605 [astro-ph.GA].

[266] B. Magnelli, D. Lutz, et al. “The evolution of the dust temperatures of galaxies in the SFR-M plane up to z $\sim$ 2”. In: 561, A86 (Jan. 2014), A86. DOI: 10.1051/0004-6361/201322217. arXiv: 1311.2956.

[267] B. Magnelli, P. Popesso, et al. “The deepest Herschel-PACS far-infrared survey: number counts and infrared luminosity functions from combined PEP/GOODS-H observations”. In: 553, A132 (May 2013), A132. DOI: 10.1051/0004-6361/201321371. arXiv: 1303.4436.

[268] R. Maiolino et al. “Evidence of strong quasar feedback in the early Universe”. In: 425 (Sept. 2012), pp. L66–L70. DOI: 10.1111/j.1745-3933.2012.01303.x. arXiv: 1204.2904.

[269] K. Małek et al. “[Ultra] luminous infrared galaxies selected at 90 μm in the AKARI deep field: a study of AGN types contributing to their infrared emission”. In: 598, A1 (Feb. 2017), A1. DOI: 10.1051/0004-6361/201527969. arXiv: 1611.07410.

[270] C. Mancuso et al. “The Quest for Dusty Star-forming Galaxies at High Redshift z 4”. In: 823, 128 (June 2016), p. 128. DOI: 10.3847/0004-637X/823/2/128. arXiv: 1604.02507.

[271] F. Mannucci et al. “A fundamental relation between mass, star formation rate and metallicity in local and high-redshift galaxies”. In: 408 (Nov. 2010), pp. 2115–2127. DOI: 10.1111/j.1365-2966.2010.17291.x. arXiv: 1005.0006.

[272] C. B. Markwardt. “Non-linear Least-squares Fitting in IDL with MPFIT”. In: Astronomical Data Analysis Software and Systems XVIII. Ed. by D. A. Bohlender et al. Vol. 411. Astronomical Society of the Pacific Conference Series. Sept. 2009, p. 251. arXiv: 0902.2850 [astro-ph.IM].

[273] D. P. Marrone et al. “Galaxy growth in a massive halo in the first billion years of cosmic history”. In: 553 (Jan. 2018), pp. 51–54. DOI: 10.1038/nature24629. arXiv: 1712.03020.

[274] G. Marsden et al. “BLAST: Resolving the Cosmic Submillimeter Background”. In: 707 (Dec. 2009), pp. 1729–1739. DOI: 10.1088/0004-637X/707/2/1729. arXiv: 0904.1205 [astro-ph.CO].

[275] G. Martin et al. “The limited role of galaxy mergers in driving stellar mass growth over cosmic time”. In: 472 (Nov. 2017), pp. L50–L54. DOI: 10.1093/mnrasl/slx136. arXiv: 1708.09396.

[276] N. S. Martis et al. “The Evolution of the Fractions of Quiescent and Star-forming Galaxies as a Function of Stellar Mass Since z = 3: Increasing Importance of Massive, Dusty Star-forming Galaxies in the Early Universe”. In: 827, L25 (Aug. 2016), p. L25. DOI: 10.3847/2041-8205/827/2/L25. arXiv: 1606.04090.

[277] Jorryt Matthee et al. “The origin of scatter in the star formation rate - stellar mass relation”. In: ArXiv e-prints, arXiv:1805.05956 (May 2018), arXiv:1805.05956. arXiv: 1805.05956.

[278] J. Matthee et al. “ALMA Reveals Metals yet No Dust within Multiple Components in CR7”. In: 851, 145 (Dec. 2017), p. 145. DOI: 10.3847/1538-4357/aa9931.

[279] Christopher F. McKee et al. “Theory of Star Formation”. In: Annual Review of Astronomy and Astrophysics 45 (Sept. 2007), pp. 565–687. DOI: 10.1146/annurev.astro.45.051806.110602. arXiv: 0707.3514.

[280] Simona Mei et al. “Star-forming Blue ETGs in Two Newly Discovered Galaxy Overdensities in the HUDF at z=1.84 and 1.9: Unveiling the Progenitors of Passive ETGs in Cluster Cores”. In: 804, 117 (May 2015), p. 117. DOI: 10.1088/0004-637X/804/2/117. arXiv: 1403.7524.

[281] E. Merlin et al. “T-PHOT version 2.0: Improved algorithms for background subtraction, local convolution, kernel registration, and new options”. In: 595, A97 (Nov. 2016), A97. DOI: 10.1051/0004-6361/201628751. arXiv: 1609.00146 [astro-ph.IM].

[282] G. R. Meurer et al. “Dust Absorption and the Ultraviolet Luminosity Density at z ˜ 3 as Calibrated by Local Starburst Galaxies”. In: 521 (Aug. 1999), pp. 64–80. DOI: 10.1086/307523. eprint: astro-ph/9903054.

[283] M. J. Michałowski, J. S. Dunlop, et al. “The stellar masses and specific star-formation rates of submillimetre galaxies”. In: 541, A85 (May 2012), A85. DOI: 10.1051/0004-6361/201016308. arXiv: 1108.6058 [astro-ph.CO].

[284] M. J. Michałowski, C. C. Hayward, et al. “Determining the stellar masses of sub-millimetre galaxies: the critical importance of star formation histories”. In: 571, A75 (Nov. 2014), A75. DOI: 10.1051/0004-6361/201424174. arXiv: 1405.2335.

[285] O. Miettinen et al. “(Sub)millimetre interferometric imaging of a sample of COSMOS/AzTEC submillimetre galaxies. II. The spatial extent of the radio-emitting regions”. In: 584, A32 (Dec. 2015), A32. DOI: 10.1051/0004-6361/201526589. arXiv: 1509.07147.

[286] George Miley et al. “Distant radio galaxies and their environments”. In: Astronomy and Astrophysics Review 15 (Feb. 2008), pp. 67–144. DOI: 10.1007/s00159-007-0008-z.

[287] Miller, S. C. Chapman, et al. “A massive core for a cluster of galaxies at a redshift of 4.3”. In: 556 (Apr. 2018), pp. 469–472. DOI: 10.1038/s41586-018-0025-2.

[288] Miller, Hayward, et al. “The bias of the submillimetre galaxy population: SMGs are poor tracers of the most-massive structures in the z 2 Universe”. In: 452 (Sept. 2015), pp. 878–883. DOI: 10.1093/mnras/stv1267.

[289] H. J. Mo et al. “On the Error Estimates of Correlation Functions”. In: 392 (June 1992), p. 452. DOI: 10.1086/171444.

[290] H. Mo et al. Galaxy Formation and Evolution. May 2010.

[291] L. Morselli et al. “Primordial environment of super massive black holes: large-scale galaxy overdensities around z 6 quasars with LBT”. In: 568, A1 (Aug. 2014), A1. DOI: 10.1051/0004-6361/201423853. arXiv: 1406.3961.

[292] Stuart I. Muldrew et al. “What are protoclusters? - Defining high-redshift galaxy clusters and protoclusters”. In: 452 (Sept. 2015), pp. 2528–2539. DOI: 10.1093/mnras/stv1449.

[293] Stuart I. Muldrew et al. “Galaxy evolution in protoclusters”. In: 473 (Jan. 2018), pp. 2335–2347. DOI: 10.1093/mnras/stx2454.

[294] J. R. Mullaney et al. “Defining the intrinsic AGN infrared spectral energy distribution and measuring its contribution to the infrared output of composite galaxies”. In: 414 (June 2011), pp. 1082–1110. DOI: 10.1111/j.1365-2966.2011.18448.x. arXiv: 1102.1425.

[295] Alejandra M. Muñoz Arancibia et al. “Properties of submillimetre galaxies in a semi-analytic model using the ‘Count Matching’ approach: application to the ECDF-S”. In: 446 (Jan. 2015), pp. 2291–2311. DOI: 10.1093/mnras/stu2237.

[296] H. Murakami et al. “The Infrared Astronomical Mission AKARI*”. In: 59 (Oct. 2007), S369–S376. DOI: 10.1093/pasj/59.sp2.S369. arXiv: 0708.1796.

[297] E. J. Murphy et al. “Radio and Mid-infrared Properties of Compact Starbursts: Distancing Themselves from the Main Sequence”. In: 768, 2 (May 2013), p. 2. DOI: 10.1088/0004-637X/768/1/2. arXiv: 1302.5704.

[298] D. Narayanan et al. “The IRX-β dust attenuation relation in cosmological galaxy formation simulations”. In: 474 (Feb. 2018), pp. 1718–1736. DOI: 10.1093/mnras/stx2860. arXiv: 1705.05858.

[299] Narayanan et al. “The formation of submillimetre-bright galaxies from gas infall over a billion years”. In: 525 (Sept. 2015), pp. 496–499. DOI: 10.1038/nature15383. arXiv: 1509.06377.

[300] M. Negrello et al. “The Herschel-ATLAS: a sample of 500 μm-selected lensed galaxies over 600 deg^2”. In: 465 (Mar. 2017), pp. 3558–3580. DOI: 10.1093/mnras/stw2911. arXiv: 1611.03922.

[301] G. Neugebauer et al. “The Infrared Astronomical Satellite (IRAS) mission”. In: 278 (Mar. 1984), pp. L1–L6. DOI: 10.1086/184209.

[302] H. T. Nguyen et al. “HerMES: The SPIRE confusion limit”. In: 518, L5 (July 2010), p. L5. DOI: 10.1051/0004-6361/201014680. arXiv: 1005.2207.

[303] Akatoki Noboriguchi et al. “Optical properties of infrared-bright dust-obscured galaxies viewed with Subaru Hyper Suprime-Cam”. In: ArXiv e-prints, arXiv:1803.09951 (Mar. 2018), arXiv:1803.09951. arXiv: 1803.09951.

[304] Noeske et al. “Star Formation in AEGIS Field Galaxies since z=1.1: The Dominance of Gradually Declining Star Formation, and the Main Sequence of Star-forming Galaxies”. In: 660 (May 2007), pp. L43–L46. DOI: 10.1086/517926. eprint: astro-ph/0701924.

[305] S. Noll et al. “Analysis of galaxy spectral energy distributions from far-UV to far-IR with CIGALE: studying a SINGS test sample”. In: 507 (Dec. 2009), pp. 1793–1813. DOI: 10.1051/0004-6361/200912497. arXiv: 0909.5439.

[306] Peder Norberg et al. “Massive dark matter haloes around bright isolated galaxies in the 2dFGRS”. In: 383 (Jan. 2008), pp. 646–662. DOI: 10.1111/j.1365-2966.2007.12583.x.

[307] R. P. Norris et al. “EMU: Evolutionary Map of the Universe”. In: 28 (Aug. 2011), pp. 215–248. DOI: 10.1071/AS11021. arXiv: 1106.3219.

[308] Kristina Nyland et al. “An Application of Multi-band Forced Photometry to One Square Degree of SERVS: Accurate Photometric Redshifts and Implications for Future Science”. In: The Astrophysical Journal Supplement Series 230, 9 (May 2017), p. 9. DOI: 10.3847/1538-4365/aa6fed.

[309] P. A. Oesch et al. “A Remarkably Luminous Galaxy at z=11.1 Measured with Hubble Space Telescope Grism Spectroscopy”. In: 819, 129 (Mar. 2016), p. 129. DOI: 10.3847/0004-637X/819/2/129. arXiv: 1603.00461.

[310] S. J. Oliver, J. Bock, et al. “The Herschel Multi-tiered Extragalactic Survey: HerMES”. In: 424 (Aug. 2012), pp. 1614–1635. DOI: 10.1111/j.1365-2966.2012.20912.x. arXiv: 1203.2562.

[311] S. J. Oliver, L. Wang, et al. “HerMES: SPIRE galaxy number counts at 250, 350, and 500 μm”. In: 518, L21 (July 2010), p. L21. DOI: 10.1051/0004-6361/201014697. arXiv: 1005.2184.

[312] Seb Oliver et al. “The European Large Area ISO Survey - I. Goals, definition and observations”. In: 316 (Aug. 2000), pp. 749–767. DOI: 10.1046/j.1365-8711.2000.03550.x. arXiv: astro-ph/0003263.

[313] J. P. Ostriker et al. “A Numerical Study of the Stability of Flattened Galaxies: or, can Cold Galaxies Survive?” In: 186 (Dec. 1973), pp. 467–480. DOI: 10.1086/152513.

[314] I. Oteo, R. J. Ivison, L. Dunne, et al. “An extreme proto-cluster of luminous dusty starbursts in the early Universe”. In: ArXiv e-prints (Sept. 2017). arXiv: 1709.02809.

[315] I. Oteo, R. J. Ivison, M. Negrello, et al. “Witnessing the birth of the red sequence: the physical scale and morphology of dust emission in hyper-luminous starbursts in the early Universe”. In: ArXiv e-prints, arXiv:1709.04191 (Sept. 2017). arXiv: 1709.04191.

[316] I. Oteo, Smail, et al. “Low-redshift analogs of submm galaxies: a diverse population”. In: ArXiv e-prints (July 2017). arXiv: 1707.05329.

[317] Masami Ouchi et al. “The Discovery of Primeval Large-Scale Structures with Forming Clusters at Redshift 6”. In: 620 (Feb. 2005), pp. L1–L4. DOI: 10.1086/428499.

[318] Overzier. “The realm of the galaxy protoclusters. A review”. In: 24, 14 (Nov. 2016), p. 14. DOI: 10.1007/s00159-016-0100-3. arXiv: 1610.05201.

[319] M. Pannella et al. “GOODS-Herschel: Star Formation, Dust Attenuation, and the FIR-radio Correlation on the Main Sequence of Star-forming Galaxies up to z 4”. In: 807, 141 (July 2015), p. 141. DOI: 10.1088/0004-637X/807/2/141. arXiv: 1407.5072.

[320] Padeli P. Papadopoulos et al. “C I Emission in Ultraluminous Infrared Galaxies as a Molecular Gas Mass Tracer”. In: 615 (Nov. 2004), pp. L29–L32. DOI: 10.1086/426059. arXiv: astro-ph/0409559.

[321] C. Pappalardo, G. J. Bendo, et al. “The Herschel Virgo Cluster Survey. XVII. SPIRE point-source catalogs and number counts”. In: 573, A129 (Jan. 2015), A129. DOI: 10.1051/0004-6361/201424549. arXiv: 1410.1879.

[322] C. Pappalardo, L. Bizzocchi, et al. “The Herschel Virgo Cluster Survey. XIX. Physical properties of low luminosity FIR sources at z 0.5”. In: 589, A11 (May 2016), A11. DOI: 10.1051/0004-6361/201528008. arXiv: 1602.02161.

[323] Isabelle Pâris et al. “The Sloan Digital Sky Survey Quasar Catalog: Fourteenth data release”. In: 613, A51 (May 2018), A51. DOI: 10.1051/0004-6361/201732445.

[324] R. B. Partridge et al. "Are Young Galaxies Visible? II. The Integrated Background". In: 148 (May 1967), p. 377. DOI: 10.1086/149161.

[325] G. Patanchon et al. "Submillimeter Number Counts from Statistical Analysis of BLAST Maps". In: 707 (Dec. 2009), pp. 1750–1765. DOI: 10.1088/0004-637X/707/2/1750. arXiv: 0906.0981 [astro-ph.CO].

[326] R. Pavesi et al. "Hidden in plain sight: a massive, dusty starburst in a galaxy protocluster at z=5.7 in the COSMOS field". In: ArXiv e-prints (Mar. 2018). arXiv: 1803.08048.

[327] C. Pearson et al. "SPIRE point source photometry: within the Herschel interactive processing environment (HIPE)". In: Experimental Astronomy 37 (July 2014), pp. 175–194. DOI: 10.1007/s10686-013-9351-4. arXiv: 1401.2036 [astro-ph.IM].

[328] Pearson, Eales, et al. "H-ATLAS: estimating redshifts of Herschel sources from sub-mm fluxes". In: 435 (Nov. 2013), pp. 2753–2763. DOI: 10.1093/mnras/stt1369. arXiv: 1308.5681.

[329] Pearson, Wang, P. D. Hurley, et al. "Main sequence of star forming galaxies beyond the Herschel confusion limit". In: ArXiv e-prints, arXiv:1804.03482 (Apr. 2018), arXiv:1804.03482. arXiv: 1804.03482.

[330] Pearson, Wang, F. F. S. van der Tak, et al. "De-blending deep Herschel surveys: A multi-wavelength approach". In: 603, A102 (July 2017), A102. DOI: 10.1051/0004-6361/201630105.

[331] P. J. E. Peebles. "Large-scale background temperature and mass fluctuations due to scale- invariant primeval perturbations". In: 263 (Dec. 1982), pp. L1–L5. DOI: 10.1086/183911.

[332] P. J. Peebles et al. "The cosmological constant and dark energy". In: Reviews of Modern Physics 75 (Apr. 2003), pp. 559–606. DOI: 10.1103/RevModPhys.75.559. eprint: astro-ph/0207347.

[333] Y.-j. Peng et al. "Mass and Environment as Drivers of Galaxy Evolution in SDSS and zCOSMOS and the Origin of the Schechter Function". In: 721 (Sept. 2010), pp. 193–221. DOI: 10.1088/0004-637X/721/1/193. arXiv: 1003.4747 [astro-ph.CO].

[334] L. Pentericci et al. “Tracing the Reionization Epoch with ALMA: [C II] Emission in z 7 Galaxies”. In: 829, L11 (Sept. 2016), p. L11. DOI: 10.3847/2041-8205/829/1/L11.

[335] G. L. Pilbratt et al. “Herschel Space Observatory. An ESA facility for far-infrared and submillimetre astronomy”. In: 518, L1 (July 2010), p. L1. DOI: 10.1051/0004-6361/201014759. arXiv: 1005.5331 [astro-ph.IM].

[336] Planck Collaboration, P. A. R. Ade, N. Aghanim, F. Argüeso, M. Arnaud, M. Ashdown, J. Aumont, C. Baccigalupi, A. Balbi, et al. “Planck early results. XIII. Statistical properties of extragalactic radio sources in the Planck Early Release Compact Source Catalogue”. In: 536, A13 (Dec. 2011), A13. DOI: 10.1051/0004-6361/201116471. arXiv: 1101.2044.

[337] Planck Collaboration, P. A. R. Ade, N. Aghanim, F. Argüeso, M. Arnaud, M. Ashdown, J. Aumont, C. Baccigalupi, A. J. Banday, et al. “Planck 2015 results. XXVI. The Second Planck Catalogue of Compact Sources”. In: 594, A26 (Sept. 2016), A26. DOI: 10.1051/0004-6361/201526914.

[338] Planck Collaboration, P. A. R. Ade, N. Aghanim, M. Arnaud, M. Ashdown, et al. “Planck 2015 results. XIII. Cosmological parameters”. In: 594, A13 (Sept. 2016), A13. DOI: 10.1051/0004-6361/201525830. arXiv: 1502.01589.

[339] Planck Collaboration, P. A. R. Ade, N. Aghanim, M. Arnaud, J. Aumont, C. Baccigalupi, A. J. Banday, R. B. Barreiro, N. Bartolo, E. Battaner, K. Benabed, A. Benoit-Lévy, et al. “Planck intermediate results. XXXIX. The Planck list of high-redshift source candidates”. In: 596, A100 (Dec. 2016), A100. DOI: 10.1051/0004-6361/201527206. arXiv: 1508.04171.

[340] Planck Collaboration, P. A. R. Ade, N. Aghanim, M. Arnaud, J. Aumont, C. Baccigalupi, A. J. Banday, R. B. Barreiro, N. Bartolo, E. Battaner, K. Benabed, Benoit-Lévy, et al. “Planck intermediate results. XXXIX. The Planck list of high-redshift source candidates”. In: 596, A100 (Dec. 2016), A100. DOI: 10.1051/0004-6361/201527206.

[341] Planck Collaboration, N. Aghanim, B. Altieri, et al. “Planck intermediate results. XXVII. High-redshift infrared galaxy overdensity candidates and lensed sources discovered by Planck and confirmed by Herschel-SPIRE”. In: 582, A30 (Oct. 2015), A30. DOI: 10.1051/0004-6361/201424790.

[342] Planck Collaboration, N. Aghanim, M. Arnaud, et al. "Planck 2015 results. XXII. A map of the thermal Sunyaev-Zeldovich effect". In: 594, A22 (Sept. 2016), A22. DOI: 10.1051/0004-6361/201525826.

[343] A. Poglitsch et al. "The Photodetector Array Camera and Spectrometer (PACS) on the Herschel Space Observatory". In: 518, L2 (July 2010), p. L2. DOI: 10.1051/0004-6361/201014535. arXiv: 1005.1487 [astro-ph.IM].

[344] M. Polletta et al. "Spectral Energy Distributions of Hard X-Ray Selected Active Galactic Nuclei in the XMM-Newton Medium Deep Survey". In: 663 (July 2007), pp. 81–102. DOI: 10.1086/518113. eprint: astro-ph/0703255.

[345] A. Pope and R.-R. Chary. "Searching for the Highest Redshift Sources in 250-500 μm Submillimeter Surveys". In: 715 (June 2010), pp. L171–L175. DOI: 10.1088/2041-8205/715/2/L171. arXiv: 1005.0386.

[346] A. Pope, R.-R. Chary, et al. "Mid-Infrared Spectral Diagnosis of Submillimeter Galaxies". In: 675, 1171-1193 (Mar. 2008), pp. 1171–1193. DOI: 10.1086/527030. arXiv: 0711.1553.

[347] A. Pope, A. Montaña, et al. "Early Science with the Large Millimeter Telescope: Detection of Dust Emission in Multiple Images of a Normal Galaxy at z 4 Lensed by a Frontier Fields Cluster". In: 838, 137 (Apr. 2017), p. 137. DOI: 10.3847/1538-4357/aa6573. arXiv: 1703.04535.

[348] Gergö Popping et al. "The dust content of galaxies from z = 0 to z = 9". In: 471 (Nov. 2017), pp. 3152–3185. DOI: 10.1093/mnras/stx1545.

[349] Francisco Prada et al. "Halo concentrations in the standard Λ cold dark matter cosmology". In: 423 (July 2012), pp. 3018–3030. DOI: 10.1111/j.1365-2966.2012.21007.x. arXiv: 1104.5130.

[350] W. H. Press et al. "Formation of Galaxies and Clusters of Galaxies by Self-Similar Gravitational Condensation". In: 187 (Feb. 1974), pp. 425–438. DOI: 10.1086/152650.

[351] Puget et al. "Tentative detection of a cosmic far-infrared background with COBE." In: 308 (Apr. 1996), p. L5.

[352] C. Ragone-Figueroa et al. "BCG mass evolution in cosmological hydro-simulations". In: 479 (Sept. 2018), pp. 1125–1136. DOI: 10.1093/mnras/sty1639.

[353] A. Raichoor et al. "The Next Generation Virgo Cluster Survey. XV. The Photometric Redshift Estimation for Background Sources". In: 797, 102 (Dec. 2014), p. 102. DOI: 10.1088/0004-637X/797/2/102. arXiv: 1410.2276.

[354] N. Rangwala et al. "Observations of Arp 220 Using Herschel-SPIRE: An Unprecedented View of the Molecular Gas in an Extreme Star Formation Environment". In: 743, 94 (Dec. 2011), p. 94. DOI: 10.1088/0004-637X/743/1/94. arXiv: 1106.5054.

[355] T. D. Rawle et al. "A complete census of Herschel-detected infrared sources within the HST Frontier Fields". In: 459 (June 2016), pp. 1626–1645. DOI: 10.1093/mnras/stw712. arXiv: 1508.00586.

[356] Renaud et al. "Starbursts triggered by intergalactic tides andinterstellar compressive turbulence". In: 442 (July 2014), pp. L33–L37. DOI: 10.1093/mnrasl/slu050. arXiv: 1403.7316.

[357] D. A. Riechers, C. M. Bradford, et al. "A dust-obscured massive maximum-starburst galaxy at a redshift of 6.34". In: 496 (Apr. 2013), pp. 329–333. DOI: 10.1038/nature12050. arXiv: 1304.4256 [astro-ph.CO].

[358] D. A. Riechers, T. K. D. Leung, et al. "Rise of the Titans: A Dusty, Hyper-luminous 870 μm Riser Galaxy at z
6". In: 850, 1 (Nov. 2017), p. 1. DOI: 10.3847/1538-4357/aa8ccf. arXiv: 1705.09660.

[359] G. H. Rieke et al. "The Multiband Imaging Photometer for Spitzer (MIPS)". In: 154 (Sept. 2004), pp. 25–29. DOI: 10.1086/422717.

[360] E. E. Rigby, N. A. Hatch, et al. "Searching for large-scale structures around high-redshift radio galaxies with Herschel". In: 437 (Jan. 2014), pp. 1882–1893. DOI: 10.1093/mnras/stt2019. arXiv: 1310.5710.

[361] E. E. Rigby, S. J. Maddox, et al. "Herschel-ATLAS: first data release of the Science Demonstration Phase source catalogues". In: 415 (Aug. 2011), pp. 2336–2348. DOI: 10.1111/j.1365-2966.2011.18864.x. arXiv: 1010.5787 [astro-ph.IM].

[362] D. Rigopoulou et al. "On the far-infrared metallicity diagnostics: applications to high- redshift galaxies". In: 473 (Jan. 2018), pp. 20–29. DOI: 10.1093/mnras/stx2311.

[363] G. Rodighiero, M. Brusa, et al. "Relationship between Star Formation Rate and Black Hole Accretion At Z = 2: the Different Contributions in Quiescent, Normal, and Starburst Galaxies". In: 800, L10 (Feb. 2015), p. L10. DOI: 10.1088/2041-8205/800/1/L10.

[364] G. Rodighiero, Daddi, et al. "The Lesser Role of Starbursts in Star Formation at z = 2". In: 739, L40 (Oct. 2011), p. L40. DOI: 10.1088/2041-8205/739/2/L40. arXiv: 1108.0933.

[365] A. Rodríguez-Puebla et al. "Halo and subhalo demographics with Planck cosmological parameters: Bolshoi-Planck and MultiDark-Planck simulations". In: 462 (Oct. 2016), pp. 893–916. DOI: 10.1093/mnras/stw1705. arXiv: 1602.04813.

[366] Eric Roebuck et al. "The Role of Star Formation and AGN in Dust Heating of z=0.3-2.8 Galaxies - II. Informing IR AGN Fraction Estimates through Simulations". In: 833, 60 (Dec. 2016), p. 60. DOI: 10.3847/1538-4357/833/1/60.

[367] I. G. Roseboom, R. J. Ivison, et al. "The Herschel Multi-tiered Extragalactic Survey: SPIRE-mm photometric redshifts". In: 419 (Feb. 2012), pp. 2758–2773. DOI: 10.1111/j.1365-2966.2011.19827.x. arXiv: 1109.2887.

[368] I. G. Roseboom, S. J. Oliver, et al. "The Herschel Multi-Tiered Extragalactic Survey: source extraction and cross-identifications in confusion-dominated SPIRE images". In: 409 (Nov. 2010), pp. 48–65. DOI: 10.1111/j.1365-2966.2010.17634.x. arXiv: 1009.1658.

[369] M. Rowan-Robinson, R. G. Mann, et al. "Observations of the Hubble Deep Field with the Infrared Space Observatory - V. Spectral energy distributions, starburst models and star formation history". In: 289 (Aug. 1997), pp. 490–496. DOI: 10.1093/mnras/289.2.490. arXiv: astro-ph/9707030 [astro-ph].

[370] M. Rowan-Robinson, S. Oliver, et al. "The star formation rate density from z = 1 to 6". In: 461 (Sept. 2016), pp. 1100–1111. DOI: 10.1093/mnras/stw1169. arXiv: 1605.03937.

[371] K. Rowlands et al. "Herschel-ATLAS: properties of dusty massive galaxies at low and high redshifts". In: 441 (June 2014), pp. 1017–1039. DOI: 10.1093/mnras/stu510. arXiv: 1403.2994.

[372] W. Rujopakarn et al. “Cospatial Star Formation and Supermassive Black Hole Growth in z $\sim$ 3 Galaxies: Evidence for In Situ Co- evolution”. In: 854, L4 (Feb. 2018), p. L4. DOI: 10.3847/2041-8213/aaa9b3.

[373] M. Safarzadeh, H. C. Ferguson, et al. “A Novel Technique to Improve Photometry in Confused Images Using Graphs and Bayesian Priors”. In: 798, 91 (Jan. 2015), p. 91. DOI: 10.1088/0004-637X/798/2/91. arXiv: 1408.2227.

[374] M. Safarzadeh, Y. Lu, et al. “Is a top-heavy initial mass function needed to reproduce the submillimetre galaxy number counts?” In: 472 (Dec. 2017), pp. 2462–2467. DOI: 10.1093/mnras/stx2172.

[375] A. Sajina et al. “The 1-1000μm spectral energy distributions of far- infrared galaxies”. In: 369 (June 2006), pp. 939–957. DOI: 10.1111/j.1365-2966.2006.10361.x. arXiv: astro-ph/0603614.

[376] Samir Salim et al. “On the Mass-Metallicity-Star Formation Rate Relation for Galaxies at z2”. In: 808, 25 (July 2015), p. 25. DOI: 10.1088/0004-637X/808/1/25.

[377] F. Salmi et al. “Dissecting the Stellar-mass-SFR Correlation in z = 1 Star-forming Disk Galaxies”. In: 754, L14 (July 2012), p. L14. DOI: 10.1088/2041-8205/754/1/L14. arXiv: 1206.1704.

[378] J. Sánchez Almeida et al. “Metallicity Inhomogeneities in Local Star-forming Galaxies as a Sign of Recent Metal-poor Gas Accretion”. In: 783, 45 (Mar. 2014), p. 45. DOI: 10.1088/0004-637X/783/1/45. arXiv: 1401.1985.

[379] D. B. Sanders et al. “Ultraluminous Infrared Galaxies and the Origin of Quasars”. In: 325 (Feb. 1988), p. 74. DOI: 10.1086/165983.

[380] D. Sanders et al. “Luminous Infrared Galaxies: Optical Morphology and Photometry, Molecular Gas Masses, and Starburst/AGN Activity versus Infrared Luminosity”. In: The Neutral ISM in Starburst Galaxies. Vol. 320. Dec. 2004, p. 230.

[381] M. T. Sargent et al. “The Contribution of Starbursts and Normal Galaxies to Infrared Luminosity Functions at z 2”. In: 747, L31 (Mar. 2012), p. L31. DOI: 10.1088/2041-8205/747/2/L31. arXiv: 1202.0290.

[382] Shobita Satyapal et al. “Buried AGNs in Advanced Mergers: Mid-infrared Color Selection as a Dual AGN Candidate Finder”. In: 848, 126 (Oct. 2017), p. 126. DOI: 10.3847/1538-4357/aa88ca.

[383] R. S. Savage et al. “Bayesian Methods of Astronomical Source Extraction”. In: 661 (June 2007), pp. 1339–1346. DOI: 10.1086/515393. eprint: astro-ph/0512597.

[384] Schaye et al. “The EAGLE project: simulating the evolution and assembly of galaxies and their environments”. In: 446 (Jan. 2015), pp. 521–554. DOI: 10.1093/mnras/stu2058. arXiv: 1407.7040.

[385] Maarten Schmidt. “Space Distribution and Luminosity Functions of Quasi-Stellar Radio Sources”. In: 151 (Feb. 1968), p. 393. DOI: 10.1086/149446.

[386] Peter Schneider. Extragalactic Astronomy and Cosmology: An Introduction. 2015. DOI: 10.1007/978-3-642-54083-7.

[387] C. Schreiber et al. “EGG: hatching a mock Universe from empirical prescriptions⋆”. In: 602, A96 (June 2017), A96. DOI: 10.1051/0004-6361/201629123. arXiv: 1606.05354 [astro-ph.IM].

[388] Schreiber, Elbaz, Pannella, Ciesla, T. Wang, and M. Franco. “Dust temperature and mid-to-total infrared color distributions for star- forming galaxies at 0 < z < 4”. In: 609, A30 (Jan. 2018), A30. DOI: 10.1051/0004-6361/201731506.

[389] Schreiber, Elbaz, Pannella, Ciesla, T. Wang, A. Koekemoer, et al. “Observational evidence of a slow downfall of star formation efficiency in massive galaxies during the past 10 Gyr”. In: 589, A35 (May 2016), A35. DOI: 10.1051/0004-6361/201527200. arXiv: 1601.04226.

[390] Schreiber, Pannella, Elbaz, et al. “The Herschel view of the dominant mode of galaxy growth from z = 4 to the present day”. In: 575, A74 (Mar. 2015), A74. DOI: 10.1051/0004-6361/201425017. arXiv: 1409.5433.

[391] Schreiber, Pannella, R. Leiton, et al. “The ALMA Redshift 4 Survey (AR4S). I. The massive end of the z = 4 main sequence of galaxies”. In: 599, A134 (Mar. 2017), A134. DOI: 10.1051/0004-6361/201629155. arXiv: 1606.06252.

[392] Jillian M. Scudder et al. “The multiplicity of 250-m Herschel sources in the COSMOS field”. In: Monthly Notices of the Royal Astronomical Society 460.1 (2016), p. 1119. DOI: 10.1093/mnras/stw1044. eprint: /oup/backfile/Content_public/Journal/mnras/460/1/10.1093_mnras_stw1044/2/stw1044.pdf. URL: +%20http://dx.doi.org/10.1093/mnras/stw1044.

[393] Serjeant, Alberto Carramiñana, et al. “The European Large Area ISO Survey - IX. The 90-μm luminosity function from the Final Analysis sample”. In: 355 (Dec. 2004), pp. 813–818. DOI: 10.1111/j.1365-2966.2004.08358.x. arXiv: 2966.2004.

[394] Serjeant, S. Dye, et al. “The SCUBA Half Degree Extragalactic Survey (SHADES) - IX. The environment, mass and redshift dependence of star formation”. In: 386 (June 2008), pp. 1907–1921. DOI: 10.1111/j.1365-2966.2008.13197.x. arXiv: 0712.3613.

[395] P. Sharda et al. “Testing star formation laws in a starburst galaxy at redshift 3 resolved with ALMA”. In: 477 (July 2018), pp. 4380–4390. DOI: 10.1093/mnras/sty886.

[396] Sheth et al. “On the environmental dependence of halo formation”. In: 350 (June 2004), pp. 1385–1390. DOI: 10.1111/j.1365-2966.2004.07733.x. arXiv: astro-ph/0402237 [astro-ph].

[397] X. W. Shu et al. “Identification of z 2 Herschel 500 μM Sources Using Color Deconfusion”. In: 222, 4 (Jan. 2016), p. 4. DOI: 10.3847/0067-0049/222/1/4. arXiv: 1512.00167.

[398] Vimal Simha et al. “Testing subhalo abundance matching in cosmological smoothed particle hydrodynamics simulations”. In: 423 (July 2012), pp. 3458–3473. DOI: 10.1111/j.1365-2966.2012.21142.x. arXiv: 1011.4964.

[399] J. M. Simpson et al. “An ALMA Survey of Submillimeter Galaxies in the Extended Chandra Deep Field South: The Redshift Distribution and Evolution of Submillimeter Galaxies”. In: 788, 125 (June 2014), p. 125. DOI: 10.1088/0004-637X/788/2/125. arXiv: 1310.6363.

[400] Simpson et al. “The SCUBA-2 Cosmology Legacy Survey: ALMA Resolves the Bright-end of the Sub-millimeter Number Counts”. In: 807, 128 (July 2015), p. 128. DOI: 10.1088/0004-637X/807/2/128. arXiv: 1505.05152.

[401] G. Siringo et al. “The Large APEX BOlometer CAmera LABOCA”. In: 497 (Apr. 2009), pp. 945–962. DOI: 10.1051/0004-6361/200811454. arXiv: 0903.1354 [astro-ph.IM].

[402] V. M. Slipher. “The radial velocity of the Andromeda Nebula”. In: Lowell Observatory Bulletin 1 (Jan. 1913), pp. 56–57.

[403] M. W. L. Smith et al. “The Herschel Exploitation of Local Galaxy Andromeda (HELGA). II. Dust and Gas in Andromeda”. In: 756, 40 (Sept. 2012), p. 40. DOI: 10.1088/0004-637X/756/1/40. arXiv: 1204.0785.

[404] V. Smolčić et al. “(Sub)millimetre interferometric imaging of a sample of COSMOS/AzTEC submillimetre galaxies. III. Environments”. In: 597, A4 (Jan. 2017), A4. DOI: 10.1051/0004-6361/201526989. arXiv: 1604.01775.

[405] T. J. Sodroski et al. “A Three-dimensional Decomposition of the Infrared Emission from Dust in the Milky Way”. In: 480 (May 1997), pp. 173–187. DOI: 10.1086/303961.

[406] B. T. Soifer et al. “The Spitzer view of the extragalactic universe.” In: Annual Review of Astronomy and Astrophysics 46 (Sept. 2008), pp. 201–240. DOI: 10.1146/annurev.astro.46.060407.145144. arXiv: 0407.14514.

[407] P. M. Solomon et al. “Molecular Gas at High Redshift”. In: Annual Review of Astronomy and Astrophysics 43 (Sept. 2005), pp. 677–725. DOI: 10.1146/annurev.astro.43.051804.102221. arXiv: astro-ph/0508481.

[408] R. S. Somerville and R. Davé. “Physical Models of Galaxy Formation in a Cosmological Framework”. In: 53 (Aug. 2015), pp. 51–113. DOI: 10.1146/annurev-astro-082812-140951. arXiv: 1412.2712.

[409] R. S. Somerville, R. C. Gilmore, et al. “Galaxy properties from the ultraviolet to the far-infrared: Λ cold dark matter models confront observations”. In: 423 (July 2012), pp. 1992–2015. DOI: 10.1111/j.1365-2966.2012.20490.x. arXiv: 1104.0669.

[410] R. M. Soneira et al. “A computer model universe - Simulation of the nature of the galaxy distribution in the Lick catalog”. In: 83 (July 1978), pp. 845–860. DOI: 10.1086/112268.

[411] J. S. Speagle et al. “A Highly Consistent Framework for the Evolution of the Star-Forming ”Main Sequence” from z 0-6”. In: The Astrophysical Journal Supplement Series 214, 15 (Oct. 2014), p. 15. DOI: 10.1088/0067-0049/214/2/15. arXiv: 1405.2041.

[412] D. N. Spergel. “The dark side of cosmology: Dark matter and dark energy”. In: Science 347 (Mar. 2015), pp. 1100–1102. DOI: 10.1126/science.aaa0980.

[413] L. R. Spitler et al. "Exploring the z = 3-4 Massive Galaxy Population with ZFOURGE: The Prevalence of Dusty and Quiescent Galaxies". In: 787, L36 (June 2014), p. L36. DOI: 10.1088/2041-8205/787/2/L36. arXiv: 1405.1048.

[414] V. Springel. "The cosmological simulation code GADGET-2". In: 364 (Dec. 2005), pp. 1105–1134. DOI: 10.1111/j.1365-2966.2005.09655.x. eprint: astro-ph/0505010.

[415] Volker Springel et al. "First results from the IllustrisTNG simulations: matter and galaxy clustering". In: 475 (Mar. 2018), pp. 676–698. DOI: 10.1093/mnras/stx3304. arXiv: 1707.03397.

[416] S. M. Stach et al. "An ALMA survey of the SCUBA-2 Cosmology Legacy Survey UKIDSS/UDS field: number counts of submillimeter galaxies". In: ArXiv e-prints, arXiv:1805.05362 (May 2018), arXiv:1805.05362. arXiv: 1805.05362.

[417] Charles C. Steidel et al. "A Large Structure of Galaxies at Redshift Z approximately 3 and Its Cosmological Implications". In: 492 (Jan. 1998), pp. 428–438. DOI: 10.1086/305073. arXiv: astro-ph/9708125.

[418] C. L. Steinhardt et al. "The Impossibly Early Galaxy Problem". In: 824, 21 (June 2016), p. 21. DOI: 10.3847/0004-637X/824/1/21. arXiv: 1506.01377.

[419] P. B. Stetson. "DAOPHOT - A computer program for crowded-field stellar photometry". In: 99 (Mar. 1987), pp. 191–222. DOI: 10.1086/131977.

[420] M. Stiavelli et al. "Evidence of Primordial Clustering around the QSO SDSS J1030+0524 at z=6.28". In: 622 (Mar. 2005), pp. L1–L4. DOI: 10.1086/429406.

[421] M. L. Strandet, A. Weiss, C. De Breuck, et al. "ISM Properties of a Massive Dusty Star-forming Galaxy Discovered at z
7". In: 842, L15 (June 2017), p. L15. DOI: 10.3847/2041-8213/aa74b0. arXiv: 1705.07912.

[422] M. L. Strandet, A. Weiss, J. D. Vieira, et al. "The Redshift Distribution of Dusty Star-forming Galaxies from the SPT Survey". In: 822, 80 (May 2016), p. 80. DOI: 10.3847/0004-637X/822/2/80. arXiv: 1603.05094.

[423] Andra Stroe et al. "The role of cluster mergers and travelling shocks in shaping the Hα luminosity function at z 0.2: 'sausage' and 'toothbrush' clusters". In: 438 (Feb. 2014), pp. 1377–1390. DOI: 10.1093/mnras/stt2286. arXiv: 1311.6812.

[424] A. M. Swinbank, J. M. Simpson, et al. "An ALMA survey of sub-millimetre Galaxies in the Extended Chandra Deep Field South: the far-infrared properties of SMGs". In: 438 (Feb. 2014), pp. 1267–1287. DOI: 10.1093/mnras/stt2273. arXiv: 1310.6362.

[425] A. M. Swinbank, Ian Smail, et al. "The Properties of the Star-forming Interstellar Medium at z = 0.8-2.2 from HiZELS: Star Formation and Clump Scaling Laws in Gas-rich, Turbulent Disks". In: 760, 130 (Dec. 2012), p. 130. DOI: 10.1088/0004-637X/760/2/130. arXiv: 1209.1396.

[426] A. M. Swinbank, I. Smail, et al. "Intense star formation within resolved compact regions in a galaxy at z = 2.3". In: 464 (Apr. 2010), pp. 733–736. DOI: 10.1038/nature08880. arXiv: 1003.3674 [astro-ph.CO].

[427] M. Symeonidis, B. M. Giblin, et al. "AGN are cooler than you think: the intrinsic far-IR emission from QSOs". In: 459 (June 2016), pp. 257–276. DOI: 10.1093/mnras/stw667. arXiv: 1603.05278.

[428] M. Symeonidis, M. Vaccari, et al. "The Herschel census of infrared SEDs through cosmic time". In: 431 (May 2013), pp. 2317–2340. DOI: 10.1093/mnras/stt330. arXiv: 1302.4895.

[429] L. J. Tacconi et al. "Submillimeter Galaxies at z ˜ 2: Evidence for Major Mergers and Constraints on Lifetimes, IMF, and CO-H_2 Conversion Factor". In: 680, 246-262 (June 2008), pp. 246–262. DOI: 10.1086/587168. arXiv: 0801.3650.

[430] Ryuichi Takahashi et al. "Full-sky Gravitational Lensing Simulation for Large-area Galaxy Surveys and Cosmic Microwave Background Experiments". In: 850, 24 (Nov. 2017), p. 24. DOI: 10.3847/1538-4357/aa943d.

[431] Yoichi Tamura et al. "Spatial correlation between submillimetre and Lyman-α galaxies in the SSA22 protocluster". In: 459 (May 2009), pp. 61–63. DOI: 10.1038/nature07947.

[432] J. A. Tauber et al. "Planck pre-launch status: The Planck mission". In: 520, A1 (Sept. 2010), A1. DOI: 10.1051/0004-6361/200912983.

[433] Tinker et al. "Toward a Halo Mass Function for Precision Cosmology: The Limits of Universality". In: 688 (Dec. 2008), pp. 709–728. DOI: 10.1086/591439. arXiv: 0803.2706 [astro-ph].

[434] Yoshiki Toba et al. "Discovery of an Extremely Luminous Dust-obscured Galaxy Observed with SDSS, WISE, JCMT, and SMA". In: 857, 31 (Apr. 2018), p. 31. DOI: 10.3847/1538-4357/aab3cf.

[435] S. Toft et al. "Submillimeter Galaxies as Progenitors of Compact Quiescent Galaxies". In: 782, 68 (Feb. 2014), p. 68. DOI: 10.1088/0004-637X/782/2/68. arXiv: 1401.1510.

[436] Jun Toshikawa, Nobunari Kashikawa, Kazuaki Ota, et al. "Discovery of a Protocluster at z 6". In: 750, 137 (May 2012), p. 137. DOI: 10.1088/0004-637X/750/2/137.

[437] Jun Toshikawa, Nobunari Kashikawa, Roderik Overzier, et al. "A First Site of Galaxy Cluster Formation: Complete Spectroscopy of a Protocluster at z = 6.01". In: 792, 15 (Sept. 2014), p. 15. DOI: 10.1088/0004-637X/792/1/15.

[438] Benny Trakhtenbrot et al. "Fast-growing SMBHs in Fast-growing Galaxies, at High Redshifts: the Role of Major Mergers as Revealed by ALMA". In: ArXiv e-prints, arXiv:1801.01508 (Jan. 2018), arXiv:1801.01508. arXiv: 1801.01508 [astro-ph.GA].

[439] Chao-Wei Tsai et al. "The Most Luminous Galaxies Discovered by WISE". In: 805, 90 (June 2015), p. 90. DOI: 10.1088/0004-637X/805/2/90. arXiv: 1410.1751.

[440] C. Megan Urry et al. "Unified Schemes for Radio-Loud Active Galactic Nuclei". In: Publications of the Astronomical Society of the Pacific 107 (Sept. 1995), p. 803. DOI: 10.1086/133630. arXiv: astro-ph/9506063.

[441] E. Valiante et al. "The Herschel-ATLAS data release 1 - I. Maps, catalogues and number counts". In: 462 (Nov. 2016), pp. 3146–3179. DOI: 10.1093/mnras/stw1806. arXiv: 1606.09615.

[442] L. Vallini et al. "On the [CII]-SFR Relation in High Redshift Galaxies". In: 813, 36 (Nov. 2015), p. 36. DOI: 10.1088/0004-637X/813/1/36.

[443] Ivan Valtchanov et al. "Serendipitous detection of an overdensity of Herschel-SPIRE 250 μm sources south of MRC 1138-26". In: 436 (Dec. 2013), pp. 2505–2514. DOI: 10.1093/mnras/stt1753.

[444] J. D. Vieira et al. "Dusty starburst galaxies in the early Universe as revealed by gravitational lensing". In: 495 (Mar. 2013), pp. 344–347. DOI: 10.1038/nature12001. arXiv: 1303.2723.

[445] M. P. Viero et al. "The Herschel Stripe 82 Survey (HerS): Maps and Early Catalog". In: 210, 22 (Feb. 2014), p. 22. DOI: 10.1088/0067-0049/210/2/22. arXiv: 1308.4399.

[446] L. Vincoletto et al. "Cosmic star formation rate: a theoretical approach". In: 421 (Apr. 2012), pp. 3116–3126. DOI: 10.1111/j.1365-2966.2012.20535.x. arXiv: 1201.1751.

[447] M. Vogelsberger et al. "Introducing the Illustris Project: simulating the coevolution of dark and visible matter in the Universe". In: 444 (Oct. 2014), pp. 1518–1547. DOI: 10.1093/mnras/stu1536. arXiv: 1405.2921.

[448] Fabian Walter et al. "ALMA Spectroscopic Survey in the Hubble Ultra Deep Field: Survey Description". In: 833, 67 (Dec. 2016), p. 67. DOI: 10.3847/1538-4357/833/1/67.

[449] Wang et al. "HerMES: point source catalogues from Herschel-SPIRE observations II". In: 444 (Nov. 2014), pp. 2870–2883. DOI: 10.1093/mnras/stu1569. arXiv: 1312.0552.

[450] J. L. Wardlow et al. "The Interstellar Medium in High-redshift Submillimeter Galaxies as Probed by Infrared Spectroscopy*". In: 837, 12 (Mar. 2017), p. 12. DOI: 10.3847/1538-4357/837/1/12. arXiv: 1701.03112.

[451] Wardlow, S. Malhotra, et al. "Constraining the Lyα Escape Fraction with Far-infrared Observations of Lyα Emitters". In: 787, 9 (May 2014), p. 9. DOI: 10.1088/0004-637X/787/1/9. arXiv: 1312.4963.

[452] Wardlow, Simpson, et al. "An ALMA survey of CO in submillimetre galaxies: companions, triggering, and the environment in blended sources". In: 479 (Sept. 2018), pp. 3879–3891. DOI: 10.1093/mnras/sty1526.

[453] A. Weiß, C. De Breuck, et al. "ALMA Redshifts of Millimeter-selected Galaxies from the SPT Survey: The Redshift Distribution of Dusty Star-forming Galaxies". In: 767, 88 (Apr. 2013), p. 88. DOI: 10.1088/0004-637X/767/1/88. arXiv: 1303.2726.

[454] A. Weiß, R. J. Ivison, et al. "First Redshift Determination of an Optically/Ultraviolet Faint Submillimeter Galaxy Using CO Emission Lines". In: 705 (Nov. 2009), pp. L45–L47. DOI: 10.1088/0004-637X/705/1/L45. arXiv: 0909.3177 [astro-ph.CO].

[455] K. E. Whitaker et al. “Galaxy Structure as a Driver of the Star Formation Sequence Slope and Scatter”. In: 811, L12 (Sept. 2015), p. L12. DOI: 10.1088/2041-8205/811/1/L12. arXiv: 1508.04771.

[456] A. Wilkinson et al. “The SCUBA-2 Cosmology Legacy Survey: the clustering of submillimetre galaxies in the UKIDSS UDS field”. In: 464 (Jan. 2017), pp. 1380–1392. DOI: 10.1093/mnras/stw2405. arXiv: 1604.00018.

[457] Christina C. Williams et al. “The JWST Extragalactic Mock Catalog: Modeling Galaxy Populations from the UV through the Near-IR over 13 Billion Years of Cosmic History”. In: The Astrophysical Journal Supplement Series 236, 33 (June 2018), p. 33. DOI: 10.3847/1538-4365/aabcbb.

[458] G. W. Wilson et al. “The AzTEC mm-wavelength camera”. In: 386 (May 2008), pp. 807–818. DOI: 10.1111/j.1365-2966.2008.12980.x. arXiv: 0801.2783.

[459] W. E. Wilson et al. “The Australia Telescope Compact Array Broad-band Backend: description and first results”. In: 416 (Sept. 2011), pp. 832–856. DOI: 10.1111/j.1365-2966.2011.19054.x. arXiv: 1105.3532 [astro-ph.IM].

[460] A. Wootten et al. “The Atacama Large Millimeter/Submillimeter Array”. In: IEEE Proceedings 97 (Aug. 2009), pp. 1463–1471. DOI: 10.1109/JPROC.2009.2020572. arXiv: 0904.3739 [astro-ph.IM].

[461] E. L. Wright et al. “The Wide-field Infrared Survey Explorer (WISE): Mission Description and Initial On-orbit Performance”. In: 140, 1868-1881 (Dec. 2010), pp. 1868–1881. DOI: 10.1088/0004-6256/140/6/1868. arXiv: 1008.0031 [astro-ph.IM].

[462] Jun-Qing Xia et al. “Clustering of submillimetre galaxies in a self-regulated baryon collapse model”. In: 422 (May 2012), pp. 1324–1331. DOI: 10.1111/j.1365-2966.2012.20705.x.

[463] F. Yuan et al. “The spectral energy distribution of galaxies at z 2.5: Implications from the Herschel/SPIRE color-color diagram”. In: 582, A90 (Oct. 2015), A90. DOI: 10.1051/0004-6361/201425497. arXiv: 1506.07397.

[464] M. S. Yun et al. “Radio Properties of Infrared-selected Galaxies in the IRAS 2 Jy Sample”. In: 554 (June 2001), pp. 803–822. DOI: 10.1086/323145. eprint: astro-ph/0102154.

[465] J. A. Zavala, I. Aretxaga, et al. “The SCUBA-2 Cosmology Legacy Survey: The EGS deep field - II. Morphological transformation and multiwavelength properties of faint submillimetre galaxies”. In: 475 (Apr. 2018), pp. 5585–5602. DOI: 10.1093/mnras/sty217. arXiv: 1801.07718.

[466] J. A. Zavala, A. Montaña, et al. “An amplified dusty star-forming galaxy at z=6: unveiling an elusive population of galaxies”. In: ArXiv e-prints, arXiv:1707.09022 (July 2017). arXiv: 1707.09022.

[467] F. Zwicky. “Die Rotverschiebung von extragalaktischen Nebeln”. In: Helvetica Physica Acta 6 (Jan. 1933), pp. 110–127.

APPENDIX A

Published papers

Astronomy & Astrophysics manuscript no. output
February 19, 2018

Towards a census of high-redshift dusty galaxies with *Herschel*

A selection of "500 μm-risers"

D. Donevski[1], V. Buat[1], F. Boone[2], C. Pappalardo[3,4], M. Bethermin[1,7], C. Schreiber[5], F. Mazyed[1], J. Alvarez-Marquez[6], and S. Duivenvoorden[8]

[1] Aix Marseille Univ, CNRS, LAM, Laboratoire d'Astrophysique de Marseille, Marseille, France, e-mail: darko.donevski@lam.fr
[2] Universite de Toulouse; UPS-OMP; IRAP; Toulouse, France
[3] Centro de Astronomia e Astrofísica da Universidade de Lisboa, Observatório Astronómico de Lisboa, Tapada da Ajuda, 1349-018 Lisboa, Portugal
[4] Instituto de Astrofísica e Ciencias do Espaço, Universidade de Lisboa, OAL, Tapada da Ajuda, 1349-018 Lisboa, Portugal
[5] Leiden Observatory, Leiden University, 2300 RA Leiden, The Netherlands
[6] Departamento de astrofisica, Centro de Astrobiologia (CAB, CSIC-INTA), Carretera de Ajalvir, 28850 Torrejón de Ardoz, Madrid, Spain
[7] European Southern Observatory, Karl-Schwarzschild-Str. 2, 85748 Garching, Germany
[8] Astronomy Centre, Department of Physics and Astronomy, University of Sussex, Brighton BN1 9QH, UK

Received ; accepted

ABSTRACT

Context. Over the last decade a large number of dusty star-forming galaxies has been discovered up to redshift $z = 2 - 3$ and recent studies have attempted to push the highly confused *Herschel* SPIRE surveys beyond that distance. To search for $z \geq 4$ galaxies they often consider the sources with fluxes rising from 250 μm to 500 μm (so-called "500 μm-risers"). *Herschel* surveys offer a unique opportunity to efficiently select a large number of these rare objects, and thus gain insight into the prodigious star-forming activity that takes place in the very distant Universe.
Aims. We aim to implement a novel method to obtain a statistical sample of 500 μm-risers and fully evaluate our selection inspecting different models of galaxy evolution.
Methods. We consider one of the largest and deepest *Herschel* surveys, the Herschel Virgo Cluster Survey. We develop a novel selection algorithm which links the source extraction and spectral energy distribution fitting. To fully quantify selection biases we make end-to-end simulations including clustering and lensing.
Results. We select 133 500 μm-risers over 55 deg^2, imposing the criteria: $S_{500} > S_{350} > S_{250}$, $S_{250} > 13.2$ mJy and $S_{500} > 30$ mJy. Differential number counts are in fairly good agreement with models, displaying a better match than other existing samples. The estimated fraction of strongly lensed sources is 24^{+6}_{-5}% based on models.
Conclusions. We present the faintest sample of 500 μm-risers down to $S_{250} = 13.2$ mJy. We show that noise and strong lensing have an important impact on measured counts and redshift distribution of selected sources. We estimate the flux-corrected star formation rate density at $4 < z < 5$ with the 500 μm-risers and find it to be close to the total value measured in far-infrared. This indicates that colour selection is not a limiting effect to search for the most massive, dusty $z > 4$ sources.

Key words. Galaxies: statistics – Galaxies: evolution – Galaxies: star formation – Galaxies: high-redshift – Infrared: Galaxies: photometry: Galaxies – Submillimeter: galaxies

1. Introduction

The abundance of dusty galaxies at high-redshifts ($z > 4$) constrains our theories about early galaxy formation, since it is generally stated that they are the progenitors of massive ellipticals seen in overdense regions of the local Universe (e.g. Eales et al. 2017, Toft et al. 2014, Simpson et al. 2014, Casey et al. 2014).

The widely accepted picture is that dusty star-forming galaxies (DSFGs) occupy the most massive halos in early epochs and lie on the most extreme tail of the galaxy stellar mass function (e.g. Ikarashi et al. 2017, Fudamoto et al. 2017, Oteo et al. 2016, Mancuso et al. 2016, Michałowski et al. 2014). These DSFGs are usually selected in the far-infrared (FIR) regime where the star formation rates can be directly measured.

Large FIR surveys, such as those conducted with the *Herschel* Space Observatory (Pilbratt et al. 2010), provide an opportunity to build a thorough census of prodigious starbursts over cosmological redshifts using a wide and blind search concept. The *Herschel* SPIRE photometer (Griffin et al. 2010) was often used for mapping large areas at wavelengths of 250 μm, 350 μm and 500 μm. The redshift peak of most *Herschel*-detected sources matches with the redshift where galaxies have formed most of their stars ($z \sim 2$, Pearson et al. 2013, Lapi et al. 2011, Amblard et al. 2010). Considering that rest-frame dust spectral energy distribution (SED) of a galaxy typically peaks between 70 and 100 μm, colours of sources in *Herschel* SPIRE bands were used to select candidate high-redshift dusty objects. To search for $z \gtrsim 4$ candidates, there is a particular interest to exploit the sources with red SPIRE colours, with rising flux densites from 250 to 500 microns (so-called "500 μm-risers"). Such galaxies should lie at $z \geqslant 4$ unless they have dust temperatures that are

notably lower than is seen in local FIR-bright equivalents (Asboth et al. 2016, Yuan et al. 2015, Dowell et al. 2014, Roseboom et al. 2012).

If the selection of 500 μm-risers is free of contaminants such are blended systems and powerful non-thermal sources (e.g. quasars), it is expected to provide us insight into very distant and dusty, star-forming galactic events. Recently, literature on dusty high-z galaxies has rapidly flourished, including a handful of serendipitously discovered 500 μm-risers (e.g. Daddi et al. 2009, Cox et al. 2011, Capak et al. 2011, Combes et al. 2012, Vieira et al. 2013, Miettinen et al. 2015, Negrello et al. 2017). However, these findings had serious shortcomings - they were limited to few objects with red SPIRE colours.[1]

Being primarily focused on individual (usually strong lensing) candidates or millimeter-selected samples regardless of the galaxy colour, they poorly constrained the statistics of 500 μm-risers. To derive a larger number of potentially unlensed 500 μm-risers and analyse them in a more standardised manner, several works used map-search technique (Asboth et al. 2016, Dowell et al. 2014, Ivison et al. 2016). These led to the discovery of the most distant dusty starburst galaxies known to date: SPT0311-58 at $z = 6.902$ (Strandet et al. 2017), HFLS3 at $z = 6.34$ (Riechers et al. 2013) and G09-83808 at $z = 6.02$ (Zavala et al. 2017, Fudamoto et al. 2017).Furthermore, selecting the 500 μm-risers from lowest-resolution *Herschel* SPIRE-maps, Dowell et al. (2014) and Asboth et al. (2016)) claimed significant overprediction of observed number of 500 μm-risers, one order of magnitude higher than predicted by the existing models (e.g. Hayward 2013, Béthermin et al. 2012).

Even if *Herschel* offers a direct insight into the IR emission of high-z objects, there are critical limitations, such as sensitivity of detectors and low spatial resolution. These are responsible for biases such as source confusion. The sensitivity of SPIRE allows for the direct detection of only the brightest and thus rarest objects at the tip of the luminosity function (Cowley et al. 2015, Karim et al. 2013, Oliver et al. 2010), and we therefore need large surveys to increase the statistics. The study of Dowell et al. (2014) analysed maps of three different extragalactic fields observed as part of the HerMES (*Herschel* Multi-tiered Extragalactic Survey, Oliver et al. 2010) program, while Ivison et al. (2016) and Asboth et al. (2016) probed much wider but shallower areas of the *H*-ATLAS and HeLMS (HerMES Large Mode Survey) fields, respectively (see Section 2.1 for details about field properties).

In this work we aim to introduce a slightly different approach to building a statistically significant sample of red, potentially $z > 4$ sources. The new selection scheme we propose is motivated by the size and the depth of the field we chose to investigate. *Herschel* Virgo Cluster Survey (HeViCS, Davies et al. 2010) is deeper than the one used in the analysis of Asboth et al. (2016) and Ivison et al. (2016), and larger than the area analysed by Dowell et al. (2014).

The paper is organised as follows: in Section 2 we describe the methods we used for the data analysis and our new selection criteria for 500 μm-risers. In Section 3 and Section 4 we present expected redshift/luminosity trend of selected galaxies and differential number counts. In Section 5 we compare our results to different models. We perform simulations to review all selection biases and highlight the necessity of a further refinement of selection criteria in searches for $z \gtrsim 4$ sources. The nature of 500 μm-risers and our main conclusions are outlined in Section 6 and Section 7, respectively. We assume a Planck Collaboration et al. (2016a) cosmology.

[1] Throughout the text we adopt the following terminology regarding colours of IR-detected sources: red colours and red sources refer to 500 μm-risers, while "350 μm peakers" refer to galaxies having SED peak at 350 μm.

2. Data analysis

2.1. HeViCS field

HeViCS is a fully sampled survey that covers a region centered at the Virgo cluster (Davies et al. 2010, Davies et al. 2012). It is one of the largest uniform Herschel surveys, and its main advantage is its sensitivity and uniformity of data. In this survey, *Herschel* observed four overlapping fields (fields V1-V4) in fast parallel-mode. The total entire survey region is 84 square degrees, where 55 square degrees are observed at unvarying depth with eight orthogonal cross scans (see Auld et al. 2013 and Pappalardo et al. 2015 for more details).

HeViCS observations reached a depth close to the confusion limit at the shortest SPIRE wavelength (250 μm). Because of the number of repeated scans, instrumental noise is significantly reduced in HeViCS maps, giving the 1σ levels of 4.9, 4.9, and 5.5 mJy at 250 μm, 350 μm, and 500 μm, respectively (Auld et al. 2013). In the overlapped, deeper regions recorded by 16 scans, these values are even smaller, namely 3.5, 3.3, and 4.0 mJy. Due to the presence of bright sources (see Section 2.3), global noise estimation is not a straightforward task. We excluded bright sources from the map by masking them, and after their removal the global noise was derived from the variance of the map. It reaches the 1σ values of 6.58, 7.07, and 7.68 mJy (250 μm, 350 μm, and 500 μm, respectively) for a major area covered by eight cross-scans. The extensive contributor to the overall noise measured in HeViCS maps is confusion noise, usually defined as the the variance in the sky map due to the fluctuations of unresolved sources inside the SPIRE beam. We calculate confusion using the relation $\sigma_{\rm conf} = \sqrt{\sigma^2_{\rm tot} - \sigma^2_{\rm inst}}$, where $\sigma_{\rm tot}$ is the total noise measured in the map, and $\sigma_{\rm inst}$ is the instrumental noise. Values determined for the confusion noise are 4.4, 5.2, and 5.5 mJy at the 250 μm, 350 μm, and 500 μm bands, respectively, and are almost identical to the ones presented in Auld et al. (2013). These values are also close to the confusion noise measured in HerMES maps, within twice the uncertainty of 3σ-clipping estimates from Nguyen et al. (2010) (3.8 mJy, 4.7 mJy, and 5.2 mJy at the 250 μm, 350 μm, and 500 μm bands, respectively). In this work we use only SPIRE data. In parallel, each HeViCS tile has been observed by the *Herschel* PACS instrument, but the depth of PACS data ($5\sigma_{\rm tot}$ =70 mJy at 100 μm, Pappalardo et al. 2016) is not sufficient to directly detect our FIR-rising sources. PACS data at 100 μm and 160 μm will be added together with a deep optical-NIR map from the Next Generation Virgo Cluster Survey (NGVS, Ferrarese et al. 2012) in a following paper analysing ancillary data.

2.2. An overview of other Herschel fields

There are several large *Herschel* fields (e.g. with an observed area $\theta > 10$ deg^2) used for detection of 500 μm-risers. A summary of their properties is shown in Table 1. All the values are taken from the literature (Oliver et al. 2012, Wang et al. 2014). The *H*-ATLAS survey (Eales et al. 2010) is used to select red candidates by Ivison et al. (2016). *H*-ATLAS is designed to uniformly cover 600 deg^2 of sky, but with its two scans, the survey did not reach the level of confusion noise at 250 μm. Stud-

Table 1: Properties of different large fields mapped by *Herschel*

Field	Mode	N(rep)	Time [hr]	Area [deg^2]	Noise level in *m*Jy 5σ at 250 μm
(1)	(2)	(3)	(4)	(5)	(6)
HeViCS	Parallel	8	286	55	30.5
H-ATLAS	Parallel	2	600	550	56.0
HerMES					
FLS	Parallel	2	17.1	6.7	25.8
Bootes NDWFS	Parallel	2	28	10.5	25.8
ELAIS-N2	Parallel	2	28	12.28	25.8
Lockman-Swire	Parallel	4	71.2	16	13.6
XMM-LSS SWIRE	Parallel	4	71.2	18.87	25.8
HeLMS	Sp.Fast	2	103.4	274	64.0

Notes: Columns (1) Name of the field observed by *Herschel*; (2) *Herschel* observing mode ; (3) The total number of repeats of the observing mode in the set; (4) Total time of observations; (5) Field area of good pixels; (6) Total noise from the literature. Noise is calculated using the relation $\sigma_{\rm tot} = \sqrt{\sigma^2_{\rm conf} + \sigma^2_{\rm inst}}$; The bottom six fields are areas with different design levels nested as a part of HerMES: Total area covered in HerMES is 380 deg^2. Shallow HeLMS field covers the area of 274 deg^2, and deeper Level 1 - Level 6 fields cover the total area of about 80 deg^2. FLS and Lockman-SWIRE have been used to probe 500 μm-risers selection by Dowell et al. (2014), while Asboth et al. (2016) applied the same selection method in the HeLMS field.

ies by Asboth et al. (2016) and Dowell et al. (2014) acquired data from different fields which are part of the HerMES survey (Oliver et al. 2012). The HerMES survey observed 380 deg^2 of the sky. The survey has a hierarchical structure containing seven levels, ranging from very deep observations of clusters to wider fields with varying size and depth. The largest (and the shallowest) observed area is HeLMS, with its 274 square degrees. HeViCS maps consist of two or four times more scans compared to other fields listed in Table 1. This leads to a reduction of instrumental noise by a factor of $\sqrt{2}$. The global 250 μm noise in HeViCS is smaller than in *H*-ATLAS and HeLMS. However, it is still higher than in other HerMES fields, showing that confusion is a very compelling supplier to the noise budget for point sources in the HeViCS field. We clarify that statement by repeating our analysis of regions overlapped between the tiles, which have greater coverage. We found no significant noise reduction, implying that the maps are dominated by confusion noise.

2.3. Map filtering

Prior to performing source extraction on SPIRE maps, we reduce the background contamination. The 250 μm map of V2 field in HeViCS is strongly affected by galactic cirrus emission. This contamination peaks at around 150-200 μm (Bracco et al. 2011, Valiante et al. 2016), implying that it is the brightest in the shortest SPIRE bands. The main effect of cirrus emission is to increase the confusion in the maps, but the small-scale structure within it can also lead to spurious detections in the catalogues.

We follow the method applied by Pappalardo et al. (2015). Using the `SExtractor` (Bertin & Arnouts 1996) we re-grid the 250 μm map into meshes larger than the pixel size. The `SExtractor` makes an initial pass through the pixel data, and computes an estimator for the local background in each mesh of a grid that covers the whole adopted frame. We apply repetitive iterations to estimate the mean and standard deviation of the pixel value distribution in boxes, removing outlying pixels at each iteration. An important step in this procedure is the choice of the box size, since we do not want the background estimation to be affected by the presence of objects and random noise. The box size should generally be larger than the typical size of sources in the image, but small enough to encapsulate any background variations. We therefore fix the mesh size to 8 pixels, adopting the result from Pappalardo et al. (2015). The local background is clipped iteratively to reach $\pm 3\sigma$ convergence around its median. After the background subtraction, the number of sources appears uniform for regions with different cirrus emission. We use the background subtracted map as an input for the source-extraction process described in the following subsection.

2.4. Extraction of sources

Blind SPIRE source catalogues have been produced for HeViCS (Pappalardo et al. 2015). Nonetheless, when the density of sources is very high, which is the case in the highly crowded HeViCS field, blind source extraction cannot separate blended point sources in an efficient way. Additionally, it remains difficult to properly cross-match sources at different wavelengths, since central positions from blind catalogues are not well constrained. To deal with source multiplicity we chose to perform extraction of 350 μm and 500 μm fluxes at the exact a priori position of 250 μm band detections, allowing much more precise identification. The potential limitation of such a method is that we might be eventually miss some 500 μm-risers that are not included in the prior list after the first iteration of source extraction. We thus run our method iteratively and add new sources that may appear in the residuals at each iteration.

We use SUSSEXtractor (Savage & Oliver 2007), a source-finding algorithm optimised for isolated point-sources, to create the catalogue of galaxies detected in the 250 μm map as a prior to extract the flux densities at longer wavelengths. We then implement our novel technique (see Section 2.6) where source deblending and single temperature modified blackbody (MBB) fitting are combined in the same procedure. In the following we explain our source-extraction pipeline (see Fig.1 for a graphical description):

1. We run SUSSEXtractor using a fully overlapping HeViCS 250-micron map. SUSSEXtractor works on the flux-calibrated, Level 2 *Herschel* SPIRE maps. We create a point response function (PRF)-filtered image, smoothed with the PRF. In SUSSEXtractor, the PRF is assumed to be Gaussian by default, with the full-width-at-half-maximum (FWHM) provided by the FWHM parameter. We apply values of 17.6", 23.9", and 35.2" at 250, 350, and 500 μm, respectively. Subsequently, pixel sizes at these bands are 6", 10", and 14". The algorithm searches for a local maximum which is the highest pixel value within a distance defined by pixel region. The position assigned to the possible source is then refined by fitting a quadratic function to certain pixels in the PRF-filtered image.
2. To search for even fainter sources that are closer to the confusion limit and usually masked/hidden in highly confused fields like HeViCS, we perform an additional step looking for detections in our residual maps.
   Applying such an additional step, we increase the total number of sources by around 4%. Errors in the position estimated to be a source are determined as 0.6 times the ratio of the FWHM to the signal-to-noise ratio (S/N), up to a maximum of 1.0 pixel, as suggested in the literature (Ivison et al. 2007).
3. We build an initial list of 250 μm sources selecting all point sources above the threshold=3 (Bayesian criteria in SUSSEXtractor). We also impose the flux density cut choosing values equal to or higher than 13.2 mJy, which corresponds to $S_{250} \gtrsim 3\sigma_{\rm conf}$. As a result of our source extraction pipeline at 250-micron maps, we listed 64309 sources, similarly distributed among the four (V1-V4) fields.
4. List of 250 μm detections is then divided into a "no-neighbour" list of sources (250 μm sources without another detection inside the 500 μm beam) and a "close-neighbour" list where we add all sources that have another 250 μm detection within the 500 μm beam. Prior to assigning the initial 250 μm list as an input to our modified blackbody fitting procedure, we remove potentially extended sources from the catalogue.

2.5. Extended sources

The Virgo cluster is one of the richest local clusters and we expect to have a significant number of extended sources. Objects that are extended on the SPIRE beam scale (see Wang et al. 2014 or Rigby et al. 2011) are not expected to be accurately identified with point-source extracting codes, and large galaxies may be misidentified as multiple point sources. To solve this problem, we implement the same method as used in Pappalardo et al. (2015). They define a mask using the recipe of SExtractor, which detects a source when a fixed number of contiguous pixels is above a σ-threshold estimated from the background map. We keep the same value tested in Pappalardo et al. (2015) - 70 contiguous pixels above 1.2σ. In this case, most of the sources larger than 0.7 arcmin^2 are rejected from the sample. Additionally, we

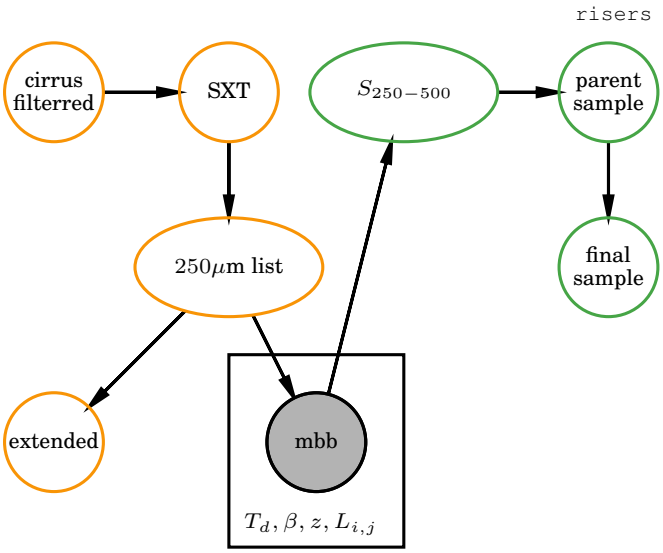

Fig. 1: Schematic representation of selection of 500 μm-risers in the HeViCS field. Coloured in orange are segments of source extraction prior to using MBB-fitter; these are (from upper left, following the arrows) subtraction of strong cirrus emission; SUSSEXtractor list of initial (threshold=3) 250 μm detections; and assumed a priori list cleaned from extended sources. Enveloped by smaller black squares are parameters considered for the fitting procedure with MBB-fitter corresponding to all pixels in the map where we have 250 μm detections. Coloured in green are segments of our selection after performing the photometry: MBB photometry ($S_{250-500}$) at SPIRE wavelengths using 250 μm priors; parent list of 500 μm-risers (140 sources in total), not cleaned from strong synchrotron contaminants; and the final list (133 in total) of 500 μm-risers after excluding local radio sources. We apply the following selection criteria for the final sample: $S_{500} > S_{350} > S_{250}$, $S_{250} > 13.2$ mJy, and $S_{500} > 30$ mJy.

cross-match all remaining HeViCS 250 μm detections with their nearest (within 36") counterpart in the *2MASS* Extended Source Catalog (Jarrett et al. 2000). We remove any detection supposed to be a counterpart with a Kron elliptical aperture semi-major larger than 9". In total we suppressed 812 sources from the analysis, thus decreasing the number of 250 μm detections in our parent list from 64309 to 63497.

The list of sources detected at 250 μm down to 13.2 mJy, cleaned from galactic cirrus contaminants and extended sources, is further used as an a priori list for our simultaneous modified blackbody fitting.

2.6. Modified blackbody fitter

As described in Section 2.1, our maps are limited by confusion noise caused by the high density of sources relative to the resolution of the *Herschel* instrument. In cases where SPIRE images have multiple sources per beam, measured fluxes might be biased if we treat several blended sources as one. Several different approaches for source "de-blending" exist in the literature. We can separate these into three groups: Firstly, there are deblending methods that use only positional priors as input information (e.g. Elbaz et al. 2010, Swinbank et al. 2014, Béthermin et al. 2010, Roseboom et al. 2010). The second group of deblenders consists of methods which combine positional informa-

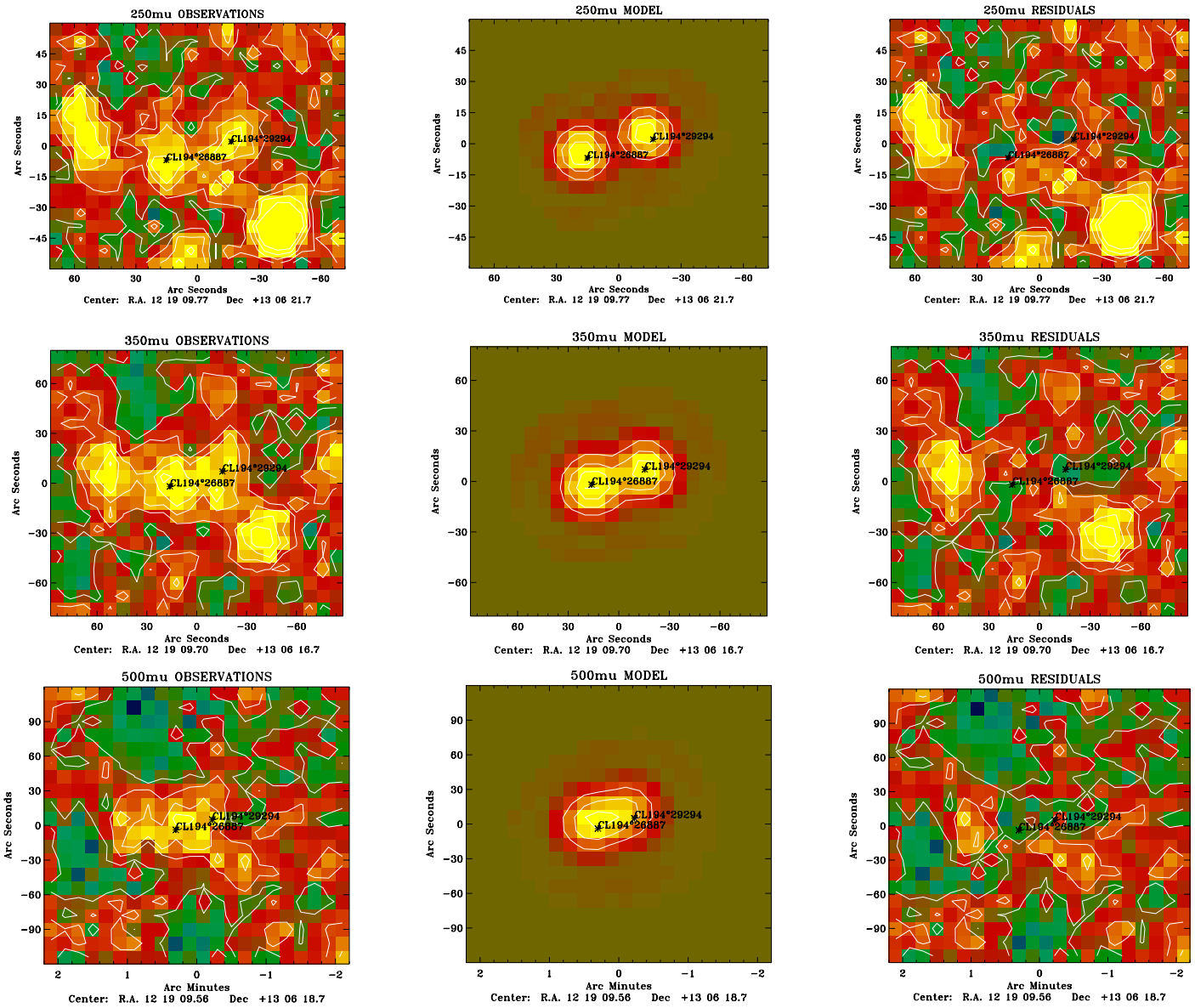

Fig. 2: Example of simultaneous prior-source deblending with `MBB-fitter`. Sources are taken from our "neighbour" list of 250 μm detections. Columns from left to right: 250 μm, 350 μm, and 500 μm maps of sources (first column), subtracted models (second column) and residuals (third column). We note that in this example two central sources are considered for the fitting.

tion with statistical techniques (Hurley et al. 2017, Safarzadeh et al. 2015); for example, Safarzadeh et al. (2015) and Hurley et al. (2017) developed the codes based on the Monte Carlo Markov Chain (MCMC) sampling for prior source detections, and while Safarzadeh et al. (2015) used Hubble Space Telescope (HST) H-band sources as a positional argument, Hurley et al. (2017) developed a similar MCMC-based prior-extraction for Spitzer 24 μm detections. Such algorithms are efficient in obtaining Bayesian PDFs for all priors, however they might still have some limitations, the most important being the potential inability to unveil the true high-z sources in cases where they are not included in the initial list. Finally, a third group of deblenders consists of those using SED modelling as an addition to positional arguments (MacKenzie et al. 2014, Shu et al. 2016, Merlin et al. 2016, Liu et al. 2017).

Due to the lack of *Spitzer* 24 μm data for the HeViCS field, and unsufficiently deep existing optical images, we have no opportunity to use positional priors from shorter-wavelength surveys, and we based our analysis on SPIRE data instead. We use models to test the whole procedure of selecting 500 μm-risers in Sect. 5.

`MBB-fitter` is a code developed to extract sources from multiwavelength bolometric observations (Boone et al, in prep.) combining positional priors and spectral information of sources such that SEDs of fitted galaxies follow modified blackbody (MBB) shape as defined by Blain et al. (2003). Our MBB deblending approach is thus very similar to the method applied by MacKenzie et al. (2014). Although such a model can only encapsulate a segment of the general complexity of astrophysical processes in a galaxy, it can account for the SED data for a wide variety of dusty galaxies. The `MBB-fitter` method is described

in detail and is tested on simulations in Boone et al. (in prep.). We summarise here the main points. In `MBB-fitter`, the map (M) of a sky region is described as a regular grid corresponding to the sky flux density distribution convolved by the point spread function (PSF) of an instrument and sampled in pixels. Thus, $M_i = M(\alpha_i, \delta_i)$ refers to the value of the map at the $i^{\rm th}$ pixel with coordinates α_i, δ_i. We further assume that the sources have a morphology independent of the frequency. The flux density distributions in the three-dimensional (3D) space $s_k(\alpha, \delta, \nu)$, where ν is frequency, can therefore be decomposed into a spatial distribution term (morphology) and an SED term:

$$M_{ij} = M(\alpha_i, \delta_i, \nu_j) = [\sum_{k=1}^{N_{\rm sources}} f_k(\nu_j)\tilde{s}_k(\alpha - \alpha_k, \delta - \delta_k) \otimes PSF_j]_i, \quad (1)$$

where PSF_j is the PSF of the map at a given frequency (ν_j), and $N_{\rm sources}$ is the number of sources considered for the fitting, with its reference coordinates ($\alpha_\kappa, \delta_\kappa$). Here we assume that the thermal continuum SED of galaxies in the FIR domain can be modelled as a modified blackbody of the form (Blain et al. 2003)

$$f(\nu, T_{\rm d}, \beta, \gamma) \propto \begin{cases} \nu^{3+\beta}/[\exp(h\nu/kT_{\rm d}) - 1], & \text{if } \nu < \nu_{\rm w} \\ \nu^{-\gamma}, & \text{if } \nu \geq \nu_{\rm w} \end{cases}, \quad (2)$$

where $\nu_{\rm w}$ is the lower boundary of Wien's regime, h is the Planck constant, and k is the Stefan-Boltzmann constant. Thus, Eq.1 describes a general model for a set of maps at different wavelengths, and each source SED is defined by a set of parameters arranged into a vector of the form $P_\kappa = [L_{{\rm IR}_\kappa}, T_{{\rm d}_\kappa}, z_\kappa, \beta_\kappa, \gamma_\kappa]$, where z_κ is the redshift of a given source, β_κ is its emissivity index, γ_κ is the index of the power law to substitute the Wien's regime, and $L_{\rm IR}$ is the IR luminosity of a source. This model is parametrized by the source SED parameters, P_κ, and coordinates $\alpha_\kappa, \delta_\kappa$. The total number of parameters is therefore $N_{\rm par}$=$N_{\rm s} \times (N_{{\rm SED}_{\rm par}} + 2)$, where $N_{{\rm SED}_{\rm par}}$ is the number of SED parameters and $N_{\rm s}$ is the number of sources.

The introduced set of parameters reflects the global properties of the source. There are potential degeneracies, meaning that different values of parameters may give very similar SEDs. This is the most prolific challenge when using the FIR peak as a redshift indicator; dust temperature and the redshift are completely degenerate (see e.g. Pope & Chary 2010).

A defined model can be compared to a set of observed maps and its fidelity can be assessed with a figure of merit such as the chi-square, exemplified as the sum of the pixel deviations:

$$\chi(P)^2 = \sum_i^{N_{\rm pix}} \sum_j^{N_{\rm freq}} \frac{(M_{ij}(P) - \tilde{M}_{ij})^2}{\sigma_{ij}^2}, \quad (3)$$

where $\tilde{M}_{ij}$ is the multiwavelength set of maps, σ_{ij} is the Gaussian noise level of the i-th pixel of the map at the j-th frequency, $N_{\rm pix}$ is the number of accounted pixels, while $N_{\rm freq}$ represents the number of maps, which is equal to the number of different frequencies used.

We use the Levenberg-Marquardt algorithm to find the minimum of the chi-square function in the space of parameters. The algorithm also returns an estimation of the errors on the parameters based on the covariance matrix. We note that it is not necessary to include all the pixels of maps in the chi-square computation; it can be restricted to a subset of pixels (contiguous or not), and sky regions without prior sources can be excluded.

We impose our list of 250 μm detected sources as a prior list, and use `MBB-fitter` to perform two-step photometry: (1) simultaneously fitting the sources affected by surrounding source-blend (12135 sources in total), and (2) performing the photometry of sources that are more isolated without a surrounding companion inside the beam (51362 sources in total). We set emission spectral slope and dust temperature at $\beta = 1.8$, and $T_{\rm d} = 38 \pm 7$ K. These values are chosen to provide a very good description of the data and they are based on our current knowledge of dust temperatures in SPIRE-detected sources (e.g. Yuan et al. 2015, Swinbank et al. 2014, Symeonidis et al. 2013, Lapi et al. 2011, see also Schreiber et al. 2017b). An example of simultaneous MBB deblending is illustrated in Fig.2.

2.7. Final data sample of 500 μm-risers

We select the final list of 133 500 μm-risers over the area of 55 deg^2. Selected sources fulfil criteria accepted for the final cut: $S_{500} > S_{350} > S_{250}$, $S_{250} > 13.2$ mJy and $S_{500} > 30$ mJy. The full catalogue is presented in Table 8.

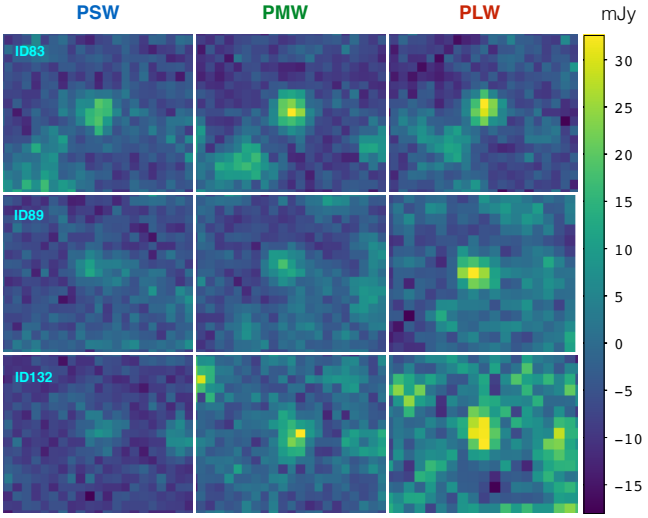

Fig. 3: 2D image cutouts as an illustration of 500 μm-risers that fulfil our final selection criteria. Presented examples are drawn from our "no-neighbour" list, that is, sources without a clear 250 μm detection within a radius of at least 36" around their centres. Colourbar shows fluxes measured in mJy.

We performed several tests and chose to set the flux density cut in the 500 μm band at $S_{500} \simeq 30$ mJy, which is related to 4σ above total noise measured in HeViCS maps. Using this value, we reach a completeness level of $\sim$ 80% at 500 μm (see Fig. 5) avoiding larger uncertainties in colours due to lower S/Ns (see Table 5 and Section 5.2). A 250 μm flux cut ($S_{250} > 13.2$ mJy) corresponds to $S_{250} > 3\sigma_{\rm conf}$ after applying an iterative 3σ clipping to remove bright sources (see Section 2.1). Amongst the final 500 μm-risers (133 in total) we have 11 red candidates with one or two additional 250 μm detections inside the 500 μm beam. Example two-dimensional (2D) cutouts of several 500 μm-risers from our final sample are presented in Fig.3 (see also Appendix C). Strong radio sources that have flat spectra and very prominent FIR emission (7 objects in total) have been removed from our final list of 500 μm-risers in the HeViCS field; these objects may have colours similar to those of dusty, star-forming systems that we are interested in selecting. Contamination due to radio-bright galaxies is eliminated by cross-matching existing radio

catalogues: HMQ (Flesch 2015), NVSS (Condon et al. 1998), FIRST (Helfand et al. 2015) and ALFA ALFA (Giovanelli et al. 2007). Identified radio-bright sources are classified as quasars. [2]

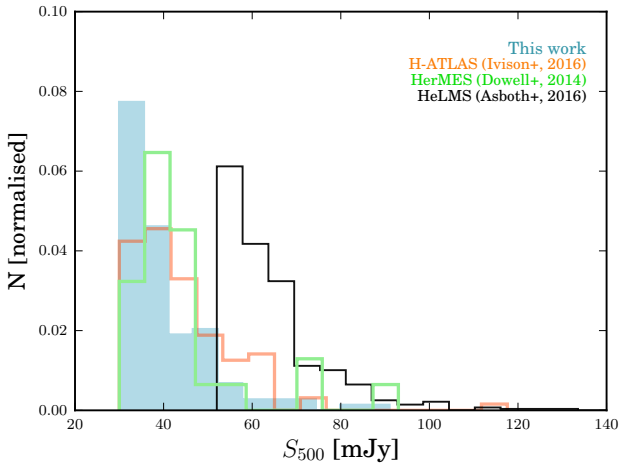

Fig. 4: Normalised distribution of 500 μm fluxes of 500 μm-risers. The filled blue area indicates our sample, while samples of Ivison et al. (2016), Dowell et al. (2014) and Asboth et al. (2016) are represented by orange, green and black lines, respectively.

In Fig.4 we show actual flux distribution of 500 μm-risers selected in this work, along with red sources from other studies. We see that our catalogue contains, on average, more fainter objects than other existing samples. The median 500 μm flux of our sample is 38 ± 4 mJy, while median fluxes found in Dowell et al. (2014), Asboth et al. (2016), and Ivison et al. (2016) are 45 mJy, 65 mJy, and 47 mJy, respectively. Therefore, our selection is arguably the faintest sample of 500 μm-risers available. We note that the underlying flux distribution of selected galaxies might still be affected by strong gravitational lensing, which we discuss in detail in Section 6.2. Along with galaxy-galaxy lensing, cluster-lens amplification might affect measured fluxes. The effect is the strongest when the deflector is located half-way between the observer and the lensed object (e.g. Kneib & Natarajan 2011). Strong lensing events are thus more numerous for clusters at $0.1 < z < 0.5$ (Johnson et al. 2014). Virgo cluster is very close along the line of sight ($z = 0.003$) and for this reason we expect negligible impact on SPIRE fluxes of 500 μm-risers. Colours of sources selected in this work, together with colours of 500 μm-risers with spectroscopic redshifts from other studies, are plotted in Fig.6. The median observed colour of our sample is $S_{500}/S_{350} = 1.11 \pm 0.10$, whereas median colours from Dowell et al. (2014), Asboth et al. (2016), and Ivison et al. (2016) are $S_{500}/S_{350} = 1.08$, $S_{500}/S_{350} = 1.12$, and $S_{500}/S_{350} = 1.23$, respectively. In Section 5.1.5 and Section 5.2 we illustrate and discuss the impact of the noise on observed counts and colours.

2.8. Completeness and flux accuracy

We check the quality of our data analysis by performing tests of completeness and flux accuracy. To determine these values, we use real "in-out" simulations. We calculate completeness by considering the number of injected sources with certain flux density S that are recovered in the simulated maps as real detections. Since our selection is based on a priori 250-μm positions, in this test we mostly inspect that band.

Table 2: The completeness fraction at SPIRE wavebands measured by injecting artificial sources into real SPIRE maps. Input fluxes are given in the first column, while percentages of detected sources (average values per bin) are given in the subsequent columns.

Flux [mJy]	V1 [250 μm]	V2 [250 μm]	V3 [250 μm]	V4 [250 μm]
5	0.18	0.14	0.17	0.19
10	0.37	0.40	0.39	0.38
15	0.59	0.64	0.63	0.61
25	0.84	0.91	0.93	0.93
35	0.94	0.97	0.96	0.97
45	0.97	0.98	0.98	0.98
55	0.98	0.99	0.99	0.99
65	0.98	1.0	1.0	0.99
75	0.99	1.0	1.0	1.0
85	1.0	1.0	1.0	1.0
95	1.0	1.0	1.0	1.0
	[350 μm]	[350 μm]	[350 μm]	[350 μm]
5	0.14	0.19	0.12	0.11
10	0.30	0.43	0.29	0.28
15	0.57	0.64	0.53	0.55
25	0.79	0.83	0.78	0.76
35	0.92	0.94	0.93	0.93
45	0.97	0.98	0.98	0.97
55	0.98	0.99	0.99	0.98
65	0.99	1.0	0.99	0.99
75	0.99	1.0	1.0	1.0
85	1.0	1.0	1.0	1.0
95	1.0	1.0	1.0	1.0
	[500 μm]	[500 μm]	[500 μm]	[500 μm]
5	0.10	0.09	0.11	0.11
10	0.21	0.20	0.18	0.18
15	0.39	0.44	0.43	0.42
25	0.69	0.68	0.68	0.73
35	0.91	0.88	0.89	0.94
45	0.98	0.99	0.98	0.99
55	0.99	0.99	0.99	0.99
65	0.99	1.0	1.0	0.99
75	0.99	1.0	1.0	1.0
85	1.0	1.0	1.0	1.0
95	1.0	1.0	1.0	1.0

We use Monte-Carlo simulation, artificially adding Gaussian sources and projecting them at randomised positions to our real 250 μm data, before convolving with the beam. Simulated sources in 350 μm and 500 μm maps are then placed at the same positions. The FWHM values that we used to convolve are 17.6", 23.9", and 35.2", that is, values we consider for our `SUSSEXtractor` detections. In each HeViCS field we add sources spanning the wide range of flux densities separated in different flux bins (first bin starts from 1-5 mJy, then 5-10 mJy, 10-20 mJy, 20-30 mJy and so on, up to 90-100 mJy). We

[2] For the detailed description of this category of dusty, radio sources, see Appendix A.

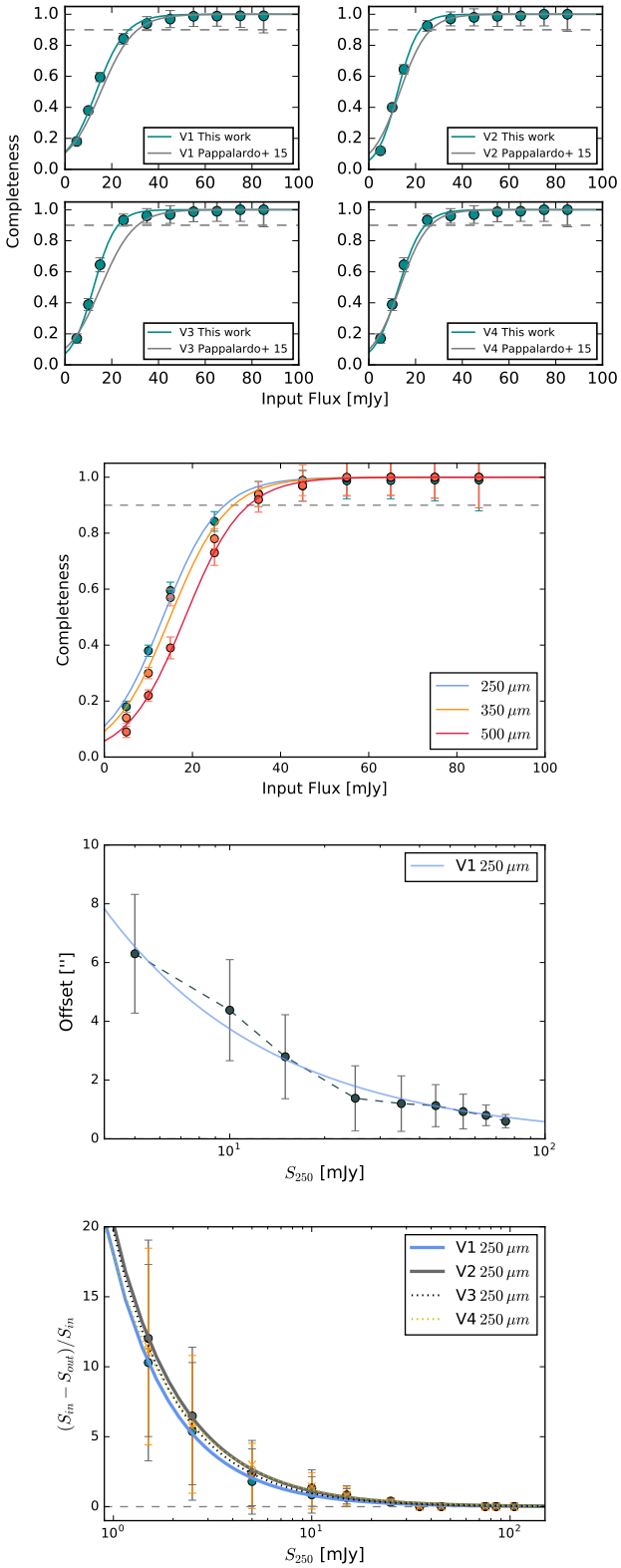

Fig. 5: For the HeViCS fields: Completeness at 250 μm band compared to Pappalardo et al. 2015, SPIRE completeness for the V1 field, positional accuracy (average radial offset), and flux boosting (the flux difference as a function of input flux) are shown from top to bottom. Simulated (input) flux $S_{\rm in}$ is plotted on the x-axis for all subplots, while $S_{\rm out}$ refers to observed flux.

perform the source extraction pipeline extracting the list of recovered point sources using `SUSSEXtractor` and searching for matched detections.

The HeViCS field is significantly crowded and we can perform missmatch with an unrelated source close to the input (x, y) coordinate. We match the input to output catalogue considering source distances smaller than half of the 250 μm beam size (9"), measured from the centre of the 250 μm detection. Quality assessment results are summarised in Table 2 and Fig.5. The plotted completeness curves are the best-fitting logistic functions, describing the completeness as a function of input flux. We can see that positions of recovered sources do not show any significant offset to assigned inputs. More than 70 % of sources with $S_{250} > 13.2$ mJy have an offset lower than 6", which is smaller than a 250 μm pixel size. Completeness and flux accuracy are consistent over all four HeViCS fields. The top panel in Fig.5 shows our completeness result compared to one obtained by Pappalardo et al. (2015), confirming that our results do not change notably when using different methods of flux estimation.

With measured numbers in hand, we can adjust the detection cut to see variations in completeness, which are connected to the function of input flux density. The completeness of our 250 μm maps shows a trend of fast decrease below $\sim$ 25 mJy, and reaches $\sim$ 50% at $\sim$ 13.2 mJy, the value we choose as the lowest cut for our prior S_{250} list. The fitting logistic function reaches saturation at the level of 250 μm fluxes larger than 40 mJy. For the 500 μm band, our completeness is above 80% at $S_{500} > 30$ mJy. We apply this 500 μm flux as the threshold for the final selection of 500 μm-risers. The bottom panel in Fig.5 shows that fluxes of sources below $S_{250} = 7 - 10$ mJy are systematically overestimated due to "flux-boosting".

A reliability test is performed to quantify eventual spurious detections. This is an important value for measuring the total number counts rather than for selection of 500 μm-risers, since we expect that eventually spurious sources would be present in one waveband but not in all three SPIRE bands. However, since our prior list is based on faint 250 μm detections close to the confusion limit, we perform an analysis of possible false detections by injecting fake sources into noise maps. We also quantify the range of statistical outliers present in our measurements. Outlier contamination is measured as a function of output flux density. Sources are considered as contaminants if their output fluxes are more than 3σ above the value inferred for injected sources. Considering the lowest detection threshold in the 250 μm band (13.2 mJy) we found a low sample contamination of 2.7%.

3. Expected $L_{\rm IR}$ and z distribution of 500 μm-risers

Without known interferometric positions and confirmed spectroscopic redshifts of our sources, we are limited to the properties of FIR SEDs of selected 500 μm-risers. Nevertheless, our data may be very useful in providing approximate redshift/luminosity distributions of large samples and candidates for follow-ups. To fit an MBB model to our photometric data, we consider a degeneracy between $\beta - T_{\rm d}$, and $T_{\rm d} - z$ (Blain et al. 2003, Pope & Chary 2010). The peak of the SED is determined by the $\nu/T_{\rm d}$ term (see Eq.2), given that a measurement of the colours alone constrains only $(1 + z)/T_{\rm d}$ ratio. However, assuming reasonable priors (in our case β and $T_{\rm d}$) it is possible to estimate a qualitative redshift distribution of 500 μm-risers (see $T_{\rm d} - z$ degeneracy illustrated in Fig.B.1).

We fit a single-temperature MBB model to the data. We fix the power-law slope $\beta = 1.8$ and dust temperature $T_{\rm d} = 38$ K, and we determine a median redshift of 4.22 ± 0.49. The choice of

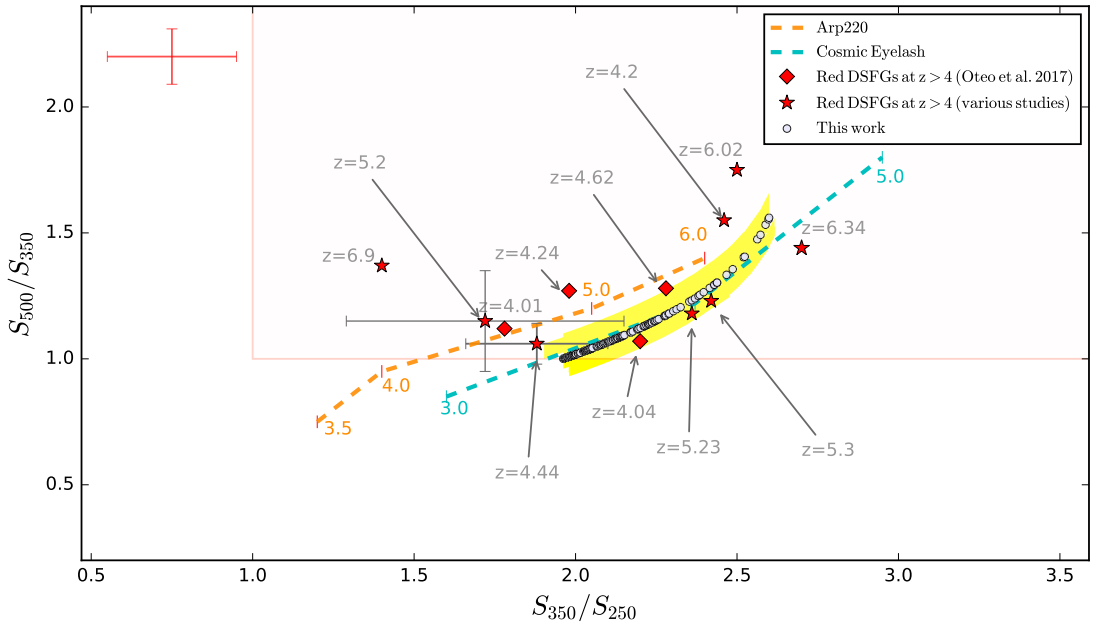

Fig. 6: SPIRE colour-colour diagram of 500 μm-risers, overlaid with redshift tracks of Arp 220 (Rangwala et al. 2011) and Cosmic Eyelash (Swinbank et al. 2010). Galaxies selected in this work are represented with circles, while yellow shaded regions describe uncertainties related to the chosen emissivity ($1.5 < \beta < 2.1$). For comparison we show 500 μm-risers selected in different studies and with known spectroscopic redshifts. Sources marked with red stars are: $z = 6.34$ (HFLS3 , Riechers et al. 2013), $z = 6.02$ (G09-8988, Zavala et al. 2017), $z = 4.44$ (FLS 5, Dowell et al. 2014), $z = 5.3$ (FLS 1, Dowell et al. 2014), $z = 5.2$ (HELMS-RED4, Asboth et al. 2016), $z = 4.04$ (GN20, Daddi et al. 2009), and $z = 4.2$ (SPT0113-46, Weiß et al. 2013). Sources marked with red diamonds are from Oteo et al. (2017b). For some of known sources we plot their colour uncertainties. Representative colour uncertainty for our sample is plotted in the upper-left corner.

β is arbitrary, likely $1.5 < \beta < 2.0$ (Casey et al. 2014, MacKenzie et al. 2014, Roseboom et al. 2012), and here we chose the value which is in the middle of that range. Due to the aforementioned degeneracy in $(1+z)/T_{\rm d}$ space, decreasing the dust temperature, for example from 38 K to 30 K for the fixed β, the peak of the redshift distribution decreases to $z = 3.57$ (with 33% of sources at $z > 4$). Modelled redshift tracks for different MBB parameters are provided in Appendix B (see Fig.B.1).

To further investigate the possible redshift/luminosity range, we consider a collection of SEDs of extensively studied IR-bright galaxies both from the local and higher-z Universe, namely: the compact local starburst M82, the typically interacting, local dusty system Arp220, and the "Cosmic Eyelash", a strongly cluster-lensed dusty galaxy at $z = 2.3$ (Swinbank et al. 2010).

The sample of dusty galaxies at $z > 4$ is expected to be comprised of a combination of intrinsically luminous starbursts and strongly lensed systems (Béthermin et al. 2012, Casey et al. 2014). It has been shown that a lack of observational constraints caused some SEDs to express overly low fluxes on the long λ-side of the FIR peak (Lutz 2014, Elbaz et al. 2010). Another important point considered here is that ultra-luminous infrared galaxies (ULIRGs) at higher redshifts express a wider variance in dust temperatures compared to their local analogues (e.g. Smith et al. 2014, Symeonidis et al. 2013). To overcome these differences we use an empirical template representative of *H*-ATLAS galaxies (Pearson et al. 2013). The template is built from a subset of 40 *H*-ATLAS survey sources with accurately measured redshifts covering the range from 0.5 to 4.5. It adopts two dust components with different temperatures and has already been used in the literature as a statistical framework for characterising redshifts of sources selected from SPIRE observations (see Ivison et al. 2016). With different templates in hand we can better characterise the systematics and uncertainties of measured redshifts. Shifting these templates to fit with our FIR fluxes, we forecast redshift ranges of 500 μm-risers in the HeViCS field. We built a probability distribution function (PDF) based on fitted χ^2 values that allows us to derive an estimate of the median redshift. With this we calculate a median redshift of 500 μm-risers of 3.87 if we apply "Cosmic Eyelash" template, 4.14 for Arp220 and 4.68 for M82. Subsequently, we apply a *H*-ATLAS empirical template accepting the following best-fit parameters: $T_{\rm cold} = 23.9$ K, $T_{\rm hot} = 46.9$ K, and the ratio between the masses of cold and warm dust of 30.1, as in Pearson et al. (2013). The result is shown in Fig.7. We determine a median redshift $\hat{z} = 4.28$, and an interquartile range of 4.08-4.75. This estimate matches the 1σ uncertainty range of photometric redshifts calculated by Dowell et al. (2014) and Asboth et al. (2016). To determine an average photometric redshift for red sources selected from several HerMES fields, Dowell et al. (2014) used the affine invariant method (Foreman-Mackey et al. 2013) to fit the MBB model with fixed emissivity and rest-frame wavelength peak for each source. They found $\langle z \rangle = 4.7 \pm 0.9$. The median photometric redshift estimated in Ivison et al. (2016) is somewhat lower ($\hat{z} = 3.7$), but we note that not all the sources in their catalogue of high-z candidate DSFGs are 500 μm-risers. In Section 5.2 we analyse how the noise and resolution effects might impact the observed colours of DSFGs and thus the redshift distribution of selected 500 μm-risers.

To compute the IR luminosity, which is defined as the integral over the rest frame spectrum between 8 μm and 1000 μm, we rely on the same approach. Our results favour the presence

of very luminous systems regardless of the chosen template - in 90% of cases selected 500 μm-risers have $L_{\rm IR} \geq 10^{13} L_{\odot}$, with minimum and maximum values of $L_{\rm IR} = 8.1 \times 10^{12} L_{\odot}$ and $L_{\rm IR} = 5.1 \times 10^{13} L_{\odot}$, respectively. Concerning the MBB model, we obtain $\hat{L_{\rm IR}} = 2.14 \times 10^{13} L_{\odot}$, but it is worth noting that the model accounts for mid-IR excess using a very simplified method (see Eq.2). Furthermore, we apply the *H*-ATLAS representative template to determine corresponding median rest-frame IR luminosity $\hat{L_{\rm IR}} = 1.94 \times 10^{13} L_{\odot}$. The result is again in consistency with Dowell et al. (2014) and Ivison et al. (2016). These studies performed SED modelling of the sources with known photometric or spectroscopic redshifts, concluding that 500 μm-risers have, on average, $L_{\rm IR} \geq 10^{13} L_{\odot}$. For example, Ivison et al. (2016) report the median value $L_{\rm IR} = 1.3^{+0.7}_{-0.5} \times 10^{13} L_{\odot}$. The corresponding luminosities in their sample range from $L_{\rm IR} = 6.0 \times 10^{12} L_{\odot}$ to $L_{\rm IR} = 5.8 \times 10^{13} L_{\odot}$.

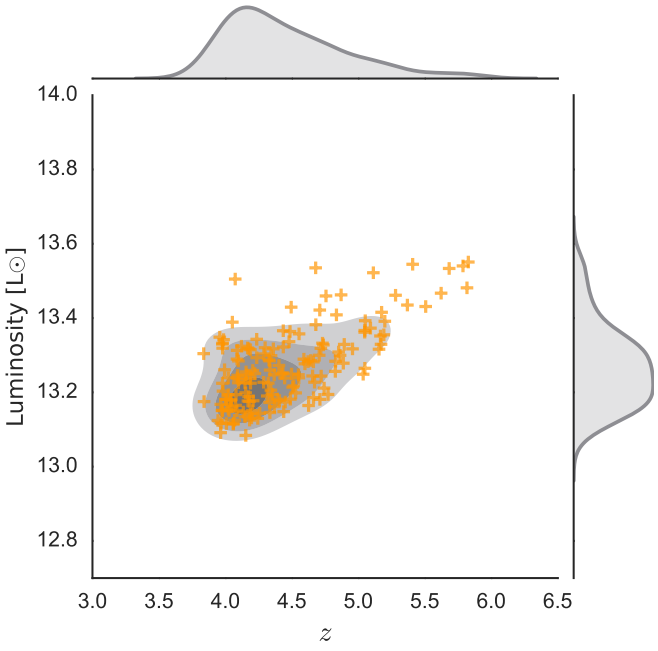

Fig. 7: Infrared luminosity of our 500 μm-risers (y-axis) as a function of redshift. Orange crosses are values estimated applying the empirical template made from *H*-ATLAS galaxies covering the redshift range from $z = 0.5$ to $z = 4.5$ (Pearson et al. 2013). We imposed the same fitting parameters as used for *H*-ATLAS galaxies: $T_{\rm cold} = 23.9$ K, $T_{\rm hot} = 46.9$ K, and a cold-to-hot dust mass ratio equal to 30.1.

In Fig.7 we illustrate the $L_{\rm IR}$-redshift trend of our 500 μm-risers. We see that the expected redshift distribution is heavy-tailed towards the higher redshifts. This indicates that very red submillimetre galaxies are present at redshfits above the interquartile range, but could also indicate strong gravitational lensing or unresolved blending. We should consider using a much wider range of $L_{\rm IR} - z$ values under larger uncertainties in dust temperatures. The IR luminosity emitted by an MBB source at a given $T_{\rm d}$ depends on the emissivity and size of the radiation area. Therefore, eventual gravitationally lensed candidates would lead to an apparent boost in dust luminosity at a given $T_{\rm d}$ due to a larger magnification (Greve et al. 2012). We consider and quantify the effects of strong lensing in our selection (see Section 5.1.5 and Section 6.2). We should emphasise here that the proper "training" of selected templates requires addition of higher-resolution data, and only when these are available is it possible to estimate systematic uncertainties and reject unreliable templates.

Comparison to red sources from the literature

In Fig.6 we show how the sources from this work relate to some of the 500μm-risers with known redshifts selected from the literature. Redshift tracks of Arp 220 and Cosmic Eyelash are added for comparison. We see that the colours of our sources agree very well with a large number of red DSFGs at $z > 4$ found in different studies. There are some exceptions, one of them being the most distant 500 μm-riser, SPT0311-58 at $z = 6.9$ (Strandet et al. 2017). The possible reason for this might be an additional contribution from AGN, since it has been shown that SPT0311-58 experiences additional mechanical energy input, probably via AGN-driven outflows. There are also examples of sources with redshifts somewhat lower than what would be expected from their very red colours. These sources usually have much lower $T_{\rm d}$ compared to the median dust temperature of 500 μm-risers at $z > 4$. Such an example is the 500μm-riser at $z = 4.2$ (Weiß et al. 2013), a strongly lensed red source with colours very similar to those of known 500 μm-risers at $z > 6$. However this source has an estimated $T_{\rm d}$ of 30 K, compared to 50K for all other known 500 μm-risers at $z > 6$ (Zavala et al. 2017, Strandet et al. 2017, Riechers et al. 2013).

We draw attention to some interesting 500μm-risers selected in this work. According to the MBB model introduced in Section 2.6 , it is plausible to expect a source at $z \sim 6$ if it has $T_{\rm d} \geq 45$ K and satisfies colour criteria $S_{500}/S_{350} > 1.3$ and $S_{350}/S_{250} > 2.4$ (see Fig.B.1 in Appendix B). In the literature two out of the three 500 μm-risers at $z > 6$ fulfil these so-called "ultra-red" requirements (Zavala et al. 2017, Riechers et al. 2013). We have seven such sources in our sample, and we highlight them as suitable very high-redshift candidates. They are catalogued as HVS 5, HVS 6, HVS 21, HVS 35, HVS 47, HVS 75, HVS 85 and HVS 94. We also stress that five of our 500μm-risers (HVS27, HVS60, HVS 64, HVS115 and HVS 130) reside in potential overdense regions unveiled by *Planck* (Planck Collaboration et al. 2016b). If these overdensities are not just part of random fluctuations in the galaxy number density within the *Planck* beam, this makes them candidate protoclusters of high-z DSFGs (Greenslade et al. 2018, Smolčić et al. 2017, Oteo et al. 2017a, Clements et al. 2016).

4. Differential number counts

We measure the raw 500 μm differential number counts and test our selection in respect to previous studies (this section), but also models of galaxy evolution (Section 5). We determine our counts placing 133 500 μm-risers in seven logarithmic flux bins between 30 mJy and 100 mJy. The resulting plot is shown in Fig.8. The total raw number density of 500 μm-risers in 55 deg^2 of HeViCS is $N = 2.41$ sources per deg^2, with the corresponding 1σ uncertainty of 0.34. We note that this value is uncorrected for non-red contaminants and completeness. In Section 5.2 we fully inspect and quantify biases that affect observed distribution, correcting for these effects. Furthermore, the presented differential number counts ignore eventual source multiplicity. Without interferometric data at longer wavelengths, our counts should be interpreted as the density of sources in respect to the beam resolution. Potential impact of SPIRE source multiplicity on our "FIR-riser" selection is discussed in Section 6.

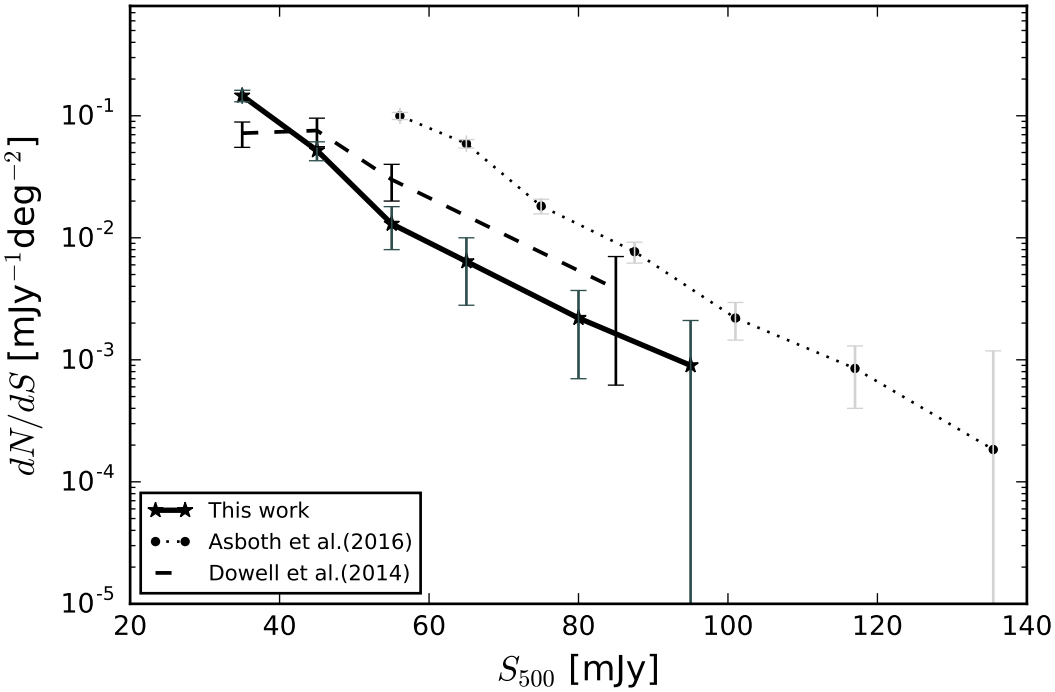

Fig. 8: Raw differential number counts of red sources from several studies. HeViCS number counts are presented with black stars, connected with a full, black line. Counts from Asboth et al. (2016) are indicated with black circles and connected with dotted lines, whilst observational findings of Dowell et al. (2014) are presented with dashed black lines. Filled points have Poisson 1σ error-bars added, and for the brightest flux bins with low statistics of sources, we plot the upper 95% confidence levels.

In Table 3 we present raw differential and integral number counts. In Fig.8 we plot our differential number counts along with values from studies of Asboth et al. (2016) and Dowell et al. (2014). They applied the so-called difference map method (*DMAP*) to select red sources. The method homogenizes beams to the size of 500 μm, and creates the *DMAP* where SPIRE images are all smoothed to an identical angular resolution. Prior to source identification, a weighted combination of the SPIRE maps is formed applying the relation $D = 0.920 \times M_{500} - 0.392 \times M_{250}$, where M_{500} and M_{250} are the smoothing values after matching SPIRE maps to the 500 μm resolution. To select 500 μm-risers, they performed a red colour map-based search, starting from lowest-resolution 500 μm maps.

From Fig.8 it can be seen that differential number counts notably differ, especially in the lowest two flux bins where our measurements are consistent with Dowell et al. (2014). The slope obtained by Dowell et al. (2014) in the first two flux bins is almost flat, which is different from the HeViCS curve where a steeper decrease is present. While our number counts show fairly good agreement with those measured by Dowell et al. (2014) especially in lower flux bins, they are well below the values measured by Asboth et al. (2016). Depending on the chosen flux bin, the discrepancy factor ranges from 3 to 10. We note that discrepancy between our number counts and those from Asboth et al. (2016) are due to several effects. Asboth et al. (2016) included possible blends in their final catalogue under the assumption that at least one component of a blend is a red DSFG. This introduces a non-negligible number of contaminants, which is the effect we analyse in Section 5.2. The effect of blending on our number counts is reduced since we apply a new technique of source extraction based on positional and SED priors. Additionally, Bethermin et al. (2017) simulated the same process of source extraction and selection as in Asboth et al. (2016) and found the number of observed 500 μm-risers to be higher by a factor of eight compared to the number of genuine (modelled) 500μm-risers. They concluded that a combination of noise, resolution effects, and the steepness of flux density distributions produces numerous red artefacts that match 500 μm-risers criteria. In Section 5.1.5 and Section 5.2 we present a detailed analysis of the effect of noise on our selection.

Table 3: Differential and integral number counts.

Flux (500 μm)		Diff. counts	Int.counts [(1)]
$S_{\rm min}$	$S_{\rm max}$	dN/dS	$N(>S_{\rm min})$
[mJy]	[mJy]	[$\times 10^{-4}$mJy^{-1}deg^{-2}]	[deg^{-2}]
30	40	1527± 164	2.41± 0.22
40	50	581± 90	0.91±0.14
50	60	145±51	0.29±0.09
60	70	72±36	0.14±0.05
70	90	27±15	0.07±0.03
90	110	9±5	0.02±0.01

(1) In order to calculate the cumulative (integral) number counts we have summed over all the 500μm-risers above the specified flux density ($S_{\rm min}$). Here we present raw differential and integrated number counts.

Table 4: Comparison of models used in our analysis.

	Models		
	B12 Béthermin et al. (2012)	B17 Bethermin et al. (2017)	S16 Schreiber et al. (2016)
Formalism(1)	2SFM	2SFM	2SFM
sSFR(2)	evolves up to $z = 2.5$	evolves up to $z = 4$	evolves continuously
Dispersion ($\sigma_{\rm MS}$)(3)	0.15 dex	0.3 dex	0.3 dex
Strong lensing	Yes	Yes	No
Passive galaxies	Yes	Yes	Yes
Evolution of $T_{\rm d}$	up to $z = 2$	up to $z = 4$	continuous
AGN contribution	Yes	Yes	No

(1) All the models are based on two SF mode formalism. Stellar mass function (SMF) is described by a double Schechter function: $\phi(\mathrm{M}_*)\mathrm{d}(\mathrm{M}_*) = \exp(-\frac{\mathrm{M}_*}{\mathrm{M}^*})[\Phi_1^*(\frac{\mathrm{M}_*}{\mathrm{M}^*}) + \Phi_2^*(\frac{\mathrm{M}_*}{\mathrm{M}^*})]$, where M^* is the characteristic mass of the Schechter break. The M^* is the redshift invariant in the Béthermin et al. (2012) model, and evolves with redshift in the other two presented models. For redshifts $z > 4$, the model of Bethermin et al. (2017) assumes a single Schechter function fixing Φ_1^* at zero, while the model of Schreiber et al. (2016) adopts double Schechter fitting to results of Grazian et al. (2015) for $4.5 < z < 7$. (2) The specific star-formation rate, defined as sSFR=SFR/M_*. In Béthermin et al. (2012) the sSFR increases with redshift up to $z = 2.5$ and than flattens. This trend is independent of the chosen range of stellar masses. In the latter two models the evolution is different, see Eq. 6 in Bethermin et al. (2017); (3) Modelled width of the main sequence (as log-normal scatter).

Apart from the samples mentioned above, it is possible to find other 500 μm-risers in the literature, but they are not selected in a uniform manner (e.g. Casey et al. 2012, Miettinen et al. 2015, Negrello et al. 2017). 500 μm-risers are serendipitously detected in relatively wide and shallow surveys that use wavelengths longer than 500 μm for initial detection (e.g. South Pole Telescope, see Vieira et al. 2013). These samples contain some of brightest 500 μm-risers, all of them significantly amplified by gravitational lensing ($S_{500} > 100$ mJy).

5. Comparison to models of galaxy evolution

In this section we compare our results with expectations from the most recent models of galaxy evolution. To evaluate our selection method, we perform simulations by generating realistic SPIRE maps from catalogues of simulated galaxies.

5.1. Models

In the literature there is a number of methods aiming to predict the evolution of number counts at different IR wavelengths. In this work we consider galaxy evolution models based on multi-band surveys. In general such models rely on the combination of observed SED templates of galaxies and luminosity functions. It has been shown (Dowell et al. 2014) that some galaxy evolution models, mostly from "pre-Herschel era", underpredict either the total number of high-z, red sources (Le Borgne et al. (2009), or the number of red sources which lie at $z > 4$ (Béthermin et al. 2011). There are some exceptions (e.g. Franceschini et al. 2010), that anticipate larger number of red, high-z galaxies, but predicts at the same time large amount of very low-z ($z < 2$) red objects which seems unphysical. Additionally, we expect that "almost red" sources (described as sources having a peak in their FIR SEDs at wavelengths between 350 and 500 μm) contaminate the sample of "500 μm-risers", making observational artefacts caused by the noise. It is then very important to have models that predict significant number of such sources, to check the systematics in the detection rate of these contaminants. In this work we consider phenomenological models of Béthermin et al. (2012), Schreiber et al. (2016) and Bethermin et al. (2017), hereafter denoted as B12, S16 and B17 respectively. These models were built on *Herschel* data and accurately match the total IR number counts. A summary of the models and their main ingredients is given in Table 3. Common to all models is their usage of stellar mass function (SMF) as a starting point from which properties of galaxies are generated. They share the same general description of star-forming galaxies, with star formation rate (SFR) assigned based on the dichotomy model of Sargent et al. (2012). It decomposes the bolometric FIR-luminosity function with main sequence (MS) and starburst (SB) galaxies. The MS galaxies are described as secularly evolving galaxies tightly relating stellar mass and SFR, while SB galaxies show an offset from the MS, expressing very high specific SFRs (sSFR = SFR/$\mathrm{M}_\star$). The shape of the SEDs is controlled by the galaxy type (MS or SB) and the mean intensity of the radiation field $\langle U \rangle$, which couples with the temperature of dust. Differences between the models are described briefly in the following subsections - the most important are scatter from the MS, parameters chosen to fit stellar masses, and redshift evolution of a dust temperature. Models presented here also have a slightly different description of mergers.

5.1.1. Béthermin et al. (2012) model

The B12 model describes the SMF with a Schechter function with a redshift invariant characteristic mass parameter (see Eq. 4 in Béthermin et al. 2012, but also Peng et al. 2010). Here, the infrared SED template is based on Draine & Li (2007) models, with the mean radiation field $\langle U \rangle$ evolving with redshift up to z = 2.0 (Magdis et al. 2012). The dispersion of the MS log-normal distribution is $\sigma_{\rm MS}$=0.15 dex, following Sargent et al. (2012) and Salmi et al. (2012). The model takes into account strong lensing effects reckoning the magnification rate PDF from Hezaveh & Holder (2011). These lensed sources contribute $\sim$ 20% to the bright-end submillimetre counts (PLW $\gtrsim$ 100 mJy). The AGN contribution is statistically associated based on results from Aird et al. (2012) and Mullaney et al. (2011).

5.1.2. Bethermin et al. (2017) model

The B17 model is based on similar prescriptions as B12, but implies several improvements in order to match recent interferometric results that disclosed notable overestimation of submillimetre number counts due to source blending (Karim et al. 2013, Simpson et al. 2015). The model includes detailed consideration of clustering and resolution effects. To describe the physical clustering, an abundance matching procedure is used to populate the dark-matter halos of a light cone constructed from the Bolshoi-Planck simulation (Rodríguez-Puebla et al. 2016).The MS scatter is updated ($\sigma_{\rm MS}$=0.3 dex) in order to match the measurements of Ilbert et al. (2015) and Schreiber et al. (2015). The model uses a new parametric form to fit the redshift evolution of the radiation field $\langle U \rangle$. The evolution of the dust temperature of MS star-forming galaxies stops at z = 4 (instead at z = 2.0 as in B12) and remains constant at higher values. Contribution of AGNs and strong lensing effects are modelled as in B12. The weak lensing regime is modelled with magnifications that are randomly drawn from a Gaussian distribution. Their width and mean values are derived based on a cosmological simulation of Hilbert et al. (2007).

5.1.3. Schreiber et al. (2016) model

Similarly to B12 and B17, the S16 model is based on the MS-SB dichotomy. MS galaxies are modelled based on a stellar mass and redshift from Schreiber et al. (2015) and Pannella et al. (2015). The scatter of the main sequence $\sigma_{\rm MS}$=0.3 dex. Randomly-selected galaxies (5%) are placed in the SB mode by enhancing their SFR by a factor of approximately five. The distribution of stellar masses is described by a double power-law Schechter fit, with parameters evolving with redshift. These parameters are chosen according to observational data from Schreiber et al. (2015) (see also Grazian et al. 2015). A new set of template SEDs is used to model the dust emission of star-forming galaxies. These SEDs are based on the physically motivated dust model of Galliano et al. (2011). Redshift evolution of a dust temperature is modelled as

$$T_{\rm d}[{\rm K}] = \begin{cases} 4.65 \times (z-2) + 31, & \text{for MS} \\ T_{\rm d}^{\rm MS} + 6.6 \times \log_{10}({\rm R_{SB}}), & \text{for SB} \end{cases} . \quad (4)$$

The "starburstiness" term $\rm R_{SB}$ is used to quantify the SFR offset between MS and SB galaxies ($\rm R_{SB}$ = SFR/$\rm SFR_{MS}$). Dependence of sSFR on the stellar mass shows that sSFR is constant at lower masses, and drops at the highest masses, $M > 10^{10.5} M_*$ (e.g. Schreiber et al. 2015, Whitaker et al. 2015, Magnelli et al. 2014). This trend is similar to the one used in B17, but different from the fit used in B12. To summarise, in S16 both sSFR and $T_{\rm d}$ evolve continuously with redshift, which is not the case for the other two models (see Table 3). Effects of strong lensing and AGNs are not included in the model.

5.1.4. Mock catalogues

We set mock catalogues based on models described in the previous section. Our goal is to compare the number counts of observed 500 μm-risers to the ones predicted by models.[3] The catalogues based on B12, B17, and S16 cover sufficiently large areas to offer accurate inspection of our observational criteria in the HeViCS field. Namely, for the B12 model we used the catalogue which is a result of 500 deg^2 simulations (Béthermin et al. 2012). We also used the catalogue created by the B17 model covering the area of 274 deg^2 (Simulated Infrared Dusty Extragalactic Sky, SIDES, Bethermin et al. 2017). The size of the simulated area is equal to the size of the HeLMS field, thus perfectly suited for a comparison of our selection technique to the one used by Asboth et al. (2016). With the S16 model, we generated a mock catalogue covering the size of the HeViCS field (55 deg^2).

We further apply our 500 μm-risers selection criteria ($S_{500} > S_{350} > S_{250}$, $S_{250} > 13.2$ mJy and $S_{500} > 30$ mJy) to modelled sources. In Fig.9 we see that observed counts are in a fairly good agreement with models, while corresponding power-law slopes show no significant difference from the slopes anticipated by models. Observed values are steep at the fainter end and flatter at the brighter end ($S_{500} > 80 - 90$ mJy) which is due to flux magnification by gravitational lensing. Our HeViCS differential number counts show a perfect agreement with B12, but we must note some recent evidence (see Bethermin et al. 2017 for more details) suggesting that the simulated catalogue based on the B12 model overpredicts the number counts at 500 μm fluxes below 50 mJy by a factor of two to three. The number of sources satisfying our selection in B17 and S16 is 0.45 deg^{-2} and 0.40 deg^{-2} , respectively. Predictions of B17 and S16 are consistent with the 1σ error bars of observed counts in the higher flux bins (60 mJy$< S_{500} <$ 100 mJy). In lower flux bins (30 mJy$< S_{500} <$ 60 mJy) discrepancy factors are between 1 and 6 depending on the chosen bin. In Section 5.1.5 we discuss in more detail potential reasons for these differences. However, it is clear that we have a much better agreement with empirical models than previous studies (Asboth et al. 2016) who claim observational discrepancy of an order of magnitude.

5.1.5. Effects of noise on measured counts

The results described in Section 5.1.4 neglect the effect of noise on the number counts of 500 μm-risers. Therefore, we simulate the effect of both confusion and instrumental noise by adding a random Gaussian noise drawn from the values measured in the HeViCS field (Section 2.1). The comparison between observations and models with simulated Gaussian noise is illustrated in the right panel of Fig.9. The significant increase of counts in the lowest two flux bins is clearly seen, while their slopes do not express significant change compared to intrinsic ones (left panel in Fig.9).

Considering the addition of noise, the number of simulated sources that appear as 500 μm-risers in B17 jumps to 473, re-

[3] In the following, we make the distinction between intrinsic and observed quantities. The former ones are the true, modelled properties of galaxies, free of measurement errors and systematics. The latter are measured values, affected by biases.

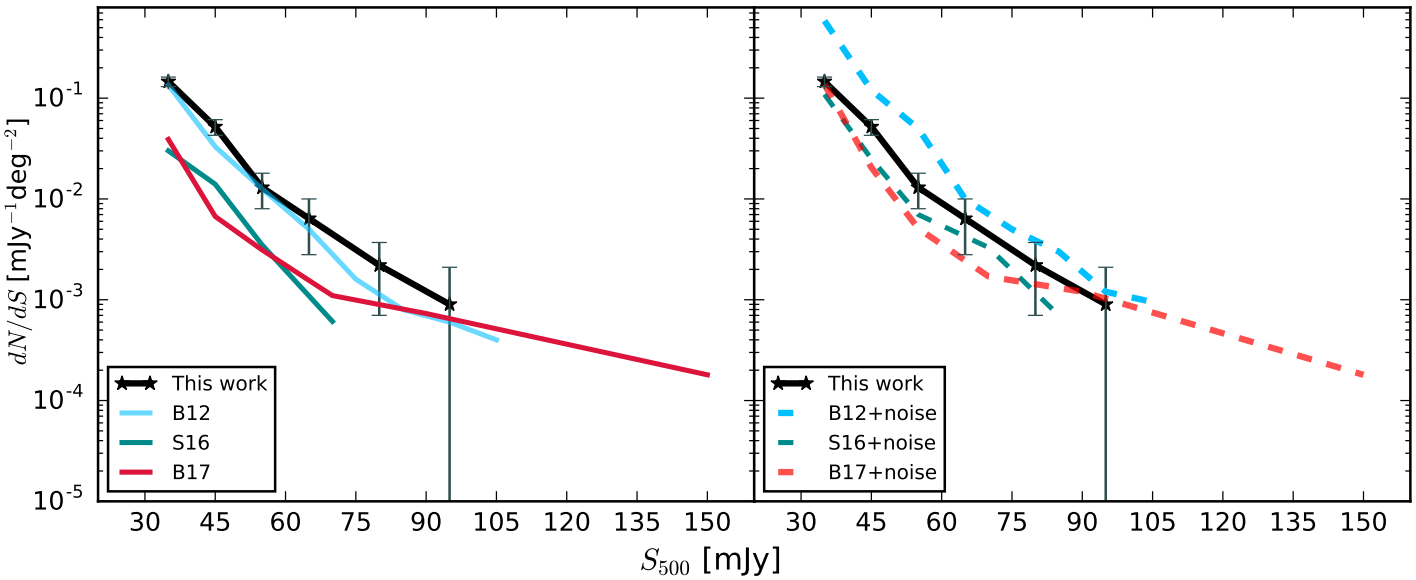

Fig. 9: Observed differential number counts of 500 μm-risers in the HeViCS field (black line) compared to models. Expected values from models are overplotted as coloured lines. *Left*: Comparison of observed and modelled counts. Models are represented by full, coloured lines: cyan for B12 (Béthermin et al. 2012), red for B17 (Bethermin et al. 2017), and green for S16 (Schreiber et al. 2016). The effect of simulated noise is ignored. *Right*: Comparison between observed and modelled counts if the effect of noise is simulated. The effect of confusion and instrumental noise is simulated by adding a random Gaussian noise to the modelled fluxes. Differential counts are then represented by dashed, coloured lines.

sulting in an increase of number counts from 0.45 per deg^2 to 1.73 per deg^2. We obtain a very similar result with S16 - a number density increases from 0.4 per deg^2 to 1.54 per deg^2. As a consequence, observed HeViCS values match predictions of the B17 and S16 models even in the faintest 500 μm flux regime. [4] We find that noise often tends to increase the number of genuinely red sources that are slightly below our 500 μm flux cut. These galaxies have modelled flux densities $S_{500} < 30$ mJy, but they can pass our final 500 μm-risers selection after the addition of a Gaussian noise. As shown in Table 5, contribution of these sources to the modelled 500 μm-risers varies between 52 and 67%. In Section 4, we mentioned that for the wide and shallow HeLMS field, Bethermin et al. (2017) found an increase of observed number counts by a factor of eight compared to their modelled values. This strong increase is caused by the combination of noise and clustering, and it is two times higher than the noise-driven increase of density of detected 500 μm-risers in the HeViCS field (see Table 5). We thus conclude that the effect of noise is more prominent for shallower fields, while for deeper fields (e.g. HeViCS and deep HerMES fields analysed in Dowell et al. 2014) the noise has only a mild impact on measured number counts.

Table 5: Comparison of modelled number counts before and after adding the Gaussian noise. Counts are calculated by imposing our criteria to select 500 μm-risers.

	Predicted density of 500 μm-risers (1)	Faint 500 μm-risers (2) ($S_{500} < 30$ mJy)
B17	0.45 deg^{-2} (51% lensed)	-
B17 + noise	1.73 deg^{-2} (24% lensed)	52 %
S16	0.4 deg^{-2}	-
S16 +noise	1.54 deg^{-2}	67 %

(1) Modelled density of 500 μm-risers before and after the addition of random Gaussian noise. Criteria used to select 500 μm-risers are: $S_{500} > S_{350} > S_{250}$, $S_{250} > 13.2$ mJy and $S_{500} > 30$ mJy. Numbers reported in brackets refer to the percentage of strongly lensed galaxies; (2) Contribution of intrinsically red but faint sources ($S_{500} < 30$mJy) to the population of modelled sources that match our 500 μm-risers selection criteria after the addition of modelled Gaussian noise.

The effect of noise also changes the relative contribution of modelled lensed and unlensed 500 μm-risers. The percentage of weakly lensed and non-lensed 500 μm-risers in B17 increases from 49% (modelled values) to 76% (modelled values+Gaussian noise). Closer inspection reveals that weak lensing ($1 < \mu < 2$) is a contributor to the flux budget for a non-negligible number of sources (166 out of 473, or 35%). Fainter, weakly lensed red sources can pass our final 500 μm-risers criteria more often if they are on a positive fluctuation of the magnification. This has an important role in producing observed 500 μm-risers without the support of strong lensing.

5.2. Simulated maps

Mock mapping simulations are needed to explore the exact nature of selected sources and possible biases of our *Herschel* SPIRE selection. These are mostly induced by the limited angular resolution combined with the noise effects. Having used two different models, we can uncover systematic uncertainty sur-

[4] In B17, SFR is limited to a maximum 1000 M$_\odot$yr^{-1}.

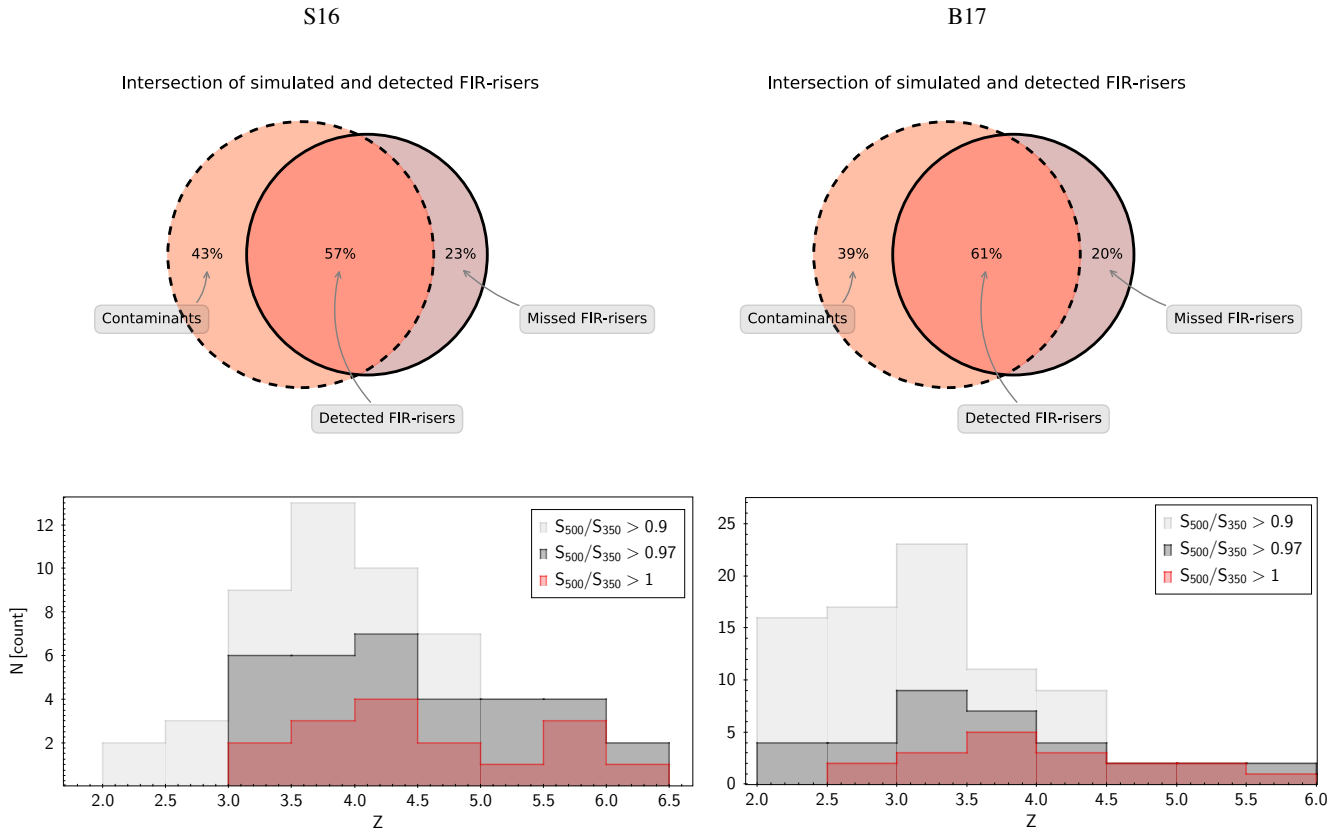

Fig. 10: *Upper panels*: Galaxies detected in mock maps. "FIR-riser" criteria are imposed as for real HeViCS maps ($S_{500} > S_{350} > S_{250}$, $S_{250} > 13.2$ mJy, $S_{500} > 30$ mJy). Intersected area coloured in dark orange depicts recovered red sources. Light orange area represents detected contaminants. Violet area represents missed sources. Those genuinely red galaxies are present in our catalogue, but not as 500 μm-risers. *Lower panels*: Redshift distribution of modelled galaxies. Different S_{500}/S_{350} colour cuts are imposed. These cuts are related to statistical properties of the confusion noise, which is the greatest contributor to colour uncertainties. (see also Table 6). Left and right panels refer to S16 and B17, respectively.

rounding the purity of detected sources. This is a crucial step if we want to investigate our photometric pipeline of 500μm-risers, since it is necessary to count the numbers of sources we potentially miss and to determine fraction of contaminants.

We generated a set of simulated SPIRE maps with the use of Empirical Galaxy Generator Code (EGG, Schreiber et al. 2017a). We filled our mock maps with sources drawn from S16 and B17 mock catalogues. We converted mock catalogues into maps, assigning theoretical *Herschel* PSF and the same noise properties as measured in our real HeViCS images. We chose to simulate clustering. The mock galaxies from the catalogues are then placed on the sky at coordinates with a fixed angular two-point correlation function to implement this effect. Positions of galaxies in S16 are clustered by default using of Soneira & Peebles (1978) algorithm, which produces a two-point correlation function with a power-law shape. To assign clustered coordinates for mock maps created from B17, we follow prescriptions from a simulation described in Bethermin et al. (2017), which adopts a sophisticated clustering model with the sub-halo abundance matching procedure used to populate the dark-matter halos of a light cone constructed from the Bolshoi-Planck simulation (Rodríguez-Puebla et al. 2016). With this we ensure that simulated maps contain a realistic background of clustered sources that can contribute to the confusion noise.

Due to computational dependencies, we generated maps covering the area of one of the four HeViCS fields (16 deg^2 each). As shown in Section 2.4, our source extraction lead to a homogeneous distribution of sources over all HeViCS fields, so we can easily extrapolate our results for the whole observed area of 55 deg^2. We use the methods described above and perform the same source-detection pipeline as we did in our raw HeViCS maps. We also check positional and flux accuracies in the same way we did for real HeViCS images.

Results from our simulations are summarised and presented in Fig.10. We detected all modelled 500 μm-risers via our detection procedure, but not all of them are characterised using their intrinsic colours.We thus disclose three groups of sources described below.

1. *Recovered 500 μm-risers*
   The dark orange region in Fig. 9 indicates the fraction of recovered 500 μm-risers. These are intrinsically red sources selected as 500μm-risers when we applied the same selection criteria as for the real HeViCS maps ($S_{500} > S_{350} > S_{250}$, $S_{250} > 13.2$ mJy and $S_{500} >$30 mJy). The percentage of recovered 500 μm-risers is around 60% for both models (57% for S16 and 61% for B17).

   As expected from the mock catalogue analysis (Sec-

tion 5.1.4), the population of recovered risers is a mix of both lensed and unlensed galaxies. We confirm that our criteria to select 500 μm-risers unveil a significant group of dusty and potentially very high-z sources that are not biased towards higher magnifications.

As introduced in Section 5.1.5, noise effects might produce colours somewhat redder than original ones. We quantify this as a "reddening", namely:

$$\Delta = \left(\frac{S_{500} + \sigma_{PLW}}{S_{350} + \sigma_{PMW}}\right) - \frac{S_{500}}{S_{350}}, \quad (5)$$

where σ_{PLWm} and σ_{PMW} are 1σ total noise ratios measured for appropriate bands in the HeViCS field (see Section 2.1). The differences between intrinsic and observed colours of recovered 500 μm-risers are presented in Table 6. We see that the largest difference is for the lowest flux bin, where we also expect the largest flux uncertainties due to the lower S/N. The redshift distribution of recovered 500 μm-risers in Fig.10 reflects differences between models. Following S16, all red galaxies are at $z > 3$, and most of them (70%) are at $z > 4$. The mean redshift value is $\langle z \rangle = 4.56 \pm 0.94$. The B17 model has a comparable high redshift tail, but this model peaks at lower redshift, causing the mean value ($\langle z \rangle = 3.89 \pm 0.9$) to be lower than in S16.

2. *Contaminants*
The light-orange region in Fig.10 indicates a fraction of contaminants. Sources are detected as 500 μm-risers, but having assigned their modelled colours and fluxes, they should not pass our selection criteria. The total percentage of contaminants is 39% for B17 and 43% for S16. They consist of two different populations of sources: The first ones are genuinely red, but are fainter galaxies, with modelled 500 μm fluxes not bright enough for the final catalogue inclusion ($S_{500} < 30$ mJy). Nonetheless, their observed fluxes and colours are sufficiently high to pass "500 μm-risers" criteria. The relative contribution of these contaminants is 60% for B17 and 72% for S16. The second population of contaminants are non-red sources with narrowly ranged intrinsic colours in the range $0.95 < S_{500}/S_{350} < 1.0$. They are weakly lensed or unlensed "almost red" sources. We also find that non-red contaminants are accompanied with sources clustered at $1 < z < 2$. The largest 500 μm excess is caused if clustered neighbours are at $z = 1.3 \pm 0.1$. These sources are massive galaxies with $M_* > 10^{9.8} M_\odot$. This confirms the conclusion from Section 5.1.4 that combined with weak lensing, confusion which arises from clustering and noise has a tendency to increase the number of observed red sources.

Having exploited both models, we see that all detected contaminants are high-z dusty galaxies, with just one source at $z < 3$. Redshift distribution of contaminants peaks at 3.48 for B17 ($z_{min} = 2.2$ and $z_{max} = 5.11$), and 4.17 for S16 ($z_{min} = 3.28$ and $z_{max} = 5.86$). Additionally, according to both models, contaminants are galaxies with warm dust temperatures ($40\ \mathrm{K} < T_\mathrm{d} < 50\ \mathrm{K}$).

3. *Missed 500 μm-risers*
With our extraction procedure we detected all modelled 500 μm-risers from simulated maps. However there is a fraction of sources for which we failed to properly characterize their colours with `MBB-fitter`. The violet region in Fig.10 indicates sources with $S_{500}/S_{350} < 1$ or $S_{500} < 30$ mJy. In this way we failed to select around 20% of the genuine 500 μm-risers. According to models, missed 500 μm-risers have colours and fluxes very close to the lowest selection threshold. In our simulated maps, they often immerse in complex blends, having a nearby, unresolved blue source at $0.5 < z < 1.0$ inside the 250 μm beam. Therefore, missed sources pass both 250 μm and 500 μm flux selection cuts but their observed colours are non-red. We find that the difference between observed and modelled colours of missed 500 μm-risers is shifted bluewards by a factor of approximately 0.03, thus giving negative Δ. Interestingly, not just the observed, but also the modelled Δ of missed sources exhibits negligible change due to noise effects; they tend to make their colours marginally redder or even bluer compared to the average value we measure for 500 μm-risers ($\langle\Delta\rangle = 0.01$ for the whole population, while for missed sources $\langle\Delta\rangle < 0.003$ having consulted both models). The final colour-criterion is thus highly sensitive to multiple effects including the strong clustering of blue sources. The redshift distribution of missed 500 μm-risers shows that 50% of them are weakly lensed galaxies at $z > 4$. It becomes vital to account for the missed population of red sources while searching for $z > 4$ dusty galaxies.

Table 6: Intrinsic vs. observed colours of simulated 500 μm-risers. Catalogue and maps are based on B17.

Flux bin	$S_{500}/S_{350}^{(1)}$ [B17$_{\mathrm{cat}}$]	$S_{500}/S_{350}^{(2)}$ [B17$_{\mathrm{map}}$]	$\Delta^{(3)}$
30-40 mJy	1.03± 0.09	1.07± 0.1	0.04 (0.012)
40-50 mJy	1.10± 0.05	1.12±0.06	0.02 (0.009)
> 50 mJy	1.15±0.11	1.16±0.18	0.01 (0.008)

(Column 2) Catalogued colours from B17. Noise is not added to initial flux values; (Column 3) Measured colours in simulated maps; (Column 4) Colour difference between observed and simulated flux values. It is quantified as "reddening" ($\Delta = \left(\frac{S_{500} + \sigma_{PLW}}{S_{350} + \sigma_{PMW}}\right) - \frac{S_{500}}{S_{350}}$). Values in brackets show the difference between catalogued fluxes before and after the additon of modelled Gaussian noise.

Modifying criteria to select galaxies at $z > 4$?

The percentage of simulated red sources recovered by our detection pipeline is not as high as the values presented in Asboth et al. (2016) and Dowell et al. (2014). These studies reported purity of almost 90%. Yet, there is an important and significant difference between our simulations. While we created mock images assuming the colours of sources that have been drawn directly from the simulated catalogues, Asboth et al. (2016) and Dowell et al. (2014) omitted modelled red sources from their maps, injecting 500 μm-risers with SPIRE colours fixed to the median value measured in their raw maps. Such an approach may lead to a bias, since we found (see Section 5.1) that most unlensed 500 μm-risers have S_{500}/S_{350} very close to one. Additionally,

S16 and B17 predict a large number of almost red FIR sources (e.g. $0.9 < S_{500}/S_{350} < 1.0$ and $S_{250} > 13.2$ mJy). The modelled number density of such defined sources is between 8 and 10 per deg^2. They are included in our initial "prior" catalogue, and due to effects of noise, clustering and/or lensing, some of them might be observed "redwards", thus being responsible for lower purity index.

Considering the colour differences (parameter Δ in Table 6), it appears clear that distinguishing between the population with $S_{500}/S_{350} = 0.97$ and $S_{500}/S_{350} = 1$ is very troublesome in crowded environments, even for fields with significantly reduced instrumental noise. As expected, colour uncertainties increase towards the lower fluxes. We conclude that some flexibility on a colour threshold is needed to account for noise and environmental effects. Here we test several colour cuts. The goal of such a test is twofold: to find the colour threshold that increases the number of true (modelled) 500 μm-risers, and to introduce at the same time low contamination of $2 < z < 4$ sources. We quantify the contribution of these lower-z objects for each colour limit. The result of the analysis are summarised in Table 7 and histograms in the lower panel of Fig.10. Having imposed $S_{500}/S_{350} > 0.9$ we anticipate that almost all 500 μm-risers will be found independently of the chosen model. Nevertheless, contribution of $2 < z < 4$ sources is significant, and varies from 57% (S16) to 77% (B17). Redshift distribution peaks at $z = 3.25$ for B17 and $z = 3.92$ for S16. If we increase the colour cut requirement to $S_{500}/S_{350} > 0.97$, the percentage of detected simulated intrinsic 500 μm-risers ranges between 82 and 85%. Contamination is heavily reduced, and just a few galaxies are at $z < 3$ (e.g. in S16 all the galaxies that satisfy this colour cut are at $z > 3$). Furthermore, redshift peak shifts to higher values, $z = 3.68$ for B17 and $z = 4.29$ for S16.

Following these results, we suggest that a cut at $S_{500}/S_{350} > 0.97$ might be imposed to search for $z \gtrsim 4$ galaxies in the future. It is a good compromise that accounts for several effects which decrease the percentage of recovered red galaxies. At the same time, it works well against the lower-z contaminants, especially those at $z < 3$, limiting their contribution to a maximum of 15%. Recent follow-up observations of red sources selected in the H-ATLAS field (Ivison et al. 2016) also support our reasoning for modifying 500 μm-risers colour criteria. They report that just 30% of sources selected as 500 μm-risers are lying at $z > 4$, claiming that such a low fraction is perhaps due to significant number of spurious-red contaminants in their catalogue. To account for a high level of noise in the H-ATLAS field, authors agreed that some refined selection technique is needed. In this paper we keep our final selection based on the traditional threshold of $S_{500}/S_{350} > 1$ for ease of comparison with existing studies.

Table 7: Relation of different colour cuts to the number of observed/missed red sources and their redshift distributions. Sources observed in simulated SPIRE maps are divided into three columns according to different colour limits ($S_{500/350} > 0.9$, $S_{500/350} > 0.97$, $S_{500/350} > 1.0$). For each of these columns m gives a percentage of missed genuine 500 μm-risers, while column $z > 4$ gives the percentage of $z > 4$ sources contained in selected populations.

Models	Colour-cuts					
	$S_{500/350} > 0.9$		$S_{500/350} > 0.97$		$S_{500/350} > 1.0$	
	m	$z > 4$	m	$z > 4$	m	$z > 4$
S16	3%	43%	18%	62%	23%	72%
B17	0%	23%	15%	33%	20%	47%

6. What are 500 μm-risers?

6.1. Problem of multiplicity

The potential problem in performing refined selection criteria for 500 μm-risers is our limited knowledge of source multiplicity. Different rates of multiplicities are claimed by studies found in the literature (e.g. Cowley et al. 2015, Simpson et al. 2015). Their conclusions are tightly related to selection criteria and instruments used to measure the flux (single dish or interferometer). Some observations suggest that multiplicity fraction may be dependent on the observed FIR flux, where is more liable for brighter sources to have multiple components (Karim et al. 2013, Bussmann et al. 2015). This assumption includes strongly lensed sources as well, since they are known to be very bright in SPIRE bands. A more recent SPIRE multiplicity study was done by Scudder et al. (2016). They used an improved version of the XID+ code (Hurley et al. 2017) to search for many potential contributing sources per 250 μm detection. They considered dusty galaxies covering a wide range of photometric redshifts and 250 μm flux densities. For 250 μm fluxes between 30 mJy and 45 mJy they found that a combination of the two brightest components accounts for approximately 90% of the flux in the 250 μm source. Additionally, the brightest component contributes more than 60% of the total flux.

Since we work with SPIRE data only, our multiplicity analysis is based on simulations. We perform photometry on simulated SPIRE maps and compare the flux emitted from the brightest galaxy to the total single-dish flux ratio. For each source detected as a 500 μm-riser in our mock maps, we assign the brightest component in the radius no larger than half of the 250 μm beam (9"). We then measure the ratio between the flux of this brightest galaxy from mock catalogues and the measured single-dish flux in our simulated maps. We place computed values in several flux bins. Our results are presented in Fig.11. For galaxies detected as 500 μm-risers, we found that 72 to 85% of observed 250 μm flux is emitted by the brightest galaxy (78% on average).

Overall, we see almost insignificant change for S16 and B17, with the trend expressing a slight increase towards higher 250 μm fluxes. Repeating the same analysis for the 500 μm beam we find the similar trend with a somewhat lower brightest-galaxy fraction (64 % on average) due to stronger resolution effects. Even from such a simple multiplicity analysis, it seems plausible to expect that selection of red sources from prior 250 μm detections does not experience strong resolution effects. The situation is somewhat different for missed red sources - the contribution of brightest components is lower (47-65%) with a tendency to decrease towards larger 250 μm fluxes. This is due to a presence of "blue" blends close to the position of 500 μm-risers ($r < 9''$).

Scudder et al. (2016) found the ratio of the fraction of the brightest 250 μm components to the total flux measured in simulated maps to be higher than one. They used deep multiwavelength data and applied a different definition of the flux density fraction. Additionally, their analysis considered sources regardless of SPIRE colours making a direct comparison difficult here. Our multiplicity predictions appear to be in good agreement with the measurements of Greenslade et al. (in prep.). They performed a Submillimeter Array (SMA) follow up program for 36 500 μm-risers selected from various fields and found a multiplicity rate

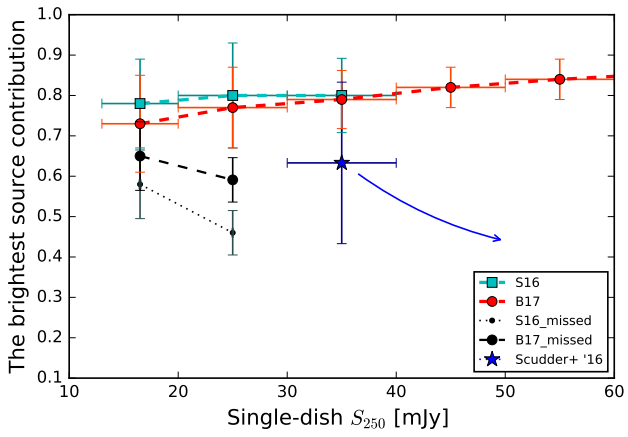

Fig. 11: Multiplicity of red sources detected in mock maps. Average fraction of the 250 μm flux density emitted by the brightest galaxy in the *Herschel* beam is plotted as a function of total, single-dish 250 μm flux measured in our simulated maps. Horizontal error bars indicate the width of the chosen flux bin, while vertical error bars show the standard deviation of the distribution. The blue star refers to the study of Scudder et al. (2016), and the blue arrow indicates the observed trend they found towards brighter fluxes.

of 33% with brightest components contributing 50 – 75% of the SMA flux. To shed new light on this issue, the contamination of sources at intermediate redshifts ($1 < z < 2$) seen in deep NGVS and PACS images will be discussed in a following paper.

6.2. Lensing and clustering

Considering the increase with redshift of the optical depth to lensing and the magnification bias, we account for the possibility that some of our 500 μm-risers are strongly lensed (Bethermin et al. 2017, Negrello et al. 2017, Cai et al. 2013). Without interferometric data allowing us to identify the true lensing fraction of our 500 μm-risers, we cannot precisely correct for the lensed population in our final sample. We thus investigate their relative contribution by making the comparison with recent ALMA/NOEMA follow-up results of 500 μm-risers selected in other fields (*H*-ATLAS, HerMES and HeLMS, Oteo et al. 2017b, see also Fudamoto et al. 2017), and using predictions from B17. Our findings are summarised in Fig.12 and Table 8.

The sample used for high-resolution ALMA follow-up in Oteo et al. (2017b) contains 44 red DSFGs. They were chosen from complete samples of red DSFGs presented in Ivison et al. (2016), Asboth et al. (2016), and Dowell et al. (2014). The sources span the wide range of 500 μm fluxes, from 30 mJy to 162 mJy. We note here that the sample is highly incomplete, accounting for only the reddest sources whose colours are consistent with high photometric redshifts, estimated to be $z \sim 4 - 6$. Observed total fraction of strongly lensed galaxies in Oteo et al. (2017b) is 40 % (18 out of 44). However, most of the lensed sources are in the bright flux regime of red DSFGs ($S_{500} > 52$ mJy) [5] . To make the sample suitable for comparison with our sources and model predictions, we split it into three subsamples according to methods used for their selections: 21 sources from Ivison et al. (2016), 13 sources from Asboth et al. (2016), and 10 sources from Dowell et al. (2014). In Fig.12 we show 500 μm flux distribution of our sample alongside the sub-samples drawn from Oteo et al. (2017b). We see that 500 μm-risers selected in this work have average fluxes fainter than other presented galaxies. We show the observed number of strongly lensed objects in *H*-ATLAS, HerMES, and HeLMS in the second column of Table 8. The sub-sample of 500 μm-risers in HeLMS contains the largest fraction of lensed sources (75%), while the lowest observed fraction is for *H*-ATLAS (23%).

We further use B17 and consider the same selection criteria as initial studies (Ivison et al. 2016, Asboth et al. 2016, Dowell et al. 2014). For each sub-sample we examine the range of fluxes identical to what is presented in Oteo et al. (2017b) and simulate the effect noise as explained in Section 5.1.5. From Table 8 we see a very good match between model predictions and observations. We estimate the predicted contribution of strongly lensed sources to our sample of 500 μm-risers. Applying our selection criteria we find that B17 predicts 24^{+6}_{-5}% fraction of strongly lensed 500 μm-risers in our sample. More precisely, 17% of the strongly magnified galaxies are expected to lie at a fainter flux regime ($S_{500} < 52$ mJy) where most of our sources reside (119 out of 133, or 89%). The median redshift of modelled, strongly lensed sources is $\hat{z} = 4.2 \pm 0.4$, whilst median magnification differs by $\hat{\mu} = 5.3 \pm 3$ and $\hat{\mu} = 8.1 \pm 5$ for the fainter and brighter flux regime, respectively. This implies that strong lensing can affect the observed luminosity function of our 500 μm-risers and lowers the fraction of intrinsically bright sources. After correcting for lensing, we expect to have 24% of galaxies with luminosities falling in the range $1.3 \times 10^{12} L_\odot < L_{\rm IR} < 10^{13} L_\odot$ (classified as ULIRGs), and 76% of sources with $L_{\rm IR} > 10^{13} L_\odot$, classified as hyperluminous IR galaxies (HyLIRGs).

Apart from strong lensing, clustering might be responsible for producing observed excess in number counts of 500 μm-risers. Several studies of the clustering of submillimetre bright galaxies at $1 < z < 3$ (e.g. $M_* > 10^{11} M_\odot$, and $L_{\rm IR} > 10^{12} L_\odot$, see Farrah et al. 2006, Wilkinson et al. 2017) have shown that they are hosted in moderately strongly clustered massive halos. *Herschel* detected that star-forming galaxies are on average more strongly clustered at higher redshifts ($z \sim 2$) than nearby objects (Béthermin et al. 2014, Ono et al. 2014). Since the beam size in *Herschel* is a direct function of the wavelength, we expect the largest SPIRE beam (500 μm) to be more affected than the other two beams. Bethermin et al. (2017) have studied in detail the influence of clustering on FIR continuum observations. They found that the confusion which arises from clustering increases the number of observed 500 μm-risers. The number of such contaminants causes the peak of intrinsic redshift distribution of 500 μm-risers to be somewhat lower than what would be expected from observed SPIRE colours. [6] Therefore, future spectroscopic confirmations of full samples of selected 500 μm-risers are needed to quantify and compare the exact fraction of sources at $z > 4$.

Simulations presented in Section 5.2 have some limitations in that they are affected by cosmic variance beyond simple Poissonian, and thus contain under- or overdensities at some redshifts. Furthermore, a purely probabilistic treatment is used to model the lensing, lacking the physical connection to the over-

[5] Here we distinguish between fainter ($S_{500} < 52$ mJy), and brighter 500 μm-risers ($S_{500} > 52$ mJy). The chosen separation is based on model predictions (B17), where highly magnified sources are contributing more than 50% to the population of red DSFGs at fluxes higher than $S_{500} > 52$ mJy.

[6] Ivison et al. (2016) and Duivenvoorden et al. (2018) found that more than half of DSFGs from their samples have $z_{\rm phot} < 4$. Photometric redshifts are estimated from SPIRE and SCUBA-2/LABOCA data.

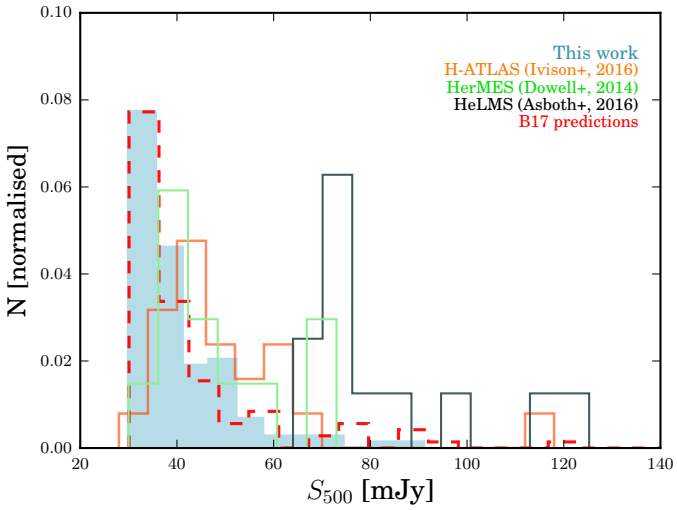

Fig. 12: Flux distribution of 500 μm-risers from this work (coloured blue area) compared to 500 μm-risers considered for a submillimetre interferometric follow-up in different studies. Orange, black, and green stepfilled lines represent sub-samples selected from Ivison et al. (2016), Asboth et al. (2016), and Dowell et al. (2014), respectively. Flux distribution of red sources from the B17 that are modelled applying the same selection criteria presented in this work is represented by the dashed red line.

Table 8: A relative contribution of strongly lensed sources to 500 μm-risers selected in different studies (1):

	Median S_{500} [mJy]	Lensed [observed]	Lensed [modelled (B17)]
H-ATLAS	45 ± 14	23^{+13}_{-11} % (5/21)	28^{+8}_{-9} %
HeLMS	78 ± 19	69^{+21}_{-25} % (9/13)	75^{+10}_{-13} %
HerMES	47 ± 9	40^{+10}_{-8} % (4/10)	36^{+9}_{-7} %
This work	38 ± 4	-	24^{+6}_{-5}%

Notes: Flux distribution of 500 μm-risers from this work compared to 44 red DSFGs presented in Oteo et al. (2017b). These are *H*-ATLAS, HerMES, and HeLMS sub-samples observed with ALMA and NOEMA at 870 μm, 1 mm, and 3 mm (Oteo et al. 2017b, Fudamoto et al. 2017). The second column shows median 500 μm fluxes along with the median 500 μm flux from this work. The relative contribution of observed, strongly lensed sources in various selections is shown in the third column. The fourth column shows the relative contribution of modelled, strongly lensed sources from B17. A relative contribution of strongly lensed sources is modelled applying the same selection cuts of 500 μm-risers for tabulated extragalactic fields.

density of lower-z systems. To improve our understanding of how lensing and clustering might shape 500 μm-riser selection, different solutions can be considered. Along with deeper, interferometric observations, more complex cosmological simulations are needed. They should include larger halo volumes, high-resolution to unveil fainter galaxies responsible for confusion, environmental effects, and refined treatment of a lens modelling.

6.3. Star-formation rate density

Bright, individually detected 500 μm-risers are important for understanding the evolution of massive systems. Here we test if such a selection is suitable to measure the total SFR density (SFRD). We make a rough estimate of the SFRD assuming the statistical properties of selected 500 μm-risers. We determine SFRD at $4 < z < 5$ applying the equation (Vincoletto et al. 2012, Hogg 1999):

$$\rho_*(z) = \frac{\sum \mathrm{SFR_{IR}}}{\frac{4\pi}{3}\int_{z=4}^{z=5} \frac{c/H_0}{\sqrt{\Omega_M(1+z)^3+\Omega_\Lambda}} dz}, \quad (6)$$

where $\rho_*(z)$ is SFRD, defined as a total sum of SFRs per co-moving volume, while $\mathrm{SFR_{IR}}$ is determined from IR luminosity. The denominator in Eq.6 is the co-moving volume contained within $4 < z < 5$, and IR luminosity is converted to SFR applying the standard conversion formula from Kennicutt (1998):

$$\mathrm{SFR_{IR}}(\mathrm{M_\odot\ yr^{-1}}) = 1.71 \times 10^{10}\ L_{\mathrm{IR}}\ (L_\odot). \quad (7)$$

We apply our selection criteria to model (B17). Since B17 provides a magnification factor for each source, we further use the modelled, lensing-corrected luminosities and redshift distribution of 500 μm-risers. We then correct for the number of missed and contaminant sources applying the result from our simulations (Fig.10, Section 5.2). We place IR luminosities in a wide bin by the co-moving volume per deg^2. Scaling with the observed area and applying cosmological parameters Ω_M = 0.307, Ω_Λ = 0.693, and H_0 = 67.8 km/s/Mpc (Planck Collaboration et al. 2016a), we find that SFRD = 1.99×10^{-4} M$_\odot$ yr^{-1} Mpc^{-3} for 500 μm-risers at $4 < z < 5$. This result is shown with a filled red star in Fig.13. Large uncertainties ($\pm 1.4 \times 10^{-4}$) determined by Monte Carlo bootstrapping are due to the Poisson noise and the fact that we make constraints with SPIRE data only. We additionally cross-check this result and make the same estimation of SFRD but adopting median IR luminosity (1.94×10^{13} $L_\odot$) from observed $L_{IR} - z$ distribution (see Section 3.).

Based on the expected fraction of strongly amplified objects found in Section 6.2 (24%), we randomly chose sources from our catalogue to correct for lensing, namely 17% of sources at $S_{500} < 52$ mJy, and 83% at $S_{500} > 52$ mJy. These percentages correspond to predictions from B17. We then adopt a median magnification from B17 that corresponds to a chosen flux-regime ($\mu = 5.3$ for fainter, and $\mu = 8.1$ for brighter "500 μm-risers"), and produce the observed, lensing-corrected luminosity distribution. We find SFRD = 2.87×10^{-4} M$_\odot$ yr^{-1} Mpc^{-3}. Our model-based SFRD estimation is consistent with recent observational findings from Duivenvoorden et al. (2018). We note also that offset between the study of Dowell et al. (2014) and our own may be explained by the fact that the estimation by Dowell et al. (2014) assumed substantially higher IR luminosities and purity ratios.

Furthermore, we can use the shape of the luminosity function to correct for the fainter red sources. We extrapolate the contribution of 500 μm-risers to SFRD - firstly we remove the 500 μm flux limit (thus accounting for red sources fainter than $S_{500} < 30$ mJy), and then we remove the lower 250 μm flux cut, thus accounting for all 500 μm-risers below the *Herschel* sensitivity limit. Extrapolated contributions are depicted by empty red triangles in Fig.13). Here we assume the luminosity distribution from B17, but we should mention that we obtain a very similar result (higher by a factor of 1.2) by applying the luminosity function from S16. As expected, the largest portion of sources responsible for a stellar budget at $z > 4$ is missed due to sensitivity limitations of *Herschel* instruments and not to colour selection.

The contribution of the emission of DSFGs to the total IR luminosity functions up to $z = 5$ is partially investigated (e.g. Koprowski et al. 2017, Bourne et al. 2016, Rowan-Robinson et al. 2016, Madau & Dickinson 2014, Gruppioni et al. 2013, Burgarella et al. 2013). However, there is no consensus on whether or not UV estimates have notably underestimated the contribution of dust-enshrouded star formation in DSFGs because our knowledge at $z > 3$ is severely incomplete, mostly due to optical obscuration. Attempting to extend the cosmic SFRD up to $z = 6$, Rowan-Robinson et al. (2016) exploited existing 500 μm *Herschel* selections of 500 μm-risers. They report no decline in dust-obscured SFRDs in the range $z = 3 - 6$, and very high SFRD values at $4 < z < 5$, an order of magnitude higher than our estimation. However, our result is in much better agreement with studies of Bourne et al. (2016) (marked with diamonds in Fig.13), who used very deep millimetre imaging to reduce the effects of confusion on cosmic SFRD measurements.

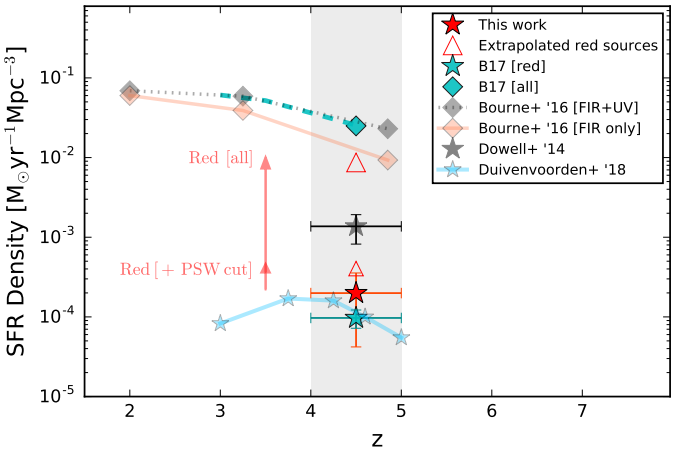

Fig. 13: SFRD as a function of redshift. The filled red star indicates our measurement. The estimated SFRDs of extrapolated 500 μm-risers are shown with empty red-edged triangles: smaller when 250 μm cut is imposed ($S_{250} > 13.2$ mJy), and larger if all flux cuts are removed. Flux corrections are annotated with arrows. We show for comparison results from other 500 μm-riser selections: B17 (cyan), Dowell et al. (2014) (black) and Duivenvoorden et al. (2018) (blue). Horizontal bars reflect the bin size. FIR and total FIR+UV observed SFRD (Bourne et al. 2017), as well as total simulated SFRD (B17), are marked with diamonds.

7. Conclusions

We have performed a systematic search of dusty background galaxies on a 55 deg^2 area. We introduce an innovative method for selecting 500 μm-risers ($S_{500} > S_{350} > S_{250}$). In order to estimate the 250-500 μm flux of blended sources, we use the multiwavelength `MBB-fitter` code. We assign positions of galaxies detected in the 250 μm map as a prior to extracting the flux densities at longer wavelengths, iteratively fitting their SEDs as modified blackbodies. We select 133 500 μm-risers that fulfil the following criteria: $S_{500} > S_{350} > S_{250}$, $S_{250} > 13.2$ mJy and $S_{500} > 30$ mJy. We reject all strong synchrotron sources by cross-matching available radio catalogues.

We use statistical properties of selected galaxies and estimate a median redshift value of $\hat{z} = 4.28$ and a corresponding median rest-frame IR luminosity of $\hat{L_{IR}} = 1.94 \times 10^{13} L_\odot$.

The total raw number density of selected sources is 2.41 $\pm$ 0.34 deg^{-2}. To evaluate our results, we retrieve mock catalogues based on models of Béthermin et al. (2012), Bethermin et al. (2017), and Schreiber et al. (2016). Differential number counts are fairly consistent with model predictions. Namely, towards the brighter end ($S_{500} > 70$ mJy), HeViCS counts have both slope and values identical to those anticipated by models. At the lowest flux end, discrepancy is the effect of noise and lensing. We find that noise tends to increase number counts of 500 μm-risers. It may be high enough to fully match with observations within 1σ uncertainty. We confirm that selecting 500 μm-risers applying our selection criteria is a direct way to detect a significant population of unlensed, dusty, high-z galaxies.

We build simulated maps. Clustering and lensing are modelled in order to fully resolve effects that produce colour uncertainties. We propose a modified colour criterion ($S_{500}/S_{350} > 0.97$) that should be probed in future selections of potentially $z > 4$ dusty sources. Motivation to apply this criterion is twofold: it would account for colour uncertainties that arise from effects

of noise, clustering, and lensing, and it increases the sample of candidate $z > 4$ galaxies. Anticipated contribution of $2 < z < 3$ contaminants satisfying this colour cut is small, and reaches the maximum of 13%.

We inspect the effect of multiplicity working with simulated SPIRE data. The brightest galaxy inside the beam contributes on average 75% and 64% to the total single-dish flux measured at 250 μm and 500 μm, respectively.

We use the model of Bethermin et al. (2017) and find that 24^{+6}_{-5}% of 500 μm-risers selected with our criteria would be strongly lensed. After correcting measured luminosities for lensing, we expect 24% of sources to have luminosities of $10^{12} L_{\odot} < L_{\rm IR} < 10^{13} L_{\odot}$ (classified as ULIRGs) and 76% of sources to have $L_{\rm IR} > 10^{13} L_{\odot}$ (classified as HyLIRGs).

We use the statistical properties of our galaxies to determine the role of 500 μm-risers in the SFRD for $4 < z < 5$. We show that after correcting for fainter sources, the projected contribution of 500 μm-risers is just a factor of 2 below the total, dust-corrected SFRD.

Acknowledgements. We are thankful to the anonymous referee for very constructive comments and points which significantly improved this paper. We would like to acknowledge David Corre, Denis Burgarella, Alessandro Boselli, Tom Bakx and Eric Jullo for useful discussions. The project leading to this publication has received funding from Excellence Initiative of Aix-Marseille University - A*MIDEX, a French "Investissements d'Avenir" programme (ANR-11-IDEX-0001-02) and from the OCEVU Labex (ANR-11-LABX-0060). d'Avenir" French government program managed by the ANR. C.P. acknowledges support from the Science and Technology Foundation (FCT, Portugal) through the Postdoctoral Fellowship SFRH/BPD/90559/2012, PEst-OE/FIS/UI2751/2014, PTDC/FIS-AST/2194/2012, and through the support to the IA activity via the UID/FIS/04434/2013 fund.
HeViCS is a *Herschel* open time key program (PI Davies, Davies et al. 2010). All the data are publicly available through Herschel Science Archive `http://archives.esac.esa.int/hsa/whsa/#home`.
Herschel is an ESA space observatory with science instruments provided by European-led Principal Investigator consortia and with important participation from NASA. SPIRE has been developed by a consortium of institutes led by Cardiff University (UK) and including Univ. Lethbridge (Canada); NAOC (China); CEA, LAM (France); IFSI, Univ. Padua (Italy); IAC (Spain); Stockholm Observatory (Sweden); Imperial College London, RAL, UCL-MSSL, UKATC, Univ.Sussex (UK); and Caltech, JPL, NHSC, Univ. Colorado (USA). This development has been supported by national funding agencies: CSA (Canada); NAOC (China); CEA, CNES, CNRS (France); ASI (Italy); MCINN (Spain); SNSB (Sweden); STFC (UK); and NASA (USA). This publication makes use of public data products from the Two Micron All Sky Survey (2MASS), which is a joint project of the University of Massachusetts and the Infrared Processing and Analysis Center California Institute of Technology, funded by the National Aeronautics and Space Administration and the National Science Foundation. We express our gratitude to `Daft` `https://github.com/dfm/daft`, a probabilistic graphical model available under the MIT License.

References

Aird, J., Coil, A. L., Moustakas, J., et al. 2012, ApJ, 746, 90
Amblard, A., Cooray, A., Serra, P., et al. 2010, A&A, 518, L9
Asboth, V., Conley, A., Sayers, J., et al. 2016, Monthly Notices of the Royal Astronomical Society, 462, 1989
Auld, R., Bianchi, S., Smith, M. W. L., et al. 2013, MNRAS, 428, 1880
Bertin, E. & Arnouts, S. 1996, A&AS, 117, 393
Béthermin, M., Daddi, E., Magdis, G., et al. 2012, ApJ, 757, L23
Béthermin, M., Dole, H., Cousin, M., & Bavouzet, N. 2010, A&A, 516, A43
Béthermin, M., Dole, H., Lagache, G., Le Borgne, D., & Penin, A. 2011, A&A, 529, A4
Béthermin, M., Kilbinger, M., Daddi, E., et al. 2014, A&A, 567, A103
Bethermin, M., Wu, H.-Y., Lagache, G., et al. 2017, ArXiv e-prints, arXiv:1703.08795 [`arXiv:1703.08795v2`]
Blain, A. W., Barnard, V. E., & Chapman, S. C. 2003, MNRAS, 338, 733
Bourne, N., Dunlop, J. S., Merlin, E., et al. 2017, MNRAS, 467, 1360
Bourne, N., Dunne, L., Maddox, S. J., et al. 2016, MNRAS, 462, 1714
Bracco, A., Cooray, A., Veneziani, M., et al. 2011, MNRAS, 412, 1151
Burgarella, D., Buat, V., Gruppioni, C., et al. 2013, A&A, 554, A70
Bussmann, R. S., Riechers, D., Fialkov, A., et al. 2015, ApJ, 812, 43
Cai, Z.-Y., Lapi, A., Xia, J.-Q., et al. 2013, ApJ, 768, 21
Capak, P. L., Riechers, D., Scoville, N. Z., et al. 2011, Nature, 470, 233
Casey, C. M., Berta, S., Béthermin, M., et al. 2012, ApJ, 761, 140
Casey, C. M., Narayanan, D., & Cooray, A. 2014, Phys. Rep., 541, 45
Clements, D. L., Braglia, F., Petitpas, G., et al. 2016, MNRAS, 461, 1719
Combes, F., Rex, M., Rawle, T. D., et al. 2012, A&A, 538, L4
Condon, J. J., Cotton, W. D., Greisen, E. W., et al. 1998, AJ, 115, 1693
Cowley, W. I., Lacey, C. G., Baugh, C. M., & Cole, S. 2015, MNRAS, 446, 1784
Cox, P., Krips, M., Neri, R., et al. 2011, ApJ, 740, 63
da Cunha, E., Groves, B., Walter, F., et al. 2013, ApJ, 766, 13
Daddi, E., Dannerbauer, H., Stern, D., et al. 2009, ApJ, 694, 1517
Davies, J. I., Baes, M., Bendo, G. J., et al. 2010, A&A, 518, L48
Davies, J. I., Bianchi, S., Cortese, L., et al. 2012, MNRAS, 419, 3505
Delhaize, J., Smolcic, V., Delvecchio, I., et al. 2017, ArXiv e-prints, arXiv:1703.09723 [`arXiv:1703.09723`]
Dowell, C. D., Conley, A., Glenn, J., et al. 2014, The Astrophysical Journal, 780, 75
Draine, B. T. & Li, A. 2007, ApJ, 657, 810
Duivenvoorden, S., Oliver, S., Scudder, J. M., et al. 2018, ArXiv e-prints [`arXiv:1801.07266`]
Eales, S., de Vis, P., Smith, M. W. L., et al. 2017, MNRAS, 465, 3125
Eales, S. A., Smith, M. W. L., Wilson, C. D., et al. 2010, A&A, 518, L62
Elbaz, D., Hwang, H. S., Magnelli, B., et al. 2010, A&A, 518, L29
Farrah, D., Lonsdale, C. J., Borys, C., et al. 2006, ApJ, 641, L17
Ferrarese, L., Côté, P., Cuillandre, J.-C., et al. 2012, ApJS, 200, 4
Flesch, E. W. 2015, PASA, 32, e010
Foreman-Mackey, D., Hogg, D. W., Lang, D., & Goodman, J. 2013, PASP, 125, 306
Franceschini, A., Rodighiero, G., Vaccari, M., et al. 2010, A&A, 517, A74
Fudamoto, Y., Ivison, R. J., Oteo, I., et al. 2017, MNRAS, 472, 2028
Galliano, F., Hony, S., Bernard, J.-P., et al. 2011, A&A, 536, A88
Giovanelli, R., Haynes, M. P., Kent, B. R., et al. 2007, AJ, 133, 2569
Grazian, A., Fontana, A., Santini, P., et al. 2015, A&A, 575, A96
Greenslade, J., Clements, D. L., Cheng, T., et al. 2018, MNRAS[`arXiv:1712.07141`]
Greve, T. R., Vieira, J. D., Weiß, A., et al. 2012, ApJ, 756, 101
Griffin, M. J., Abergel, A., Abreu, A., et al. 2010, A&A, 518, L3
Gruppioni, C., Pozzi, F., Rodighiero, G., et al. 2013, MNRAS, 432, 23
Hayward, C. C. 2013, MNRAS, 432, L85
Helfand, D. J., White, R. L., & Becker, R. H. 2015, ApJ, 801, 26
Hezaveh, Y. D. & Holder, G. P. 2011, ApJ, 734, 52
Hilbert, S., White, S. D. M., Hartlap, J., & Schneider, P. 2007, MNRAS, 382, 121
Hogg, D. W. 1999, ArXiv Astrophysics e-prints, arXiv:astro-ph/9905116 [`astro-ph/9905116`]
Hurley, P. D., Oliver, S., Betancourt, M., et al. 2017, MNRAS, 464, 885
Ikarashi, S., Ivison, R. J., Caputi, K. I., et al. 2017, ApJ, 835, 286
Ilbert, O., Arnouts, S., Le Floc'h, E., et al. 2015, A&A, 579, A2
Ivison, R. J., Greve, T. R., Dunlop, J. S., et al. 2007, MNRAS, 380, 199
Ivison, R. J., Lewis, A. J. R., Weiss, A., et al. 2016, ApJ, 832, 78
Jarrett, T.-H., Chester, T., Cutri, R., et al. 2000, AJ, 120, 298
Johnson, T. L., Sharon, K., Bayliss, M. B., et al. 2014, ApJ, 797, 48
Karim, A., Swinbank, A. M., Hodge, J. A., et al. 2013, MNRAS, 432, 2
Kennicutt, Jr., R. C. 1998, ARA&A, 36, 189
Kneib, J.-P. & Natarajan, P. 2011, A&A Rev., 19, 47
Koprowski, M. P., Dunlop, J. S., Michałowski, M. J., et al. 2017, MNRAS, 471, 4155
Lapi, A., González-Nuevo, J., Fan, L., et al. 2011, ApJ, 742, 24
Le Borgne, D., Elbaz, D., Ocvirk, P., & Pichon, C. 2009, A&A, 504, 727
Liu, D., Daddi, E., Dickinson, M., et al. 2017, ArXiv e-prints, arXiv:1703.05281 [`arXiv:1703.05281`]
Lutz, D. 2014, ARA&A, 52, 373
Ma, Z. & Yan, H. 2015, ApJ, 811, 58
MacKenzie, T. P., Scott, D., Smail, I., et al. 2014, MNRAS, 445, 201
Madau, P. & Dickinson, M. 2014, ARA&A, 52, 415
Magdis, G. E., Daddi, E., Béthermin, M., et al. 2012, ApJ, 760, 6
Magnelli, B., Lutz, D., Saintonge, A., et al. 2014, A&A, 561, A86
Mancuso, C., Lapi, A., Shi, J., et al. 2016, ApJ, 823, 128
Merlin, E., Bourne, N., Castellano, M., et al. 2016, A&A, 595, A97
Michałowski, M. J., Hayward, C. C., Dunlop, J. S., et al. 2014, A&A, 571, A75
Miettinen, O., Novak, M., Smolčić, V., et al. 2015, A&A, 584, A32
Mullaney, J. R., Alexander, D. M., Goulding, A. D., & Hickox, R. C. 2011, MNRAS, 414, 1082
Negrello, M., Amber, S., Amvrosiadis, A., et al. 2017, MNRAS, 465, 3558
Nguyen, H. T., Schulz, B., Levenson, L., et al. 2010, A&A, 518, L5
Norris, R. P., Hopkins, A. M., Afonso, J., et al. 2011, PASA, 28, 215
Oliver, S. J., Bock, J., Altieri, B., et al. 2012, MNRAS, 424, 1614
Oliver, S. J., Wang, L., Smith, A. J., et al. 2010, A&A, 518, L21
Ono, Y., Ouchi, M., Kurono, Y., & Momose, R. 2014, ApJ, 795, 5

Oteo, I., Ivison, R. J., Dunne, L., et al. 2017a, ArXiv e-prints [arXiv:1709.02809]
Oteo, I., Ivison, R. J., Dunne, L., et al. 2016, ApJ, 827, 34
Oteo, I., Ivison, R. J., Negrello, M., et al. 2017b, ArXiv e-prints, arXiv:1709.04191 [arXiv:1709.04191]
Pannella, M., Elbaz, D., Daddi, E., et al. 2015, ApJ, 807, 141
Pappalardo, C., Bendo, G. J., Bianchi, S., et al. 2015, A&A, 573, A129
Pappalardo, C., Bizzocchi, L., Fritz, J., et al. 2016, A&A, 589, A11
Pearson, E. A., Eales, S., Dunne, L., et al. 2013, MNRAS, 435, 2753
Peng, Y.-j., Lilly, S. J., Kovač, K., et al. 2010, ApJ, 721, 193
Pilbratt, G. L., Riedinger, J. R., Passvogel, T., et al. 2010, A&A, 518, L1
Planck Collaboration, Ade, P. A. R., Aghanim, N., et al. 2016a, A&A, 594, A13
Planck Collaboration, Ade, P. A. R., Aghanim, N., et al. 2016b, A&A, 596, A100
Pope, A. & Chary, R.-R. 2010, ApJ, 715, L171
Rangwala, N., Maloney, P. R., Glenn, J., et al. 2011, ApJ, 743, 94
Riechers, D. A., Bradford, C. M., Clements, D. L., et al. 2013, Nature, 496, 329
Rigby, E. E., Maddox, S. J., Dunne, L., et al. 2011, MNRAS, 415, 2336
Rodríguez-Puebla, A., Behroozi, P., Primack, J., et al. 2016, MNRAS, 462, 893
Roseboom, I. G., Ivison, R. J., Greve, T. R., et al. 2012, MNRAS, 419, 2758
Roseboom, I. G., Oliver, S. J., Kunz, M., et al. 2010, MNRAS, 409, 48
Rowan-Robinson, M., Oliver, S., Wang, L., et al. 2016, MNRAS, 461, 1100
Safarzadeh, M., Ferguson, H. C., Lu, Y., Inami, H., & Somerville, R. S. 2015, ApJ, 798, 91
Salmi, F., Daddi, E., Elbaz, D., et al. 2012, ApJ, 754, L14
Sargent, M. T., Béthermin, M., Daddi, E., & Elbaz, D. 2012, ApJ, 747, L31
Savage, R. S. & Oliver, S. 2007, ApJ, 661, 1339
Schober, J., Schleicher, D. R. G., & Klessen, R. S. 2017, MNRAS, 468, 946
Schreiber, C., Elbaz, D., Pannella, M., et al. 2016, A&A, 589, A35
Schreiber, C., Elbaz, D., Pannella, M., et al. 2017a, A&A, 602, A96
Schreiber, C., Pannella, M., Elbaz, D., et al. 2015, A&A, 575, A74
Schreiber, C., Pannella, M., Leiton, R., et al. 2017b, A&A, 599, A134
Scudder, J. M., Oliver, S., Hurley, P. D., et al. 2016, Monthly Notices of the Royal Astronomical Society, 460, 1119
Shu, X. W., Elbaz, D., Bourne, N., et al. 2016, ApJS, 222, 4
Simpson, J. M., Smail, I., Swinbank, A. M., et al. 2015, ApJ, 807, 128
Simpson, J. M., Swinbank, A. M., Smail, I., et al. 2014, ApJ, 788, 125
Smith, D. J. B., Jarvis, M. J., Hardcastle, M. J., et al. 2014, MNRAS, 445, 2232
Smolčić, V., Miettinen, O., Tomičić, N., et al. 2017, A&A, 597, A4
Soneira, R. M. & Peebles, P. J. E. 1978, AJ, 83, 845
Strandet, M. L., Weiss, A., De Breuck, C., et al. 2017, ApJ, 842, L15
Swinbank, A. M., Simpson, J. M., Smail, I., et al. 2014, MNRAS, 438, 1267
Swinbank, A. M., Smail, I., Longmore, S., et al. 2010, Nature, 464, 733
Symeonidis, M., Vaccari, M., Berta, S., et al. 2013, MNRAS, 431, 2317
Toft, S., Smolčić, V., Magnelli, B., et al. 2014, ApJ, 782, 68
Valiante, E., Smith, M. W. L., Eales, S., et al. 2016, MNRAS, 462, 3146
Vieira, J. D., Marrone, D. P., Chapman, S. C., et al. 2013, Nature, 495, 344
Vincoletto, L., Matteucci, F., Calura, F., Silva, L., & Granato, G. 2012, MNRAS, 421, 3116
Wang, L., Viero, M., Clarke, C., et al. 2014, MNRAS, 444, 2870
Weiß, A., De Breuck, C., Marrone, D. P., et al. 2013, ApJ, 767, 88
Whitaker, K. E., Franx, M., Bezanson, R., et al. 2015, ApJ, 811, L12
Wilkinson, A., Almaini, O., Chen, C.-C., et al. 2017, MNRAS, 464, 1380
Yuan, F., Buat, V., Burgarella, D., et al. 2015, A&A, 582, A90
Yun, M. S., Reddy, N. A., & Condon, J. J. 2001, ApJ, 554, 803
Zavala, J. A., Montaña, A., Hughes, D. H., et al. 2017, ArXiv e-prints, arXiv:1707.09022 [arXiv:1707.09022]

Table 9: List of selected sources.

ID (HVS)	Source name	RA [J2000] [h m s]	Dec [J2000] [° ′ ″]	S_{250} [mJy]	$S^{\rm err}_{250}$ [mJy]	S_{350} [mJy]	$S^{\rm err}_{350}$ [mJy]	S_{500} [mJy]	$S^{\rm err}_{500}$ [mJy]
1	HVS J120715+1453.9	12:07:15.07	+14:53:17.9	17.81	1.75	35.07	3.46	35.94	3.54
2	HVS J120724+1430.0	12:07:24.76	+14:30:14.0	20.96	1.87	40.52	3.61	40.9	3.64
3	HVS J120909+1433.7	12:09:09.18	+14:33:26.7	14.03	1.67	32.46	3.87	38.84	4.63
4	HVS J120936+1518.0	12:09:36.01	+15:18:36.0	17.95	1.69	37.63	3.55	40.07	3.78
5	HVS J121140+1416.8	12:11:40.83	+14:16:10.8	9.86	2.23	25.62	5.86	39.8	5.68
6	HVS J121540+1307.9	12:15:40.18	+13:07:36.9	11.82	1.61	28.72	3.91	37.17	5.06
7	HVS J121847+1537.3	12:18:47.43	+15:37:39.3	18.22	1.73	36.82	3.49	38.61	3.67
8	HVS J122017+1535.9	12:20:17.55	+15:35:14.9	18.14	1.86	34.69	3.56	34.69	3.56
9	HVS J122217+1534.7	12:22:17.80	+15:34:11.7	14.62	1.74	29.46	3.52	30.18	3.61
10	HVS J123037+1207.1	12:30:37.15	+12:07:15.1	16.34	1.75	33.94	3.64	35.82	3.84
11	HVS J122654+1214.6	12:26:54.33	+12:14:22.6	15.88	1.79	31.50	3.55	31.82	3.59
12	HVS J122445+0930.7	12:24:45.12	+09:30:14.7	13.34	1.65	29.88	3.70	34.92	4.32
13	HVS J123304+1309.0	12:33:04.61	+13:09:16.0	15.45	1.77	31.86	3.65	34.05	3.90
14	HVS J123027+1237.7	12:30:27.61	+12:37:39.7	13.59	2.04	28.34	3.63	30.01	3.85
15	HVS J122438+0953.5	12:24:38.28	+09:53:41.6	17.27	1.73	35.37	3.54	37.56	3.76
16	HVS J122646+1152.1	12:26:46.27	+11:52:35.0	17.76	2.09	35.35	3.49	36.57	3.61
17	HVS J122416+1208.1	12:24:16.90	+12:08:16.1	23.64	1.79	46.08	3.49	46.82	3.56
18	HVS J122938+1355.7	12:29:38.92	+13:55:49.7	21.81	1.81	42.91	3.56	43.95	3.65
19	HVS J121814+1529.1	12:18:14.42	+15:29:36.1	15.73	1.57	36.9	3.68	45.05	4.49
20	HVS J122358+0725.1	12:23:58.59	+07:25:34.1	13.43	1.67	32.19	3.92	41.36	5.04
21	HVS J121740+1613.0	12:17:40.07	+16:13:26.0	9.3	1.72	24.17	4.48	37.71	6.99
22	HVS J121723+0418.0	12:17:23.84	+04:18:58.0	14.86	1.75	30.38	3.55	31.27	3.65
23	HVS J122816+0824.3	12:28:16.15	+08:24:02.3	13.41	1.58	31.65	3.74	39.0	4.61
24	HVS J123138+1020.0	12:31:38.77	+10:20:59.0	11.99	1.58	28.29	3.73	35.44	4.67
25	HVS J123027+1237.3	12:30:27.76	+12:37:37.3	14.32	2.14	31.91	3.56	36.42	3.70
26	HVS J123232+0701.9	12:32:32.99	+07:01:32.9	18.56	2.05	37.31	3.51	38.07	3.58
27	HVS J123435+0839.9	12:34:35.03	+08:39:47.9	15.65	1.73	31.67	3.49	33.25	3.68
28	HVS J121613+0253.1	12:16:13.80	+02:53:11.1	36.75	1.78	70.84	3.44	71.31	3.46
29	HVS J121744+0721.5	12:17:44.72	+07:21:27.5	21.99	1.85	46.42	3.46	49.75	3.39
30	HVS J121409+0516.7	12:14:09.70	+05:16:37.7	15.53	1.73	31.68	3.52	32.85	3.65
31	HVS J121801+0348.4	12:18:01.13	+03:48:10.4	14.03	2.11	31.22	3.73	35.51	4.25
32	HVS J121016+0527.1	12:10:16.25	+05:27:22.1	15.28	2.16	31.37	3.62	32.72	3.77
33	HVS J122526+0414.7	12:25:26.88	+04:14:52.7	13.68	2.15	29.71	3.62	32.83	3.98
34	HVS J122521+0407.8	12:25:23.23	+04:07:18.8	12.45	2.38	28.51	3.84	33.64	4.53
35	HVS J122821+0407.4	12:28:21.13	+04:07:32.4	12.81	1.60	32.32	4.04	45.43	5.67
36	HVS J123917+1112.4	12:39:17.85	+11:12:42.4	13.24	2.21	28.33	3.58	30.82	3.91
37	HVS J122854+1328.6	12:28:54.43	+13:28:05.6	12.72	1.65	28.21	3.67	32.57	4.23
38	HVS J122649+0502.2	12:26:49.90	+05:02:01.2	13.34	1.65	29.03	3.62	32.78	4.11
39	HVS J121755+0721.2	12:17:55.74	+07:21:00.2	12.69	1.63	29.85	3.87	36.63	4.73
40	HVS J122505+0735.6	12:25:05.61	+07:35:44.6	24.77	1.77	50.85	3.25	53.04	3.07
41	HVS J121654+1604.8	12:16:54.97	+16:04:14.8	14.05	1.73	29.65	3.65	31.78	3.91
42	HVS J122446+0540.0	12:24:46.52	+05:40:18.0	14.22	1.79	29.09	3.67	30.25	3.81
43	HVS J122031+1551.5	12:20:31.49	+15:51:26.5	16.36	1.65	37.25	3.72	43.61	4.35
44	HVS J123419+1054.2	12:34:19.79	+10:54:00.2	17.46	1.57	40.73	3.66	49.37	4.48
45	HVS J122810+0512.6	12:28:10.78	+05:12:02.6	15.66	1.73	31.94	3.58	33.11	3.66
46	HVS J123200+0821.9	12:32:00.58	+08:21:37.9	18.42	1.86	41.18	3.65	47.19	3.67
47	HVS J121443+0344.0	12:14:43.75	+03:44:29.0	10.08	1.63	25.98	4.19	38.98	6.3
48	HVS J123220+1214.0	12:32:20.88	+12:14:37.0	13.46	1.67	28.0	3.53	30.18	3.80
49	HVS J121851+0301.8	12:18:51.09	+03:01:53.8	16.38	1.69	34.8	3.59	37.58	3.87
50	HVS J122000+0422.0	12:20:00.48	+04:22:01.0	18.28	1.61	40.2	3.54	45.09	3.97
51	HVS J122744+0948.1	12:27:44.28	+09:48:01.1	12.12	1.59	27.86	3.66	33.04	4.34
52	HVS J122623+0621.1	12:26:23.79	+06:21:26.1	16.81	1.55	40.81	3.78	52.72	4.88
53	HVS J122939+1355.5	12:29:39.00	+13:55:49.5	18.62	1.73	39.84	3.53	44.21	3.64
54	HVS J122000+0524.9	12:20:00.60	+05:24:12.9	17.27	1.77	34.4	3.54	34.89	3.59
55	HVS J122124+0911.4	12:21:24.48	+09:11:46.4	18.33	1.65	37.64	3.40	39.28	3.55
56	HVS J120934+1526.0	12:09:34.04	+15:26:47.0	29.55	1.69	60.62	3.48	63.18	3.62
57	HVS J122728+0939.0	12:27:28.12	+09:39:00.0	16.81	1.80	35.48	3.51	38.03	3.48

Table 9: continued.

ID (HVS)	Source name	RA [J2000] [h m s]	Dec [J2000] [° ′ ″]	S_{250} [mJy]	$S^{\rm err}_{250}$ [mJy]	S_{350} [mJy]	$S^{\rm err}_{350}$ [mJy]	S_{500} [mJy]	$S^{\rm err}_{500}$ [mJy]
58	HVS J123348+0703.5	12:33:48.69	+07:03:55.5	17.86	1.69	37.32	3.54	39.62	3.76
59	HVS J122248+1635.6	12:22:48.00	+16:35:19.6	18.42	1.68	41.2	3.64	47.15	4.17
60	HVS J121346+0438.2	12:13:46.22	+04:38:36.2	19.86	1.79	41.28	3.67	43.59	3.88
61	HVS J122101+1449.9	12:21:01.77	+14:49:40.9	22.0	1.64	47.46	3.46	52.08	3.79
62	HVS J122026+0731.4	12:20:26.24	+07:31:28.4	21.89	2.18	43.96	3.37	44.9	2.89
63	HVS J122157+0526.6	12:21:57.97	+05:26:35.6	18.95	1.73	38.51	3.52	39.79	3.64
64	HVS J121349+0438.1	12:13:49.72	+04:38:28.1	31.41	1.58	73.99	3.69	90.97	4.54
65	HVS J123044+0950.7	12:30:44.45	+09:50:49.7	14.14	2.09	28.58	3.51	29.99	3.69
66	HVS J122547+1529.7	12:25:47.42	+15:29:32.7	21.98	2.13	45.11	3.53	47.04	3.68
67	HVS J122142+1611.4	12:21:42.97	+16:11:50.4	21.81	2.10	42.79	3.53	42.81	3.53
68	HVS J123312+0713.5	12:33:12.72	+07:13:27.5	15.85	2.27	30.32	3.45	30.34	3.46
69	HVS J122634+1400.0	12:26:34.07	+14:00:10.0	18.18	2.11	38.23	3.6	40.85	3.84
70	HVS J121742+0351.1	12:17:42.83	+03:51:28.1	11.77	2.19	26.34	3.69	30.18	4.23
71	HVS J122148+1443.8	12:21:48.69	+14:43:52.8	17.55	2.15	34.65	3.27	34.86	3.29
72	HVS J122415+0958.8	12:24:15.19	+09:58:41.8	22.87	2.23	46.32	3.50	47.68	3.60
73	HVS J121815+0307.5	12:18:15.98	+03:07:43.5	14.73	1.75	31.08	3.39	33.31	3.35
74	HVS J122854+1328.3	12:28:54.46	+13:28:05.3	15.08	1.54	33.27	3.41	37.45	3.84
75	HVS J121900+1550.6	12:19:00.96	+15:50:19.6	14.52	1.56	36.32	3.90	49.9	5.36
76	HVS J121949+1610.5	12:19:49.92	+16:10:09.5	17.93	1.81	37.84	3.42	40.56	3.41
77	HVS J121827+1544.7	12:18:27.36	+15:44:15.7	16.02	1.87	32.89	3.49	34.31	3.43
78	HVS J121911+1618.4	12:19:11.52	+16:18:09.4	13.02	1.67	28.65	3.67	32.79	4.21
79	HVS J123032+1014.2	12:30:32.38	+10:14:07.2	23.69	2.06	47.57	3.38	48.59	3.02
80	HVS J123000+0415.5	12:30:00.59	+04:15:21.5	19.6	1.61	40.25	3.31	42.0	3.47
81	HVS J122024+1434.2	12:20:24.48	+14:34:23.2	12.5	1.64	28.23	3.72	33.34	4.39
82	HVS J122610+1027.9	12:26:10.56	+10:27:02.9	20.16	1.78	42.07	3.62	45.49	3.92
83	HVS J123346+1007.0	12:33:46.32	+10:07:03.0	13.78	2.17	28.29	3.60	30.1	3.84
84	HVS J121604+1246.7	12:16:04.08	+12:46:21.7	13.34	1.75	28.85	3.68	32.37	4.14
85	HVS J123126+1249.7	12:31:26.16	+12:49:43.7	8.93	1.76	23.24	4.61	36.93	7.34
86	HVS J123120+1412.2	12:31:20.88	+14:12:38.2	13.72	1.68	28.88	3.55	30.87	3.81
87	HVS J122627+0336.6	12:26:27.53	+03:36:31.6	16.27	1.79	32.58	3.58	33.9	3.72
88	HVS J123155+1420.9	12:31:55.20	+14:20:17.9	13.41	1.71	28.45	3.63	30.66	3.91
89	HVS J121037+0517.2	12:10:37.19	+05:17:22.2	15.93	1.86	32.7	3.40	34.11	3.28
90	HVS J122212+1141.7	12:22:12.24	+11:41:33.7	15.94	1.86	32.72	3.41	34.13	3.35
91	HVS J122527+1153.0	12:25:27.12	+11:53:28.0	13.64	1.72	28.83	3.63	31.58	3.98
92	HVS J122449+0951.2	12:24:49.90	+09:51:12.2	15.92	1.71	32.89	3.53	34.51	3.74
93	HVS J122727+0525.6	12:27:27.06	+05:25:29.6	23.19	2.13	46.57	3.40	47.57	2.97
94	HVS J121601+1231.4	12:16:01.18	+12:31:11.4	14.78	2.13	36.54	3.84	48.96	5.18
95	HVS J122845+0929.8	12:28:45.36	+09:29:34.8	14.58	1.73	29.13	3.46	30.23	3.59
96	HVS J123007+1338.1	12:30:07.92	+13:38:45.1	21.29	2.05	42.75	3.30	43.67	2.90
97	HVS J122508+0756.7	12:25:08.64	+07:56:02.7	11.9	1.63	26.49	3.63	30.72	4.21
98	HVS J121843+0328.8	12:18:43.68	+03:28:10.8	18.27	1.81	35.72	3.54	36.38	3.61
99	HVS J121713+1202.9	12:17:13.96	+12:02:42.9	18.93	2.09	38.0	3.42	38.82	3.57
100	HVS J122519+0518.1	12:25:19.92	+05:18:40.1	16.7	1.78	31.94	3.42	31.96	3.62
101	HVS J122709+0856.1	12:27:09.42	+08:56:26.1	17.52	1.68	38.42	3.69	42.96	4.13
102	HVS J122156+1527.0	12:21:56.03	+15:27:57.0	18.44	2.02	37.86	3.41	39.49	3.77
103	HVS J123003+1318.3	12:30:03.80	+13:18:04.3	22.1	1.77	46.63	3.47	49.98	3.69
104	HVS J122619+0443.7	12:26:19.44	+04:43:37.7	14.24	1.82	30.05	3.47	32.21	3.77
105	HVS J121735+0413.8	12:17:35.04	+04:13:42.8	15.58	1.98	31.98	3.52	33.36	4.37
106	HVS J121451+0412.5	12:14:51.58	+04:12:44.5	11.74	1.67	26.36	3.75	30.31	4.32
107	HVS J121617+0408.0	12:16:17.76	+04:08:21.0	13.08	1.62	29.6	3.66	35.0	4.33
108	HVS J123427+0714.0	12:34:27.98	+07:14:54.0	25.39	2.03	50.99	3.31	52.08	3.93
109	HVS J121543+0619.5	12:15:43.92	+06:19:12.5	16.35	1.75	33.65	3.61	35.9	3.85
110	HVS J123007+1332.1	12:30:07.93	+13:32:07.1	18.17	1.92	37.3	3.42	38.91	3.54
111	HVS J122414+1014.6	12:24:14.05	+10:14:36.6	21.98	2.02	45.12	3.38	47.06	3.78
112	HVS J121304+0519.0	12:13:04.30	+05:19:28.0	11.33	1.66	25.84	3.74	30.3	4.42
113	HVS J122517+1121.3	12:25:17.75	+11:21:56.3	13.98	2.53	30.82	3.46	34.68	3.87
114	HVS J122100+1306.9	12:21:00.68	+13:06:51.9	30.94	2.13	62.14	3.38	63.47	3.95
115	HVS J122709+0540.2	12:27:09.60	+05:40:00.2	20.09	2.86	38.74	3.52	39.02	3.57

Table 9: continued.

ID (HVS)	Source name	RA [J2000] [h m s]	Dec [J2000] [° ′ ″]	S_{250} [mJy]	$S^{\rm err}_{250}$ [mJy]	S_{350} [mJy]	$S^{\rm err}_{350}$ [mJy]	S_{500} [mJy]	$S^{\rm err}_{500}$ [mJy]
116	HVS J123213+0740.8	12:32:13.44	+07:40:30.8	12.36	2.68	27.12	3.70	30.92	4.21
117	HVS J122109+0946.9	12:21:09.49	+09:46:33.9	30.53	2.12	61.3	3.30	62.62	3.83
118	HVS J121904+1338.9	12:19:04.56	+13:38:53.9	25.03	1.96	51.39	3.44	53.6	3.21
119	HVS J123619+0909.5	12:36:19.04	+09:09:44.5	26.06	2.13	52.33	3.31	53.45	3.84
120	HVS J121818+0506.4	12:18:18.40	+05:06:48.4	35.85	2.05	71.98	3.38	73.53	3.04
121	HVS J122611+1518.8	12:26:11.82	+15:18:33.8	24.69	2.02	50.7	3.41	52.88	3.23
122	HVS J123032+0641.8	12:30:32.44	+06:41:54.8	31.33	2.04	62.91	3.29	64.26	3.93
123	HVS J121110+1220.3	12:11:10.88	+12:20:35.3	24.74	2.06	49.68	3.30	50.75	3.90
124	HVS J123113+1220.1	12:31:13.14	+12:20:43.1	16.38	2.14	33.62	3.44	35.07	3.29
125	HVS J122646+1049.3	12:26:46.02	+10:49:06.3	16.22	1.66	34.18	3.50	36.57	3.75
126	HVS J121900+1516.5	12:19:00.34	+15:16:49.5	21.75	1.92	44.65	3.41	46.57	3.23
127	HVS J122806+0928.7	12:28:06.04	+09:28:11.7	39.83	2.03	79.97	3.32	81.69	3.97
128	HVS J123000+0803.6	12:30:00.33	+08:03:26.6	21.04	1.99	43.19	3.41	45.05	3.15
129	HVS J121609+1601.2	12:16:09.60	+16:01:59.2	14.11	1.64	31.25	3.64	36.04	4.19
130	HVS J122241+0708.4	12:22:41.71	+07:08:26.4	21.1	1.71	44.93	3.65	49.44	4.03
131	HVS J122335+1108.0	12:23:35.52	+11:08:56.0	12.35	1.63	26.86	3.61	30.33	4.08
132	HVS J123304+1326.6	12:33:04.80	+13:26:27.6	14.75	1.68	32.51	3.70	37.26	4.25
133	HVS J123317+1235.2	12:33:17.76	+12:35:31.2	14.29	1.77	28.74	3.58	30.03	3.74

Column descriptions:

Column 1: Catalogue numbers (HVS);

Column 2: Full source name (source names are based on their positions for the J2000).

Columns 3-4: Coordinates of sources (RA, Dec);

Column 4-9: SPIRE fluxes (S_{250}, S_{350}, S_{500}) and accompanied errors in the flux estimation ($S^{\rm err}$). Flux errors are estimated as explained in Section 2.6. We note, however, that errors are strongly correlated, since we performed "forced" MBB photometry at SPIRE wavelengths.

Appendix A: Dusty radio sources

As mentioned in Section 2.5, our final list of 500 μm-risers has been cleared of strong radio sources and quasars (QSOs, 7 objects in total). We measure significant FIR emission close to position of these sources, and here we briefly investigate its nature. Radio emission from quasars may be due to star formation in the quasar host galaxy, to a jet launched by the supermassive black hole, or to relativistic particles accelerated in a wide-angle radiatively driven outflow. Our MBB fitting approach realtively efficiently "protects" star-forming selection against the flat (in terms of SED) and dusty synchrotron sources. When `MBB-fitter` photometry of such flat sources is performed, most of the χ^2 values lie outside the range we accept as good for our final selection ($\chi^2 < 3.84$, see Appendix B). Between the seven objects removed from the final list, three of them are defined as radio-loud quasars (QSO) or blazars, with catalogued L-band 1.4 GHz radio emission larger than 1 mJy (5.04 mJy, 799.97 mJy and 6.2 mJy respectively), and their redshifts span the range from 0.6 to 0.965. An example is the brightest radio source catalogued as HVS387 in our catalogue or J122222.5+041316 in the FIRST database. It has IR excess and very strong UV and gamma-ray emission. The source has a spectroscopic redshift of $z = 0.964$ and according to the classical PSF-fitting photometry performed with, for example, `SUSSEXtractor` or `DAOphot` it could pass our red source criteria, but it cannot be fitted accurately using the `MBB-fitter`. Since they may have colours similar to those of high-z DSFGs, heterogeneously selected 500 μm-risers that exist in the literature thus should be considered with caution, since they may be polluted by synchrotron-dominated sources whose IR energy is not star-formation related. Another possibility is that some of those QSOs act as a foreground lens, amplifying the signal from the higher-redshift, dusty system.

Another four QSO-like sources are found by cross-matching with the Half Million Quasar catalogue (HMQ, Flesch 2015). They are optically bright, high-z QSO-like sources close to the position of our SPIRE detection (r<3"). They have high photometric redshifts - on average $z = 2.74$, with one source lying at $z > 4$. To fully inspect the relation of these objects to the population that we aimed to select in the current study, in our following paper we consider optical and PACS data, together with archival WISE data. Here we can determine the expected radio emission of our final group of 133 500 μm-risers implementing FIR-radio correlation:

$$q_{\rm IR} = \log\left(\frac{F_{\rm FIR}}{3.75\times10^{12}{\rm Wm^{-2}}}\right) - \log\left(\frac{S_{1.4}}{{\rm Wm^{-2}Hz^{-1}}}\right), \quad (A.1)$$

where $S_{1.4}$ is the continuum radio emission flux at 1.4 GHz per frequency such that $S_{1.4} \propto \nu^{-\alpha}$ and α is the radio spectral index, positive in the vast majority of sources. $F_{\rm FIR}$ is the rest-frame FIR dust emission flux. There is considerable evidence that local star-forming galaxies express a tight FIR-radio correlation. For example, Yun et al. (2001) analysed the sample of 1800 *IRAS* galaxies and measured this value to be $q_{\rm IR} = 2.37 \pm 0.01$ with a dispersion of 0.25 dex. From this we estimate that for our $z \sim 4$ candidates 1400 MHz flux densities are in the range between 25 μJy and 90 μJy. Assuming the faintest level of existing radio surveys covering Virgo (~0.75-1 mJy at 1.4 GHz), we can reveal just local cluster members and radio bright quasars, but not dusty background, star-forming galaxies.

However, FIR-radio correlation cannot be implemented accurately in order to estimate expected radio flux of optically selected quasars which have radio flux below the FIRST (NVSS) limit. As we add QSO contribution to both radio and IR, correlation could break down. This could be particularly due to the origin of the FIR/submm emission which includes a small contribution from the AGN torus, being predominantly linked to (kpc-scale) heated dust by the AGN. Recent studies have enlarged the sample of *Herschel* -detected optically selected QSOs (e.g. Ma & Yan 2015). They, however, claimed a statistically large group of objects for which SEDs are due to the cold-dust components within the host galaxies, consistent with being heated by active star formation. Lacking the L_{IR} correlation with the black hole masses or the X-ray QSO luminosities of the quasars, this could support a scenario where their thermal SED is not AGN-driven. Thus, our subsample of QSO-like objects could be a very interesting case study for probing the connection between AGN activity and host galaxy star-formation. Existing large sky radio catalogues are not deep enough to distinguish between very dusty radio-dominated galaxies at higher redshifts and star-forming systems. This issue will be addressed with deep radio observations performed over the area covering Virgo; Evolutionary Map of the Universe (EMU survey, Norris et al. (2011) will make a deep (10", *rms*=10 μJy/beam) continuum maps.

It is clear that in addition to FIR/submm data, radio data are of significant importance to further uncover the true nature of selected dusty sources. Since photometric redshifts calculated using the SPIRE data alone are highly uncertain, the addition of radio data (via FIR-radio correlation) might be expected to improve the photometric redshift accuracy, for example to $\Delta z/(1+z) = 0.15$ (Roseboom et al. 2012). From this, it is vital to understand the true nature of the FIR to radio correlation at redshifts higher than 2, since some recent results have claimed much larger scatter and even break at redshifts larger than 4 (e.g. Miettinen et al. (2015), Delhaize et al. (2017), see also Schober et al. 2017). Thus the redshift independent FIR-radio correlation cannot be used straightforwardly to break temperature-redshift degeneracy as suggested in most previous papers found in the literature (e.g. Pope & Chary 2010). Approaching existing and future interferometers (JVLA, SKA), we can put constraints on the photometric redshifts of our red sources, and can also uncover the sizes of their star-forming regions and investigate how they compare to other tracers such as FIR or CO.

Appendix B: Colour-redshift diagram related to the MBB model

In the FIR regime, SED peak is provoked by thermal emission from dust of different temperatures, and it can be used in extragalactic surveys such as *Herschel* to identify objects in a specific redshift range. To test our theory that selecting 500 μm-risers is the way to select $z \gtrsim 4$ candidates, we run a Monte Carlo simulation to sample all possible colours as a function of redshift. We test which range of redshifts we should expect assuming the MBB model with the fixed various ranges of parameters. We confirm that if sources are not sufficiently cold, they reside at $z \gtrsim 4$. Thus, we are particularly interested in unveilling MBB-fitted sources with $S_{500}/S_{350} > 1$ and $S_{500}/S_{250} > 2$. Plotted in Fig. B.1 are some such examples, where we applied different combinations of fixed $T_{\rm d}$ and β. At redshifts $z > 6$ the heating of dust by the cosmic microwave background (CMB) could be more significant and we take that into account in our modelling of observed SED following da Cunha et al. (2013).

Appendix C: An example of faint and deblended 500 μm-risers

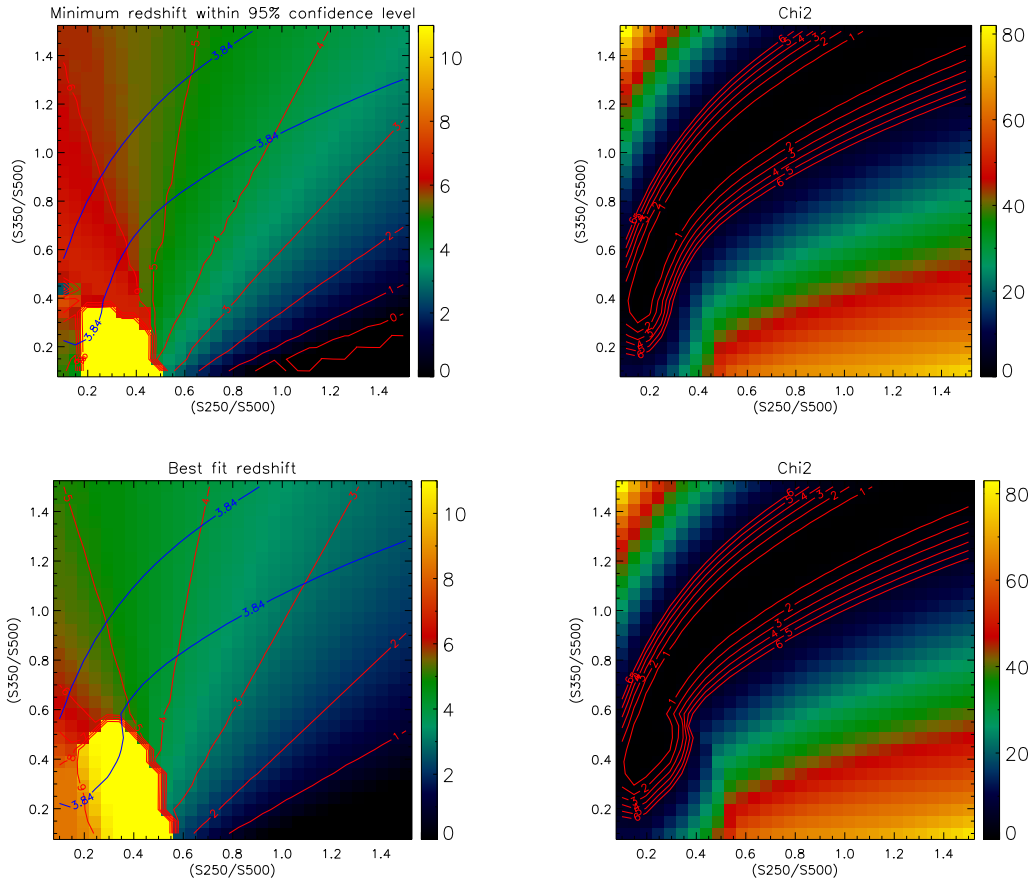

Fig. B.1: Criteria for selecting 500 μm-risers. Plotted is a SPIRE colour diagram related to the MBB model. The plot is a result of a Monte Carlo simulation in which we start with a single-temperature modified blackbody with the flux S_{500}=30 mJy. The mock SEDs are generated to account for different fixed $T_{\rm d}$ and β illustrating temperature-redshift degeneracy. Plotted against all possible colours are simulated sources with $T_{\rm d}$=45 K and β = 1.8 (upper panel) and $T_{\rm d}$=38 K and β = 1.8 (lower panel). *Left* : Colour-redshfit plot. Red lines represent redshift tracks rising from right to left. The coloured background indicates the average redshift in these colour-colour spaces. Blue lines define the 95% confidence limit region. A correction factor due to modelled effect of CMB heating on colours is applied. However, our simulations show that we do not expect a major contribution from that effect at sources lying below $z \sim 7$; *Right* : Different chi-square fitting values reflected on SPIRE colour-colour ratios. For our final 500 μm-risers selection we kept only those sources whose chi-square resides inside the 95% confidence limit region ($\chi^2 < 3.84$).

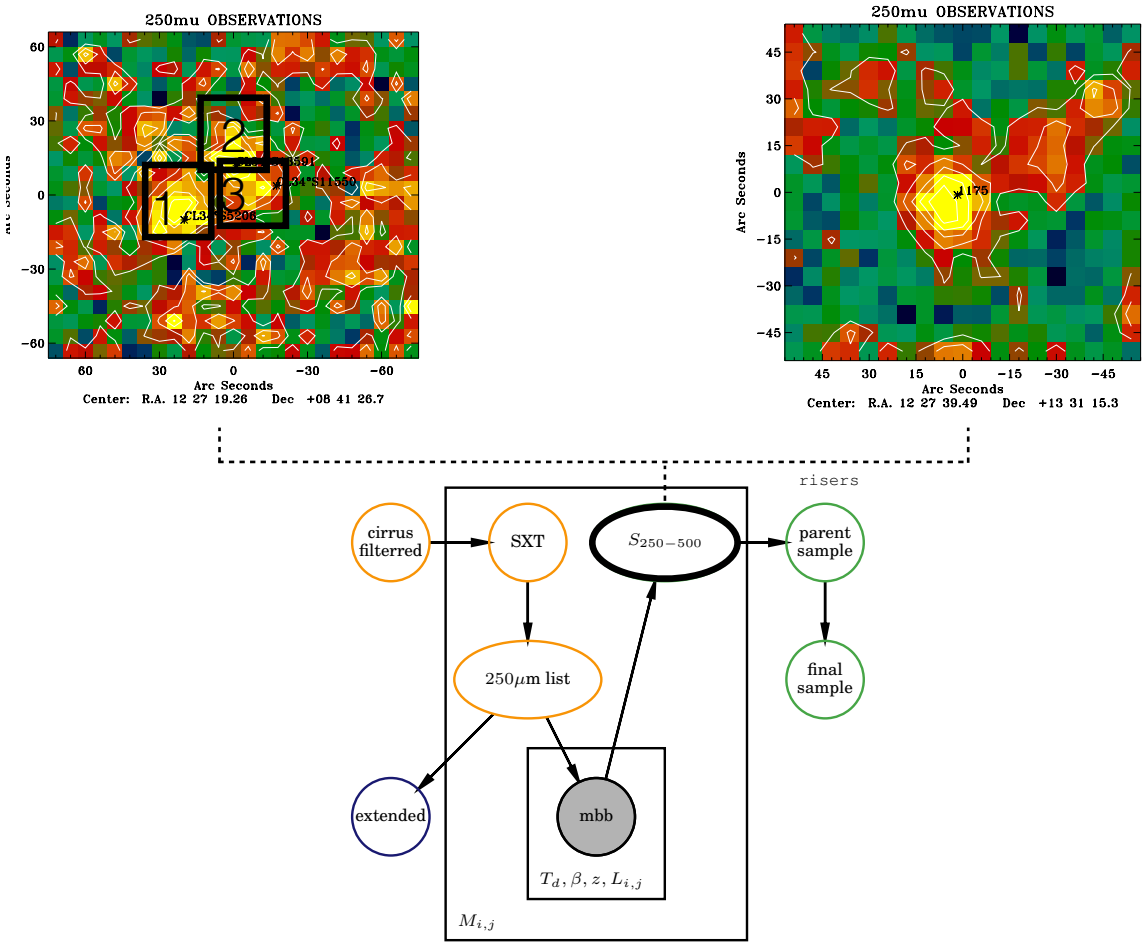

Fig. C.1: Example 2D cutouts of confused (left) and isolated point source detections (right) from our 250 μm catalogue. The first group of sources are fitted simultaneously, while the second is fitted as a single source.

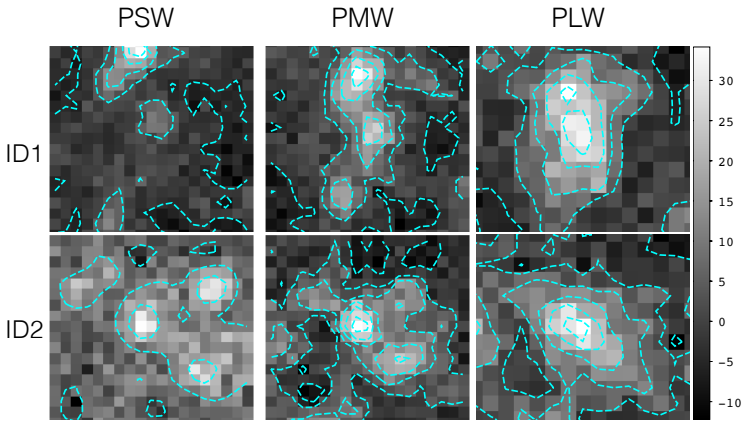

Fig. C.2: Example 60"x 60" cutouts of 500 μm-risers from our final sample. Both sources are detected in the second iteration of our extraction procedure, when we add sources that appeared bright in our residual maps. Upper panel: 250 μm, 350 μm and 500 μm cutout of a multisource case where two sources are de-blended for their 350 μm and 500 μm emission. Lower panel: An isolated case, without a prominent 350 μm or 500 μm blend with respect to the beam.

APPENDIX B

Searching for overdensities beyond the SPIRE data: HSC-SCUBA2 Protocluster Project

This spring I have been invited to join Subaru Hyper Supreme Camera (HSC)-Protocluster Survey Project (PI: Y. Matsuda). I started the collaborative work on two projects that aimed to investigate large scale structures at $z > 5 - 6$ initially discovered in deep optical surveys. The main aim of the projects is to characterise dust properties of some of the most distant overdensities confirmed to date. In the following paragraphs I will describe the main lines of project along with my contribution. Results that are described below will soon appear in two papers submitted to ApJ: Harikane et al. (submitted) and Fujimoto et al. (submitted).

In order to find the rare population of very high-z ($z > 5 - 6$) protoclusters, a systematic survey of galaxy overdensities has been carried out with the broadband and narrow-band HSC observations. Masami Ouchi et al. 2005 have identified an overdensity of $Ly\alpha$ emitters (LAEs) at $z = 5.7$ from a deep Subaru narrow-band imaging

($5\sigma = 26.5$ magAB) over a 1 deg^2 area. Toshikawa, Kashikawa, Ota, et al. 2012 have found an overdensity of i-dropout galaxies (LBGs) at $z \sim 6$ from deep broadband imaging with the 5σ limiting magnitudes are (R, i', z'=28.4, 27.7, 27.1) magAB over a 0.25 deg^2. The latest result of the HSC narrow-band imaging ($5\sigma = 26$ magAB) over a 34 deg^2 have newly identified LAE overdensity at $z = 6.6$, where a known, remarkably giant SB galaxy dubbed "Himiko", resides at $z = 6.595$ (Tamura et al. 2009).

The extensive follow-ups with VLT/VIMOS, Keck/DEMOS, Subaru/FOCAS, and Gemini/GMOS probe the area of $6' \times 6'$ (14 Mpc x 14 Mpc in comoving units at $z \sim 6$), the size suggested from aforementioned cosmological simulations. The extensive observations reveal that overdensity cores at $z = 5.69, 6.01,$ and 6.57 are composed of 12, 10, and 9 member LAEs and LBGs respectively, confirmed via their $\mathrm{Ly}\alpha$ line detections. In addition to that, the estimated DM halo masses are likely evolve into $> 10^{14} M_\odot$ halos at $z = 0$ based on the simulations (Toshikawa, Kashikawa, R. Overzier, et al. 2014). However, all these protocluster candidates were identified based on the optical-NIR selection bands, and it became clear that further exploration of their dust obscured star-formation is needed.

The first project I am involved in (Harikane et al, submitted to ApJ) make use of a large spectroscopic sample of 167 LAEs in order to inspect the two overdense regions at $z = 5.7$ and $z = 6.6$. Combined with the recent Gemini/GMOS observations, the team at the University of Tokyo (PI: Harikane) produced the 3D maps of the Universe traced with the LAEs in the $\sim 200 \times 200 \times 80$ co-moving Mpc^3. The scope of the project is detection of dusty galaxies and the further investigation of the correlation between the LAEs and DSFGs, along with their stellar properties, in order to probe the environmental dependence of galaxy properties. To place the result in the cosmological context, we also compare our observational results with recent numerical simulations.

My main contribution to the project were analyses of SPIRE and SCUBA-2 data (PI:K.Kodama). We aim to statistically evaluate contribution of DSFGs to observed cluster progenitors. Firstly, I identify 500 μm-risers using the same method described in Chapter 2 of the Thesis, but with the difference that detection threshold is pushed down to S_{250}=8mJy and $S_{500} = 21$ mJy, correspondingly to noise levels of the HSC fields. As a result, I find that $6' \times 6'$ regions centred around protocluster cores contain 101 SCUBA-2 sources detected above 4σ, of which 73 are detected in SPIRE. We cross-match the SCUBA-2 sources with ALMA sources (Fujimoto et al. in prep.) within 10", and measure fluxes at the positions of the ALMA counterparts in the HSC images. The ALMA data we use

are taken in band 7, with typical 1σ noise level and angular resolution at 0.2 mJy/beam and $0.''2$, respectively. For more than 70% of the SCUBA- 2 sources we identified ALMA counterparts, and most of the rest are not observed with ALMA. Interestingly, among SCUBA-2 sources whose ALMA counterparts are identified, more than 90% of sources have single ALMA detection, which either place the constraint on very low multiplicity fraction, or indicates that fainter contributing sources are below the detection limit. I then evaluate the overdensity parameters related to SCUBA-2 number counts and 500 μm-risers, and check their significance by using randomly injected 1000 apertures. I find the number density of SCUBA-2 sources with S/N>5 by factor of 3-5 higher than in the field. For those SCUBA-2 sources with SPIRE detections, I find the excess of the number of 500 μm-risers in all three structures, as illustrated in Fig.B1.The detection of a large number of DSFGs is than used in Harikane et al. (submitted to ApJ) for measuring the clustering signal between the LAEs and red DSFGs (500 μm-risers). The significant 5.6σ cross-correlation signal has been measured between the $z = 5.7$ LAEs and 500 μm-risers, assuming the FIR-colour based photometric redshifts for all optically obscured DSFGs. When we performed the same analysis with spectroscopically confirmed sources only, the correlation is still significant, $> 3.5\sigma$. It is worth to note here that the clustering signal between 500 μm-risers and LAEs overcomes the strength of the signal measured between LAEs-LAEs and LAEs-normal DSFGs pairs. It indicates that LAE-red DSFGs pairs are common even at high-z ($z > 4$), and that their correlation can be detected at scales < 20" more often than LAEs-LAEs pairs. Y.Harikane additionally performed SED fitting analysis using the sources with secure optical-NIR detections and generate model SEDs with the SED-fitting tool `Beagle` (Chevallard et al. 2016). As a result of the best-fit parameters, the stellar population analyses suggest that LAEs in higher dense regions are more actively forming stars than those in lower dense regions. We suggest that the enhanced star formation of LAEs in the overdense regions may be due to high inflow rates in overdensities whose halos are massive, similar as it is observed in Harikane, Masami Ouchi, Takatoshi Shibuya, et al. 2018.

Additionally, lurking at SCUBA-2 sources that are not detected in SPIRE maps, I find an interesting case where one source close to the centre of $z = 5.69$ protocluster is resolved in the archival ALMA continuum 870 μm map. It consists of two detections, and given that these sources are faint in all deep optical-NIR bands, it suggests they reside on very high-redshifts (Fujimoto et al. in prep.). For galaxies with both SPIRE and SCUBA-2 detections, I calculate the z_{phot} in the same manner as I do in Section

3.1. I find that redshift of these galaxies span the wide range ($1.23 < z < 6.79$), where $\sim 8\%$ of SCUBA-2 detections have z_{phot} consistent within $\Delta = 0.016$ to their signposts. However, we cannot fully confirm their final connection to our $z \sim 6$ protoclusters since we need to improve the accuracy of their positions/redshifts.

To meliorate the problem, we thus propose ALMA Band 6/7 [CII] observations for 101 DSFGs potentially associated to the structures observed at $z = 5.69, 6.01,$ and 6.57 (PI: S.Fujimoto). We chose the [CII] because its structure transition at 158 μm is the dominant cooling line of cool interstellar gas, and is the brightest of emission lines from star forming galaxies in FIR/submm, almost unaffected by dust attenuation. It is thus a great gas and SFR tracer, although it has been found strongly dependent on the metallicity (Vallini et al. 2015). The importance here is that [CII] can also be used to measure the systemic redshift of the galaxies (Pentericci et al. 2016). With ALMA we are planning to derive the line luminosity functions, and measure the abundance of [CII] emitters (Aravena et al. 2016). Confirming which DSFGs are associated to the overdensities, and unveiling their positions relative to LAEs, we can understand interplay between massive starburst galaxies and galaxy protoclusters at the earliest stages. At the time of writing this thesis, we were waiting for the results of our proposal. Nonetheless, along with necessity of deep ALMA data, our results demonstrate that quantifying the time evolution of the fraction of dust-obscured SFRD in rich environments is an important cosmological probe, particularly waiting for support of future surveys (JWST, Euclid, SKA, ng-VLA).

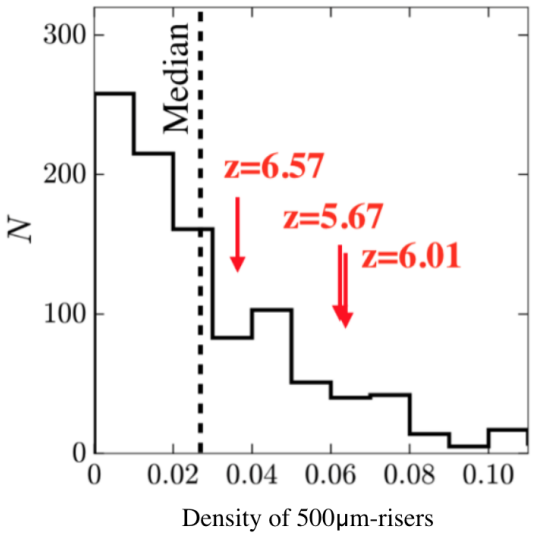

Figure B.1.: Density histogram of SCUBA-2 sources which are observed as 500 μm-risers in SPIRE images. The histogram is estimated by 1000 apertures with the radius of 6′, randomly injected in UDS field. The rad arrows indicate the SCUBA-2 detections with red SPIRE colours around $z = 5.69, 6.01$, and 6.57 overdensities.

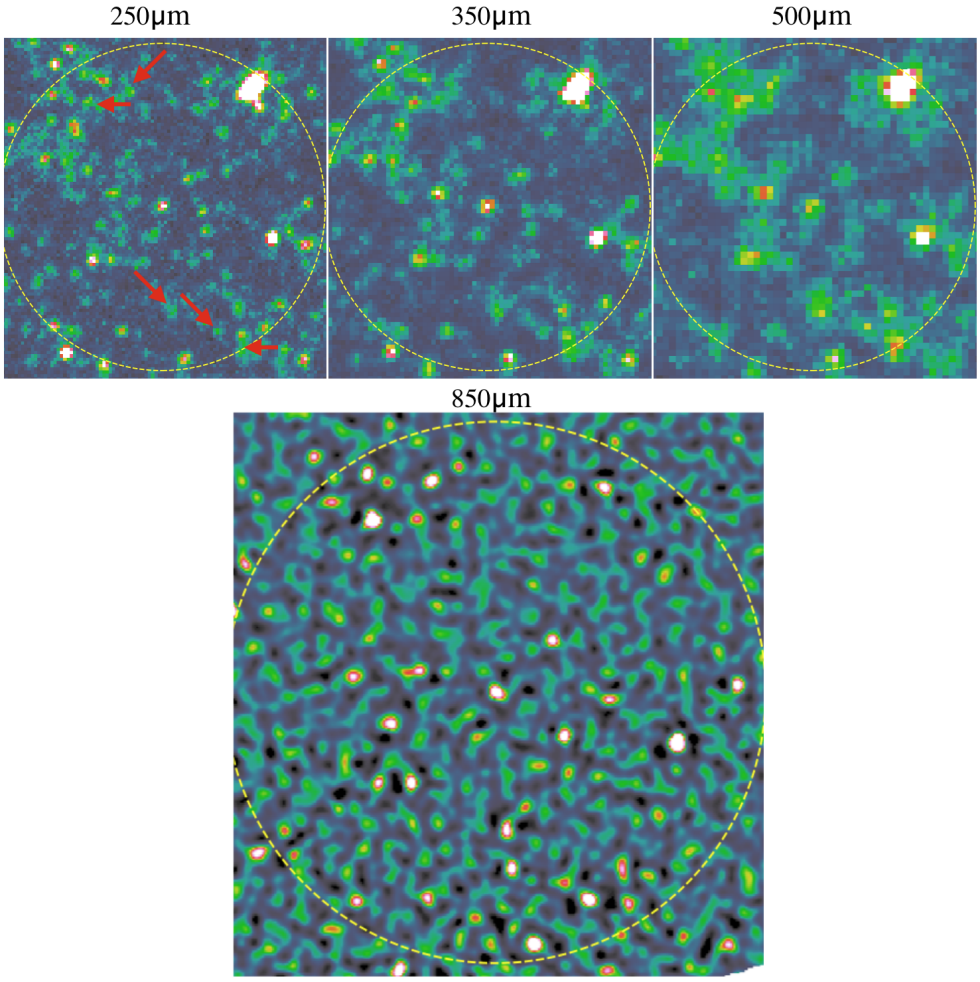

Figure B.2.: Postage stamp SPIRE and SCUBA-2 images (upper and lower panel respectively), showing the DSFG overdensity centred around candidate cluster progenitor at $z = 5.69$. Red arrows indicate sources observed as 500 μm-risers. In total 32 sources with S/N>4 are detected with SCUBA-2 inside the probed aperture with the radius of 3' (depicted with yellow circle).

APPENDIX C

Observing 500 μm-risers with IRAM 30m telescope

The goal of this project is to measure the spectroscopic redshifts of the four galaxies from the complete sample of 133 500 μm-risers selected with our method, described in Chapter 2. It has been known (e.g. Solomon et al. 2005, Carilli et al. 2013) that a promising route for determining the redshift of high-z DSFGs is through observations of CO emission lines at cm or mm-wavelengths. These spectral lines arise from the molecular gas in star formation process, and can be related unambiguously to the dust continuum source. As a PI I was granted with 69 observing hours at the IRAM 30m telescope. Unfortunately, our observations were conducted under very bad weather conditions and strong wind/storm stopped our investigation after just 15 hours of completed observations. Calibration of obtained data was accomplished following the standard procedures, using `GILDAS`. Towards two of our sources, single emission lines were detected, insufficient to determine the true distance to the source unambiguously, as the species and/or transition of molecular emission lines are unknown. However, combining the global redshift constraint that is possible by virtue of FIR colour, and excluding

the contribution of NGVS-detected sources, only a few of strong emission lines become plausible candidates. I find that two of our sources have assigned single CO lines detected with more than 2.5σ. For source ID 132, the line is detected with 4σ, with the peak at 95.6 GHz, implying a possible combination of redshifts $z = 3.85$ or $z = 5.06$. For source ID 30, the line is detected with 2.9σ, with the peak at 98.56 GHz, implying a possible combination of redshifts $z = 3.68$ or $z = 4.85$. Our photometric redshifts estimated from IR data are consistent with combination of redsfhits linked to CO lines, however further follow-up investigations are required to determine unambiguous redshifts for these galaxies. I am currently writing a proposal for NOEMA interferometer, which is much more powerful in terms of sensitivity and resoluton than IRAM single-dish telescope. With its new and wide instantaneous bandwidth, correlator PolyFix will allow us to fully cover the 3 mm band (70.5 to 115GHz) with only two different tunings. With this, we will significantly decrease the observing time needed for 3 mm spectral scan of our "500 μm-risers".

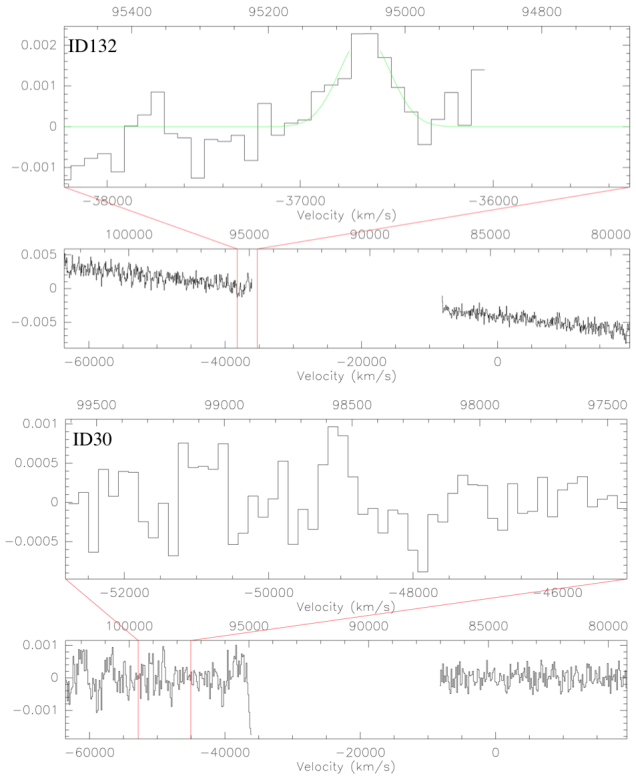

Figure C.1.: IRAM30m spectra in the E0 band (76-115 GHz) for two of our DSFGs.

Unveiling high-z dusty galaxies in the *Herschel* Virgo Cluster Survey

P.I.: Darko Donevski

1 Scientific Background

Dusty star forming galaxies at high-redshifts are generally believed to be the progenitors of massive ellipticals observed at current epoch (e.g.[Casey et al.(2014)]). Their contribution to the cosmic star formation rate density at high-redshifts ($z > 4$) is still unknown, due to the limited availability of statistically significant samples at such a high-redshifts. Conjointly, at $z > 4$ they are often undetectable at shorter wavelengths, thus the determination of the photometric redshifts becomes uncertain. To study the contribution of the high redshift dusty galaxies to the star formation rate density we need a way to select these objects based on their properties in the available far-infrared (FIR) datasets alone. The large FIR surveys, such as those conducted with the *Herschel* Space Observatory, provide a unique opportunity to construct a complete census of these distant objects using blind searches across wide areas. Since the dust Spectral Energy Distribution (SED) of a galaxy typically peaks around 100μm, we can use the colours of sources whose SED in SPIRE bands is rising from 250μm to 500μm (so-called **"FIR-risers"**). They are likely to lie at $z > 4$ unless their dust temperatures are substantially lower than is seen in local equivalents [Pope & Chary(2010)]. the shape of the counts could hint to the evolution of the observed population.

2 FIR-risers in the *Herschel* Virgo Cluster Survey (HeViCS)

Aiming to build statistically significant sample of dusty, high-redshift sources, we chose to study background galaxies in the Virgo Cluster. The *Herschel* Virgo Cluster Survey (HeViCS) is a fully-sampled, blind survey [Pappalardo et al.(2015)]. **The main advantages of HeViCS are a large field of view (55 square degrees), depth of its FIR observations, and deep, complementary optical data**. The selection of "FIR-rasers" is challenging due to high confusion in *Herschel* maps. A new method of source selection is performed (Donevski et al.2016, in prep): we used peak finding algorithm optimized for isolated sources (SUSSEXtractor) to obtain positions of SPIRE sources based on their "a-priori" position at 250μm. To de-blend the source fluxes we implemented new technique where source de-blending and SED fitting are combined in the same procedure, modelling each source SED as modified blackbody (Boone 2016, in prep.). We have built sample of 169 "FIR-risers" which satisfy following criteria: $S_{500} > S_{350} > S_{250}$, SNR$> 5$ and $S_{500} >$30mJy. Contamination of this selection by non-thermal sources is eliminated cross-matching existing radio catalogues (NVSS,FIRST and ALFAALFA). However, assuming the faintest level of these radio surveys ($\sim$1mJy at 1.4 GHz) we can reveal just local cluster members and known blazars, but not background galaxies.

To strengthen our analysis we complemented optical data from Next Generation Virgo Cluster Field Survey (NGVS)[Ferrarese et al.(2012)]. NGVS data reach the point source depth of 26 AB mag in r-band (S/N=5). There are two main scientific benefits of these deep data in our study: to search for a possible counterparts of SPIRE selected objects; and to reveal gravitationally lensed objects, because red sources we are seeing at these redshifts have prodigious luminosities, typically $\geq 10^{13} L_{\odot}$, indicating very high star-formation rate or lensing. Most of previous studies are limited to few "red" objects (e.g. [Daddi et al.(2009)]; [Riechers et al.(2013)]), and only allowed us to measure their total number above some flux density limit. Similarly as in [Asboth et al.(2016)], our selection is large enough to obtain the shape of differential number counts of these high-z candidates. We used [Béthermin et al.(2012)] empirical model to compare raw number of observed/predicted red galaxies satisfying our detection criteria. The observed number density of "FIR-risers" (3.07/deg^2) is almost five times larger then model prediction. Reason for existing discrepancy could be multiplicity of sources inside the SPIRE beam (e.g.[Scudder et al.(2016)]), or notably more lensing effects at high redshifts than expected. Understanding of these effects will give robust analysis of dusty star formation at high-z, and put the new and quantitative insights into models. Analysing NGVS maps, we divided our sample into three categories: (1) Category 1 (117 in total) - multiple optical sources are present close (r$\leq$5") to the catalogued SPIRE source entailing many potential

contributing objects per 250μm detection; (2) Category 2 (23 in total) - gravitationaly lensed candidates and/or counterparts; and (3) Category 3 (29 in total) - no optical associations close to the SPIRE detection.

All of Category 3 sources populate flux range between 30-48mJy at 500μm. Following our selection criteria, [Béthermin et al.(2012)] model anticipate that all such sources should lie at $z > 3$, while vast majority of these galaxies are not expected to be strongly lensed. Increasing the spectroscopically confirmed number of Category 3 galaxies is a necessary step towards to understanding of their contribution to the whole population. Such a confirmation could be done in submm looking for redshifted CO or [CII] lines.

3 Planned observations

The aim of this proposal is to measure the spectroscopic redshifts of the four FIR-risers falling in the Category 3 of objects (sources without NGVS detections inside the ∼18" beam). This category is important to understand prototypical case of sources that are extremely obscured by dust, and imply how many such galaxies at high-z might not be included in the optical star formation history. This will be the first milimeter scan of "FIR-risers" systematicaly selected according to lack of their optical associations. After shifting several well-known templates of local ULIRG's and scaling them to fit our SPIRE data, we concluded our galaxies should indeed be invisible in our NGVS images. **With this selection we therefore expect to discover new very high-z ($z \geq 4$), intrinsicaly bright dusty galaxies**. The line shape will let us measure the dynamical mass of the galaxies.

This is a pilot program and depending on the outcome of this project we might extend the redshift search to the rest of Category 3 targets. Knowledge of exact redshift distribution of these sources will allow us to construct the infrared luminosity functions at $z \geq 4$, infering the evolution of the star formation rate density at high-z. For our Category 2 sources, we will also consider follow-up observations with NOEMA to resolve the multiple images of brightest, lensed systems and the different components in case of mergers. High-resolution optical maps will be used for interpretation of highly confused sources from Category 1, as well as to identify optical counterparts without ambiguity.

4 Technical justification

According to a standard modified black-body fit to the SPIRE measurements these galaxies are most likely at $z \geq 3$. With its 16GHz bandwith spectral line receiver EMIR (Eight MIxer Receiver) will allow us to fully cover the E0 band (79 to 115 GHz) with only three different tunings. This corresponds to $1.04 < z < 8.7$ for CO lines with transitions from $J = 2 - 1$ to $7 - 6$. There is only a small gap for $1.9 < z < 2.0$ but our targets are expected to lie at higher redshifts. To estimate the CO line flux we convert the FIR luminosity derived from the modified black body fit at $z = 3$ to a CO luminosity using the FIR-CO correlation. We use the relationship found by [Dessauges-Zavadsky et al.(2015)] for lensed dusty galaxies, namely, $\log(L_{\rm FIR}) = 1.17 \times \log(L_{\rm CO}) + 0.28$. We then assume a line width of 300 km s^{-1} to derive the peak flux of the line. The results are summarized in the Table 1. These estimates are subject to large uncertainties mainly due to the unknown excitation of the high-J CO lines. In strong starbursts the CO spectral line energy distribution (SLED) could be rising up to high-Js but in more normal star forming galaxies the SLED could be flatter and decreasing at high Js [Dessauges-Zavadsky et al.(2015)]. However, we note that assuming $z = 3$ is conservative and for higher redshifts the estimated fluxes would be higher for a flat SLED (30% higher for $z = 4$).

The four galaxies have a CO peak flux $S_{\rm CO}$ ∼6-8 mJy. To detect the line with a S/N> 3 we therefore need to reach a sensitivity of 2 mJy noise RMS. Assuming 6 Jy per K this corresponds to a T_A^* RMS of 0.33 mK. A spectral resolution of 100 km s^{-1} is sufficient to identify a line and it maximizes the S/N. For a typical elevation of 45.0 degrees in winter conditions, an observing frequency of 110.0 GHz and a spectrometer resolution of 100.0 km/s, the time estimator tells us that we will need a telescope time of 8.2 hr to reach a sensitivity of 0.5 mK with average conditions (4.0 mm of pwv, Tsys 149.7 K[Ta*] mean per pixel).

We assume an average of 2 tunings per source to determine the redshift (two lines detected or one line detected and a possible ambiguity rejected). We therefore require $4 \times 2 \times (8.2 + 0.5) = 69.6$ hours of observing time in total (this includes the 30 min for each tuning).

5 Supporting material

References

[Asboth et al.(2016)] Asboth, V., Conley, A., Sayers, J., et al. 2016, arXiv:1601.02665

[Béthermin et al.(2012)] Béthermin, M., Daddi, E., Magdis, G., et al. 2012, ApJ Letter, 757, L23

[Bourne et al.(2014)] 2014MNRAS.444.1884B Bourne, N., Maddox, S. J., Dunne, L., et al. 2014, MNRAS, 444, 1884

[Carilli et al.(2013)] Carilli, C.L., Riechers, D., Walter, F., et al. 2013, ApJ, 763, 120

[Casey et al.(2014)] 2014PhR...541...45C Casey, C. M., Narayanan, D., & Cooray, A. 2014, , 541, 45

[Daddi et al.(2009)] 2009ApJ...694.1517D Daddi, E., Dannerbauer, H., Stern, D., et al. 2009, ApJ, 694, 1517

[Dessauges-Zavadsky et al.(2015)] Dessauges-Zavadsky, M., Zamojski, M., Schaerer, D., et al. 2015, A&A, 577, A50

[Dowell et al.(2014)] Dowell, C. D., Conley, A., Glenn, J., et al. 2014, ApJ, 780, 75

[Ferrarese et al.(2012)] 2012ApJS..200....4F Ferrarese, L., Côté, P., Cuillandre, J.-C., et al. 2012, ApJS, 200, 4

[Frayer et al.(2011)] Frayer, D. T., Harris, A. I., Baker, A. J., et al. 2011, ApJ Letter, 726, L22

[Nayyeri et al.(2016)] Nayyeri, H., Keele, M., Cooray, A., et al. 2016, arXiv:1601.03401

[Pappalardo et al.(2015)] Pappalardo, C., Bendo, G. J., Bianchi, S., et al. 2015, A&A, 573, A129

[Pope & Chary(2010)] 2010ApJ...715L.171P Pope, A., & Chary, R.-R. 2010, ApJ Letter, 715, L171

[Riechers et al.(2013)] 2013Natur.496..329R Riechers, D. A., Bradford, C. M., Clements, D. L., et al. 2013, Nature, 496, 329

[Rowan-Robinson et al.(2014)] Rowan-Robinson, M., Wang, L., Wardlow, J., et al. 2014, MNRAS, 445, 3848

[Scudder et al.(2016)] 2016MNRAS.460.1119S Scudder, J. M., Oliver, S., Hurley, P. D., et al. 2016, MNRAS, 460, 1119

[Wardlow et al.(2013)] Wardlow, J. L., Cooray, A., De Bernardis, F., et al. 2013, ApJ, 762, 59

[Weiß et al.(2009)] Weiß, A., Ivison, R. J., Downes, D., et al. 2009, ApJ Letter, 705, L45

[Zavala et al.(2015)] Zavala, J. A., Yun, M. S., Aretxaga, I., et al. 2015, MNRAS, 452, 1140

Table 1: Properties of our 500 μm risers from Category 3.

ID	S_{500} (1) [mJy]	$L_{\rm FIR}$ (2) [$10^{13} L_\odot$]	$L_{\rm CO}$ (3) [$10^{10} L_\odot$]	$S_{\rm CO}$ (4) [mJy]
1	48.08	1.08	8.00	8.13
2	43.04	0.85	6.46	6.56
3	44.48	0.98	7.37	7.49
4	47.18	1.04	7.74	7.86

(1) Flux at 500 μm; (2) FIR luminosity derived from the modified blackbody fit to the SPIRE fluxes with $z = 3$; (3) CO luminosity derived from $\log(L_{\rm FIR}) = 1.17 \times \log(L_{\rm CO}) + 0.28$ [Dessauges-Zavadsky et al.(2015)]; (4) CO line peak flux assuming at line width of 300 km s^{-1}.